Physical Properties of Wolf-Rayet Stars at Infra-red Wavelengths

Christopher K. Rosslowe

Department of Physics & Astronomy
The University of Sheffield

A dissertation submitted in candidature for the degree of Doctor of Philosophy at the University of Sheffield

September, 2015

Declaration

I declare that no part of this thesis has been accepted, or is currently being submitted, for any degree or diploma or certificate or any other qualification in this University or elsewhere.

This thesis is the result of my own work unless otherwise stated.

Acknowledgements

I would like to thank Paul for his superb guidance throughout my studies, for showing endless patience, providing me with fantastic opportunities, and always finding time to deal with any issue big or small.

I am grateful to have had the support of many friends, both those that I have made in the Astronomy group and more widely across the University. There are too many to mention individually, but you know who you are. We've shared plenty of laughs along the way and I hope our friendships will persist for many years to come. Special thanks go to Liam for showing kindness and understanding during the most difficult times, and Rik for being an exemplary flatmate for over 2 years.

Finally, a special thank you goes to my parents Jean and Alan for constantly believing in me. Their unconditional support has been the foundation of my success.

Summary

Wolf-Rayet (WR) stars represent the ultimate phase of evolution for the most massive stars in the Universe. Hot and luminous - they drive dense outflows, giving rise to rich emission-line spectra featuring nitrogen, carbon, and/or oxygen, as deeper layers of nuclear-processed material are revealed. This stripped nature implicates them as Type Ib/c supernovae progenitors, yet how the majority reach this state is unclear. The standard view of line-driven mass-loss producing WR stars is seceding to binary processes.

The goal of this thesis is to combine statistics for the Galactic WR population, with physical properties of specific objects, to assess how well these can be explained by stellar models - of single and multiple massive stars. This has been achieved through observations in the infra-red - an increasingly important wavelength regime, abetted by low interstellar extinction and rapidly advancing instrumentation.

I present a map of 356 Galactic WR stars, created using calibrated (1–8μm) absolute magnitudes by spectral subtype, and a refined near-IR classification scheme. I compare WR subtype variations with metallicity to population synthesis outputs, finding little evidence for ubiquitous fast stellar rotation. I produce a toy model of the total Galactic WR population using spatial information gleaned.

Oxygen abundances in 7 WC and WO stars are determined using *Herschel* PACS scans of [OIII] 88.36μm. These are combined with other recent analyses to argue for a reduction in the $^{12}\mathrm{C}(\alpha,\gamma)^{16}\mathrm{O}$ reaction rate in stellar models.

I present a spectroscopic analysis of the largest coeval population of WR stars in the Galaxy - that of the Westerlund 1 cluster. The youth of this cluster prohibits $\lesssim 40\,M_{\odot}$ progenitors, hence the physical properties derived - particularly low luminosity - suggest a binary origin for most.

Contents

List of Figures

List of Tables

Chapter 1

Introduction

Massive stars are incredibly rare yet vastly influential constituents of the cosmos. Throughout their short lives they are profuse sources of ionising (Lyman continuum) radiation, which together with their fast stellar winds and eventual supernova explosions, dominate the energy balance of the Interstellar Medium (ISM). These effects are most profound for massive stars in the Wolf-Rayet (WR) phase - the ultimate stage of evolution for initial mass $M_i \gtrsim 25\,M_\odot$ stars - which drive powerful outflows and radiate intensely in the far-UV. Our understanding of these objects has progressed remarkably since the first three examples were discovered in Cygnus by Wolf & Rayet (1867), but remains far from complete. In this chapter I will begin by emphasising the central role played by massive stars in a number of astrophysical contexts. The evolution of massive stars in isolation will then be outlined from a theoretical perspective, before a discussion of how binary effects may perturb stars from these courses. I will then present the observational studies of WR stars that have helped shape our current understanding of their evolutionary state, before presenting a summary of their physical parameters and the techniques typically used to measure these.

1.1 Universial importance of massive stars

1.1.1 General properties of massive stars

Stars born with an initial mass greater than $\sim 10\,M_\odot$ proceed through all stages of nuclear burning to form an inert iron-rich core, the sudden collapse of which signifies their death as supernovae. Such stars are considered 'massive'. They consume their nuclear fuel over a much shorter time that solar-type stars, which can be understood by

considering the mass-luminosity (M–L) relation for MS stars,

$$L \propto M^{\alpha}, \tag{1.1}$$

where the exponent, $\alpha \sim 3$, was predicted by Eddington's 'standard model' (Eddington, 1924). It was later confirmed observationally using the masses of binary stars (Kuiper, 1938), and shown to decrease from ~ 4.5 for solar-type stars to ~ 2.5 for massive stars. It follows that a star's MS lifetime (τ_{MS}) will be proportional to the amount of nuclear fuel available (M) divided by the rate of consumption of that nuclear fuel (represented by stellar energy output, L), such that

$$\tau_{MS} \propto \frac{M}{L} \propto M^{1-\alpha}. \tag{1.2}$$

Thus, the lifetimes of massive stars are vanishingly small on galactic timescales, resulting in a strong correlation between their number and the amount of gas available for star formation in a galaxy. The mass distribution of stars formed at any given time within a given volume, with masses in the interval $(M, M + dM)$ is observed to be solely a function of mass,

$$dN = \phi(M)dM. \tag{1.3}$$

The form of this so-called birth function was determined by Salpeter (1955),

$$\phi(M) \propto M^{-2.35}, \tag{1.4}$$

and still holds approximately to this day, with the power law becoming shallower for lower masses below $\sim 0.5\,M_{\odot}$ (Kroupa, 2001; Chabrier, 2003). Hence the rarity of massive stars at any one time in a galaxy is an inevitable consequence of their large masses.

Modern spectroscopic classification of stars derives from the two dimensional scheme of Morgan, Keenan & Kellman (1943). The relative strengths of absorption lines in stellar spectra are used to arrange them into a temperature sequence, labelled by letters OBAFGKM, with subdivisions 1–9 from hot (early) to cool (late). The second dimension uses roman numerals I–V to ascribe a 'luminosity class', judged by the width of absorption lines as a gauge of atmospheric pressure and surface gravity, and hence luminosity. MS/dwarf stars (class V) have high surface gravity ($\log(g) \simeq 4$) and lower luminosity for a given temperature, and vice-versa for supergiant stars (class I) ($\log(g) \simeq 3$–0, from O to M, in cgs units). For O-stars, only luminosity classes I, III and V are employed, and numbering extends as early as O2 (Walborn et al., 2002).

A $\sim$10 $M_{\odot}$ star will emerge on the main sequence as a B1.5V star. Hence, this spectral type approximately marks the boundary between massive and intermediate mass stars. As O and early-B stars begin to evolve away from the MS, their radii increase and temperatures drop, becoming what are known as Blue SuperGiant (BSG) stars (classes OBA I–III). Depending on the initial mass (see Section 1.2), this redward evolution may continue into a Yellow HyperGiant (YHG)/Red SuperGiant (RSG) phase (classes FG/KM I) where exceptionally large radii of $\log(r/R_{\odot}) \simeq 2$–3 are reached. On the blue side of the MS, stars with comparable luminosity to O-stars are observed with spectra dominated by broad emission lines of nitrogen, carbon and in some cases oxygen. These stars bear the name of their discoverers Wolf & Rayet (1867). Gamow (1943) was the first to suggest surface enrichment by the products of H-burning as an explanation of these unusual spectra, implying a post-MS nature. These WR stars are the focus of this thesis, and their classification and observed properties are discussed further in Section 1.3.

A unifying property of massive stars is the emission of radiation capable of ionising Hydrogen, i.e, $\lambda < 912$Å, at some point during their evolution, owing to their high temperatures. The rate of these so-called Lyman continuum photons ($N(Lyc)\ s^{-1}$) is a strong function of temperature, varying from $\log\big(N(Lyc)\big) \simeq 46$ for B2 stars ($T_{eff} = 21$ kK) to 49 for O3 ($T_{eff} = 45$ kK). As a consequence of this high luminosity in the UV regime, large bolometric corrections of 3–4.5 magnitudes must be applied to visual magnitudes of O-stars with T_{eff}= 30–50 kK.

During their tour of the upper H-R diagram, the high luminosity and temperature of massive stars conspire to drive outflows of material. Beals (1929) was the first to suggest stellar winds to explain the spectra of WR stars. Direct evidence in the form of P Cygni line profiles emerged following the first rocket-borne UV measurements of OB stars (Morton, 1967). It has become clear that an exchange of momentum between photons and atoms through spectral lines, particularly in the UV wavelength regime, provides the acceleration in hot star winds. Castor et al. (1975) developed a robust theoretical treatment for massive star winds, in which acceleration occurs up to a maximum velocity v_{∞}, and mass is removed from the star at a rate $\dot{M}$. The physics of mass-loss and stellar winds will be discussed further in Section 1.4.1. Wolf-Rayet stars are more extreme with regard to effective temperatures and stellar winds than their O-star predecessors. Some WR types reach temperatures high enough ($\sim$200 kK) to doubly ionise helium, $\lambda < 228$Å and generally they possess the highest wind momenta of any type of massive star, excluding outbursts from unstable LBV stars near the Eddington limit (e.g., η Carinae).

The dominant physical processes involved in massive star formation still remain highly uncertain (see Zinnecker & Yorke 2007 for a review). However, the idea that nearly all stars form in clusters (Lada & Lada, 2003) has been the general consensus for decades. Indeed, for massive stars locally, there exist few, if any, convincing candidates for massive star formation in isolation (de Wit et al., 2005; Gvaramadze et al., 2012). This is not to say that massive stars only form in extremely massive clusters, such as NGC 3603 or Wd1, where stellar densities exceed 10^4 stars pc^{-3}. Massive star formation has also been proven to occur in loose associations with stellar densities $\sim 10^2$ stars pc^{-3} (Wright et al., 2014).

It has long been known that the fraction of O-stars with relatively massive companions (within a factor of a few in mass) is high (Abt & Levy, 1978; Garmany et al., 1980). The most recent estimates of the O-star binary fraction *at birth* stand at $\sim$70% (Mason et al., 2009; Chini et al., 2012; Sana et al., 2013). Furthermore, massive binaries are frequently created by disk fragmentation in hydrodynamic simulations of accreting protostars (Krumholz et al., 2009; Kratter et al., 2010). With the confirmation of this high binary fraction has come the realisation that the *majority* of stars born as O-type will interact with a companion star before exploding as a supernova (Sana et al., 2012). The implications this has for stellar evolution are explored further in Section 1.2.2, with a focus on producing WR stars, but suffice it to say that the evolutionary paths followed by massive stars can be modified significantly.

There is now unequivocal proof that massive stars end their lives as core-collapse supernovae. The B3I progenitor of the peculiar Type IIb SN 1987A (Sonneborn et al., 1987) is the only one to have been confirmed spectroscopically. The detection of a significant neutrino flux preceding the supernova light was confirmation of the core-collapse process (Arnett et al., 1989). Since then, RSG stars have been identified at the locations of Type II-P (H-rich) Supernova (SN) in serendipitous pre-SN imaging (Smartt et al., 2009). Direct progenitor identifications have been restricted to type II SN; the progenitor(s) of H-free Type Ia/b/c SN remain unknown, but much can be learned form their explosion spectra. Type Ia SNe are thought to be thermonuclear explosions of white dwarf stars exceeding the Chandrasekhar limit, and are not discussed further here. Type Ib/c are characterised by the presence/absence of spectral features associated with helium. Heavily stripped massive stars, i.e., WR stars, have been mooted as progenitor candidates for decades (e.g., Begelman & Sarazin 1986, Gaskell et al. 1986). However, no progenitors consistent with WR stars have yet been identified in pre-images of Type Ib/c SN (Eldridge et al., 2013). What's more, the observed rate of these SN appears

too high for them to originate exclusively from single WR stars (Smith et al., 2011), if they originate from $M_i \gtrsim 25\,M_\odot$ stars, as expected from evolutionary models (Maeder & Meynet, 2000).

1.1.2 Feedback and chemical enrichment of the ISM

The gas between stars is a major baryonic component of galaxies, and exists in a variety of physical states at any one time. The ISM is too rarefied to achieve thermal equilibrium with the stellar radiation which pervades it, yet it is this radiation - particularly high energy photons from massive stars - that dictates the energy of the gas. Temperatures in the ISM vary from $\sim$10–20 K in dense molecular clouds ($\sim$1000 cm^{-3}) shielded from stellar UV radiation, to 10^{4-6}K in the diffuse ISM ($\sim$10–0.01 cm^{-3}) surrounding massive stars. Regions of the ISM where Lyman continuum photons have ionised hydrogen - and partially ionised other elements such as carbon, nitrogen and oxygen - are known as HII–regions. The most famous example is the Orion nebula, which is powered almost entirely by the 4 O-stars of the Trapezium cluster. The resultant emission nebulae display permitted lines of neutral hydrogen and neutral and ionised helium, as well as forbidden emission lines of C, N and O. The radii of HII-regions are well approximated by the Strömgren radius, R_S, given by

$$R_S = (\frac{3}{4\pi}\frac{S_\star}{n^2\beta})^{1/3}, \tag{1.5}$$

where n is the density of hydrogen atoms (nuclei), $S_\star$ is the ionising flux ($\lambda < 912$Å) and β the recombination rate.

The large bolometric luminosities of massive stars, $\log(L_{Bol}/L_\odot) = 5$–6, provide large radiative momenta, L_{Bol}/c. The momentum flux of stellar winds $\dot{M}/v_\infty$ amounts to $\sim$30% of this for typical O-stars (Conti et al., 2008); in terms of energy, the mechanical luminosity, $1/2\dot{M}v_\infty^2$, is only a few percent of the radiative luminosity. However, as stellar winds intensify during post-MS phases, particularly WR, mechanical luminosities may rise to comparable values, with significant implications for the kinematics of their circumstellar environments. In Figure 1.1 I show the evolution of radiative and mechanical luminosity for a model of a 60 $M_\odot$ star (Langer et al., 1994). The integrated kinetic energy transferred to the ISM over the course of a typical massive star lifetime (10^7 yr) is 10^{51} erg - comparable to that of a typical supernova explosion (Garcia-Segura et al. 1996a, Garcia-Segura et al. 1996b). Therefore, O-stars tend to evacuate their surroundings of gas, before evolving away from the MS. Weaver et al. (1977) provide a

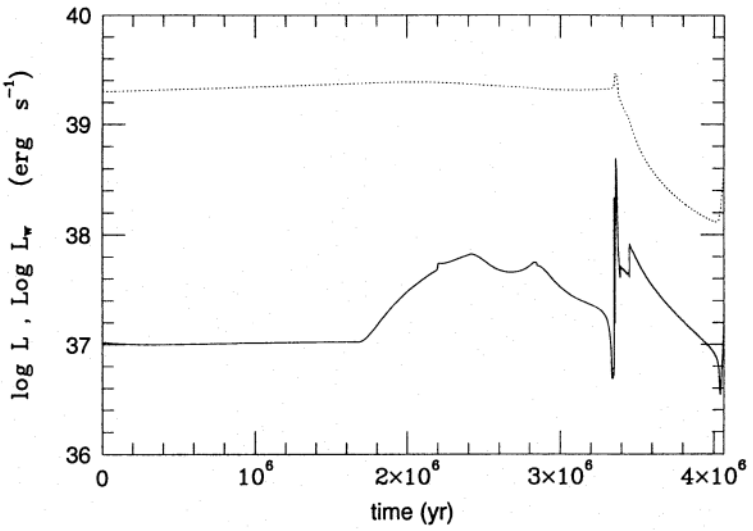

Figure 1.1: Evolution of mechanical (solid) and radiative luminosity (dotted) in a 60 $M_\odot$ stellar model (Langer et al., 1994). Taken from Garcia-Segura et al. (1996a).

mathematical description of these so-called wind-blown bubbles, and predict a structure - driven by gas pressure - consisting of four main parts: the cool expanding wind, hot shocked wind, cool swept-up ISM, and ambient ISM. Typical bubble radii are $\sim$10 pc, with expansion velocities $\sim$10 kms^{-3}.

Such wind blown bubbles around O-stars are often unobservable, as they cannot produce enough shock compression to sufficiently raise the density of swept-up material. This changes however when the star evolves into a supergiant phase. Higher mass ($\gtrsim 60\,M_\odot$) O-stars are expected to remain on the blue side of the H-R diagram, and experience episodic mass-loss as they approach their Eddington luminosities, resembling a LBV phase (Langer et al. 1994, see Section 1.2.1). Lower mass O-stars will become RSG stars, characterised by mass-loss rates $\sim 10^{-4} M_\odot$/yr (de Jager et al., 1988) several orders of magnitude higher than O-stars, ejected at much lower speeds ($\sim$ 10 kms^{-1}). As stars in both mass ranges enter a WR phase, wind speeds recover (10^3 kms^{-1}) and carry with them large amounts of mass ($\sim 10^{-5} M_\odot$/yr) (Nugis & Lamers, 2000). The complex interplay between WR star winds and slower moving material ejected during previous phases produces a plethora of nebula morphologies. Garcia-Segura et al. (1996b) present hydrodynamical simulations of a circumstellar environment of a 60 $M_\odot$ star, predicting visible nebula during late LBV and early WR times, containing $\sim 10\,M_\odot$ of material with CNO abundances consistent with nuclear burning (N enriched, C & O depleted). Similarly, Garcia-Segura et al. (1996a) predict a visible nebula with quite a different morphology for a post-RSG WR star, containing similar amounts of mass, albeit with

Figure 1.2: Image of the Crescent nebula, NGC 6888, taken with the Wide Field Camera on the INT. Colour composite of narrow-band filters selecting emission from H-α and OIII, coded in the image as red, green (25% H-α and 75% OIII) and blue. The central WR star (WR 136), can be seen as the bright point-source near the centre. Credit: Daniel Lopez.

lower N enrichment. Johnson & Hogg (1965) were the first to detect nebulae around WR stars, and many have been associated with a variety of massive stars since (e.g., Wachter et al. 2010). Most WR nebulae consist of ejected rather than swept-up material. Stock & Barlow (2010) estimate 5–6% of Galactic WR stars have such nebulae, a prominent example of which is NGC 6888, shown in Figure 1.2.

It is therefore clear that massive stars are capable of imparting enormous amounts of radiative and kinetic energy into the ISM, even before their death as SN. Massive stars are thought to be important sources of α-elements (CNO) in the early universe (Henry et al., 2000), and pollution of natal material by massive stars has been invoked to explain recently discovered multiple populations in globular clusters (Salaris & Cassisi, 2014). The role of WR stars as significant polluters of the ISM with nitrogen is supported by observations of N-enriched ejecta nebulae around some Galactic WR stars (Stock et al., 2011), and enhanced N and He abundances measured in star-forming galaxies showing WR features in their integrated spectra (Pagel et al., 1986; Brinchmann et al., 2008; López-Sánchez & Esteban, 2010). It is less clear whether evolved massive stars are dominant producers of C and O, as these are more challenging to measure in the gas

phase of ejecta nebulae (Stock et al., 2011) or by analysis of stellar photospheres (see Section 1.3.1). Competing sources of carbon are Type II SNe (Woosley & Weaver, 1995) and dredge-up in Asymptotic Giant Branch (AGB) stars (Frost & Lattanzio, 1996). From synthetic populations of high and intermediate-mass stars, Dray et al. (2003) conclude that massive stars *are* comparable to intermediate-mass stars in their C production at solar metallicity, whereas O enrichment is dominated by SNe. Efforts are underway to detect the chemical imprints of the first generation of massive stars (Population III) in low-mass stars with ages comparable to that of the Universe (e.g., Chiappini et al. 2011).

As well as enriching the ISM, energetic feedback from massive stars may potentially play a role in regulating star formation. Given the clustered nature of star formation, and apparent universality of the IMF, most clusters will contain at least a few reasonably massive stars. Most stars will therefore form in the vicinity of a massive star, and hence be subject to their strong feedback effects. HII-regions act as significant sources of energy for turbulence in Giant Molecular Clouds (GMCs) (Matzner, 2002), preventing further collapse of the cloud into protostars. O-stars are the principal agents of GMC dispersal (Williams & McKee, 1997), and it has been shown theoretically that radiation pressure from massive stars can evacuate young clusters of natal gas (Boily & Kroupa, 2003; Dale et al., 2005), bringing accretion onto protostars to a halt. Not all massive star feedback is necessarily negative. Momentum injected into the ISM through stellar winds and SN explosions is a key component of the proposed 'collect and collapse' scenario (Elmegreen, 1998), in which further massive star formation is induced in swept-up material. Recent evidence for triggered star formation in the Milky Way was provided by the Milky Way Project (Kendrew et al., 2012).

Any process which affects star formation will also have consequences for galaxy formation and evolution, as galaxies build up their baryonic mass by converting gas into stars. The Kennicutt-Schmidt (KS) relation relates the surface gas density of a Galaxy to its star formation rate density (Kennicutt, 1998), and implies that star formation occurs on timescales of $\sim$50 dynamical times. However, it has been shown that without stellar feedback, gas inside galaxies is predicted to cool too efficiently, and forms stars on shorter timescales than this (Bournaud et al., 2010; Hopkins et al., 2011; Tasker, 2011; Dobbs et al., 2011). Consequently, in cosmological simulations, star formation peaks at higher redshifts where galaxies are gas-rich (e.g., Springel & Hernquist 2003), and modern-day stellar masses become higher than observed (White & Frenk, 1991; Katz et al., 1996; Cole et al., 2000), providing especially poor fits to the low end of the stellar mass function. Furthermore, observational evidence of galactic-scale gaseous outflows

in starburst galaxies is abundant (Heckman et al., 2000; Martin, 2005; Veilleux et al., 2005), showing that massive stars play a key role in regulating star formation, both through altering the physical conditions and outright quantity of gas available. Hopkins et al. (2014) show that it is necessary to account for massive star feedback in all forms (radiation pressure, wind momentum, SNe) if the KS relation and galactic winds are to be reproduced in simulations of galaxies over a broad range in halo mass. Another observational canon of galaxy evolution, the Tully-Fischer relation, is also better predicted when SNe feedback is accounted for (de Rossi et al., 2010).

1.1.3 Massive stars as cosmic probes

Virtually all Star Formation Rate (SFR) tracers are fundamentally tracers of massive star formation, as these dominate the radiated energy of a stellar population. Extensive reviews of SFR diagnostics are given by Kennicutt (1998) and Kennicutt & Evans (2012), and their use to determine the evolution of star formation with redshift (Madau & Dickinson, 2014). Different observational tracers are sensitive to different stellar mass ranges, hence they respond differently as a function of age. Observational tracers of photoionised regions are sensitive to the shortest-lived OB-stars and WR stars with ages < 10 Myr, whereas the near to far-UV continuum is produced by stars over a broader mass range with longer lifetimes (20–100 Myr). An understanding of the underlying massive stellar population is therefore crucial for the correct interpretation of the majority of SFR indicators, with crucial parameters including ionising luminosities and the lifetimes of the most influential evolutionary phases.

The UV luminosity of a galaxy is the most direct measure of the instantaneous SFR density (e.g., Schiminovich et al. 2005). The far-UV luminosity, L_{FUV}, around (rest-frame) 1500 Å is commonly used as a diagnostic. Absorption by the neutral Inter-Galactic Medium (IGM) is too severe shortward of this. An advantage of this method is that this portion of a galaxy's SED is shifted to optical wavelengths at intermediate redshift ($z > 1.4$), allowing ground-based observation. The conversion between L_{FUV} and SFR is not straightforward. It is in principle possible to predict the UV output of a stellar population and its evolution with age (e.g., Schaerer & Vacca 1998), however these predictions are sensitive to the assumed IMF, and the specific models of stellar evolution used, particularly for the most massive stars. In Figure 1.3 I show an example of the predicted far-UV luminosity for populations of single-stars at $Z_\odot$ and $^1/_{10}Z_\odot$, showing the dominance of young massive stars. Populations of single-stars are often assumed, yet binary interactions can significantly alter the integrated radiative output of a population

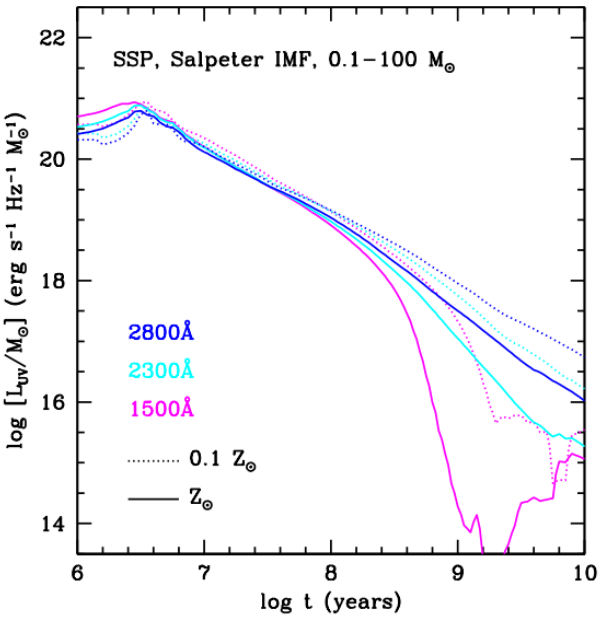

Figure 1.3: The evolution of luminosity at three different UV wavelengths in a single stellar population, at metallicities $Z_\odot$ (solid) and $0.1\,Z_\odot$ (dotted). Adapted from Madau & Dickinson (2014).

of massive stars (Eldridge, 2009). The most significant drawback of UV methods is dust extinction, as UV wavelengths are heavily attenuated by even modest column densities. Calzetti (2001) review the effects of dust extinction on UV-derived SFRs.

To supplement direct UV-based SFR indicators, various indirect measures exist, taking advantage of the effects massive stars have on their surroundings. Dust that absorbs UV photons re-radiates the energy at mid and far-IR wavelengths, and the IR ($\sim$10–300 μm) luminosity of a galaxy is generally considered to be directly proportional to this absorbed energy from star formation (Kennicutt, 1998). The far-IR luminosity of nearby late-type (star-forming) galaxies has shown consistency with other SFR indicators (Lonsdale & Helou, 1985; Sauvage & Thuan, 1992; Buat & Xu, 1996), but in quiescent galaxies it is thought lower-mass stars are the primary dust heaters, resulting in overestimates of SFR. Observations of both rest-frame far-UV and far-IR luminosities should therefore measure all energy from star formation in a galaxy. This is possible for nearby galaxies, whose resolvable stellar contents may provide essential calibrations between UV and IR methods (e.g., Doran et al. 2013). However, while optical (and near-IR) observations can select 'normal' star-forming galaxies to increasingly high redshift (z>4, Bouwens et al. 2015), the most sensitive far-IR observatories such as *Herschel* are

limited to extreme objects above $z \simeq 2$ (Madau & Dickinson, 2014).

Recombination lines such as H-α, Ly-α, and Pa-α are commonly used (see Moustakas et al. 2006 for a comparison), as these trace photoionisation of the ISM caused by the UV radiation from young massive stars. In some galaxies, an Active Galactic Nucleus (AGN) may contribute to these lines, corrupting SFR measurements. However, the harder ionising source in such galaxies can be readily diagnosed using emission lines of other elements (O & N) (Baldwin et al., 1981).

Finally, the comoving volumetric core-collapse supernova (ccSN) rate - signalling the death rate of massive stars - also contains information about the SFR. Observationally, this has been estimated to $z \simeq 1$ (Dahlen et al., 2012), showing good agreement with the other tracers discussed. This method does, however, require assumptions about the maximum stellar mass producing ccSN, which remains uncertain (Heger et al., 2003). Long Gamma Ray Bursts (GRBs) have been associated with some type Ic SNe at low redshift (e.g., Galama et al. 1998), and have been detected to very high redshifts ($z \sim 9$, Cucchiara et al. 2011). Porciani & Madau (2001) argue that the long-GRB rate may be used as an independent measure of SFR in the early universe, but their association with massive stars is metallicity-dependent and difficult to model (see Woosley & Bloom 2006 for a review). They have also been shown to be biased SFR tracers, occurring more frequently per unit stellar mass at earlier times (Kistler et al., 2009; Robertson & Ellis, 2012).

As well as being central to SFR diagnostics, massive stars in large numbers can have a profound effect on integrated galaxy spectra. Galaxies undergoing extraordinary star-formation ($\sim$100 $M_{\odot}\mathrm{yr}^{-1}$), known as 'starburst' galaxies, have spectra featuring nebular emission lines from gas photoionised by massive stars. Such galaxies were first associated with higher than average star formation rates by Searle & Sargent (1972). Nearby starburst galaxies are generally observed as either blue and irregular, or very IR luminous resulting from a high dust content. The latter are often referred to as (Ultra) Luminous Infra-Red Galaxys (LIRGs).

Prior to the previous two decades, few galaxies of any kind were known at redshifts, $z > 1$. This changed with a technique pioneered by Steidel & Hamilton (1993), utilising the sharp flux discontinuity (or 'break') at the Lyman limit (912 Å), to detect large samples of star-forming galaxies at $z \sim 2$–3, for which this 'Lyman-break' is shifted to optical wavelengths where adjacent filters may be used to measure a colour excess. Far-UV emission from hot stars emphasises this flux discontinuity, as it is absorbed by Hydrogen both in the atmospheres of some hot stars and the ISM, at wavelengths < 912 Å.

Lyman Break Galaxies (LBGs) have become a target of abundance measurements (Pettini, 2004), predominantly by two approaches: direct observation of stellar UV features, or analysis of nebular lines. Rix et al. (2004) showed that the integrated rest-frame UVspectra of Lyman Break Galaxy (LBG)s could be used to measure metallicity to $z{\sim}3$, by comparing the observed photospheric and wind lines of OB-stars to those in synthetic spectra. Heckman et al. (1998) also show that for nearby starburst galaxies, the equivalent widths of some UV wind lines are proportional to O/H - as a result of stronger stellar winds at higher metallicity. Such methods are of course subject to our understanding of massive star evolution, and the metallicity-dependence of stellar winds (see Section 1.4.1). Indeed, some spectral features in the bright rest-frame UV spectra of gravitationally lensed systems cannot as yet be reproduced by population spectral synthesis (e.g., Quider et al. 2009). Despite the potential of rest-frame UV diagnostics, well-established nebular diagnostics using H Balmer lines, such as the R_{23} (McGaugh, 1991) and N2 (Pettini & Pagel, 2004) methods, have tended to prevail. For example, Pettini et al. (2001) detect such nebular diagnostic in near-IR spectra of LBGs at $z \sim 3$, finding consistency between star formation rates derived using Hβ and L_{FUV}, and subsolar oxygen abundances that seem to exceed other structures at similar redshifts (e.g., damped Lyα systems, Wolfe et al. 2005). Such measurements provide constraints on nucleosynthesis in massive stars when the Universe was only $\sim 15\%$ of its current age. However, limited atmospheric transmission in the near-IR makes it challenging to obtain nebular diagnostics for LBGs at such redshifts, making rest-frame UV diagnostics more appealing. Any improvements in our understanding of massive star evolution, particularly metallicity-dependent effects, will therefore aid this exciting pursuit.

1.2 Evolution of massive stars

The primary goal of this thesis, broadly, is to use both statistically large samples and detailed observations of Galactic WR stars to test current theoretical models of massive star evolution. In this section I summarise this theoretical picture, from core processes to predicted surface properties. I will highlight the theoretical uncertainties which render our understanding incomplete, and require further observational constraints. The observational characteristics of WR stars are deferred to Section 1.3. For now it is sufficient to regard a WR star as an evolved massive star stripped by mass-loss, such that nuclear processed material appears at the surface.

1.2.1 Single-star evolution

Most models of stellar evolution agree on a lower initial mass limit of $\sim 25\,M_{\odot}$ for single stars entering a WR phase (e.g., Meynet & Maeder 2005). I will therefore focus on the evolution of stars above this mass, which have an O spectral type on the main sequence.

Core evolution

The mass-luminosity relation (Equation 1.1) for stars in this mass regime is shallower than for lower masses ($\alpha \sim 1.75$, Conti et al. 2008). Therefore, there is a smaller dispersion of lifetimes amongst $>25\,M_{\odot}$ stars, all less than 10 Myr, with approximately 90% of this spent on the hydrogen-burning MS. During this time, core temperatures are sufficiently high that hydrogen burning proceeds through the CNO cycle, whereby these elements act as catalysts in transforming 4 protons into an alpha particle by the following reaction chains:

CN

$$^{12}\mathrm{C} + {}^{1}\mathrm{H} \rightarrow {}^{13}\mathrm{N} + \gamma$$
$$^{13}\mathrm{C} \rightarrow {}^{13}\mathrm{C} + e^{+} + \mu_{e}$$
$$^{13}\mathrm{C} + {}^{1}\mathrm{H} \rightarrow {}^{14}\mathrm{N} + \gamma$$
$$^{14}\mathrm{N} + {}^{1}\mathrm{H} \rightarrow {}^{15}\mathrm{O} + \gamma$$
$$^{15}\mathrm{O} \rightarrow {}^{15}\mathrm{N} + e^{+} + \mu_{e}$$
$$^{15}\mathrm{N} + {}^{1}\mathrm{H} \rightarrow {}^{12}\mathrm{C} + {}^{4}\mathrm{He}$$

ON

$$^{15}\mathrm{N} + {}^{1}\mathrm{H} \rightarrow {}^{16}\mathrm{O} + \gamma$$
$$^{16}\mathrm{O} + {}^{1}\mathrm{H} \rightarrow {}^{17}\mathrm{F} + \gamma$$
$$^{17}\mathrm{F} \rightarrow {}^{17}\mathrm{O} + e^{+} + \mu_{e}$$
$$^{17}\mathrm{O} + {}^{1}\mathrm{H} \rightarrow {}^{14}\mathrm{N} + {}^{4}\mathrm{He}$$

The energy generation rate of the CNO cycle has a much steeper temperature dependence ($q_{CNO} \propto \rho T^{16}$) than that of the p-p chain - the H-burning mechanism in lower

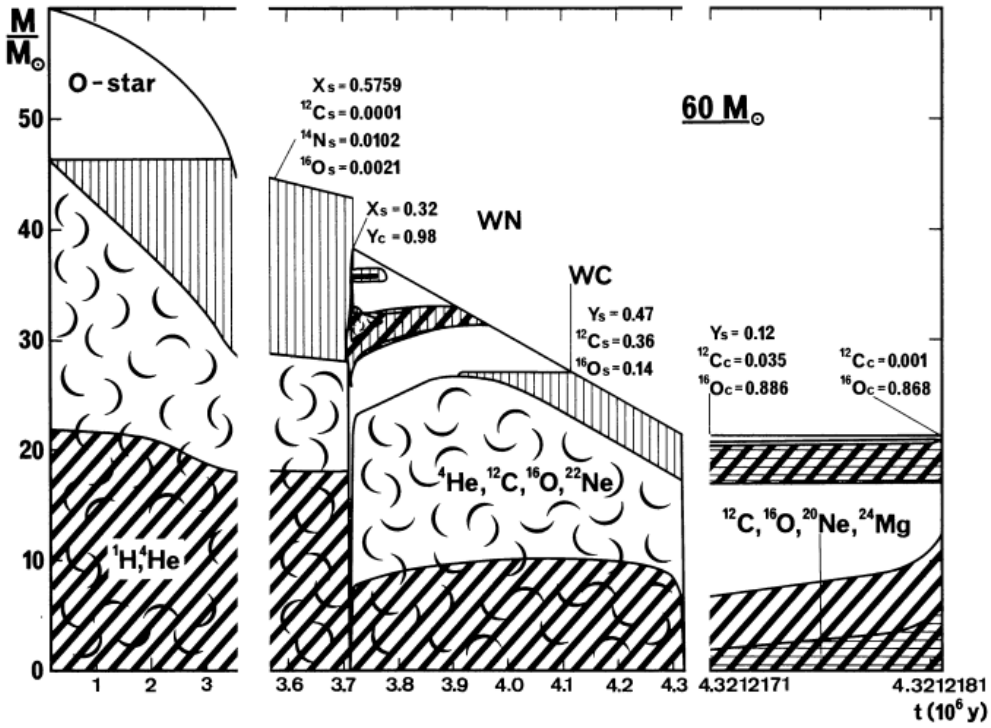

Figure 1.4: Kippenhahn diagram for a 60 $M_\odot$ star, showing internal structure up until central C-exhaustion. Cloudy regions indicate convective zones, and heavy diagonals indicate zones of intense nuclear energy generation ($> 10^3$ erg g^{-1}s^{-1}). Vertically hatched regions are zones of variable H and He contents, and the horizontally hatched regions are zones of variable ^{12}C, ^{16}O, and ^{20}Ne contents. The observable status of the star is indicated. The total mass of the star decreases with time due to mass-loss via a stellar wind. Abundances are indicated at various stages, where subscript "c" denotes core, and "s" surface. Taken from Maeder & Meynet (1987).

(solar-type) stars ($q_{p-p} \propto \rho T^4$). Such steep temperature gradients in massive stellar cores make them unstable to convection. Thermonuclear reactions therefore occur in large convective cores, involving 60–80% of the mass of the star for initial masses 25–100 $M_\odot$ (Maeder & Meynet, 1987).

The extent of this convective core is frequently defined by the Schwarzchild radius, R_S, where the adiabatic gradient equals the radiative gradient. However, the velocity of convective elements may cause an extention beyond this boundary, or 'overshoot'. The extent of convective overshooting, parameterised as αR_S in stellar evolution models, can encompass an extra $\sim 10\,\%$ (5%) by mass at the beginning of H (He) burning (Maeder & Meynet, 1987). This has the effect of mixing more nuclear fuel into the core, lengthening the H-burning phase. In Figure 1.4 I show the evolution of internal structure for a 60 $M_\odot$ star, showing convective zones and regions of nuclear energy production.

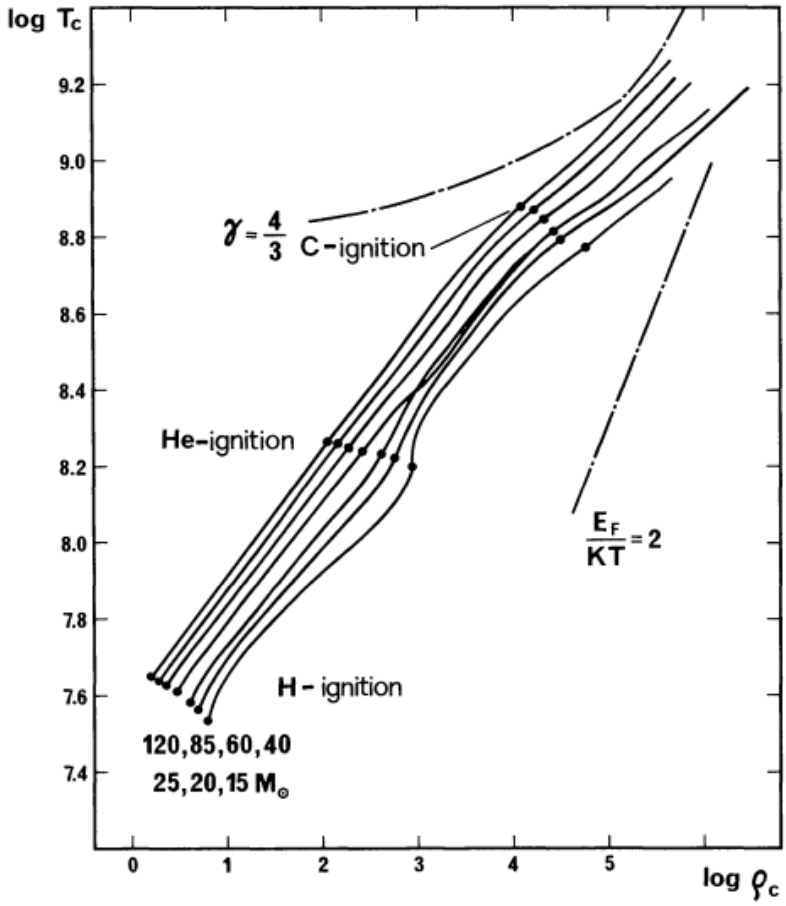

Figure 1.5: Evolution of stellar models with initial mass 15, 20, 25, 40, 60, 85, and 120 $M_\odot$ in the $\log(T_c)$ vs $\log(\rho_c)$ plane (central temperature vs central density). Stars evolve from bottom left to top right. For a given ρ_c, before He-ignition, T_c increases monotonically with initial mass. Taken from Maeder & Meynet (1987).

Convective motions maintain a uniform chemical composition throughout the core, (Figure 1.4), mixing fresh hydrogen into the centre where energy generation is strongly concentrated. As a result, the exhaustion of hydrogen in the core occurs abruptly. Core hydrogen exhaustion sees nuclear energy production in the core diminish, causing a decrease in the temperature gradient, and a temporary halt to convection. Schönberg & Chandrasekhar (1942) showed there is a critical mass for an isothermal sphere of ideal gas, above which internal pressure cannot sustain the weight of the overlying envelope. For stars of initial mass $\gtrsim 2M_{\odot}$, H-depleted cores exceed this, hence further collapse is inevitable. Indeed, from hydrogen burning onwards, core temperatures and densities increase essentially monotonically, with an approximate relationship, $\rho_c \propto T_c^3$, as expected for the non-adiabatic contraction of an ideal gas in successive hydrostatic equilibria. In Figure 1.5 I show the evolution of core temperature and density with time for various initial masses at solar composition. Gravitational energy released by this contraction heats material surrounding the He core, igniting a shell of H-burning, at which point the outer layers respond by expanding.

Once central temperatures exceed $\sim 10^8$ K, helium nuclei (alpha particles) are sufficiently energetic to tunnel through their coulomb barriers and fuse to form ^{8}Be. This nucleus is very unstable to fission, decaying on timescales of 10^{-16}s, however this is longer than the mean transit time of two alpha particles in the core (10^{-19}s), such that a stable ^{12}C nucleus may be formed:

$$^4\mathrm{He} + {}^4\mathrm{He} \rightarrow {}^8\mathrm{Be},$$
$$^8\mathrm{Be} + {}^4\mathrm{He} \rightarrow {}^{12}\mathrm{C} + \gamma.$$

This process, seeing the combination of three alpha particles to form ^{12}C, is know as triple α (3-α). Once sufficient carbon nuclei have accumulated, further α captures may produce oxygen,

$$^{12}\mathrm{C} + {}^4\mathrm{He} \rightarrow {}^{16}\mathrm{O} + \gamma$$

Competition between these processes producing carbon and oxygen dictates the C/O ratio in the core when He is exhausted. The rate of $^{12}\mathrm{C}(\alpha,\gamma)^{16}\mathrm{O}$ (above) is uncertain, and has been subject to many revisions (Kettner et al. 1982; Weaver & Woosley 1993; Kunz et al. 2002, see also Section 4.1. Dearborn & Blake (1979) note that the C/O ratio also depends on the central temperature during He-burning, which is correlated with initial core (stellar) mass (Figure 1.5). Overshooting acts to increase the core size and mass, and as expected one finds lower (core) C/O ratios in models with overshooting

(Maeder & Meynet, 1987) than without (Maeder, 1981).

Helium burning by these reactions dominates energy production for the last $\sim 10\%$ of the stellar lifetime, with further burning stages occurring fleetingly and in rapid succession. Further α capture as a means to create elements heavier than oxygen is ineffective. Instead, carbon burning ignites at temperatures $> 5 \times 10^8$ K. Neon produced by carbon burning captures α particles at temperatures $> 1.5 \times 10^9$ K, followed by oxygen burning at $> 2 \times 10^9$ K.

Energy removal from the core by neutrinos becomes significant during carbon burning. The nuclear energy source must compensate for this, as well as the stellar luminosity. With the fusion of heavier elements releasing less energy per unit mass than lighter elements, nuclear fuel is consumed rapidly. The time between central He exhaustion and C exhaustion is only $\sim$1% of the MS lifetime, or a few thousand years. The light particles (p and α particles) produced by C and O burning are quickly absorbed by other nuclei, as temperatures are extremely high and coulomb barriers relatively low. Thus, secondary reactions form many different isotopes. As the oxygen abundance builds, photodisintegration of nuclei competes with α captures to form a state of nuclear statistical equilibrium, e.g., $^{16}\mathrm{O} + \mathrm{He} \rightleftharpoons^{20} \mathrm{Ne} + \gamma$. Heavy nuclei disintegrate into light particles, which in turn are absorbed by other heavy nuclei. The equilibrium is not perfect, and a leakage occurs to stable Fe-group nuclei, eventually resulting in an iron-nickel core. This core is surrounded by burning shells, formed in an analogous way to the first H-burning shell, of successively lighter elements - Si, O, Ne, C, He - towards the stellar surface.

As the inert Fe core contracts, the electron gas becomes degenerate, and several nuclear processes conspire to remove the main pressure sources, accelerating collapse. Heavy nuclei capture electrons, and as the temperature rises, photons become energetic enough to disintegrate Fe nuclei,

$$^{56}\mathrm{Fe} \rightarrow \ 13\,^4\mathrm{He} + 4\mathrm{n},$$

which is highly endothermic. Further temperature increases see α particles disintegrated into protons and neutrons, which is again endothermic. Densities eventually become high enough for free protons to capture electrons, forming neutrons, and releasing vast quantities of neutrinos. A neutron star is produced if the ensuing neutron degeneracy pressure is sufficient to halt further collapse, otherwise a black hole is formed.

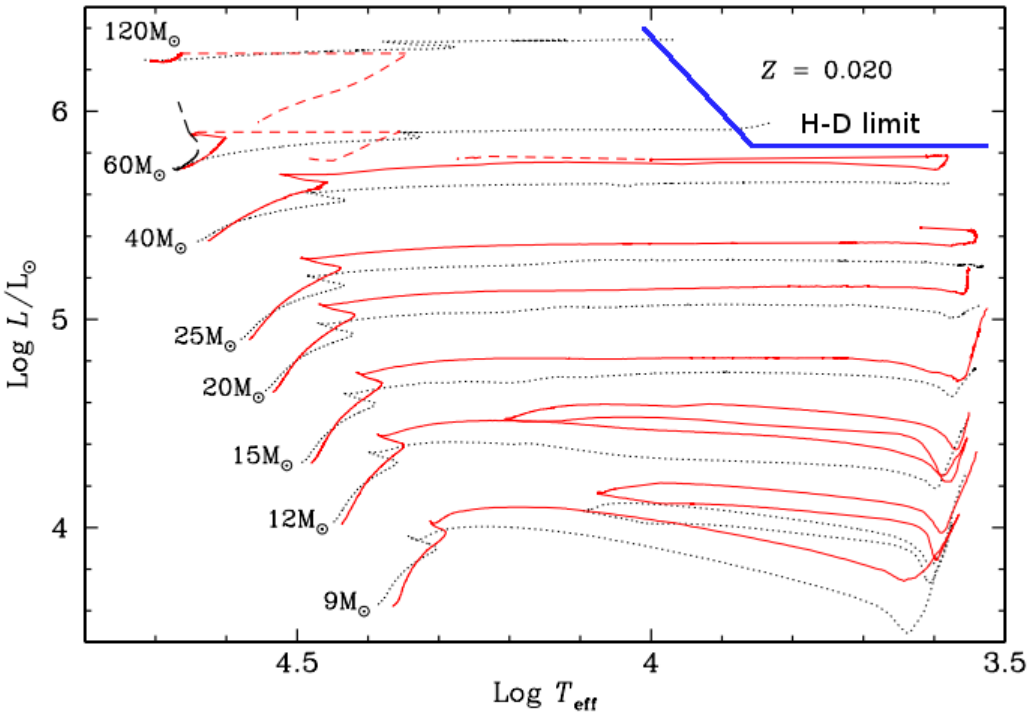

Figure 1.6: Hertzsprung-Russell (H-R) diagram showing the evolution of rotating ($300\,\mathrm{kms}^{-1}$) and non-rotating stars at solar metallicity ($Z = 0.02$), as solid (red) and dotted (black) lines respectively. Dashed portions of the tracks correspond to WR phases, although their full bluewards evolution is not shown, for clarity. The solid black line shows the evolution of a $60\,M_{\odot}$ star with very fast rotation ($500\,\mathrm{kms}^{-1}$), which essentially follows chemically homogeneous evolution and stays blue. The solid blue line represents the Humphrey-Davidson limit. Adapted from Meynet & Maeder (2000).

Massive stars in the H-R diagram - red vs blue

The first 1D stellar evolution models to account for mass-loss via stellar winds demonstrated a profound effect on the paths followed by massive stars in the H-R diagram (Chiosi et al., 1978; Stothers & Chin, 1979; Maeder, 1981). For a given initial mass, the He-C-O core produced by constant-mass and mass-losing stars are very similar (cf. Chiosi & Maeder 1986). Hence, mass-loss does not significantly alter the picture of core evolution outlined above. It can however shift the initial mass boundary between stars that evolve redward to become RSGs after core H exhaustion, thus affecting the average predicted duration of RSG/YHG and BSG/WR star phases.

In the classical picture of red giant/supergiant formation, core contraction following H depletion is accompanied by envelope expansion on a thermal timescale. This can be understood on the basis of the virial theorem. If core contraction occurs quasi-statically, i.e., over a time much longer than the dynamical time, virial equilibrium can be assumed to hold. Furthermore, if the total energy of the star changes slowly (thermal equilibrium is maintained), thermal as well as gravitational energy is conserved. Therefore, contraction and heating of the core must result in expansion and cooling of the envelope. This takes a star quickly to the red side of the H-R diagram, where evolution continues on a slower nuclear timescale. The precise physical processes driving envelope expansion are still a matter of debate (see Renzini 1984).

In Figure 1.6 I show the anticipated evolution of stars with various initial masses at solar metallicity, with and without stellar rotation, according to the models of Meynet & Maeder (2003). A discussion of the effects of rotation is deferred to the following section. It can be seen that for masses greater than $\sim$50–60 $M_{\odot}$, redward evolution is prevented. This is consistent with the observed absence of red supergiants with bolometric luminosity exceeding, $\log(L_{bol}/L_{\odot}) \simeq 5.8$ (Fig. 1.6, Humphreys & Davidson 1979). Stripping of the hydrogen envelope by mass-loss is the dominant reason for these stars remaining blue. The helium cores of these stars occupy a larger fraction of the total mass than in lower mass stars, meaning the convective envelopes that develop are relatively chemically homogenious. As H is the dominant source of opacity in these envelopes, its reduced abundance limits radius expansion and also favours blueward evolution (Stothers & Chin, 1976; Maeder et al., 1980). Further mass-loss stripping in these stars as they evolve blueward will successively expose layers of CNO processed material and the products of partial helium burning, resulting in WN and WC Wolf-Rayet stars respectively.

Langer et al. (1994) further investigate stellar evolution is this mass regime by mod-

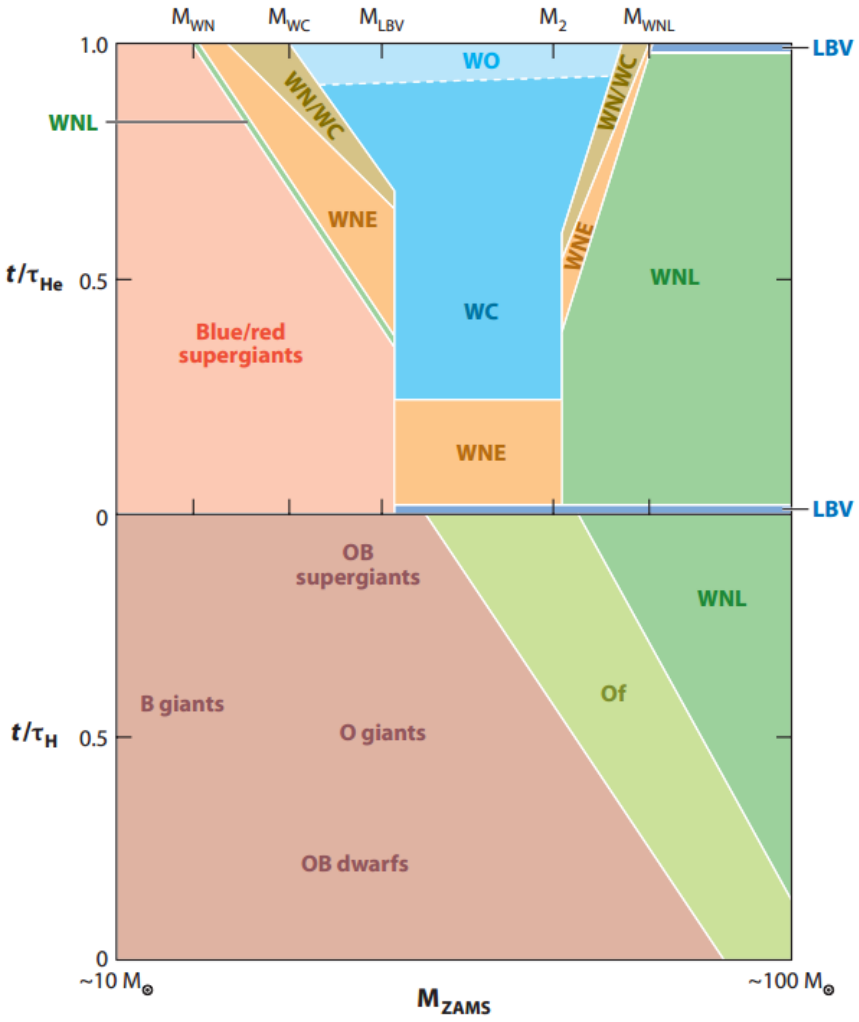

Figure 1.7: Schematic (spectroscopic) phase diagram for the MS (lower half) and post-MS (upper half) evolution of massive stars at solar metallicity. A star of a given mass on the zero-age MS (bottom axis) evolves vertically upwards in this diagram. The vertical path through each coloured region measures the fraction of core hydrogen or helium burning time spent in the corresponding phase. Taken from Langer (2012).

elling the evolution of a 60 $M_{\odot}$ star, including pulsational instabilities during the BSG phase, which enhance the average mass-loss rate. They associate such behaviour with that observed in LBV stars (Conti, 1984), previously known as 'Hubble-Sandage' variables (Hubble & Sandage, 1953). Briefly, these stars are observed to undergo so-called 'S Doradus' cycles, varying in T_{eff} at approximately constant L_{Bol} (see Humphreys & Davidson 1994). LBV winds exhibit large mass-loss rates, capable of removing H envelopes in $\sim 10^4$yr. A subset have been observed to undergo violent eruptions, such as η Car, evidenced by a $\sim 10\,M_{\odot}$ ejecta nebula (Smith, 2006). If such a phase is prevalent for stars above the RSG mass limit, it could be vital in providing the mass-loss required to create WR stars. Smith & Owocki (2006) argue for the necessity of an LBV phase, as O-star winds are insufficient to completely remove H-rich layers.

In the mass range 25–40 $M_{\odot}$, smaller He cores and less extended convective zones favour redward evolution, and stars quickly become RSGs after core H exhaustion. These stars are predicted to return to the blue side of the H-R diagram to become BSG and WR stars if/when stellar mass-loss causes the He core to occupy some critical fraction, q_c, of the total stellar mass (Stothers & Chin 1979; Chiosi et al. 1978, q_c= 0.67 for 60 $M_{\odot}$, and 0.77 for 30 $M_{\odot}$). Hence, the fraction of the helium burning lifetime (t_{He}) spent as a WR star as opposed to RSG strongly increases with initial mass and pre-WR mass-loss, since $t_{He} \simeq (t_{WR} + t_{RSG})$. Single stars of mass $\lesssim 25\,M_{\odot}$ are incapable of removing their H-rich envelopes before the end of He burning (Meynet & Maeder, 2005; Ekström et al., 2012), and therefore never enter a WR phase.

The following approximate evolutionary scenarios are borne out by evolutionary models for non-rotating single stars:

$M_i < 25\,M_{\odot}$
O-star → BSG → RSG

$25\,M_{\odot} < M_i < 60\,M_{\odot}$
O-star → BSG → RSG/YHG → WN (H-poor) → WC

$M_i > 60\,M_{\odot}$
O-star → WN (H-rich) → BSG/LBV → WN (H-poor) → WC/WO

In evolutionary models, WN and WC stars are usually defined by their surface properties, as model outputs are not routinely coupled to stellar atmosphere calculations (although see Groh et al. 2014). Stars are typically categorised as WNL when $X_H < 0.3$–0.4, WNE when $X_H < 10^{-5}$, and WC when $X_C > X_N$. Transition Type Wolf-Rayet (WN/C) stars are defined as having $0.1 < X_C/X_N < 0.9$ (Meynet & Maeder, 2005). These defini-

Table 1.1: Lifetimes in Myr for various core (H and He) burning phases, and surface appearances. I have assumed $t_{He} = (t_{WR} + t_{RSG})$, and hence neglected a possible LBV phase in $M > 60\,M_{\odot}$ stars. Initial equatorial rotational velocity, v_{ini}, is in kms^{-1}, and masses M in $M_{\odot}$. Data from (Meynet & Maeder, 2005).

M	v_{ini}	t_H	t_{He}	$t_{RSG/YHG}$	t_{WR}	t_{WN}	t_{WC}
120	0	2.74	0.36	0.00	0.68	0.38	0.30
	300	3.14	0.41	0.00	1.39	1.10	0.29
85	0	3.09	0.37	0.00	0.48	0.21	0.27
	300	3.69	0.40	0.00	1.41	1.20	0.21
60	0	3.62	0.37	0.00	0.37	0.17	0.22
	300	4.30	0.37	0.00	0.75	0.51	0.24
40	0	4.56	0.48	0.41	0.07	0.07	0.00
	300	5.54	0.42	0.05	0.37	0.18	0.19
25	0	6.59	0.69	0.69	0.00	0.00	0.00
	300	8.07	0.63	0.42	0.21	0.21	0.00

tions apply for the rest of this discussion.

In Figure 1.7 I show a schematic of massive star evolution as a function of initial stellar mass, at solar metallicity, based on theoretical and observational evidence (Langer, 2012). In this diagram, the upper limit on RSG progenitor masses can be seen, with more massive stars experiencing LBV and H-rich (WNL) WR phases. I note that H-free WR stars are predicted to descend from both RSG and LBV/WNL stars, and have a wider range in initial mass - only overlapping slightly with WNL stars.

In Table 1.1 I show the predicted lifetimes for each evolutionary phase for a range of masses. The total duration of the WR phase is predominantly controlled by mass-loss. With faster stripping, CNO processed material is revealed at an earlier stage of evolution, prolonging the observed WR phase. Up until this point, mass-loss has little effect on the core evolution, but further mass-loss can affect the relative duration of WN and WC phases, i.e., more mass-loss during the WN phase will produce WC stars with lower mass cores, inside which nuclear reactions will proceed with less vigour, prolonging this phase. In Figure 1.8**a** I present the predicted lifetimes of WR phases as a function of initial mass. A general increase of t_{WR} with initial mass can be seen, due to the larger cores of more massive stars being exposed at an earlier phase (but not necessarily age) by stronger stellar winds. Stellar rotation affects the mass-loss properties of massive stars, and induces various mixing processes in their interiors, both of which alter their evolution through the H-R diagram compared to the single-star picture outlined thus far.

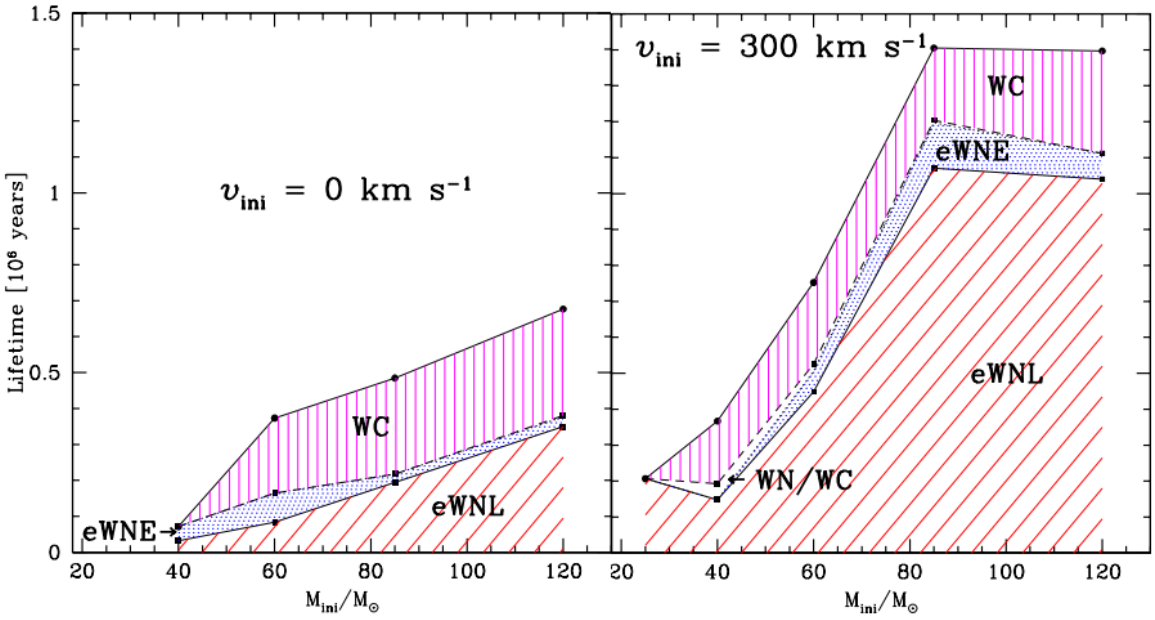

Figure 1.8: **a**(*Left*) Average duration of WNE, WNL, and WC phases as a function of initial stellar mass, for a population of non-rotating single stars at solar metallicity ($Z = 0.02$). **b**(*Right*) As left, for single stars rotating with an initial equatorial velocity of 300 kms^{-1}. Adapted from Meynet & Maeder (2003).

Effects of rotation

Rotation modifies the internal structure of massive stars, and the manner in which mass is lost from their surfaces. Meynet & Maeder (1997) detail how the theoretical treatment of Zahn (1992) is incorporated into stellar structure equations used to compute 1D evolutionary models. Meynet & Maeder (2000) explore the consequences for positions of stars in the H-R diagram, and the topic is reviewed by Maeder & Meynet (2000). Rotation was included following several deficiencies of non-rotating models when it came to reproducing observations. These included the surface enrichment of He in fast-rotating O-stars (Herrero et al., 1992), widened cluster main sequences (Maeder & Meynet, 1989), and the observation of transition WN/C type WR stars (Langer, 1991).

Centrifugal acceleration - by lowering effective gravity at the equator - introduces a latitude dependence to the surface temperature of a rotating star (von Zeipel, 1924),

$$T_{eff}(\theta) \propto g_{eff}(\theta)^{1/4}. \tag{1.6}$$

This so-called 'gravity darkening' has been confirmed observationally (Domiciano de Souza et al., 2005). The local radiative flux provides momentum to drive a stellar wind,

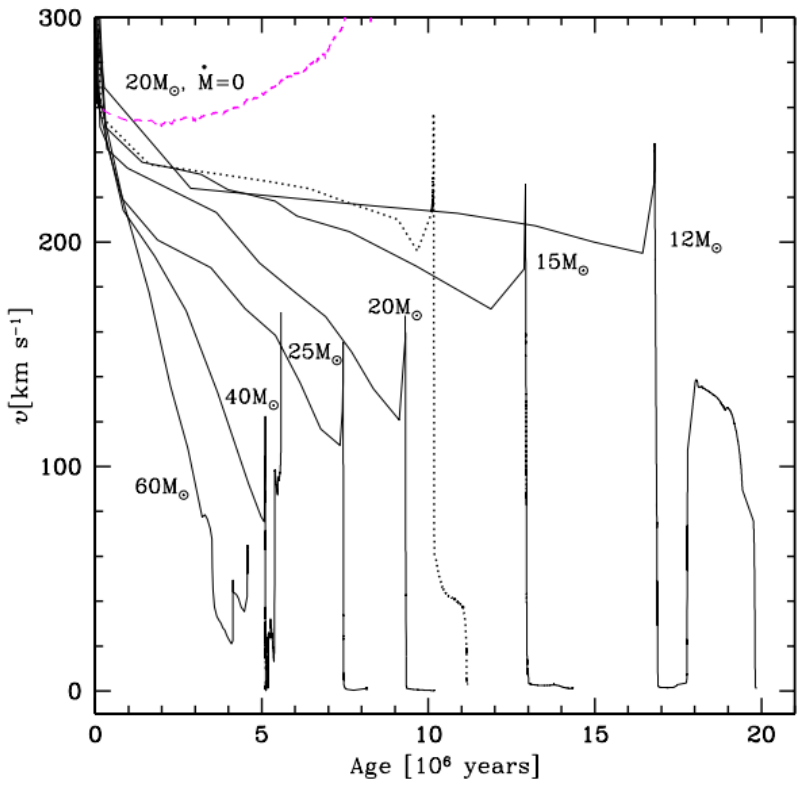

Figure 1.9: Evolution of surface equatorial velocity as a function of time for various initial stellar masses. Solid lines refer to solar metallicity ($Z = 0.02$), the dotted line corresponds to a $20\,M_{\odot}$ model at $Z = 0.004$ (weaker wind). The Purple dashed line shows a $20\,M_{\odot}$ star without mass-loss. Taken from Meynet & Maeder (2000).

and since this is proportional to the local effective gravity - which is lower at the equator - mass-loss is enhanced at the poles of a rotating star. In general, the surface-averaged mass-loss rate of a rotating massive star is predicted to be higher than in the non-rotating case (Maeder & Meynet, 2000; Puls et al., 2008), however Müller & Vink (2014) have recently challenged this.

Removal of angular momentum by stellar winds acts to gradually reduce rotational velocities, such that rotational velocities of 100s kms^{-1} can be reduced to zero. In Figure 1.9 I show the predicted evolution of rotation as a function of age in stellar models at solar metallicity. This spin-down is more effective at higher metallicity, due to enhanced stellar winds (see Section 1.4.1).

Internally, 'shellular rotation' is implemented in models, where angular momentum, $\Omega(R)$, is constant on isobars (Meynet & Maeder, 1997). This is underpinned by the assumption that turbulence in horizontal directions is much stronger than vertical. In a rotating star, following von Zeipel's theorem, equipotential surfaces are closer together

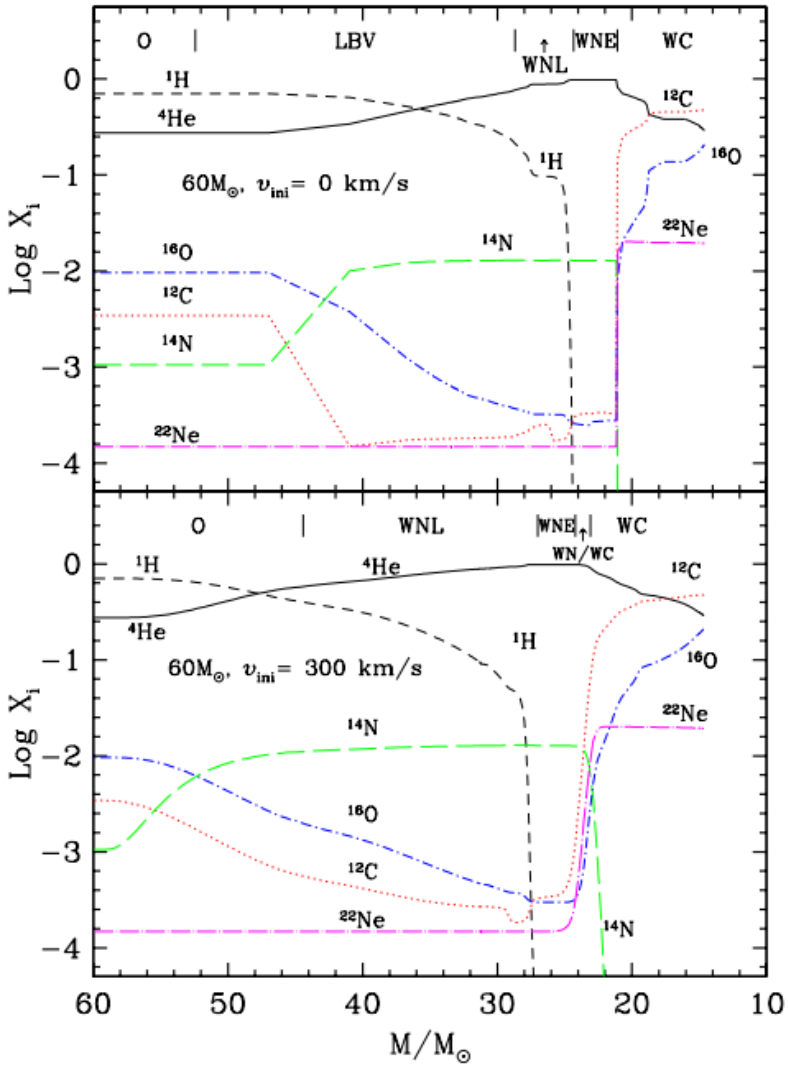

Figure 1.10: Evolution of abundances (as mass fraction) at the surface of a non-rotating (upper panel) and rotating (lower panel) 60 $M_\odot$ stellar model, as a function of the total mass of the star (decreasing with time due to mass-loss via a stellar wind). Note the less abrupt changes in surface composition, and earlier ascendance of N and C caused by rotation. Anticipated spectroscopic appearance is labelled at the top of each panel. Adapted from Meynet & Maeder (2003).

along the polar axis. Heating is generally higher in these directions as a result, driving large-scale motions rising at the poles and descending at the equator, known as meridional circulations. These are the dominant method of angular momentum transport from the cores to the surfaces of massive stars. Another form of instability, shear turbulence, results from the interaction of differentially rotating layers in the stellar interior. This turbulence acts to mix chemical elements, and can be treated as a diffusive process (Maeder & Meynet, 2000), thus smoothing out strong chemical discontinuities which are seen in non-rotating models. This can be seen in Figure 1.10, where I show the predicted evolution of surface abundances for a $60\,M_{\odot}$ star with and without rotation. More gradual surface abundance changes in the rotating case signify the smoother chemical gradients within. A more gradual transition from N to C-rich WR stars helped to explain the frequency of WN/C stars, as this transition phase is negligibly short in the non-rotating case.

Three effects of stellar rotation are particularly important for the WR phase:

1. Rotating cores are larger than non-rotating cores, with similar consequences to convective overshooting, extending the H-burning lifetime.

2. Chemically enriched layers are shifted outwards from the core, and hence are revealed by mass-loss more readily.

3. A more homogeneous chemical composition in the atmosphere lowers opacity, inhibiting redwards evolution, and lowering the upper mass limit for stars becoming RSG stars before WR.

A higher He abundance mixed into the atmospheres of rotating massive stars has the effect of lowering opacity, thus reducing radii and slightly increasing temperatures on the MS (see Figure 1.6). A combination of increased surface-averaged mass-loss and the transport of CNO processed layers outwards results in these layers being revealed at an earlier stage of evolution. The WN phase is therefore prolonged (Meynet & Maeder, 2003), as can be seen in Figure 1.8**b**. Rotation also lowers the initial mass limit for (single) stars entering the WR phase, from $\sim 37\,M_{\odot}$ to $\sim 22\,M_{\odot}$ at solar metallicity (Meynet & Maeder, 2003).

1.2.2 Binary evolution

There is overwhelming evidence that binary interactions play a major role in the evolution of massive stars, and hence the formation of some fraction of WR stars. Not only does the high observed binary fraction and distribution of orbital parameters in massive binaries point to this (Sana et al., 2012), but several observations require it. The observed binary fraction amongst Galactic WR stars is ∼40 % (van der Hucht, 2001), not accounting for observational bias towards easily detectable systems. The present-day orbital parameters of many of these can only be explained by previous mass and angular momentum exchanges (Petrovic et al., 2005). Indirectly, the observed rate of H-free ccSN (assumed to come from WR stars) is too high to arise exclusively from massive single WR stars (Smith et al., 2011), and the cosmic long-GRB rate is easier to reproduce with models including a binary channel (Bissaldi et al., 2007; Trenti et al., 2015). The qualitative evolutionary scenario for WR stars as a result of binary interaction was introduced by Paczyński (1967). Compared to single-star models, however, the addition of extra variables (orbital period, eccentricity, mass ratio, etc.), complicates binary models considerably. Furthermore, important uncertainties exist, including the efficiency of the mass-transfer process (Cantiello et al., 2007; de Mink et al., 2007), and the subsequent response of the secondary to gaining mass and angular momentum (de Mink et al., 2013)

As the primary star in a binary system expands (see Section 1.2.1), its outer layers might extend beyond the Roche Lobe, inside which material is gravitationally bound to the star. Material will subsequently flow through the inner Lagrangian point (L_1) towards the less-evolved secondary. This process is known as Roche Lobe Over-Flow (RLOF). Kippenhahn & Weigert (1967) categorise these events according to the evolutionary state of the primary at the onset of mass transfer; Case A during the MS, Case B during H-shell burning, and Case C during core/shell He-burning. Case A will occur in binaries with periods of a few days, Case B up to ∼ 1000 days assuming a circular orbit and one component expanding to RSG proportions, and Case C up to a few thousand days (Podsiadlowski et al., 1992). If *both* stars fill their Roche Lobes - as a result of mass gained by the secondary or its own evolutionary expansion - a Common Envelope (CE) phase will result. The orbit will decay due to dynamical friction, and a merger may occur before the primary explodes (Podsiadlowski et al., 1992).

Mass transfer may be conservative (mass transfer efficiency=1) or non-conservative (mass transfer efficiency < 1), depending on how amenable the secondary is to accepting mass. The rotation rate of the secondary is an important determining factor for mass transfer efficiency. Significant amounts of angular momentum may be transferred with

the mass, such that the mass gainer can be spun up to a substantial fraction of its critical rotation rate ($g_{eff} = 0$ at equator) after increasing in mass by as little as 5–10% (Packet, 1981). Depending on the secondary radius (evolutionary stage), and the orbital separation, material flowing through L_1 may form an accretion disk capable of spinning-up the whole star to critical velocity, effectively halting accretion. Mass transfer efficiency is therefore expected to decrease for wider systems, which are more likely to form accretion disks, and lower mass ratios ($q = M_2/M_1$), where a smaller fraction of primary mass is required to spin-up the secondary (cf. Langer 2012). The latter has been proven by observations of massive WR binaries (Petrovic et al., 2005). These spun-up secondaries may display CNO enhancements, due to the accreted material and rotational mixing (Section 1.2.1). The efficiency of mass transfer remains a crucial unknown in binary modelling.

I will now assess the likelihood of H-depleted He-burning stars, i.e., WR stars, being produced by each case, as either primaries or secondaries. Case A mass transfer occurs on a nuclear timescale, and systems with periods $\lesssim$2d and $q < 0.6$ may evolve into contact (CE) (Pols, 1994), causing a probable merger in $\gtrsim$50 % of Case A systems (de Mink et al., 2011). Case A primaries that avoid such a CE phase will promptly lose their H envelopes upon ignition of H-shell burning, resulting in a H-depleted primary with a potentially more luminous secondary, in a close (of order $\sim$10d) orbit.

Mass transfer in Case B systems is less well understood due to the large convective envelopes involved. For periods up to $\sim$100 days, mass transfer may lead to a CE phase - as proposed for the progenitor of SN 1987A (Podsiadlowski et al., 1992) - and a subsequent merger is favourable for low mass ratios. The merger product will not be a rejuvenated star, as Hydrogen is unable to mix into the primary's He core. Instead, the resulting star will be core He-burning with an under-massive core for its total mass. This type of star stays blue, and reaches core collapse as a BSG, or WR if sufficiently massive (Braun & Langer, 1995; Claeys et al., 2011). CE evolution is highly uncertain, but it is thought that if a merger does not result from Case B interaction, the CE can be ejected at the expense of orbital energy (Paczyński, 1967), leading to a close binary with a H-deficient core He-burning component (Taam & Sandquist, 2000). If a Case B system remains detached, the primary will become a H-deficient He-burning star, retaining an envelope with anything up to a few $M_\odot$ of hydrogen. It is possible that the secondary star will outshine the primary at this point, as it will be rejuvenated due to gained mass (assuming it is still core H-burning), and mimic a higher mass star. However, as noted by Langer (2012), the capability of Case B/C mass transfer producing WR stars is limited

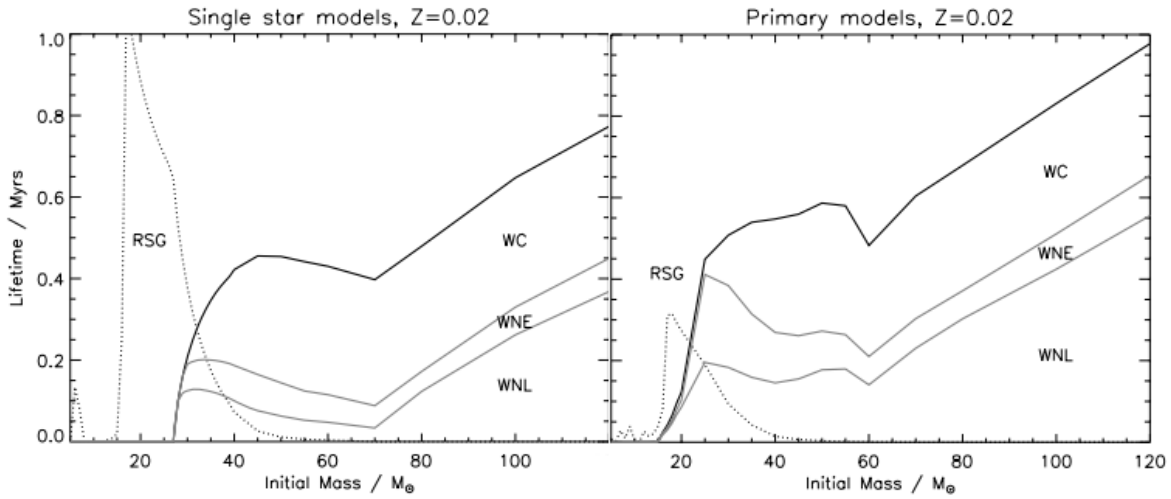

Figure 1.11: (*Left*) Average duration of RSG, WNL, WNE and WC phases (labelled) as a function of initial mass, for a population of non-rotating single stars at approximately solar metallicity ($Z = 0.02$). (*Right*) As left, for primary stars in binary systems, averaged over a range of orbital parameters. Adapted from Eldridge et al. (2008).

to lower luminosities, as $> 30\,M_{\odot}$ stars are not expected to expand to RSG dimensions.

In summary, core He-burning stars with H-depleted surfaces (essentially WR stars) are most likely to arise from *i*) Case A systems which avoid merging, resulting in a close binary ($P < 10$d) with a similarly (if not more) luminous less-evolved companion, *ii*) post-CE Case B systems, resulting in a close binary with a relatively low-luminosity primary ($\log(L/L_{\odot}) \lesssim 5.6$), potentially with surrounding nebula containing the ejected envelope, *iii*) Case B systems with $P \gtrsim 100$ d which avoid a CE phase, resulting in WR-like primaries of luminosity similar to (*ii*), and secondaries whose luminosities are heavily dependent on the mass transfer efficiency.

Population synthesis models taking binary evolution into account (e.g., Vanbeveren et al. 1998) predict very different relative numbers of massive star types than those based solely on single stars (e.g., Meynet 1995). Outstanding problems to single-star population synthesis include the BSG/RSG ratio (Langer & Maeder, 1995; Massey & Olsen, 2003), the RSG/WR ratio (Massey, 2003), and to a lesser extent the WC/WN ratio; the lack of a complete sample larger than those of the LMC and SMC has limited comparison of the latter to observations. In Figure 1.11 I show average lifetimes predicted for RSG and WR (divided into WNE, WNL and WC) stars as a function of initial mass, for single stars (as in Figure 1.8a) and the primary stars of binary systems, according to the population synthesis models of Eldridge et al. (2008). In the binary scenario, average WR lifetimes moderately increase and RSG lifetimes are dramatically reduced.

This is due to RLOF assisting the removal of H-rich layers, revealing CNO products with a larger fraction of t_{He} remaining. The most significant difference is a decrease in the minimum initial masses producing a WR star, from $\sim$27 $M_{\odot}$ to $\sim$15 $M_{\odot}$. The lengthening of average WR lifetimes is manifest mainly in the WN phase, in qualitative agreement with other studies (Vanbeveren et al., 2007).

1.3 Observational characteristics of Wolf-Rayet stars

The optical spectra of WR stars consist of strong broad emission lines, representing a range of ionisation and excitation, on top of a blue continuum. Such spectra have their origins in dense stellar winds, meaning the stellar photosphere (optical depth of order unity) arises in outflowing material, and emission lines form even further out. Their wind properties are discussed further in Section 1.4. The first examples were recognised by Wolf & Rayet (1867) as peculiar emission line sources in the Cygnus star-forming region, and since then over 600 have been discovered in the Galaxy (see Chapter 2). Their distribution in the solar neighbourhood is strikingly similar to massive OB stars, indicating an evolutionary connection (Divan & Burnichon-Prévot, 1988; Conti, 1988). WR spectra come in three main flavours, all showing He enrichment (Smith, 1973; Willis, 1982), and displaying lines of either nitrogen, carbon, or oxygen, denoted as WN, WC, and WO types respectively. Conti (1975) first proposed an evolutionary sequence connecting these subtypes, whereby mass-loss from stellar winds (Beals, 1929) progressively reveals nuclear processed material (Paczynski, 1973); first from the CNO cycle (WN), followed by the products of partial helium burning (WC & WO). This has come to be known as the 'Conti scenario'.

The interpretation of WR stars as evolved objects was challenged (e.g., Underhill 1983), on the basis that insufficient radiative momentum is available to drive the necessary outflows ($\sim 10^{-5}\, M_{\odot}\mathrm{yr}^{-1}$, e.g., Bieging et al. 1982). Instead it were proposed that WR stars are massive Pre-Main Sequence (PMS) objects with solar abundances, with apparently anomalous abundances put down to ionisation effects, and wind features originating from a disk of natal material. Lamers et al. (1991) discussed the observational evidence for PMS and post-MS interpretations, and strongly favoured the latter, based on the existence of WR binaries with evolved components and the comprehensive absence of circumstellar matter.

1.3.1 Observational techniques

Classification

Historically, the classification of WR stars has been based on optical spectral features, arising from ionised Helium and other elements in their atmospheres. Beals (1939) was first to define a classification scheme, which was mainly qualitative, and was successively modified by Hiltner & Schild (1966) and Smith (1968a). The advent of linear detectors facilitated the development of fully quantitative WR classification schemes.

A three dimensional system for WN star classification was devised by Smith et al. (1996), in which stars are arranged between WN2-WN9 (extended to WN11 by Smith et al. 1994) from high to low ionisation. The primary diagnostic for this is the ratio between HeII 5411/HeI 5875 Å lines, with NV 4603/NIII 4640 Å also providing distinctions. Some exemplary optical WN spectra are shown in Figure 1.12**a**. WN stars of ionisation type ≤ 6 are more broadly referred to as early-type (WNE), and others late-type (WNL). The second and third dimensions of this system relate to the strength of hydrogen features and FWHM of He lines in the optical spectrum. Hiltner & Schild (1966) introduced a broad-line distinction (denoted by 'b'), noting that such stars encompass a smaller range in ionisation (typically WN4–7). The presence of hydrogen (denoted by 'h') is revealed by an oscillating Pickering decrement, where lines formed of H+He clearly exceed adjacent pure He lines. The threshold hydrogen abundance for this is estimated to be $H^+/He^{++} = 0.5$ by number (Smith et al., 1996). WN stars showing a weak oscillation of the Pickering decrement, i.e., $0 < (H^+/He^{++}) < 0.5$, are denoted '(h)'. WN stars classified as broad-line rarely show hydrogen in their spectra, hence 'b' also implies hydrogen-free.

A subset of H-rich WN stars display weak hydrogen emission and *intrinsic* hydrogen absorption lines, referred to here as WN#ha stars (see Smith & Conti 2008; Crowther & Walborn 2011). Spectroscopically, they represent a continuation of Of type (emission line) stars (Bohannan & Crowther, 1999), with strong winds at a relatively early evolutionary stage. WN#ha stars also tend to be more luminous that H-free WN stars (Hamann et al., 2006), and are almost uniquely found in young clusters, suggesting current masses $>65\,M_\odot$ from cluster turn-offs (Crowther et al., 1995a). I will further discuss the evolutionary context of WN stars in the following section.

For WC and WO stars, the quantitative one dimensional schemes of Smith et al. (1990) and Kingsburgh et al. (1995) respectively were refined and unified by Crowther et al. (1998). WC and WO spectral sequences are generally well-behaved and there is a smooth transition between the two. Ionisation types WC4–9 are chiefly discriminated by

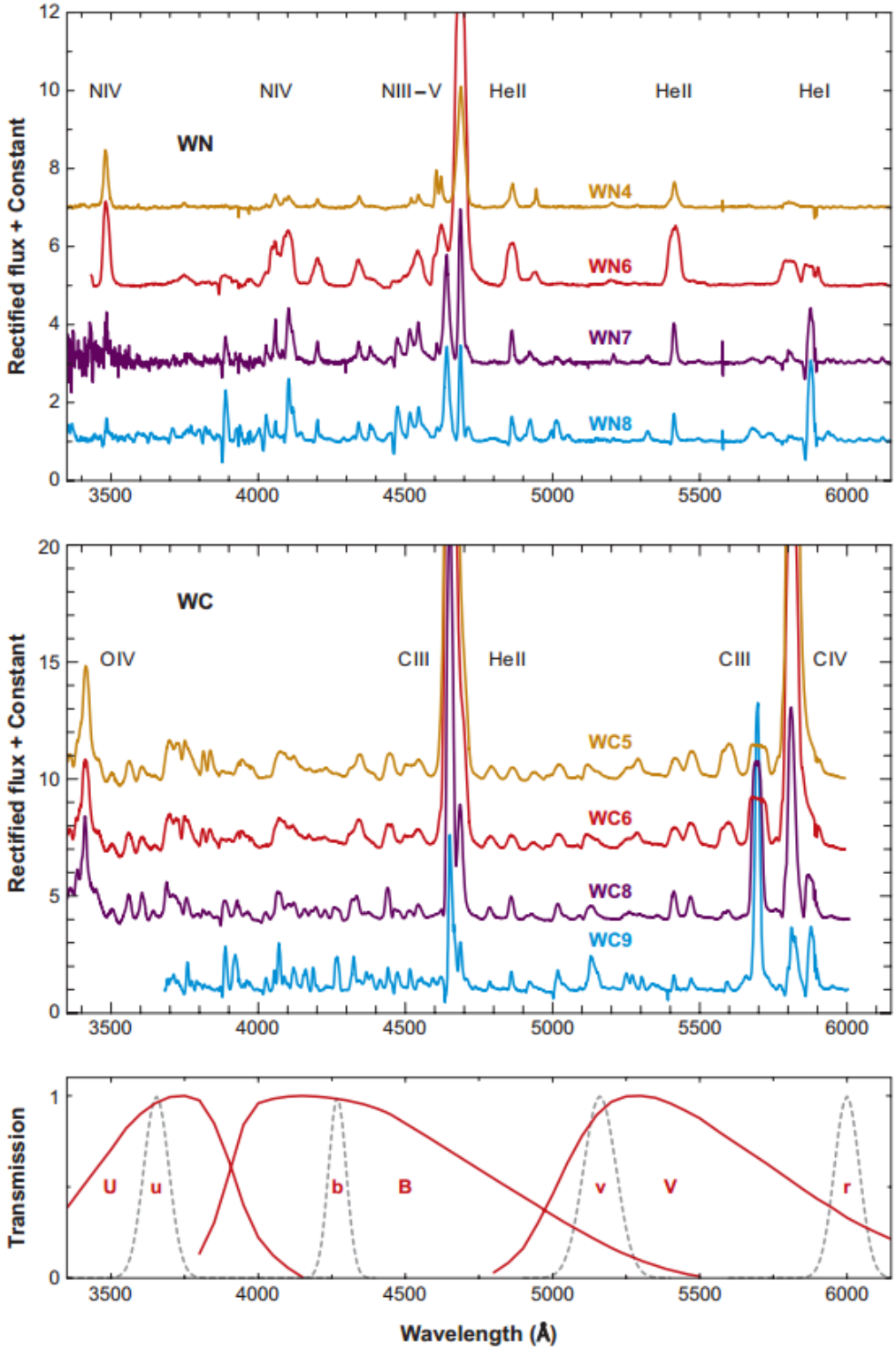

Figure 1.12: **a**(*Top*) Montage of optical WN spectra. **b**(*Middle*) Montage of optical WC spectra. **c**(*Bottom*) Wavelength coverage of commonly used photometric filters; Johnsnon UBV, and narrow ubvr introduced specifically for WR stars by Smith (1968b) and Massey (1984). Taken from Crowther (2007).

the CIV 5801/CIII 5696Å ratio. Subtypes WC4–6 are regarded as early-type, and WC7–9 as late-type. As CIII lines are absent in the spectra of the hotter WO stars, WO1–4 are classified by OVI 3811/OV 5590Å. I show exemplary optical WC spectra in Figure 1.12**b**.

Abundances

The development of non-LTE atmospheres has allowed accurate abundance measurements for WR stars. The physics of these atmosphere models will be the topic of Section 1.4. A subtype trend exists amongst Galactic WN stars regarding their H abundance, with WNL type stars generally showing $X_H = 5$–25% and WNE being H-free, although there are exceptions. A larger fraction of WN stars of all ionisation subtypes display H at lower metallicity (Foellmi et al., 2003). The luminous WNha stars are universally H-rich with $X_H \sim 50\%$ (Crowther et al., 1995b), reinforcing the interpretation of these as very massive core-H burning objects. Analyses of CNO abundances in WN stars reveals a pattern consistent with nuclear burning, with $X_N \sim 1\%$ and $X_C = 0.05\%$ (e.g., Crowther et al. 1995c).

The spectra of WC and WO stars show no H or N lines. For WC stars, non-LTE analyses have measured $20\% < X_C < 55\%$, with no dependence on subtype (e.g., Koesterke & Hamann 1995). Many carbon diagnostics are found at optical/IR wavelengths, but oxygen features are more sparse, and the most suitable are located in the UV. Where such data are available, analyses have found $X_O \sim 5$–10% (Crowther et al., 2002). Detailed analysis of WC9 optical spectra has recently indicated lower oxygen abundances in these than earlier subtypes ($X_O = 1$–4%; Williams et al. 2015).

WO stars are extremely C and O-rich, as a consequence of their highly evolved nature (Kingsburgh et al., 1995). Tramper et al. (2015, in prep) present a comprehensive spectroscopic analysis of the majority of WO stars known, deriving $X_C = 0.45$–0.6 and $X_O = 0.1$–0.25. I give a more detailed summary of oxygen abundances in WC and WO stars in Section 4.1.

Intrinsic brightness and colours

Using standard UBV photometry, WR stars cannot be distinguished from other hot stars. Strong WR emission lines (Fig 1.12) contribute up to 1.0 mag, but more typically 0.5 mag, in the visual. For the study of true WR continua, narrow ubv filters avoiding strong WR emission features were employed by Smith (1968b), to which r was added by Massey (1984). These are shown in Figure 1.12**c**. Continuum slopes measured using these filters can provide reddening estimates when compared to expectations of *intrinsic* continuum

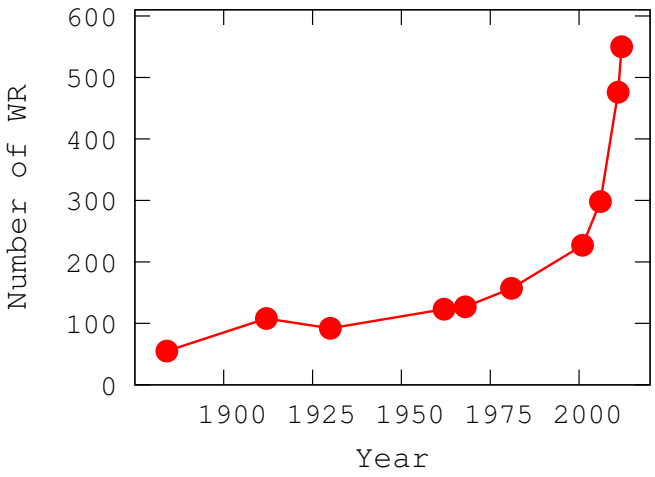

Figure 1.13: The number of spectroscopically confirmed Galactic WR stars since Campbell (1894). Other points refer to the catalogs of Fleming & Pickering (1912), Gaposchkin (1930), Roberts (1962), Smith (1968c), van der Hucht et al. (1981), van der Hucht (2001), van der Hucht (2006), and Crowther, Baker & Kus[1].

slopes (e.g., Morris et al. 1993). Such reddening estimates allow absolute magnitudes to be calculated for WR stars residing in clusters at known distance. Absolute visual magnitudes have been shown to vary with subtype, most notably for WN stars (Smith, 1968b), with $M_V \simeq -3$ for early WN, and -6 (H-poor) to -7 (H-rich) for late WN (van der Hucht, 2001; Hamann et al., 2006). A smaller range is seen for WC stars, with $M_V \simeq -3.5$ for early and -5 for late-types, with a ~ 0.5 mag scatter in each subtype.

In principle, such absolute magnitude-subtype calibrations should allow a distance measurement to any classified Galactic WR. This mapping was indeed done when the population stood at <150 lightly reddened examples (Smith, 1968c). However, in Figure 1.13 I show how the known population has expanded since the dawn of large all-sky and Galactic plane IR surveys. High visual extinction prohibits spectroscopic classification of this emerging population, limiting the usefulness of the aforementioned optical calibrations.

Galactic distribution and total population estimates

Our knowledge of the Galaxy's WR content rests on the successive achievements of tailored imaging surveys. The use of narrow-band selection techniques was pioneered by Massey & Conti (1983) and Moffat & Shara (1983) to identify extra-galactic WR stars, using filters centred on and off strong WR star emission lines at optical wavelengths.

[1] http://pacrowther.staff.shef.ac.uk/WRcat/

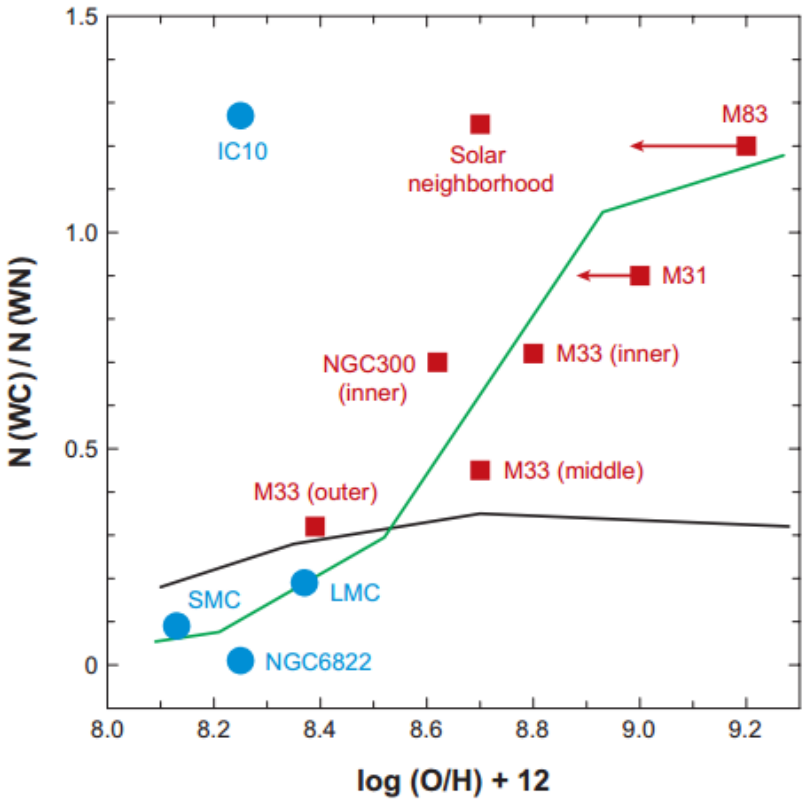

Figure 1.14: The N_{WC}/N_{WN} ratio measured by direct stellar counts in Local Group galaxies, as a function of their metallicity. Predictions are shown as lines (green: Eldridge & Vink 2006, black: Meynet & Maeder 2005 rotating) based on the duration WC and WN phases in stellar models, weighted to the IMF. Taken from Crowther (2007).

Shara et al. (1991, 1999) applied similar methods to push the extent of the known Galactic population beyond 5 kpc from the Sun, and extension to near-IR wavelengths has facilitated yet deeper investigation of the Galactic disk (Shara et al., 2009, 2012).

Such surveys have shown the absolute number and subtype distribution of WR stars to vary from galaxy to galaxy (Massey, 2003). The number of WR stars to O-stars is lower in metal-poor environments, with $N_{WR}/N_O \sim 0.15$ in the solar neighbourhood, while $N_{WR}/N_O \sim 0.01$ in the SMC. Lower metallicity also favours WN over WC stars, with the former exceeding the latter ten-fold in the SMC, while WC slightly outnumber WN in the metal-rich inner Milky Way (Section 2.3). I show N_{WC}/N_{WN} as a function of metallicity in Figure 1.14. However, one must be mindful of the bias in narrow-band imaging techniques against WNE stars, due to their intrinsically weaker emission lines. It is likely for this reason that galaxy IC 10 appears well above the N_{WC}/N_{WN} trend in Figure 1.14.

Another distinctive feature of WR stars - the near-IR excess caused by free-free emission in their winds - has been exploited to yield further discoveries in the Galaxy (Homeier et al., 2003; Hadfield et al., 2007; Mauerhan et al., 2011). The efficiency of these broad-band techniques is enhanced by the inclusion of $>2\,\mu$m photometry, and the association of candidates with X-ray sources in the Galactic plane (Mauerhan et al., 2010a), typically reaching $\sim$20%. These exploit common properties of colliding-wind WR+O binary systems; X-rays from the shock-heated collision region (Stevens et al., 1992), and thermal emission from dust (peaking at $\sim5\,\mu$m) condensing in the interaction region between C-rich WC winds and H-rich O-star winds (e.g., Williams et al. 1990a). These, together with many serendipitous discoveries (e.g., Clark et al. 2005, Mauerhan et al. 2010a) have brought the currently recognised population to $\sim$660 (May 2015).

Several attempts have been made to determine the total number of WR stars in the Galaxy. Maeder & Lequeux (1982) used the then-known 157 WR stars to arrive at a total of $\sim$1,200 by assuming the surface density of WR stars to vary with Galactocentric radius (R_G) in the same way as giant HII-regions, including a dearth at $R_G \lesssim 3$kpc. To emphasise the need for IR investigation, Shara et al. (1999) created a model WR star population featuring a stellar disk of exponentially increasing density towards $R_G = 0$. From this they inferred a total of 2,500 Galactic WR stars, or 1,500 if few WR stars inhabit the region $R_G \lesssim 3$kpc, as the decline in gas density suggests (barring the inner 500 pc). van der Hucht (2001) arrived at a much higher 6,500 WR stars by extrapolating the surface density of local WR stars (7kpc$< R_G <$ 12kpc) across the entire disk, neglecting the decrease in star formation rate interior to $R_G \sim 3$kpc. Most recently, in the light of numerous WR star discoveries in IR surveys, Shara et al. (2009) presented an updated population model - still featuring an exponential disk of stars - yeilding a total of 6,400. The same work also suggested that observations of WR stars as faint as $K \simeq 15.5$ mag are necessary to achieve a completeness of 95%.

1.3.2 Evolutionary status of WR stars

Here I summarise what may be inferred from the physical properties of WR stars about their evolutionary state, and how they fit into the picture of massive star evolution. Many recent observations have challenged the simplistic evolutionary scenarios presented in Section 1.2.1, causing a major re-think of the evolutionary connections between different types of massive star.

Cluster turn-offs provided the first indications of progenitor mass ranges for WR stars (Schild & Maeder, 1984; Massey et al., 2001). By comparison to single-star models of

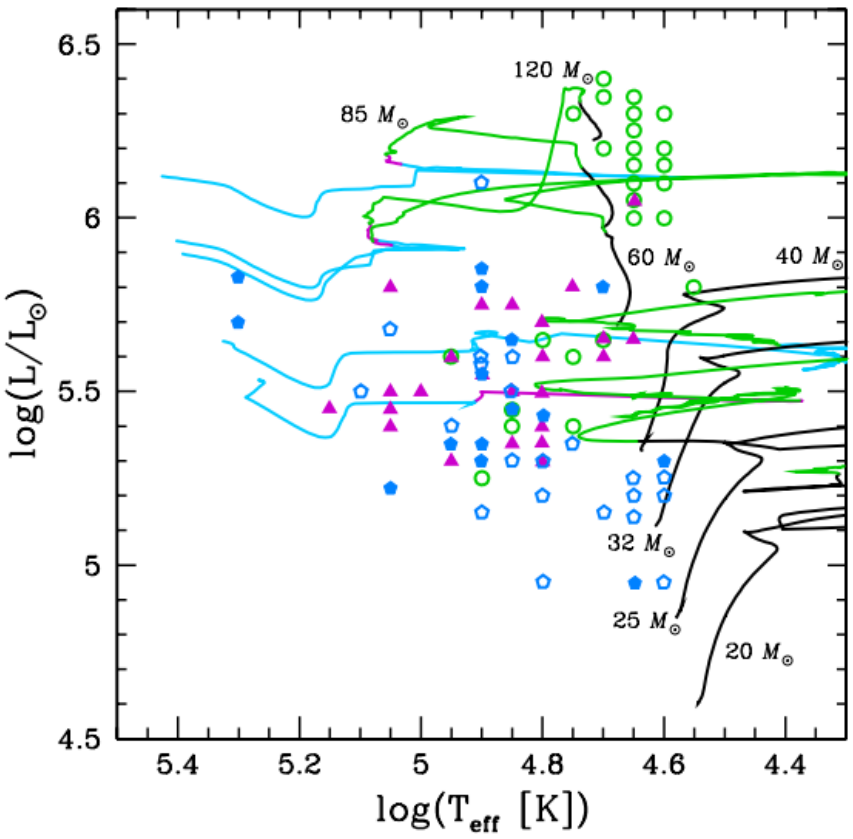

Figure 1.15: Hertzsprung-Russell (H-R) diagram showing the measured positions of H-rich WN stars (green open circles), H-free WN stars (purple triangles), and WC stars (blue pentagons. Known distance filled; unknown distance open). The two hottest stars $\left(\log(T_{eff}[K]) = 5.3\right)$ are WO (Hamann et al., 2006; Sander et al., 2012). Single-star rotating evolutionary tracks (Ekström et al., 2012) are overlaid, coloured appropriately for they expected spectral types (Green: H-rich WN - Purple: H-poor WN - Blue: WC). Initial model stellar masses are labelled. Taken from Georgy et al. (2012).

the day, the observed clusters suggested a higher minimum mass for WC stars than for H-free WN, with the former descending from $> 45\,M_{\odot}$ stars and the latter from $\gtrsim 20\,M_{\odot}$. However, such studies inherently assume of that the WR stars seen in massive clusters are representative of the whole population. This may not be the case, as Smith & Tombleson (2015) show some WR types are less clustered than others (see also Section 2.3). It is true however that H-rich WNL stars (WNha) are largely exclusive to massive clusters, indicating very massive ($>$60–70 $M_{\odot}$) progenitors. The high luminosities of these stars ($\log(L/L_{\odot}) \gtrsim 6.0$), and their similar spectral morphology and smooth progression of mass-loss properties with Of type stars, is consistent with WNha being a continuation of the upper main-sequence (Crowther et al., 1995b).

The locations of Galactic WN and WC stars in the H-R diagram (Hamann et al., 2006; Sander et al., 2012) can be seen in Figure 1.15, along with current single-star evolutionary models with rotation (Georgy et al., 2012). It can be seen that $>60\,M_{\odot}$ tracks reproduce the location of WNL stars well, but their subsequent bluewards evolution at constant L_{bol} to become very luminous WC and WO stars is not seen observationally. The WNL must therefore lose their H envelopes - to avoid redward evolution past the Humphrey-Davidson limit - without evolving bluewards from their current locations. Clumping-corrected mass-loss rates during the O-star phase seem insufficient to perform this H-envelope removal (Mokiem et al., 2007), hence some other mechanism is required. Indeed, Smith (2014) argues that the MS mass-loss rates employed in stellar models are too high, increasing the need for additional mass-loss mechanisms to explains the current WR star population. Enhanced mass-loss in close proximity to the Eddington limit has been suggested to explain the WNha stars (Gräfener et al., 2011; Bestenlehner et al., 2014). Langer (1987) proposed that very massive stars could spend the entirety of He burning on the blue side of the H-R diagram, while retaining an envelope containing some fraction of hydrogen. Under this scenario, supported by the models of Langer & El Eid (1986), very massive stars ($\gtrsim 60\,M_{\odot}$) would end their lives as WNL stars. This prediction is compatible with indications that approximately 8–9% (Smith et al., 2011) of core-collapse supernovae have LBV-like progenitors, evidenced by narrow emission lines in their spectra arising from explosion into a dense circumstellar medium.

There is little overlap in luminosity between WNL and WNE stars (Figure 1.15), suggesting either that WNE are not the progeny of WNL, or that the luminosity of some WNL is reduced to that of WNE by an unknown process on a timescale much shorter than either phase duration. The high luminosity of WO stars observed by Sander et al. (2012) is puzzling, because under the Conti scenario these would have WC or WNE progenitors of comparable or higher luminosity, which are not observed (Figure 1.15). Langer (2012) propose that the least massive WNL stars - having had the longest time during He burning to enrich the layer surrounding their He cores with C - might evolve rapidly bluewards via a WN/C phase to become WO. The existence of one such luminous WN/C star WR 26 ($\log(L/L_{\odot}) = 6.1$, Fig. 1.15, Sander et al. 2012) is tantalising evidence for this.

The majority of WNE and WC stars (with the exception of WC9) have similar measured luminosities ($\log(L/L_{\odot}) = 5.3$–5.7), supporting an evolutionary connection. The similarity in temperature of WNE and WC stars is also expected from models of He-stars enriched with carbon and oxygen (Langer, 1989). There exists a tight theoretical

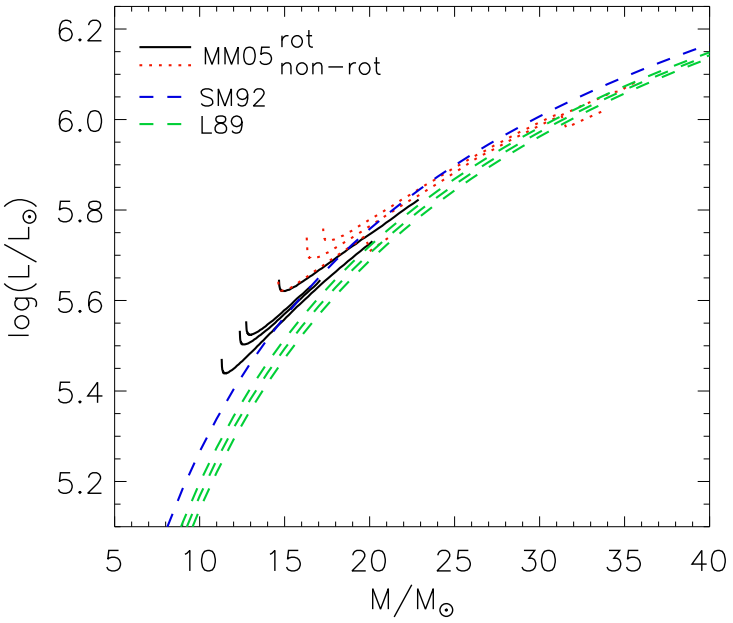

Figure 1.16: Mass-luminosity relationships for H-free WR stars, according to Langer (1989) (green dashed), Schaerer & Maeder (1992) (blue dashed), and the models of Meynet & Maeder 2005 (solid rotating, dotted non-rotating).

mass-luminosity relationship for H-free stars (Langer, 1989; Schaerer & Maeder, 1992), which I show in Figure 1.16. Following this, the observed luminosity of WNE and WC stars corresponds to actual masses in the range 10–30 $M_{\odot}$. Binary-derived masses for a few WC stars range between 9–16 $M_{\odot}$ (Crowther, 2007), consistent with but low compared to the mass-luminosity relationship. Single-star models predict 10–30 $M_{\odot}$ He cores from stars with initial mass 25–60 $M_{\odot}$, but currently assumed mass-loss rates are almost certainly overestimated (Smith, 2014), further suggesting that most WNL do not evolve into WNE. A H-rich WNL phase is not expected for post-RSG stars, as removal of the entire H-rich envelope is required before returning to the blue. The detection of hydrogen ($X_H \sim 0.1$) in some lower luminosity WN therefore suggests that some WNE have descended from blue progenitors. Two single-star channels into the WNE phase are therefore implied, as shown in Figure 1.7; stars above $\sim 40\,M_{\odot}$ enter via a blue supergiant phase, possibly as a result of LBV mass ejections, and below $40\,M_{\odot}$ evolution proceeds via an RSG phase. Both scenarios produce He stars of similar mass (luminosity), because stars following the RSG path may grow their helium cores before they are uncovered as WNE, unlike those following the BSG route which are uncovered at the start of He-burning. Hence WNE luminosity alone cannot be used to determine the

evolutionary path taken. Rotation rates may provide clues, as these should be higher at an earlier stage of He-burning, while rotation in post-RSG stars can be strongly reduced by magnetic coupling (Heger et al., 2005) or shear mixing (Meynet & Maeder, 2003). This two channel picture may help to explain the peculiar broad-line WN#b stars, which have been linked to fast rotation (Shenar et al., 2014).

The WC9 stars are observed with low luminosity ($\log(L/L_{\odot}) \simeq 5.1$) and in close proximity to the H-burning MS. This is currently unexplained by any proposed evolutionary scenario leading to surface carbon enrichment. According to the Conti scenario, every WC star should have a H-free WN (WNE) progenitor, presumably of comparable luminosity (mass) and slightly lower T_{eff}, yet no such WNE stars are observed (Hamann et al., 2006). The atmospheres of cool WC9 stars are the most challenging to model of any WR class, owing to the complex model atoms required, hence extreme care must be taken when using model spectra to derive temperatures. It could be the case that model-grid approaches (e.g., Sander et al. 2012) are too coarse and simplistic to derive accurate temperatures. I return to this problem in Section 1.4.2, where I also discuss the possibility that sub-photospheric envelope inflation (Gräfener et al., 2012) distorts our understanding of WR radii and hence temperatures.

The clustering of WR stars has recently been evaluated by Smith & Tombleson (2015), who measure the projected separations of different WR classes from massive O-stars in the Galaxy and LMC (via SIMBAD[2]). Massive O-stars are well recognised indicators of young stellar populations, and are rarely found in isolation (Gvaramadze et al., 2012), such that increasing spatial correlation with these should indicate increasing initial masses. To a lesser extent, relative ages may be also be inferred, as older stars have longer to roam from their birth sites (as shown in Section 2.3.2). In Figure 1.17 I show the nearest O-star neighbour statistics found by Smith & Tombleson (2015), showing that WC stars are more dispersed than H-free WN, which in turn are more dispersed than H-rich WN. A subset of H-rich WN stars are very tightly clustered, corresponding to the core H-burning WNha stars (Smith & Conti, 2008). The higher dispersal of WC stars relative to H-free WN stars is significant. It is strongly suggestive of a lower initial mass range, contrary to conclusions from cluster turn-offs (Massey et al., 2001). Although WC stars are indeed regarded as older than WN, an age effect can be largely ruled out by considering the higher clustering of mid O-type stars, which have similar MS lifetimes to the combined H and He-burning lifetimes of WC stars in evolutionary models (Meynet & Maeder, 2005). A lower mass range for WC than WNE

[2] http://simbad.u-strasbg.fr/simbad/

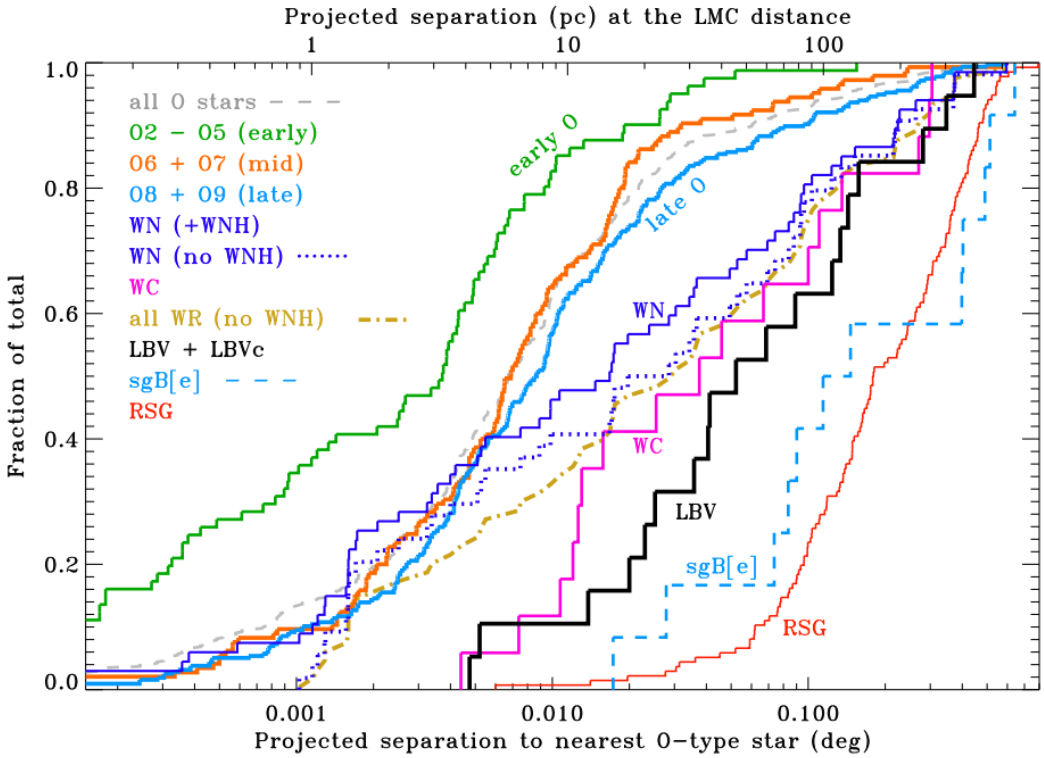

Figure 1.17: Cumulative distribution plot illustrating degrees of isolation for various types of massive star in the LMC. Separation from the nearest O-star is plotted on a log scale. Classes of object that are more clustered with O-stars appear further to the left. Taken from Smith & Tombleson (2015).

stars is impossible to account for in current single-star evolutionary scenarios, leaving binary processes as the only viable explanation.

1.4 Physics of Wolf-Rayet atmospheres

Stellar winds are a ubiquitous property of massive stars. The suggestion that radiation pressure on spectral lines could drive these outflows was put forward by Milne (1926). It was later shown to be theoretically plausible (Lucy & Solomon, 1970), and Castor, Abbott & Klein (1975) introduced what is known as the CAK line-driven wind theory. The basic principal is that photon absorptions occur preferrentially in the radial direction, with re-emission isotropic, hence absorptions impart net radial momentum to ions in the atmosphere. Puls et al. (2008) give a recent review of mass-loss via stellar winds in hot masive stars, elaborating on the 1D standard model of line driven winds. The mass-loss rates of WR stars are so large, and their atmospheres so extended, that an optical depth of unity arises in the outflowing stellar wind. An understanding of these winds and how to parameterise them is therefore crucial, if one is to derive fundamental stellar parameters for the star by spectroscopic analysis. In this section I will give an overview of standard radiation-driven wind theory, and its difficulty in accounting for strong WR winds. I will then summarise frequently used mass-loss and wind velocity diagnostics, and evidence for inhomogeneous winds. I will conclude the introduction with an overview of WR atmosphere analysis techniques and their key results.

1.4.1 Stellar winds and mass-loss

Primarily, stellar winds are parameterised by mass-loss ($\dot{M}$) and terminal (maximum) velocity (v_∞). For a spherical, steady-state wind, mass-loss is related to velocity and density by the continuity equation,

$$\dot{M} = 4\pi r^2 \rho(r) v(r). \tag{1.7}$$

The equation of motion is given by:

$$v\frac{dv}{dr} = -\frac{GM}{r^2} - \frac{1}{\rho}\frac{dp}{dr} + g_{rad}, \tag{1.8}$$

depicting a competition between the inwards force of gravity ($g_{grav} = GM/r^2$), and outwards forces due to the gas pressure gradient (dp/dr) and total radiative acceleration

(g_{rad}). The prime challenge is computing g_{rad}, which is provided by a combination of continuum and line opacity ($g_{rad} = g_{rad}^{cont} + g_{rad}^{line}$).

Electron (Thompson) scattering dominates the continuum opacity in hot stars, which is wavelength-independent and may be estimated by;

$$g_e = \frac{4\pi}{c}\frac{q\sigma_e}{m_H}\sigma T_{eff}^4. \tag{1.9}$$

However, scattering from bound electrons is much stronger that free electrons, so that line scattering is a much stronger source of opacity. It is a combination of a plethora of spectral lines in the same spectral region as the maximum photospheric flux (far-UV) that provides efficient driving of hot star winds (Gayley, 1995). For a given spectral line in a static atmosphere, interaction with photospheric radiation will only be effective in the lower layers of the atmosphere, due to the limited frequency range for the interaction. A way around this was proposed by Sobolev (1960), who realised that motion in the atmosphere would cause gas moving radially outwards to 'see' a redshifted photosphere. Hence, photospheric photons emitted blueward of a spectral line may travel unimpeded until they are redshifted into resonance with the spectral line. The geometric width of this resonance region (the Sobolov length) is given by $v_{th}/(dv/dr)$, where v_{th} is the ion thermal speed. This is smaller that the typical scale of variations in the outflow (of velocity gradient and opacity), such that for a single line at frequency ν with optical depth τ, line acceleration can be approximated by local quantities,

$$g_{rad}^{line} = \frac{L_\nu \nu}{4\pi r^2 c^2}\left(\frac{dv}{dr}\right)\frac{1}{\rho}(1 - e^{-\tau}). \tag{1.10}$$

For optically thin lines ($\tau < 1$), line scattering has the same $1/r^2$ dependence as electron scattering (Eq. 1.9), however it is optically thick lines ($\tau > 1$) which are important in driving winds in WR and some O-stars. In this limit,

$$g_{thick} \simeq \frac{L_\star}{\dot{M}c^2} v\frac{dv}{dr}, \tag{1.11}$$

thus, optically thick line force is independent of opacity, and scales with the velocity gradient. Neglecting gravity and pressure in Eq. 1.8, $v(dv/dr) \simeq g_{line}$, and substituting this into Eq. 1.11 gives $\dot{M} \propto L_\star/c^2$. In reality, winds are driven by multiple thick lines, and mass-loss also scales with the number of these. Assuming these lines are spread through the spectrum and do not overlap, this naturally leads to an upper limit on the line force, known as the single-scattering limit, given by

$$\eta = \frac{\dot{M} v_\infty}{L_\star / c} \leq 1, \tag{1.12}$$

where η is the wind efficiency parameter. Typical values of η lie in the range 1–5 for WR stars (Crowther, 2007), clearly showing that in the single-scattering approximation there is insufficient momentum to drive their powerful winds.

In the CAK approach, lines are summed in the form of a line-strength distribution function, approximated by a power law in opacity. This allows the total line acceleration to be calculated by integration (see Puls et al. 2000, for example). This approach provided the first self-consistent wind solution for hot stars. One of many key predictions was the velocity structure of stellar winds, the so-called 'β law',

$$v(r) = v_\infty \left(1 - \frac{R_\star}{r}\right)^\beta, \tag{1.13}$$

where $\beta = 0.5$ if the star is treated as a point source. A more realistic treatment considering the angular extent of the disk gives $\beta \simeq 0.8$ for hot O-stars (Friend & Abbott, 1986). CAK theory also predicts a "wind momentum-luminosity relation" (e.g., Puls et al. 1996), which was extended to predict a metallicity dependence for stellar winds,

$$\dot{M} \propto Z^\alpha, \tag{1.14}$$

where $\alpha \sim 0.6$ (Kudritzki & Puls, 2000).

An alternative approach to CAK, invoking a Monte-Carlo method, was developed by Abbott & Lucy (1985). Photons are tracked on their journey outwards, and crucially multiple-scattering events are accounted for, which become important in dense winds. Multiply scattered photons can add radial momentum to the wind, exceeding the single-scattering limit. Vink et al. (2000) used a Monte-Carlo method to produce a theoretical mass-loss recipe, as a function of stellar parameters L, M, T_{eff}, v_∞, and v_{esc} (escape velocity). The Vink et al. prescription is valid for effective temperatures $27.5\,\mathrm{kK} < T_{eff} < 50\,\mathrm{kK}$, and is almost universally adopted in models of stellar evolution for MS stars (Langer, 2012). This mass-loss recipe predicts at exponent for the $\dot{M}(Z)$ relation of 0.69 ± 0.10, which is consistent with measurements of O-star winds across the Galaxy, LMC, and SMC (Mokiem et al., 2007) which give 0.83 ± 0.16, as shown in Figure 1.18. Vink & de Koter (2005) perform Monte-Carlo mass-loss computations as a function of metal abundance for late-type WR stars, predicting a similar $\dot{M}$–Z relation for WN stars due to the dominating influence of millions of far-UV Fe lines. Indeed, theoretical calculations have shown heavy complex elements such as Fe to be principal

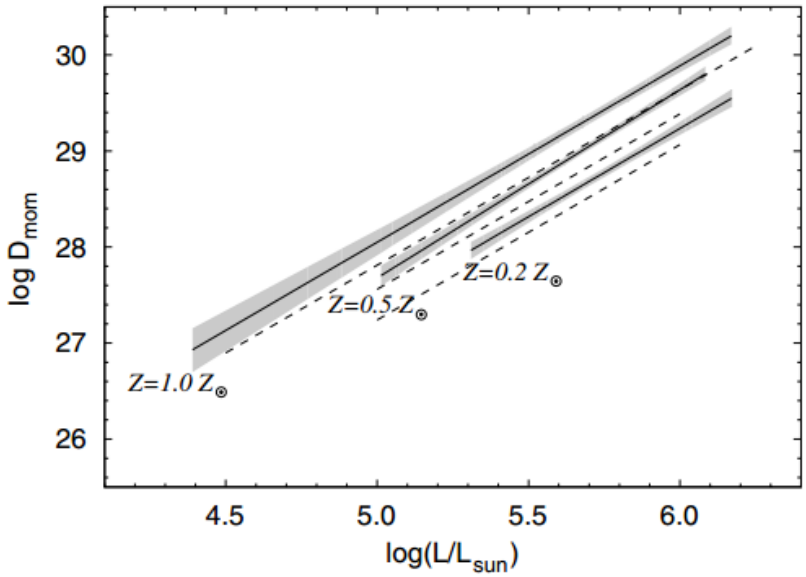

Figure 1.18: Empirical wind momenta ($D_{mom} = \dot{M} v_\infty R_\star^{0.5}$) of Galactic, LMC, and SMC stars (top to bottom, solid lines), compared to theoretical predictions of Vink et al. (2001) (dashed lines). Mass-loss rates are not corrected for clumping. Taken from Mokiem et al. (2007).

line-drivers in the inner subsonic wind, while CNO take over in the outer supersonic part (Puls et al., 2000; Vink et al., 2000). For this reason, WC stars are expected to show a weaker mass-loss increase with nascent metallicity, as they are heavily self-enriched with C & O. Weaker mass-loss rates are indeed observed in LMC WC stars by Crowther et al. (2002). A decrease of wind density with metallicity goes some way to explaining the prevalence of early-spectral types at low metallicity. Weaker winds are more transparent to ionising radiation, and less prone to recombination, hence a higher ionisation balance can be maintained throughout the wind.

It remains a challenge to explain the strength of WR winds by radiation pressure alone. The metallicity dependence of WR winds is evidence for line-driven winds, as opposed to alternative structural origins such as vibrational instability (Maeder, 1980) and pulsations (Scuflaire & Noels, 1986). Monte-Carlo simulations including multiple scattering have consistently failed to provide sufficient driving in the inner winds of WR stars (Lucy & Abbott, 1993; Springmann, 1994). However, the analytical study of Nugis & Lamers (2002) found that the opacity peak due to Fe at 160 kK can produce observed WR mass-loss rates, and (Gräfener & Hamann, 2005) established that highly ionised Fe ions (Fe IX–XVII) provide the necessary opacity to initiate the wind of WC5 star WR 111.

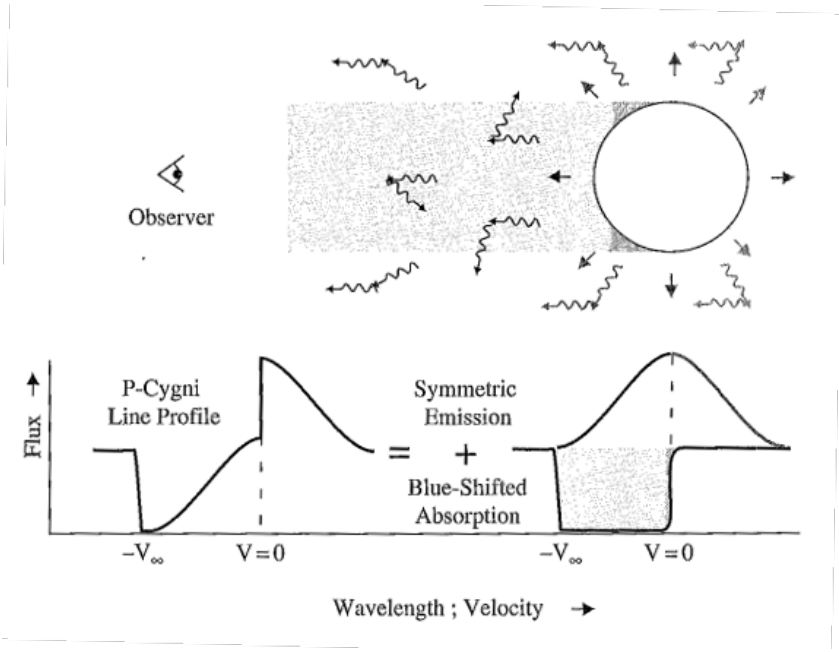

Figure 1.19: Schematic showing the formation of a P Cygni line profile in a stellar wind. Taken from Conti et al. (2008).

Mass-loss measurements and the impact of inhomogeneous winds

Wind solutions discussed thus far - the CAK theory and Monte-Carlo schemes - all describe spherically symmetric homogeneous outflows. Until recently, most measurements of stellar winds were based on this assumption. Returning to Equation 1.7, a measurement of stellar mass-loss requires a knowledge of both wind density and velocity.

Emission line profiles give a measure of v_∞ in WR stars. The most readily observable emission lines in WR spectra - optical/IR recombination lines - are formed over large and varied radial extensions, and hence velocities, so that their widths do not give an accurate measurement of v_∞ without the assumption of a velocity law. UV P Cygni profiles provide a direct measure of v_∞ (Prinja et al., 1990). Such profiles, illustrated in Figure 1.19, typically arise from resonance transitions of ions such as SIV and CIV. Outflowing material in a column towards the observer causes blueshifted absorption in these lines. In addition, photons scattered back towards the observer from either side of this column create a symmetric emission profile, which together with the absorption component creates an asymmetric profile. Alternatively, far-IR fine structure lines such as [NeIII]15.5 μm are formed at very low densities and large radii, where the terminal velocity has been reached, and hence their line widths directly correspond to v_∞ (e.g., Barlow et al. 1988, see also Section 4.3.2).

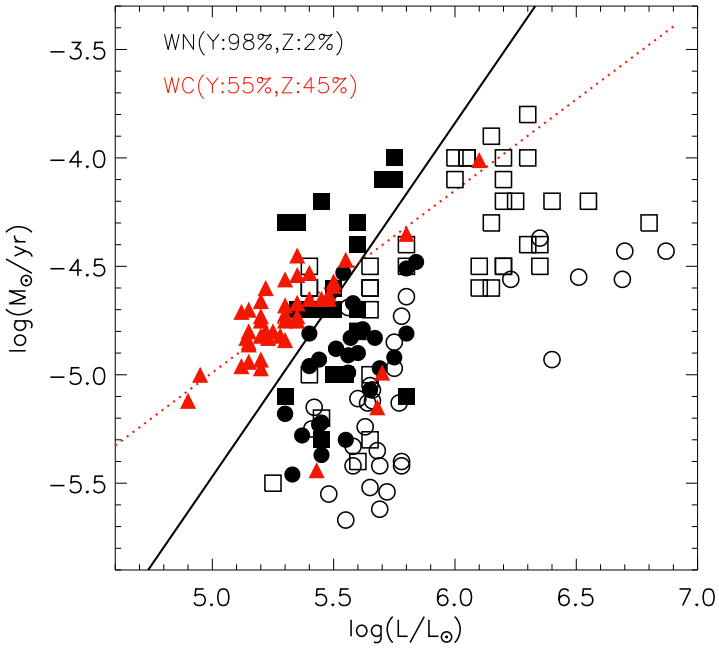

Figure 1.20: Mass-loss rates versus luminosity for Galactic WC stars (red triangles; Sander et al. 2012), Galactic WN stars (black squares; filled WNE, open WNL; Hamann et al. 2006), and LMC WN stars (black circles; filled WNE, open WNL; Hainich et al. 2014). Lines show the empirical $\dot{M}(L, Y, Z)$ relation of Nugis & Lamers (2000), for typical Galactic WC (red dotted) and H-free WN (black solid) abundances.

One of the most direct measures of wind density is free-free emission from electrons in the outer wind, detectable at IR and radio wavelengths. Simple analytic relations reveal that continuum flux, S_ν, in a spherical, isothermal envelope expanding at v_∞, scales with ν^α, where $\alpha \simeq 0.6$. The emergent flux is then set by the mass-loss, distance to the star, and terminal velocity. The strength of optical/IR recombination lines (most commonly Hα) can also be used to gauge wind density (Lamers & Leitherer, 1993). Since the physical origin of emission from both recombination and free-free processes is the collision of two particles, both diagnostics are proportional to the square of density (ρ^2). The strength of P Cygni absorption features can also probe wind density (Puls et al., 2008), and this method is linearly proportional to density.

Measured mass-loss rates using ρ^2 and ρ diagnostics will only give consistent values if winds are homogeneous. This is essentially because $\langle\rho^2\rangle \neq \langle\rho\rangle^2$ in a wind comprised of clumpy material. There is indeed substantial evidence for clumping in hot star winds. Analyses of WR spectra as early as Hillier (1991) found electron scattering wings ($\propto \rho$) were overestimated compared to line centres ($\propto \rho^2$). Shocks embedded in the wind, re-

sulting from collisions between slow moving overdense clumps and fast rarefied material, are currently the leading explanation for soft X-rays detected from hot stars. The most likely physical origin for these clumps in an instability in the line-driving process (Owocki et al., 1988). An inconsistency between mass-loss diagnostics in O-stars was highlighted by Fullerton et al. (2006), suggesting that ρ^2-derived mass-loss rates may need to be reduced by a factor of up to 10 to correct for clumping. More moderate reductions of a factor of ~ 3 are required by Bouret et al. (2005) for early O-stars.

The reduction in empirical O-star mass-loss rates caused by clumping have led Smith (2014) to call for a reduction of mass-loss rates applied to models of stellar evolution on the MS (i.e., the Vink et al. prescription). Empirical mass-loss relations for WR stars (Nugis & Lamers, 2000), routinely applied to models of stellar evolution, are in reasonable agreement with recent clumping-corrected mass-loss rates (cf. Crowther 2007). In Figure 1.20 I compare measured mass-loss rates for Galactic and LMC WR stars to the empirical relation of Nugis & Lamers (2000).

1.4.2 Analysis of WR atmospheres

Determining the physical properties of WR stars, such as effective temperature T_{eff}, stellar luminosity (L), chemical abundances, and wind parameters, requires detailed modelling of the emergent spectral energy distribution and absorption/emission features. Modelling the state of gasses constituting a Wolf-Rayet atmosphere, with the goal of creating a synthetic spectrum, is a task littered with complexities. For cooler stars like the Sun, the assumption of local thermal equilibrium (LTE) can be applied to the gasses in their photospheres; in which case, the equilibrium relations of statistical mechanics and thermodynamics yield occupation numbers for bound and free energy levels based solely on the *local* temperature and density. For hot stars like WRs, however, radiative transitions dominate the state of the gas. Consequently, the simplifying assumption of LTE in invalid, and the equations of statistical equilibrium must be used to calculate energy level occupation numbers (as described by Mihalas 1978). The solution of the equations of statistical equilibrium is an iterative process, as the radiation field is dependent on these populations, which in turn rely on the radiation field.

A further complication arises from the extended nature of WR atmospheres compared to their O-star precursors. WR radii are characterised by $R_\star$, where the Rosseland optical depth is high ($\tau_{Ross} = 10$–100). Observed optical continuum radiation is emitted from larger stellar radii ($R_{2/3}$) where the Rosseland optical depth, $\tau_{Ross} = 2/3$. The separation between $R_{\frac{2}{3}}$ and the inner boundary of the atmosphere ($R_\star$), is comparable to the stellar

radius itself, prohibiting simplification of the radiative transfer equation by the commonly applied plane-parallel approximation (Gray, 2005).

The quantitative analysis of WR atmospheres requires extremely complex model atoms, which can be computationally demanding. This problem is alleviated by grouping together atomic levels with similar energies and properties in to a 'super-level' (Anderson, 1989). This allows the population of an individual atomic level to be calculated assuming it has the same departure coefficient (from LTE) as the super-level to which it belongs. The simplification brought about by this approach allows thousands of individual levels to be reduced to hundreds, allowing the inclusion of highly complex Fe atoms with millions of transitions, which have a profound effect on the radiation field throughout the atmosphere - known as 'line-blanketing'.

Two codes well-suited to modelling WR atmospheres are in common usage: `PoWR` (Hamann & Schmutz, 1987; Gräfener et al., 2002) and `CMFGEN` (Hillier, 1987; Hillier & Miller, 1998). Both codes solve the radiative transfer equation in the co-moving frame, subject to statistical and radiative equilibrium, assuming an expanding spherically symmetric atmosphere. Both have also been updated to account for line-blanketing by the super-level approach, and include an approximation to clumped winds. Wind clumping is parameterised by a volume-filling factor, whereby a fraction (f) of the stellar wind is occupied by clumps, which are separated by voids. Alternatively, a clumping factor, $D_{cl} = 1/f$, is sometimes quoted. Values of $f \sim 0.05$–0.25 generally provide adequate fits to line profiles of stars with strong winds (Hillier & Miller, 1999; Dessart et al., 2000; Crowther et al., 2002; Hillier et al., 2003).

Typical parameters and disagreement with theory

The physical parameters derived by spectral analyses of WR stars are summarised by Crowther (2007), and in Table 1.2 I show typical values by subtype. I have touched upon many of the key parameters of WR stars throughout this section. In the remainder I will highlight some important trends and challenges.

The measured luminosities of H-free WN, and WC stars fall consistently below the predictions from single-star evolutionary models (see Figure 1.15). This is observed in large samples not only in the Galaxy (Hamann et al., 2006; Sander et al., 2012), where distance uncertainties are large, but also in the LMC (Hainich et al., 2014) which has a well-known distance. I discuss this problem further in Section 5.4.3, in relation to the WR stars in Galactic cluster Westerlund 1.

Widespread acknowledgement of inhomogeneous winds in WR stars has brought the

Table 1.2: Typical parameters of Galactic WR stars by subtype. Data are taken from Herald et al. (2001) and Hamann et al. (2006) for WN stars; and Sander et al. (2012), Tramper et al. (2015, in prep), and Williams et al. (2015) for WO and WC stars.

Sp. type	$T_\star$(kK)	$\log(L/L_\odot)$	$\log\left(\dot{M}(M_\odot yr^{-1})\right)$	$v_\infty(\mathrm{kms}^{-1})$	M_v
			WN		
3	85	5.34	-5.3	2200	-3.1
4b	85	5.3	-4.9	1800	-4.0
5	60	5.2	-5.2	1500	-4.0
6b	70	5.2	-4.8	1800	-4.1
7	50	5.54	-4.8	1300	-5.4
8	45	5.38	-4.7	1000	-5.5
9	32	5.7	-4.8	700	-6.7
6ha	45	6.18	-5.0	2500	-6.8
9ha	35	5.86	-4.8	1300	-7.1
			WC & WO		
WO	170	5.4	-5.0	5000	-2.8
5	83	5.3	-4.62	2800	-3.6
6	78	5.5	-4.61	2300	-3.6
7	71	5.3	-4.8	2000	-4.5
8	60	5.3	-4.8	1800	-4.0
9	40	5.0	-5.0	1000	-4.6

clumping factor (f) to the fore in determining mass-loss rates. Typical f values of 0.05–0.25 cause a factor of 2–4 reduction in $\dot{M}$ relative to homogeneous wind models ($\dot{M} \propto f^{-1/2}$). Any resulting reduction in the mass-loss rates assumed by stellar models, as proposed by Smith (2014), would only worsen the aforementioned luminosity problem, by predicting more massive and hence luminous WR stars. Indeed, evolutionary models with artificially *enhanced* mass-loss rates have previously been proposed to account for low-luminosity WNE and WC stars (Meynet et al., 1994), which can now be ruled out. During the WR phases, models of stellar evolution adopt mass-loss rates dictated by empirical relations based on luminosity and chemical composition (Nugis & Lamers, 2000). Clumping-corrected mass-loss rates from spectroscopic analyses are required to thoroughly test the adequacy of these relations.

The temperatures of WR stars are measured by modelling the intensity ratios of adjacent ionisation stages of a particular element (typically HeII/HeI in WN, and CIV/CIII/CII in WC). However, due to the extension of WR atmospheres, these spectral features originate from layers well above the hydrostatic domain - typically where temperatures are defined in stellar models. WR temperatures, $T_\star$, must therefore defined at (unobservable) radii, where the optical depth is high ($R_\star$), for meaningful comparisons to models. This relies on an assumption that the same velocity law holds throughout the wind. Differences between $R_\star$ and $R_{2/3}$ can be extreme when the stellar wind is strong. For example, in HD 50896 (WN4b), $R_\star = 2.9\,R_\odot$ and $R_{2/3} = 7.7\,R_\odot$, corresponding to $T_\star = 85\,\mathrm{kK}$ and $T_{2/3} = 52\,\mathrm{kK}$ (Morris et al., 2004). Differences in weak-lined WN stars are less extreme, as $R_\star \sim R_{2/3}$.

Furthermore, temperatures and mass-loss rates must be derived simultaneously using non-LTE atmosphere codes, due to the highly stratified winds of WR stars. This is because an increase in mass-loss rate would raise wind density, leading to more efficient recombination from high to low ionisation stages, thus affecting the ionisation-based temperature diagnostics. In Figure 1.21 I show the predicted wind structure of a WC8 star as a function of radius.

Values of $R_\star$ derived by spectroscopic analysis (Table 1.2) are consistently an order of magnitude higher than radii predicted by stellar structure models for H-free WR stars (e.g., Schaerer & Maeder 1992). Consequently, a comparison between the measured $T_\star$ and T_{eff} predicted by evolutionary models (at the hydrostatic surface) is not straightforward. To explain this radius discrepancy, it has been proposed that some WR stars close to the Eddington limit consist of a small hydrostatic core within an 'inflated' sub-photospheric envelope - the so-called "core-halo" model (Ishii et al., 1999; Petrovic

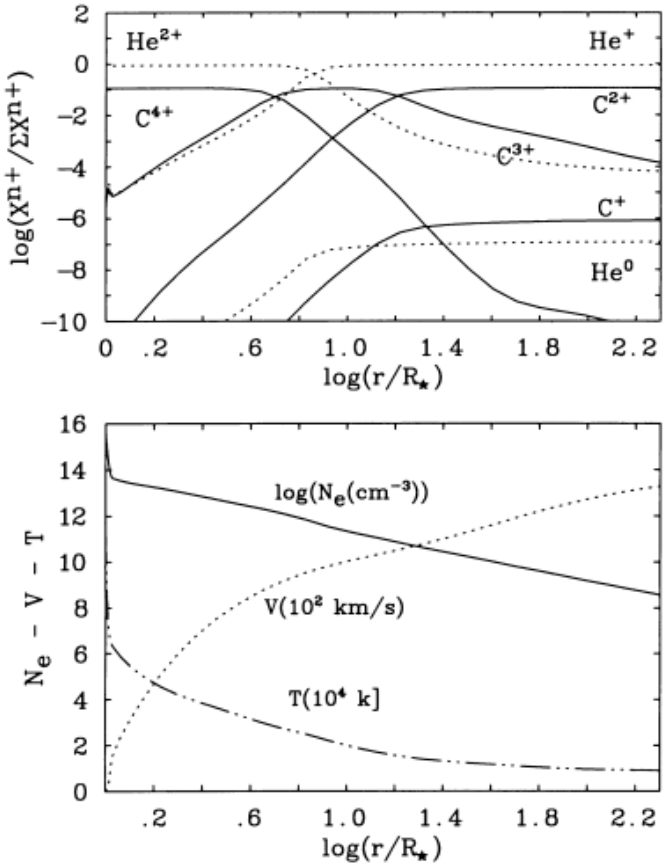

Figure 1.21: Stellar wind structure as a function of radius given by a extttCMFGEN model for a WC8 star (WR 135). *(Top)* Wind ionisation stratification showing carbon (solid) and helium (dotted). Note, $R_{2/3}$ occurs at several $R_\star$. *(Bottom)* Electron density (N_e, solid), wind velocity (v, dotted), and temperature (T, dot-dashed). Taken from (Dessart et al., 2000).

et al., 2006). Consequently, hydrostatic cores may be smaller and hotter than derived from atmosphere analyses. Such a scenario would also alleviate the radius problem in WR stars. Gräfener et al. (2012) have recently shown that envelope inflation may not restricted to high-L H-rich WR stars, but may occur in H-free WR stars, or in a lower mass regime if the clumping factor of the wind is high enough.

1.5 Motivations

IR surveys are rapidly revealing the full extent of the Galactic WR population - the largest *spatially resolved* population of WR stars. In Section 1.3 I explained how mapping the distribution of these stars, and extrapolating the observed population to estimate a total, can constrain models of stellar evolution. The most applicable method of measuring distances to a single WR stars uses absolute magnitude-spectral subtype calibrations. However, spectral classification currently relies on optical diagnostics, which are unavailable for the newly discovered population. An IR classification scheme is therefore required, in order to fully exploit the large number statistics of the Galaxy. For example, the relative lifetimes - and hence numbers - of WC to WN stars predicted by stellar models with and without rotation differ significantly. As it is not possible to measure the rotation rates of WR stars directly, this subtype ratio gauges the the importance of stellar rotation in creating WR stars. In Chapter 2, I develop an improved quantitative near-IR classification scheme, and use this to calibrate the absolute magnitudes of WR stars, using the large numbers that reside in obscured clusters. I go on to map the distribution of WR stars in the Galaxy, and compare their relative numbers to the predictions of stellar evolution models. I use the observed distribution to inform a model of the Galactic WR population, in Chapter 3, which is used to make predictions relevant to future surveys.

In Section 1.3 I also described how non-LTE model atmospheres have become the primary tool for measuring chemical abundances in WR atmospheres. Spectral analyses have delivered accurate H, He, N & C abundances in subtypes with these present. The surface C/O ratio is a key prediction of stellar models, as it is sensitive to many influential and uncertain processes in massive stars. Since WC and WO stars, by definition, show the products of Helium burning in their atmospheres, measurements of C/O can constrain nuclear reaction rates. As discussed in Section 1.2.1, the C/O ratio in the stellar core is determined by competition between 3–α and $^{12}\mathrm{C}(\alpha,\gamma)^{16}\mathrm{O}$, but latter reaction rate is very uncertain. It is the combined action of internal chemical mixing

and mass-loss that exposes these products on the stellar surface, making C/O a probe of these processes also. Carbon abundances are well-known in WC and WO stars. The same cannot be said for oxygen, as O features in UV-IR spectra are often more sensitive to ionisation than abundance. Fine-structure lines of Oxygen, such as [OIV] 25.9μm, [OIII] 51.81μm, & [OIII] 88.36μm offer less model-dependant abundances. Yet, due to the need for space-borne instrumentation, these have only been observed in a handful of objects. In Chapter 4 I present Herschel PACS observations of [OIII] 88.36μm in 7 WC/WO stars, significantly increasing the sample with accurate C and O measurements.

The Conti scenario, outlined in Section 1.3, provides a natural explanation for the WR phenomenon, and is supported by models of stars evolving in isolation (Section 1.2.1). Analysis of the Galactic field population has partially validated this scenario, yet, as discussed in Section 1.3.2, some WR types occupy unexpected regions of the H-R diagram, with no clear progenitors or progeny. Two important mechanisms are currently absent from the standard view of massive star evolution; *i*) irregular/eruptive mass-loss in single stars, and *ii*) binary interactions (Section 1.2.2). Inclusion of these in a quantitative manner is challenging, as the frequency of such events - amongst other things - is uncertain. While analysis of large populations of massive stars is useful, there is a need for detailed analyses of single-age populations at known distances. These provide a snapshot of stellar evolution, whereby the presence or absence of specific stellar types may rule out evolutionary pathways that appear plausible from multiple-age populations. Furthermore, the luminosities of H-free WR stars at a particular age provides a tight constraint on their mass-loss history, given the theoretical M–L relation. The Galactic cluster Wd1 contains the largest known co-eval WR population, which I analyse in Chapter 5.

Chapter 2

The distribution of Galactic Wolf-Rayet stars from infra-red surveys

The majority of the work presented in this chapter has been published in Rosslowe & Crowther (2015b).

Systematic testing of the theoretical predictions of massive star evolution requires statistically large, unbiased samples of massive stars. In the case of WR stars, such a sample is only currently available in the Galactic disk. However, as Galactic WR discoveries progress to greater distances and higher extinctions, optical methods are ineffective. This is presently the case, as fewer than 5% of WR stars discovered since and including the survey of Shara et al. (2009) have published spectra short-ward of 1 μm. These developments also limit the usefulness of v-band absolute magnitude-subtype calibrations (van der Hucht, 2001) for determining distances to WR stars. It is apparent that improved IR tools are necessary to characterise the full Galactic WR population, allowing accurate distances and classifications to be obtained.

In this chapter I begin in Section 2.1 by developing a refined near-IR classification scheme for WR stars, building on the work of Crowther et al. (2006b). In Section 2.2 I present a sample of Galactic WR at known distances - mostly by cluster membership - for which I review spectral types and compute a new calibration of near-IR absolute magnitudes for each WR subtype. I use these calibrations to map the majority of the remianing population in Section 2.3, allowing the distribution of subtypes to be assessed across the Galactic metallicity gradient and comparisons to be made with theoretical

population synthesis. Finally, in Section 2.4 I describe an observing campaign of spectroscopic follow-up of IR-selected WR star candidates in the Galactic plane.

2.1 Spectral classification of WR stars at infra-red wavelengths

Crowther et al. (2006b) presented a rudimentary WR classification scheme based on near-IR emission line ratios, designed to be consistent with optical methods. Here I present a more detailed investigation into the potential of near-IR diagnostics for WR classification.

2.1.1 Spectroscopic data and line measurements

I primarily used a set of 29 IRTF SpeX[1] 1–5μmspectra of WR stars (Vacca, priv. comm) to refine near-IR classification diagnostics. This is presented in Table 2.1, and consisted of 16 WN of all ionisation classes, 10 WC of all ionisation classes, 1 WO and 2 WN/C stars. All stars have robust optical classifications by the schemes of Smith et al. (1996) (for WN) or Crowther et al. (1998) (for WC).

I used line equivalent width (W_λ) as a measure of emission-line strength, contrary to Smith et al. (1996) who use line peaks. This was possible due to the relative sparsity of emission lines at IR compared to optical wavelengths, meaning line blending was less of an issue. I used line peak height ratios in some cases where lines of interest fall close together, e.g., CIV 1.191μm and CIII 1.199μm, to limit the effects of line blending. Peak heights were measured in continuum units, where the continuum level is equal to 1. All line strengths I discuss here are measured in W_λ unless stated.

I measured W_λ and line width (FWHM) using the `elf` routines in the `Starlink DIPSO` software package[2]. Emission lines were fitted with Gaussian profiles, after spectra had been rectified by dividing by a polynomial fit to the continuum. A single Gaussian profile provided a satisfactory fit to all emission lines, except the flat-topped HeI 1.083μm triplet in stars with broad lines (WN#b), where three closely spaced Gaussian profiles provided a more appropriate fit. In these cases I summed W_λ over the three profiles and measured FWHM by eye.

I initially used the IRTF spectra to define a set of classification diagnostics in each

[1] SpeX, medium-resolution spectrograph on the NASA Infra-Red Telescope Facility
[2] `http://www.starlink.rl.ac.uk/docs/sun50.htx/sun50.html`

near-IR band, consistent with optical diagnostics. I then carried out blind tests of these diagnostics using lower-quality IR spectra of other WR stars with optical classifications. I show this test sample in Table 2.2. These blind tests revealed several degeneracies between subtypes that were not apparent using the smaller, high-quality IRTF sample. This allowed me to refine the boundaries between subtypes, and assess the accuracy of specific diagnostics. All line measurements used to construct the present near-IR classification scheme, for both IRTF and test samples, are given in Appendix A.

Table 2.1: Summary of WR stars primarily used to refine near-IR classification diagnostics. All IRTF/SpeX spectra were provided by W. Vacca. Line measurements based on these spectra are given in Appendix A.

WR#	Sp. Type	Telescope/Instrument	Range (μm)
106	WC9d	IRTF/SpeX	1–5
119	WC9d	IRTF/SpeX	1–5
121	WC9d	IRTF/SpeX	1–5
135	WC8	IRTF/SpeX	1–5
137	WC7pd+O9	IRTF/SpeX	1–5
140	WC7pd+O4–5	IRTF/SpeX	1–5
5	WC6	IRTF/SpeX	1–5
154	WC6	IRTF/SpeX	1–5
146	WC4–6	IRTF/SpeX	1–5
111	WC5	IRTF/SpeX	1–5
142	WO2	IRTF/SpeX	1–5
105	WN9h	IRTF/SpeX	1–5
108	WN9ha	IRTF/SpeX	1–5
116	WN8h	IRTF/SpeX	1–5
123	WN8o	IRTF/SpeX	1–5
130	WN8(h)	IRTF/SpeX	1–5
158	WN7h	IRTF/SpeX	1–5
145	WN7/C	IRTF/SpeX	1–5
134	WN6b	IRTF/SpeX	1–5
136	WN6b(h)	IRTF/SpeX	1–5
138	WN6o	IRTF/SpeX	1–5
153	WN6/C+O6I	IRTF/SpeX	1–5
155	WN6o+O9II–Ib	IRTF/SpeX	1–5
133	WN5o+O9I	IRTF/SpeX	1–5
157	WN5o+?	IRTF/SpeX	1–5
1	WN4b	IRTF/SpeX	1–5
6	WN4b	IRTF/SpeX	1–5
3	WN3ha	IRTF/SpeX	1–5
2	WN2b	IRTF/SpeX	1–5

Table 2.2: Summary of 'test sample'. All NTT/SOFI spectra were provided by N. Homeier. Line measurements based on these spectra are given in Appendix A.

WR#	Sp. Type	Telescope/Instrument	Range (μm)
103	WC9d	NTT/SOFI	1.6–2.4
57	WC8	NTT/SOFI	0.98–1.60
60	WC8	NTT/SOFI	0.98–2.4
56	WC7	NTT/SOFI	0.98–1.60
64	WC7	NTT/SOFI	0.98–1.60
90	WC7	NTT/SOFI	0.98–2.4
107a	WC6	NTT/SOFI	0.98–1.60
4	WC5+?	NTT/SOFI	1.6–2.4
52	WC4	NTT/SOFI	0.98–2.4
143	WC4+?	NTT/SOFI	1.6–2.4
16	WN8h	NTT/SOFI	1.6–2.4
40	WN8h	NTT/SOFI	1.6–2.4
66	WN8h	NTT/SOFI	0.98–1.60
82	WN8(h)	NTT/SOFI	0.98–1.60
22	WN7ha	NTT/SOFI	1.6–2.4
55	WN7o	NTT/SOFI	0.98–1.60
78	WN7h	NTT/SOFI	1.6–2.4
84	WN7o	NTT/SOFI	0.98–1.60
120	WN7o	NTT/SOFI	1.6–2.4
131	WN7h	NTT/SOFI	1.6–2.4
24	WN6ha	NTT/SOFI	1.6–2.4
25	WN6ha	NTT/SOFI	1.6–2.4
68a	WN6o	NTT/SOFI	0.98–1.60
115	WN6o	NTT/SOFI	1.6–2.4
75	WN6b	NTT/SOFI	0.98–1.60
110	WN5–6b	NTT/SOFI	0.98–1.60
54	WN5o	NTT/SOFI	0.98–1.60
61	WN5o	NTT/SOFI	0.98–1.60
83	WN5o	NTT/SOFI	0.98–1.60
62a	WN4–5o	NTT/SOFI	0.98–1.60
128	WN4(h)	NTT/SOFI	1.6–2.4
93a	WN2.5–3o	NTT/SOFI	0.98–1.60

2.1.2 WN star classification

The strongest emission lines in the near-IR spectrum of a WN star are those of HeI and HeII, these therefore provide primary ionisation diagnostics, with weaker nitrogen features providing secondary information. Near-IR hydrogen features are relatively weak,

but in each spectral region (YJHKLM) I have attempted to identify features that indicate the presence of hydrogen, in a similar manner to Smith et al. (1996). In each band I also identify a HeII line suitable for classifying broad-line WN. Classification diagnostics are summarised in Table 2.3.

Y & J-bands

It has been shown by Vreux et al. (1990), and more recently Crowther et al. (2006b), that
HeII 1.012μm/HeI 1.083μm can discriminate WN subtypes. The proximity of these lines is also advantageous, as they are not affected by wavelength-dependent line dilution, i.e, from a companion star. I therefore employed this as the primary ionisation diagnostic, and show values of this ratio versus FWHM HeII 1.012μm in Figure 2.1 for WN4–9 subtypes. Subtypes WN8, WN7, WN6 and WN5 overlap in this ratio, but some ranges are unique to one subtype. HeI 1.083μm is not present in the only WN3 (WR 3) in the IRTF or test samples. Figure 2.1 includes stars WR 110 and WR 62a from the test sample, however these are not considered when quantifying the ranges of values in HeII 1.012μm/HeI 1.083μm (Table 2.3) as they have atypical optical classifications of WN5–6b and WN4–5o respectively.

Some subtypes have overlapping values in the primary diagnostic, but may be discriminated using secondary information. I found it possible to separate WN8 and WN9 stars using the SiIV 1.1904μm line, which is stronger with respect to the nearby HeII 1.163μm line in WN9 stars (see Table 2.3). I found the degeneracy in primary diagnostic between narrow-line WN4 and WN6 subtypes can be lifted using NV 1.111μm, which is present in the former only. However, broad-line WN4b and 6b subtypes have near identical spectra in this region, both showing NV 1.111μm. I found no quantifiable way of discriminating these subtypes.

I attempted to quantify a diagnostic for the presence of Hydrogen in WN stars, by comparing the strength of Hydrogen and Helium emission lines. Numerous Hydrogen lines are present in this spectral region, most notably Pa δ 1.005μm and the blend Pa β+HeII 1.2812–1.2818μm. The sample of WN stars available contained WN7 and WN8 stars with and without Hydrogen according to their optical classifications. In Table 2.4 I show measurements of Pa δ+HeII 1.2812–1.2818μm/HeII 1.163μm and Pa δ/HeII 1.012μm. Peak heights (in continuum units) were used to measure the latter ratio, due to the proximity of the lines. It can be seen that in WN7 and WN8 subtypes, H-rich 'h' stars show significantly higher values in both ratios, but stars showing less

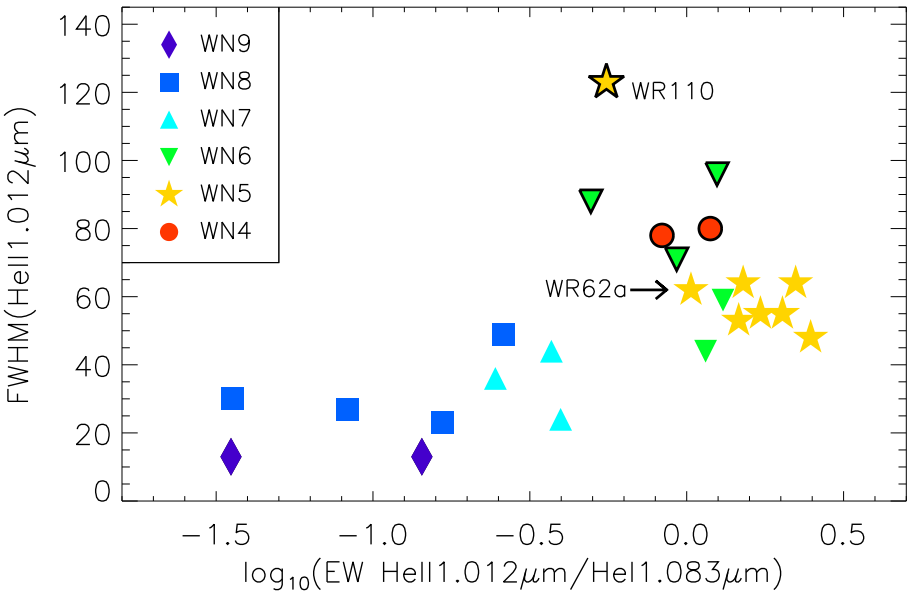

Figure 2.1: The primary Y & J-band classification diagnostics for WN stars, He II 1.012μm / He I 1.083μm, against FWHM He II 1.012μm. Errors are smaller than or of the same order as symbol sizes. Broad-line stars are indicated by a black symbol outline. Symbols representing stars with uncertain optical classifications (WR 110 and 62a) are labelled. The stars shown are drawn from the IRTF and test samples (line measurements given in Appendix A).

obvious optical Hydrogen signatures (the '(h)' stars) do not follow a clear trend.

He II 1.012μm or He II 1.163μm act as adequate broad-line diagnostics, with a FWHM threshold of 70Å.

Table 2.3: Summary of quantitative near-IR classification diagnostics for WN stars. All line ratios are calculated using line W_λ, unless 'peak' is indicated for line peak values. Ranges shown in bold give a definitive classification.

subtype	HeII 1.012μm/ HeI 1.083μm	SiIV 1.1904μm/ HeII 1.163μm	HeII 2.189μm/ HeII+Brγ 2.165–2.166μm	peak NV 2.099μm/ HeI+HeII+NIV 2.11–2.12μm
WN9	<0.14	$>$ **0.55**	<0.25	
WN8	0.04–**0.14**–**0.25**	**0.10**–**0.55**	<0.25	
WN7	**0.25**–**0.50**	<0.10	**0.25**–**0.72**	
WN6	**0.50**–**0.83**–1.30		0.72–**0.95**–**1.38**–2.50	**0.91**–**0.95**
WN5	$>$ **1.30**		>1.38	**0.95**–**1.01**
WN4	0.83–1.19		>1.72	$>$ **1.01**
		HeII+NV 3.545μm/ HeII+Pfγ 3.740μm	HeII 4.765μm/ HeII+Pfβ 4.653μm	
WN9		$<$ **0.05**	$<$ **0.10**	
WN8		**0.05**–**0.19**	**0.10**–**0.37**–0.50	
WN7		**0.19**–**0.68**–0.73	0.37–**0.50**–**2.12**	
WN6		0.68–1.40	**2.12**–**2.68**–4.48	
WN5		0.79–1.62	2.68–4.77	
WN4		1.53–**1.62**–**1.71**	4.72–4.77, $>$ **4.77**	

Table 2.4: Summary of potential Hydrogen diagnostics for WN7–8 stars.

WR#	subtype	$W_\lambda \frac{\text{Pa}\,\beta+\text{HeII}\,1.2812-1.2818\mu\text{m}}{\text{HeII}\,1.163\mu\text{m}}$	peak $\frac{\text{Pa}\,\delta}{\text{HeII}\,1.012\mu\text{m}}$
55	WN7o	0.93	0.41
84	WN7o	0.70	0.34
82	WN7(h)	2.28	0.69
158	WN7h	2.18	0.66
123	WN8o	3.47	0.60
130	WN8(h)	2.50	0.56
66	WN8(h)	1.45	0.61
116	WN8h	10.40	0.97

H-band

The H-band is of limited use for WN classification due to the lack of a single strong HeI emission line. The strongest HeI line (HeI 1.700μm) is highly crowded amongst other strong lines in the 1.67–1.71μm region. To overcome the crowding in this region I explored the potential of emission line peak ratios as ionisation diagnostics. Spectral morphology readily distinguishes WN9 subtypes, as HeII 1.692μm is very weak or absent and HeI 1.700μm dominates. Using the peak ratio of these two lines, it is only possible to separate WN8–3 into early and late-type WN. Several high lines in the hydrogen Brackett series are present in the H-band, but these features are too weak - even in H-rich WN stars - to be used as quantitative hydrogen diagnostics. HeII 1.692μm is an adequate broad-line diagnostic with a FWHM threshold of $\sim$120Å.

K-band

Following Crowther et al. (2006b) I employed the ratio HeII 2.189μm/HeII+Brγ 2.165–2.166μm as the primary K-band ionisation diagnostic. I plot values of this versus FWHM HeII 2.189μm in Figure 2.2 for WN4–9 subtypes. It can be seen that WN stars may be classified into WN9–8, WN7 and WN6–4 subtypes by this ratio alone.

Once again, I found WN8 and WN9 stars to be degenerate in the primary ionisation diagnostic. However, the WN9 showing the highest value in the primary diagnostic - indicative of a higher ionisation - is WR 105, which displays very weak HeII 2.189μm. Weak HeII is a distinguishing feature of WN9 stars. The degeneracy between WN8 and WN9 is caused by varying amounts of hydrogen contributing to Brγ, as these subtypes are almost universally H-rich. Based on the two WN9 stars available, I found W_λ

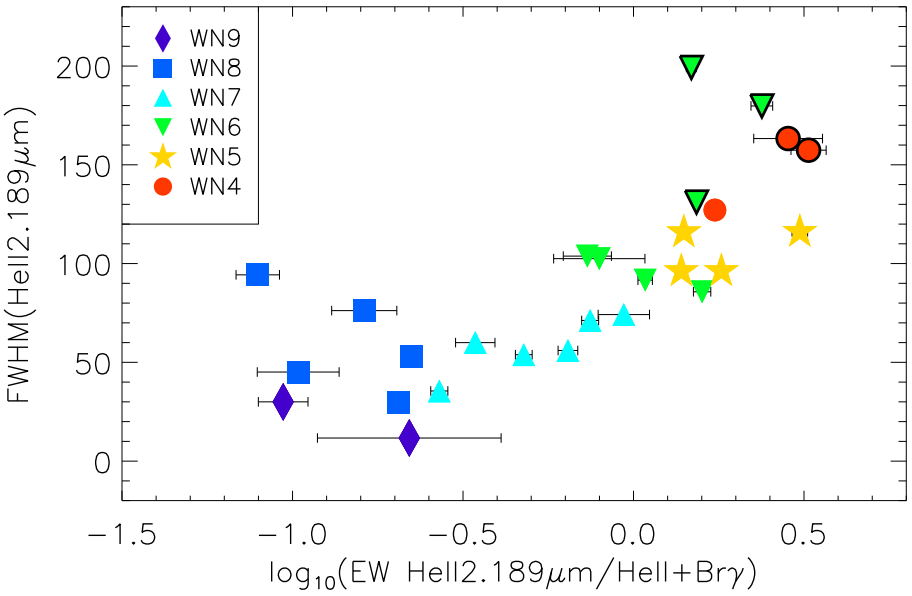

Figure 2.2: The primary K-band classification diagnostic for WN stars, HeII+Brγ 2.165–2.166μm / HeII 2.189μm, against FWHM HeII 2.189μm. Broad-line stars are indicated by a black symbol outline. Error bars represent uncertainties from the Gaussian fitting process, generated by `DIPSO elf`. All stars shown are drawn from the IRTF and test samples (line measurements given in Appendix A).

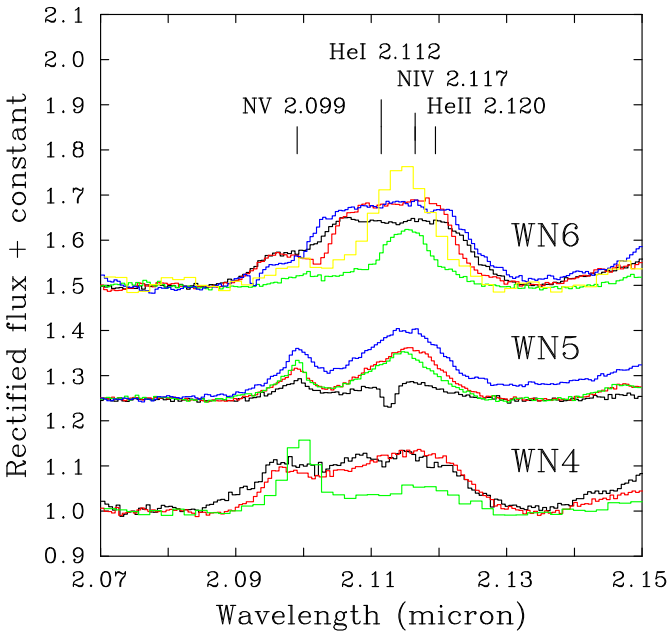

Figure 2.3: Spectral morphology of WN4–6 over the region where these subtypes may be distinguished. Subtypes are offset vertically, with individual stars plotted in different colours.

HeII 2.189μm $<$ 7Å for WN9 stars. In addition to this, the HeII 2.189μm line shows signs of absorption, which given the lack of evidence for a bright OB star companion to WR 108 or WR 105 must be intrinsic to the WN9 subtype. This has previously been noted for WR 108 by Crowther et al. (1995a).

I attempted to separate WN4–6 stars by inspecting the spectral morphology over 2.09–2.13μm, containing a blend of NV 2.099μm, HeI 2.112μm, NIV 2.117μm, and HeII 2.120μm. In Figure 2.3 I show the spectra of several WN4–6 stars in this region. It can be seen that NV 2.099μm is prominent in WN4 subtypes, and weakens through WN5 and WN6 subtypes as emission at $\sim$2.115μm in the form of HeI 2.112μm+NIV 2.117μm begins to dominate. As noted by Crowther et al. (2006b), we find severe blending prohibits the use of these lines for classification in broad-line WN4–6b subtypes. Line peak ratios of capable of distinguishing narrow-line WN4–6 stars are presented in Table 2.3.

The strongest hydrogen feature in the K-band is Brγ; since this forms part of the primary ionisation diagnostic, it is not possible to quantitatively identify hydrogen from K-band spectra of WN stars. HeII 2.189μm acts as an adequate broad-line diagnostic with a FWHM threshold of 130Å.

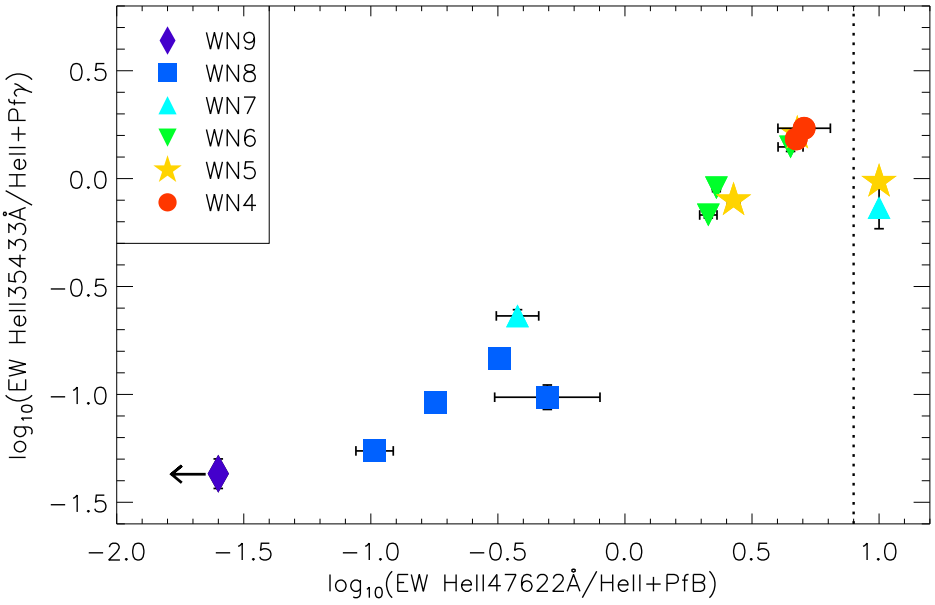

Figure 2.4: The primary L and M-band classification diagnostics for WN stars. Symbols to the right of the dotted line represent stars with only a measurement of HeII+NV 3.545μm/HeII+Pfγ 3.740μm available. Error bars represent uncertainties from the Gaussian fitting process, generated by `DIPSO elf`. All stars shown are drawn from the IRTF and test samples (line measurements given in Appendix A).

L & M-bands

At longer wavelengths, the most effective classification diagnostic is HeII+NV 3.545μm/HeII+Pfγ 3.740μm. I found this ratio capable of separating WN9, WN8, WN7, WN7–5, and WN5–4 subtypes. In Figure 2.4 I plot values of this ratio, along with the best M-band diagnostic, HeII 4.765μm/HeII+Pfβ 4.653μm. This diagnostic ratio is similar in effect to the chosen L-band diagnostic, which was expected as they both have a hydrogen contribution in the denominator. The M-band diagnostic clearly distinguishes WN9 and WN8 subtypes, with earlier types have increasingly overlapping values (Fig 2.4).

2.1.3 WC star classification

The near-IR spectra of WC stars is dominated by Carbon emission lines, with CIV prevailing in early-types and CIII and CII becoming stronger in late-types. Adjacent ionisation stages of carbon provide primary classification diagnostics, while HeII/HeI is also of use. I have avoided using line ratios of He to C, or vice versa, as these would be subject carbon abundance as well as ionisation. Classification diagnostics are summarised in Table 2.5.

The IRTF sample contains WR 146, a peculiar object classified as WC5 by Crowther et al. (1998) and WC6 by Dougherty et al. (2000). It is a visual binary system with non-thermal radio index, indicating colliding stellar winds (Niemela et al., 1998; Dougherty et al., 1996). The radio emission was resolved into several components by Dougherty et al. (2000), the relative positions of which suggest a higher than expected wind momentum for the O-type companion star, suggesting it may also harbour a WC component. In Figures 2.5, 2.6 and 2.7 of this section I show line measurements from the composite spectrum of WR 146, assuming a WC5 subtype, but do not consider these when defining the classification scheme outlined in Table 2.5.

Y & J-bands

The helium ratio HeII 1.012μm/HeI 1.083μm and carbon CIV 1.191μm/CIII 0.972μm are effective at distinguishing WC ionisation subtypes, with little overlap. However, as CIII 0.972μm suffers from lower atmospheric transparency, fewer measurements of this line were available. Notably, I did not have access to this line in WR 52 - the only WC4 star in the sample. I was therefore unable to define the boundary between WC5 and WC4 stars in this ratio. I measured another carbon ratio that proved to be effective,

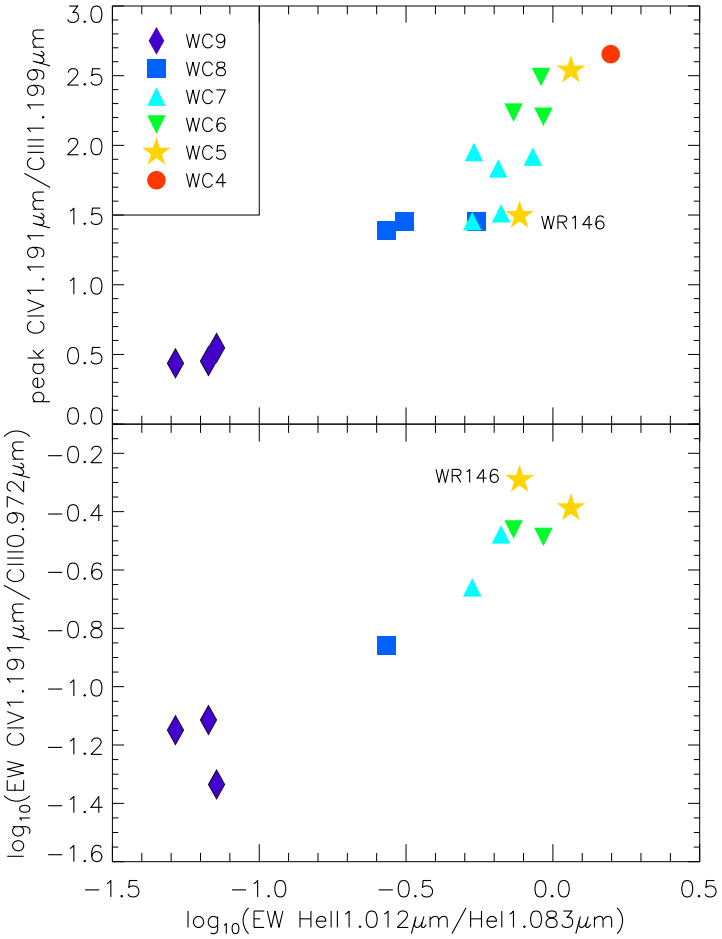

Figure 2.5: Y & J-band classification diagnostics for WC stars. The most effective helium ratio, HeII 1.012μm / HeI 1.083μm, plotted against two carbon diagnostics, CIV 1.191μm / CIII 0.972μm (lower panel) and peak CIV 1.191μm / CIII 1.199μm (upper panel). Errors are smaller than or of the same order as symbol sizes. The stars shown are drawn from the IRTF and test samples (line measurements given in Appendix A).

CIV 1.191μm/CIII 1.199μm, using line peak values to overcome blending. In Figure 2.5 I show all three diagnostic ratios discussed. The use of two diagnostics will give exact subtype, and in most cases a single ratio is sufficient.

Table 2.5: Summary of quantitative near-IR classification diagnostics for WC stars. All line ratios are calculated using line W_λ, unless 'peak' is indicated for line peak values. Ranges shown in bold give a definitive classification.

subtype	HeII 1.012μm/ HeI 1.083μm	CIV 1.191μm/ CIII 0.972μm	peak CIV 1.191μm/ CIII 1.199μm	CIV 2.070–2.084μm/ CIII+HeI 2.112–2.137μm
WC9	$<$ **0.17**	$<$ **0.11**	$<$ **0.97**	$<$ **1.46**
WC8	**0.17–0.54**–0.55	**0.11–0.18**	**0.97–1.45**–1.46	**1.46–3.23**
WC7	0.54–**0.55–0.73**–0.85	**0.18–0.33**	1.45–**1.47–2.08**	**3.23–4.00**
WC6	0.73–**0.85–1.04**	**0.33–0.38**	**2.08–2.52**	$>$ 4.80
WC5	**1.04–1.36**	$>$ 0.38	**2.52–2.60**	$>$ 4.00
WC4	$>$ **1.36**	$>$ 0.38	$>$ **2.60**	$>$ 4.00
	CIV 2.427/ CIII 2.480μm	CIV 3.281μm/ CIII+CIV+HeII 3.089–3.091μm	HeII 3.543μm/ HeII+HeI 3.737–3.738μm	
WC9	$<$**1.03**	CIV 3.281μm **absent**	HeII 3.543μm **absent**	
WC8	**1.03–2.04**	$<$ **0.36**	$<$ **0.73**	
WC7	**2.04–2.67**	**0.36–0.44**	**0.73–1.04**	
WC6	**2.67–3.31**–3.51	0.44–0.51	**1.04–1.19**–1.20	
WC5	$>$ 3.31	$>$ 0.51	$>$ 1.20	
WC4				

H-band

This spectral region contains limited diagnostic information for classification of WC stars. No single ratio of lines in this region can be used to classify WC stars. I constructed a rudimentary classification scheme, primarily based on the prominence of CII 1.785μm and OV 1.554μm in WCL and WCE respectively. Indeed, OV 1.554μm is the only line capable of quantifying a distinction between WC6–4 subtypes. The scheme is as follows:

WC9 unique in that W_λ CIV 1.736μm < CII 1.785μm,

WC8 W_λ CIV 1.736μm > CII 1.785μm and HeII 1.693μm < HeI 1.701μm,

WC7 HeII 1.693μm > HeI 1.701μm and CII 1.785μm is present.

WC6 HeII 1.693μm > HeI 1.701μm and CII 1.785μm is not present. OV 1.554μm is weak; peak OV 1.554μm/(HeII+CIII) 1.574μm < 0.92,

WC4–5 HeII 1.693μm > HeI 1.701μm and OV 1.554μm is strong; peak OV 1.554μm/(HeII+CIII) 1.574μm > 0.92

The CIV 1.736μm line is strong in all WC subtypes excluding WC9. This is the shortest wavelength line to be significantly diluted by thermal emission from circumstellar dust in some WC stars, and hence is a useful indicator of ongoing or recent dust production. The strength of this line in dust-free WC stars is given in Table A.4.

K-band

Following Crowther et al. (2006b), I used CIV 2.070–2.084μm/CIII+HeI 2.112–2.137μm as the primary classification diagnostic in this region and found it capable of separating WC9, WC8, WC7 and WC6-4 subtypes. Equally effective is CIV 2.427/CIII 2.470–2.480μm. However, this pair of carbon lines is located in a region of low atmospheric transparency, requiring a higher signal-to-noise spectrum, hence measurements are only available for WC stars in the IRTF sample. In Figure 2.6 I plot both diagnostics for all WC subtypes. I also measured of the ratio HeII 2.165μm/HeII 2.189μm and found it to be ineffective at distinguishing subtypes, unlike in WN stars where the contribution Brγ distinguishes late-types. I found no quantifiable means to distinguish WC4–6 subtypes, which are degenerate in the primary diagnostic (Fig 2.6). Dilution of The CIV 2.070–2.084μm triplet is the most conspicuous indicator of circumstellar dust in 'd' stars, as this is the strongest K-band line in late-types.

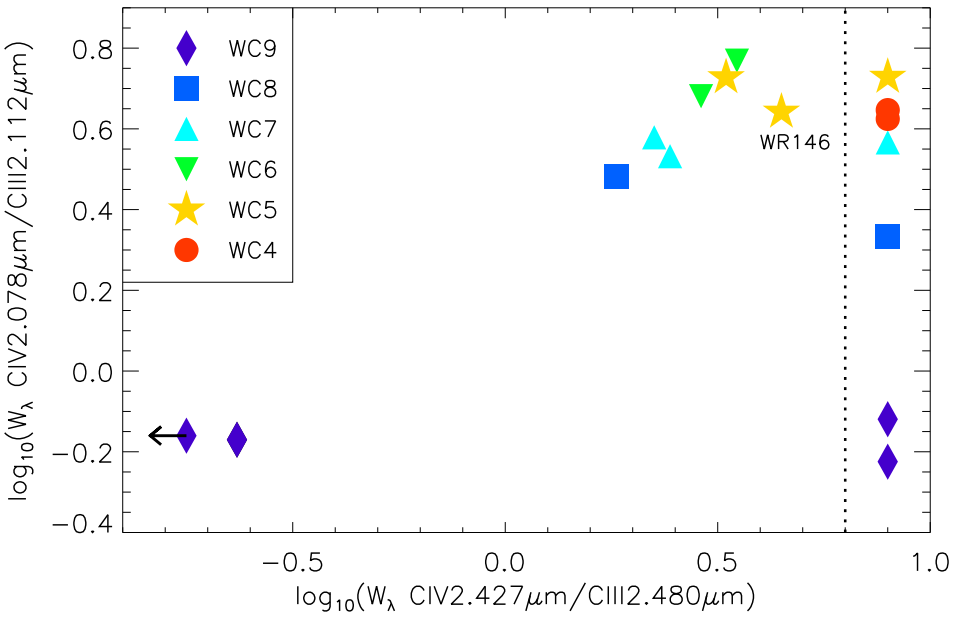

Figure 2.6: Primary K-band classification diagnostics for WC stars, CIV 2.427 / CIII 2.470–2.480μm against CIV 2.070–2.084μm / CIII+HeI 2.112–2.137μm. Errors are smaller than or of the same order as symbol sizes. Symbols to the right of the vertical dotted line do not have CIV 2.427 / CIII 2.470–2.480μm measurements available. All stars shown are drawn from the IRTF and test samples (line measurements given in Appendix A).

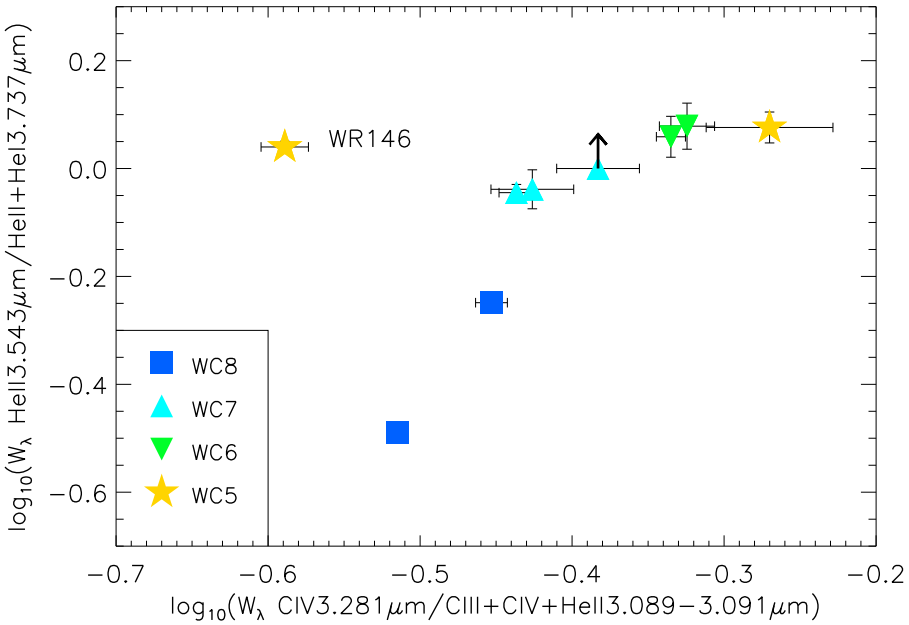

Figure 2.7: Primary L-band classification diagnostics for WC stars. Error bars represent uncertainties from the Gaussian fitting process, generated by `DIPSO elf`. All stars shown are drawn from the IRTF and test samples (line measurements given in Appendix A).

L-band

At longer wavelengths there is an effective classification diagnostic in CIV 3.281μm/CIII+CIV+HeII 3.089–3.091μm, which is capable of separating WC9, WC8, WC7, WC6 and WC5 stars. CIV 3.281μm is absent in all three WC9 stars in the IRTF sample - a property unique to this subtype. I was unable to measure these lines in any WC4 star, so could not define the boundary between WC5 and WC4 in this ratio. Additionally, I found the ratio HeII 3.543μm/HeII+HeI 3.737–3.738μm capable of distinguishing WC9, WC8, WC7, WC6–5. HeII 3.543μm is absent in all three WC9 stars in the IRTF sample - a property unique to this subtype. In Figure 2.7 I show these two classification diagnostics; an exact subtype can be assigned if both are utilised.

2.1.4 WO stars

Several distinctive spectral features are present in the near-IR spectra of WO and WN/C stars. The near-IR spectra of WO stars are characterised by very broad CIV emission lines, enhanced OV compared to early-WC stars, and a complete absence of CIII. In Figure 2.8 I compare IRTF spectra of WR 111 (WC5) to WR 142 (WO2) in two important

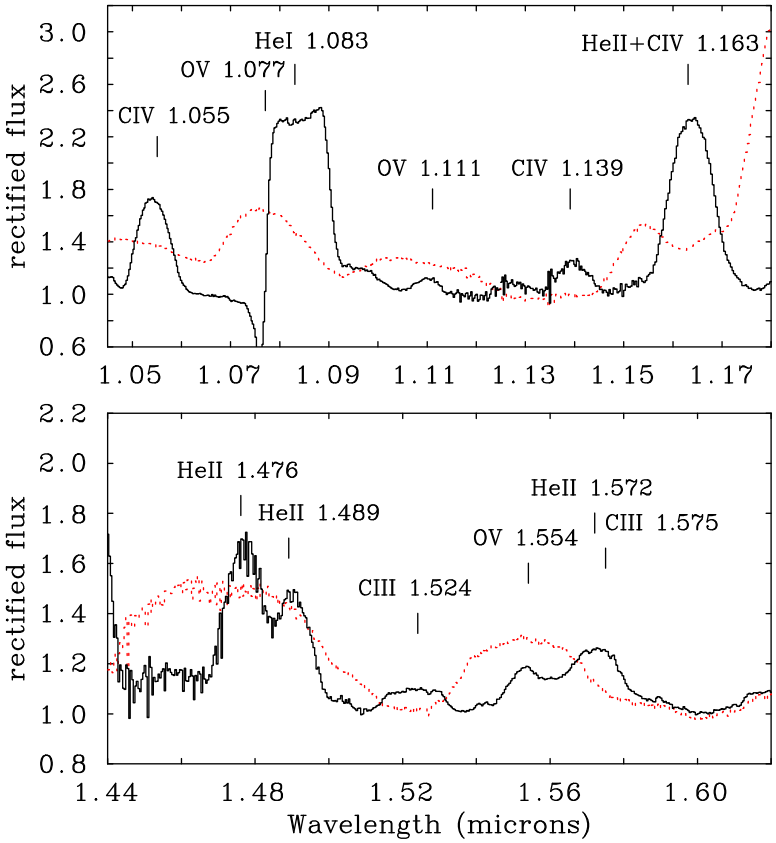

Figure 2.8: A comparison between IRTF spectra of WR 111 (WC5, black solid) and WR 142 (WO2, red dotted) in regions showing prominent oxygen features. The strongest lines are identified by labels indicating the atomic species and wavelength (μm). Both spectra have been divided by a polynomial fit to the continuum level.

regions for distinguishing WO from early WC stars. It is immediately obvious that OV 1.111μm is stronger and broader in the WO than in the WC5 star. WR 142 shows no emission associated with HeI 1.083μm, unlike WR 111, and instead OV 1.077μm is prominent. In the H-band, WR 142 shows no emission associated with CIII 1.524μm or CIII 1.575μm - both seen in WR 111 - and OV 1.554μm is significantly stronger and broader in WR 142 compared to the surrounding HeII features (e.g., HeII 1.476).

2.1.5 WN/C stars

Transition-type WN/C stars reveal themselves in the near-IR through the presence - albeit weakly - of the strongest carbon lines found in a WC spectrum. In Figure 2.9 I show IRTF spectra of two WN/C stars (**WR 145**: WN7/C & **WR 153**: WN6/C+O6I),

along with WN stars of similar ionisation in the helium spectrum (**WR 158**: WN7h & **WR 155**: WN6+O9II-Ib). In the 1μm region, C III 0.972μm is absent in WN7 stars but can clearly be seen in the WN7/C star WR 145. However, this line is not seen in the rectified spectrum of WN6/CE star WR 153, as in the 'normal' WN6 star WR 155 (Fig 2.9, top panel). The same can be said for another strong carbon feature in the J-band, C IV 1.191μm, which is enhanced relative to He in WR 145 compared to WR 158, but absent in WR 153, as in WR 155. The absence of these C III and C IV lines in WR 153 rules out ionisation effects as the cause, because one would expect C IV features to be more prominent in WR 153 than WR 145, due to its higher ionisation subtype.

The strongest carbon feature in the H-band, C IV 1.736μm, is not present in the IRTF spectra of WR 145 or WR 153, and therefore is not a suitable diagnostic for transition type stars. In the K-band, C IV 2.070–2.084Å and C III+He I 2.112–2.137μm are clearly enhanced relative to He in WR 145 compared to WR 158 (Fig 2.9, bottom panel). No such enhancement can be seen in WR 153.

The distinctive carbon features seen in WR 145 show that some WN/C stars are identifiable from their near-IR spectra alone, but the absence of such features in WR 153 shows that some may evade detection this way. The absence of C IV in the spectrum of WR 153 indicates that detection of carbon is not restricted to specific ionisation classes. A low carbon abundance in WR 153 is a possible explanation for its WN-like appearance. Crowther et al. (1995d) measure C/N ~ 2 for WR 145 by spectral analysis, but similar measurements for WR 153 are unavailable.

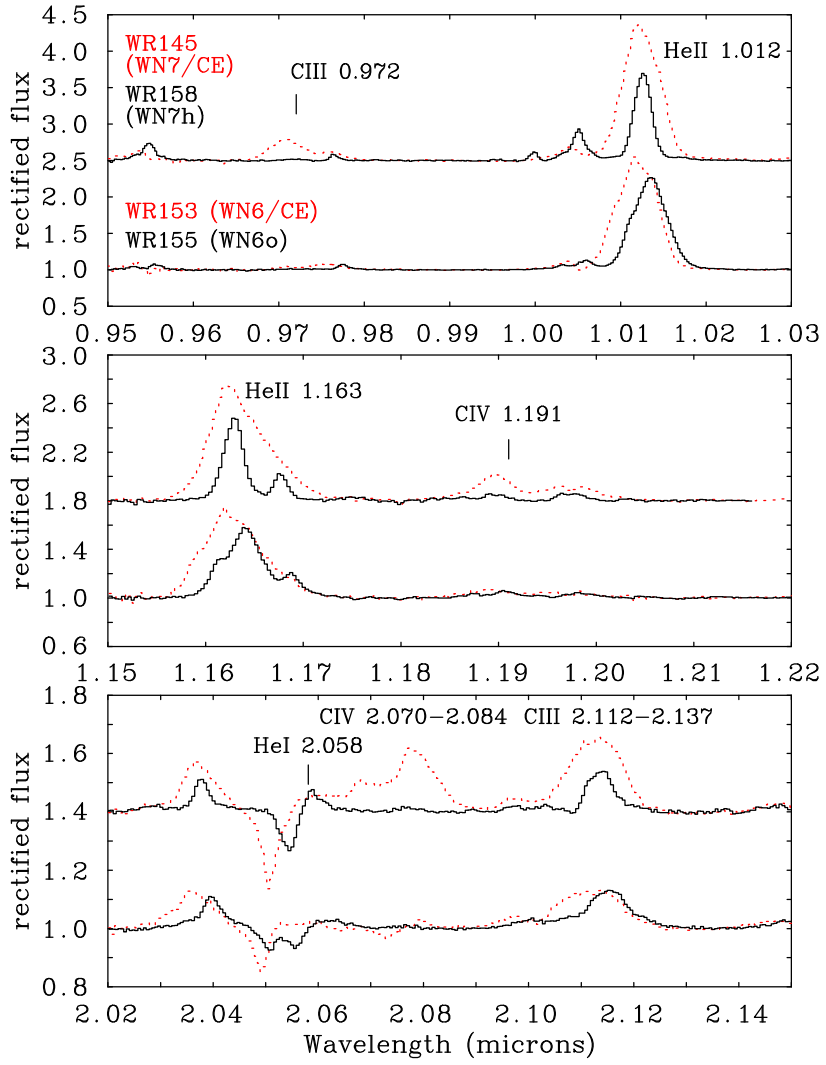

Figure 2.9: A comparison between IRTF spectra of WR 145 (WN7/CE, red dotted) and WR 158 (WN7h, black solid); WR 153 (WN6/CE, red dotted) and WR 155 (WN6o, black solid). The spectra of WR 145 and WR 158 are given a positive offset in each spectral window. Prominent lines of helium and carbon are labelled with species atomic species and wavelength (μm). All spectra have been divided by a polynomial fit to the continuum level.

2.2 Calibration of infra-red absolute magnitudes for WR stars

In this section I present a calibration of absolute magnitudes over the wavelength range 1–8μm for each WR spectral type, extending earlier results by Crowther et al. (2006b) via additional WR stars located within star clusters that have been discovered in the past decade.

2.2.1 Calibration sample

Adopted distances and spectral types for the WR stars used to calibrate IR absolute magnitudes are shown in Tables 2.6, 2.7 & 2.8 for WC/WO stars, WN stars, and WR stars in binary systems with OB companions, respectively. This sample is drawn from an updated online catalogue of Galactic WR stars[3] and totals 126, with 91 inhabiting clusters, 26 in OB associations and 9 appearing 'isolated'. By subtype, 85 of these are WN, 40 WC, and 1 WO. type. For OB associations that have been historically well studied at optical wavelengths, membership is taken from Lundström & Stenholm (1984). For WR stars in obscured clusters I have generally accepted the membership conclusions of the discovering author(s), except where noted.

For most star clusters and associations considered, there is typically more than one distance measurement to be found in the literature. Where these measurements are in general agreement I favour methods of OB-star spectrophotometry over main-sequence fitting. A small number of WR stars, in relative isolation, have kinematic distances derived from velocity measurements of an associated nebula; I use these distances but remain wary of kinematic distance estimates in general because of their sensitivity to the assumed Galactic rotation curve and local perturbations to the Galactic disk.

Where multiple consistent distance estimates are found in the literature I take an average of the reported distances - weighted by the square of the inverse uncertainty reported on each (e.g., Westerlund 1 and Car OB1) - indicated by multiple references in Tables 2.6–2.8. Cases in which inconsistent distances have been reported in the literature are discussed further in Appendix B.

[3] http://pacrowther.staff.shef.ac.uk/WRcat/

Table 2.6: Apparently single dust-free WO and WC stars, and dust-producing WC stars of known distance used to calibrate near-IR absolute magnitudes by spectral type.

Sp. Type	WR#	Cluster	Association	Distance (kpc)	Ref	J	H	K_S	Ref	$A^J_{K_S}$	$A^H_{K_S}$	$\bar{A}_{K_S}$	M_{K_S}
WO2	142	Berkeley 87		1.23 ± 0.04	1	9.54	8.89	8.60	a,a,a	0.40	0.41	0.41 ± 0.01	-2.26 ± 0.07
WC4	144		Cyg OB2	1.40 ± 0.08	2	9.41	8.59	7.71	a,a,a	0.51	0.43	0.48 ± 0.02	-3.50 ± 0.13
WC5	111		Sgr OB1	1.9 ± 0.2	3, 4	7.28	7.14	6.51	a,a,a	0.07	0.07	0.07 ± 0.01	-4.95 ± 0.23
	114		Ser OB1	2.05 ± 0.09	5, 6	8.98	8.43	7.61	a,a,a	0.36	0.34	0.35 ± 0.02	-4.30 ± 0.10
WC6	23		Car OB1	2.6 ± 0.2	7, 8	7.89	7.60	7.06	a,a,a	0.10	...	0.10 ± 0.03	-5.12 ± 0.17
	*48-4	Danks 1		4.16 ± 0.60	9	13.16	11.82	10.78	a,a,a	0.84	0.65	0.75 ± 0.03	-3.06 ± 0.32
	154		Cep OB1	3.5 ± 1.0	10	9.30	9.01	8.29	a,a,a	0.19	0.20	0.19 ± 0.01	-4.62 ± 0.62
WC7	14		Anon Vel a	2.0 ± 0.1	11	7.49	7.25	6.61	a,a,a	0.12	0.07	0.11 ± 0.01	-5.00 ± 0.11
	68		Cir OB1	3.6 ± 0.3	12	9.90	9.39	8.75	a,a,a	0.25	0.08	0.20 ± 0.02	-4.23 ± 0.18
WC8	48-3	(G305.4+0.1)/Danks 1		4.16 ± 0.60	9	10.75	9.57	8.77	a,a,a	0.74	0.59	0.67 ± 0.03	-4.99 ± 0.32
	48-2	Danks 2		4.16 ± 0.60	9	10.83	9.83	8.98	a,a,a	0.67	0.66	0.67 ± 0.03	-4.78 ± 0.32
	77g	Westerlund 1		4.0 ± 0.2	13, 14	11.81	10.40	9.53	b,b,b	0.88	0.69	0.81 ± 0.04	-4.29 ± 0.13
	102k	Quintuplet		8.00 ± 0.25	15, 16	16.71	13.45	11.19	d,d,a	2.49	2.55	2.50 ± 0.08	-5.83 ± 0.12
	*124-1	Glimpse 20		4.45 ± 0.65	17	...	10.38	9.19	a,a	...	1.14	1.14 ± 0.10	-5.20 ± 0.33
	135		Cyg OB3	1.9 ± 0.2	18	7.23	7.11	6.66	a,a,a	0.07	0.10	0.08 ± 0.01	-4.81 ± 0.23
WC9	77p	Westerlund 1		4.0 ± 0.2	13, 14	10.12	9.09	8.29	b,b,b	0.76	0.76	0.76 ± 0.05	-5.48 ± 0.16
	101f	GC		8.00 ± 0.25	15, 16	18.78	15.43	13.11	e,e,e	2.65	2.78	2.72 ± 0.04	-4.12 ± 0.08
	101oa	GC		8.00 ± 0.25	15, 16	18.48	15.43	13.01	e,e,e	2.56	2.92	2.72 ± 0.04	-4.23 ± 0.08
	102h	Quintuplet		8.00 ± 0.25	15, 16	16.62	13.51	11.34	d,d,a	2.47	2.58	2.50 ± 0.08	-5.68 ± 0.12
WC8d	53			4.00 ± 1.00	19	8.75	7.92	6.84	a,a,a	...	...	$0.29 \pm 0.09^{\ddagger}$	-6.43 ± 0.55
	102e	Quintuplet		8.00 ± 0.25	15, 16	17.5	13.3	10.4	d,d,d	...	...	$3.1 \pm 0.5^{\dagger}$	-7.22 ± 0.51
	102f	Quintuplet		8.00 ± 0.25	15, 16	...	...	10.4	c	...	...	$3.1 \pm 0.5^{\dagger}$	-7.22 ± 0.51
	113			2.0 ± 0.2	20	7.02	6.28	5.49	a,a,a	...	...	$0.38 \pm 0.01^{\ddagger}$	-6.37 ± 0.22
WC9d	65		Cir OB1	3.6 ± 0.3	12	8.46	7.28	6.17	a,a,a	...	...	$0.91 \pm 0.04^{\ddagger}$	-7.45 ± 0.19
	77aa	Westerlund 1		4.00 ± 0.25	13,14	10.04	8.21	6.72	b,b,b	...	...	$1.01 \pm 0.14^{\dagger}$	-7.30 ± 0.20
	77b	Westerlund 1		4.00 ± 0.25	13,14	9.69	7.84	6.41	b,b,b	...	...	$1.01 \pm 0.14^{\dagger}$	-7.61 ± 0.20

Continued on next page

Table 2.6 – *Continued from previous page*

Sp. Type	WR#	Cluster	Association Distance (kpc)	Ref	J	H	K_S	Ref	$A^J_{K_S}$	$A^H_{K_S}$	$\bar{A}_{K_S}$	M_{K_S}
	77i	Westerlund 1	4.00 ± 0.25	13,14	10.13	7.64	6.90	b,b,b	...	...	$1.01 \pm 0.14^{\dagger}$	-7.12 ± 0.22
	77l	Westerlund 1	4.00 ± 0.25	13,14	10.31	8.56	7.38	b,b,b	...	...	$1.01 \pm 0.14^{\dagger}$	-6.64 ± 0.20
	77m	Westerlund 1	4.00 ± 0.25	13,14	11.26	9.51	8.23	b,b,b	...	...	$1.01 \pm 0.14^{\dagger}$	-5.79 ± 0.20
	77n	Westerlund 1	4.00 ± 0.25	13,14	9.85	7.97	7.28	b,b,b	...	...	$1.01 \pm 0.14^{\dagger}$	-6.74 ± 0.20
	95	Trumpler 27	2.5 ± 0.5	21	8.29	6.67	5.27	a,a,a	...	...	$0.66 \pm 0.03^{\dagger b}$	-7.38 ± 0.44
	101ea	GC	8.00 ± 0.25	15,16	17.79	13.46	10.50	f,f,f	...	...	3.2 ± 0.2	-7.22 ± 0.22
	102-2	Quintuplet	8.00 ± 0.25	15,16	...	...	10.30	c	...	...	$3.1 \pm 0.5^{\dagger}$	-7.32 ± 0.51
	102-3	Quintuplet	8.00 ± 0.25	15,16	15.49	11.71	9.32	d,d,d	...	...	$3.1 \pm 0.5^{\dagger}$	-8.30 ± 0.51
	104		2.6 ± 0.7	4	6.67	4.34	2.42	a,a,a	...	...	$0.86 \pm 0.02^{\ddagger}$	-10.44 ± 0.64
	111a	SGR 1806-20	8.70 ± 1.65	22	...	13.76	11.60	g,g	...	...	$3.0 \pm 0.3^{\dagger}$	-6.10 ± 0.51
	118-1	Quartet	6.3 ± 0.2	17	13.22	10.14	8.09	a,a,a	...	...	$1.6 \pm 0.4^{\dagger}$	-7.51 ± 0.41

*Indicates updated spectral types based on an improved near-IR classification scheme. Since publication of this work (Rosslowe & Crowther, 2015b), WR124-1 has been resolved into two WC stars and a O6 If star (de la Fuente et al., 2015).

Distance references: (1)Turner et al. (2006), (2)Rygl et al. (2012), (3)Mel'Nik & Dambis (2009), (4)Tuthill et al. (2008), (5)Hillenbrand et al. (1993), (6)Djurašević et al. (2001), (7)Smith (2006), (8)Hur, Sung & Bessell (2012), (9)Davies et al. (2012), (10)Cappa et al. (2010), (11)Lundström & Stenholm (1984), (12)Vázquez et al. (1995), (13)Kothes & Dougherty (2007), (14)Koumpia & Bonanos (2012), (15)Reid et al. (2009), (16)Gillessen et al. (2013), (17)Messineo et al. (2009), (18)Reid et al. (2011), (19)Martín, Cappa & Testori (2007), (20)Esteban & Rosado (1995), (21)Crowther et al. (2006b), (22)Bibby et al. (2008).

Photometry references: (a)2MASS, (b)Crowther et al. (2006b), (c)Liermann, Hamann & Oskinova (2009), (d)Figer, McLean & Morris (1999), (e)Dong, Wang & Morris (2012), (f)Eikenberry et al. (2004), (g)Bibby et al. (2008).

Extinction: †Average of parent cluster, $^{\ddagger}A_v$ taken from van der Hucht (2001) and converted using $A_K = 0.12A_v$.

Table 2.7: Apparently single WN stars (and those with an insignificant companion contribution at IR wavelengths) of known distance used to calibrate near-IR absolute magnitudes by spectral type.

Sp. Type	WR#	Cluster	Association	Distance (kpc)	Ref	J	H	K_S	Ref	$A^J_{K_S}$	$A^H_{K_S}$	$\bar{A}_{K_S}$	M_{K_S}
WN2b	2		Cas OB1	2.4 ± 0.8	23	10.04	9.78	9.45	a,a,a	0.33	0.52	0.40 ± 0.02	-2.86 ± 0.72
WN3b	46		Cru OB4	4.00 ± 0.85	24, 25	10.20	10.08	9.83	a,a,a	0.23	0.39	0.27 ± 0.01	-3.45 ± 0.46
WN4b	1		Cas OB7	2.3 ± 0.5	3	8.21	7.86	7.48	a,a,a	0.17	0.15	0.17 ± 0.01	-4.49 ± 0.47
	6			1.80 ± 0.27	26	6.35	6.23	5.89	a,a,a	0.04	0.09	0.05 ± 0.01	-5.44 ± 0.33
	7			5.5 ± 0.5	27	9.97	9.67	9.27	a,a,a	0.16	0.19	0.17 ± 0.01	-4.60 ± 0.20
	18		Car OB1	2.6 ± 0.2	7, 8	8.57	8.21	7.68	a,a,a	0.25	0.36	0.27 ± 0.02	-4.67 ± 0.17
	35b	Sher 1		10.0 ± 1.4	28	10.95	10.35	9.76	a,a,a	0.39	0.46	0.41 ± 0.03	-5.65 ± 0.31
WN6b	*102c	Quintuplet		8.00 ± 0.25	15, 16	...	13.12	11.53	d,d	...	1.78	1.78 ± 0.38	-4.77 ± 0.44
	111c	SGR 1806-20		8.70 ± 1.65	22	...	14.03	12.16	f,f	...	2.25	2.25 ± 0.15	-4.79 ± 0.44
	134		Cyg OB3	1.9 ± 0.2	18	6.72	6.52	6.13	a,a,a	0.10	0.17	0.12 ± 0.01	-5.39 ± 0.23
	136		Cyg OB1	1.3 ± 0.2	29	6.13	5.90	5.56	a,a,a	0.09	0.10	0.09 ± 0.01	-5.10 ± 0.33
WN7b	77sc	Westerlund 1		4.0 ± 0.2	13, 14	10.34	9.11	8.37	b,b,b	0.76	0.66	0.74 ± 0.05	-5.38 ± 0.16
	111-2	Cl 1813-178		3.6 ± 0.7	30	9.62	8.60	7.94	a,a,a	0.62	0.55	0.59 ± 0.03	-5.44 ± 0.42
WN3	152		Cep OB1	3.5 ± 1.0	10	10.49	10.32	10.04	a,a,a	0.26	0.43	0.31 ± 0.02	-2.99 ± 0.62
WN5	77e	Westerlund 1		4.0 ± 0.2	13, 14	11.70	10.30	9.70	b,b,b	0.87	0.62	0.79 ± 0.06	-4.10 ± 0.16
	77q	Westerlund 1		4.0 ± 0.2	13, 14	11.92	10.84	10.26	b,b,b	0.70	0.59	0.67 ± 0.04	-3.42 ± 0.13
	77sd	Westerlund 1		4.0 ± 0.2	13, 14	12.36	11.08	10.25	b,b,b	0.92	0.94	0.93 ± 0.04	-3.69 ± 0.13
WN6	67	Pismis 20	Cir OB1	3.6 ± 0.3	12	9.28	8.86	8.45	a,a,a	0.31	0.35	0.32 ± 0.02	-4.65 ± 0.18
	77sb	Westerlund 1		4.0 ± 0.2	13, 14	11.00	9.98	9.45	b,b,b	0.65	0.52	0.61 ± 0.04	-4.17 ± 0.12
	77a	Westerlund 1		4.0 ± 0.2	13, 14	11.72	10.67	10.00	b,b,b	0.73	0.72	0.73 ± 0.04	-3.74 ± 0.13
	77s	Westerlund 1		4.0 ± 0.2	13, 14	10.77	9.72	9.20	b,b,b	0.66	0.51	0.61 ± 0.04	-4.42 ± 0.12
	85			2.8 ± 1.1	31	...	7.94	7.48	a,a	...	0.43	0.43 ± 0.16	-5.19 ± 0.87
	*101o	GC		8.00 ± 0.25	15, 16	17.94	14.13	11.60	e,e,e	3.00	3.20	3.11 ± 0.04	-6.02 ± 0.08
	115		Ser OB1	2.05 ± 0.09	5, 6	7.99	7.42	6.95	a,a,a	0.41	0.44	0.42 ± 0.02	-5.03 ± 0.10
WN7	75ba			4.1 ± 0.4	32	10.22	9.29	8.91	a,a,a	0.56	0.39	0.51 ± 0.04	-4.67 ± 0.23
	77r	Westerlund 1		4.0 ± 0.2	13, 14	11.63	10.31	9.61	b,b,b	0.90	0.83	0.87 ± 0.04	-4.27 ± 0.13

Continued on next page

Table 2.7 – *Continued from previous page*

Sp. Type	WR#	Cluster	Association	Distance (kpc)	Ref	J	H	K_S	Ref	$A^J_{K_S}$	$A^H_{K_S}$	$\bar{A}_{K_S}$	M_{K_S}
	77j	Westerlund 1		4.0 ± 0.2	13, 14	11.36	9.97	9.28	b,b,b	0.93	0.82	0.89 ± 0.04	-4.62 ± 0.13
	77d	Westerlund 1		4.0 ± 0.2	13, 14	11.06	9.83	9.26	b,b,b	0.80	0.65	0.74 ± 0.04	-4.49 ± 0.13
	*77sa	Westerlund 1		4.0 ± 0.2	13, 14	12.11	10.75	10.04	b,b,b	0.92	0.85	0.89 ± 0.04	-3.86 ± 0.13
	78	NGC 6231	Sco OB1	1.64 ± 0.03	33	5.44	5.27	4.98	a,a,a	0.16	0.25	0.18 ± 0.01	-6.27 ± 0.05
	87	Halven-Moffat 1		3.3 ± 0.3	34	8.00	7.45	7.09	a,a,a	0.37	0.36	0.37 ± 0.02	-5.88 ± 0.20
	*101ai	GC		8.00 ± 0.25	15, 16	...	14.33	12.12	e,e	...	2.84	2.84 ± 0.07	-5.23 ± 0.10
	*111-4	Cl 1813-178		3.6 ± 0.7	30	10.31	9.27	8.66	a,a,a	0.72	0.70	0.71 ± 0.03	-4.84 ± 0.42
WN8	12•	Bochum 7		4.2 ± 2.1	35	8.62	8.26	7.87	a,a,a	0.29	0.40	0.32 ± 0.02	-5.57 ± 1.09
	*48-7	Danks 1		4.16 ± 0.60	9	9.81	8.48	7.65	a,a,a	0.97	1.01	0.99 ± 0.04	-6.43 ± 0.32
	66		Cir OB1	3.6 ± 0.3	12	8.93	8.48	8.15	a,a,a	0.31	0.31	0.31 ± 0.02	-4.94 ± 0.18
	77c	Westerlund 1		4.0 ± 0.2	13, 14	10.89	9.57	8.86	b,b,b	0.90	0.85	0.88 ± 0.04	-5.03 ± 0.13
	77h	Westerlund 1		4.0 ± 0.2	13, 14	10.75	9.42	8.76	b,b,b	0.89	0.77	0.84 ± 0.04	-5.09 ± 0.13
	89	Halven-Moffat 2		3.3 ± 0.3	34	7.39	6.96	6.58	a,a,a	0.32	0.39	0.34 ± 0.02	-6.36 ± 0.20
	101b	GC		8.00 ± 0.25	15, 16	...	13.53	11.43	e,e	...	2.69	2.69 ± 0.06	-5.77 ± 0.09
	101nc	GC		8.00 ± 0.25	15, 16	17.38	14.23	11.91	e,e,e	2.60	2.99	2.79 ± 0.04	-5.40 ± 0.08
	*101oc	GC		8.00 ± 0.25	15, 16	18.66	14.93	12.61	e,e,e	2.89	2.99	2.94 ± 0.04	-4.85 ± 0.08
	*101dd	GC		8.00 ± 0.25	15, 16	18.96	15.43	13.01	e,e,e	2.84	3.12	2.98 ± 0.04	-4.49 ± 0.08
	102a	Arches		8.00 ± 0.25	15, 16	17.17	13.26	11.02	h,a,a	2.94	2.88	2.91 ± 0.05	-6.40 ± 0.10
	*102ae	Arches		8.00 ± 0.25	15, 16	15.43	12.40	10.62	i,i,i	2.28	2.25	2.27 ± 0.02	-6.16 ± 0.07
	*102af	Arches		8.00 ± 0.25	15, 16	15.97	12.81	10.88	i,i,i	2.42	2.46	2.44 ± 0.03	-6.08 ± 0.07
	*102ah	Arches		8.00 ± 0.25	15, 16	15.23	12.03	10.07	i,i,i	2.45	2.50	2.48 ± 0.03	-6.92 ± 0.07
	*102al	Arches		8.00 ± 0.25	15, 16	15.11	12.09	10.24	i,i,i	2.31	2.34	2.33 ± 0.02	-6.60 ± 0.07
	124			3.35 ± 0.67	36	8.58	8.18	7.73	a,a,a	0.34	0.47	0.39 ± 0.02	-5.28 ± 0.44
WN9	*48-6	(G305.4+0.1)/Danks 1		4.16 ± 0.60	9	10.21	8.57	7.58	a,a,a	1.19	1.24	1.21 ± 0.05	-6.73 ± 0.32
	*48-10	Danks 1		4.16 ± 0.60	9	9.42	8.15	7.48	a,a,a	0.86	0.79	0.83 ± 0.04	-6.45 ± 0.32
	48-9	Danks 1		4.16 ± 0.60	9	8.26	7.27	6.61	a,a,a	0.72	0.77	0.74 ± 0.03	-7.22 ± 0.32
	77k	Westerlund 1		4.0 ± 0.2	13, 14	9.08	7.72	7.19	b,b,b	0.84	0.59	0.75 ± 0.04	-6.57 ± 0.13
	*101m	GC		8.00 ± 0.25	15, 16	16.58	13.53	11.32	e,e,e	2.50	2.84	2.67 ± 0.03	-5.86 ± 0.08

Continued on next page

Table 2.7 – *Continued from previous page*

Sp. Type	WR#	Cluster	Association	Distance (kpc)	Ref	J	H	K_S	Ref	$A^J_{K_S}$	$A^H_{K_S}$	$\bar{A}_{K_S}$	M_{K_S}
	*101e	GC		8.00 ± 0.25	15, 16	15.87	12.73	10.41	e,e,e	2.60	2.99	2.79 ± 0.04	-6.90 ± 0.08
	*102aa	Arches		8.00 ± 0.25	15, 16	...	...	11.18	j	...	...	$2.48 \pm 0.37^{\dagger}$	-5.82 ± 0.39
	*102ad	Arches		8.00 ± 0.25	15, 16	15.86	12.44	10.35	i,i,i	2.63	2.69	2.66 ± 0.03	-6.83 ± 0.08
	*102ag	Arches		8.00 ± 0.25	15, 16	15.67	12.45	10.46	i,i,i	2.48	2.55	2.52 ± 0.03	-6.58 ± 0.07
	*102ai	Arches		8.00 ± 0.25	15, 16	...	12.24	10.34	a,a	...	2.41	2.41 ± 0.19	-6.59 ± 0.22
	*102aj	Arches		8.00 ± 0.25	15, 16	16.55	13.56	11.79	i,i,i	2.26	2.24	2.25 ± 0.02	-4.98 ± 0.07
	*102bb	Arches		8.00 ± 0.25	15, 16	15.58	12.36	10.36	i,i,i	2.48	2.54	2.52 ± 0.03	-6.67 ± 0.07
	*102bc	Arches		8.00 ± 0.25	15, 16	...	13.14	11.20	i,i	...	2.47	2.47 ± 0.13	-5.79 ± 0.16
	102d	Quintuplet		8.00 ± 0.25	15, 16	15.58	12.40	10.50	d,d,c	2.41	2.42	2.42 ± 0.09	-6.43 ± 0.15
	102hb	Quintuplet		8.00 ± 0.25	15, 16	14.19	10.90	9.60	d,d,c	2.18	1.61	2.01 ± 0.09	-6.93 ± 0.15
	102i	Quintuplet		8.00 ± 0.25	15, 16	14.77	11.67	10.22	d,a,a	2.16	1.81	1.98 ± 0.05	-6.27 ± 0.10
	102j	Quintuplet		8.00 ± 0.25	15, 16	14.66	11.77	10.23	a,a,a	2.10	1.94	2.03 ± 0.03	-6.32 ± 0.08
	105		Sgr OB1	1.9 ± 0.2	3, 4	7.04	6.25	5.73	a,a,a	0.56	0.58	0.57 ± 0.02	-6.24 ± 0.23
WN6ha	20a1			8.0 ± 1.0	37	9.61	8.84	8.34	a,a,a	0.61	0.65	0.63 ± 0.03	-6.80 ± 0.38
	20a2			8.0 ± 1.0	37	9.61	8.84	8.34	a,a,a	0.61	0.65	0.63 ± 0.03	-6.80 ± 0.38
	24	Coll 228	Car OB1	2.6 ± 0.2	7, 8	6.10	6.01	5.82	a,a,a	0.14	0.23	0.16 ± 0.01	-6.42 ± 0.17
	25•	Trumpler 16	Car OB1	2.6 ± 0.2	7, 8	6.26	5.97	5.72	a,a,a	0.26	0.31	0.28 ± 0.02	-6.63 ± 0.17
	43A1	NGC 3603		7.6 ± 0.4	38	8.57	8.36	7.78	k,k,k	0.38	0.77	0.49 ± 0.05	-7.11 ± 0.16
	43A2	NGC 3603		7.6 ± 0.4	38	8.98	8.77	8.19	k,k,k	0.38	0.77	0.49 ± 0.04	-6.70 ± 0.14
	43B	NGC 3603		7.6 ± 0.4	38	7.78	7.70	7.08	k,k,k	0.34	0.83	0.47 ± 0.03	-7.80 ± 0.13
	43C•	NGC 3603		7.6 ± 0.4	38	8.49	8.13	7.81	k,k,k	0.33	0.41	0.35 ± 0.03	-6.95 ± 0.13
WN7ha	22•		Car	2.6 ± 0.2	7, 8	5.71	5.58	5.39	a,a,a	0.17	0.26	0.20 ± 0.03	-6.81 ± 0.17
	*125-3	Mercer 23		6.5 ± 0.3	39	8.65	7.84	7.33	l,l,l	0.64	0.70	0.67 ± 0.02	-7.40 ± 0.10
WN9ha	79a	NGC 6231	Sco OB1	1.64 ± 0.03	33	5.15	5.09	4.90	a,a,a	0.14	0.25	0.17 ± 0.02	-6.34 ± 0.05
	79b		KQ Sco	3.5 ± 0.5	40	6.76	6.62	6.48	a,a,a	0.16	0.19	0.17 ± 0.01	-6.41 ± 0.31

*Indicates updated spectral types based on an improved near-IR classification scheme.

•Spectroscopic binary systems with a dominant WR component at IR wavelengths ($F^{WR}/F^{sys} > 2/3$).

Binary detection: (WR 12)Fahed & Moffat (2012), (WR 25)Gamen et al. (2006), (WR 43C)Schnurr et al. (2008), (WR 22)Schweickhardt et al. (1999).

Distance references (1-22 as in Table 2.6): (23)Arnal et al. (1999), (24)Crowther, Smith & Hillier (1995c), (25)Tovmassian, Navarro & Cardona (1996), (26)Howarth & Schmutz (1995), (27)Cappa et al. (1999), (28)Moffat, Shara & Potter (1991), (29)Garmany & Stencel (1992), (30)Messineo et al. (2011), (31)Vázquez et al. (2005), (32)Cohen, Parker & Green (2005), (33)Sana et al. (2006), (34)Vázquez & Baume (2001), (35)Corti, Bosch & Niemela (2007), (36)Marchenko, Moffat & Crowther (2010), (37)Rauw et al. (2007), (38)Melena et al. (2008), (39)Hanson et al. (2010), (40)Bohannan & Crowther (1999).

Photometry references (a-g as in Table 2.6): (h)Cotera et al. (1999), (i)Espinoza, Selman & Melnick (2009), (j)Martins et al. (2008), (k)Harayama, Eisenhauer & Martins (2008), (l)Hanson et al. (2010).

Extinction: †Average of parent cluster.

Table 2.8: WR stars in confirmed binary systems (WR+non-WR) used for absolute magnitude-spectral type calibrations.

WR#	Sp. Type	Cluster/Association	Distance(kpc)	Ref	JHK_S^{sys}	Ref	Flux ratio F^{WR}/F^{sys}	Extinction	M^{WR}
11	WC8+O7.5III		0.342 ± 0.035	41	$J = 2.12$	m	0.45 ± 0.32	0.00	$M_J = -4.68 \pm 0.81$
					$H = 2.17$	m	0.48 ± 0.30	0.00	$M_H = -4.70 \pm 0.72$
					$K_S = 1.98$	m	0.60 ± 0.23	0.00	$M_{K_S} = -5.14 \pm 0.48$
77o	WN7o+?	Westerlund 1	4.0 ± 0.2	13, 14	$J = 10.34$	b	0.59 ± 0.10	2.98 ± 0.20	$M_J = -5.08 \pm 0.26$
					$K_S = 8.37$	b	0.80 ± 0.10	0.96 ± 0.05	$M_{K_S} = -5.36 \pm 0.23$
79	WC7+O5-8V	Sco OB1	1.64 ± 0.03	33	$J = 5.96$	a	0.41 ± 0.05	0.48 ± 0.03	$M_J = -4.62 \pm 0.14$
					$K_S = 5.39$	a	0.45 ± 0.05	0.16 ± 0.01	$M_{K_S} = -4.97 \pm 0.13$
93	WC7+O7-9	Pismis 24	2.0 ± 0.2	tw.	$K_S = 5.87$	a	0.73 ± 0.72	$0.58 \pm 0.03^{\ddagger}$	$M_{K_S} = -5.88 \pm 1.10$
127	WN5+O8.5V	Vul OB2	4.41 ± 0.12	42	$J = 9.18$	a	0.58 ± 0.17	0.56 ± 0.09	$M_J = -4.00 \pm 0.65$
					$H = 9.02$	a	0.59 ± 0.13	0.31 ± 0.05	$M_H = -3.93 \pm 0.26$
					$K_S = 8.76$	a	0.67 ± 0.09	0.18 ± 0.03	$M_{K_S} = -4.21 \pm 0.16$

Continued on next page

Table 2.8 – *Continued from previous page*

WR#	Sp. Type	Cluster/Association	Distance(kpc)	Ref	JHK_S^{sys}	Ref	Flux ratio F^{WR}/F^{sys}	Extinction	M^{WR}
133	WN5+O9I	NGC 6871	2.14 ± 0.07	43	$J = 6.32$	a	0.22 ± 0.05	0.55 ± 0.05	$M_J = -3.86 \pm 0.19$
					$K_S = 6.25$	a	0.23 ± 0.05	0.18 ± 0.02	$M_{K_S} = -4.04 \pm 0.19$
137	WC7+O9	Cyg OB1	1.3 ± 0.2	29	$J = 7.00$	n	0.41 ± 0.12	0.59 ± 0.07	$M_J = -3.19 \pm 0.47$
					$K_S = 6.43$	n	0.46 ± 0.13	0.19 ± 0.02	$M_{K_S} = -3.49 \pm 0.46$
139	WN5+O6III-V	Cyg OB1	1.3 ± 0.2	29	$J = 6.70$	a	0.44 ± 0.06	0.59 ± 0.06	$M_J = -3.57 \pm 0.36$
					$K_S = 6.33$	a	0.50 ± 0.07	0.19 ± 0.02	$M_{K_S} = -3.69 \pm 0.36$
141	WN5+O5III-V	Cyg OB1	1.3 ± 0.2	29	$J = 7.34$	a	0.65 ± 0.07	$0.45 \pm 0.15^{\dagger}$	$M_J = -3.21 \pm 0.34$
157	WN5+?	Markarian 50	3.46 ± 0.35	44	$J = 8.22$	a	0.47 ± 0.10	0.90 ± 0.15	$M_J = -4.53 \pm 0.30$
					$K_S = 7.73$	a	0.68 ± 0.10	0.29 ± 0.04	$M_{K_S} = -4.88 \pm 0.36$

Distance references (1-40 as in Tables 2.6 & 2.7): (41)van Leeuwen (2007), (42)Turner (1980), (43)Malchenko & Tarasov (2009), (44)Baume, Vázquez & Carraro (2004).

Photometry references (a-l as in Tables 2.6 & 2.7): (m)Williams et al. (1990b), (n)Williams et al. (2001).

Spectral types: (WR 11) De Marco & Schmutz (1999), (WR 77o) Crowther et al. (2006b), (WR 79) Smith, Shara & Moffat (1990), (WR 93) Lortet, Testor & Niemela (1984), (WR 127) de La Chevrotière, Moffat & Chené (2011), (WR 133) Underhill & Hill (1994), (WR 137) Williams et al. (2001), (WR 139) Marchenko, Moffat & Koenigsberger (1994), (WR 141) Marchenko, Moffat & Eenens (1998b), (WR 157) Smith et al. (1996).

Extinction: $^{\ddagger}A_v$ taken from van der Hucht (2001) and converted using $A_K = 0.12A_v$. †Average extinction taken from WR 136 and WR 139, also members of Cyg OB1.

Over half of the WR stars in this calibration sample reside in obscured clusters. Their spectral types had therefore been poorly determined, due to the lack of optical spectra and/or a fully developed near-IR classification scheme. I have re-assessed the spectral type of every star in the calibration sample that was not classified using an optical spectrum. To do this I used published K-band spectra of WR stars in the GC cluster (Krabbe et al., 1995; Martins et al., 2007), Arches (Cotera et al., 1999; Martins et al., 2008) and Quintuplet (Liermann et al., 2009), Danks 1 & 2 (Davies et al., 2012), and IJHK spectra of the WR stars in Westerlund 1 (Crowther et al., 2006b). Updated spectral types are indicated in Tables 2.6–2.8.

Some WR stars included in Tables 2.6 & 2.7 are known to have companions, but are included as *effectively* single provided the WR component contributes $\gtrsim 80\%$ of the near-IR flux, i.e., a WR/system flux ratio, $F^{WR}/F^{sys} \gtrsim 0.8$. To check for unseen companions, and estimate their relative flux contributions, I compiled a reference list of standard WR star emission line strengths, given in Table A.4. I ensured the strength of emission lines displayed by each WR star in Tables 2.6 or 2.7, were sufficiently strong to rule out a significant continuum contribution from an otherwise undetected companion (i.e., $F^{WR}/F^{sys} \lesssim 0.8$). Table 2.8 contains all binary calibration stars, either spectroscopically confirmed or revealed by IR line dilution, where photometry has been corrected to remove the contribution from a companion by the methods described in Section 2.2.2.

2.2.2 Photometry and extinction

For the most part I took JHK_S photometry for each WR from the Two Micron All-Sky Survey (2MASS) point source catalogue (Skrutskie et al., 2006), requiring a minimum quality flag of C. I also took IRAC [3.6]–[8.0](μm) photometry from the *Spitzer* GLIMPSE survey (Benjamin et al., 2003) for sufficiently isolated sources in the surveyed field.

Many cluster and association members are located in fields too crowded for 2MASS to be useful. In such cases I turned to dedicated observations with higher spatial resolution of the stellar groups in question (Tables 2.6–2.8).

I have attempted to ensure consistency in the JHK_S photometry used. Notably, observations of WR stars in the Galactic Centre region assembled by Dong et al. (2012), consist of Hubble Space Telescope snapshot imaging plus multiple ground-based photometry. In this case, to maintain consistency with other assembled photometry, I constructed and applied a simple algorithm to convert Dong et al. JHK_S values into the 2MASS photometric system (following their equations 7–9). However, in general

Table 2.9: Intrinsic colours adopted for each type of WR star, primarily from Crowther et al. (2006b), albeit supplemented with unpublished stellar atmospheric model results for additional types considered here (e.g. WO).

Sp. type	$(J–K)_0$	$(H–K)_0$
WO2	0.11	0.00
WC4–7	0.62	0.58
WC8	0.43	0.38
WC9	0.23	0.26
WN4–7b	0.37	0.27
WN2–4	–0.11	–0.03
WN5–6	0.18	0.16
WN7–9	0.13	0.11
WN5–6ha	–0.015	0.03
WN7–9ha	–0.04	0.005

I regard the slight differences between ground-based filter systems as insignificant, as they have a much smaller effect on calculated absolute magnitudes than that of distance uncertainties.

I calculated the extinction towards each calibration star by evaluating the colour excesses E_{J-K_S} and E_{H-K_S}, utilising intrinsic JHK$_S$ colours of WR stars given by Crowther et al. (2006b), updated in Table 2.9. Two values of K$_S$-band extinction follow;

$$A^J_{K_s} = E_{J-K_s} \times (\frac{A_J}{A_{K_S}} - 1)^{-1}, \tag{2.1}$$

and

$$A^H_{K_s} = E_{H-K_s} \times (\frac{A_H}{A_{K_S}} - 1)^{-1}. \tag{2.2}$$

The second terms in Equations 2.1 and 2.2 require knowledge of the near-IR extinction law.

Due to the growing body of evidence suggesting a difference in dust properties toward the GC, I employed two different Galactic near-IR extinction laws. For stars in the GC region ($358° < l < 2°, |b| < 1°$) I used the line-derived extinction law of Fritz et al. (2011) ($^{A_J}/_{A_{K_S}} = 3.05 \pm 0.07$, $^{A_H}/_{A_{K_S}} = 1.74 \pm 0.03$). For all other Galactic sight lines I used the law of Stead & Hoare (2009) ($^{A_J}/_{A_{K_S}} = 3.1 \pm 0.2$, $^{A_H}/_{A_{K_S}} = 1.71 \pm 0.09$) – an updated form of that provided by Indebetouw et al. (2005). For the purpose of calculating the absolute magnitude of each calibration star, we take an average ($\bar{A}_{K_S}$) from Equations 2.1 and 2.2. Since extinction in the IRAC bands is much lower, I opted for a more straightforward approach and used the relations given by Indebetouw et al. (2005) for all sight lines.

A minority of stars in the calibration sample only had single-band photometry available, preventing an extinction calculation by colour excess. For these objects I resorted to one of two alternatives; I either adopted the average cluster A_{K_S} calculated by the colour excess of other O or WR stars (where two or more were available), or I took A_v as given by van der Hucht (2001) and converted this using $A_{K_S} \simeq 0.11 A_V \simeq 0.12 A_v$ (Rieke & Lebofsky, 1985). If neither was possible I excluded the star from the sample.

For those WR stars in the calibration sample with evidence for a bright companion (Table 2.8), it was necessary to subtract the contribution of this companion to the systemic magnitudes, allowing an absolute magnitude calculation for the WR component alone. As the distance to these systems was known, a systemic absolute magnitude could be calculated in each case. It was then straightforward to estimate and subtract any companion contribution if either its absolute magnitude were known, or a WR/companion flux ratio could be calculated. In the case where the absolute magnitude of a spectroscopically classified companion were known, I used the following equations to calculate the Wolf-Rayet absolute magnitude in each band;

$$M^{WR} = M^{c} - 2.5 \log \left(\frac{F^{WR}}{F^{c}} \right), \tag{2.3}$$

and

$$\frac{F^{WR}}{F^{c}} = 10^{\frac{M^{c} - M^{sys}}{2.5}} - 1, \tag{2.4}$$

where F and M denote flux and absolute magnitude of the Wolf-Rayet (superscript WR), companion (c), and system (sys) respectively. I took values for M^c from Martins & Plez (2006) in the case of O-stars, or the *Hipparcos*-based absolute magnitudes of (Wegner, 2006) for B-stars.

When a classification was not available for the companion star, I used the dilution of IR emission lines to determined a WR/system flux ratio, so that

$$M^{WR} = M^{sys} - 2.5 \log \left(\frac{F^{WR}}{F^{sys}} \right), \tag{2.5}$$

and

$$\frac{F^{WR}}{F^{sys}} = \frac{W_\lambda^m}{W_\lambda^n}, \tag{2.6}$$

where W_λ^m and W_λ^n represent measured and 'undiluted' (Table A.4) emission line equivalent widths. If the companion is not an OB-star or is insufficiently bright to notably dilute WR emission lines, it will not make a significant contribution to the systemic flux.

Two systems in the calibration sample are WNha+WNha binaries. There are no

known 'classical' WR+WR binaries, highlighting the sensitivity of post-MS evolution to initial mass. The fact that WNha+WNha binaries *are* observed emphasises their similarity to massive O-stars. We separate the light contributions of individual stars to each system by considering mass ratios derived by spectroscopic monitoring of their orbits. The stars making up WR 20a are of identical spectral type and have very similar masses (Rauw et al., 2005), hence we assume an equal light contribution from each star in the J, H and K_S-bands, and alter the systemic photometry accordingly. Similarly, WR 43A in the NGC 3603 cluster is comprised of two stars with very high measured masses, $116 \pm 31\,M_\odot$ and $89 \pm 16\,M_\odot$ ($q = 0.8 \pm 0.2$; Schnurr et al. 2008). Using the mass-luminosity relationship for very massive stars ($M > 80\,M_\odot$) provided by Yusof et al. (2013), we arrive at a light ratio of 1.46 ± 0.47 for this system in all bands, assuming identical SEDs. We include the stars of WR 20a and WR 43A under the WN6ha spectral type in Table 2.7.

The majority of WC9, and a diminishing fraction of earlier WC stars, show evidence of periodic or persistent circumstellar dust production (e.g. WR 140, Williams et al. 1990a). Episodes of dust formation occur at perihelion passage in eccentric WC+OB systems, whereas circular orbits allow persistent dust production, enhancing the near-IR flux of the system dramatically. For completeness, we perform near to mid-IR absolute magnitude calibrations for WC8d and WC9d spectral types based on the 18 stars at known distances. However, we do not make any attempt to remove the light contribution of potential companion stars; firstly because their K_S-band flux is usually insignificant compared to that of the hot circumstellar dust, and secondly because dust production seems to be inextricably linked to the presence of these companions (Crowther, 2003).

Thermal emission from hot circumstellar dust dominates the IR colours of dusty WC systems, prohibiting extinction determination via near-IR colour excess. For the dusty systems in our calibration sample we either adopt an average A_{K_S} for the relevant cluster/association, or convert an A_v listed by van der Hucht (2001) according to $A_{K_S} \simeq 0.12 A_v$.

I made an exception of WR 137 - a member of the Cyg OB1 association comprising WC7 and O9(± 0.5) type stars - which displays periodic dust formation episodes concurrent with its 13 yr orbit. Williams et al. (2001) present JHK$_S$ photometry for this system during a quiescent phase (1992–4), allowing me to derive a K_S-band flux ratio ($F^{WR}/F^{sys} = 0.46 \pm 0.13$) using line strengths measured from IRTF/SpeX spectra taken during quiescence (Table A.3), and remove the O-star light. I include The WC7 component in Table 2.8.

2.2.3 Calibration method and uncertainties

The results of near-IR absolute magnitude calibrations for all WR subtypes are presented in Table 2.11, with mid-IR calibrations shown in Table 2.12. Figures 2.10 and 2.11 present the K_S-band absolute magnitudes for WN and WC stars, respectively. I used a weighted mean method to arrive at an average absolute magnitude for each WR subtype, computed by

$$\bar{M} = \sum_{i=1}^{n} \frac{p_i M_i}{p}, \tag{2.7}$$

using weights

$$p_i = \frac{1}{s_i^2}, \qquad p = \sum_{i=1}^{n} p_i, \tag{2.8}$$

where s_i is the error in absolute magnitude (M_i) - invariably dominated by distance uncertainty - calculated for each of the n WR stars of that subtype. We calculate a formal error (σ) on each calibrated absolute magnitude value by combining two uncertainty estimates for weighted data:

$$\sigma = \sqrt{\sigma_1^2 + \sigma_2^2}, \tag{2.9}$$

where

$$\sigma_1 = \frac{1}{\sqrt{p}}, \tag{2.10}$$

and

$$\sigma_2 = \sqrt{\frac{\sum_{i=1}^{n} p_i (M_i - \bar{M})^2}{p(n-1)}}. \tag{2.11}$$

This combination is chosen because σ_1 depends only on s_i and does not consider the spread in M_i, which is accounted for by the term σ_2.

This weighted average approach favours objects with the most accurately determined distances, but the formal uncertainty given by Equation 2.9 does not account for any *intrinsic* scatter in luminosity within a WR subtype. Such a scatter is expected as a WR spectral subtype does not represent a perfectly uniform class of objects, but the division of smoothly varying Wolf-Rayet properties at spectroscopically identifiable boundaries.

Westerlund 1, the Arches and the GC cluster individually contain enough stars of a single subtype to evaluate some basic measures of spread, effectively eliminating the scatter introduced by distance uncertainties when considering one subtype across multiple clusters. In Table 2.10 I show the range and standard deviation in M_{K_S} within a WR subtype. Ranges are typically <1mag, although WN9 stars in the Arches cluster show a larger range due to the anomalously faint WR 102aj; we classify this star

Table 2.10: Intrinsic scatter in absolute magnitude within a WR spectral type

Cluster	Stars (WR#)	M_{K_S} range	σ_{M_K}
	WN7		
Westerlund 1	77d, 77j, 77r, 77sa	0.76	0.33
	WN8		
Arches	102a, 102ae, 102af, 102ah, 102al	0.84	0.34
GC Cluster	101b, 101dd, 101nc, 101oc	1.28	0.57
	WN9		
Arches	102ad, 102ag, 102ai, 102aj, 102bb, 102bc	1.85	0.72

based on a K-band spectrum published by Martins et al. (2008) and thus can only claim ±1 accuracy on the WN9 spectral type. Typical standard deviations of 0.3–0.6 mag in M_{K_S} suggest that WR absolute magnitudes intrinsically vary by at least ±0.3 within a spectral type. Following this result, I added an uncertainty of 0.3 mag in quadrature to the results of Equation 2.9 (see Tables 2.11–2.12), and recommend the use of this combined uncertainty when applying these calibrated absolute magnitudes to WR stars in the field, as I do in Section 2.3.

Throughout the rest of this chapter I favour discussion and application of M_{K_S} calibrations, as these results are affected by lower (and more accurately determined) extinctions than those in J and H-bands, and were calculated using the largest sample. Subtypes WN4 and WN5b stars were unrepresented in our calibration sample; for completeness I take average values in each band from the adjacent ionisation types.

2.2.4 Results of near to mid-IR absolute magnitude calibrations

Both strong and weak-line WN stars show a monotonic increase in near-IR luminosity with ionisation type. This is largely due to cooler, late-type WN stars having smaller bolometric corrections. WN stars displaying intrinsic absorption features - the WNha stars - are the most luminous at these wavelengths, as consequence of their high masses. Our results show good agreement with the calibrations of Crowther et al. (2006b) for

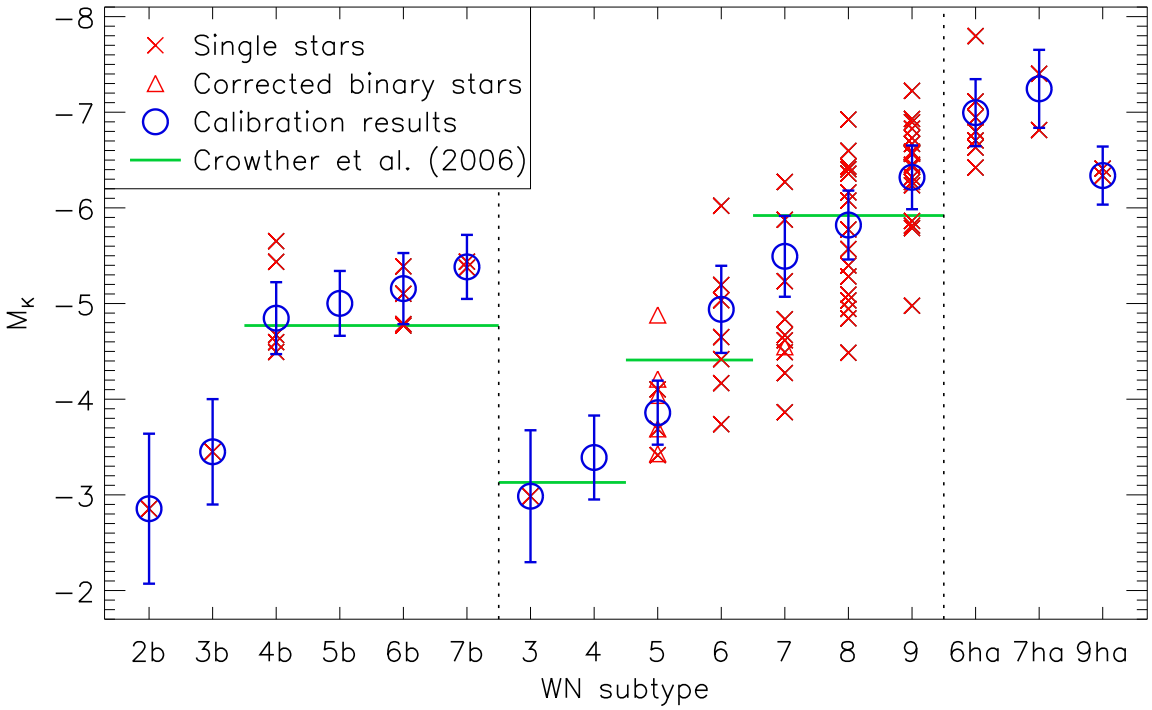

Figure 2.10: Calibration of M_{K_S} for WN spectral types. Broad-line stars are on the left, weak-line (including 'WN#o' and 'WN#h' stars) in the centre, and 'WN#ha' stars to the right. Individual single stars are represented by small (red) crosses, and stars that have been corrected for a companion(s) by (red) triangles. Larger (blue) symbols show the weighted average for each type with a combination of statistical error (Equations 2.9, 2.10 & 2.11) and the estimated intrinsic spread (0.3 mag) in M_{K_S} within a WR spectral type. Horizontal lines represent the previous calibrations of Crowther et al. (2006b).

weak-line WN stars, but suggest slightly higher IR luminosities for strong-line WN4–7b. It is interesting that for ionisation types 6–7, strong and weak line stars show similar M_{K_S}. One would expect an enhanced contribution from free-free excess in the dense winds of 'b' stars to make them brighter at IR wavelengths than weak-line stars. However, the strong-line stars of these ionisation types have higher effective temperatures (Hamann et al., 2006), so that the IR emission from free-free excess is counteracted by larger bolometric corrections in these subtypes.

Table 2.11: Calibrated near-IR absolute magnitudes for Galactic WR stars. The number of objects used to arrive at each value is indicated in adjacent parentheses. Two uncertainties are shown with each value; formal errors (parenthesised, Equation 2.9) do not account for the intrinsic spread in magnitude within a WR spectral type - estimated to be ~ 0.3 mag - which is incorporated into the final (nonparenthesised) uncertainty.

Sp. type	$\bar{M}_J$	(N)	$\bar{M}_H$	(N)	$\bar{M}_{K_S}$	(N)
WO2	$-2.15 \pm (0.08)\, 0.31$	(1)	$-2.26 \pm (0.08)\, 0.31$	(1)	$-2.26 \pm (0.07)\, 0.31$	(1)
WC4	$-2.88 \pm (0.13)\, 0.33$	(1)	$-2.92 \pm (0.13)\, 0.33$	(1)	$-3.50 \pm (0.13)\, 0.33$	(1)
WC5	$-3.80 \pm (0.27)\, 0.40$	(2)	$-3.84 \pm (0.27)\, 0.40$	(2)	$-4.40 \pm (0.25)\, 0.39$	(2)
WC6	$-4.03 \pm (0.61)\, 0.68$	(3)	$-4.06 \pm (0.62)\, 0.69$	(3)	$-4.66 \pm (0.61)\, 0.68$	(3)
WC7	$-4.21 \pm (0.20)\, 0.36$	(4)	$-4.25 \pm (0.20)\, 0.36$	(2)	$-4.84 \pm (0.21)\, 0.36$	(5)
WC8	$-4.26 \pm (0.24)\, 0.38$	(6)	$-4.35 \pm (0.22)\, 0.37$	(7)	$-5.04 \pm (0.28)\, 0.41$	(7)
WC9	$-4.42 \pm (0.39)\, 0.49$	(4)	$-4.17 \pm (0.32)\, 0.44$	(4)	$-4.57 \pm (0.38)\, 0.48$	(4)
WC8d	$-5.53 \pm (0.25)\, 0.39$	(3)	$-5.83 \pm (0.23)\, 0.38$	(3)	$-6.57 \pm (0.27)\, 0.41$	(4)
WC9d	$-6.34 \pm 0(.25)\, 0.39$	(12)	$-6.63 \pm (0.21)\, 0.37$	(13)	$-7.06 \pm (0.20)\, 0.36$	(14)
WN2b	$-2.97 \pm (0.73)\, 0.79$	(1)	$-2.89 \pm (0.73)\, 0.78$	(1)	$-2.86 \pm (0.72)\, 0.78$	(1)
WN3b	$-3.56 \pm (0.46)\, 0.55$	(1)	$-3.48 \pm (0.46)\, 0.55$	(1)	$-3.45 \pm (0.46)\, 0.55$	(1)
WN4b	$-4.48 \pm (0.23)\, 0.38$	(5)	$-4.58 \pm (0.23)\, 0.38$	(5)	$-4.85 \pm (0.23)\, 0.38$	(5)
WN5b	$-4.70 \pm (0.16)\, 0.34^a$	(0)	$-4.74 \pm (0.16)\, 0.34^a$	(0)	$-5.00 \pm (0.16)\, 0.34^a$	(0)
WN6b	$-4.93 \pm (0.23)\, 0.38$	(2)	$-4.90 \pm (0.22)\, 0.37$	(4)	$-5.16 \pm (0.22)\, 0.37$	(4)
WN7b	$-5.02 \pm (0.16)\, 0.34$	(2)	$-5.12 \pm (0.19)\, 0.36$	(2)	$-5.38 \pm (0.15)\, 0.34$	(2)
WN3	$-3.10 \pm (0.62)\, 0.69$	(1)	$-3.02 \pm (0.62)\, 0.69$	(1)	$-2.99 \pm (0.62)\, 0.69$	(1)
WN4	$-3.36 \pm (0.32)\, 0.44^a$	(0)	$-3.33 \pm (0.32)\, 0.44^a$	(0)	$-3.39 \pm (0.32)\, 0.44^a$	(0)
WN5	$-3.63 \pm (0.16)\, 0.34$	(8)	$-3.66 \pm (0.15)\, 0.34$	(4)	$-3.86 \pm (0.15)\, 0.34$	(7)
WN6	$-4.47 \pm (0.30)\, 0.43$	(6)	$-4.74 \pm (0.34)\, 0.45$	(7)	$-4.94 \pm (0.34)\, 0.46$	(7)
WN7	$-5.32 \pm (0.34)\, 0.45$	(9)	$-5.01 \pm (0.28)\, 0.41$	(9)	$-5.49 \pm (0.30)\, 0.42$	(10)
WN8	$-5.94 \pm (0.19)\, 0.35$	(15)	$-5.78 \pm (0.19)\, 0.36$	(16)	$-5.82 \pm (0.20)\, 0.36$	(16)
WN9	$-6.18 \pm (0.18)\, 0.35$	(15)	$-6.19 \pm (0.16)\, 0.34$	(17)	$-6.32 \pm (0.15)\, 0.33$	(18)
WN6ha	$-6.98 \pm (0.17)\, 0.34$	(8)	$-6.94 \pm (0.19)\, 0.36$	(8)	$-7.00 \pm (0.18)\, 0.35$	(8)
WN7ha	$-7.33 \pm (0.25)\, 0.39$	(2)	$-7.26 \pm (0.27)\, 0.40$	(2)	$-7.24 \pm (0.28)\, 0.41$	(2)
WN9ha	$-6.38 \pm (0.07)\, 0.31$	(2)	$-6.33 \pm (0.07)\, 0.31$	(2)	$-6.34 \pm (0.05)\, 0.30$	(2)

[a] Average of adjacent types since no stars of this type are available for calibration.

Table 2.12: Calibrated mid-IR (*Spitzer* IRAC filters) absolute magnitudes for Galactic WR stars. The number of objects used to arrive at each value is indicated in adjacent parentheses. Two uncertainties are shown with each value; formal errors (parenthesised, Equation 2.9) do not account for the intrinsic spread in magnitude within a WR spectral type - estimated to be ~ 0.3 mag - which is incorporated into the final (nonparenthesised) uncertainty.

WR Sp. type	$\bar{M}_{[3.6]}$	(N)	$\bar{M}_{[4.5]}$	(N)	$\bar{M}_{[5.8]}$	(N)	$\bar{M}_{[8.0]}$	(N)
WC5–6	$-4.34 \pm (0.35)\, 0.46$	(2)	$-4.75 \pm (0.35)\, 0.46$	(2)	$-5.02 \pm (0.28)\, 0.41$	(3)	$-5.32 \pm (0.29)\, 0.41$	(3)
WC7–9	$-5.96 \pm (0.29)\, 0.42$	(4)	$-6.27 \pm (0.33)\, 0.45$	(4)	$-6.06 \pm (0.33)\, 0.45$	(4)	$-6.27 \pm (0.34)\, 0.46$	(4)
WC8d	...		...		$-8.18 \pm (0.55)\, 0.63$	(1)	$-8.47 \pm (0.55)\, 0.63$	(1)
WC9d	$-6.88 \pm (0.48)\, 0.57$	(1)	$-7.25 \pm (0.50)\, 0.58$	(1)	$-9.29 \pm (0.16)\, 0.34$	(4)	$-9.36 \pm (0.16)\, 0.34$	(4)
WN3b	$-3.59 \pm (0.46)\, 0.55$	(1)	$-3.84 \pm (0.46)\, 0.55$	(1)	$-4.11 \pm (0.46)\, 0.55$	(1)	$-4.50 \pm (0.46)\, 0.55$	(1)
WN6–7b	$-5.51 \pm (0.41)\, 0.51$	(2)	$-5.88 \pm (0.40)\, 0.50$	(2)	$-6.14 \pm (0.38)\, 0.49$	(2)	$-6.41 \pm (0.44)\, 0.53$	(2)
WN4–6	$-4.18 \pm (0.13)\, 0.33$	(1)	$-4.42 \pm (0.14)\, 0.33$	(1)	$-4.71 \pm (0.15)\, 0.34$	(1)	$-5.05 \pm (0.15)\, 0.33$	(1)
WN7–9	$-5.96 \pm (0.39)\, 0.49$	(5)	$-6.23 \pm (0.36)\, 0.47$	(6)	$-6.53 \pm (0.28)\, 0.41$	(12)	$-6.79 \pm (0.30)\, 0.43$	(11)
WN7ha	...		$-7.74 \pm (0.12)\, 0.32$	(1)	$-7.87 \pm (0.12)\, 0.32$	(1)	$-8.22 \pm (0.12)\, 0.32$	(1)
WN9ha	...		...		$-6.79 \pm (0.31)\, 0.43$	(1)	$-6.90 \pm (0.31)\, 0.43$	(1)

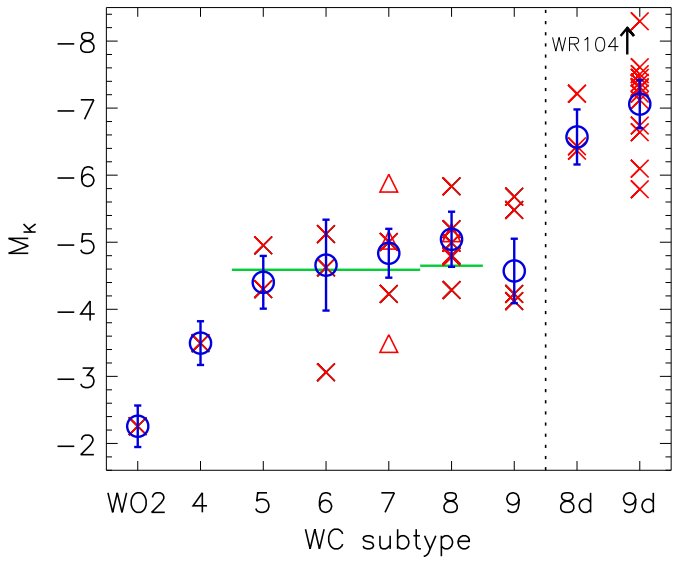

Figure 2.11: Calibration of M_{K_S} for WO and WC subtypes. To the right of the vertical dotted line are subtypes associated with circumstellar dust. WR 104 (WC9d+B) has $M_{K_S} = -10.4$, outside the range displayed here. Symbols same as Figure 2.10.

The lower number of WC stars available reveal a less obvious trend in M_{K_S} with ionisation type, yet a monotonic increase in near-IR luminosity does appear to be present for WC4–8. As expected, dusty WC stars display a large range in M_{K_S} due to varying quantities of dust and the random orbital phases sampled amongst periodic dust forming systems.

The limited area and resolution of the GLIMPSE survey results in far fewer stars available for absolute magnitude calibration at [3.6]–[8.0]μm. Hence, in some cases spectral types showing only small differences in M_{K_S} are grouped together to provide more robust estimates. For all WR types with GLIMPSE coverage we observe a brightening across [3.6]–[8.0], gradual in most cases except dusty WC stars which exhibit a dramatic $\Delta M \sim 2$ between [4.5] and [5.8].

The effects of a different Galactic Center extinction law

The results presented here were produced by applying the line-derived Fritz et al. (2011) 1–19μm law - with $A \propto \lambda^{-\alpha}, \alpha = 2.13 \pm 0.08$ over the JHK$_S$ range - to WR stars residing in the GC ($358° < l < 2°, |b| < 1°$). Alternatively, Nishiyama et al. (2009) propose a shallower law ($\alpha = 2.0$). It can be seen in Equations 2.1 and 2.2 that a shallower law would lead to lower derived extinctions by the colour excess method. I performed a second set of absolute magnitude calibrations using the Nishiyama et al.. law to quantify its effect

on our results. The biggest change is seen in calibrated absolute magnitudes for late-type WN and WC stars, as these dominate in the inner Galaxy. Compared to values presented in Table 2.11, adopting the Nishiyama et al. law changes $\bar{M}_J$, $\bar{M}_H$, and $\bar{M}_{K_S}$ of WN9 stars by −0.30, −0.31 and −0.30mag, respectively; WN8 stars by −0.26, −0.31, −0.32mag, and WC9 stars by −0.27, −0.32, −0.32mag. All differences are within the estimated uncertainties (Table 2.11) when using the Fritz et al.. law, and hence are not significant. However, as I proceeded to obtain further results based on these values I monitored their effects and will comment where discrepancies arose.

2.3 The Observed Galactic WR star Distribution

The sample of 126 WR stars involved in absolute magnitude calibrations represents approximately 20% of the current known Galactic population. The remainder either have poorly defined spectral types, uncertain binary status, or in a majority of cases do not reside in an identified cluster or association for which a distance measurement is available. For convenience, I shall refer to any WR star not in our calibration sample (i.e., Tables 2.6–2.8) as a 'field' WR star.

Up until recently it was widely accepted that most stars formed in clusters (Lada & Lada, 2003), so the low frequency of WR stars presently in clusters arose via dynamical ejection or rapid cluster dissolution. It is now recognised that a high fraction of star formation occurs in relatively low density regions (Bressert et al., 2010), so the low fraction of WR stars in clusters does not require an unusually high rate of ejection. Smith & Tombleson (2015) compare the association of WR stars (and Luminous Blue Variables) in the Milky Way and Magellanic Clouds with O stars. They find WR stars to be less clustered than O-type stars, with WC stars in particular showing weak spatial coincidence with O-stars and H-rich WN. The sizes of WN and WC calibration samples presented here echo this finding, with approximately half as many WC stars residing in clusters or associations with distance measurements. The typical velocity dispersion of cluster stars is not high enough to account for the isolation of WC stars considering their greater age. The relative isolation of WC stars challenges the commonly accepted evolutionary paradigm that this phase follows the WN phase in the lives of the most massive stars. Two alternative scenarios may explain the locations of WC stars; either they descend from a lower initial mass regime than other WR types, or the runaway fraction of WC and H-free WR stars in general is higher. Further detailed modelling of cluster collapse and the ejection of massive stars is needed to explain these emerging

statistics.

In this section I present an analysis of the spatial distribution of WR stars, where distances to 246 field WR stars are obtained by application of absolute magnitude calibrations. Runaway WR stars are discussed further in Section 2.3.2.

2.3.1 Applying M_{K_S} Calibrations

Photometry and the derived spatial information of 246 field WR stars are given in Tables 2.13 and 2.14. For any non-dusty field WR star with a well-defined spectral type and no evidence of a significant binary companion - either spectroscopically or through dilution of near-IR emission lines - I have applied M_{K_S} calibrations to obtain a distance. For these straightforward cases I applied the following equation,

$$d(\mathrm{kpc}) = 10^{(m_{K_S} - \bar{M}_{K_S} + 5 - A_{K_S})/5.0}, \tag{2.12}$$

once again using 2MASS photometry and extinction calculated by the method described in Section 2.2.2.

Regarding rare WO stars, although only one star (WR 142, WO2) is available for calibration, I apply the absolute magnitude of this star to the other three field WO stars in the Galaxy, spanning WO1–4 spectral types.

I found the spectral type and binary status of many field WR stars to be uncertain. The majority of the field sample are heavily reddened stars discovered by near-IR surveys, with typically only a K-band (and occasionally H-band) spectrum available in the literature. I included these stars in the field sample by applying the classification scheme presented in Section 2.1, requiring an accuracy of ± 1 subtype. Of the field WR stars included in this distribution analysis, I modified the previously claimed spectral types of $\sim$25% of those with *only* IR data available, indicated in Tables 2.13 & 2.14. For the remaining 75%, I either agreed with previous spectral types based on near-IR spectra, or adopted an optically assigned spectral type which were always assumed to be reliable.

Binary status is unknown of the majority of field WR stars, particularly late-WC stars, as IR line-dilution could be a result of thermal emission from circumstellar dust *or* the continuum of a bright companion. I cross-checked the IR emission line strengths of all WR stars discovered in near-IR surveys with the standard values given in Table A.4 to identify those showing unusually weak lines. I considered emission lines to be significantly diluted if two or more prominent lines across J, H, K_S were below $\sim 80\%$ of their standard strength. For WR stars of subtype other than WC7–9 showing IR line dilution, but with

no spectroscopically classified companion, I used equation 2.6 to measure a WR/system flux ratio in all bands with a line W_λ measurement. I then used the following equation to obtain an apparent magnitude for the WR component alone,

$$m^{WR} = m^{sys} - 2.5 \log \left(\frac{F^{WR}}{F^{sys}} \right). \tag{2.13}$$

The dilution of optical lines can also be used, as the uniformity of OB-star intrinsic (V-K_S) colours (Martins & Plez, 2006) makes it straightforward to translate a V-band flux ratio to the near-IR. I used the HeII 5411Å line to calculate a V-band flux ratio in WR 29, 38b, 39, 41, 50, 51, 63, using W_λ values published by Smith et al. (1996) or (Conti & Massey, 1989), compared with single WR stars from the same sources.

If line measurements are available across two bands, I was able to calculate an extinction to these diluted emission line WR stars using the colour excess method described in Section 2.2.2. However, the paucity of published line strengths typically results in a flux ratio only being measurable in one near-IR band. When this is the case, I either adopted A_v from the literature and converted using $A_K = 0.12 A_v$ (indicated in Table 2.14) or excluded the star from the analysis.

A small sample of field WR stars are SB2 systems where both components are spectroscopically classified. In these cases, I used the WR absolute magnitudes presented here, together with companion absolute magnitudes (M^c) from Martins & Plez (2006) for O-stars or Wegner (2006) for B-stars, to calculate a flux ratio,

$$\frac{F^c}{F^{WR}} = 10^{(\bar{M}^{WR} - M^c)/2.5}. \tag{2.14}$$

Using this ratio, I was then able to obtain the apparent magnitude of the WR star using the equation

$$m^{WR} = m^{sys} + 2.5 \log \left(1 + \frac{F^c}{F^{WR}} \right). \tag{2.15}$$

The SB2 method is applicable to periodic dust-forming WC systems, provided the systemic apparent magnitude is taken from a quiescent period. Another advantage of this method is it provides a WR star apparent magnitude in each band, allowing extinction to be calculated by the colour excess method.

To determine the nature of late-WC stars displaying diluted emission lines, I took photometry from the WISE all-sky survey (Wright et al., 2010), and constructed a simplistic 1–22μm SED for these sources. I interpreted a peak energy output at $\gtrsim 5\mu$m as evidence for circumstellar dust emission. Stars showing this in their mid-IR SEDs

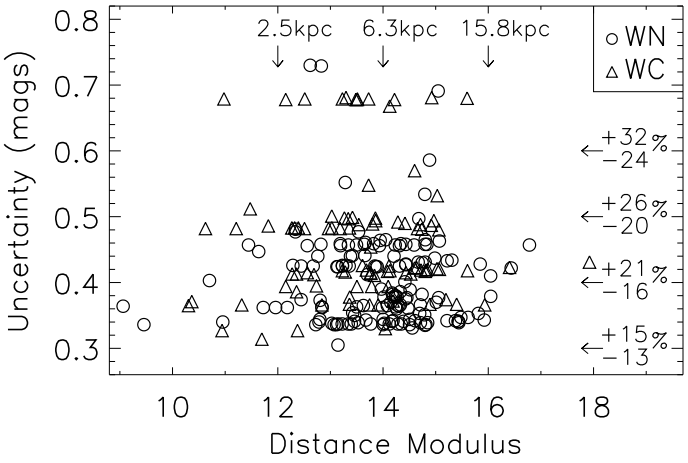

Figure 2.12: Distance modulus uncertainty for field WR stars, with equivalent distances indicated by vertical arrows and percentage errors by horizontal arrows.

were excluded from the analysis, as dust forming systems are a heterogeneous group and therefore cannot be assigned near-IR absolute magnitudes. I identified only one line-diluted late-WC, WR 42 (WC7+O7V), to be conclusively dust-free, and included this star in the field sample with a corrected J-band apparent magnitude (Equations 2.6 and 2.13).

In Figure 2.12 I show uncertainties on distance modulii derived for field WR stars. It can be seen that $\Delta DM \sim 0.4$ mag typically applies, and minimum distance uncertainties are approximately $\pm 14\%$.

The field WR star sample consists of 246 objects; 18 of these were corrected for a companion by the line dilution technique, and 3 corrected for a spectroscopically classified companion. Note that with the currently known population standing at ~ 660, approximately 290 WR stars are unaccounted for in the calibration and field samples. Of these, the majority have uncertain spectral types, and lack spectra of sufficient quality (or spectral range) to obtain the required subtype precision. I also excluded stars with inconclusive evidence for a companion, and subtypes for which calibrated near-IR absolute magnitudes could not be assumed (dusty WC stars, WN/C stars, WN10–11 stars).

A complete list of WR stars discovered between the Annex to the VIIth WR catalogue (van der Hucht, 2001, 2006) and March 2014 was provided by Rosslowe & Crowther (2015b), including an explanation of revised nomenclature.

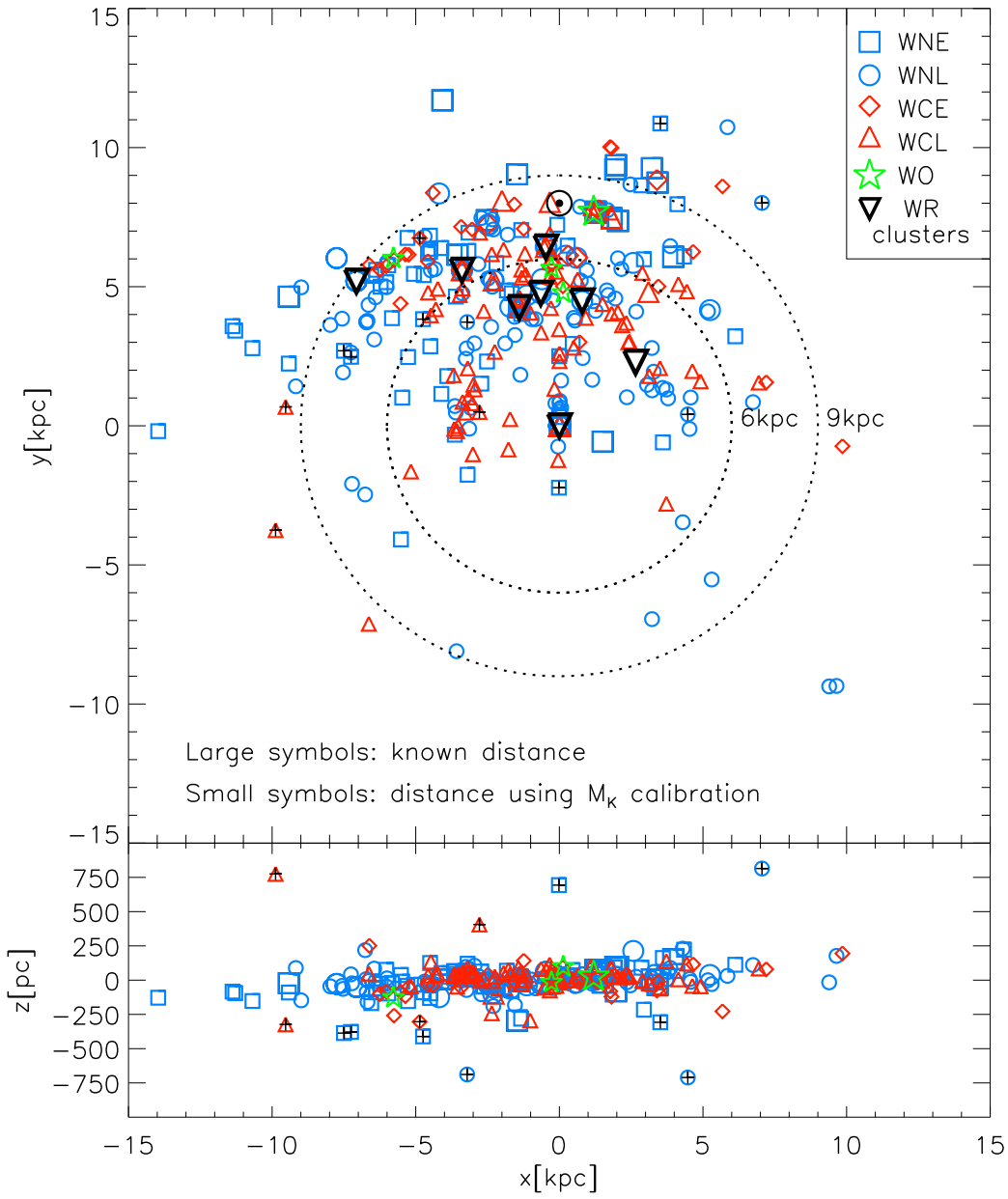

Figure 2.13: Positions of 354 WR stars projected on the Galactic plane (top) and viewed edge-on (bottom) in Cartesian coordinates, with the GC at (0,0,0). Galactic longitude increases anti-clockwise about the Sun, which is represented by the standard symbol. Stars with known distances (calibration sample) are represented by larger symbols, whereas those with photometric distances (field sample) are represented by smaller symbols. Stars located at $|z| > 300$ kpc are marked with black crosses. Dotted lines at $R_G = 6$ kpc and 9 kpc delineate the three chosen metallicity zones. From left to right, the displayed clusters from which > 1 WR stars are taken are: NGC 3603 [–7.07, 5.20], Danks 1&2 [–3.39, 5.59], Westerlund 1 [–1.40, 4.25], Havlen-Moffat 1&2 [–0.65, 4.76], NGC 6231 [–0.47, 6.43], GC [0.0, 0.0], Arches & Quintuplet [0.02, 0.0], Cl 1813-178 [0.79, 4.49] and Quartet [2.65, 2.29].

Table 2.13: Calculated spatial locations of the 228 'field' WR stars showing no conclusive evidence for an IR-bright companion, to which our calibrated absolute magnitudes have been assigned. Shown for each object are the adopted spectral type, 2MASS photometry (unless stated), derived K_S-band extinction, heliocentric distance (d), Galactocentric radius (R_G) and vertical distance from the Galactic midplane (z). A full version of this table is given in Appendix C.

WR#	Sp. Type	ref	J	H	K_S	$\bar{A}_{K_S}$	d(kpc)	R_G(kpc)	z(pc)
3	WN3ha	1	10.24	10.13	10.01	0.18 ± 0.02	4.53 ± 1.15	11.41 ± 1.18	-308 ± 83
4	WC5	2	8.75	8.57	7.88	0.13 ± 0.01	2.69 ± 0.49	10.15 ± 0.55	-121 ± 25
5	WC6	2	8.63	8.34	7.65	0.16 ± 0.02	2.69 ± 0.84	10.18 ± 0.88	-82 ± 32
13	WC6	2	10.14	9.64	8.86	0.29 ± 0.02	4.42 ± 1.38	9.46 ± 1.40	-40 ± 19
15	WC6	2	7.85	7.34	6.60	0.28 ± 0.02	1.57 ± 0.49	8.11 ± 0.55	-10 ± 9
16	WN8h	2	6.97	6.71	6.38	0.24 ± 0.02	2.77 ± 0.46	7.95 ± 0.52	-104 ± 20
17	WC5	2	9.93	9.74	9.17	0.07 ± 0.02	5.02 ± 0.91	8.31 ± 0.95	-303 ± 59
17-1	WN5b	3	11.73	10.38	9.53	0.85 ± 0.05	5.43 ± 0.86	8.58 ± 0.89	-41 ± 10
19	WC5+O9	4,5	9.75	9.13	8.53	0.20 ± 0.02	3.52 ± 0.64	7.93 ± 0.69	-54 ± 13
19a	WN7(h)	2	9.07	8.13	7.50	0.71 ± 0.04	2.41 ± 0.47	7.78 ± 0.53	-23 ± 8
...	...	...	...	...	...	...	...	...	...

Spectral types: (1)Marchenko et al. (2004), (2)van der Hucht (2001), (3) this work, (4)Crowther et al. (1998), (5)Williams et al. (2009b), ...

Table 2.14: Calculated spatial locations of 18 binary 'field' WR stars to which our calibrated absolute magnitudes have been assigned. Shown for each object are the adopted spectral type(s), systemic 2MASS photometry (unless stated), calculated K_S-band (unless stated otherwise in parentheses) WR/system flux ratio, derived K_S-band extinction, heliocentric distance (d), Galactocentric radius (R_G) and vertical distance from the Galactic midplane (z).

WR#	Sp. Type	ref	J^{sys}	H^{sys}	K_S^{sys}	F^{WR}/F^{sys}	$\bar{A}_{K_S}$	d(kpc)	R_G(kpc)	z(pc)
29	WN7h+O5I	1	9.91	9.46	9.12	0.49 ± 0.16	0.51 ± 0.19	9.48 ± 2.56	10.27 ± 2.57	-148 ± 45
30	WC6+O6-8	2	10.06	9.76	9.21	$0.75^{+0.25}_{-0.66}$	$0.25^{+0.37}_{-0.25}$	6.11 ± 3.44	8.29 ± 3.45	-258 ± 157
30a	WO4+O5-5.5	3	10.25	9.83	9.56	0.13 ± 0.04	0.40 ± 0.04	5.67 ± 1.18	8.17 ± 1.21	-117 ± 28
31	WN4+O8V	2	9.17	8.96	8.69	0.46 ± 0.23	0.30 ± 0.22	3.34 ± 1.12	7.63 ± 1.15	21 ± 1
35a	WN6h+O8.5V	4	10.47	9.98	9.65	$0.80^{+0.20}_{-0.33}$	0.37 ± 0.14	7.81 ± 1.99	9.13 ± 2.00	12 ± 2
41	WC5+OB	2	11.53	10.98	10.12	$0.93^{+0.07}_{-0.53}$	0.47 ± 0.27	6.69 ± 2.06	8.40 ± 2.07	-101 ± 37
42	WC7+O7V	5	7.59	7.52	7.08	0.53 ± 0.10(J)	0.14 ± 0.03	2.96 ± 0.53	7.47 ± 0.58	-6 ± 5
47	WN6+O5.5	6	8.32	7.92	7.55	$0.93^{+0.07}_{-0.12}$(J)	0.37 ± 0.03	2.12 ± 0.44	7.10 ± 0.50	11 ± 2
50	WC7+OB	2	9.75	9.38	8.81	$0.86^{+0.14}_{-0.59}$	$0.21^{+0.37}_{-0.21}$	5.23 ± 2.18	6.49 ± 2.19	45 ± 11
51	WN4+OB?	2	10.90	10.33	9.89	$0.77^{+0.23}_{-0.30}$	$0.72^{+0.86}_{-0.72}$	3.70 ± 1.80	6.55 ± 1.82	35 ± 7
63	WN7+OB	2	8.60	8.07	7.64	$0.89^{+0.11}_{-0.44}$	0.43 ± 0.27	3.68 ± 1.23	5.85 ± 1.26	-6 ± 8
86	WC7+B0III	7	7.44	7.14	6.67	0.77 ± 0.26	0.31 ± 0.02	1.97 ± 0.47	6.05 ± 0.53	83 ± 15
125	WC7ed+O9III	2	9.26^{8}	8.74^{8}	8.25^{8}	0.46 ± 0.07	0.25 ± 0.12	5.45 ± 1.05	6.56 ± 1.08	120 ± 19
138	WN5+OB	2	6.97	6.80	6.58	0.61 ± 0.11	0.27 ± 0.10	1.38 ± 0.26	7.76 ± 0.36	46 ± 5
143	WC4+Be	9	8.58	8.10	7.46	0.53 ± 0.17	0.60 ± 0.06	1.33 ± 0.30	7.82 ± 0.39	18 ± 1
151	WN4+O5V	2	9.76	9.36	9.01	0.73 ± 0.10	0.40 ± 0.11	2.93 ± 0.65	9.10 ± 0.70	91 ± 16
155	WN6+O9II-Ib	2	7.48	7.34	7.16	0.70 ± 0.07	0.14 ± 0.08	2.56 ± 0.56	9.02 ± 0.61	-38 ± 13
158	WN+OB?	2	8.64	8.20	7.81	$0.84^{+0.16}_{-0.28}$	0.40 ± 0.03	6.46 ± 1.38	12.23 ± 1.40	31 ± 3

(1)Gamen et al. (2009), (2)van der Hucht (2001), (3)Gosset et al. (2001), (4)Gamen et al. (2014), (5)Davis, Moffat & Niemela (1981), (6)Fahed & Moffat (2012), (7)Lépine et al. (2001), (8)Williams et al. (1992): average of quiescent photometry in 1989, (9)Varricatt & Ashok (2006).

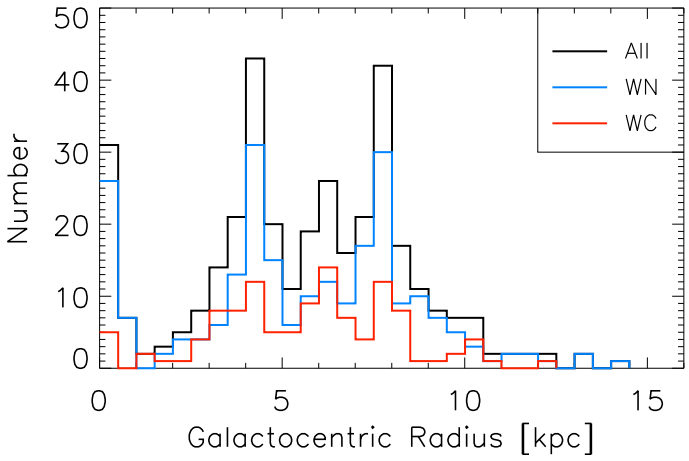

Figure 2.14: The distribution of Galactocentric radii for 354 WR stars, in 0.5 kpc bins

2.3.2 Spatial properties

The Galactic locations of 354 WN and non-dusty WC stars comprising calibration and field samples are shown in Figure 2.13.

Radial distribution

Figure 2.14 shows the radial distribution of 354 WR stars in the Milky Way. As expected, the majority of WR stars are located at Galactocentric distances of 3.5–10 kpc, with an additional peak at $R_G < 500$ pc owing to significant star formation within the central molecular zone (CMZ), reminiscent of OB-star forming regions (Bronfman et al., 2000).

Two conspicuous sub-peaks, consisting mostly of WN stars, can be seen at $R_G \sim 4.5$ kpc and ~ 7.5 kpc. Both may be viewed as superpositions on the underlying WR population, the innermost and outermost are largely attributable to the WR content of Westerlund 1 (~ 20 WR) and the nearby Cygnus star-forming region (~ 15 WR, $l \sim 75°$, $d = 1.3$–1.9 kpc) respectively.

z - distribution

Figure 2.15 shows that, as expected, WR stars are largely confined to the thin disk. This strict confinement to $z = 0$ resembles a Cauchy distribution. Indeed, a non-linear least squares fit of a Lorentzian function (Equation 2.16) matches well the distribution of vertical heights (z) of WR stars from the Galactic plane,

$$N(z) = A\left(\frac{\gamma^2}{(z - z_o)^2 + \gamma^2}\right), \tag{2.16}$$

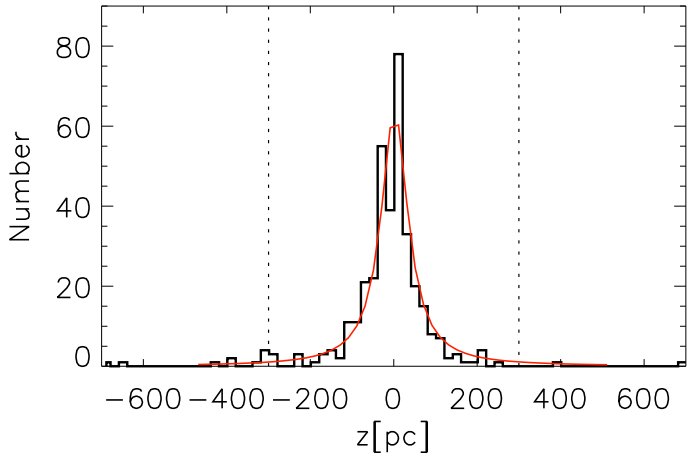

Figure 2.15: z distribution of 354 Galactic WR stars shown in 20pc bins (thick black line) with a fitted three-parameter Lorentzian function (thin red line, Equation 2.16). Stars at $|z|>300$pc (outside dotted lines) are listed in Table 2.15.

where γ is the half width at half maximum (HWHM), z_o is the location of the peak and A is an intensity. Assuming the Sun lies 20 pc above the Galactic midplane (Humphreys & Larsen, 1995), our fit yields $\gamma = 39.2$ pc and $z_o = 1.9$ pc (Figure 2.15).

Unlike other young stellar population tracers, I found no evidence for flaring of the WR star disk with increasing R_G, although this is likely due to the small number of WR stars identified beyond the solar circle. Paladini, Davies & De Zotti (2004) perform a Gaussian fit to the z-distribution of 456 Galactic H II regions interior to the solar circle, finding $\sigma \simeq 52$ pc (full width half maximum, FWHM ~ 125 pc). Although different in form, this distribution is broader than what I find for WR stars. The thickness of the OB star forming disk interior to the solar circle is measured by Bronfman et al. (2000), who find a FWHM of 30–50 pc - slightly narrower than the WR star disk - flaring to > 200 pc beyond $R_G = 12$ kpc.

WR stars at large distances from the Galactic disk

A small fraction of WR stars are found at high vertical distances from the Galactic disk. Additional details of the 12 WR stars at $|z| > 300$ pc ($\gtrsim 7\gamma$) are shown in Table 2.15, all of which are presumably runaways from star formation sites in the thin disk. I have included WR 124 in Table 2.15 which is identified as an extreme runaway by its high peculiar radial velocity (156 kms^{-1}; Moffat et al. 1982). Here we briefly discuss the possible events leading to the runaway status of these 13 WR stars, and summarise the evidence for each.

Table 2.15: Properties of 12 WR stars observed at $|z| > 300$ pc, plus WR 124 which is known to be an extreme runaway.

WR#	Sp. type	z(pc)	Binary status	L_X (ergs s^{-1})	Hα Nebula?
17	WC5	-303 ± 59	single	not detected[d]	...
3	WN3ha	-308 ± 83	single	2.5×10^{32} [c]	...
56	WC7	-323 ± 58	single	not detected[d]	No
54	WN5	-378 ± 61	single	not detected[d]	No
49	WN5(h)	-386 ± 63	single	not detected[d]	No
75c	WC9	406 ± 78	single	...	No
61	WN5	-411 ± 66	single	$< 5.0 \times 10^{30}$ [c]	No
71	WN6	-689 ± 139	Binary? (SB1)[a]	not detected[d]	Yes[e]
93a	WN3	694 ± 214	single	...	No
123	WN8	-711 ± 120	single	not detected[d]	No
64	WC7	775 ± 127	single	not detected[d]	No
148	WN8h	814 ± 131	Binary (SB1)[b]	$< 1.6 \times 10^{32}$ [c]	...
124	WN8h	213 ± 39	single	$< 2.0 \times 10^{32}$ [c]	Yes[e]

[a]Isserstedt et al. (1983), [b]Drissen et al. (1986), [c]Oskinova (2005), [d](ROSAT, Pollock, Haberl & Corcoran 1995), [e]Stock & Barlow (2010).

First, we address the possibility that some of these objects are much fainter (thus less distant) WR-like central stars of planetary nebulae (CSPN). Both WC-like ([WC], e.g., Depew et al. 2011) and WN-like ([WN], e.g., Miszalski et al. 2012 and Todt et al. 2013) CSPN have been observed in the field, although [WC]-type are far more common. These objects are almost identical in spectral appearance to their high-mass analogues (Crowther et al., 2006a), yet are intrinsically fainter by several magnitudes.

We conduct a search for nebulosity around each $|z| > 300$ pc WR star by inspection of SuperCOSMOS Hα images (Parker et al., 2005) and any other published Hα imaging. Identification of a surrounding nebula cannot alone prove any of these objects to be CSPN, as some WR stars are seen to possess ejecta nebulae (Stock & Barlow, 2010), yet it would provide a strong indication. Nebulosity is only observed around WR 71, which is known to be a genuinely massive, potential WR+compact object binary system (Isserstedt et al., 1983). We therefore conclude that none of these 12 high-z WR stars are incorrectly classified CSPN.

There are two leading mechanisms by which massive stars can be ejected from their birthplaces: the binary supernova scenario where a massive binary system becomes unbound after a SN explosion (Blaauw, 1961), and the dynamical ejection scenario where close encounters in a dense cluster can eject massive single or binary stars (Poveda, Ruiz & Allen, 1967).

A WR star at $|z| = 700$ pc (similar to the highest observed), assuming $z = 0$ at birth and a time since ejection of 5 Myr (typical WR star age), would require an average velocity in the z direction of 140 kms^{-1}. In the case of dynamical interaction between massive single and binary stars, a typical ejection velocity is given by $v_{ej}^2 = GM_b/a$ ($M_b =$ total mass of binary with semi-major axis a) according to Fujii & Portegies Zwart (2011), and the ejected star usually has the lowest mass of the three. By this reasoning, assuming a $M \gtrsim 25$ M$_\odot$ WR progenitor limit, a M_b=50 M$_\odot$ (160 M$_\odot$) binary with a period up to 170d (550d) would be capable of ejecting a WR progenitor star with at least $v_{ej} = 140$ kms^{-1}. Ejection of the binary system is also possible in such an interaction, which one might expect thereafter to be associated with considerable hard X-ray flux from the collision of stellar winds. In Table 2.15 I include available X-ray observations for these 12 stars, showing that only WR 3 is conspicuous, lying on the L_X/L_{bol} relation for spectroscopic O-star binaries (Oskinova, 2005). However, Marchenko et al. (2004) find no evidence for short period ($<$ 2yr) radial velocity changes, concluding that WR 3 is likely a single star.

Alternatively, the locations of these stars may be explained by momentum gained from the supernova explosion of a companion. Dray et al. (2005) estimate that $^2/_3$ of massive runaways are produced this way. Isserstedt, Moffat & Niemela (1983) show that kick velocities of ~ 150 kms^{-1} may be imparted on a surviving star, and that this star and the resulting supernova remnant may remain bound if less than half the total system mass is lost during the supernova. Therefore, one would expect a fraction of massive runaway stars to have compact companions. Indeed, WR 148 is an SB1 (Drissen et al., 1986) and the strongest Galactic candidate after Cyg-X3 for a WR+compact object binary. Low amplitude photometric and spectroscopic variations have been observed in WR 71 and WR 124 (Isserstedt et al., 1983; Moffat et al., 1982), suggesting they may also be SB1 systems with small mass functions. However, the absence of X-ray emission from accretion onto a compact object remains unexplained in all 3 cases. We note that the (WR+OB) binary fraction amongst this sample is very low, and quite possibly zero.

It has been suggested that WN8–9 subtypes are more frequently observed as WR runaways (Moffat, 1989). Considering only the most extreme examples, i.e., those with $|z| > 500$ pc plus WR 124, it can be seen from Table 2.15 that 3/6 are of the WN8 subtype. Although numbers are small, a preference seems to exist for WN8 runaways. Moffat (1989) argue that a WN8 spectral appearance may arise from mass accretion from a binary companion. Combined with the unusually low (WR+OB) binary fraction and the low-mass companion of WR 148, this evidence favours a binary supernova origin for the most extreme WR runaways.

Two of the runaway stars listed in Table 2.15, WR 61 and WR 93a, are observed at similar Galactic longitudes to the G 305 complex and GC clusters, respectively. Considering typical distance uncertainties (Figure 2.12), ejection from these massive star forming regions is a possible explanation for their large distance from the Galactic plane.

2.3.3 Subtype distributions across the Galactic metallicity gradient

Here I assess how WR subtypes vary across the Milky Way disk and compare this to the predictions of metallicity (Z)-dependent evolutionary models for massive stars. By including WR stars in the LMC and SMC, it was possible to probe massive star evolution over a metallicity range $Z = 0.002$–0.04. A constant star formation rate was implicitly assumed in all regions considered, allowing the relative numbers of WR types observed to be directly associated the relative duration of each phase.

I began by dividing the Galaxy into three broad zones of super-solar ($R_G < 6$ kpc), solar ($6 < R_G < 9$ kpc), and sub-solar ($R_G > 9$ kpc) metallicity. Based on the HII-region metallicity analysis of Balser et al. (2011), I assigned approximate Oxygen abundances ($\log[O/H] + 12$) of 8.85, 8.7 and 8.55 (± 0.1dex) to each zone respectively; I chose each value based on their Figure 8, and their derived (azimuthally averaged) $\log[O/H]$ gradient of -0.05 ± 0.02 dex kpc^{-1}. According to the distribution analysis of 354 WR stars presented here, I find 187, 133 and 34 to inhabit the super-solar, solar, and sub-solar metallicity zones respectively. Additionally, there are 148 known WR stars in the LMC (Breysacher et al. 1999; Neugent et al. 2012 and references therein; Massey et al. 2014) for which the Oxygen abundance is $(\log[O/H] + 12) = 8.38$ (Rolleston, Trundle & Dufton, 2002), and 12 WR stars in the SMC (Massey & Duffy, 2001; Massey et al., 2003) for which $(\log[O/H] + 12) = 8.13$ (Rolleston et al., 2003).

As recently highlighted by Groh et al. (2014), there is not a straightforward correspondence between spectroscopic and evolutionary phases in massive stars, particularly post-main sequence. When comparing the duration of an observed spectroscopic phase to the duration of an evolutionary phase, one must take care to be sure that the two represent the same physical state of the star.

Spectroscopically, any WN showing surface Hydrogen (WN#h or (h)) or with ionisation type ≥ 7 is identified as late-type (WNL), while H-free WN of ionisation type ≤ 6 or those displaying broad emission lines (WN#b) are early-type (WNE). I followed these definitions, noting that the lack of near-IR hydrogen diagnostics is unlikely to significantly affect our measured N_{WNE}/N_{WNL}, as Galactic WN ≤ 7 stars are generally

Table 2.16: Observed Wolf-Rayet number ratios in the Galaxy, LMC and SMC. Galactic WC stars counted here show no evidence of circumstellar dust, results incorporating an estimated 28% of neglected (dusty) WC stars are parenthesised. The 4 WO stars are counted as WCE. An indication of uncertainty is given assuming $\sqrt{N}$ errors on each count.

Region ($\log[^{O}/_{H}]+12$)	N_{WR}	N_{WC} (N_{WCd})	N_{WN}	N_{WC}/N_{WN} ($N_{(WC+WCd)}/N_{WN}$)	N_{eWNE}/N_{eWNL}	$N_{(WCE+WO)}/N_{WCL}$
Inner Galaxy (8.85 ± 0.1)	187	63 ($\sim$22)	124	0.51 ± 0.08 (0.69)	0.23 ± 0.05	0.05 ± 0.03
Mid Galaxy (8.7 ± 0.1)	132	46 ($\sim$16)	86	0.53 ± 0.10 (0.73)	0.79 ± 0.17	1.00 ± 0.28
Outer Galaxy (8.55 ± 0.1)	35	10 ($\sim$4)	25	0.40 ± 0.16 (0.57)	1.27 ± 0.58	1.5 ± 0.97
LMC (8.38 ± 0.05)	148	26	122	0.21 ± 0.05	1.93 ± 0.37	26/0
SMC (8.13 ± 0.05)	12	1	11	0.10 ± 0.09	11/0	1/0

H-free (Hamann, Gräfener & Liermann, 2006), so division by ionisation type alone is sufficient. This assumption is less applicable in the lower metallicity regions of the outer Galaxy, however, low extinction in these directions means optical (Hydrogen) diagnostics are commonly available. The division in WC stars is more straightforward, with WC4–6 defined as early (WCE) and WC7–9 as late-type (WCL). In Table 2.16 I show the subtype breakdown of WR stars observed in each Galactic metallicity region.

In stellar models, WR stars have historically been matched with the aforementioned spectroscopic WR types using basic surface abundance and effective temperature (T_{eff}) criteria. For example, Meynet & Maeder (2005) employ $T_{eff} > 10^4$ K and $X_H < 0.4$ as the definition of a WR star in their models, while Eldridge, Izzard & Tout (2008) add a further constraint of $\log(L/\mathrm{L}_{\odot}) > 4.9$. This T_{eff} boundary is too low, since even the coolest WR stars (WN8–9) are found to have $\log(T_{eff}) \simeq 4.6$ (Hamann et al., 2006). A surface temperature of 10^4 K is more typical of late-B/early-A supergiants (Przybilla et al., 2006). Also, recent spectroscopic analysis of WC stars by Sander, Hamann & Todt (2012) indicate that some WC9 stars are very close to this lower luminosity limit. The transition between eWNE and eWNL phases (where 'e' denotes the definition in evolutionary models) is regarded to occur when $X_H < 10^{-5}$, and the eWC phase begins when carbon dominates nitrogen by mass (Meynet & Maeder, 2005). By computing model spectra from evolutionary models, Groh et al. (2014) have shown that spectroscopic WNE and WNL lifetimes can differ radically from eWNE and eWNL lifetimes,

as a star may have a WNE spectrum while retaining some surface hydrogen, hence this is a poor indicator. The problem is not so severe regarding the transition from WN to WC stars, as the change in surface carbon abundance is a rapid process, meaning the eWC phase corresponds well to the spectroscopic WC phase.

Incompleteness of the sample

Before comparing observed numbers with evolutionary model predictions, it is necessary to comment on two selection effects - one in our distribution analysis and one inherent to WR star surveys - that affect the star counts I present.

Firstly, since reliable near-IR absolute magnitudes cannot be assumed for dusty WC stars they have been excluded from this distribution analysis. In Table 2.16 I have counted only those WC stars showing no evidence for circumstellar dust. However, by inspection of a local volume-limited ($d < 3$ kpc) sample of WR stars (see Section 3.3.2 for full details), I have estimated that $27(\pm 9)\%$ of WC stars shown evidence of circumstellar dust. To account for these neglected WC stars, I include an enhanced set WC/WN number ratios, along with those directly counted from Table 2.16. As this information is only available in the solar neighbourhood, I was forced to assume an unvarying fraction of dust-forming WC stars across the whole Galaxy. Late-type WC stars are known to dominate at higher metallicity, and it is predominantly these that are seen forming dust, hence I expect this fraction in reality to be higher towards the GC. The slight downturn in N_{WC}/N_{WN} at $R_G < 6$ kpc could be due to a higher number of late WC stars omitted from this analysis in that region.

Secondly, the two most widely employed WR star survey techniques are both least effective at identifying weak-lined WNE stars. Narrow-band IR imaging surveys are biased against WNEs due to low photometric excesses from their weak emission lines. The IR excess emission from free-free scattering - exploited by broad-band selection techniques - is also weaker in WNE stars as their wind densities are lower than other WR subtypes. For these reasons, and considering their modest IR luminosities, I expect WNE stars to be slightly under-represented in the total sample of 354 WR stars, especially beyond the solar neighbourhood. Therefore, future observations will likely refine the numbers presented here by marginally decreasing N_{WC}/N_{WN} and increasing N_{WNE}/N_{WNL}.

Comparison to evolutionary predictions

In Figure 2.16 I plot the observed N_{WC}/N_{WN} in different regions of the Galaxy, and the Magellanic Clouds, alongside predictions from population synthesis of massive stars

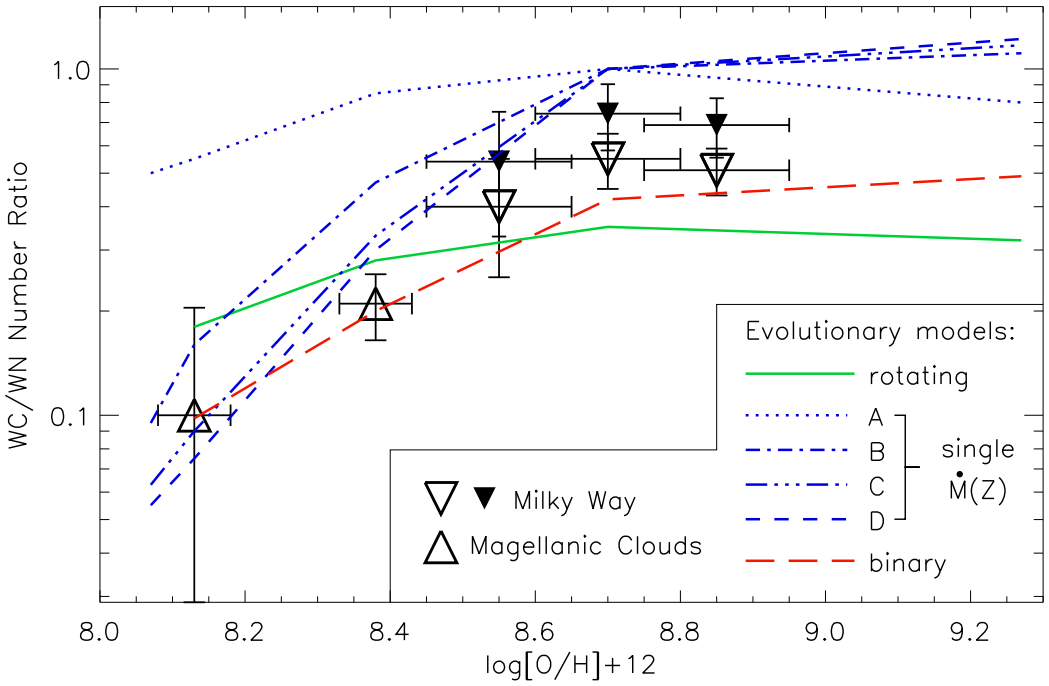

Figure 2.16: Number ratio of WC/WN stars in the LMC and SMC (triangles), and across three Milky Way regions (upsidedown triangles) where results omitting dusty WC stars (as in Table 2.16) are plotted as larger open symbols and smaller filled symbols represent the case where 28% of all WC stars possess hot circumstellar dust (Section 3.3.2). Solid (green) line shows the predictions of Meynet & Maeder (2005) for rotating single stars. Long-dashed (red) line shows the predictions of Eldridge et al. (2008) for a population of massive binaries. All other lines (blue) represent non-rotating single-star evolutionary predictions of Eldridge & Vink (2006) for four different $\dot{M}-Z$ dependencies. Errors on the number ratios shown are estimated assuming $\sqrt{N}$ counting errors in N_{WC} and N_{WN}. An uncertainty of 0.1 dex is assumed for each Galactic $^{O}/_{H}$ value.

using various evolutionary models. Rotating single-star models are taken from Meynet & Maeder (2005), non-rotating single-star models with various $\dot{M}(Z)$ dependencies are taken from Eldridge & Vink (2006), and predictions for a population of non-rotating massive binaries exhibiting metallicity dependent mass-loss are taken from Eldridge et al. (2008) (BPASS[4]).

All models predict an increasing number of WC compared to WN stars with metallicity, due to increasingly rapid exposure of nuclear burning products caused by stronger stellar winds in more metal-rich environments (recall Section 1.4.1). The observed values show only a modest variation of N_{WC}/N_{WN} (0.4–0.55) across the Galactic disk, whereas the ratio drops considerably to 0.2–0.1 at LMC and SMC metallicities. At all metallicities the observed N_{WC}/N_{WN} lies between the predictions from a population of binary stars (Eldridge et al., 2008) and single non-rotating stars. The addition of an estimated 28% of neglected (dusty) WC stars at Galactic metallicities does not significantly alter this. However, the predictions of evolutionary models including rotation lie ubiquitously lower than the observations at Galactic metallicities. Fast rotation has the effect of lengthening WR lifetimes, manifest predominantly in the eWNL phase (Figure 1.8), thus reducing N_{WC}/N_{WN} (Meynet & Maeder, 2005). However, it is not expected that all massive stars are formed rotating as quickly ($v_i^{rot} = 300\,\mathrm{km\,s^{-1}}$) as those generated in these models (Penny & Gies, 2009).

Figure 2.17 shows the number ratio of early to late WN stars in each Galactic metallicity zone, as well as in the LMC and SMC. An increase in the proportion of WNE can be seen with decreasing metallicity, and no WNL stars are known in the SMC. Contrary to this, the rotating models of Meynet & Maeder (2005) produce a *shorter* relative eWNE phase at lower metallicity, due to less efficient removal of the H-rich stellar envelope during prior evolutionary phases. Furthermore, rotationally induced mixing allows stars to become WRs earlier in their evolution and experience an extended eWNL phase. The extreme sensitivity of the eWNE/eWNL transition to the chosen hydrogen surface abundance criterion clearly has a major influence on predictions (Groh et al., 2014). Therefore I interpreted the disparity between observed and predicted N_{eWNE}/N_{eWNL} largely as a symptom of these definitions, rather than a serious conflict with evolutionary theory.

These results reinforce the idea that the WN phase of WR stars at sub-solar metallicities is almost entirely spent with a WNE spectral appearance, whereas the WNL spectral type endures longer on average at super-solar metallicities.

[4] http://www.bpass.org.uk/

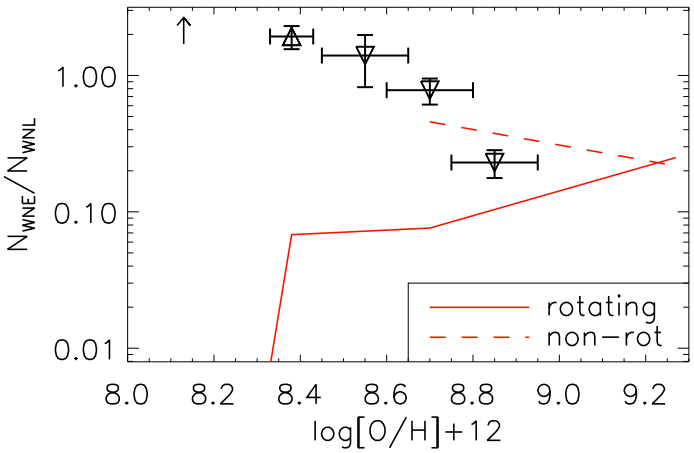

Figure 2.17: Number ratio of WNE/WNL stars across three metallicity zones in the Milky Way, LMC and SMC. Red lines show eWNE/eWNL predictions from rotating (solid) and non-rotating (dashed) evolutionary models (Meynet & Maeder, 2005).

2.4 The Potential of WISE and IPHAS to identify new Galactic Wolf-Rayet Stars

Only ∼40 WR are known beyond the solar circle (R_G= 8kpc). Identifying and characterising massive stars in this region is important for testing evolutionary predictions as a function of metallicity (e.g., Section 2.3.3), as it provides a bridge between the solar neighbourhood and LMC. Furthermore, calibrated absolute magnitudes for WR stars (Section 2.2) allow them to be used as tracers of Galactic structure.

As discussed in Section 1.3.1, recently developed near-IR selection techniques for WR stars have helped deliver a 3-fold in the number of known Galactic WR stars over the past ∼ 15 years. However, spectroscopic follow-up of candidates has been exclusively focused on the inner Galaxy. In Figure 2.18 I show the GLIMPSE field of view, which has been extensively searched for WR star candidates, with published spectroscopic follow-up to K≃12 mag (Hadfield et al., 2007; Mauerhan et al., 2011). In the same figure I show the area surveyed with narrow-band imaging (Shara et al., 2009, 2012), to identify WR stars by photometric excess caused by emission lines. While the density of massive star tracers on the sky decreases outside these areas, there are reasons to expect a population of massive stars outside of them. The lines of sight corresponding to the longitude limits of the GLIMPSE survey are tangential to a circle of 7.25 kpc in Galactocentric radius. According to the distribution of WR stars presented in Section 2.3, this radius encloses ∼ 68% of those known. Furthermore, the molecular gas disk of the Galaxy - with which

one expects massive star formation to be associated - truncates at $\sim 15\,\mathrm{kpc}$. There also exists several young open clusters beyond the solar circle (e.g. NGC1893, h+χ Persei) hosting populations of massive stars (Marco & Negueruela, 2002; Currie et al., 2010).

In September 2013, I led a 2-night observing run on the Isaac Newton Telecsope (INT), using the IDS to take optical spectra of IR-selected WR star candidates. I selected candidates using a combination of photometric criteria based on the properties of known WR stars in the 2MASS, WISE and IPHAS surveys (Section 2.4.2). The area of sky targeted (see Fig 2.18) coincides with a local enhancement of HII-regions in the Northern hemisphere, indicative of massive star formation. Galactic structure is also uncertain along the chosen line-of-sight (in the second quadrant, Q2), as explained in Section 2.4.1.

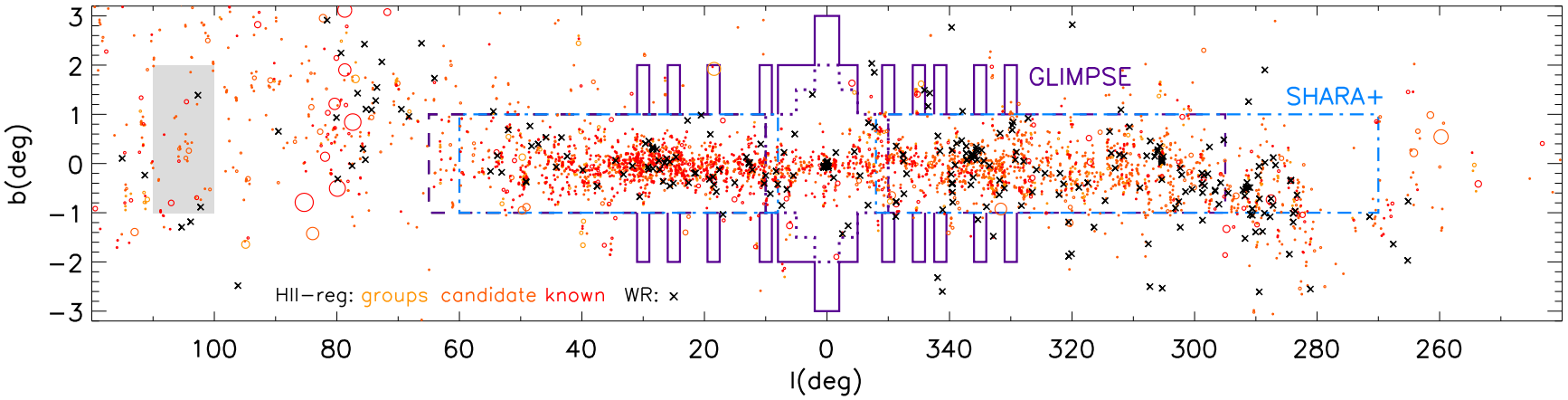

Figure 2.18: The Galactic plane (excluding the anti-centre $120° < l < 240°$). The locations of 354 known WR stars (calibration and field samples, presented in this chapter) are shown as black crosses. The locations of Galactic HII-regions are taken from Anderson et al. (2014) and shown as circles, plotted to scale and enlarged for visibility. Colours represent known (red), candidate (orange) and groups of (yellow) HII-regions. The GLIMPSE survey footprint is enclosed by a purple border, including GLIMPSE I (dashed), GLIMPSE II (dotted) and GLIMPSE 3D (solid). The area surveyed by Shara et al. with narrow-band imaging is enclosed by a blue (dash-dot) border. The area from which WR candidates were selected for follow-up using INT/IDS is shaded grey.

2.4.1 Selection of Survey Area

The existence of an outer spiral arm (or Cygnus arm) was suggested by Kimeswenger & Weinberger (1989), revealed by a statistically significant gap in optical tracers between the Perseus arm and a more distant feature at 5–7 kpc. I show a schematic of this proposed structure in Figure 2.19. This distant spiral arm has been seen in velocity measurements of molecular gas (e.g., Dame et al. 2001). However, Russeil (2003) notes that velocity departures between the Perseus and Outer arm - in opposite directions - have led many authors to incorrectly measure kinematic distances in Q2, highlighting the need for more direct optical/IR tracers of spiral structure. Negueruela & Marco (2003) measured spectroscopic parallaxes of ∼60 OB stars throughout Q2, finding that those between l=150−180° sparsely trace a further spiral arm. Similarly, Raddi et al. (2013) measured spectroscopic parallaxes of ∼60 classical Be stars between l=120−140°, finding a significant number at the outer arm distance, but with a distribution equally consistent with a spiral or flocculent morphology.

I selected WR star candidates from Galactic longitude and latitude ranges $100° < l < 110°$, $-1° < b < +2°$, shown in Figure 2.18. The positive bias in latitude was included to account for warping of the stellar disk, seen to reach +1° at $l \simeq 100°$ (Momany et al., 2006). The chosen longitude range contained only 6 known WR stars prior to our observing campaign, and displays an enhanced density of HII-regions according to the distribution presented by Paladini et al. (2004). In Figure 2.18 I include an updated and considerably more complete map of Galactic HII-regions (Anderson et al., 2014). The over-density of HII-regions visible in the Paladini et al. sample between $100°<l<110°$ is less obvious in this updated sample, however, several small groups are present.

Vallée (2008) report a distance to the outer arm of $d = 4$–5 kpc at $l = 180°$, increasing to $d = 6$–7 kpc at $l = 90°$. Assuming $d = 6$ kpc, the intrinsically faintest WR subtypes ($M_K \simeq -4.0$ mag, Sec 2.2) would have K ≃ 11.0 mag if reddened by $A_{K_S} \simeq 0.3$ mag (equivalent to $A_r = 2.5$ mag - median reddening of Be stars in Q2 surveyed by Raddi et al. 2013). This would translate into $R \simeq 16$ mag, meaning the requisite signal-to-noise for spectroscopic classification (~ 50) could be achieved in approximately 40 minutes[5] with the IDS instrument in the configuration used (Section 2.4.3). Therefore, any WR stars discovered by this observing campaign could serve as a direct tracers of spiral structure (the outer arm) in this region.

[5]calculated using the ING exposure time calculator.

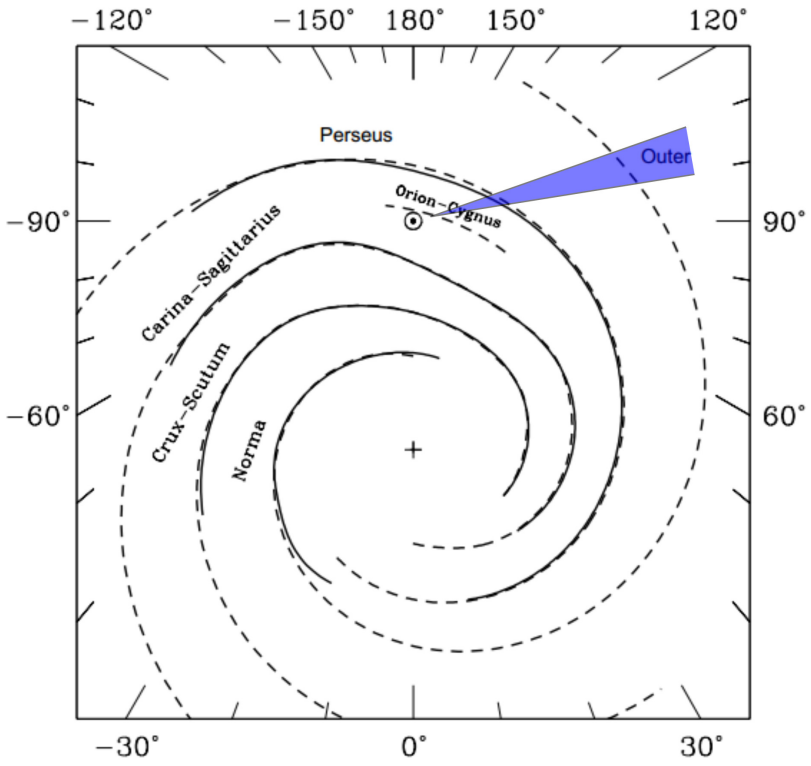

Figure 2.19: Schematic top-down view of the Milky Way's spiral structure, showing confirmed (solid) and proposed (dashed) spiral arms (Georgelin & Georgelin, 1976). The shaded area shows the longitude range from which candidate WR stars were selected for follow-up with INT/IDS (shaded), intersecting the Perseus and Cygnus (outer) spiral arms.

2.4.2 Colour Selection of Candidates

It has been shown that using photometric criteria involving $>2\mu$m data significantly improves the efficiency WR star candidate selection (Mauerhan et al., 2011). The all-sky WISE survey facilitates the extension of near to mid-IR colour selection techniques to areas not surveyed by *Spitzer* GLIMPSE. The IPHAS Hα survey provides a further tool in the search for Northern hemisphere WR stars, since emission in HeII(6560Å)+Hα is common to all WR subtypes.

I selected candidates using a combination of photometric criteria based on the properties of known WR stars in the 2MASS, WISE and IPHAS surveys. Mauerhan et al. (2011) identify colour 'sweet-spots' (see their figure 1), i.e., areas of near to mid-IR colour space from which WR star candidates are most effectively selected. I attempted to replicate these colour criteria using WISE bands W1 (3.4μm) & W2 (4.6μm) as a proxy for GLIMPSE [3.6μm] & [4.5μm].

In Figure 2.20 I show 2MASS and WISE colours for a sample of Northern Hemisphere WR stars[6]. I also show samples of field dwarf stars (Bilir et al., 2011); dwarf, giant and supergiant O-stars[7]; and Be-stars taken from the sample of Jones et al. (2011). I retrieved and inspected 2MASS K_S, W1 & W2 images for every star included in the WR, O-star and Be-star samples shown in Figure 2.20, ensuring each source was unblended and consistent between the different surveys. Be stars are included because they are a common contaminant of colour-selected WR star candidates, along with OB supergaints, owing to the IR excess from their winds (Mauerhan et al., 2011). Be stars also show Hα emission, leading to possible confusion when IPHAS data is taken into account. It can be seen in Figure 2.20 that WR stars are well separated from these other stellar types in WISE+2MASS colour space.

In Figure 2.21 I show IPHAS colours for a sample of WR stars, along with a randomly selected sub-sample of Be stars from Raddi et al. (2015), and all point sources within $2'$ of $l=105°, b=0.5°$ (centre of the searched field). I extracted IPHAS photometry for Northern Hemisphere WR from the initial data release (González-Solares et al., 2008). Witham et al. (2008) give a catalogue of Hα emission sources in the IPHAS field, defining a threshold in $(r-H\alpha)$ vs $(r-i)$. This threshold, shown in Figure 2.21 as a dotted line, only identifies approximately half of known WR stars as Hα emitters. I therefore decided to adopt a more conservative limit (dashed line, Fig 2.21), encompassing all known WR in the available sample.

[6]selected from the Galactic WR star catalogue
[7]selected from the Galactic O-star catalogue (Maíz Apellániz et al., 2013)

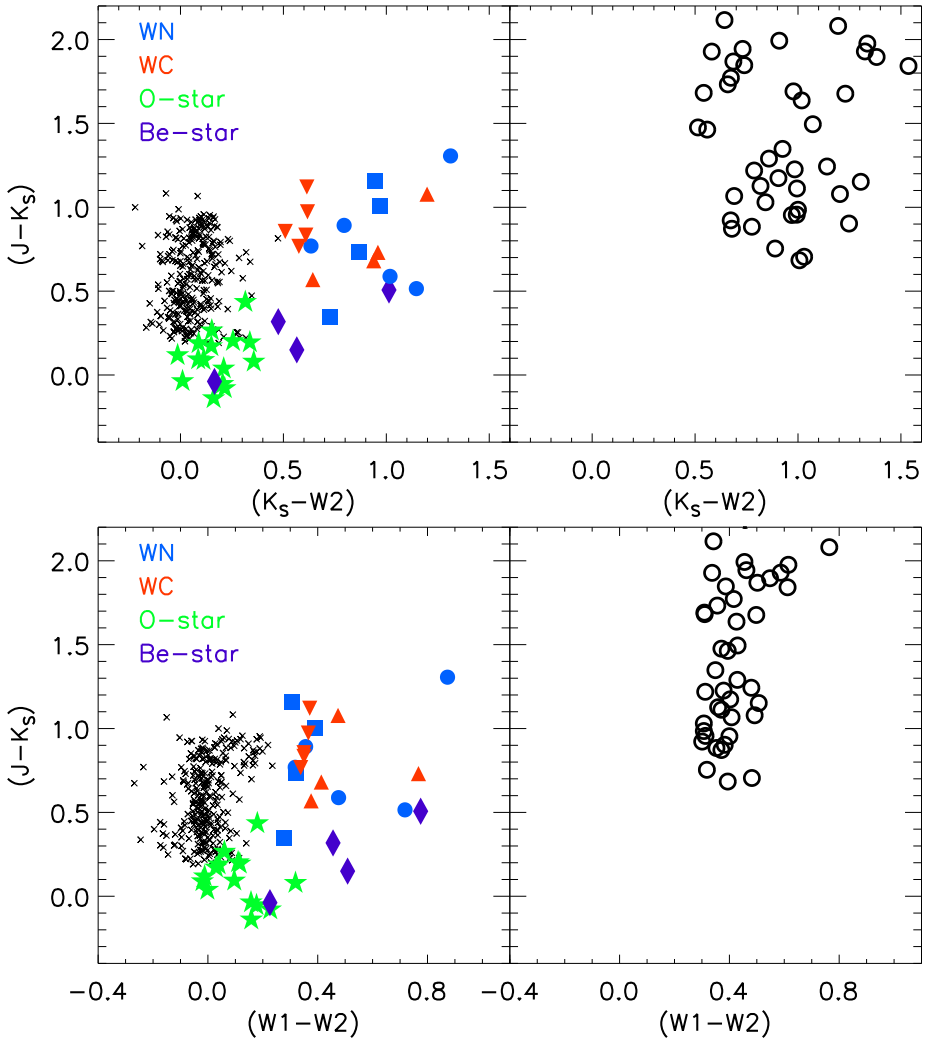

Figure 2.20: *Left*: near to mid-IR (2MASS and WISE) colours for samples of known stellar types, including common WR impostors (field dwarf stars shown as crosses; O-stars stars; Be-stars diamonds; WNE squares; WNL circles; WCE down triangles; WCL up triangles). *Right*: same colours as left for selected WR star candidates in the search field ($100° < l < 110°$, $-1° < b < +2°$).

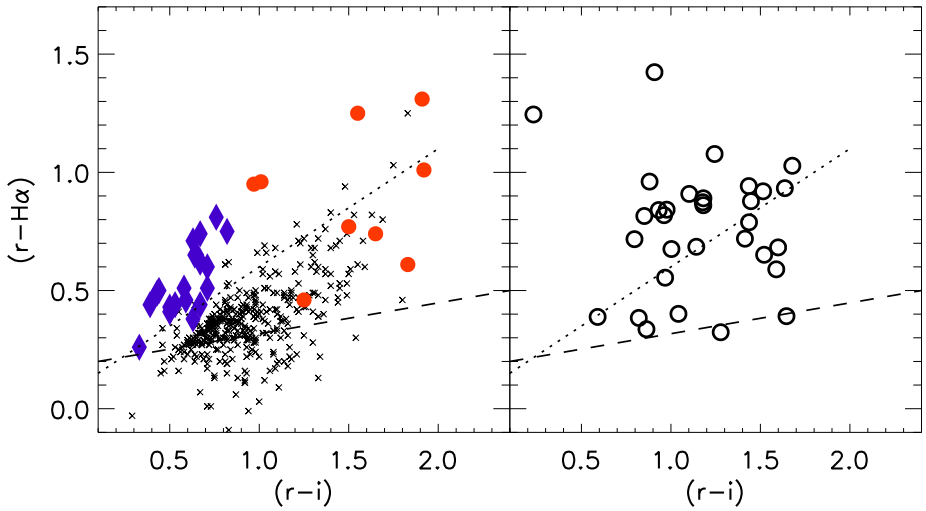

Figure 2.21: *Left*: optical colours of every point source from the IPHAS initial data release within 2′ of the centre of the search field ($l = 105°, b = 0.5°$, black crosses), Be stars (purple diamonds) and WR stars (red circles). *Right*: same colours for selected WR candidates in the search field ($100° < l < 110°$, $-1° < b < +2°$). Black dotted line shows the Hα emitter threshold devised by Witham et al. (2008). The lower black dashed line indicates the threshold above which WR candidates were selected.

I selected WR candidates from the WISE point-source catalog (Wright et al. 2010), requiring the satisfaction of three independent criteria;

i). WISE/2MASS colours; $0.5 < (J-K_S) < 5.0$, $0.3 < (W1-W2) < 0.8$ and $(K_S-W2) > 0.5$. Designed to mimic the WR colour 'sweet spots' highlighted by Mauerhan et al. (2011).

ii). K_S<11 mag - the expected brightness of an intrinsically faint WR ($M_K \sim -4$) at the distance of the outer arm with $A_K \simeq 0.3$mag,

iii). Sources coexistent with an IPHAS Hα(+HeII 6560Å) emission source (see Figure 2.21) within 6″, corresponding to the spatial resolution of WISE images.

I inspected by-eye the W1 & W2 images of all sources satisfying these criteria, rejecting sources coincident with extended emission, ensuring the mid-IR colours used were purely stellar in origin. I also inspected by-eye 2MASS JHK$_S$ and DSS images to verify each target was a single source. The candidate sources satisfying all above criteria are shown in the right panels of Figures 2.20 & 2.21.

The characterisation of WR stars in IR surveys, specifically WISE, has since been investigated in much greater detail by Faherty et al. (2014). The colour-selection crite-

ria devised by these authors are more sophisticated but in good agreement with those presented here.

2.4.3 Observations and results

Over 2 nights I observed 47 candidate WR stars using the INT/IDS. The R300V grating was used with 235mm camera and the EEV10a detector, providing a wavelength dispersion of 1.9Å/per pixel in the V-band and a spatial scale of .4″/pixel. The wavelength range covered ($\sim$4000–9000Å) contains key emission line diagnostics for the classification of WR by the methods of Smith et al. (1996) and Crowther et al. (1998) for WN and WC stars respectively. The ratio HeII 5411Å/HeI 5875Å providing the primary ionisation diagnostic for WN stars, and CIV 5801–12Å/CIII 5696Å for WC stars. I opted to use a 4 pixel (1.6″) slit width to minimise light losses, whilst providing adequate spectral resolution for WR classification. In addition to determining the ionisation subclass of any identified WN stars, the resulting spectra would allow the presence/absence of Hydrogen to be identified by oscillation of the Pickering decrement over the wavelength range 4200–5400Å.

Poor weather during the first night of observation allowed only 11 candidates to be observed, none of which were genuine WR stars. Following this low success rate, I included several additional candidates in the Cygnus star-forming region ($l \sim 80°$), motivated by other IR discoveries of WR there (e.g., Pasquali et al. 2002). Despite including 9 candidates in Cygnus, the second night also failed to deliver any WR star discoveries.

In addition to the 47 candidate WR stars, I acquired spectra of 7 known WR stars (WR138-1, 140, 142, 142a, 142-1, 149, 159). This provided the first optical spectrum of WR142a, which was confirmed as a WC8 as estimated from its H+K spectrum (Pasquali et al., 2002).

I began the data reduction process by bias and flat-field correcting all frames using IRAF. I then performed wavelength calibration using internal arc maps, and the `Starlink FIGARO` package. I optimally extracted all stellar spectra using IRAF. I used observations of several spectrophotometric standard stars taken at regular intervals during both nights to generate calibration curves. I used these to flux calibrate the spectra of all WR stars observed, and a few typical WR impostors.

The majority of sources observed showed strong Hα emission and in most cases Hβ. I show a typical example in Figure 2.22. These are consistent with classical T Tauri stars, which have optical spectra characterised by H Balmer and Ca H & K emission

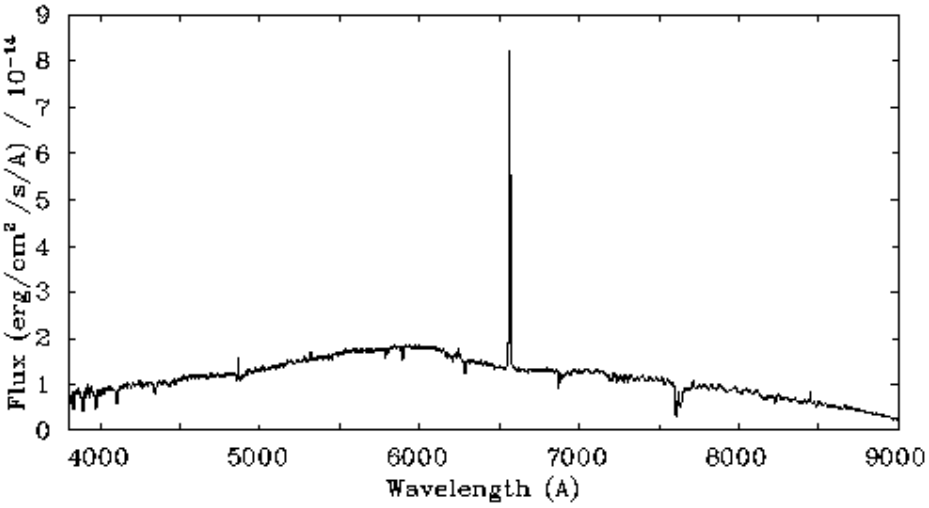

Figure 2.22: INT/IDS spectrum of WR candidate 2MASS 22220600+5743389 (HBHA 5705-56), a classical T Tauri star.

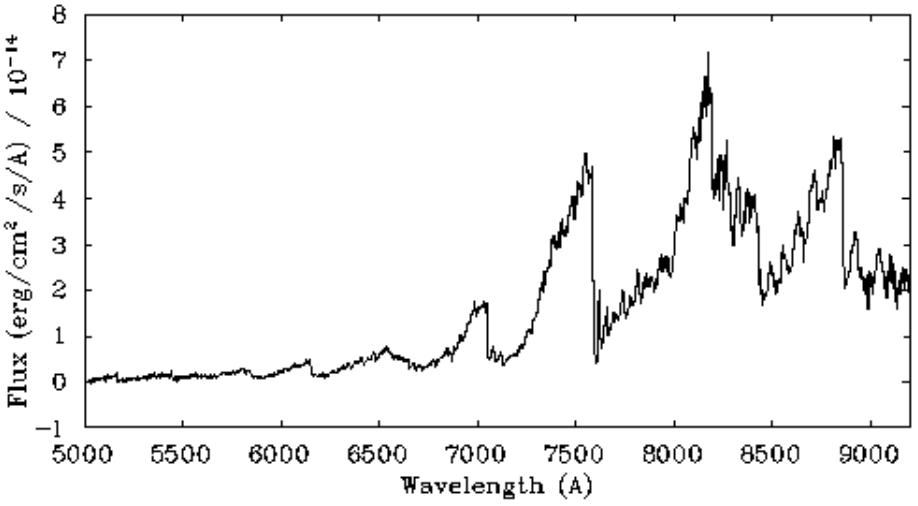

Figure 2.23: INT/IDS spectrum of WR candidate IRAS 23037+6145, an M-type star.

lines (Appenzeller & Mundt, 1989). I could not identify the most prominent Ca H & K lines (3968.5Å & 3933.7Å) as they are situated at the blue extreme of the spectra taken here. It is also common also common to see a P Cygni profile in Hα due to outflows in T Tauri stars, but the resolution of observed spectra was insufficient to show this. T Tauri stars possess IR excess that is attributed to a their circumstellar disks (Strom et al., 1993), explaining their presence in the sample of WR candidates.

In Figure 2.23 I also show the observed spectrum of IRAS 23037+6145, one of two observed candidates showing TiO absorption bands. This source was identified as a Hα emitter by Mikami & Ogura (2001), but to my knowledge no spectrum has been published. The combination of a red spectral shape and strong TiO bands suggests an M spectral type. By comparison to the atlas of Kirkpatrick et al. (1991), IRAS 23037+6145 has a spectral type between M5–8V.

In Figures 2.24 and 2.25, I show flux calibrated spectra of the 7 WR stars observed. I measured the equivalent widths of all primary classification lines in these spectra, and confirm the WC8 spectral type for WR142a estimated by Pasquali et al. (2002) using IR classification diagnostics. The spectral types I concluded for all other WR stars observed were in agreement with those previously published.

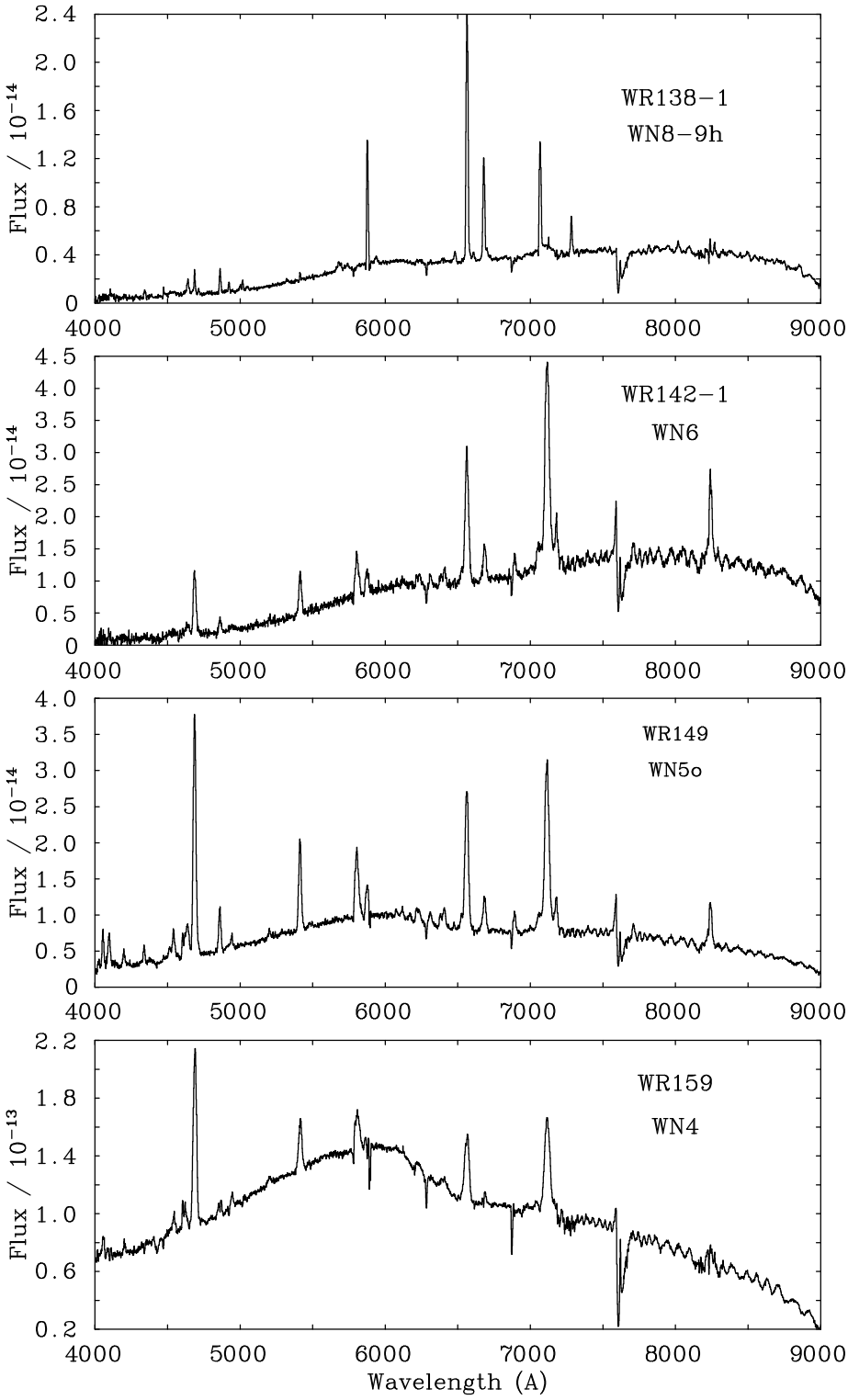

Figure 2.24: Flux calibrated spectra of 4 WN stars, taken with INT/IDS. Flux is in units of erg $s^{-1}\,cm^{-2}\,Å^{-1}$.

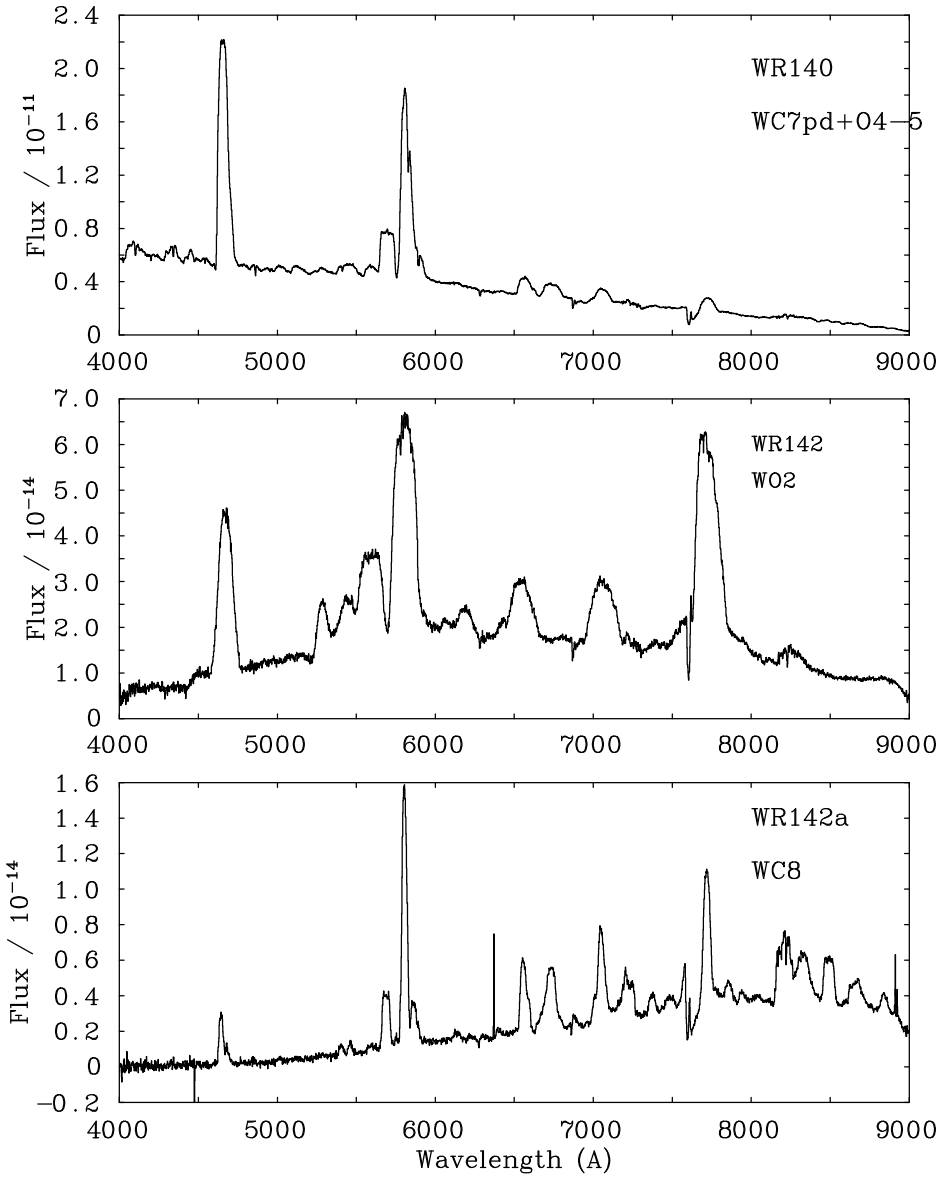

Figure 2.25: Flux calibrated spectra of 2 WC and one WO star, taken with INT/IDS. Flux is in units of erg $s^{-1}\,cm^{-2}\,Å^{-1}$.

2.5 Summary

In this chapter I have presented a refined near-IR classification scheme for WR stars, advancing the work of Crowther et al. (2006b) by using superior data. Testing of this revised scheme revised scheme has shown it to be consistent with optical schemes in common use. Using this I confirmed and updated spectal types of heavily obscured WR stars, allowing me to calibrate near-IR absolute magnitudes by spectral subtype. This was achieved using 126 WN, WC & WO stars with known distances (mostly by cluster or OB association membership). Applying these calibrations I have derived distances to a further 246 WR stars and present a 3D map of their locations. Approximately half as many WC stars are available for calibration as cluster/association members than WN, consistent with the findings of Smith (2014) than WC stars are generally more isolated (recall Section 1.3.2). This challenges the idea that WC stars descend directly from WN, which in turn descend from the most massive O-stars. I have found the heights of WR stars from the Galactic midplane to be Cauchy distributed with HWHM = 39.2 pc, where 12 stars reside at $|z| > 300$ pc. The low binary fraction and a preference for WN8 subtypes in this small sample of runaway stars indicates a binary supernova origin for the most extreme examples.

Exploiting the variation of metallicity across the Galactic disk, I compared subtype number ratios measured in the inner Galaxy, solar neighbourhood, and outer Galaxy to the predictions of various metallicity-dependent stellar models. At Galactic metallicities, N_{WC}/N_{WN} is significantly higher than predicted by stellar models including fast rotation (Meynet & Maeder, 2005), suggesting that the predicted lengthened WNL and shortened WC phases are not widely observed at ($Z \gtrsim Z_{\odot}$). Similarly, a shortened eWNE phase in such models, particularly at lower metallicity, is not manifest in our observations. Single-star models without rotation (Eldridge & Vink, 2006) and models that account for the various effects of binary interaction (Eldridge et al., 2008) reproduce our measurements of N_{WC}/N_{WN} more appropriately. Hence, to a first approximation a population consisting of non-rotating (or slowly rotating) single stars and interacting binaries would be consistent with the subtype ratios we observe. However, I cautioned that all comparisons of this nature are subject to how the physics of stellar models translates into observable properties of the stars, which is currently based on simple criteria involving surface abundances and temperatures. These may not be appropriate (Groh et al., 2014), particularly for the transition between eWNE and eWNL subtypes.

Finally, I presented the results of an observing campaign designed to identify new WR stars beyond the solar circle, in the direction of the Perseus spiral arm. I developed a

novel candidate selection technique, designed to exploit both the characteristic IR excess and line emission of WR stars. The WISE all-sky survey was used to mimic well constrained near-IR colour criteria in the *Spitzer* bands, and the IPHAS survey to identify candidates showing HeII(6560Å)+Hα emission. The colour selection criteria performed well using test samples containing known WR stars, however, optical spectroscopy of 46 candidates with the INT/IDS returned no positive identifications. The false positives were dominated by pre-MS stars, showing strong Hα emission.

Chapter 3

Predicting the Total Wolf-Rayet Population of the Milky Way

The work presented in this chapter has been published in Rosslowe & Crowther (2015b) and a subsequent erratum (Rosslowe & Crowther, 2015a).

Several attempts have been made to determine the total number of WR stars in the Galaxy. Estimates range from ∼1000–6500, mainly as a result of differing extrapolations of the locally observed population across the whole Galaxy. I summarised these population estimates in Section 1.3.1. Combined with an assumed Galactic SFR and IMF, the average WR phase duration may be estimated from their total current numbers. This an important prediction of stellar models, as it is when massive stars have the strongest dymanical influence on their surroundings (recall discussion of ejecta nebulae, Section 1.1.2), and may emit very hard (< 228Å) ionising radiation.

With knowledge of how WR subtypes vary with Galactocentric radius, and the intrinsic near-IR brightness of each subtype, it is possible to predict the observational properties of the whole Galactic WR population. To this end I developed a 3D, azimuthally symmetric "toy" model of the population, scalable to different total numbers of WR stars. The construction of this model is described in Section 3.1 of this chapter. I applied a simple Galactic dust distribution (Section 3.2) to redden this model population, and subsequently derived apparent magnitude distributions in various bands for various total numbers of WR stars. An estimate of the size of the total population followed by comparing predicted magnitude distributions to the observed population (Section 3.3).

3.1 Constructing the model

In this section I describe how spatial coordinates $[r(\mathrm{pc}), \theta, z(\mathrm{pc})]$ were attributed to every WR star in the model population. These coordinates have their usual meanings in the cylindrical coordinate system; r represents Galactocentric radius, z the vertical distance from the Galactic midplane, and θ the azimuthal angle. I placed the Galactic centre at the origin of this coordinate system, meaning the Sun resides at $(8000, 0°, 20)$, assuming a Galactocentric distance of 8 kpc (Reid et al., 2009; Gillessen et al., 2013) and a vertical distance from the midplane of 20 pc (Humphreys & Larsen, 1995). I populated the model in two stages, considering central ($r < 3$ kpc) and disk (3 kpc$<r<$15 kpc) regions separately, containing N_{WR}^{cent} and N_{WR}^{disk} WR stars respectively.

I did not attempt to incorporate complex structural features such as spiral arms or the Galactic bar into the model WR population, as my aim was to derive basic observational characteristics of the whole population, smoothing over any local enhancements. I therefore distributed model WR stars in an azimuthally symmetric disk, with the same thickness as the observed population. I generated a z-coordinate for each star (independent of r and θ) so they would be Cauchy distributed, by computing

$$z_i = \gamma \tan(\pi r_{01} - \frac{1}{2}), \tag{3.1}$$

where r_{01} is a randomly generated number between 0 and 1 and γ is the observed HWHM (39.2 pc, Sec. 2.3.2). The z-distribution was truncated at $z = \pm 1$ kpc in accordance with the most extreme runaway WR stars observed.

To populate the model Galactic disk with N_{WR}^{disk} WR stars in a realistic way, I had to account for their variations in number and subtype (i.e., luminosity) with Galactocentric radius. To do this I split the model disk into 24 annuli of 0.5 kpc in width spanning radii $r =$ 3–15 kpc, and populated each in turn. To dictate the total number of WR stars in each annulus, I constructed a normalised version of the radial HII-region distribution presented by Paladini et al. (2004). This was preferred over the observed radial distribution of WR stars presented here (Sec. 2.3.2) since HII-regions trace hot young stars over a larger Galactic extent, owing to their easy detection at radio wavelengths. This normalised HII-region distribution consisted of a 1D array of 24 values, summing to 1, by which N_{WR}^{disk} could be multiplied to obtain a number of WR stars in each annulus. Within each annulus, the resulting number of stars were pseudo-randomly assigned radii between the lower and upper radius limits, by implementing a Box-Muller transform. Simlarly, each star was assigned an angle θ, between 0 and 2π.

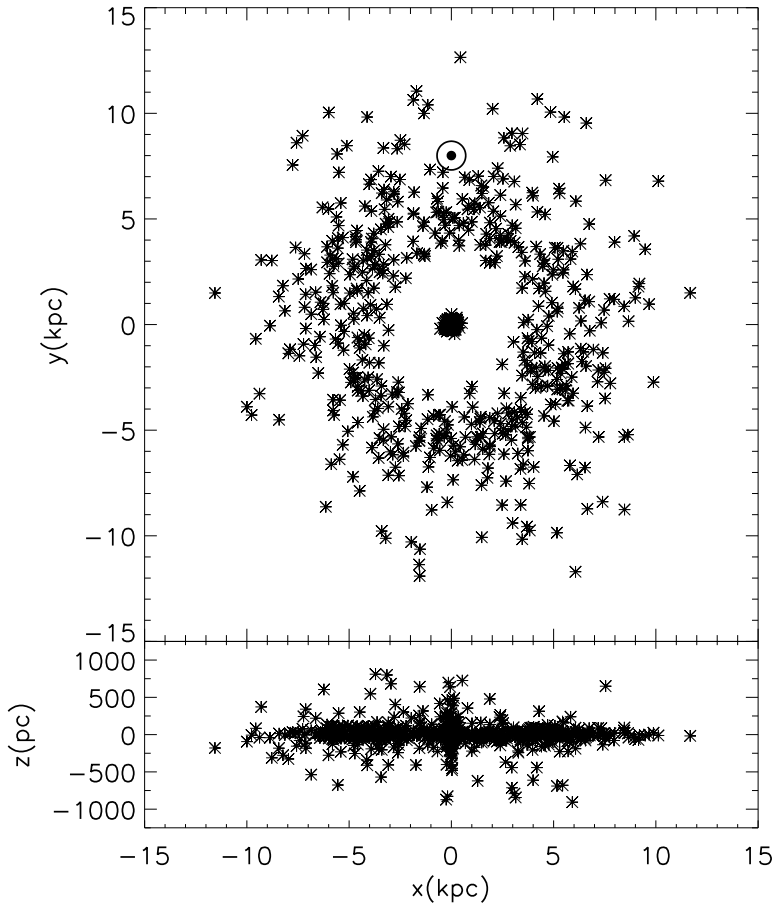

Figure 3.1: An example model WR population mimicking that of the Galaxy, containing 550 stars at R_G= 3–15 kpc and 250 at R_G< 3 kpc, shown in Cartesian coordinates. The location of the Sun is indicated by the standard symbol at (0,8 kpc) in the top panel.

In the central 3 kpc, where star formation is suppressed outside the Central Molecular Zone (CMZ), I included a fixed number of WR stars in every model. Dong et al. (2012) report on a Pa-α survey covering the central $\sim 0.6°$ (~ 80 pc) of the Galaxy, including the three massive clusters there (Arches, Quintuplet and GC). Within this region they identify as many emission line sources (i.e., evolved massive star candidates) outside of these clusters as in them; given that ~ 80 WR stars are known to reside in these clusters, it follows that ~ 150 WR stars should present in the Dong et al. survey area. The CMZ is approximately 3° (400 pc) across, and the density of gas in this extreme environment is strongly centrally peaked. Using the molecular gas distribution mapped by Ferrière (2008) I estimated that approximately 40% of the CMZ gas lies within the Dong et al. survey area. Assuming the non-cluster population of WR stars can be traced by this molecular gas, this implies a further ~ 100 WR stars in the CMZ. The inner Galaxy ($R_G < 3$ kpc) contains little star formation outside the CMZ, I therefore assumed $N_{WR}^{cent} = 250$ in each model. I gave these central stars a Gaussian distribution in r, centred on $r = 0$ with $\sigma = 200$ pc. Each central WR star was assigned a random azimuthal angle, θ, between 0 and 2π, in an identical manner to the disk stars. I show an example model WR population in Figure 3.1.

The number of WR stars in each of the 25 radial sections (24 annuli + central region) of the model was divided into four components, representing WNE, WNL, WCE and WCL type stars. I defined the relative numbers of each WR type to match those observed at each radius (see Tab. 2.16). To do this I implemented linearly varying number fractions $N_{WC}/N_{WN}(r)$, $N_{WNE}/N_{WNL}(r)$ and $N_{WCE}/N_{WCL}(r)$. I defined these by extrapolating between the observed values in each Galactic metallicity zone (Sec. 2.3.3), using representative radii of R_G=3 kpc, 7.5 kpc and 10 kpc. For each radial section, these fractions were evaluated at the midpoint in radius, and multiplied by the aforementioned number fractions to deliver $N_{WCE}, N_{WCL}, N_{WNE}, N_{WNL}$, with results rounded to the nearest integer. To each WR type, I assigned absolute magnitudes $M_{K_S} = -4.31$ (WNE), -6.01 (WNL), -4.45 (WCE) and -4.89 (WCL), based on averaging calibration results (Sec. 2.2.4) over the individual subtypes constituting these broader types. I discuss in Section 2.2.4 how assuming a shallower extinction law towards the GC (Nishiyama et al., 2009) resulted in brighter near-IR absolute magnitudes for WNL and WCL types. To investigate the effect this would have on the magnitude distributions derived from model populations, I created some in which WNL and WCL were assigned $M_{K_S} = -6.26$ and -5.09 respectively. I did not include WO or WN/C stars in any model population, as they constitute a negligible fraction (1–2%) of the observed population.

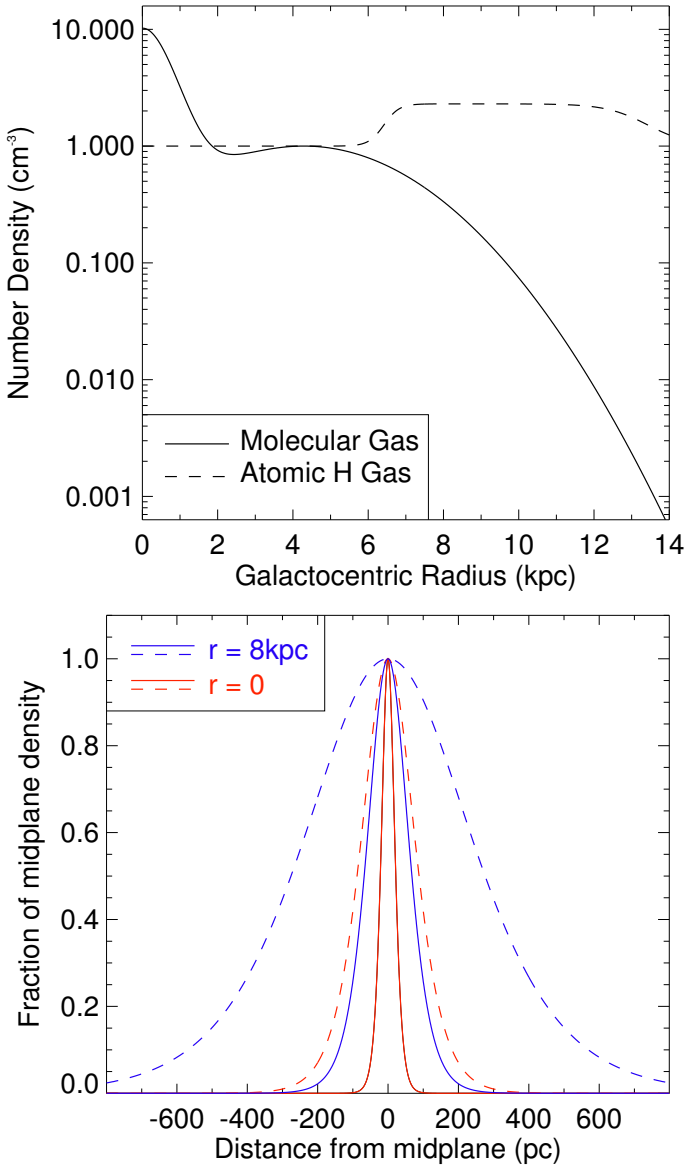

Figure 3.2: Functions describing the radial and vertical dependence of molecular and atomic gas density, used to govern the dust distribution in model WR star populations. *Top*: midplane number density of molecular H_2 ($D_m^{mol}(r)$, solid) and atomic H ($D_m^{atom}(r)$, dashed) gas. (Equations 3.3 and 3.4, respectively). *Bottom*: vertical dependence of number density, $D_h(r,z) = \mathrm{sech}^2(\zeta)$, showing values of ζ at $r = 0\,\mathrm{pc}$ (red) and $r = 8\,\mathrm{pc}$ (blue).

3.2 A dust model for the Milky Way

To approximate an extinction to each model WR star, I superimposed two dust components to the model WR star disk; one associated with molecular (H_2) gas, the other with atomic H gas. I applied the same dust-to-gas mass ratio for each component. This assumption followed from Bohlin et al. (1978) who derive a total neutral hydrogen to colour excess ratio, implying that each atom of H is responsible for a set amount of extinction, whether in molecular or atomic form. Both dust components were included as two dimensional functions in r and z, motivated by the observed spatial distribution of their respective gas species. I used the gas measurements of Nakanishi & Sofue (2006) and Nakanishi & Sofue (2003) for molecular (traced using CO) and atomic gas respectively.

Functions describing each dust component have the form $D_m(r) \times D_h(r,z)$, where $D_m(r)$ describes the dependence of *midplane* density on Galactocentric radius, and $D_h(r,z)$ describes how the density drops with vertical distance from the midplane.

Both dust components were included with a vertical dependence of the form $D_h(r,z) = \mathrm{sech}^2(\zeta)$, where

$$\zeta(r,z) = \log(1+\sqrt{2})\frac{z}{z_{1/2}(r)}, \tag{3.2}$$

and $z_{1/2}(r)$ is the height at which the density falls to half of the midplane value, which increases linearly with Galactocentric radius for both gas species. I present these functions for atomic and molecular gas in the lower panel of Figure 3.2. For molecular gas, $z_{1/2}(r{=}0) = 25\,\mathrm{pc}$ increasing to 90 pc at $r = 10\,\mathrm{kpc}$ (Nakanishi & Sofue, 2006). For atomic gas, $z_{1/2}(r{=}0) = 100\,\mathrm{pc}$ increasing to 500 pc at $r = 15\,\mathrm{kpc}$ (Nakanishi & Sofue, 2003).

To represent the midplane density of molecular gas, I constructed the following function:

$$D_m^{mol}(r) = N_0^{mol}\,\mathrm{sech}^2\left(\frac{r}{800pc}\right) + \exp\left[\frac{-(r-4300pc)^2}{2(2500pc)^2}\right][\mathrm{cm}^{-3}], \tag{3.3}$$

which is shown in the top panel of Figure 3.2. The numerical values in Equation 3.3 and $N_0^{mol} = 10\,\mathrm{cm}^{-3}$ were chosen to reproduce observations (Nakanishi & Sofue, 2006).

To represent the midplane density of atomic gas, I employed a summation of two

step functions:

$$D_m^{atom}(r) = N_0^{atom}\Big[1 + \frac{1.3}{1+\exp(\frac{-(r-6500pc)}{200pc})}... \\ ... - \frac{1.3}{1+\exp(\frac{-(r-13200pc)}{550pc})}\Big][\mathrm{cm}^{-3}] \tag{3.4}$$

as shown in Figure 3.2 (top panel). Once again, I chose the numerical values and N_0^{atom}= 0.08 cm^{-3} to reproduce observations (Nakanishi & Sofue, 2003).

Summing molecular and atomic dust components gives the total dust function;

$$D(r,z) = (D_m^{mol} \times D_h^{mol}) + (D_m^{atom} \times D_h^{atom}), \tag{3.5}$$

Once this global dust distribution had been defined, a total amount of dust along the sight line from the Sun to each WR star in the model was calculated. This calculation was performed in a Cartesian coordinate system (x, y, z) for simplification. In Cartesian coordinates, the Galactic Centre is at $(0, 0, 0)$ and the Sun at $(x_0, y_0, z_0) = (0.0, 8000, 20)$ in pc. To evaluate the dust function (Eq 3.5) in Cartesian coordinates, the following transformations were used;

$$r = \sqrt{x^2 + y^2}, \tag{3.6}$$

and

$$z = z. \tag{3.7}$$

Each line-of-sight through the dust distribution was treated as a straight line through a three dimensional scalar field. A line integral was performed along each line-of-sight by parameterising the path C, such that x=$x(t)$, y=$y(t)$, z=$z(t)$, for $0 < t < 1$. For a straight line between points at (x_0, y_0, z_0) and (x_1, y_1, z_1):

$$x(t) = (1-t)x_0 + x_1 t, \tag{3.8}$$

$$y(t) = (1-t)y_0 + y_1 t, \tag{3.9}$$

$$z(t) = (1-t)z_0 + z_1 t. \tag{3.10}$$

The amount of obscuring dust is then given by:

$$dust = \int_C D\big(x(t), y(t), z(t)\big)\frac{\mathrm{d}s}{\mathrm{d}t}\mathrm{d}t, \tag{3.11}$$

where

$$\mathrm{d}s = \sqrt{\mathrm{d}x^2 + \mathrm{d}y^2 + \mathrm{d}z^2} \tag{3.12}$$

Each component of ds (an infintesimal segment of path C) can be written in parameterised form:

$$\mathrm{d}x = \frac{\mathrm{d}x}{\mathrm{d}t}dt, \tag{3.13}$$

$$\mathrm{d}y = \frac{\mathrm{d}y}{\mathrm{d}t}dt, \tag{3.14}$$

$$\mathrm{d}z = \frac{\mathrm{d}z}{\mathrm{d}t}dt. \tag{3.15}$$

Substituting these into Equation 3.12 gives:

$$\mathrm{d}s = \sqrt{\left(\frac{\mathrm{d}x}{\mathrm{d}t}\right)^2 + \left(\frac{\mathrm{d}y}{\mathrm{d}t}\right)^2 + \left(\frac{\mathrm{d}z}{\mathrm{d}t}\right)^2}\,\mathrm{d}t. \tag{3.16}$$

By differentiating Equations 3.8–3.10 and substituting them into Equation 3.16, one obtains:

$$\frac{\mathrm{d}s}{\mathrm{d}t} = \sqrt{(x_0 - x_1)^2 + (y_0 - y_1)^2 + (z_0 - z_1)^2} = L. \tag{3.17}$$

This is a constant, hence $\frac{\mathrm{d}s}{\mathrm{d}t}$ can be factorised out of the total dust integral (Eq 3.11).

I employed the trapezium rule to compute the resulting integral. The number of steps, N, was defined by dividing the total path length by a fixed step size of 10 pc. The parameter t was then iterated in steps of 1/N in order to progress x, y, z coordinates along the path, from $(x(t_0), y(t_0), z(t_0))$ to $(x(t_N), y(t_N), z(t_N))$. Numerically, Equation 3.11 became:

$$dust = \frac{10(pc)L}{2}\sum_{k=0}^{N}\Big(D\big(x(t_k), y(t_k), z(t_k)\big) + D\big(x(t_{k+1}), y(t_{k+1}), z(t_{k+1})\big)\Big). \tag{3.18}$$

Finally, I attributed the amount of dust given by Equation 3.18 to an extinction in K-band magnitudes, assuming a liner relationship between the two. To calibrate this relationship, I calculated the amount of dust along the Sun–GC line of sight, and equated this with $A_{K_S} = 2.42$ mag, in accordance with hydrogen emission line measurements of gas clouds residing there (Fritz et al., 2011).

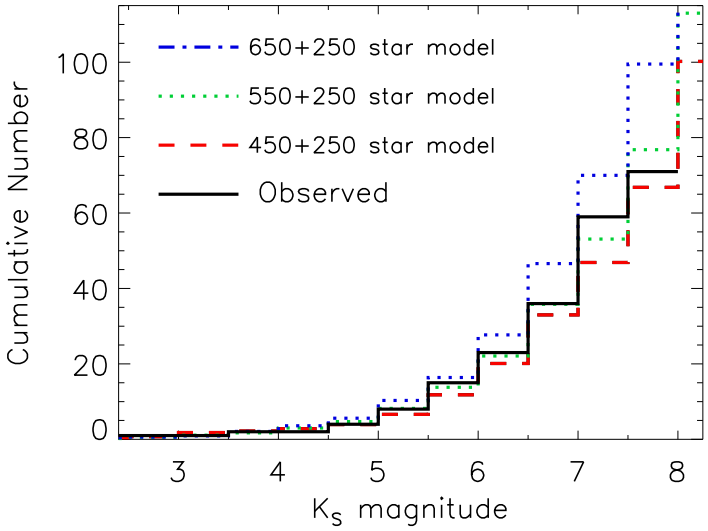

Figure 3.3: The cumulative number of observed WR-dominated systems (black solid line) in bins of 0.5 K_S mag, compared with that of three different model WR populations.

3.3 Quantifying the total population

Combining model WR star populations (Section 3.1) with the extinction calculations described in the previous section, I was able to generate global magnitude distributions for populations containing any number of WR stars. It follows that a comparison between modelled and observed apparent magnitude distributions allows an estimate of the total number of Galactic WR stars.

Before proceeding, it was important to consider what the model WR stars truly represent. As their absolute magnitudes are based on the calibrated values for WR stars, they represent what I refer to as 'WR-dominated' systems, i.e., where any companion star(s) do not affect the systemic magnitude by more than 0.4 mag (typical error on the absolute magnitude calibrations), i.e., $(m_K^{\rm WR} - m_K^{Sys}) > 0.4$, corresponding to a WR/system flux ratio of $F_K^{\rm WR}/F_K^{sys} > 0.7$. Also, these model stars do not represent WO, WN/C or dust-producing WC stars. Therefore, to achieve a like-for-like comparison to observations, I initially only considered *observed* WR-dominated systems, and in Section 3.3.2 I estimate the contribution of neglected WR types.

3.3.1 Comparison to a magnitude-limited sample

I assembled a magnitude-limited sample of real WR-dominated systems, for comparison to model K_S-band magnitude distributions. I used the agreement between real and

predicted magnitude distributions, up to a limiting magnitude, as a measure of how well each model represented the real population. Regarding the choice of limiting magnitude, I note that $< 5\%$ of WR stars discovered since the year 2011 are brighter than $K_S = 8$ mag (Mauerhan et al., 2011; Shara et al., 2012; Smith et al., 2012; Chené et al., 2013). Therefore, I adopted this as the current completeness limit in *systemic* magnitude.

In Figure 3.3 I present predicted K_S-band magnitude distributions for WR populations totalling 700, 800 and 900 WR, with 450, 550 and 650 between $R_G = 3$–15 kpc respectively, plus 250 central stars at $R_G < 3$ kpc. Also shown is the number of observed WR-dominated systems with systemic $K_S < 8$ mag. In spite of providing too few systems with $7.5 < K_S < 8.0$, the best agreement is found with the $550 + 250$ WR star model. I therefore take forward 800 ± 100 as the number of Galactic WR-dominated systems, with an approximate uncertainty based on the comparison shown in Figure 3.3.

To assess the implications of a shallower GC extinction law on this result, I performed identical comparisons using model populations with brighter WCL and WNL stars. I found greater consistency with models containing $\sim$100 fewer WR stars. Hence, the assumption of a shallower GC extinction law would not affect this result beyond the uncertainty already assumed.

3.3.2 Fractions of dusty and companion-dominated WR systems in a volume-limited sample

Each point in one of these model populations represents a stellar system with a WR star as the dominant or sole near-IR source. To gain an insight into how many dusty and companion-dominated WR systems are neglected in these models - and hence the initially deduced population of 800 - I created a volume-limited sample of nearby WR systems. In Table 3.1 I list all known WR stars within 3 kpc of the Sun, where distances are taken from this work where possible (non-dusty WR stars), or by utilising $\bar{M}_v$-subtype calibrations (van der Hucht, 2001). A v-band magnitude can be used to determine distances to dusty WC stars, as hot dust emission does not contribute to the continuum flux at these wavelengths. I inspected the near-IR properties of the WR stars in Table 3.1, catagorising each as either WR-dominated ($F_K^{WR}/F_K^{sys} > 0.7$), having a significant companion ($F_K^{WR}/F_K^{sys} < 0.7$), or dusty WC.

Table 3.1: Closest ($d < 3$kpc) WR stars listed in ascending heliocentric distance. In the fourth column I class each system as WR-dominated ($m_K^{\rm WR} - m_K^{sys} > 0.4$; WR), companion-dominated (C), or dust-producing (D). References are given for spectral types of stars not present in Tables 2.6–2.8, 2.13 or 2.14.

WR#	Spectral type	Distance (kpc)	Class
11	WC8+O7.5III	0.34 ± 0.08	C
147	WN8(h)+OB	0.73 ± 0.12	WR
94	WN5	0.78 ± 0.12	WR
90	WC7	1.15 ± 0.19	WR
136	WN6b(h)	1.3 ± 0.2	WR
137	WC7+O9	1.3 ± 0.2	D
139	WN5+O6III-V	1.3 ± 0.2	C
141	WN5+O5III-V	1.3 ± 0.2	C
143	WC4+Be	1.33 ± 0.33	C
138	WN5+OB	1.38 ± 0.26	C
144	WC4	1.40 ± 0.08	WR
52	WC4	1.54 ± 0.23	WR
110	WN5b	1.55 ± 0.24	WR
9	WC5+O7*	$1.57 \pm 0.58^\star$	C
15	WC6	1.57 ± 0.49	WR
81	WC9	1.64 ± 0.34	WR
78	WN7	1.64 ± 0.03	WR
79	WC7+O5-8V	1.64 ± 0.03	C
79a	WN9ha	1.64 ± 0.03	WR
140	WC7pd+O5fcIII-I[1]	1.67 ± 0.03[2]	D
142-1	WN6	1.70 ± 0.34	WR
6	WN4b	1.80 ± 0.27	WR
121	WC9d*	$1.8 \pm 0.4^\star$	D
142a	WC7	1.83 ± 0.31	WR
105	WN9	1.9 ± 0.2	WR
111	WC5	1.9 ± 0.2	WR
134	WN6b	1.9 ± 0.2	WR
135	WC8	1.9 ± 0.2	WR
86	WC7+B0III	1.97 ± 0.47	WR
113	WC8d+O8-9*	2.0 ± 0.2	D
14	WC7	2.0 ± 0.1	WR
93	WC7+O7-9	2.0 ± 0.2	WR
114	WC5	2.05 ± 0.09	WR
115	WN6	2.05 ± 0.09	WR
70	WC9vd+B0I*	$2.1 \pm 0.4^\star$	D
47	WN6+O5.5	2.13 ± 0.44	WR
133	WN5+O9I	2.14 ± 0.07	C
70-5	WC9	2.17 ± 0.45	WR
48	WC6+O6-7V[3]... ...+O9.5/B0Iab*	$< 2.3^\star$	C

Continued on next page

Table 3.1 – *Continued from previous page*

WR#	Spectral type	Distance (kpc)	Class
1	WN4b	2.3 ± 0.5	WR
103	WC9d*	$2.3 \pm 0.5^\star$	D
59	WC9d*	$2.3 \pm 0.5^\star$	D
2	WN2b+B[4]	2.4 ± 0.8	WR
106	WC9d*	$2.4 \pm 0.6^\star$	D
19a	WN7	2.41 ± 0.47	WR
101	WC8	2.46 ± 0.43	WR
40	WN8h	2.48 ± 0.41	WR
95	WC9d*	2.5 ± 0.5	D
60	WC8	2.55 ± 0.45	WR
155	WN6+O9II-Ib	2.56 ± 0.56	WR
117-1	WN7	2.59 ± 0.50	WR
18	WN4b	2.6 ± 0.2	WR
22	WN7ha+O9III-V	2.6 ± 0.2	WR
23	WC6	2.6 ± 0.2	WR
24	WN6ha	2.6 ± 0.2	WR
25	O2.5If*/WN6[5]+OB	2.6 ± 0.2	C
104	WC9d+B0.5V*	2.6 ± 0.7	D
88	WC9	2.67 ± 0.54	WR
4	WC5	2.69 ± 0.49	WR
5	WC6	2.69 ± 0.84	WR
72-1	WC9	2.73 ± 0.56	WR
16	WN8h	2.77 ± 0.46	WR
85	WN6	2.8 ± 1.1	WR
111-3	WC8	2.80 ± 0.49	WR
69	WC9d+OB*	$2.8 \pm 0.6^\star$	D
75b	WC9	2.82 ± 0.58	WR
124-8	WN6	2.84 ± 0.56	WR
113-1	WN7	2.88 ± 0.56	WR
151	WN4+O5V	2.93 ± 0.65	WR
42	WC7+O7V	2.96 ± 0.53	C
57	WC8	2.97 ± 0.52	WR
75a	WC9	2.98 ± 0.60	WR

*van der Hucht (2001), (1) Fahed et al. (2011), (2) Monnier et al. (2011), (3) Hill et al. (2002), (4) Chené et al. (2014), (5) Crowther & Walborn (2011).

Of the 72 WR stars in this volume-limited sample, 41 are WC type of which 11 show evidence of circumstellar dust, indicating that $15 \pm 5\%$ of WR stars and $28 \pm 9\%$ of WC stars display circumstellar dust. A companion star dominates the near-IR continuum in 11 of the remaining 61 non-dusty WR systems ($18 \pm 6\%$). Uncertainties on these fractions are calculated assuming a $\sqrt{N}$ uncertainty on each number count.

The fractions derived from this volume-limited sample imply the previously derived population of 800 represents only 82% of the non-dusty population, as ∼18% (150) will have an IR bright companion. Furthermore, this non-dusty population of 1050 (=800+150) represents only 85% of the total population, as a further ∼15% (150) will be dusty WC stars.

Correcting the deduced population size using statistics from this volume-limited sample implicitly assumes no Galactocentric radial dependence of either, *i*) the fraction of massive binaries, or *ii*) dust-producing WC stars. The binary fraction of massive stars has been observed to remain constant over a range of metallicities (Neugent & Massey, 2014), validating assumption (*i*). However, dust producing WC stars are predominantly late-type, and the fraction of WCL stars does increase with metallicity (Tab 2.16). This means the adopted 15% of dust-producing WR is likely an under-estimate at super-solar metallicity, which is a preferential environment for WC stars (Fig 2.16). From Table 2.16, it is possible to estimate an upper limit on the fraction of dust-producing WR stars at super-solar metallicity. In the inner Galaxy ($R_G < 6$ kpc), WC stars are approximately half as numerous as WN. Furthermore, WCL stars constitute 95% of WC stars. If 100% of these WCL were dust-producing, this would equate to 31% of the total WR population. Therefore, taking 15% as a Galaxy-wide average fraction of dust-producing WR stars, and 31% as an upper limit, I deduce there are 1200^{+300}_{-100} Galactic WR stars.

3.3.3 Expectations from star formation arguments

By combining the measured Milky Way SFR with an IMF, it is possible to derive the average duration of the Wolf-Rayet phase ($\tau_{\rm WR}$) necessary to sustain a population of ∼1200 WR stars. I took the Milky Way SFR to be $1.9\,{\rm M}_\odot{\rm yr}^{-1}$ (Chomiuk & Povich, 2011), and adopted a three-part Kroupa IMF (Kroupa & Weidner, 2003) for this calculation. Assuming only stars with an initial mass $>25\,{\rm M}_\odot$ experience a WR phase (Meynet & Maeder, 2005), the derived population can be sustained if $\tau_{\rm WR} \simeq 0.25$ Myr.

The latest solar metallicity stellar models with (without) rotation display $\tau_{\rm WR} = 0.45$ Myr (0.006 Myr) at $M_i = 32\,{\rm M}_\odot$ increasing with mass to 1.2 Myr (0.4 Myr) at $M_i = 120\,{\rm M}_\odot$ (Georgy et al., 2012). Lifetimes of rotating stellar models exceed 0.25 Myr at all masses, whereas the range of τ_{WR} in non-rotating models is consistent with this. Models including binary evolution at solar metallicity span $\tau_{\rm WR} = 0.5$ Myr at $M_i = 30\,{\rm M}_\odot$ to 1.0 Myr at $120\,{\rm M}_\odot$ (Eldridge et al., 2008). Although, binary evolution favours lower WR progenitor masses, so the model populations presented here may not correspond to all WR stars formed via a binary channel. Previously claimed population sizes exceeding 6,000 (van

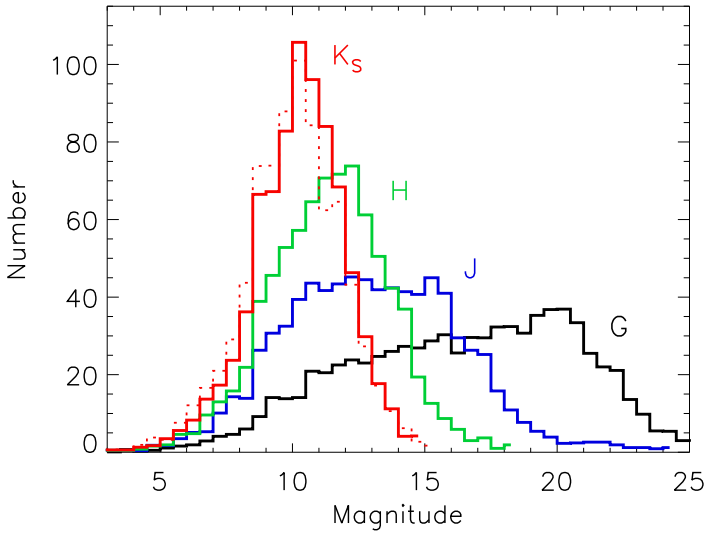

Figure 3.4: Histogram of 2MASS JHK$_S$ and G-band (*Gaia*) magnitudes predicted for the preferred model Galactic WR star population. Each distribution shown is an average over 10 model repetitions. Two K$_S$-band distributions are plotted, the dotted line represents a model population where 28% of WC stars are dust forming (WC8d/9d, $M_{K_S} = -6.95$, Table 2.11). All solid lines represent populations consisting of WN and non-dusty WC stars.

der Hucht, 2001; Shara et al., 2009) are difficult to reconcile with the measured Galactic SFR and a progenitor mass limit $M > 25\,\mathrm{M}_\odot$, as WR lifetimes in excess of 1 Myr would be required.

The CMZ accounts for an estimated ∼4–5% of Galactic star formation (Longmore et al., 2013), yet I have estimated it contains ∼250 (13%) of the Galactic WR star population. The discrepancy between these fractions would suggest either we have underestimated WR numbers in the Galactic disk, or this CMZ star formation rate is insensitive to the most recent episodes of massive star formation.

3.3.4 Implications for future spectroscopic surveys

Near-IR surveys, both broad and narrow-band, continue to add to our knowledge of the obscured Galactic Wolf-Rayet population. A question of fundamental importance to spectroscopic follow-up campaigns is: how deep do spectroscopic surveys need to go? Figure 3.4 shows multi-band magnitude distributions derived from the preferred model WR star population. From this, I estimate that to achieve 95% completeness, spectra of candidate WR stars need to be taken to a depth of K$_S \simeq 13.5$ mag, $H \simeq 15.2$ or $J \simeq 18.6$ - shallower by ∼2 mag in K$_S$ than the 95% limit estimated by Shara et al. (2009).

The ESA *Gaia* mission will perform precision astrometry for a billion stars down to visual magnitudes of 20, and acquire low-resolution spectra of objects brighter that magnitude 16. To investigate the potential of *Gaia* in the search for and characterisation of WR stars, I derived a G-band distribution from the favoured model population (see Figure 3.4). To do this, I assigned an appropriate M_v to each model WR star based on its type (van der Hucht, 2001), along with intrinsic $(b-v)$ colours from Morris et al. (1993). Utilising magnitude transformations provided by Jordi et al. (2010), the G-band magnitude of a model WR star was then given by;

$$\mathrm{G} = v - 0.0424 - \left[0.0851 \times (b-v)\right] - \left[0.3348 \times (b-v)^2\right] + \left[0.0205 \times (b-v)^3\right]. \quad (3.19)$$

Upon inspection of the resulting G-band magnitude distribution (Fig 3.4), I predicted that approximately 600 (∼45% of total) Galactic WR stars are within *Gaia*'s $6 < G < 20$ observing range, with ~ 300 brighter than the magnitude limit for spectroscopy. With the known population currently totalling ~ 635, *Gaia* is unlikely to discover significant numbers of Galactic WR stars via spectroscopy, but the majority of those known will have distances measured to a significantly higher level of accuracy than is currently possible.

3.4 Summary

Consolidating information gained about the spatial distribution, subtype variation, and intrinsic IR brightness of WR stars, I have presented a scalable toy model of the Galactic WR population. By applying a 3D dust distribution to this model - spatially congruous with the gas content of the Galaxy - I derived observable properties for populations of various sizes at multiple wavelengths. Comparison of these model-derived observables to the observed population of non-dusty, WR-dominated ($m_K^{\mathrm{WR}} - m_K^{sys} > 0.4$) systems to a completeness limit of $m_K^{sys} < 8$ indicates a total of ≃800 in the Galaxy. Using a volume-limited sample ($d < 3$kpc) I estimated such systems represent $\sim 69\%$ of the whole, implying a total Galactic WR population of 1200^{+300}_{-100}.

An average WR phase duration of 0.25 Myr is necessary to sustain thsi estimated population, assuming a Kroupa IMF and a constant Milky Way star formation rate of $1.9\,\mathrm{M_\odot yr^{-1}}$. This is consistent with τ_{WR} in non-rotating stellar models at solar metallicity, but shorter than that given by rotating models.

Looking to the future, I used the favoured model WR population to estimate a

required depth of $K_S < 13$ for spectroscopic surveys to achieve 95% completeness in Galactic WR stars. I also predicted the ESA *Gaia* mission will not deliver a significant number of WR star discoveries via low-resolution spectroscopy, but should provide improved distance measurements for the majority of the currently recognised population.

Chapter 4

Oxygen Abundances in WC and WO stars from Herschel PACS detection of [OIII]88.36 μm

4.1 Oxygen in Wolf-Rayet stars

The majority of oxygen and other α-elements in the universe are created in massive stars and core-collapse SN. Such stars not only achieve requisite temperatures to synthesise heavy elements, but during late evolutionary phases inject immense mechanical energy to mix these fresh ingredients into the ISM. Evidence for chemical enrichment of the ISM by WR winds has been observed in the circumstellar nebulae of individual WR stars (Esteban et al., 1992; Stock et al., 2011), and invoked to explain an increased N/O ratio in galaxies displaying WR spectral features (Brinchmann et al., 2008; López-Sánchez & Esteban, 2010).

WC & WO stars represent the final evolutionary stages of $M_{ini} \gtrsim 40 M_{\odot}$ stars (Meynet & Maeder, 2003) (recall Sec. 1.3.2). Following a lifetime of extreme mass-loss, these 'naked' helium stars offer a unique window into the chemical evolution of massive stellar cores. Accurate measurement of abundances in WC & WO stars stars can therefore provide important constraints on nuclear reaction rates and the efficiency of various internal mixing processes (Sec. 1.2.1).

The abundance of helium and carbon in WC atmospheres is well known. Non-LTE atmosphere codes such as `CMFGEN` and `PoWR` (Hillier & Miller, 1998; Gräfener et al., 2002) have been applied to the plethora of carbon recombination lines in WC near-UV/optical/near-IR spectra, typically revealing C/He = 0.1–0.4 by number ($X_C = 0.2$–0.5)

(Hillier & Miller, 1999; De Marco et al., 2000; Crowther et al., 2002; Gräfener & Hamann, 2005; Sander et al., 2012) (Sec. 1.3).

The precise amount of oxygen produced in massive stars has long been a contentious issue. As stated by Fowler (1984);

> "determination of the ratio $^{12}C/^{16}O$ produced in Helium burning is a problem of paramount importance in nuclear astrophysics. This ratio depends in a fairly complicated manner on the density, temperature, and duration of Helium burning, but it depends directly on the relative rates of the $3\alpha \rightarrow {}^{12}C$ process and the $^{12}C(\alpha,\gamma)^{16}O$ process".

The rate of $3\alpha \rightarrow {}^{12}C$ has recently been revised (Fynbo et al., 2005), but a significant uncertainty remains regarding the rate of $^{12}C(\alpha,\gamma)^{16}O$, as laboratory measurements are challenged by a prohibitively large coulomb barrier at the low energies relevant to astrophysical conditions. Theoretical extrapolation of measured cross-sections to lower energies are model-dependent, and despite numerous experimental investigations (Tang et al., 2007; Makii et al., 2009; Schürmann et al., 2012) a significant scatter remains in measured values, with a considerable uncertainty ($\sim 20\%$) on each.

Despite the prevalence of oxygen lines in WC and particularly WO spectra, the measurement of abundances by spectroscopic modelling has been challenging, as the strength of many O features are more sensitive to ionisation than abundance (Gräfener et al., 1998; Hillier & Miller, 1999; Crowther et al., 2002). The most appropriate and commonly used O lines in WC spectra are found in the near-UV (3000–3500$\mathring{A}$), and are therefore severely affected by dust extinction in the Galactic plane. Using space-based UV observations of six WC stars in the LMC, Crowther et al. (2002) measure oxygen abundances of O/He = 0.01–0.05 by number ($X_O = 0.02$–0.10); at the lower end of the range predicted by evolutionary models including the effects of stellar rotation (Meynet & Maeder, 2003, 2005). Another problem has been the complexity of model atoms required to accurately compute radiative transfer solutions in the winds of WC and WO stars, particularly for late-type WC stars abundant in C^+ & C^{2+}. Williams et al. (2015) recently presented O abundance determinations in WC9 stars, based on CMFGEN model atmosphere analyses of optical spectra, obtaining $X_O = 0.01$–0.04.

One would expect to measure higher chemical enrichment (C+O/He) in WO than WC stars, as their position in the H-R diagram suggests they have evolved beyond the Helium Zero Age Main-Sequence (He-ZAMS), where most WC stars are found (Sander et al., 2012). Tramper et al. (2015, in prep) present comprehensive spectroscopic CMFGEN model atmopshere analysis from near-UV to near-IR of 6 WO stars: 3 Galactic,

Table 4.1: Observation log of the *Herschel* PACS programme and measured [OIII] 88.36μm line fluxes (or upper limits). $\Delta\lambda$ is the scan width in microns.

Object name	other	Exposure time (ks)	Date	Proposal ID	$\Delta\lambda$ (μm)	F [OIII] 88.36μm (10^{-13}erg s^{-1}cm^{-2})
WR 11	γVel	2.383	7 Dec 2012	OT2_pcrowthe_2	3.41	34.1
WR 23	HD 92809	4.763	26 Jan 2013	OT1_pcrowthe_1	3.41	1.43[a]
WR 90	HD 156385	4.763	5 Oct 2012	OT2_pcrowthe_2	3.41	5.47
WR 111	HD 165763	2.383	4 Oct 2012	OT2_pcrowthe_2	3.41	<1.0
WR 140	HD 193793	3.011	23 Dec 2012	OT2_pcrowthe_2	4.20	5.13
WR 142	Sand 5	14.229	23 Dec 2012	OT2_pcrowthe_2	6.41	<4.8
WR 144	[HM60] 1	3.011	24 Dec 2010	OT1_pcrowthe_1	4.20	<1.7

[a]A total line flux of 1.75 is measured, minus 0.32 nebular emission.

2 LMC, and 1 in the extremely metal-poor galaxy IC1613. By matching helium-to-carbon line ratios and the strength of OVI 5290Å and OV 5571–5607Å lines, they derive C/He = 0.6-1.5 and O/He = 0.20–0.45 by number in Galactic and LMC cases. Their results agree with the only previous UV to near-IR analysis of a WO star, Sand 2 in the LMC, for which Crowther et al. (2000) find C/He = 0.7 and O/He = 0.15. Indeed, higher C and O abundances measured in WO stars support their status as more evolved than WC stars, however the O/C ratios obtained by these methods, in WO *and* WC stars, are ubiquitously lower than predicted by stellar models.

A more straightforward indicator of elemental abundance is provided by forbidden fine-structure lines. These are typically formed at low densities and large radii $> 10^3 R_\star$, where $R_\star$ is the radius with Rosseland optical depth 10 and temperature $T_\star$. The flux in these lines is directly proportional to the fractional abundance (γ_i) of the emitting ionic species (Barlow et al. 1988, BRA88). This method was adapted for clumped winds by (Dessart et al. 2000, DCH00), who use mid-IR spectroscopy of Neon and Sulphur lines to calculate ionic abundances of these elements in WC stars.

Fine splitting in the ground state of O^{2+} generates the [OIII] 88.36μm ($^3P_1 - ^3P_0$) forbidden fine-structure line. With a critical density of $\sim$500 cm^{-3}, this line is expected to originate from radii of a few $\times 10^5 R_\star$ in WC stars. Before the launch of ESA's *Herschel Space Telescope*, this line was only observationally accessible in the nearest WR star (γVel), by the ISO-LWS. This instrument was vastly superseded in efficiency by *Herschel*'s PACS. Here I present PACS spectra of 6 Galactic WC and 1 WO star in the vicinity of [OIII] 88.36μm. Using the flux measured in each detected line, it was my aim to provide oxygen abundances in these stars to a level of accuracy unachievable by spectroscopic modelling using current stellar atmosphere codes.

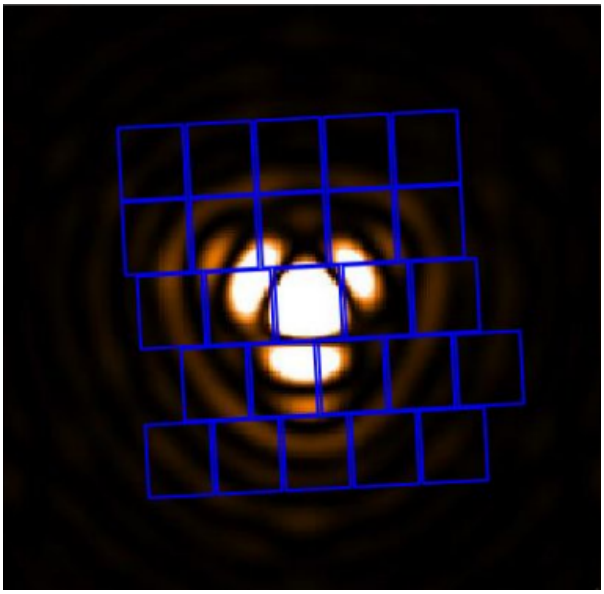

Figure 4.1: *Herschel* PACS detector sampling of the PSF at 77μm. Blue squares represent spaxels. Colour scaling is chosen to enhance lobes and wings of the PSF. Taken from PACS Observer's manual v2.5.1[1]

4.2 Observations

Observations of 6 WC stars and one WO star were carried out by the Photodetector Array Camera and Spectrometer (PACS) (Poglitsch et al., 2008) on-board the *Herschel Space Telescope*. Details of these observations are given in Table 4.1. The PACS instrument is an imaging photometer and integral field line spectrometer capable of low-resolution spectroscopy (R=1000–5000) at wavelengths 55–210μm. PACS was operational from 2009 to 2013, when its coolant was extinguished. In spectroscopy mode, PACS imaged a field of view approximately 50 × 50 arcseconds, resolved into 5″ × 5″ spectroscopic pixels, or 'spaxels'. This field of view is rearranged via an image slicer on to two 16 × 25 Ge:Ga detector arrays, providing simultaneous 55–105μm & 105–210μm spectroscopy (Poglitsch et al., 2008).

Scans covering 86.9–89.9μm with high spectral sampling density were carried out for the 6 WC stars. This wavelength range corresponds to $\pm$5000 kms^{-1} - approximately twice the width of anticipated emission lines, estimated as $2v_\infty$ (v_∞=1500–2500). In the case of the WO star WR 142, this scan width was doubled to account for a high terminal wind velocity (v_∞~5000kms^{-1}, Kingsburgh et al. 1995). The [OIII] 88.36μm line was observed in second order in chopping/nodding mode with a small chopper throw, and

[1]Available at: http://herschel.esac.esa.int/Docs/PACS/pdf/pacs_om.pdf

an additional window was simultaneously observed at 176μm in first order.

Exposure times were estimated using the only previous observation of [OIII] 88.36μm in a WC star - ISO-LWS observations of WR 11 - which measured a flux density of 16.5 Jy in the line (Barlow, priv. comm). The line flux in other programme stars was estimated by taking measurements of C/He by number, assuming C/O $\sim$ 4 from theoretical models (Meynet & Maeder, 2003), and taking the flux to scale linearly with oxygen (O^{2+}) abundance. WR 142 was an exception to this, requiring a longer exposure as only an estimated 20% of oxygen may be in the form of O^{2+} in the [OIII] 88.36μm formation region (Crowther, priv. comm).

In Figure 4.1 I show the arrangement of spaxels in the PACS detector, and their sampling of the PSF. All stars were centred on the central spaxel for observation. Distances to the programme stars range from a few hundred parsecs to $\sim$2 kpc, corresponding to spaxel scales of $\sim$0.008–0.05 pc (5″). The critical density of [OIII] 88.36μm occurs in the winds of WC stars at radii $> 10^5 R_\star$ ($\sim$ 0.005 pc), comparable to the spaxel scale for the nearest programme star(s). Indeed, in the case of WR 11, the line is detected in the outermost spaxels. Considering the PSF in Figure 4.1, one can see that an emitting region larger than 1.5 spaxels in radius would result in these spaxels receiving signal. At the distance to WR 11, 1.5 spaxels corresponds to $\gtrsim$ 0.012 pc, putting a lower limit on the emitting radius of $r \gtrsim 2.6 \times 10^5 R_\star$. In PACS scans of the second most distant programme star, WR 90 ($D = 1.2$ kpc), detection was largely confined to the central spaxel, with tentative signal in some adjacent spaxels - consistent with an unresolved point source. Non-detection of the line in the outermost spaxels constrains the physical extent of the emitting region to < 1.5 spaxels, corresponding to < 0.045 pc at the distance of WR 90, i.e., $r < 10^6 R_\star$. Detection of [OIII] 88.36μm in WR 23 and WR 140 was also largely confined to the central spaxel. Thus, the raw data confirm that the densities for [OIII] 88.36μm emission arise between 2.6–10 $\times 10^5 R_\star$ in WC star winds.

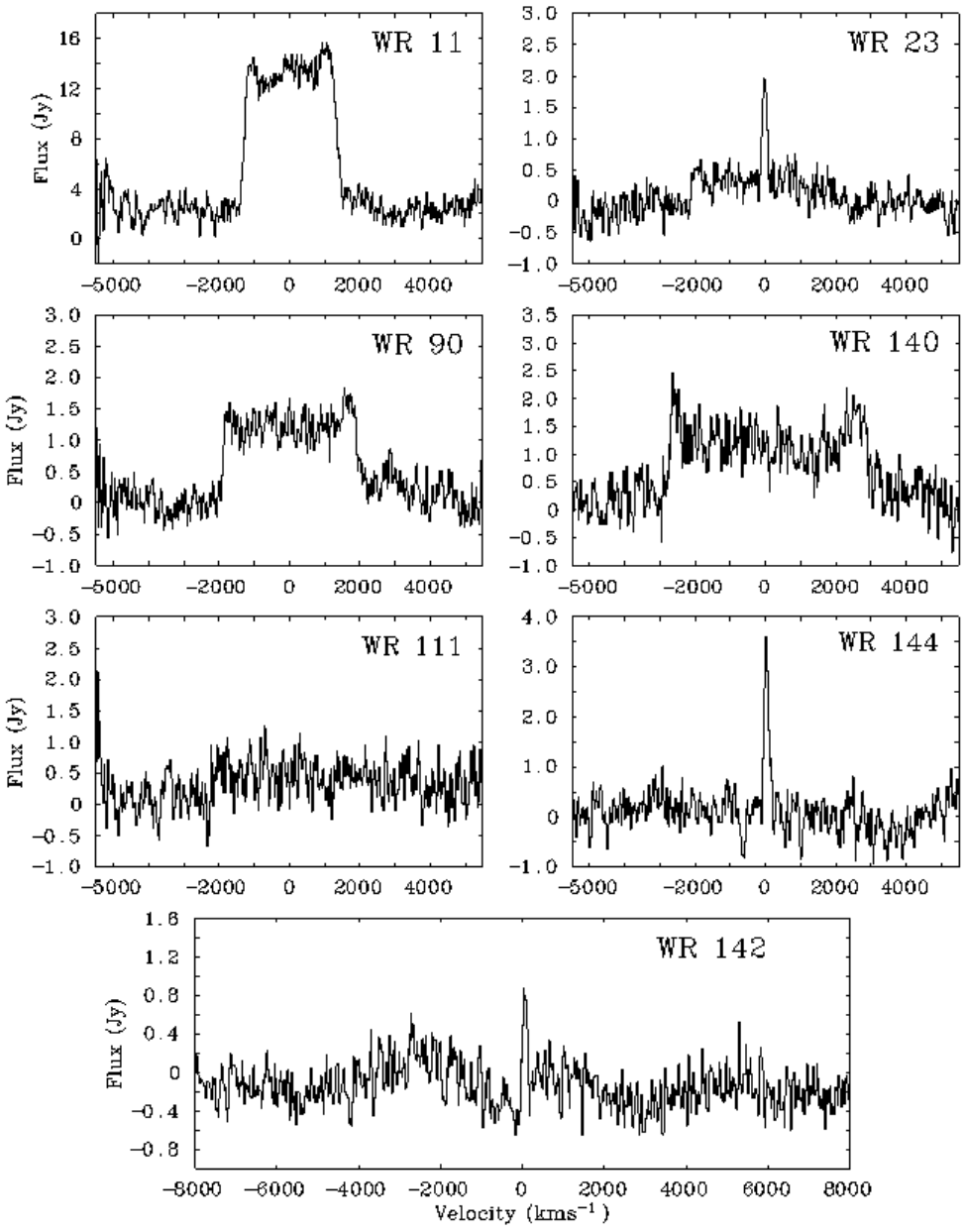

Figure 4.2: *Herschel* PACS scans of all programme WC stars. The observed signal from the central PACS spaxel is shown in each case, with the exceptions of WR 11 and WR 90 where the plotted spectra are the sum of all spaxels displaying emission - 16 and 3 spaxels respectively. Each spectrum is plotted in velocity space, about the central wavelength of [OIII] 88.36μm. Narrow nebular emission can be seen, superimposed on any stellar [OIII] 88.36μm present, in stars WR 23, 142 and 144.

4.3 [OIII] Line measurements

In Figure 4.2 I show the PACS scans at 88.36μm of all 7 programme stars. I measured the line flux of each detected broad [OIII] 88.36μm emission line using the `FLUX` routine in the Starlink `DIPSO` package[2], after converting the flux units of the PACS spectra from Janskys to ergs^{-1}cm^{-2}. Definite detections of the [OIII] 88.36μm line in four programme stars (WR 11, 23, 90 and 140) were obtained, shown in the top four panels of Figure 4.2. For the three programme stars without a clear detection, I derived upper limits on the [OIII] line flux, by methods described in Section 4.3.1. All [OIII] 88.36μm line flux measurements and upper limits are given in Table 4.1.

Of all the stars observed, only WR 11 displays significant flux in the continuum, both adjacent to [OIII] 88.36μm and in the longer wavelength (first order) window at 177μm. To measure the [OIII] line flux in this star I first performed a second order polynomial fit to selected continuum regions either side of the emission line (-3930 to $-1890\,\mathrm{kms}^{-1}$, and $+2190$ to $+4900\,\mathrm{kms}^{-1}$), avoiding the noisiest portions of the spectrum, and subtracted the result before using `FLUX`. The only other WR star potentially displaying a signal in the continuum at 88μm was WR 140. However, unlike in WR 11 the flux was observed to steadily decline towards the edges of the observed window. The origin of this uneven background was unclear, but I fitted and subtracted it as for WR 11 (selected continuum regions: -4645 to $-3000\,\mathrm{kms}^{-1}$, and $+3360$ to $+4960\,\mathrm{kms}^{-1}$) before measuring line flux using `FLUX`. In all other spectra presented in Figure 4.2 I assumed the continuum level to be at zero.

Three programme stars (WR 23, 144 and 142) displayed narrow nebular [OIII] emission as a consequence of their locations in star-forming complexes (Carina and Cygnus). In WR 23 this narrow emission is superposed on genuine broad stellar [OIII] 88.36μm emission. To measure and remove this nebular flux contribution, I fitted the feature with a Gaussian profile, using selected regions of the flat-topped broad emission feature (-1760 to $-310\,\mathrm{kms}^{-1}$, and $+330$ to $+1820\,\mathrm{kms}^{-1}$) as a pseudo 'continuum'. I then subtracted the measured nebular flux from the *total* [OIII] emission measurement given by `FLUX`. For completeness, I also performed Gaussian fits to the nebular emission seen in the spectra of WR 142 and 144, measuring their flux and width. Measurements for all nebular lines are given in Table 4.2.

[2]Available at: http://starlink.eao.hawaii.edu/starlink

Table 4.2: Measurements of nebular [OIII] 88.36μm emission associated with three programme stars.

WR#	Flux (10^{-14}erg s^{-1}cm^{-2})	Central velocity (kms^{-1})	FWHM (kms^{-1})
23	3.2 ± 0.2	-234 ± 4	146 ± 8
142	1.11 ± 0.04	-153 ± 2	105 ± 4
144	6.1 ± 0.2	-182 ± 3	152 ± 6

The uneven 'continuum' level in the the spectrum of WR 142 contributes additional uncertainty to this flux measurement, greater than the Gaussian fitting error given here.

4.3.1 Marginal detections

In the spectrum of WR 111 a broad emission feature is barely, if at all, visible (Fig 4.2). A subtle flux discontinuity is visible at precisely the expected velocity of the blue emission edge (-2300 kms^{-1}), and one could claim a subtle flux enhancement above zero redward of this feature. However, the lack of a corresponding edge at the red extreme of the line ($+2300$ kms^{-1}) restricted the line flux measurement to an upper limit.

The PACS spectrum of WR144 does not show uniform [OIII] emission attributable to the WR-star across the expected velocity range. However, reminiscent of WR 111, a small amount of emission can be seen at the expected location of the blue edge of the line (-3100 kms^{-1}). The presence of this feature suggests that the true signal is not far below the current detection limit, but once again the corresponding red edge is absent.

The spectrum of WR 142 is the noisiest obtained in this campaign, reflecting its status as the faintest of these WR-stars at IR wavelengths. Uniform [OIII] emission was not seen within the expected velocity range (-5000 to $+5000$ kms^{-1}). However, an increase in the flux above zero on the blue side of the line can be seen centred at approximately -2600 kms^{-1}. Once again, the lack of an equivalent enhancement on the red side restricted line flux measurement to an upper limit.

To determine upper limits on all three marginal detections, I created an [OIII] emission line template, of which I added increasing amounts to each spectrum showing no firm detection, until a broad emission line was discernible. To create this emission template I used the central spaxel of the strongest PACS detection (WR 11) as a representative emission profile. I subtracted a polynomial fit to the continuum (as when measuring [OIII] line flux in WR 11), before smoothing the result with a Gaussian filter ($\sigma = 200$ kms^{-1}), thus creating a generic flat-topped emission profile. Before adding this template to each spectrum, I scaled it in velocity to the expected terminal wind velocity of the star in question (Table 4.3) and measured its flux using `FLUX`. As an upper limit

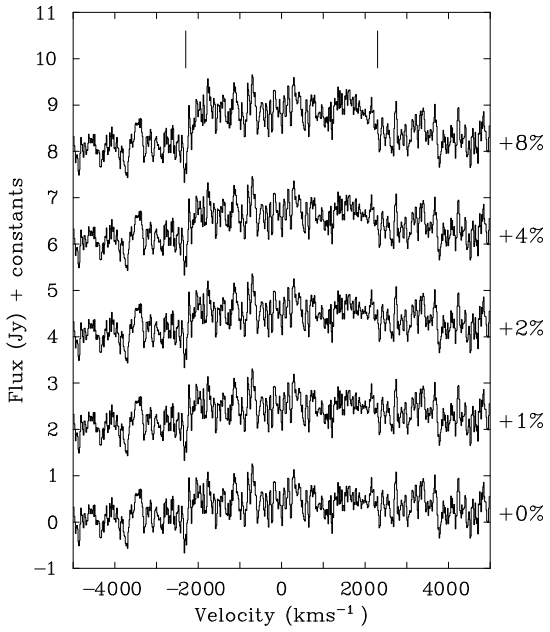

Figure 4.3: The observed PACS spectrum of WR 111 is shown (bottom), plotted in velocity space about the central wavelength [OIII] 88.36μm, with increasing amounts (indicated to the right) of an [OIII] emission line template added. The added template is scaled to the expected terminal velocity of WR 111 (2300 kms^{-1}), indicated by two vertical lines at the top of the figure.

on the line flux, I took the amount of template flux that had to be added for an emission line to become clearly discernible.

In Figures 4.3–4.5, I show this process of adding emission line template flux to the PACS spectra of WR 111, 144 and 142. In WR 111 I declared an emission feature visible upon the addition of 3–4% of the template, corresponding to an upper limit on the line flux of 4% scaled template flux, i.e., $I_{ul} < 1.0 \times 10^{-13}$ erg s^{-1}cm^{-2}.

Similarly for WR 144, I declared a broad emission feature visible upon addition of 4% of the emission template, corresponding to an upper limit on the line flux of $I_{ul} < 1.7 \times 10^{-13}$ erg s^{-1}cm^{-2}.

In the case of WR 142, it was necessary to add 8% of the scaled emission line template before a notable enhancement of the flux above zero across the *whole* expected velocity range could be seen. This corresponds to an higher upper limit on the line flux of $I_{ul} < 4.8 \times 10^{-13}$ erg s^{-1}cm^{-2}.

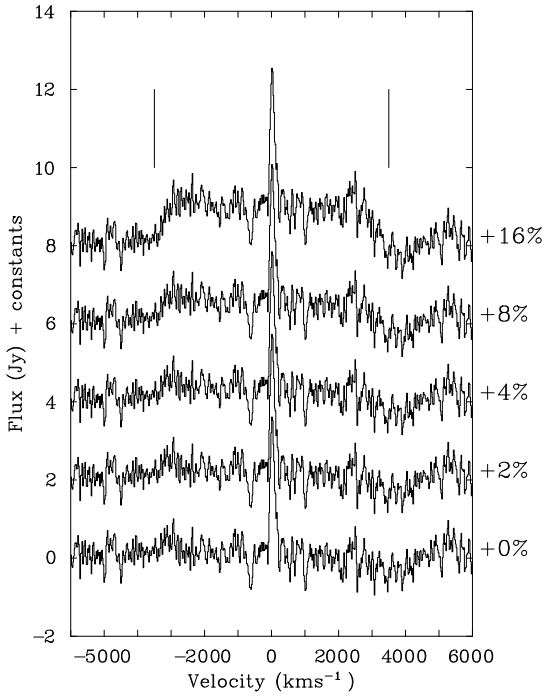

Figure 4.4: As Figure 4.3, but for WR 144. The added emission line template is scaled to $v_\infty = 3500\,\mathrm{kms}^{-1}$.

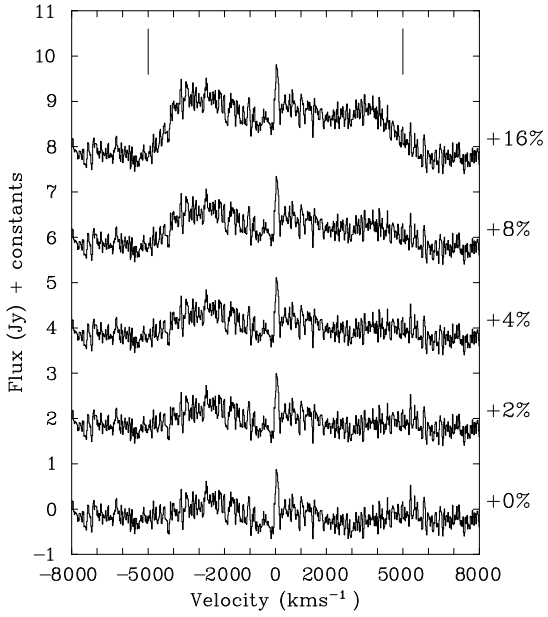

Figure 4.5: As Figure 4.3, but for WR 142. The added emission line template is scaled to $v_\infty = 5000\,\mathrm{kms}^{-1}$.

Table 4.3: Terminal wind velocities measured using detected [OIII] 88.36μm emission lines, compared to alternative measurements in the literature for the programme stars.

WR#	v_∞ ([OIII] 88.36μm) $\pm$100 kms^{-1}	v_∞ (UV) kms^{-1}	other kms^{-1}
11	1460	1415^a,1550^b	1520^c
23	2070	2280^a	-
90	1960	2045^a	-
111	-	2415^a	2300^d
140	2820	2900^a	-
142	-	-	4900^e, 5500^f
144	-	-	3500^g, 3300^h

(a)Prinja et al. (1990), (b)St.-Louis et al. (1993), (c)([NeII] 12.8μm) BRA88, (d)Hillier & Miller (1999), (e)Tramper et al. (2015, in prep), (f)Kingsburgh et al. (1995), (g)Sander et al. (2012), (h)Torres et al. (1986).

4.3.2 Terminal wind velocity measurements

Forbidden fine-structure lines such as [OIII] presented here (Fig 4.2) provide the most direct means of measuring terminal wind velocities in WR stars, as they originate entirely from the asymptotically flowing region of the stellar wind (BRA88). Since the [OIII] line is optically thin, the emission line is expected to be flat-topped and rectangular. The full width of the emission line should therefore correspond to twice v_∞. However, in reality, the line profile will be modified by the instrumental profile, making emission lines slightly non-rectangular. For stars showing a sufficiently clear [OIII] detection, I took the Full Width at Zero Intensity (FWZI) as twice v_∞, and measured this in all cases following subtraction of any continuum signal present. I estimate a $\pm$100 kms^{-1} uncertainty on v_∞ measured this way, considering the difficulty of identifying by-eye where the emission line reaches zero intensity. The FWHM of detected nebular lines (Table 4.2) also indicates that this is a reasonable estimate of the instrumental resolution. In Table 4.3 I give measured terminal wind velocities, and here I briefly discuss how these compare to literature values for the same stars obtained by other methods.

Prinja et al. (1990) present measurements of terminal wind velocities for WR stars, measured using the absorption edges of UV P Cygni profiles (v_{black}), predominantly CIV 1550Å. Unlike spectroscopic modelling, this method is free from assumptions about the form of the velocity law in the accelerating part of the wind, so provides a reasonably direct measurement of v_∞ (recall Sec. 1.4.1). All four programme stars with detected [OIII] 88.36μm are also measured by Prinja et al. (1990). The two methods agree well, with only WR 23 inconsistent - [OIII] gives a lower velocity by $\sim$200 kms^{-1}.

Being the nearest example of a WR, $\gamma\,Vel$ (WR 11) has been comprehensibly studied

and many v_∞ measurements are available. BRA88 measure $v_\infty = 1520\,\mathrm{kms}^{-1}$ using the [NeII] 12.8μm fine-structure line (also formed in the asymptotically flowing outer wind), in good agreement with [OIII]. St.-Louis et al. (1993) report on the variation of UV line profiles with phase in $\gamma\,Vel$ (WR 11), helping them to identify pure WC components which they use to measure $1550\,\mathrm{kms}^{-1}$, slightly greater than measurements using [OIII] & [NeII], but in agreement within the uncertainties.

For WR 111, 142 and 144, [OIII] is not firmly detected (Section 4.3.1) and no other observations of fine-structure lines have been published. However, good agreement between fine-structure lines and the blue edges of UV P Cygni profiles allows us to confidently adopt values obtained by the latter method for these stars. WR 111 is the only one of these three stars studied by Prinja et al. (1990), who measured $v_\infty = 2415\,\mathrm{kms}^{-1}$. For WR 142, Kingsburgh et al. (1995) argue that FWZI/2 of CIV5801,12Å agrees with v_{black} from UV P Cygni lines, and took advantage of this to measure $v_\infty = 5500\,\mathrm{kms}^{-1}$. Tramper et al. (2015) update this measurement using UV P Cygni profiles in addition to FWZI/2 of optical lines, and I adopted their result of $4900\,\mathrm{kms}^{-1}$. No direct measurements of v_∞ are available for WR 144. Sander et al. (2012) obtain $3500\,\mathrm{kms}^{-1}$ by matching the widths of optical lines in their model grid analysis. This is the value I adopted, which is supported by Torres et al. (1986) who obtained $3300\,\mathrm{kms}^{-1}$, also from the widths of optical emission lines.

4.4 Analysis method

With measurements of line flux obtained, all that is needed in addition are accurate stellar parameters to measure the fractional ionic abundance of O^{2+} in each programme star. The method I used to derive the ionic abundance of O^{2+} is similar in concept to BRA88, originally devised to measure the ionic neon abundance in WR 11 (γ *Vel*). DCH00 re-derived the BRA88 formulation to incorporate wind clumping. It is this method, briefly outlined here, that I applied to the programme stars.

4.4.1 Calculation of fractional ionic abundances

The following abundance determination is applicable to an emission line formed by electronic transition between two fine-structure energy levels (u and l), occurring in the asymptotic region of a clumpy stellar wind, where material is on average flowing at a velocity v_∞ following a r^{-2} density distribution. If a flux I_{ul} is observed in the fine structure line of a star residing at a distance D, the total power emitted by the star in

this line is

$$4\pi D^2 I_{ul} = \int_0^\infty n_u A_{ul} h\nu_{ul} 4\pi r^2 f \, \mathrm{d}r \quad erg\, s^{-1}, \tag{4.1}$$

where $h\nu_{ul}$ is the energy of a transition with probability A_{ul} (s^{-1}) of occurrence, n_u is the density of ions in the upper level, and f the volume filling (clumping) factor in the line-formation region. The incorporation of this clumping factor is a modification to the original method of BRA88, adhering to the standard simplification of no inter-clump material. The value of f has commonly been assumed constant throughout the wind, but here I denote f_{out} as the clumping factor in the [OIII] line-forming region ($R \sim 10^5 R_\star$). It has been suggested this may differ from the value routinely assumed for the inner wind, $f_{in} \simeq 0.1$ ($R \lesssim 10 R_\star$), which successfully reproduces the electron scattering wings of lines formed in these regions (Hillier, 1991).

The density of ions in the upper level can alternatively be expressed as

$$n_u = f_u n_i \quad cm^{-3}, \tag{4.2}$$

where n_i is the species ion density, of which a fraction f_u is in the upper level. Following DCH00 I used values of f_u calculated by solving the equations of statistical equilibrium for the O^{2+} ion, using the `EQUIB` code (Adams & Howarth, priv comm), at 13 electron densities over the range 10^0 to 10^{12}cm^{-3}, and electron temperatures $T = 5$–14 kK.

In determining n_i it is necessary to know the stellar mass-loss rate and terminal wind speed. These properties are combined in the mass-loss parameter $A = \dot{M}/(4\pi\mu\, m_H v_\infty)$, (BRA88) so that:

$$n_u = \frac{f_u \gamma_i A}{f_{out} r^2} \quad cm^{-3}, \tag{4.3}$$

where γ_i is the fraction of *all* ions that are species i (i.e., $\gamma(O^{2+})$, the desired result). Combining equations 4.1 and 4.3, the filling factor cancels and one is left with:

$$I_{ul} = \frac{\gamma_i}{D^2} A_{ul} h\nu_{ul} A \int_0^\infty f_u(r, f_{out}, T) \, \mathrm{d}r \quad erg\, s^{-1} cm^{-2}. \tag{4.4}$$

At this point I followed DCH00 by integrating over electron density, N_e, removing the dependency of f_u on A (and hence $\dot{M}$) and filling factor.

Converting the integral in equation 4.4 to one over N_e and re-arranging for the fractional ionic abundance, one obtains:

$$\gamma_i = \frac{(4\pi\mu m_H v_\infty)^{1.5}}{ln(10)} \left(\frac{\sqrt{f_{out}}}{\dot{M}^{1.5}}\right) \frac{1}{F_u(N_e,T)} \frac{2D^2 I_{ul}}{\sqrt{\gamma_e} A_{ul} h\nu_{ul}}, \tag{4.5}$$

where

$$F_u(N_e,T) = \int_0^\infty \frac{f_u(N_e,T)}{\sqrt{N_e}} \,\mathrm{d}\log(\mathrm{N_e}). \tag{4.6}$$

Equation 4.5 is ultimately what I used to calculate $\gamma(\mathrm{O}^{2+})$.

4.4.2 Wind clumping at large radii

Clumping in the inner winds (1–10 $R_\star$) of massive stars is likely a consequence of intrinsic instability in the line driving mechanism (Owocki & Rybicki, 1984). It explains many observational features unaccounted for by homogeneous wind models, such as the strength of electron scattering wings in WR spectra (Hillier, 1991). For WR stars, consistency with observations has most commonly been found for inner wind clumping with volume filling factor $f_{in} \simeq 0.1$ (Morris et al., 2000; Kurosawa et al., 2002). However, the radial extent to which clumping persists, and the extent to which the filling factor varies with radius, remains unknown.

There is both theoretical and observational evidence to suggest that f varies with radius. Runacres & Owocki (2002) perform 1D simulations of a line-driven hot-star wind out to 100 $R_\star$. A highly structured wind is generated, consisting of strong reverse shocks and weaker forward shocks confining high density regions, separated by high-speed rarefied material. They find that collisions of these dense regions allow structure to persist up to the largest radii considered, with the so-called clumping factor ($1/f$) rising to a maximum of ~ 10 around 20 $R_\star$, falling to ~ 5 and remaining approximately constant beyond 50 $R_\star$. As an extension to these simulations, Runacres & Owocki (2005) take advantage of the diminishing radiative force beyond $\sim 30\, R_\star$ to analyse the evolution wind structure out to 1300 $R_\star$ in a purely hydrodynamical sense. Once again, persistent structure is seen out to the largest radii, characterised by a clumping factor ~ 4 ($f = 0.25$) between 300–1300 $R_\star$. Admittedly these simulations remain two orders of magnitude in radius below the formation region of [OIII] 88.36μm, but show it is theoretically possible for structure in a line-driven wind to survive well beyond the region where it is formed.

Variations in wind clumping are hinted at observationally by the discrepancy in mass-loss rates derived using diagnostics originating from different depths in a stellar wind. For example, Puls et al. (2006) reveal a factor of two difference between H-α derived $\dot{M}$ ($\sim 2\, R_\star$) and radio derived $\dot{M}$ ($\sim 100\, R_\star$) in O supergiants, under the assumption of

constant clumping factor, implying a lower clumping factor in the radio emitting region. Additionally, the non-thermal radio spectrum of some O-stars requires wind shocks to be present out to a minimum of 500 $R_\star$ (Van Loo et al., 2004), further supporting the existence of wind structure at large radii.

The emerging consensus is that clumping persists to large radii (at least 10^3 $R_\star$) in a line-driven wind, characterised by a clumping (volume filling) factor which decays to a minimum of 4–5 ($f = 0.2$–0.25) (Runacres & Owocki, 2005). I assumed a similar wind structure in the [OIII] 88.36μm forming region (10^5 $R_\star$) of the programme stars, applying volume filling factor of $f_{out} = 0.25$ in all calculations. However, I accept that the available evidence permits values in the range $0.1 < f_{out} < 0.5$, and consider this when estimating uncertainties in $\gamma(O^{2+})$ calculations (see Section 4.6.2).

4.4.3 Predicted structure of WC star winds

The ionic oxygen fraction, $\gamma(O^{2+})$, in each star will represent the absolute oxygen abundance only if O^{2+} is the dominant ion of oxygen in the region of the wind where [OIII] 88.36μm is formed, i.e., at the critical density of $\sim$500cm^{-3}. For a typical WC star with an r^{-2} density law holding throughout its terminally flowing wind, these conditions are expected to occur at a few $\times 10^5 R_\star$, which is far beyond the consideration of most model atmosphere calculations published to date, which mostly focus on $r < 10^3 R_\star$ (e.g., Hillier & Miller 1999; Crowther et al. 2002).

To investigate the conditions found in the winds of WC stars at larger radii, I utilised a CMFGEN model atmosphere solution extending to $10^5 R_\star$ (Crowther, priv. comm). This was calculated using the stellar parameters of WR 23, which has an intermediate temperature amongst the programme stars. I show the resulting wind properties as a function of radius in Figure 4.6. It can be seen that density (N_e) declines exponentially with radius, and if extrapolated beyond the displayed range suggests the critical density of [OIII] 88.36μm (500cm^{-3}) occurs at a few $\times 10^5 R_\star$. Beyond $10^3 R_\star$ the temperature in the wind is stable at approximately 8000K, and the terminal velocity has been reached, as anticipated. I assumed this temperature when evaluating Equation 4.6 for all programme stars.

The CMFGEN model for WR 111 (WC5) presented by Hillier & Miller (1999) predicts that O^{2+} becomes the dominant oxygen ion over O^{3+} below $N_e \sim 10^{11}$cm^{-3} ($10^{1.5} R_\star$), and remains as such out to at least $N_e \sim 10^9$cm^{-3} ($10^{2.5} R_\star$), with the fraction of O^{3+} remaining in steady decline and no significant increase in O^+. Crowther et al. (2002) present models for hotter WC4 stars, showing O^{2+} becoming dominant at a lower density of 10^{11}cm^{-3}

($10^{2.0} R_\star$), still well above (interior to) the critical density of [OIII] 88.36μm. In Figure 4.7 I show the radial dependence of ionisation for oxygen, neon and sulphur as predicted by the large-radius CMFGEN model atmosphere for WR 23. This model predicts O^{2+} as the dominant ionisation stage of oxygen in the [OIII] 88.36μm line forming region. This simple model assumes a smoothly flowing wind, with clumping taken into account via a volume-filling factor approach, neglecting the effects of shocks in the wind resulting from clump-clump interactions (Runacres & Owocki, 2005). These neglected effects may provide additional heating and hence alter the ionisation balance in localised regions of the wind. In Figure 4.7 I indicate the formation regions of other fine-structure lines commonly observed in WC stars winds. In Section 4.6.1 I use observations of these lines in WR 23 and WR 11, together with stellar parameters reviewed in the next section, to test this predicted ionisation structure.

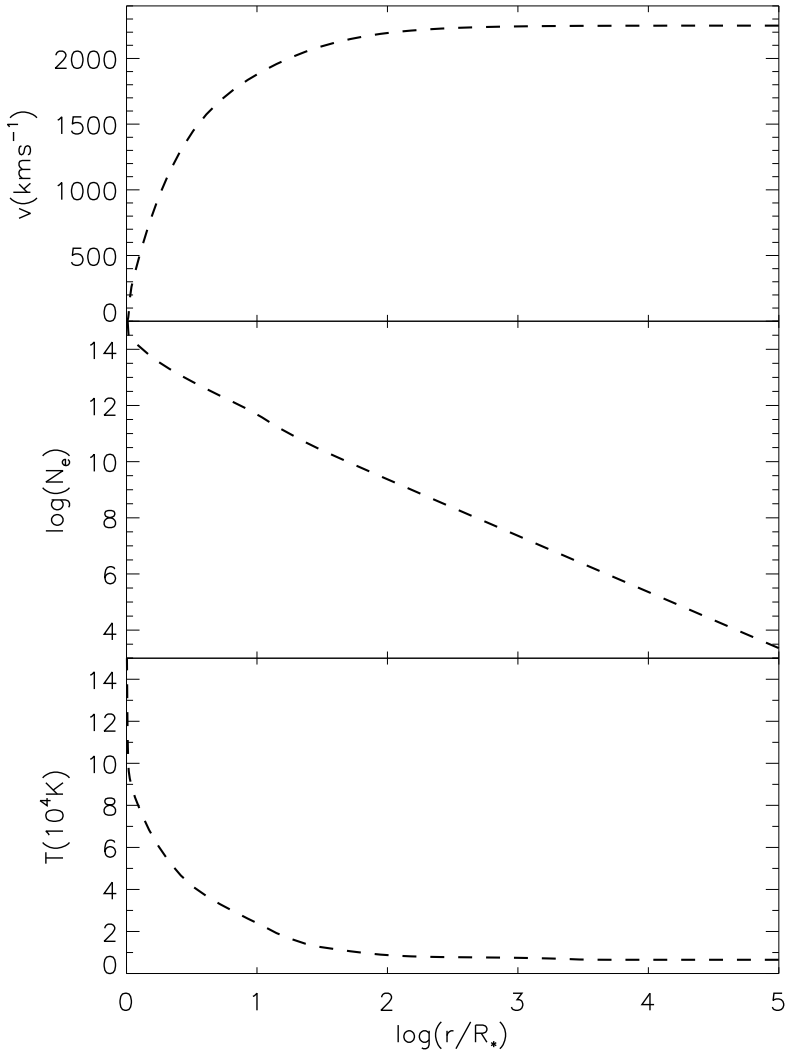

Figure 4.6: Radial dependence of wind velocity (upper panel), temperature (middle) and density (lower) in a CMFGEN model atmosphere, generated with the parameters of WR 23 (Tab. 4.4). Radius is in units of $R_\star$ - the inner boundary of the model atmosphere, located where τ_{ross}=10.

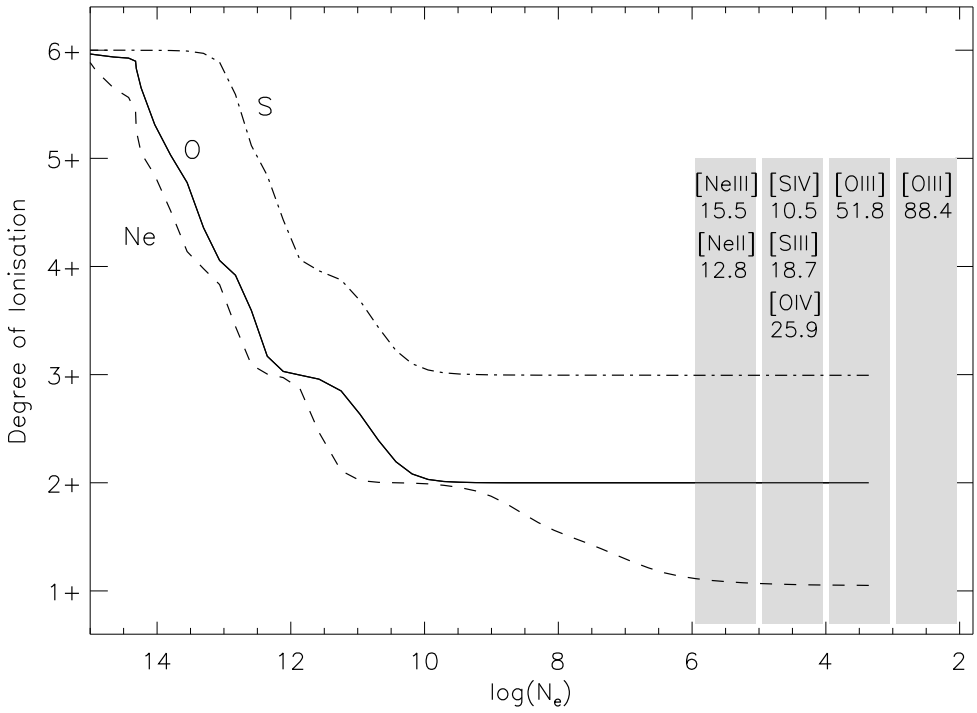

Figure 4.7: Ionisation stratification of oxygen, neon and sulphur in a CMFGEN model atmosphere (generated with the parameters of WR 23) as a function of electron density $\big(\log(N_e) \propto 1/\log(r/R_\star)\big)$. Shaded areas show approximate critical densities of formation for various far-IR fine-structure lines (labelled within) of the elements shown.

4.5 Review of Stellar Parameters

Here I present a review of stellar parameters for the programme stars. Most are collected from the literature, but some are remeasured or adjusted to account for an updated distance estimate. Parameters necessary for the calculation of fractional ionic abundance by the BRA88 method are mass-loss ($\dot{M}$), terminal wind velocity (v_∞), distance (D) and C+O abundances. Requirement of a prerequisite oxygen abundance indicates a circular method, but the quantities derived from this (C+O) abundance (γ_i and μ, Section 4.4.1) are relatively homogeneous in WC stars, and show a greater dependence on carbon abundance in WC and WO stars. Where oxygen abundance estimates were unavailable, I initially assumed C/O = 4 (Hillier & Miller, 1999). Final adopted stellar parameters are given in Table 4.4.

All programme stars have mass-loss rates measured by spectroscopic analysis of UV/optical/IR spectra. The quantity actually derived by this method is $(\dot{M}/\sqrt{f})$ (DCH00). Using notation adopted here, $f = f_{in}$, and throughout this section I implicitly assume $f_{in} = 0.1$. Furthermore, spectroscopically derived mass-loss rates scale as $\dot{M} \propto D^{1.5}$ (DCH00).

Terminal wind velocities have already been discussed in Section 4.3.2. I adopted measurements of v_∞ from those listed in Table 4.3 in order of preference; (1) [OIII] 88.36μm, (2) UV v_{black}, (3) 'other'.

WR 11 (γ *Vel*)

A component of the $\gamma\,Velorum$ system, comprising WC8+O7.5III stars, WR 11 is the closest known example of a WR star. As such it is the only WR with a *Hipparcos* parallax measurement, giving a distance of 334^{+40}_{-32}pc (van Leeuwen, 2007), revised from an initially lower 258^{+41}_{-31}pc. This revised parallax measurement is in broad agreement with interferometric distances of 336^{+8}_{-7}pc (North et al., 2007) and 368^{+38}_{-13}pc (Millour et al., 2007). I adopted a distance of 340 pc to this system.

A detailed spectral analysis of the WR component in this system has been carried out at optical and near-IR wavelengths by De Marco et al. (2000), utilising the non-LTE line-blanketed model atmosphere code CMFGEN. Their analysis yields $\log(L/L_\odot) = 5.0$, $T_{eff} = 57$kK, $(\dot{M}/\sqrt{f}) = 9.0\times10^{-6} M_\odot yr^{-1}$, and C/He=0.15, based on the initial (low) *Hipparcos* distance. Both $\log(L/L_\odot)$ and $\dot{M}$ increase to 5.2 and $1.4\times10^{-5} M_\odot yr^{-1}$ respectively at 340 pc.

WR 23 (HD 92809)

WR 23 is a WC6 star located in the Carina Nebula, and is located $\sim 20'$ north of the open cluster Bochum 10, but is likely not a member (Lundström & Stenholm, 1984). Several individual objects and open clusters associated with the Carina Nebula have measured distances, however, persistent uncertainty surrounding the form of the extinction law has maintained a spread in reported values. The enigmatic η Carinae - a member of the Tr16 open cluster - has been shown to lie at a distance of 2.35 ± 0.05 kpc by proper motion measurement of its surrounding *Homunculus* nebula (Smith, 2006). This distance is slightly lower than that found for the Tr14 and Tr16 clusters, at 2.7 kpc and 2.9 ± 0.3 kpc according to the photometric studies of Tapia et al. (2003) and Hur et al. (2012) respectively. Additionally, Freyhammer et al. (2001) derive a distance of 2.6 ± 0.1 kpc to the binary system Tr16-1. Assuming WR 23 was formed and remains within the Carina star forming complex, I adopted a distance of 2.6±0.2 kpc, consistent with these four estimates.

A CMFGEN spectroscopic analysis of WR 23 has been carried out at optical and near-IR wavelengths by Smartt et al. (2001), who also assume $D \simeq 2.6$kpc. From this I adopted $\log(L/L_{\odot}) = 5.3$, $T_{eff} = 75$kK, $\dot{M} = 1.6 \times 10^{-5} M_{\odot} yr^{-1}$ and C/He = 0.30.

WR 90 (HD 156385)

WR 90 is an apparently single WC7 star not belonging to any known cluster or association. I therefore adopted a distance based on the average K_S-band absolute magnitude of other WC7 stars, giving 1.2 ± 0.2 kpc (Table C.1).

DCH00 carried out a detailed near-UV/optical/near-IR spectral analysis of WR 90 using the CMFGEN model atmosphere code. They obtained $\log(L/L_{\odot}) = 5.5$, $T_{eff} = 71$kK, $\dot{M} = 2.5 \times 10^{-5} M_{\odot} yr^{-1}$, C/He = 0.25 and O/He = 0.03 - obtained by fitting OIV lines in the UV spectrum, providing a useful comparison to the results of [OIII] 88.36μm measurements. This luminosity and mass-loss rate were based on a distance of 1.5 kpc, obtained by the application of an average V-band absolute magnitude for WC7 stars. I chose to adopt the M_{K_S}-derived distance, as reddening uncertainties are reduced at near-IR wavelengths. At this lower distance, $\log(L/L_{\odot})$ and $\dot{M}$ become 5.2 and $\dot{M} = 1.8 \times 10^{-5} M_{\odot} yr^{-1}$ respectively.

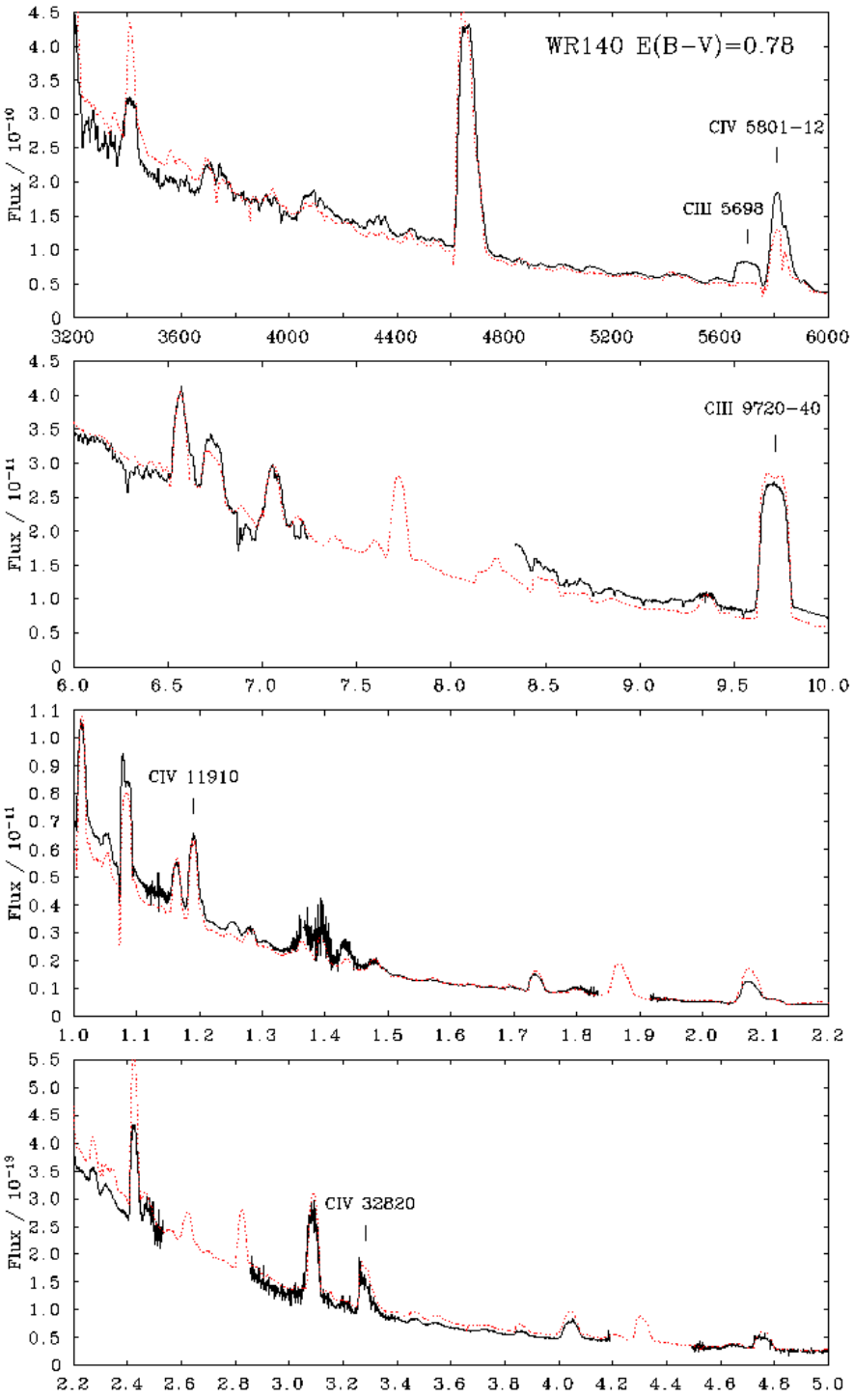

Figure 4.8: Optical and near-IR flux-calibrated spectra of WR 140 (black solid) with best fitting CMFGEN model (red dotted), reddened using E(B-V)=0.78 and R_V=3.1. Labelled are the carbon emission lines primarily used to determine C/He. Flux units are erg $s^{-1}cm^{-2}$, wavelength is in Angstroms ($\times 10^{-4}$ in lower three panels).

WR 111 (HD 165763)

WR 111 is an apparently single WC5 star and a purported member of the Sgr OB1 association (Lundström & Stenholm, 1984). Mel'Nik & Dambis (2009) placed this association between 1.3–1.9 kpc based on *Hipparcos* trigonometric parallaxes. Objects thought to be associated with Sgr OB1 include the open cluster NGC 6383, at a distance of 1.7 kpc (Paunzen et al., 2007), and more speculatively the dust-producing Wolf-Rayet binary WR 104 (WC9d+OB) (Crowther, 1997), indicated by the proper motion of its surrounding 'pinwheel' nebula to lie at a distance of 2.6 ± 0.7 kpc (Tuthill et al., 2008). I adopted a distance of 1.9 kpc to WR 111, consistent with the three existing estimates.

A detailed near-UV/optical/near-IR spectroscopic analysis of WR 111 has been carried out by Hillier & Miller (1999) in their seminal demonstration of the CMFGEN model atmosphere code. Their analysis gave $\log(L/L_{\odot}) = 5.3$, $T_{eff} = 91$kK, $\dot{M} = 1.5{\times}10^{-5} M_{\odot} yr^{-1}$, and C/He = 0.4 at an assumed distance of 1.55 kpc. At the greater distance assumed here, $\log(L/L_{\odot}) = 5.5$ and $\dot{M} = 2.0{\times}10^{-5} M_{\odot} yr^{-1}$.

WR 140 (HD 193793)

WR 140 is a well studied colliding-wind binary comprising WC7+O5 stars (Williams et al., 2009a) and does not belong to any known open cluster or OB association. The distance to WR 140 is well determined as 1.67 ± 0.03 kpc by Monnier et al. (2011), who resolve the system over a complete (7.9 yr) orbit using interferometry.

To date, uncertainty concerning the exact nature (luminosity class) of the O-star in WR 140 has prevented a detailed spectroscopic analysis to reveal the WR star parameters. However, Monnier et al. (2011) measured a H-band flux ratio between the system components of F_{WR}/F_{O}=1.37 ± 0.03, providing an essential constraint for the spectroscopic analysis of this system. To perform this analysis I utilised flux-calibrated 3000–7000Å (INT/IDS) and 1–5μm (IRTF/SpeX; Vacca, priv. comm) spectra. P. Crowther provided an appropriate model spectrum, consisting of the sum of a Kurucz model (Castelli & Kurucz, 2004) for the O component and a `CMFGEN`-computed spectrum, satisfying the observed H-band flux ratio. The reddening towards WR 140 was determined using this model by anchoring the ∼5μm flux (essentially unaffected by extinction), and varying E(B–V) until a good match was found to the optical spectrophotometery, resulting in E(B–V) = 0.78 (assuming $A_V = 3.1$). In Figure 4.8 I show these observed spectra along with the best fitting Kurucz+CMFGEN model for WR 140, from which I obtained WR parameters: $\log(L/L_{\odot}) = 5.7$, $T_{eff} = 70$kK, $\dot{M} = 1.6{\times}10^{-5} M_{\odot} yr^{-1}$, and C/He = 0.12.

Table 4.4: Adopted stellar parameters for each programme star. Volume-filling factor, $f = f_{in} = 0.1$, is assumed in all cases. See text (Section 4.5) for references.

Object	Sp. Type	Distance pc	T_* kK	$\log(L/L_\odot)$	v_∞ kms^{-1}	$\log(\dot{M})$ $M_\odot$yr^{-1}	C/He #
WR11	WC8+O7.5III	340	57	5.5^s	1500	−4.85^s	0.15
WR23	WC6	2600	75	5.3	2070	−4.80	0.30
WR90	WC7	1200	71	5.3^s	1960	−4.74^s	0.25
WR111	WC5	1900	91	5.5^s	2300	−4.69^s	0.40
WR140	WC7pd+O5	1670	70	5.7	2820	−4.79	0.12
WR142	WO2	1750	200	5.4	4900	−4.94	1.00
WR144	WC4	1400	112	5.0^s	3500	−4.60^s	0.25^a

^{s}scaled to a revised distance. ^{a}Average of spectroscopically derived C/He in LMC WC4 stars (Crowther et al., 2002).

Complementary to the above analysis, Pittard & Dougherty (2006) use hydrodynamical modelling of the wind-collision region to interpret radio and X-ray emission from this system, hence deriving $\dot{M}$ independently. They compute mass-loss rates required to reproduce the observed thermal X-ray flux as a function of the wind momentum ratio (η) suggesting $\dot{M}(\mathrm{WR}) = 2\text{–}4\times10^{-5} yr^{-1}$. Fahed et al. (2011) monitored the 2009 periastron passage in WR 140, and fitted the spectroscopic variability using a Luhrs model to obtain $\eta = 0.039\pm0.016$, which gives $\dot{M} = 3 \times 10^{-5} yr^{-1}$ when combined with the modelling of Pittard & Dougherty (2006). This mass-loss rate is higher than that given by the spectroscopic analysis of WR 140 presented here, however, Pittard & Dougherty (2006) adopt a greater distance to WR 140 (1.85 kpc) and assume a higher carbon abundance (C/He = 0.25). Updating these parameters to those in Table 4.4 has consequences for their predicted X-ray flux, since this is proportional to C/He, $\dot{M}^2$, and D^{-2}. Decreasing C/He acts to reduce the predicted X-ray flux, whereas a decrease in distance to WR 140 acts to enhance it. In total, updating these parameters decreases the predicted X-ray flux by 40%, requiring an increase in $\dot{M}$ by a factor ∼1.3 to maintain consistency with the observed X-ray flux. Therefore the predictions of Pittard & Dougherty (2006) and Fahed et al. (2011) become less consistent with the spectroscopically derived value when revised parameters are included. Nevertheless, I adopt the spectroscopically derived $\dot{M} = 1.6 \times 10^{-5} M_\odot yr^{-1}$, as this incorporates contemporary information about the O-star companion.

WR 142 (Sand 5)

With spectral type WO2 (Crowther et al., 1998), WR142 is the only oxygen-type WR star included in the observing programme. It is located 3.5′ South(East) from, and is a likely member of the open cluster Berkeley 87. Distance estimates for this cluster vary. Using spectroscopic parallax of OB stars Massey et al. (2001) and Turner et al. (2006) report distances of 1.6 and 1.23 kpc respectively. Reddening estimates are consistent between these two studies, so the distance discrepancy must originate either in the spectroscopic classification of cluster members or their assumed absolute magnitudes. In addition, Knödlseder et al. (2002) report a distance of 1.9 kpc, using a reddening-free parameter approach, yielding a reddening consistent with the other studies. In order to facilitate easy comparison of our results to those of Tramper et al. (2015, in prep), we adopt the same distance of 1.75 kpc to WR 142.

Tramper et al. present a tailored analysis of WR 142 with the CMFGEN model atmosphere code. From this, I adopted $T = 200$kK, $\log(L/L_{\odot}) = 5.39^{+0.23}_{-0.15}$, $\dot{M} = 1.15\times10^{-5} M_{\odot}\mathrm{yr}^{-1}$ and C/He = 1.00. WR 142 is also one of the two WO stars included in the non-LTE line-blanketed model grid analysis of Sander et al. (2012). The mass-loss rate obtained by Sander et al. is ∼10% lower than that given by Tramper et al. - within the typical uncertainties of spectroscopically-derived $\dot{M}$. Despite assuming a lower distance of 1.23 kpc, Sander et al. measure a higher luminosity of $\log(L/L_{\odot}) = 5.7$, corresponding to a discrepancy of $\Delta\log(L/L_{\odot}) = 0.6$ at 1.75 kpc. One reason for this is the different treatment of reddening between the two studies. Tramper et al. derive E_{B-V} by matching the slope of their flux-calibrated spectrum to that of a CMFGEN model at Galactic metallicity, under the standard assumption of $R_V = 3.1$ which is allowed to vary. Sander et al. adopt a similar approach, fitting their model spectrum to an SED constructed from optical and mid-IR spectra and near-IR photometry, with E_{B-V}, luminosity, and R_V as free parameters. Both studies derive identical E_{B-V}, however, Tramper et al. find $R_V = 2.85$ is optimal, whereas Sander et al. find the standard $R_V = 3.1$ sufficient. Consequently, these studies infer absolute magnitudes with $\Delta M_V = 0.5$, accounting for a factor of ∼1.5 in luminosity, short of the factor ∼4 difference between their results. I adopted the Luminosity derived by Tramper et al., as this is measured using a more uniform data set, allowing a more accurate determination of R_V towards WR 142.

Previous abundance estimates are given for WR 142 by Kingsburgh et al. (1995), who use the strength of optical recombination lines to derive C/He = 0.52 and O/He = 0.1. Abundances given by Kingsburgh et al. (1995) for other WO stars are in good agreement with more sophisticated model analyses, e.g., Sand 2 in the LMC (Crowther et al., 2000).

However, I favoured the results of Tramper et al. as they performed a more sophisticated model analysis using data covering the largest wavelength range available.

WR 144

WR 144 is an apparently single WC4 star belonging to the Cygnus OB2 association, part of the larger Cygnus X complex, shown to lie at a distance of 1.40 ± 0.08 kpc by trigonometric parallax measurements of water and methanol masers (Rygl et al., 2012).

The optical spectrum of WR 144 was analysed by Sander et al. (2012) using a grid of PoWR WC models, yielding $T_{eff} = 112$kK, $\log(L/L_{\odot}) = 5.2$ and $\dot{M} = 2.5{\times}10^{-5} M_{\odot}\mathrm{yr}^{-1}$, at a distance of 1.8 kpc. At the revised distance of 1.40 kpc, these become $\log(L/L_{\odot}) = 5.0$ and $\dot{M} = 1.7{\times}10^{-5} M_{\odot}\mathrm{yr}^{-1}$. Sander et al. do not derive an individual carbon abundance for WR 144. To gain an insight into the likely carbon abundance, I looked to spectral analysis of other WC4 stars in the LMC (Crowther et al., 2002). Near-UV to near-IR spectral analysis of three WC4 stars, and an optical to near-IR of three more, utilising the CMFGEN model atmosphere code, reveals a reasonably narrow range in C and O abundances (C/He =0.10–0.35, O/He =0.01–0.06). Noting that the difference in metallicity between LMC and Milky Way is not expected to have a significant effect on the abundances in self-enriched WR atmospheres, I adopted representative WC4 abundances of C/He = 0.25 and a *preliminary* O/He = 0.03 for WR 144.

Table 4.5: For each programme star: Atomic constants (μ, γ_e) calculated using adopted C/He abundances (Tab. 4.4) and preliminary O/He estimates; fractional oxygen abundance ($\gamma(O^{2+})$, Eq. 4.5); O^{2+}/He by number (= O/He in WC ≥ 5 stars, as argued in Sec. 4.6); surface oxygen mass fraction (assuming $X_O + X_C + X_{He} = 1$); (C+O)/He by number. Values shown in brackets represent upper limits regarding the abundance of O^{2+}, but may underestimate the quantity of oxygen in total due to uncertainty in the behaviour of other ionic species (see Sec. 4.6).

Object	Subtype	γ_e	μ	$\gamma(O^{2+})$ (10^{-3})	O^{2+}/He	X_O	(C+O)/He
WR11	WC8+O7.5III	1.153	5.322	$3.7^{+1.2}_{-0.9}$	$4.3^{+1.7}_{-1.3} \times 10^{-3}$	0.012	0.16
WR23	WC6	1.275	6.435	$15.4^{+4.8}_{-3.9}$	$0.020^{+0.007}_{-0.006}$	0.040	0.34
WR90	WC7	1.219	5.844	$8.5^{+2.6}_{-2.1}$	$0.011^{+0.004}_{-0.003}$	0.025	0.28
WR111	WC5	1.333	6.933	$< 5.6^{+1.7}_{-1.4}$	$< 7.9^{+2.8}_{-2.1} \times 10^{-3}$	< 0.014	< 0.41
WR140	WC7pd+O5	1.099	4.829	$26.4^{+8.2}_{-6.6}$	$0.030^{+0.012}_{-0.009}$	0.081	0.20
WR142	WO2	1.383	7.309	$< 163^{+51}_{-41}$	$< 0.39^{+0.17}_{-0.12}$	(< 0.28)	(< 1.3)
WR144	WC4	1.219	5.844	$< 9.5^{+3.0}_{-2.4}$	$< 0.012^{+0.004}_{-0.003}$	(< 0.027)	(< 0.28)

Table 4.6: Atomic data for [OIII] 88.36μm and [OIII] 51.81μm fine-structure lines.

Transition	λ μm	ω_u	ω_l	A_{ul} (s^{-1})	Ref	Ω_{ul} 8000K	Ref	$\log(N_e^{crit})$ cm^{-3}
$^3P_2 - ^3P_1$	51.814	5	3	9.76×10^{-5}	a	1.27	b	3.5
$^3P_1 - ^3P_0$	88.356	3	1	2.62×10^{-5}	a	0.54	b	2.7

(a)Nussbaumer & Storey (1981), (b)Aggarwal (1983).

4.6 Ionic oxygen Abundances

Measurements and upper limits on $\gamma(O^{2+})$ for the programme stars are presented in Table 4.5, with the relevant atomic data used for their calculation given in Table 4.6.

I calculated the number fraction, O^{2+}/He, using the equation

$$\frac{O^{2+}}{He} = \frac{(1+\frac{C}{He})\gamma O^{2+}}{1-\gamma O^{2+}}, \tag{4.7}$$

assuming a purely He+C+O composition. For the programme stars in which [OIII] 88.36μm is unambiguously detected, I measured $\gamma(O^{2+})$ in the range 0.004–0.026, corresponding to $O^{2+}/He = 0.004$–0.03. The abundance of O^{2+} as measured by [OIII] 88.36μm corresponds to the total abundance of oxygen if this ion is dominant in the region where [OIII] 88.36μm is formed (Fig. 4.7). In Section 4.4.3 I used a CMFGEN model atmosphere for WR 23, extending to large radii, to show that this is theoretically predicted to be the case. Here I summarise observational insights into the ionisation structure of Oxygen in WC & WO star winds, and what one may infer from this about oxygen abundances given by [OIII] 88.36μm in these stars.

4.6.1 Probing ionisation stratification in WC star winds

The [OIII] 51.81μm fine-structure line

To some degree, ionisation stratification in WC star winds can be probed using fine-structure lines of different ionisation stages of the same atomic species formed at different densities (radii). Regarding oxygen, unfortunately the ground state configuration of O^{+} does not provide a suitable transition, but an alternative O^{2+} line is available in [OIII] 51.81μm ($^3P_2$–$^3P_1$). This line has a critical density $\sim$3000cm^{-3} ($\sim 10^{4.5} R_\star$) - an order of magnitude higher than that of [OIII] 88.36μm - providing an insight into how the fractional abundances of other oxygen ions vary across this density (radius) range. Specifically, if the abundance of O^{+} (O^{3+}) were to substantially increase (decrease) between 3000–500cm^{-3} one would derive different values of $\gamma(O^{2+})$ using [OIII] 88.36μm and [OIII] 51.81μm.

Spectroscopy at 52μm exists for one of the WC stars observed in this programme, WR 11 ($\gamma\,Vel$), which was observed by ISO-LWS covering 43−197μm (P.I Barlow). I extracted these data from the ISO archive[3], specifically the average fluxed spectrum of back and forth scans carried out by LWS. In Figure 4.9 I plot this spectrum in velocity

[3] http://iso.esac.esa.int/ida/

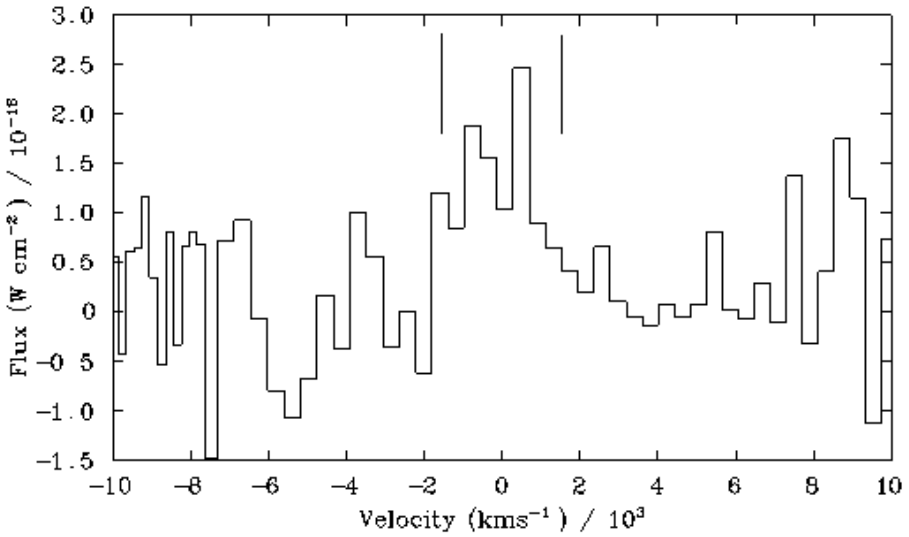

Figure 4.9: ISO-LWS spectrum of WR 11 ($\gamma\,Vel$), an average of back and forth scans, plotted in velocity space about a central wavelength 51.81μm. Vertical lines indicate the expected extent of the emission line $v_\infty = 1500\,\mathrm{kms}^{-1}$.

space, about the central wavelength 51.81μm, where I have used the anticipated width ($2v_\infty$) to identify the emission line.

The ISO-LWS spectrum of WR 11 is very noisy, making the measurement of line flux problematic, as the continuum level was difficult to determine. I proceeded by measuring the line flux in two ways; firstly using `DIPSO`'s `FLUX` command between the expected velocity limits (as for [OIII] 88.36μm) after subtraction of a *by-eye* estimate of the continuum, and secondly by fitting a Gaussian profile to the line using `DIPSO`'s `ELF` suite after subtraction of a (2nd order) polynomial fit to the continuum. Although this emission line is expected to be flat-topped and highly non-Gaussian, this structure is lost in the noise, permitting the use of Gaussian fitting as an approximation. Multiple measurements by the `FLUX` method gave an average line flux of $I_{21} = 8.1 \pm 0.6(2\sigma) \times 10^{-12}\mathrm{erg\,s^{-1}cm^{-2}}$, and Gaussian fitting gave a compatible $7.8 \pm 1.6 \times 10^{-12}\mathrm{erg\,s^{-1}cm^{-2}}$. Considering both measurements, I took the flux in this line to be I_{21}=$8.0 \times 10^{-12}\mathrm{erg\,s^{-1}cm^{-2}}$. As for the calculation of $\gamma(\mathrm{O}^{2+})$ using [OIII] 88.36μm, I used the [OIII] 51.81μm flux and identical stellar parameters for WR 11 (and atomic data from Table 4.6) to calculate $\gamma(\mathrm{O}^{2+})$=4.0×10^{-3}. This is in excellent agreement with $4.3^{+1.7}_{-1.3} \times 10^{-3}$ given by the PACS measurements (Tab. 4.5). The concurrence of these results, both derived using [OIII], provided strong evidence that at least in late-type WC stars the ionisation balance of oxygen is stable across a broad range of density and radius in the outer wind. It is clear that in WR 11

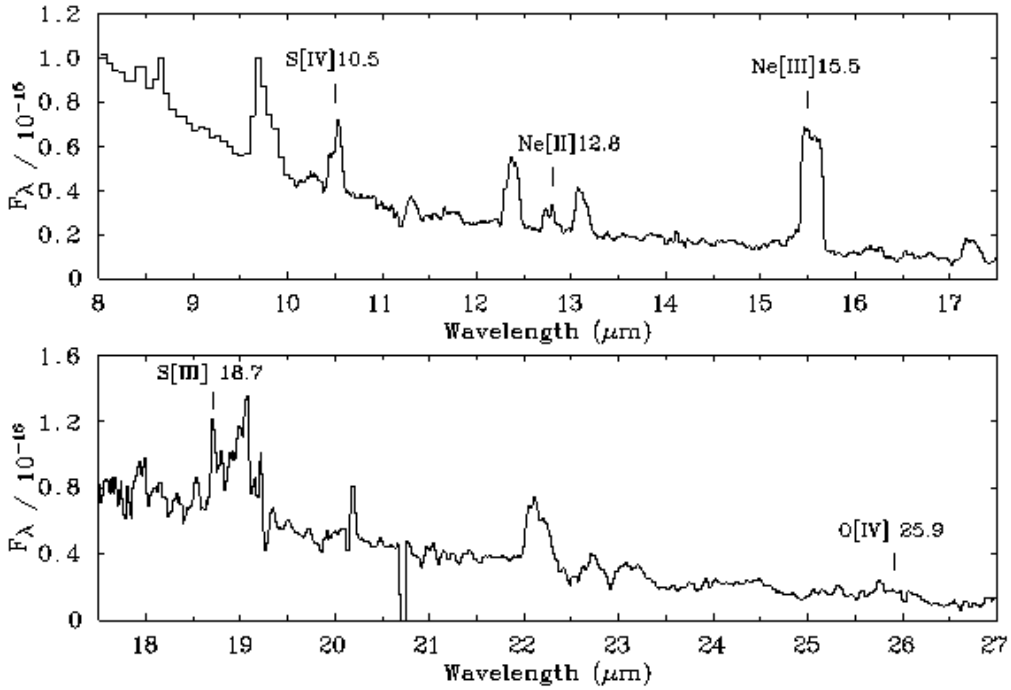

Figure 4.10: Spitzer IRS mid-IR spectrum of WR 23. Fine-structure lines of neon, sulphur and oxygen are labelled, with wavelength given in microns.

neither O^{3+} or O^{+} are dominant at 3000 cm^{-3} or 500 cm^{-3} respectively.

Fine-structure lines of Ne, S, and O^{3+} in WR 23

The consistency between $\gamma(O^{2+})$ measurements at $\log(N_e[cm^{-3}])$=3.5–2.5 in WR 11 support the predicted ionisation structure of oxygen shown in Figure 4.7. More generally, these predictions may be tested using fine-structure lines of other elements, namely Ne and S, which are commonly observed in the mid-IR spectra of WC stars. In Figure 4.10 I present a *Spitzer* IRS 8–27μm spectrum of WR 23 (P.I Crowther), with fine-structure lines of O, Ne and S indicated. In Figure 4.11 I plot the identified lines in velocity space, along with the *Herschel* PACS 88μm spectrum of WR 23 for reference, and in Figure 4.7 I indicate their critical densities with respect to the predicted ionisation stratification of Ne and S in a CMFGEN model for WR 23. Lines of [NeIII] 15.5μm, [SIV] 10.5μm and [NeII] 12.8μm are clearly detected in the IRS spectrum. I measured the flux in these lines using the `FLUX` command in `DIPSO`, after subtracting a 2nd order polynomial fit to surrounding continuum regions. The asymmetry observed in [SIV] is due to a blend with HeI(12–8) 10.52μm and CIII(20–17) 10.54μm, estimated to contribute ∼15% to the flux

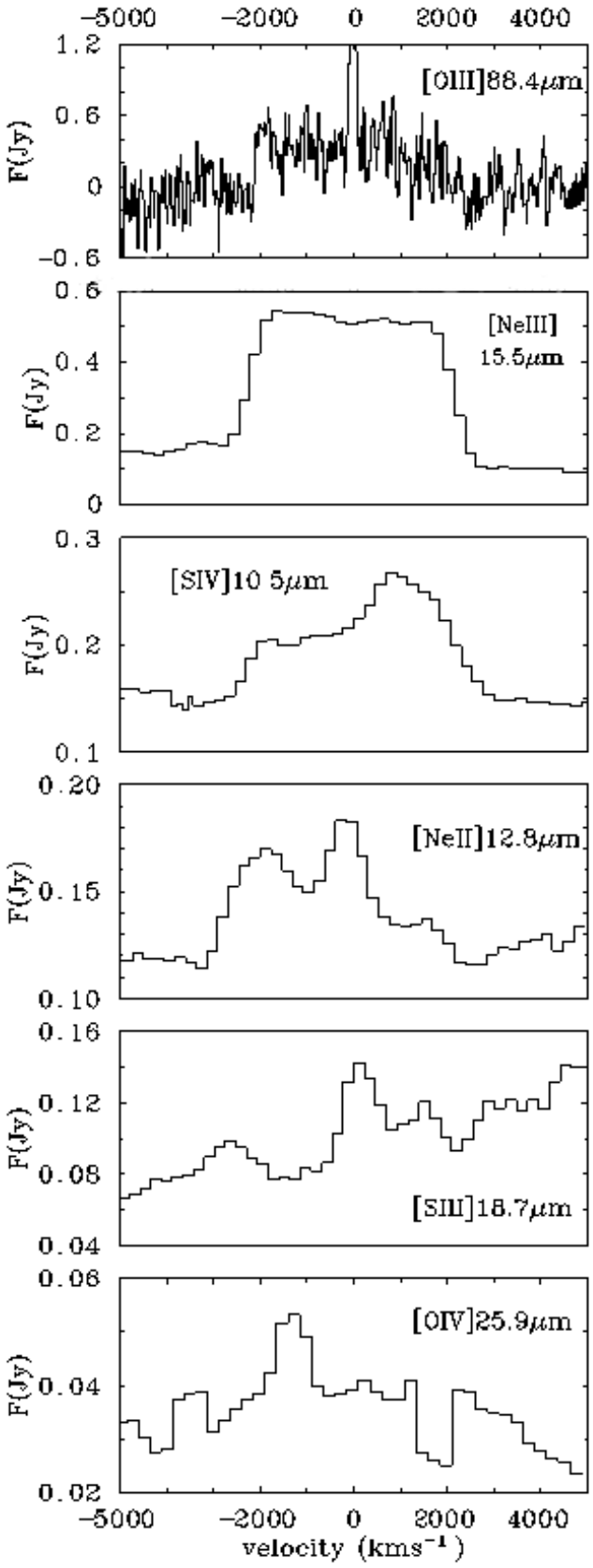

Figure 4.11: Fine-structure lines in the mid-IR *Spitzer* IRS and far-IR *Herschel* PACS spectra of WR 23, plotted in velocity space about the central wavelength of each line. All lines are formed at $\log(N_e(\mathrm{cm}^{-3})) < 6$ $\left(\log(r/R_\star) > 4\right)$ (see Figs 4.6 & 4.7).

Table 4.7: Flux of fine-structure lines (units of $\times 10^{-12}$erg s^{-1}cm^{-2}. All measurements for WR 11 are taken from BRA88, measured using the UCL spectrometer at the AAT, with the exception of [OIII]51.8μm which we measure from an ISO-LWS spectrum (see text). All measurements for WR 23 make us of the *Spitzer* IRS spectrum shown in Fig. 4.10.

WR	[OIII] 51.8μm	$\gamma(O^{2+})$ ($\times 10^{-3}$)	[NeII] 12.8μm	$\gamma(Ne^{+})$ ($\times 10^{-4}$)	[NeIII] 15.5μm	$\gamma(Ne^{2+})$ ($\times 10^{-3}$)	[SIV] 10.5μm	$\gamma(S^{3+})$ ($\times 10^{-5}$)	[SIII] 18.7μm	$\gamma(S^{2+})$ ($\times 10^{-5}$)
11	8.0	4.0	17	4.7	90	2.2	19	4.2	<1.8	<2.5
23	-	-	0.14	3.8	1.2	2.9	0.37*	6.7	<0.05	<8.3

*Value before subtraction of an estimated 15% contribution from HeI(12–8) 10.52μm and CIII(20–17) 10.54μm.

of the line (DCH00). A further Sulphur line in [SIII] 18.7μm has a marginal detection in the IRS spectrum. A 2$^{\text{nd}}$ order polynomial continuum fit revealed that the emission was not present across the full anticipated velocity extent of [SIII], therefore I estimated an upper limit on the [SIII] line flux by using `FLUX` to measure any signal above this continuum fit. In Table 4.7 I give line flux measurements for these lines in WR 23, in addition to measurements of the same lines in WR 11, given by DCH00.

Using the method introduced in Section 4.4 and atomic data from DCH00 (their Table 9), I used these S and Ne line flux measurements to calculate the fractional abundances of the respective ionic species in WR 23 and WR 11, also given in Table 4.7. This provided an insight into two ionisation balances at different locations in the wind: Ne^{2+}/Ne^{+} at $\log(N_e)$=5–6 and S^{3+}/S^{2+} at $\log(N_e)$=4–5. Neon is predicted to be singly ionised at the formation density of [NeII] & [NeIII] (Fig. 4.7), however, in both WR 23 and WR 11 the fractional abundance of Ne^{2+} is an order of magnitude higher that that of Ne^{+}. This strongly suggests that the model presented in Figures 4.7 & 4.6 overestimates the rate of decline in ionisation with radius in the case of neon. Fractional abundance measurements of sulphur are consistent with $S^{3+} \gtrsim S^{2+}$ at the formation density of [SIV] & [SIII] - an order of magnitude lower in density than the neon lines. As I was only able to obtain an upper limit on the flux of [SIII] in WR 11 and WR 23, I could not rule out S^{3+} being the dominant ion, as predicted. However, the tentative detection of [SIII]18.7μm in WR 23 and WR 11 suggest that S likely exists as a mixture of S^{3+} and S^{2+} at $\log(N_e) = 4$-5.

The ionisation energy of $O^{2+} \rightarrow O^{3+}$ (55eV) is higher than that of $Ne^{+} \rightarrow Ne^{2+}$ (41eV) and $S^{2+} \rightarrow S^{3+}$ (35eV). Hence, the dominance of Ne^{2+} at $\log(N_e) = 5$–6 suggests that sufficient energy in the form of collisions could be available to sustain a large population of O^{3+} at these densities, but the mixture of S ionisation stages at $\log(N_e) = 4$–5 implies that insufficient energy is present to sustain a significant population of O^{3+} at lower

densities. The oxygen ionisation stratification inferred from these energy arguments is consistent with the model shown in Fig. 4.7, which despite overestimating the rate of decline in Ne ionisation, is closer to producing the observed ionisation balance of S at lower densities and larger radii - closer to [OIII] 88.36μm formation.

A more direct insight into the radial extent of O^{3+} is offered by [OIV] 25.9μm ($^2P^0_{1/2}$–$^2P^0_{3/2}$), which with a critical density of 10^4cm^{-3} is formed interior to both [OIII] lines considered thus far. As shown in Figure 4.11, this line is not robustly detected in the *Spitzer* IRS spectrum of WR 23. Furthermore, this line is not detected in *Spitzer* IRS spectra of 4 additional WC≥5 stars (Crowther, priv comm). The non-detection of this line is consistent with the predictions of the CMFGEN model atmosphere calculated for WR 23, which predicts a transition from O^{3+} to O^{2+} at densities ∼6 orders of magnitude higher than where [OIV]25.9μm would form. These observations suggest that in cooler WC (≥5) stars, the fractional abundance of O^{3+} must be negligible at the formation density of [OIV]25.9μm, and even more-so at the lower density of [OIII] 88.36μm. However, [OIV]25.89μm is detected in 1/2 IRS spectra of WC4 stars, indicating that some amount of O^{3+} is present in hotter WC stars at densities log N_e = 4–5 (2 orders of magnitude greater than where [OIII] 88.36μm is predominantly formed).

In summary, consistent $\gamma(O^{2+})$ measurements from different [OIII] lines in WR 11 support a stable oxygen ionisation state in the extreme outer wind where [OIII] 88.36μm is formed. A CMFGEN model atmosphere for a WC star with the parameters of WR 23 predicts that oxygen will be predominantly doubly ionised in this region. As WR 11 is purportedly the coolest WC star observed (Table 4.4), it is unlikely that other programme stars differ by accommodating large amounts of O^+ in the [OIII] 88.36μm formation region, so this ion is unlikely to affect calculated oxygen abundances. The predicted decline of $\gamma(O^{3+})$ at radii interior to the [OIII] 88.36μm formation region is supported in WR 23 by the observed mixture of S^{3+}/S^{2+}at higher densities. With a lower ionisation energy than $O^{2+}\rightarrow O^{3+}$, if S^{3+} is not dominant at the critical density of [SIV] & [SIII], O^{3+} is highly unlikely to be present in significant quantities in the same region, interior to [OIII] 88.36μm formation. However, I could not rule out the possibility that in hotter WC stars some amount of O^{3+} exists at the critical density of [OIV] 25.9μm. I therefore concluded that *fractional* O^{2+} *abundances derived using* [OIII] 88.36μm *represent total oxygen abundances in* WC≥5 *stars* (WR 11, 23, 90, 111, 140), but may provide underestimates in hotter stars where some oxygen could be present as O^{3+} in the [OIII] 88.36μm formation region.

4.6.2 Oxygen abundance uncertainties

Several parameters involved in the calculation of $\gamma\,(\mathrm{O}^{2+})$ (Equation 4.5) are coupled, e.g., $\dot{M}$ when derived by model atmosphere analysis is dependent on both the inner wind volume filling factor (f_{in}) and distance D, such that only the quantity $\dot{M}/\sqrt{f_{in}}$ is measured, and $\dot{M} \propto D^{1.5}$. These dependencies conspire to make the determination of a formal uncertainty on $\gamma\,(\mathrm{O}^{2+})$ challenging. Nevertheless, inspection of equation 4.5 allows one to identify which stellar parameters most critically affect the calculated $\gamma\,(\mathrm{O}^{2+})$, and hence which uncertainties dominate. Here I discuss one-by-one the typical uncertainty in each adopted stellar parameter, and the relative impact each has on the calculation of $\gamma\,(\mathrm{O}^{2+})$.

For the computation of $\gamma\,(\mathrm{O}^{2+})$, I calculated the mean molecular weight (μ) and mean number of electrons per ion (γ_e) using measured carbon and preliminary oxygen abundances (Table 4.4). Upon recalculation of μ and γ_e using the oxygen abundances calculated here (Table 4.5), these values typically change by $\sim 5\%$, causing small changes of 7% and 2.5% in $\gamma\,(\mathrm{O}^{2+})$ respectively. I estimate terminal wind velocities measured directly using [OIII] 88.36μm or v_{black} (Sec. 4.3.2) to have an accuracy of 100 kms^{-1} ($\sim$5%), whereas those determined using the width of optical/IR recombination lines are typically accurate to 200 kms^{-1} ($\sim$10%). With $\gamma\,(\mathrm{O}^{2+}) \propto v_{\infty}^{1.5}$, this corresponds to at most a $\sim 15\%$ uncertainty in $\gamma\,(\mathrm{O}^{2+})$, reducing to $\sim$8% for directly measured v_{∞}. Although Equation 4.5 contains a D^2 term, recalling that $\dot{M} \propto D^{1.5}$ effectively weakens the dependence to $\gamma\,(\mathrm{O}^{2+}) \propto D^{-0.25}$, so that even the least certain distances adopted here ($\Delta\, D \sim 20\%$) only have a $\sim$5% effect on ionic oxygen fractions. I adopted an outer wind temperature of 8000K in all cases based on the model shown in Figure 4.6. To assess the sensitivity of $\gamma\,(\mathrm{O}^{2+})$ to the assumed temperature I also evaluated the integral $F(N_e, T)$ (Equation 4.6) at similarly plausible temperatures of 6000 K and 10,000 K, which resulted in a $\sim 5\%$ difference in F and hence ionic oxygen fraction, as $\gamma\,(\mathrm{O}^{2+}) \propto F^{-1}$.

All uncertainties commented on thus far combine to produce a $\sim 20\%$ uncertainty on $\gamma(\mathrm{O}^{2+})$. The final parameter to be considered is wind clumping, which as discussed in Section 4.4.2 I assumed to persist into the extreme outer winds of WC stars with a volume filling factor $f_{out} = 0.25^{+0.25}_{-0.15}$. To estimate the effect of this uncertainty, I evaluated $\gamma(\mathrm{O}^{2+})$ at the extremes of this range in f_{out}, with mass-loss rates fixed at the values derived using $f_{in} = 0.1$. The results of this were on average a 26% increase and 17% decrease in $\gamma\,(\mathrm{O}^{2+})$ when $f_{out} = 0.1$ and 0.5 respectively, compared to results obtained with $f_{out} = 0.25$. It is therefore evident that unknown wind clumping at large radii is the dominant source of uncertainty in this analysis. It contributes significantly to the final

assumed error of approximately $+31\%, -25\%$ on $\gamma(O^{2+})$, incorporating uncertainties on all parameters. This estimated total uncertainty on $\gamma(O^{2+})$ is used to calculate the uncertainties presented in Table 4.5. When using Equation 4.7 to calculate O^{2+}/He from C/He and $\gamma(O^{2+})$, I assume an uncertainty of ΔC/He=0.05 in all WC stars, and $\pm$0.1 in the case of WO star WR 142 - a comparable relative uncertainty given its large carbon abundance.

4.7 Comparison to evolutionary predictions

I have directly measured the surface oxygen abundance in a sample of 6 WC and 1 WO stars using [OIII] 88.36μm. This sample therefore have amongst the most accurately known oxygen and carbon abundances of any WR stars - comparable to the recent results of Tramper et al. (2015, in prep) for WO stars and Williams et al. (2015) for the very cool WC9 stars.

Uncertain nuclear burning rates may be constrained by these quantities, as the balance between Carbon and oxygen in massive stars is solely determined by the competition of $3\alpha \rightarrow {}^{12}$C and ${}^{12}C(\alpha,\gamma){}^{16}O$ processes. However, in order for surface abundances to be used as tests of core processes, other mechanisms acting within the star must be considered, e.g., internal mixing induced by rotation which can increase the efficiency with which nuclear processed material is transported to the surface, and stellar mass-loss which acts to reveal progressively deeper layers of a star. Here I discuss the current evolutionary status of the programme stars, allowing them to be placed into proposed evolutionary schemes as accurately as possible, ensuring meaningful comparisons of our observations to theoretical predictions.

4.7.1 Evolutionary status of programme stars

Following the tight relationship between luminosity and mass for hydrogen-free WR stars (Fig. 1.16), I used the luminosities given in Table 4.5 to derive current masses for the programme stars. These masses, spanning 7–19 $M_{\odot}$, are shown in Table 4.8. Rotating and non-rotating models for single stars at solar metallicity (Meynet & Maeder, 2003) produce stars at the end of Helium burning with masses between 11–31 $M_{\odot}$, and hence are capable of reproducing the masses of all programme stars, with the exception of WR 144, which has a lower $M(L)$. Any attempts to relate present-day to initial mass are highly model-dependent, as the effect of rotation is to generally enhance $\dot{M}$ over a star's lifetime, meaning higher initial mass stars may reach the end of Helium burning

Table 4.8: Measured stellar parameters of programme stars compared with typical parameters displayed by Geneva single-star models during the WC phase (Meynet & Maeder, 2003). The 40 $M_\odot$ model includes rotation. For 60 $M_\odot$ and 85 $M_\odot$ models, upper and lower rows refer to non-rotating and rotating models respectively. References for stellar parameters are as in Table 4.4. Masses, $M(L)$, are derived using the Schaerer & Maeder (1992) relation.

WR#	Sp. type	$\log(L/L_\odot)$	$M(L)$ $M_\odot$	T kK	$\log(\dot{M})$ $M_\odot\, yr^{-1}$	X_c	X_o
		Programme stars					
11	WC8+O7.5III	5.5	14.5	57	-4.85	0.30	0.012
23	WC6	5.3	11.1	75	-4.80	0.44	0.040
90	WC7	5.3	11.1	71	-4.74	0.41	0.025
111	WC5	5.5	14.5	91	-4.69	$\geq$0.53	$\leq$0.014
140	WC7pd+O5	5.7	18.9	70	-4.79	0.21	0.081
142	WO2	5.4	12.7	200	-4.94	$\geq$0.56	$\leq$0.28
144	WC4	5.0	7.4	112	-4.60	0.40	$\leq$0.027
		WO stars (Tramper et al. 2015)					
102	WO2	5.45	13.6	210	-4.92	0.62	0.25
142	WO2	5.39	12.7	200	-4.94	0.65	0.14
30a	WO3	5.30	11.1	160	-5.00	0.53	0.18
		WC9 stars (Williams, Crowther & van der Hucht 2015)					
92	WC9	5.0	7.4	39	-5.0	0.30	0.015
103	WC9	4.9	6.5	40	-5.0	0.38	0.040
$M_{ini} = 40\, M_\odot, v_{ini} = 314\,\mathrm{kms}^{-1}$		5.5	12.3	69	-4.8	0.50	0.20
$M_{ini} = 60\, M_\odot, v_{ini} = 0\,\mathrm{kms}^{-1}$		5.5	12.6	65	-4.9	0.51	0.19
$M_{ini} = 60\, M_\odot, v_{ini} = 346\,\mathrm{kms}^{-1}$		5.8	18.0	74	-4.7	0.49	0.21
$M_{ini} = 85\, M_\odot, v_{ini} = 0\,\mathrm{kms}^{-1}$		5.8	18.7	66	-4.7	0.49	0.24
$M_{ini} = 85\, M_\odot, v_{ini} = 368\,\mathrm{kms}^{-1}$		6.0	26.4	72	-4.6	0.47	0.25
$M_{ini} = 120\, M_\odot, v_{ini} = 0\,\mathrm{kms}^{-1}$		6.1	31.0	69	-4.6	0.46	0.28
$M_{ini} = 120\, M_\odot, v_{ini} = 389\,\mathrm{kms}^{-1}$		5.8	19.0	74	-4.7	0.49	0.23

with a lower mass (and L) than initially less massive stars that are born rotating more slowly. For example, Ekström et al. (2012) predict $M \sim 12 M_{\odot}$ (consistent with WR 23 and WR 90) at the end of He burning for stars of initial masses 60 or 40 $M_{\odot}$, when the former has zero rotation and the latter is formed rotating at 40% break-up velocity.

Tramper et al. (2013, 2015) use the observed Helium mass fraction (X_{He}) to estimate the current stage of He-burning in WO stars. As Helium burns at a more or less constant rate, assuming fully mixed convective cores in these stars, each star has progressed a fraction of $(1 - X_{He})$ through its Helium burning phase. By this logic, the X_C and X_O values presented in Table 4.8 for the programme stars suggest that WR 140 is the least chemically evolved WR in this sample. WR 142 appears to be the most evolved - as expected due to its WO spectral type - followed by WR 111.

In Section 1.2.2 I highlighted the importance of binary evolution in the context of WR stars. Of the 7 programme stars, only WR 11 and WR 140 are in confirmed binary systems. WR 140 is a highly eccentric system with a 7.9 yr period. By interferometric monitoring, Monnier et al. (2011) measure a periastron separation of 1.53 AU and a WR mass of $14.9 \pm 0.5\, M_{\odot}$, interestingly $\sim 4\, M_{\odot}$ less than that given by the M–L relation (Schaerer & Maeder, 1992). At this separation the O-star companion is too distant to affect the WR star evolution, unless the WR underwent a red supergiant phase - unexpected for stars of initial mass $> 40\, M_{\odot}$ at solar metallicity, which is suggested by the high present-day mass of WR 140. With a much shorter period of 78.5 days (Niemela & Sahade, 1980), it is likely that the WC8 star in WR 11 has undergone Case B (post-MS) mass-transfer with its O-star companion (Eldridge, 2009).

Non-thermal radio emission has been detected in WR 90 (Chapman et al., 1999) which is strongly indicative of a wind-collision region. Furthermore, De Becker & Raucq (2013) present a census of non-thermal radio-emitting massive stars, totalling 46, and WR 90 is one of only 6 not confirmed as a multiple system. Despite this strong indication of multiplicity, I considered WR 90 a single WR star in the absence of conclusive evidence for a companion. WR 11 is therefore the only programme star with evidence for a deviation from single-star evolution. Although the presence of hidden binary companions to these programme stars cannot be ruled out, I took them to be single, validating the comparison of results obtained to models for single star evolution at solar metallicity.

In Table 4.8 I compare measured stellar parameters to those typical of WC stars in rotating and non-rotating single-star models at $Z = 0.014$ (Ekström et al., 2012). Also included are WC9 stars Williams et al. (2015) and Galactic WO stars (Tramper et al. 2015, in prep) analysed by the CMFGEN model atmosphere code.

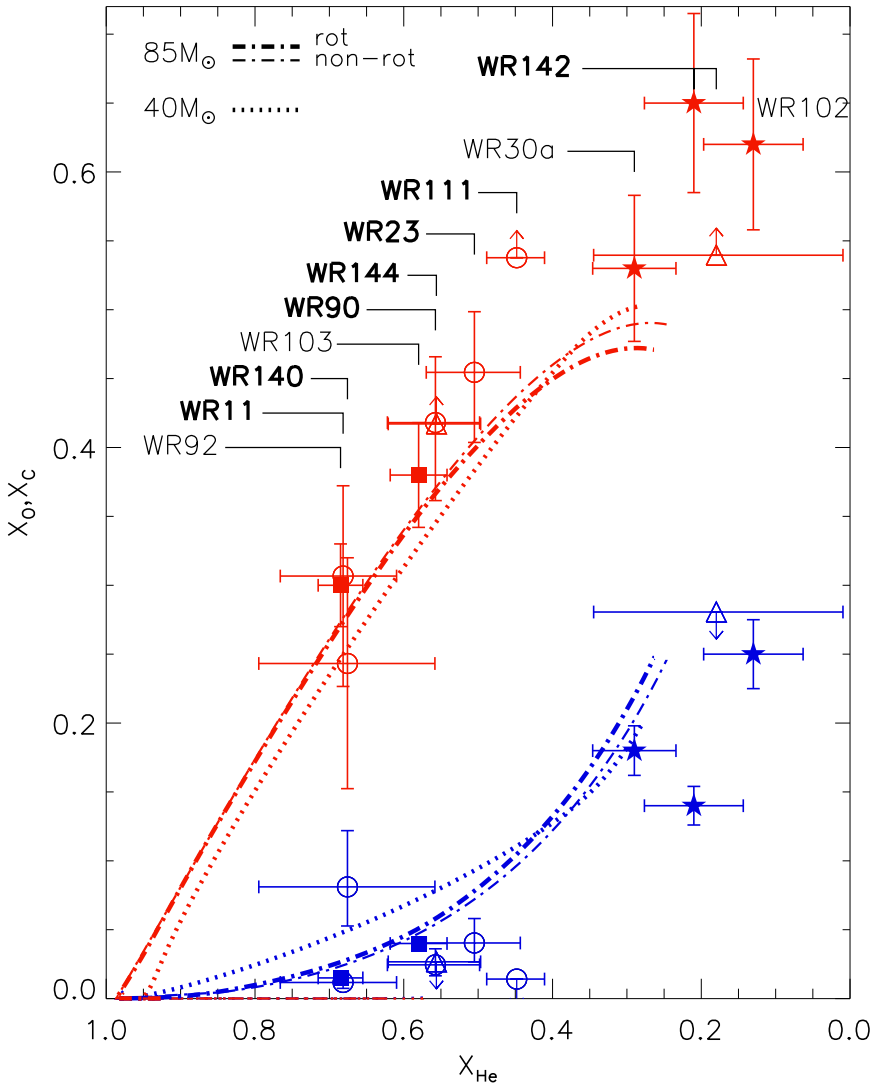

Figure 4.12: Measured abundances of carbon (X_C red) and oxygen (X_O blue) surface mass fraction, plotted against helium mass fraction (assuming $X_{He} + X_C + X_O = 1$), compared with the predictions of single-star evolutionary models. Stars included are those with X_O measured or constrained from PACS [OIII] 88.36μm observations presented here (bold labels, open symbols. WC≥5: circles, WC4 & WO: triangles), WC9 stars analysed by Williams et al. (2015) (filled squares), and Galactic WO stars analysed by Tramper et al. (2015, in prep) (filled five-point stars). Stars in the PACS sample earlier than WC5 (i.e. WR 142 and 144) are plotted as triangles, as the O abundances shown here may be underestimates because it could not be ruled out that O^{3+}contaminates the [OIII] 88.36μm line-forming region (Section 4.6.1). For WR 142, I show both the results of this work and those of Tramper et al. Uncertainties on X_O are discussed in Section 4.6.2. I assume 10% uncertainty on X_C and X_O given by Williams et al. and Tramper et al. for WC9 stars and WO stars respectively. Lines represent the evolution of X_O and X_C in Geneva models for a rotating (thick) and non-rotating (thin) $85M_\odot$ (dash-dot) and $40M_\odot$ (dotted) stars (Ekström et al., 2012). These quantities are only plotted for the phase of evolution during which $X_C > X_N$ (nominal definition of WC & WO phase). Models with initial mass $60M_\odot$ and $120M_\odot$ follow very similar paths in this diagram to the $85M_\odot$ model shown, so are not included.

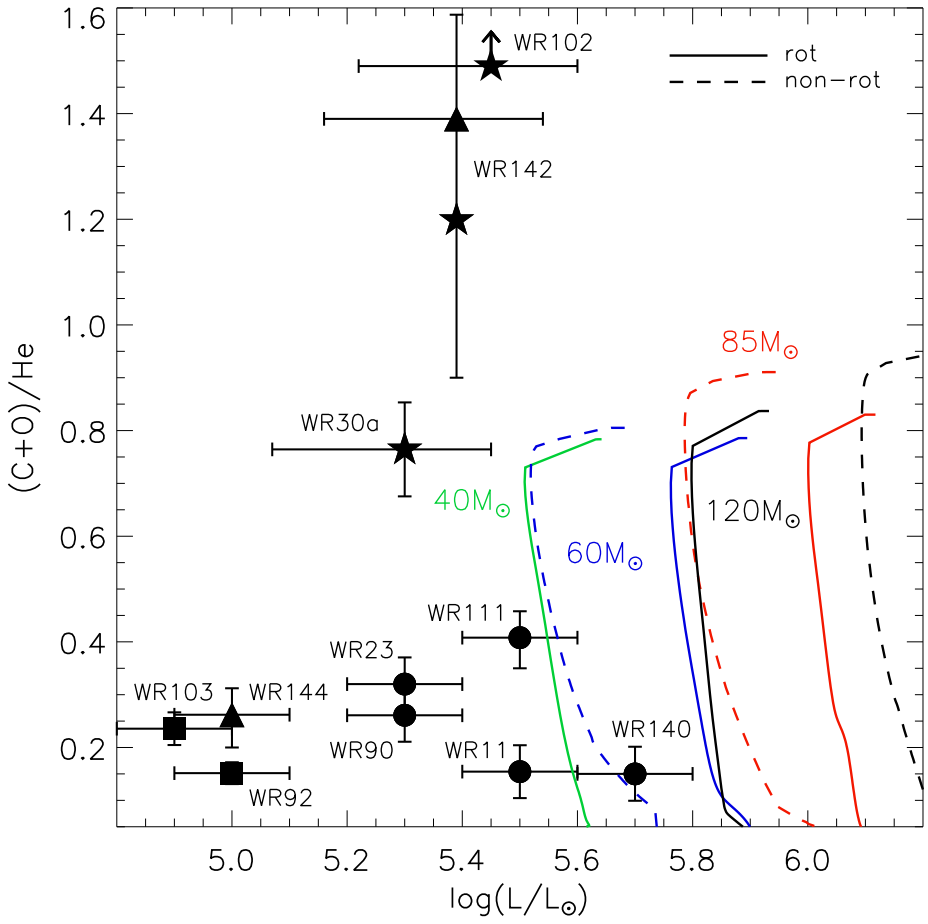

Figure 4.13: Measured abundances of carbon plus oxygen relative to Helium (by number) versus luminosity (L) for the 7 programme stars (WC≥5, circles; WC4 & WO, triangles), WO stars analysed by Tramper et al. (2015) (five-point stars), and WC9 stars analysed by Williams et al. (2015) (squares). Two symbols for WR 142 are plotted - one using O/He as measured by Tramper et al, the other using the upper limit derived in this work. For stars where only an upper limit on O/He is obtainable by the [OIII] 88.36μm measurements ,i.e., WR 111, 142 and 144, the lower extent of the error bar represents O/He = 0. A 0.1 dex uncertainty is assumed on each luminosity, based on typical distance uncertainties of 10–20%, with the exception of Galactic WO stars from Tramper et al. who estimate +0.15/-0.23 dex. Also shown is the predicted evolution of these abundances with luminosity throughout the WC phase (Ekström et al., 2012) at Z = 0.014 for four initial stellar masses, with (solid) and without (dashed) initial surface rotation.

4.7.2 Abundance predictions vs observations

In Figure 4.12 I plot surface carbon and oxygen mass fractions (X_C and X_O respectively) for all WC and WO stars in which these properties have been robustly measured, including those analysed here. I plot these properties as a function of surface helium mass fraction (X_{He}) for each star. I note that since $X_{He} + X_C + X_O$ is very close 1 in WC and WO stars, only two of these are independent, therefore the uncertainties on X_{He} follow from those of carbon and oxygen measurements. Helium burns at an almost constant rate in stars on the helium main sequence, therefore one may view the quantity X_{He} as the approximate fraction of He-burning lifetime remaining.

In Figure 4.12 I also also show the predicted evolution of X_C and X_O from single-star evolutionary models at Z = 0.014, for initial masses 40 and 85 $M_\odot$ (Ekström et al., 2012). Similar models with 60 $M_\odot$ and 120 $M_\odot$ show very similar abundance patterns to those of 85 $M_\odot$ shown, and the rotating 40 $M_\odot$ model is the lowest mass to display $X_C > X_N$ at any point during its evolution (the nominal definition of a WC star in such models). Alternative single-star models generated with and without rotation at Z = 0.013 (Chieffi & Limongi, 2013) predict an indistinguishable relationship between X_{He}, X_C and X_O over the same initial mass range.

For every star in the *Herschel* PACS sample, with the exception of WR 140, I measured a lower oxygen-to-carbon abundance ratio than predicted by single-star models of stellar evolution, far any mass capable of entering the WC phase (Ekström et al., 2012; Chieffi & Limongi, 2013). Of the four WC stars showing a robust detection of [OIII] 88.36μm three (WR 11, 23, 90) have measured X_O at least a factor of two lower than predicted for their X_{He}. This discrepancy is largest in WR 111, for which the upper limit I determined on X_O is a factor ∼5 below that expected based on its C/He abundance. As discussed in Section 4.1, several of the programme stars have alternative oxygen abundance measurements obtained by spectroscopic analysis using model atmospheres. Those analysed using near-UV spectra are of particular interest for comparison to the results presented here, as the most commonly employed O abundance diagnostics are found between 3000–3500Å.

In the case of WO star WR 142, the upper limit I obtained of $X_O < 0.28$ is consistent with the measurement of Tramper et al. (2015, in prep) (X_O= 0.14), who utilise near-UV to near-IR spectra. Both suggest a somewhat lower O abundance than the predicted $X_O > 0.3$ given the surface helium mass fraction. The O abundances given by [OIII] 88.36μm for WC stars were generally lower than those delivered by spectroscopic analysis. Specifically, DCH00 derive O/He = 0.03 ± 0.01 (X_O = 0.06) for WR 90 based

on near-UV OIV lines, which is inconsistent with my measurement of O/He = $0.011^{+0.004}_{-0.003}$ ($X_O = 0.025$). Both are below the predicted value of $X_O \sim 0.1$ given the surface helium mass fraction (Figure 4.12). Furthermore, Hillier & Miller (1999) derive O/He= 0.1 (X_O=0.15) for WR 111, again employing near-UV diagnostics, which is an order of magnitude above the upper limit I obtained of X_O<0.014. As WR 111 is the third hottest programme star, this result may in part be a consequence of O^{3+} being present in the [OIII] 88.36μm line-forming region (Section 4.6.1). However, this would need to be ten times as abundant as the O^{2+} to account for the full difference, which is quite implausible given the ionisation structure implied from other fine-structure lines in WR 23.

In Figure 4.13 I plot (C+O)/He against Luminosity, including all WC and WO stars with robust measurements of these properties, along with the predicted evolution of these properties throughout the He-burning phase (Ekström et al., 2012). Most WC & WO stars appear to be insufficiently luminous compared to model expectations; this is a well recognised problem discussed in detail by numerous authors (recall Section 1.4.2). This luminosity problem will be discussed further in Section 5.4.2. Three stars in the sample shown in Figure 4.13 are sufficiently luminous to coincide with evolutionary predictions (WR 11, 111, 140). Of these WR 11 and WR 140 appear to be the least chemically evolved. Counter-intuitively, as a confirmed long-period binary system, the WC component of WR 140 star is the most appropriate for comparison to single star evolutionary models, due to the low likelihood of binary interaction between the stars.

Oxygen created in the cores of He-burning stars, via the $^{12}C(\alpha,\gamma)^{16}O$ reaction, is transported to and revealed at the stellar surface by a combination of processes, both generally enhanced by rotation: internal mixing and mass-loss. The abundance measurements presented here suggest that the efficiency of one or both of these processes, or the $^{12}C(\alpha,\gamma)^{16}O$ reaction rate, is overestimated in contemporary stellar models.

It is apparent from Figure 4.12 that the inclusion of initial stellar rotation in the models of Ekström et al. (2012) has a minimal effect on predicted surface C and O abundances for stars with initial masses $\gtrsim 60\,M_\odot$. Their $40\,M_\odot$ model however provides an interesting case; the products of partial Helium burning only appear at the surface if rotation is included, as enhanced mass-loss in the form of an extended WNL phase is incurred. The absence of an effect of initial stellar rotation on the C/O ratio in evolutionary models is largely due to the rapid spin-down experienced by WR progenitor stars before the onset of He-burning (Fig. 1.9).

The surface abundance pattern that emerges in the $40M_\odot$ model is also much like that of higher mass models, despite them experiencing different evolution in terms of mass-

loss and rotation rate. This surface C/O ratio is not only persistent across these models, but can also be seen in the models of Chieffi & Limongi (2013), who implement a slightly different treatment of internal mixing. Furthermore, the Hydrogen-free primary stars of massive binaries modelled by Eldridge et al. (2008) only show small deviations in C vs O from the tracks shown in Figure 4.12. Agreement between these models - considering the range in mass-loss and mixing strength introduced by rotation - suggests nuclear reaction rates are more significant determinants of the surface C/O ratio. Therefore, the results I present here suggest that the $^{12}C(\alpha,\gamma)^{16}O$ reaction rate is over-estimated in current stellar evolutionary models.

The importance of the $^{12}C(\alpha,\gamma)^{16}O$ reaction rate in determining nucleosynthetic yields has been investigated by Imbriani et al. (2001), who model the evolution a 25 $M_{\odot}$ star using two different cross sections for this reaction. They find that a doubling of the reaction rate in this case halves the carbon mass fraction at the end of Helium burning, corresponding to a higher O/C ratio in the star as a whole. These authors conclude that the higher of their two considered $^{12}C(\alpha,\gamma)^{16}O$ reaction rates provides better agreement with the solar abundance pattern, in agreement with the earlier work of Weaver & Woosley (1993). It is these studies that have motivated the choice of reaction rates used in many contemporary models of stellar evolution. This preference for a higher reaction rate is at odds with the oxygen abundances presented here.

4.8 Conclusions

I have presented *Herschel* PACS scans of the [OIII] 88.36μm forbidden fine-structure line in 7 carbon and oxygen-type WR stars, reporting a firm detection in 4 objects (3 being new). Upon measurement of the flux in detected lines, and upper limits on undetected lines, I was able to derive fractional ionic abundances of the O^{2+} ion in the extreme outer winds of these stars where [OIII] 88.36μm is formed. To do this I employed the method of DCH00 - an adaptation of BRA88 for clumped winds - together with previously determined stellar parameters, mostly acquired by application of model atmosphere codes.

To place these results in a more meaningful context regarding stellar evolution, I have argued that the vast majority of oxygen in the region sampled will be in the form of (the measured) O^{2+}, confirming these as the most accurate measurements of oxygen abundances in WC stars to date. This ionisation stratification scenario was supported by a CMFGEN model atmosphere solution generated using the parameters of one pro-

gramme star WR 23, extending to $10^5 R_\star(\log(N_e[\mathrm{cm}^{-3}])\simeq 3)$. To test this predicted ionisation structure for WC winds, I measured alternative fine-structure lines of various ionic species of neon, sulphur and oxygen, originating at different densities (radii). In WR 11, ISO-LWS measurements of [OIII] 51.81μm line - which originates from a higher density region of the stellar wind than [OIII] 88.36μm - delivered an ionic fraction of O^{2+} in excellent agreement with that derived using the PACS measurements of [OIII] 88.36μm. This was indicative of a stable ionisation balance over the approximate radius range $log(r/R_\star) = 4.5{-}5$ in this WC8 star. Moreover, neon and sulphur fine-structure lines observed by *Spitzer* IRS in WR 23 showed that despite the ionisation of neon being underestimated by the CMFGEN model at $\log(N_e) \sim 6$, a mixture of S ionisation stages at lower density rules out O^{3+} being the dominant O ionisation stage there based on the lower ionisation energy of $S^{2+} \rightarrow S^{3+}$ compared with $O^{2+} \rightarrow O^{3+}$.

It is with less certainty that I assumed these conditions in hotter WC subtypes, but previous non-detections of [OIV] 25.89μm in all but WC < 5 stars suggests that O^{3+} is unlikely present in significant quantities in the [OIII] 88.36μm forming regions of WC $\geq$ 5 stars, such as the stars with detected [OIII] 88.36μm presented here.

Comparing derived surface oxygen abundances to those predicted by models of single-stars, I found surface oxygen mass fractions to be a factor of 2–5 lower than predicted. An exception to this is WR 140 - one of the least chemically evolved WR stars considered here (Figure 4.13) - which displays a high enough C/O ratio and, almost uniquely, luminosity to be compatible with single-star models (Ekström et al., 2012).

The surface C/O ratio of Helium burning WR stars is predicted to evolve in an almost identical way in single-star models with or without rotation (Meynet & Maeder, 2003; Chieffi & Limongi, 2013), and in models accounting for the effects of a massive binary companion (Eldridge et al., 2008), which may be relevant to WR 11. For this reason, I have interpreted these results as an overestimate in oxygen production relative to carbon in current models, rather than overly efficient mechanisms to transport the products of partial Helium burning to the stellar surface, or artificially high mass-loss rates revealing deeper burning layers. However, more investigation is needed into how key reaction rates, such as $^{12}C(\alpha,\gamma)^{16}O$, effect the observable properties of highly evolved massive stars. The measurements presented here stand as a stringent test to such investigations.

Chapter 5

Physical properties of Wolf-Rayet stars in the young massive cluster Westerlund 1

5.1 The Westerlund 1 cluster

Westerlund 1 (Wd1) is amongst the most massive young clusters in the Galaxy, meaning it has a stellar population that samples the IMF well at high masses. With an estimated mass of $>10^5 M_{\odot}$ (Clark et al., 2005) (C05), it is comparable to the super star clusters found in starburst galaxies (e.g., Gilbert & Graham 2007). We are witnessing this coeval collection of stars at an interesting epoch, as it contains a plethora of post-main sequence massive stars (Clark & Negueruela, 2002; Negueruela & Clark, 2005; Clark et al., 2005; Crowther et al., 2006b). The PMS population in Wd1 indicates a very narrow age spread for the cluster (Kudryavtseva et al., 2012), from which classical single-star evolution would imply the current post-MS originated from a narrow range in initial mass. Wd1 therefore provides an excellent opportunity to constrain the initial mass ranges leading to various post-MS phases, and to establish the evolutionary links between these phases, which remain unclear (see Section 1.3.2). What is more, this is an exceptionally rare example of coeval WR and cool supergiant stars, implying a narrow common initial mass range for these types of object, which has been claimed may explain the low-luminosity of some WR types compared to evolutionary predictions.

A high fraction of the WR stars in Wd1 exhibit strong indirect evidence for binarity, including dust production in WC stars (Crowther et al., 2006b) and several coincidental hard X-ray sources (Clark et al., 2008), both signposts of colliding stellar winds. There-

fore one may expect binary effects to have played a significant role in their evolution (recall Section 1.2.2). Indeed, Schneider et al. (2014) predict that after only a few Myr, the majority of a cluster's most luminous stars are the products of binary interactions. The contribution of a binary evolution channel to the WR population at large is still debated, however evidence for a significant binary channel is growing. In Section 2.3.3 I showed that the number fractions of WR types and their variation with metallicity are best reproduced by a combination of single-stars without rotation and close binaries.

Here I present tailored spectral analyses of 22 WR stars in Wd1 identified by Crowther et al. (2006b), using the non-LTE `CMFGEN` atmosphere code for spherically expanding and clumped outflows. I derive key stellar parameters: temperature ($T_\star$), luminosity (L), mass-loss rate ($\dot{M}$), terminal wind velocity (v_∞) and chemical abundances for each WR star. This chapter is structured as follows: in the remainder of this section I review the age and distance to Wd1 - crucial for the accurate analysis and interpretation of its WR stars. I also discuss the general properties of the WR star population, and summarise previous attempts to determine the form of the near-IR extinction law towards Wd1. In Section 5.2 I detail the spectroscopy and photometry used to analyse the WR stars. I present the `CMFGEN` model atmospheres used in Section 5.3, and describe the process of fitting synthetic spectra to the observations to derive stellar parameters. In section 5.4 I present the results of model atmosphere analyses, and compare these to other Galactic WR stars of similar types that have been subject to similar analyses. I also discuss how well these measurements can be reproduced by models of single-star evolution. Finally I explain how binary star evolution may alter the predictions based on single-star models, before drawing conclusions in Section 5.5.

5.1.1 Age

Stellar models predict a narrow age range for stars undergoing WR and RSG phases, with 40 $M_\odot$ representing the approximate boundary above which the RSG phase is averted, and below which the WR phase rapidly shortens (Vanbeveren et al., 1998). Hence, the simultaneous presence of WR and RSG stars in Wd1 implies either; *i*) a narrow age spread if the cluster is coeval, or *ii*) a multiple-age population, possibly superimposed along the line of sight. The high luminosity of the RSG/YHG members ($\log(L/L_\odot)$ ~5.5–5.7), approaching the empirical H-D limit (Figure 1.6), and therefore high initial mass, favours the former scenario of a coeval population. Georgy et al. (2012) find a 20 $M_\odot$ lower initial mass limit to the formation of WR stars, and Eldridge et al. (2008) conclude that close binary evolution is capable of lowering this to 15 $M_\odot$. As a consequence of their

limited initial mass range, WRs and RSGs are predicted to co-exist for $\sim$0.1 Myr by the latest Geneva models without stellar rotation, rising to $\sim$0.2 Myr when the effects of fast rotation or close binary evolution are accounted for (Ekström et al., 2012; Eldridge et al., 2008). The lack of on-going star formation in the vicinity of Wd1 is another indicator of burst-like formation. The HII-region associated with Wd1 is very faint (Kothes & Dougherty, 2007), and *Spitzer* GLIMPSE images of the cluster (see Figure 5.2) detect no nebulosity up to distances of $\sim$15 pc from the cluster. A combination of mechanical and radiative force from the hot star winds appears to have evacuated the cluster of gas, bringing star formation to an abrupt halt.

Crowther et al. (2006b) argued that the single-star models of Eldridge & Tout (2004) best reproduce the observed fraction of WR to BSG stars at an age of 4.5–5.0 Myr. The extension of WR progenitors to lower initial masses and hence longer lifetimes, as a consequence of close binary star evolution (Eldridge et al., 2008), may increase this possible age range to $\sim$5.5 Myr. Negueruela et al. (2010) identify 55 OB supergiants in Wd1, and by comparing their absolute magnitudes (at a distance of 3.9 kpc, Kothes & Dougherty 2007) to single-star Geneva isochrones, find consistency with ages between 5–6 Myr. These authors note that binary effects will have influenced OB supergiants less than WR stars, as they are less evolved and are therefore less likely to have experienced the most common type (case-B, post-MS) mass transfer with an unseen companion.

Brandner et al. (2008) fit a combination of PMS (Palla & Stahler, 1999) and MS (Lejeune & Schaerer, 2001) isochrones to deep near-IR photometry ($K_S \lesssim 18.0$) of statistically selected Wd1 members, and derive an age of 3.6 ± 0.7 Myr. This is based on the location of the PMS–MS 'transition region', as the near-IR colours of massive star isochrones are insensitive to age. The reliability of age determinations using PMS stars has been questioned by Naylor (2009), who report a systematic offset in ages indicated by PMS and MS isochrones, with the latter typically a factor of 1.5–2 higher. Indeed, Kudryavtseva et al. (2012) fit (higher spatial resolution) near-IR photometry of proper motion-selected MS stars (between 0.5–11.5 $M_{\odot}$) to FRANEC single-star evolutionary models (Tognelli et al., 2011) to derive an age of 5.0 Myr (with a spread <0.5 Myr). This is in good agreement with ages inferred from the many varieties of post-MS stars present. Considering the uncertainties surrounding ages derived from PMS stars, I assume an age of 5.0$\pm$1.0 Myr for Wd1 in accordance with its MS and post-MS stellar population, with an age spread smaller than this adopted uncertainty.

5.1.2 Distance

Estimates of the distance to Wd1 range from 1.1–5.5 kpc. The most direct measurement comes from Kothes & Dougherty (2007) who used the velocity of neutral hydrogen associated with the cluster to measure 3.9 ± 0.7 kpc. As with any kinematic distance measurement, the measured systemic cluster velocity gives two possible distances - long and short - and both are subject to the assumed Galactic rotation curve and distance to the centre of the Galaxy. However, the uncertainty on the measurement of Kothes & Dougherty (2007) incorporates any potential for non-circular velocity from streaming motions in the environment of Wd1, and the assumption of the short distance is valid, as the long distance of ∼10 kpc is double any previously reported value. Koumpia & Bonanos (2012) use the eclipsing binary W13, for which Ritchie et al. (2010) determine accurate spectral types and hence temperatures, to measure a distance 3.7 ± 0.6 kpc. These authors assign an J-band absolute magnitude to the O9.5I component of W13, and adopt $A_{K_S} = 0.82$ (as for neighbouring star Wd1-R, Crowther et al. 2006b), which they convert to A_J using $A_J/A_{K_S} = 2.5$ (Indebetouw et al., 2005). This extinction is the dominant source of uncertainty in Koumpia and Bonanos' distance measurement, as the orbital parameters of W13 are accurately known due to its eclipsing nature. Stead & Hoare (2009) argue for an alternative near-IR extinction law, giving $A_J/A_{K_S} = 3.1$. Recalculating their distance with this alternative law gives 3.0 kpc.

These two measurements of 3.9 and 3.7(3.0) kpc agree with the upper limit of <5.5 kpc argued for by C05, as greater distances would result in YHG cluster members exceeding the Humphrey-Davidson limit. These authors also dispute the low distance estimate of Piatti et al. (1998), who claim 1.0 kpc based on isochrone fits to 'main-sequence' stars. C05 show that Piatti et al. (1998) incorrectly identify Wd1's OB supergiant population as a MS, hence drastically under-estimating intrinsic brightness (M_V) and the resulting distance modulus. In addition, C05 argue for a lower limit of 2.0 kpc based on the non-detection of WR stars (confirmed at the time) in radio continuum images. The PMS/MS isochrone fits of Brandner et al. (2008) give 3.6 ± 0.2 kpc, which is in contrast to Negueruela et al. (2010) who argue for a >5 kpc distance based on single-star Geneva isochrone fits to the OB supergiant population.

A slight distance discrepancy exists, whereby 'direct' measurements (Kothes & Dougherty, 2007; Koumpia & Bonanos, 2012) suggest $\lesssim$4 kpc, and theoretical fits to the MS and post-MS stellar populations tend towards $\gtrsim$5 kpc. I assumed a distance of 4.0 ± 0.5 kpc; this is consistent with both 'direct' measurements and pre-MS isochrone fitting, yet lower that implied by the (non-WR) post-MS population (Negueruela et al.,

2010).

5.1.3 Wolf-Rayet population

Following its discovery by Westerlund (1961), several broad-band surveys indicated the presence of a large population of early-type stars in Wd1 (Borgman et al., 1970; Lockwood, 1974; Koornneef, 1977). Initial spectroscopic investigations into the stellar content of Wd1 did not reveal any WR stars (Westerlund, 1987). It was not until Clark & Negueruela (2002) revealed 11 WRs via low-resolution optical spectroscopy that the post-MS population in Wd1 received requisite attention. Negueruela & Clark (2005) and C05 reported a further 5 and 3 WRs respectively, identified by their red optical spectra. The further discovery of a WC9 star $\sim$5′ from the cluster centre (Hopewell et al., 2005), and three WN stars (Groh et al., 2006) brought the WR population to 22. This flurry of discoveries prompted Crowther et al. (2006b) to undertake a complete near-IR census of the cluster for WR stars, achieved by taking narrow-band images (NTT/SOFI) in filters centred on and off strong WN & WC emission lines, and identifying WR candidates showing an excess in difference images. I show one of these narrow-band images in the lower panel of Figure 5.2. Spectra of these candidates using NTT/SOFI IJ and HK grisms (see Section 5.2.2) revealed one additional WR, and strong evidence of thermal dust emission in the majority of WC stars. The total number of WR stars in Wd1 stands at 23 (24 including the WNVLh star Wd1–S), with 8 WC and 15 (16) WN. Crowther et al. (2006b) devised a quantitative near-IR classification scheme for WR stars, which they applied to the WR stars to obtain spectral types. In Section 2.1 I refined this classification scheme, and consequently update the spectral type of one WR star in Wd1 (Wd1–W).

The multiplicity of massive stars in Wd1 has been the focus of several photometric (Bonanos, 2007) and spectroscopic (Clark et al., 2010; Koumpia & Bonanos, 2012) monitoring campaigns. The only bona-fide confirmed spectroscopic binary WR in Wd1 is Wd1–B (Koumpia & Bonanos, 2012). However, there are numerous indications that the multiplicity fraction amongst the WR population is high.

Bonanos (2007) detect optical variability in half of the WR stars, ranging from $\Delta I = 0.05$–0.4 mag. In two cases (Wd1–A & B) these variations are periodic, with Wd1–B showing eclipses ($P = 3.51$ d), and Wd1–A showing smooth variations with a period of 7.63 d. Bonanos (2007) also note a high coincidence between photometrically variable WR stars and those identified with X-ray point sources by Skinner et al. (2006). Colliding wind binaries typically have high X-ray luminosities (L_X=10^{32-35}erg s^{-1}, Pol-

lock 1987). Indeed, Skinner et al. (2006) identify WN stars Wd1–A and Wd1–B as the most X-ray luminous WR stars in Wd1, with $\log(L_X[\mathrm{erg\,s^{-1}}]) = 33.9$ and 33.6 respectively, significantly above the median 32.2 for WN stars in Wd1. The X-ray properties of Wd1's massive star content are investigated further by Clark et al. (2008), who also highlight Wd1–A and Wd1–B as the most X-ray luminous, with Wd1–U (WN6) and Wd1–F (WC9d) also having L_X an order of magnitude above the median for WN stars. Clark et al. (2008) also reveal that, of the 12 detections of WR stars, all but Wd1–E and Wd1–U show hard X-ray spectra, which is also thought to be indicative of colliding winds. Notably, amongst the detected hard X-ray sources are WC stars Wd1–F and N, which, given the lack of single WC star X-ray sources (Oskinova et al., 2003), provides strong evidence for them being binaries.

Furthermore, these two WC stars are also amongst the 6 (out of 8) WC stars showing evidence for warm circumstellar dust, in the form of a large near-IR excess and heavily diluted emission lines at $\sim 2\,\mu$m. Such properties amongst late-type WC stars are strongly linked to colliding winds (Crowther et al., 2002; Williams et al., 2005). Three WR stars in Wd1 are detected in radio observations reported by Dougherty & Clark (2007), these are Wd1–A, Wd1–B and Wd1–V. All have flat radio spectra ($\alpha \sim 0$ for $S_\nu \propto \nu^{-\alpha}$), implying contributions from thermal and non-thermal emission mechanisms as expected in colliding wind systems.

To summarise, in addition to Wd1–B, only Wd1–A of the remaining WN stars displays sufficiently hard and luminous X-ray emission to be considered a colliding wind system beyond doubt. With its flat radio spectrum and periodic variability, I took this as conclusive evidence for a binary companion in Wd1–A. I consider all other WN stars to be single for the purpose of modelling their spectra, but cannot rule out the possibility that some are undetected binaries. Of the WC stars, I consider the presence of circumstellar dust as sufficient evidence for a binary companion. This is supported in the cases of Wd1–N and Wd1–F by their detection as hard X-ray sources (albeit with modest L_X), as this is particularly unusual for WC stars. I consider the non-dusty WC stars Wd1–E and Wd1–K to be single, despite the detection of Wd1–E as an X-ray source, because it shows a soft spectrum with low luminosity ($L_X < 10^{32}\mathrm{erg\,s^{-1}}$).

5.1.4 Form of the near-IR reddening law

The high visual extinction ($\mathrm{A_V} \sim 12$) to Westerlund 1 was soon realised upon its discovery (Westerlund, 1961). Colour-magnitude diagrams constructed by Piatti et al. (1998) revealed a scatter in the cluster sequence, greater than could be attributable to photo-

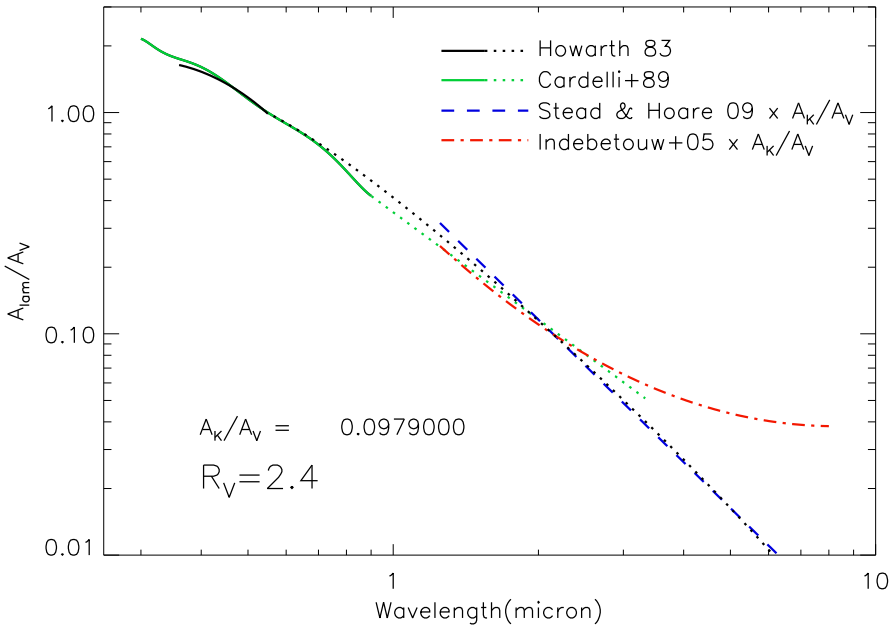

Figure 5.1: Comparison of near-IR extinction laws in the literature, with $R_V = 2.4$ (previously derived towards Wd1). The laws of Indebetouw et al. (2005) and Stead & Hoare (2009) are converted from A_λ/A_K to A_λ/A_V by multiplying by $A_K/A_V = 0.0979$, as given by Howarth (1983). It can be seen that the UV/optical/near-IR formulation of Howarth (1983) is in good agreement with the more recent near-IR law given by Stead & Hoare (2009), whereas Indebetouw et al. (2005) deviates significantly.

metric error, indicating significant differential reddening across the cluster. This finding is supported by C05, who in addition report no detectable gradient in reddening across the cluster. C05 also present evidence for a non-standard reddening law towards Wd1, i.e., $R_V \neq 3.1$, which they require to bring the absolute visual extinctions derived from the colour-excess of YHGs ($A_V \simeq 11.0$) and OB supergiants ($A_V \simeq 11.0$) - under the assumption of $R_V = 3.1$ - into agreement. However, Negueruela et al. (2010) revisit the OB supergiants in Wd1, finding a good fit to the ratio of colour excesses E_{V-I}/E_{V-R}, in agreement with a standard extinction law. A poorer correlation between E_{B-V}/E_{V-I} leads Negueruela et al. (2010) to propose a problem with the B–band photometry presented by C05, possibly due to inappropriate selection of photometric standards. Recently, Clark et al. (2014) modelled the SED of the peculiar B-type hypergiant Wd1–5, and were able to fit B through K_S photometry with a model SED reddened using a non-standard $R = 2.35$.

In Figure 5.1 I plot several reddening laws from the literature, using R_V=2.4 (Clark et al., 2014), namely; Howarth (1983) (UV/optical/IR), Cardelli et al. (1989) (UV/optical),

Table 5.1: Summary of imaging and spectroscopic data used in the analysis of WR stars in Wd1.

Instrument	Filter	Pixel scale ($''$/pixel)	Seeing (FWHM)	Epoch
VLT/FORS2	R_SPECIAL	0.125	0.7	2004-06-10
MPG ESO 2.2m/WFI	I_C	0.238	0.9	2002-07-07
NTT/SuSI2[a]	UBVRI	-	-	2001-08-21
Instrument	**Wavelength range**	**Resolution ($R=\lambda/\Delta\lambda$)**	**Stars**	**Epoch**
AAO/UK 6dF[b]	6230–6780 Å	3000	T	2004-03-27
NTT/EMMI[c]	6440–7150 Å	6000	M	2003-06-06
NTT/EMMI[c]	(3850)5550–10000 Å	(260)610	(N),A,B,C,K	2003-06-06
VLT/FORS2	4500–11000 Å	∼300	C,E,H,K	2005-06-11
NTT/SOFI[d]	0.94–2.50 μm	1000	all	2005-06-29/30

(a)C05, (b)Hopewell et al. (2005), (c)Negueruela & Clark (2005), (d)Crowther et al. (2006b).

Indebetouw et al. (2005) (near-IR), and Stead & Hoare (2009) (near-IR). I adopted the law of Howarth (1983) (black dotted line, Fig. 5.1), which agrees well with that of Cardelli et al. and Stead & Hoare over the respective wavelength ranges, but deviates from Indebetouw et al. in the IR. To accommodate potential variations in reddening across the cluster, I kept both R_V and E(B–V) as free parameters, to be determined for each star individually.

5.2 Data

In Table 5.1 I present details of all imaging and spectroscopic data used in the analysis of the WR stars in Wd1. All photometry for the WRs, both collected and measured, is given in Table 5.2.

Table 5.2: Photometry and spectral types of WR stars in Wd1.

Wd1–	WR#	Sp. type	B[a]	V[a]	R	I	J	H	K_S	[3.6]	[4.5]	[5.8]	[8.0]	E(B–V)
A	77sc	WN7b+?	-	19.69	16.76	13.67	10.34	9.11:	8.37:	-	-	-	-	5.6
B	77o	WN7+?	-	20.99	17.69	14.36	10.91	9.79	9.18	-	-	-	-	6.0
C	77m	WC9d	-	-	18.00	14.61	11.26	9.51	8.23	-	-	-	-	6.3
D	77r	WN7	-	-	18.04	15.43	11.63	10.31	9.61	8.47	8.17	-	-	5.6
E	77p	WC9	-	-	15.61	13.15	10.12	9.09	8.29:	7.13	6.71	-	6.14	5.3
F	77n	WC9d	21.7	17.86	15.39[a]	12.90[a]	9.85	7.97	7.28	-	-	-	-	4.6
G	77j	WN7	22.7	20.87	17.91	14.62	11.36	9.97	9.28	-	-	-	-	5.4
H	77l	WC9d	23.0	18.55	17.47	14.19	10.31	8.56	7.38	-	-	-	-	6.4
I	77c	WN8	-	-	17.23	14.22	10.89	9.57	8.85	-	-	7.32	6.96	5.4
J	77e	WN5	-	-	18.37	15.28	11.7:	10.3:	9.7:	-	-	-	-	6.1
K	77g	WC8	-	-	17.81	14.69	11.81	10.40	9.53	-	-	-	-	5.7
L	77k	WN9h	22.6	18.86	15.80	12.39	9.08	7.72	7.19	-	-	-	-	-
M	77i	WC9d	-	19.79	16.84	13.85	10.13	7.64	6.9:	-	-	-	-	5.7
N	77b	WC9d	-	-	16.7[b]	13.5[b]	9.69	7.84	6.41	-	-	4.32	4.17	6.2
O	77sb	WN6	-	-	16.89	14.00	11.00	9.98	9.45	-	-	-	-	5.3
P	77d	WN7	-	-	16.96	14.26	11.06	9.83	9.26	-	-	-	-	5.2
Q	77a	WN6	-	-	17.43	14.81	11.72	10.67	10.00	-	-	-	-	5.1
R	77q	WN5	-	-	17.56	14.99	11.92	10.84	10.26	-	-	-	-	5.1
T	77aa	WC9d	19.3	-	15.7[b]	13.5[b]	10.04	8.21	6.72	-	-	4.04	4.05	5.0
U	77s	WN6	-	-	17.14	14.33	10.77	9.72	9.20	-	-	-	-	5.7
V	77h	WN8	-	-	16.60	13.77	10.75	9.42	8.76	-	-	-	-	5.4
W	77sa	WN7*	-	-	19.49	15.91	12.11	10.75	10.04	-	-	-	-	6.3
X	77sd	WN5	-	-	18.4[b]	16.4[b]	12.36	11.08	10.25	-	-	-	-	5.5

(a)C05, (b)USNO B1.0 (Monet et al., 2003), :uncertain value, *updated spectral type from Crowther et al. (2006b).

5.2.1 Optical spectroscopy

Red optical spectra of WC stars Wd1–C, E, H & K, taken using the FOcal Reducer and low dispersion Spectrograph (FORS2) on the VLT, were provided by I. Negueruela (program ID 073.D-0327(B)). These provided a resolving power R ∼ 300 over the range 4500–11000 Å, however, were only useful long-wards of ∼6500 Å due to severe degradation of S/N in the blue.

Intermediate and and low-resolution spectra taken with ESO Multi-Mode Instrument (EMMI) on the NTT were also provided by I. Negueruela (program ID 071.D-0151). These spectra covered wavelength ranges 6440–7150 Å and (3850)5550–10000 Å for stars Wd1–M and (N)ABCK, with R = 6000 and R = (260)610, respectively. In addition to these, the discovery spectrum of Wd1–T presented by Hopewell et al. (2005) was provided by M. J. Barlow.

I was unable to obtain any archival spectra short-ward of 0.9μm for WN stars Wd1–D, G, I, J, O, P, Q, R, U, V, W, X and WC star Wd1–F.

5.2.2 Near-IR spectroscopy

I utilised a uniform set of flux-calibrated spectra taken using NTT/SOFI with IJ and HK grisms, provided by P. A. Crowther (program ID 075.D-0469). These had R∼1000 covering 0.9–2.5μm for every WR star in Wd1. The spectra are presented in full by Crowther et al. (2006b). The reader is referred to that work for full details of data extraction and processing.

5.2.3 Optical Photometry

C05 present BVRI photometry for 41 sources in a 5.5′×5.5′ field of view centred on Wd1, including 7 of the WR stars. These measurements were based on images taken with the SUperb-Seeing Imager 2 (SuSI2) direct imaging camera on the NTT. Photometry in the R and I-bands is particularly important to constrain the reddening to individual stars in Wd1, as extinction begins to have a major effect on stellar SEDs at these wavelengths (see the recent analysis of Wd1–5 by Clark et al. 2014). Mindful of this, I re-derived a consistent set of photometry in the R and I-bands for as many Wd1 WR stars as possible. The images I used for this are detailed in Table 5.1 and discussed further below. I took B and V-band photometry given by C05 where available (Table 5.2).

To measure photometry in the R-band, I utilised an archival 4′×7′ VLT/FORS2 (Appenzeller et al., 1998) image taken in the `R_SPECIAL` filter, observed under program

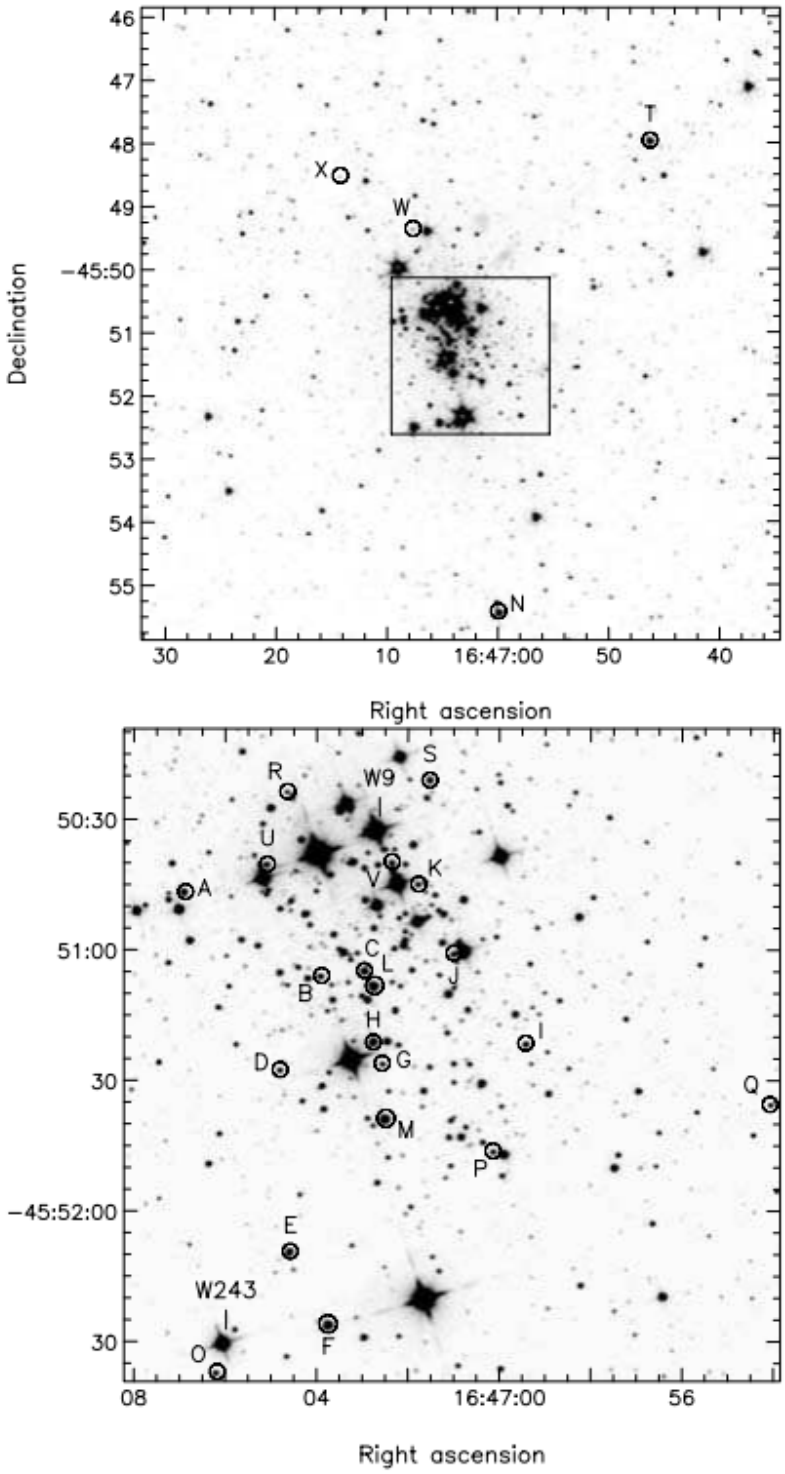

Figure 5.2: (*Upper*) *Spitzer* [3.6] μm image of the $10' \times 10'$ field (11.6×11.6 pc at a distance of 4 kpc) around Wd1. (*Lower*) NTT/SOFI Brγ image of the central $2.5' \times 2.5'$ (2.9×2.9 pc at 4 kpc) of Wd1. The known WR stars are indicated (see Table 5.2) along with sgB[e] W9 and LBV W243. North is up and east to the left in both images. Adapted from Crowther et al. (2006b) with permission.

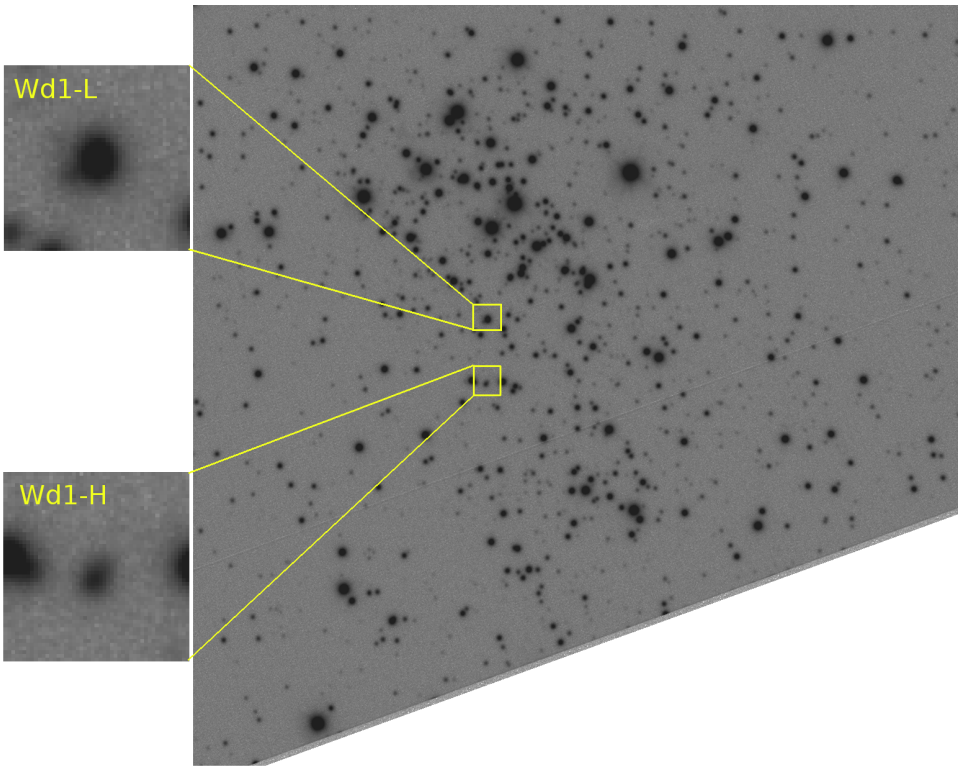

Figure 5.3: VLT image of Wd1, in the R_SPECIAL filter, used to derive R-band photometry for the WR stars. Shown on the same scale as the lower panel of Fig. 5.2. Panels on the left show expanded sections centred on Wd1-L (upper) and Wd1-H (lower), which were resolved into muiltiple components by `DAOPHOT`. North is up and east is left.

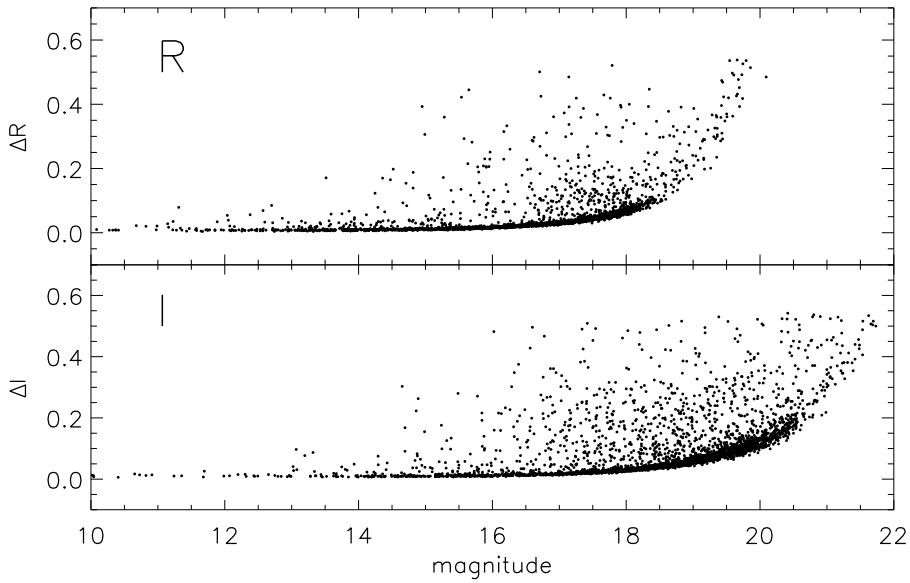

Figure 5.4: Results of PSF fitting photometry. Magnitude vs estimated uncertainty on 2406 and 3109 sources extracted by `DAOPHOT`, respectively, when applied to R-band VLT/FORS2 and I-band MPG ESO 2.2m/WFI images of Wd1.

ID 073.D-0327(A). I show this image in Figure 5.3. The image was taken with the high resolution collimator, providing a pixel scale of 0.125″/pixel. A short exposure time of 1s avoided saturation in the brightest sources in the Wd1 field. I estimated the seeing to be ∼0.7″ from the average FWHM of isolated sources across the image. Unfortunately, stars Wd1–F, N, O, T and X were outside the bounds of this image, but all other WR stars were robustly detected below the saturation limit.

To measure I-band photometry, I utilised a 5′×5′ image of Wd1 taken with the WFI on the MPG/ESO 2.2m telescope (Baade et al., 1999) in the I_c filter, observed under program ID 69.D-0327(B). This image had a pixel scale of 0.238″/pixel, and I estimated the seeing to be ∼0.9″. An integration time of 3.3s avoided saturation in the brightest sources, and all WR stars were robustly detected below the saturation limit. Stars Wd1–N, T and X lay outside the bounds of this image.

I performed PSF fitting photometry on these R and I-band images using the IRAF implementation of `DAOPHOT` (Stetson, 1987). Of the sources extracted by `DAOPHOT`, I selected 10 well-isolated (non-WR) stars, with R and I-band photometry given by C05, and used these to define a zero-point for each image. I then used these zero-points to calculate R and I-band magnitudes for all the WR stars in each image. As a consistency check, I repeated the entire process using a different set of stars to define the PSF for each image, and re-measured zero-points using the same stars in common with C05.

R-band magnitudes

Uncertainties on the DAOPHOT magnitudes are shown in Figure 5.4, and were typically $\lesssim$0.02 mag for the WR stars, with the exception of Wd1–J ($\pm$ 0.09 mag) which is close to a bright source. R magnitudes from repeats of the DAOPHOT analysis on the VLT/FORS2 image typically agreed to within <0.05 mag, with the exceptions of Wd1–H and Wd1–L. This was due to slight differences in the shape of the PSF fitted by DAOPHOT, causing each source to be resolved into a different number of sources (2 or 3) between analyses. Consequently, measurements of the primary sources fitted in Wd1–L and Wd1–H differed by 0.5 mag and 0.2 mag respectively. The R & I-band magnitudes I adopted were an average between repeat analyses, with the exceptions of Wd1–L and Wd1–H, where I preferred the brighter (2-PSF) solutions, to maintain consistency with other published photometry based on lower resolution images.

As a further consistency check, I compared my measured photometry for the WR stars to the 7 published by C05 and found agreement within 0.2 mag in all cases other than Wd1–L and Wd1–H. The magnitudes I measured for Wd1–L and Wd1–H were fainter than C05 by 0.4 and 2.3 mag respectively. Bonanos (2007) report optical variability amongst the WR stars in Wd1 of 0.05–0.4 mag, consistent with these $<$ 0.2 mag differences. However, the values I measured were fainter in 6/7 cases, indicating a systematic offset. The measurements of Wd1-H differ to such an extent that source confusion must be to blame. I am confident in the source identification used here, as I took the object identified as a WR in narrow-band difference imaging (Crowther, priv. comm).

Inspection of the VLT/FORS2 image of Wd1–H reveals an elliptical source, elongated from NE–SW (Figure 5.3). My preferred DAOPHOT fit to this source used two PSFs, one to the NE (R = 19.09) and one to the SW (R = 17.75). These sources would therefore have a combined R = 17.47, which is still significantly fainter than R = 15.46 given by C05. A closer inspection of this source in the narrow-band images used to identify the WR stars (provided by P. Crowther), showed a concentration of the emission line excess towards the brighter SW source. However, as the JHK and I-band photometry I used was derived from lower resolution images, I used the photometry of the total source for the analysis, mindful that it is likely a slight overestimate of the WR flux. The 0.4 mag difference in Wd1–L is less easily explained, but may be due to genuine variability given the $\sim$3 yr epoch difference between and NTT/SuSI2 and VLT/FORS2 imaging. Genuine variability is more likely considering the star's WN9h subtype, as late-type WN are prone to such behaviour (e.g., Marchenko et al. 1998a). The source appears circular in the VLT image, yet two DAOPHOT solutions resulted in 2 and 3 PSFs being used to fit the source,

with magnitudes R = 15.98 & 17.87 and R = 16.49, 16.75 & 18.76 respectively, compared to R = 15.61 given by C05 For the same reasons as Wd1–H, I adopted the sum of the 2-PSF solution, with R = 15.80.

I-band magnitudes

Uncertainties on the DAOPHOT magnitudes are shown in Figure 5.4, and were typically $\lesssim$0.02 mag, with the exceptions of Wd1–J ($\pm$0.2 mag), Wd1–K ($\pm$0.08 mag) and Wd1–U ($\pm$0.04 mag). The I-band magnitudes I calculated from repeats of the DAOPHOT analysis on the WFI image typically agreed within 0.05 mag. Comparing my photometry to the 7 WRs measured C05, I found differences $<$ 0.1 mag in all cases except Wd1–H & Wd1–L. As in the DAOPHOT analysis of the R-band image, Wd1–H and Wd1–L were fitted using 2 PSFs. The brightest extraction in each source was fainter than C05 measurements of each total source by 1.73 and 0.25 mag respectively. Again, the difference in Wd1–H is so large that source confusion must be the cause. I took the combination of the 2-PSF solution for Wd1–H which was still significantly fainter than C05 measurement. Wd1–L was resolved by DAOPHOT into sources with I = 12.77 and I = 13.71, compared to I = 12.52 given by C05 I adopted the sum of the 2-PSF solution for Wd1–L (I = 12.39), to remain consistent with other sources of photometry which do not identify Wd1-L as a visual multiple.

Three stars, Wd1–X, N & T, are located several arcminutes from the cluster core (see Figure 5.2), and consequently are not covered by the images used to measure R- & I-band photometry. For these objects, I took photometry from the USNO B1.0 catalogue (Monet et al. 2003, Table 5.2). All stars were detected in the USNO R- & I-bands, with only Wd1–T detected in the B-band. Two measurements in R were available for both Wd1–N (16.55 & 16.89) and Wd1–T (15.58 & 15.77), of which I took averages of R = 16.7 and R = 15.7 respectively.

5.2.4 Near-IR Photometry

Crowther et al. (2006b) present broad-band JHK$_S$ photometry for the WRs identified in Wd1, based on NTT/SOFI images (epoch 2004/09). The reader is referred to this paper for details of the data reduction and image analysis. Uncertainties of $\pm$0.05 mag are estimated, increasing to $\pm$0.1 mag in cases of severe crowding or near-saturation (indicated in Table 5.2). These data were supplemented by 2MASS JHK$_S$ photometry (Skrutskie et al., 2006) for WR stars lying sufficiently far from the cluster core, where

crowding is less of an issue. Brandner et al. (2008) also present JHK$_S$ photometry of cluster members, again based on NTT/SOFI images taken at an earlier epoch (2001/06). These authors derive redder (J-K$_S$) colours than Crowther et al. for the only two WR stars featuring in both studies, Wd1–U and Wd1–O, by 0.35 and 0.46 mag respectively. Wd1–O is sufficiently isolated to also have 2MASS photometry, which gives (J-K$_S$) 0.09 mag *bluer* than the data of Crowther et al., however the 2MASS K$_S$ quality flag of this detection is poor (D). Wd1–W is sufficiently isolated to have reliable 2MASS and Crowther et al.'s SOFI K$_S$ photometry, and is marginally brighter in SOFI K$_S$ by 0.13 mag. I adopted the JHK$_S$ photometry (with uncertainties) of Crowther et al. for WRs in the cluster centre, and 2MASS JHK$_S$ for isolated sources (Wd1–W, X, N, T). However, I treated the J (and to a lesser extent H) magnitudes given by Crowther et al. as less certain than K$_S$, following the colour discrepancy highlighted by Brandner et al. (2008). This is likely due to a systematic error in J, given the reasonable agreement between 2MASS and SOFI K$_S$ for Wd1–W.

A subset of WR stars were sufficiently separated from the cluster core to feature in the *Spitzer* GLIMPSE-I point source catalogue (Benjamin et al., 2003). Namely, the WC stars Wd1–E, N & T, and WN stars Wd1–D & I. These data (Table 5.2) were particularly valuable in determining the thermal dust contribution in WC9d stars Wd1–N & T, as the dust flux exceeds the stellar flux by an order of magnitude at these wavelengths.

5.3 Analysis by model atmospheres

To model the observed WR spectra and SEDs, I used the non-LTE `CMFGEN` model atmosphere code (Hillier & Miller, 1998, 1999). A detailed introduction to the physical principles of this code is given in Section 1.4.2. I show the model atoms used in the computation of WN and WC models in Table 5.3.

The inner boundary of the `CMFGEN` models, $R_\star$, is located at high Rosseland optical depth ($\tau \sim 10$) where the effective temperature, $T_\star$, is defined by the usual Stefan-Boltzmann relation. `CMFGEN` does not compute consistently the density (and velocity) structure of the extended atmosphere. The standard procedure is to adopt a pseudo-hydrostatic structure at small radii (less than an few $R_\star$) which develops into a "β velocity law" at larger radii. Such a structure is expected theoretically (Pauldrach et al., 1986). I adopted a standard β velocity law of the form

$$v(r) = \frac{v_0 + (v_\infty - v_0)(1 - R_\star/r)^\beta}{1 + v_0/v_{core}\exp(R_\star - r)/h_{eff}}, \tag{5.1}$$

Table 5.3: Summary of atomic data used in `CMFGEN` models for different broad WR types. N_F is the number of full levels, N_S is the number of super-levels. The following stars fall under each catagory; WC: C, E, F, H, K, N, M & T; WNL: B, D, G, I, P, V & W; WNE (weak): J, O, Q, R, U & X; WNE (broad): A.

WC			WNL			WNE (weak)			WNE (broad)		
Species	N_F	N_S	Species	N_F	N_S	Species	N_F	N_S	Species	N_F	N_S
HeI	87	49	HI	30	20	HI	10	10	HeI	87	49
HeII	30	20	HeI	59	41	HeI	71	47	HeII	30	30
CII	338	104	HeII	30	13	HeII	30	20	CIV	18	13
CIII	144	74	CIII	38	21	CIV	18	13	NIII	78	39
CIV	64	49	CIV	14	9	NIII	90	47	NIV	60	34
OII	178	79	NII	41	21	NIV	70	44	NV	55	43
OIII	154	60	NIII	90	47	NV	41	33	OIII	154	60
OIV	72	30	NIV	70	44	SiIV	38	28	OIV	72	30
OV	60	24	NV	25	17	FeIV	280	21	OV	78	28
OVI	15	9	OII	57	19	FeV	182	19	OVI	39	33
NeII	96	22	OIII	45	25	FeVI	80	10	NeIII	50	19
NeIII	102	39	OIV	25	11	FeVII	153	14	NeIV	109	30
NeIV	52	17	NeII	96	22				MgIII	201	29
SiIII	45	25	NeIII	102	39				MgIV	264	27
SiIV	33	23	NeIV	52	17				SiIV	20	12
SIII	41	21	MgII	21	13				PhIV	9	5
SIV	77	29	AlIII	65	21				PhV	43	23
SV	31	13	SiIII	29	17				SIV	53	25
SVI	20	12	SiIV	33	23				SV	35	23
ArIV	107	23	SIV	77	29				ClV	80	26
ArV	50	21	SV	31	13				ClVI	44	18
FeIII	607	65	SVI	20	12				ClVII	28	17
FeIV	280	21	FeIII	607	65				ArIV	61	19
FeV	182	19	FeIV	280	21				ArV	39	20
FeVI	80	10	FeV	182	19				ArVI	51	16
			FeVI	80	10				ArVII	41	19
									CaV	121	45
									CaVI	108	47
									CrV	223	30
									CrVI	215	30
									MnV	80	16
									MnVI	181	23
									MnVII	203	20
									FeIV	280	21
									FeV	182	19
									FeVI	80	10
									FeVII	153	14
									NiIV	214	40
									NiV	168	43
									NiVI	235	50
									NiVII	170	47

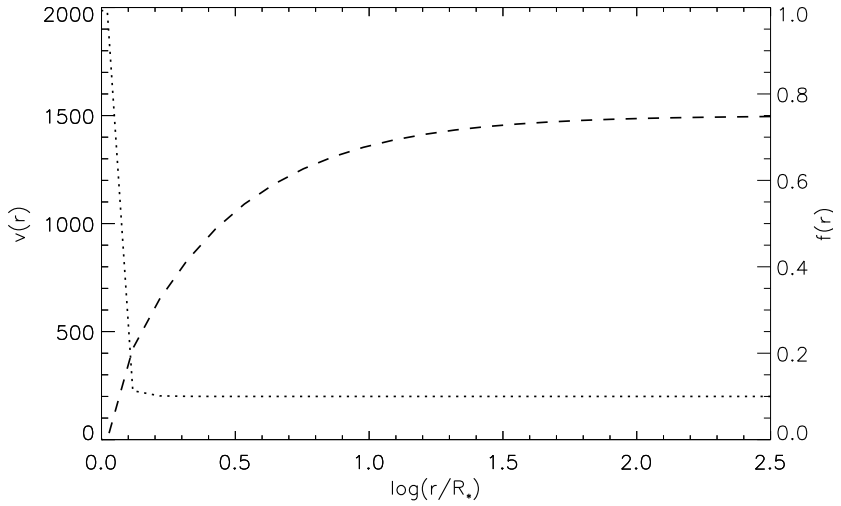

Figure 5.5: Representative radial structure of wind velocity (Eq 5.1, dashed, left y-axis) and clumping factor (Eq 5.2, dotted, right y-axis) in `CMFGEN` models. See text for typical parameters used. This is plotted with $v_\infty = 1500\,\mathrm{kms}^{-1}$.

where v_{core} is the velocity at $R_\star$ (typically a few kms^{-1}), v_0 is the photospheric velocity (typically $100\mathrm{kms}^{-1}$), and h_{eff} is the scale height of the photosphere which specifies the density structure at low velocities. These parameters were chosen to mimic a hydrostatic structure in the innermost regions of the wind, interior to the effective photosphere in WR stars. In Figure 5.5 I show this typical velocity structure as a function of radius, where it can be seen that the majority of wind acceleration occurs at radii $\lesssim 10\,R_\star$. There is evidence for wind acceleration occurring at larger radii than this adopted structure suggests (e.g. Lépine & Moffat 1999). However, modifications which take this into account, such as that proposed by Najarro et al. (1997), only significantly affect spectra features originating from the deepest visible layers of the wind (Hillier & Miller, 1999). I therefore did not adopt a slower accelerating wind structure, as most IR spectral features are formed at larger radii. I adopted $\beta = 1.0$, which is commonly assumed for WR star winds (e.g., Hillier & Miller 1999, Hamann et al. 2006). This assumption is appropriate because the high wind density of WR stars means the photosphere is beyond the hydrostatic layers, so model WR spectra are relatively insensitive to the β exponent (e.g., Hillier 1991).

Clumping is taken into account in the `CMFGEN` models presented here by a volume-filling factor approach (see Section 1.4.2). The filling factor is parameterised according to:

$$f(r) = a + (1 - a)\exp(-v(r)/b), \tag{5.2}$$

where $v(r)$ is the velocity law (Equation 5.1), a describes the density contrast and b the location in the wind at which clumping becomes important. I adopted values of $a = 0.1$ and $b = 100 \times 10^{10}$cm ($\sim 10\,R_\star$) for all `CMFGEN` models computed, meaning that $f = 0.1$ in the outer wind, i.e, $r > 10R_\star$, with clumping less pronounced interior to this as f converges to unity at $r = R_\star$. I show this expected evolution of clumping with radius in Figure 5.5. Such an approach is motivated by the findings of Owocki & Rybicki (1991) that radiation instabilities - the origin of clumped wind structure - are not expected to be important in the inner wind.

5.3.1 Initial parameter estimates and modelling technique

Individual line-blanketed co-moving frame calculations are generally computationally demanding, which limits the speed at which a large parameter space can be explored. To reduce the scope of parameter space for each star, I utilised published grids of line-blanketed model atmosphere solutions generated by the non-LTE `PoWR` code (Gräfener et al., 2002). These grids are 2 dimensional, with models characterised by a combination of temperature ($T_\star$) and transformed radius (R_t). The transformed radius, shown in Equation 5.3, is a combination of wind properties which Schmutz et al. (1989) note largely dictates the emergent emission-line spectra from stellar winds. I initially searched the database of `PoWR` models[1] for the closest match to the spectra of Wd1 WR stars. This method is not appropriate for determining final stellar parameters, as in order to cover a wide range of parameters, various important aspects of the models were fixed at generic values. For example, the abundance of carbon in WC stars and hydrogen in WN stars - which give valuable insights in to the evolutionary state of these stars - were not modelled. I used the parameters of the best fitting `PoWR` models as initial estimates for tailored `CMFGEN` models.

$$R_t = R_\star \left[\frac{v_\infty}{2500\,\mathrm{kms}^{-1}} \Big/ \frac{\dot{M}/\sqrt{f}}{10^{-4} M_\odot \mathrm{yr}^{-1}} \right]^{\frac{2}{3}} \tag{5.3}$$

I compared `PoWR` models to rectified NTT/SOFI spectra, as this data set was available for all WR stars. For the WN stars, I focused on matching the helium line ratios HeII1.012μm/HeI1.083μm and HeII2.165μm/HeII+Brγ of `PoWR` model spectra to those

[1] Available at: `http://www.astro.physik.uni-potsdam.de/~wrh/PoWR/powrgrid1.html`.

observed to obtain an estimate of temperature. This indicated temperatures in the range 40–90kK. Similarly, for the WC stars I searched the grid for model(s) best reproducing the ratios HeII1.012/HeI1.083 and CIV 2.070–2.084μm/CIII+HeI 2.112–2.137μm. This yielded low temperatures in the range 50–60 kK, as expected due to their late-type classifications (Crowther et al., 2006b).

To obtain initial estimates of mass-loss rate in WN and WC stars, I searched each grid for the model which best reproduced the absolute strength of HeI1.083μm. These models were not necessarily the same as those best reproducing the HeI/HeII temperature diagnostics. As I was comparing lines in rectified spectra (as given by `PoWR`), matching absolute the line strengths observed in binary stars or dust-producing WC stars would have provided erroneous parameter estimates, as line are diluted by companion star light or thermal dust emission. In these cases (Wd1–A, B, C, F, H, M, N & T) I compared the relative strength of HeI1.083μm to nearby lines of CIII0.992μm and CIII1.199μm, which were subject to similar amounts of dilution. Taking R_t of the best fitting model, it was possible to re-arrange Equation 5.3 to obtain an estimated mass-loss rate:

$$\frac{\dot{M}}{\sqrt{f}} = 10^{-4} \left(\frac{R_\star}{R_t} \right)^{\frac{3}{2}} \frac{v_\infty}{2500 \mathrm{kms}^{-1}}, \tag{5.4}$$

where I used the FWHM of HeI1.083μm as an initial estimate of v_∞.

With temperature and mass-loss rate estimated for each star, luminosity was the third essential parameter required for `CMFGEN` modelling. As Wd1 is at a reasonably well known distance of 4 kpc (Section 5.1.2), I was able to calculate the K-band absolute magnitude of each WR star (see Chapter 2). Each `PoWR` model in the comparison grid had a luminosity $\log(L/L_\odot) = 5.3$, and associated UBVR synthetic photometry. Using intrinsic subtype-dependent (V-K_S) colours (Crowther et al., 2006b), I calculated the absolute K_S magnitude of each best-fitting `PoWR` model. I then used the difference between absolute magnitudes calculated using synthetic and observed photometry to derive a luminosity scaling factor, by which the luminosity of the `PoWR` models could be multiplied to obtain an initial L estimate for each WR. For the dust-producing WC stars, I followed the same technique using J-band magnitudes, as thermal dust emission contributes less at these wavelengths. For stars with different models best reproducing R_t and T diagnostics, I used synthetic photometry from the model satisfying the latter. Generally, models providing the best fits to R_t and T diagnostics were close in parameter space. Initial luminosity estimates in the ranges $\log(L/L_\odot) = 5.1$–5.5 and $\log(L/L_\odot) = 5.1$–6.1 were obtained for WN and WC stars respectively.

I initially assumed a hydrogen abundance of 0.2 by number (5% by mass) for each

WN star, with the exception of Wd1-A (WN7b), lower than the $\sim$20% typical of Galactic WNLh stars. This was motivated by the observation of Crowther et al. (2006b) that most WN stars in Wd1 are hydrogen deficient. I assumed every WC star to be H-free with an initial carbon abundance of 0.15 by number.

With parameters estimated for every WR star in Wd1, I began to generate tailored `CMFGEN` models for each. In Table 5.3 I give details of the model atoms used to compute `CMFGEN` models for the main WR types in Wd1. Fitting the observed spectra and SEDs with models was an iterative process, as several free parameters - L, $T_\star$, $\dot{M}$, v_∞ and H (in WN stars) or C (in WC stars) abundances - did not act independently. For example, I determined the luminosity of each star by matching the observed K-band flux, as this is close to the SED peak whilst being less affected by extinction than J or H. However the K-band flux can be increased by raising the stellar luminosity *or* the mass-loss rate, as an increased wind density results in enhanced IR free-free emission. Therefore these parameters had to be derived in parallel. I used the ratio of different ionisation stages of the same element (He for WN stars, He and C for WC stars) to measure stellar temperatures. However, mass-loss generally influences the strength of all emission lines caused by recombination, and may even alter the observed ionisation balance by changing the ionisation structure of the wind (e.g., Najarro et al. 1997). Trivially, absolute line strengths may also be altered by changing elemental abundances. Considering many IR emission lines in WR spectra arise from a combination of atomic species, the effects of changes in abundance can be difficult to disentangle from those of mass-loss and temperature, meaning these three parameters must also be derived in combination.

Terminal wind velocity is not a genuine free parameter, as it can be readily obtained by matching the width of recombination lines, and remains invariable within $\sim$20% to reasonable changes in other parameters.

The exact modelling procedure I followed differed depending on the multiplicity, spectral type, and wavelength coverage of data available. In the following sections discuss in turn the modelling spectra and SEDs of the three broad types of WR system in Wd1: apparently single WN stars, apparently single WC stars, and confirmed binary stars (including WC9d stars).

5.3.2 Fitting procedure - single WN stars

The best fitting model spectra and SEDs for each 'single' WN star can be found in Appendix F & D respectively. I primarily used the K-band flux to measure luminosity

in the WN stars. Due to the low sensitivity of the $\sim$2 μm flux to reddening, I was able to anchor each SED using this data point, and apply the reddening required to match any shorter wavelength photometry available. I discuss the reddening law used to do this in Section 5.1.4. The SEDs of these apparently single WN stars were most straightforward to fit, and they are the most abundant type of WR in the Wd1 cluster, hence I considered them to deliver the most accurate estimates of E(B–V) and R_V. It quickly became apparent that low values of $R_V \simeq 2.3$ provided the best fits to all short wavelength (VRI) photometry simultaneously, with E(B–V) ranging from 5.1–6.3. Such an extinction law is not unusual for Wd1, as discussed in Section 5.1.4. I subsequently fixed $R_V = 2.3$ for every star, reducing the number of free parameters in more complicate cases. I include E(B–V) values derived for all Wd1 WR stars in Table 5.2.

As a temperature diagnostic I used the relative strengths of Helium lines, specifically: HeI 1.083μm, HeI 1.700μm, HeI 2.112μm, HeI+II 2.164–2.165μm, HeII 0.824μm (when available), HeII 1.012μm, HeII 1.163μm, HeII 1.281μm and HeII 2.189μm. From K-band spectra of WN stars in the GC and Arches clusters, Martins et al. (2007, 2008) claim to constrain temperature to within 2000K using similar diagnostics. Although strong in many observed spectra, I did not use the HeI 2.058μm line as a diagnostic for any parameter. As discussed at length by Najarro et al. (1994), this line is closely coupled to the UV resonance line HeI 584Å, and consequently the rate of recombination occurring through the decay channel responsible for HeI 2.058μm is highly dependent on the opacity at 584Å and hence the ionisation structure of He throughout the wind. The strength and profile of this line are therefore extremely sensitive to small changes in $\dot{M}$ or temperature - changes beyond the level of precision I claim for the parameters obtained in this study.

To determine mass-loss rates, I aimed to reproduce the strength of recombination lines in the WN spectra. I found a given increase in mass-loss would enhance the strength of HeI lines more than HeII. This is because an increase in wind density favours recombination processes, which are proportional to wind density (ρ^2), which while giving stronger emission lines in general also results in a lower ionisation throughout the wind. Hence while HeI lines - which are formed further out in the wind - are enhanced by an increase in density ($\dot{M}$), HeII lines may also be enhanced but to a lesser extent due to the tendency of He^+ to recombine to He at smaller radii. I exploited this property to determine $T_\star$ and $\dot{M}$ simultaneously, as to some extent temperature was had a greater influence on the strength of the HeII spectrum, with mass-loss largely dictating the strength of HeI. As noted earlier, changes to $\dot{M}$ flux not only affect recombination line strength but

also the K-band continuum flux, and hence inferred luminosity, which I accounted for between model iterations.

The strongest hydrogen features in the available spectral range were those of the Paschen (n=3) and Brackett (n=4) series, specifically: H(7–3) 1.005μm, H(6–3) 1.094μm, H(5–3) 1.282μm and H(7–4) 2.166μm. All of these lines fall very close to strong helium lines, with the strongest, H 1.282μm and H 2.166μm, severely blended with HeII 1.281μm and HeI+HeII 2.164–2.165μm respectively. To determine hydrogen abundance (H/He) I therefore compared the strength of H+HeII $1.281-1.282\mu$m the nearby pure HeII line at 1.163μm. Equal weight was also given to the strength of H+HeI+II 2.164–2.166μm relative to HeII 2.189μm. For a given amount of H, the strength of H+HeI+II 2.164–2.166μm would frequently be under-predicted and H+HeII $1.281-1.282\mu$m over-predicted - particularly apparent in Wd1–D (Fig F.3). In such cases, I opted for an abundance which delivered a compromise between the quality of fit for both lines. I note that the adopted super-level approximation was not expected to affect the modelling of these H diagnostics, as only levels with $n>14$ in the model H atom used in WNL models were grouped together.

I used the same diagnostics to obtain parameters for both WNE and WNL stars. However, this delivered unusually low temperatures for some WNE stars, accompanied by anomalously narrow lines in the model spectrum. The most extreme examples displaying this phenomenon were Wd1–O ($T=42$kK) and Wd1–U ($T=38$kK), which appeared to be considerably cooler than the typical $\sim$55 kK for WN5–6 stars. This is suspected to be a symptom of insufficient line-blanketing. Including more sophisticated Fe atoms - the primary agents of line-blanketing - generally increases the degree of ionisation in the inner wind, due to increased energy input by back-scattered photons, and lowers the degree of ionisation in the outer wind, due to increased opacity in the form of blocking lines. To investigate this issue further, I generated a small number of `CMFGEN` models with more sophisticated line-blanketing Fe atoms. I discuss the findings from these models in Section 5.3.5.

5.3.3 Fitting procedure - single WC stars

The best fitting model spectra and SEDs for each 'single' WC star can be found in Appendix G & E respectively. All WC stars in Wd1 belong to the coolest WC8 and WC9 subtypes. I therefore applied variations of one `CMFGEN` model to each WC star. Only two of the 8 WC stars in Wd1 show no evidence for a binary companion. Here I discuss the diagnostics used to obtain parameters for these single WC stars, but only

the determination of luminosity differs in the case of binary stars, which I discuss in the following section.

The subtypes of these WC stars alone are indicative of temperatures $T_\star \lesssim 60$kK. Therefore it was expected and indeed observed that their carbon spectra were dominated by CII and CIII lines, with weak CIV lines. Although useful in principle, the helium diagnostics used for WN stars were hampered by very weak HeII emission lines. I therefore used the relative strengths of CII to CIII lines to determine temperature, placing less emphasis on CIV. A similar methodology was adopted by Williams et al. (2015), who find CII/CIII more sensitive to temperature than CIII/CIV in the optical spectra of WC9 stars. Specifically, I prioritised the relative strengths of the following lines to measure temperature: CII 9904Å, CII 1.785μm, CIII 9705–18Å, CIII 1.199μm, CIII+HeI 2.112–2.137, CIV 2.070–2.084μmand CIV+HeI 1.733–1.736μm; additionally CII 6578-83Å, CII 7231–36Å, CIII 5696Å and CIV 5801–12Å were used where available.

Due to the complex ionisation balance of carbon in WC star winds, a good fit to all diagnostic lines across all ionisation stages was rarely achievable. I gave the greatest weight to the ratios CII 9904Å/CIII 9705–18Å and CIV 2.070–2.084μm/CIII+HeI 2.112–2.137μm, as the NTT/SOFI spectra included these lines for all stars. The lines CII 9904Å and CIII 9705–18Å were observed in the VLT/FORS2 spectra as well as NTT/SOFI, and it became apparent that their absolute strengths in rectified spectra were discrepant. In the case of Wd1–E, the peak of CIII 9705–18Å in the NTT/SOFI spectrum is almost double that in the VLT/FORS2 spectrum. Plausible reasons for this include erroneous continuum fitting during rectification, or genuine stellar variability. It was not possible to determine the cause of this difference due to the narrow overlapping wavelength range of these spectra, however I focused on modelling the VLT/FORS2 spectra.

Several lines in the red optical/near-IR spectra of cool WC stars are sensitive to mass-loss. Deriving mass-loss spectroscopically in WC stars is less straightforward than in WN stars, as the changes in ionisation structure resulting from changing wind density have a more profound and less predictable effect on the different ionisation stages of carbon present. This sensitivity to ionisation structure made it essential to derive $\dot{M}$ and $T_\star$ in unison. Owing to the sensitivity of the carbon spectrum to ionisation, I primarily aimed to reproduce the strengths of HeI 1.083μm and HeI 1.700μm lines, as in WN stars. I identified an additional suitable diagnostic in CII 1.785μm, as its predicted strength was predominantly dictated by mass-loss rather than carbon abundance.

As with other studies of WC stars, the general strength of the carbon spectrum with respect to helium was used to derive a carbon abundance (C/He). Comparisons

of pure C and He lines were favourable for this, including CIII 1.199μm/HeII 1.281μm, CIV 1.785μm/HeI 1.700μm, and CIII+HeI 2.112–2.137μm/HeII+I 2.165μm. The strength of some lines were persistently under or over-predicted, over the parameter range explored. I avoided using these to determine carbon abundance, as fitting these lines well would have required extreme parameters, at the cost of many other lines. Namely, CIII 8196Å, CIII 8500Å and CIII 2.325μm were consistently over-predicted in `CMFGEN` models, and the CII 6578–83Å lines were consistently under-predicted. In the case of CIII 2.325μm, which is over-predicted in by every best-fitting WC model, the line does not overlap with any other prominent emission feature. I therefore attributed these inconsistencies to inadequate atomic data.

5.3.4 Binary WN and dust-producing WC stars

For the binary stars highlighted in Section 5.1.3, an additional stellar component was added to each `CMFGEN` model Wolf-Rayet SED. For this component, I used a Kurucz O7V star (Castelli & Kurucz, 2004) in all cases, with a luminosity of $\log(L/L_{\odot}) = 5.1$. I treated the fractional amount of this O7V star model to be added as a free parameter. This choice of one companion SED for all cases was justified due to the homogeneous shape of O-star SEDs at near-IR wavelengths - far into the Rayleigh-Jeans tail of the SED. Furthermore, the vast majority of detected WR stars in binary systems have companions earlier than mid B-type, the near-IR SEDs of which are almost identical in shape to that of an O7V star. The addition of this extra component to the stellar SED of course affected the luminosity derived for the WR component from K-band flux. Although the IR excess of WR stars gives them redder SEDs than O-stars, this difference in shape was not sufficient to constrain the ratio of WR to O-star luminosity needed for the best SED fit, especially with the amount of reddening (E(B–V)) also essentially a free parameter. However, in the cases of Wd1–A and Wd1–B where the stellar SED consisted of only these two components, the dilution of WR emission lines provided a key constraint on the flux ratio between WR and O-star. For each star, I initially estimated the fraction of O7V flux required by comparing the total SED to the available photometric points, using an E(B–V) typical for the single WN stars. I then added this fraction of the O7V model to the `CMFGEN` model, before rectifying this to the continuum and comparing to the rectified observed spectrum. After assessing the quality of fit of the key diagnostic lines for parameters discussed in previous sections, I examined the overall strength of emission lines and altered the WR/O7V flux ratio accordingly for the next model iteration. As an increased amount of O-star flux gave a bluer SED, it was

necessary to derive the WR/O7V flux ratio and E(B–V) in combination.

The majority of WC stars in Wd1 show a large thermal IR excess (stars C, F, H, M, N, T). I interpreted this as circumstellar dust formed by the collision of two stellar winds, implying a companion star to each of these WC stars. In these cases I proceeded as for the WN binaries (stars Wd1–A and B) in adding some fraction of a Kurucz O7V star to represent the stellar companion. I approximated the emission from circumstellar dust as a black body with temperature, $T = 1400 \pm 200$ K, in accordance with previously derived dust temperatures (e.g., Williams et al. 2009a, Williams et al. 2012). A more robust treatment of this circumstellar dust would entail constructing a radiative transfer model for each star with a unique dust geometry, such as that produced by Harries et al. (2004) for their analysis of the dust-pinwheel WR 104. Crowther et al. (2006a) use such an approach to model the WC9 star WR 103, including a shell of amorphous carbon dust. However, as mid-IR *Spitzer* IRAC photometry was only obtainable for 3 of the 6 dust-producing WC stars in Wd1, I lacked the ability to constrain more detailed models such as these for all stars. I therefore opted for the more consistent approach of approximating all dust emission using black body sources. I treated the amount of black body emission (within the permitted temperature range) as a free parameter, controlled using a scaling factor as for the O7V contribution.

With two sources of radiation in addition to the WC star, the large number of free parameters made finding a unique fit to the SEDs of these systems challenging. For Wd1–F, Wd1–N, and Wd1–T, the amount of dust present was tightly constrained by [5.8] & [8.0] IRAC photometry, as the black body flux exceeded stellar sources by a factor of ∼10 at these wavelengths (Figures E.2, E.7, E.8). Fortunately, optical spectra were available for the dust-producing systems without IRAC photometry (Wd1–C, Wd1–H, Wd1–M), and I was typically able to assess the amount of WR emission line dilution across ∼0.6–2.5μm. The black body flux (dust) contribution reduced sharply at the short end of this wavelength range, meaning any line dilution there was attributable largely to the companion star flux. Conversely, the black body emission representing dust typically peaked at 2.5μm with a flux far in excess of both stellar components, meaning line dilution at longer wavelengths was entirely due to the black body (dust) flux. This variation of line-diluting source with wavelength provided an important constraint on the ratio between of O7V model and black body flux being added to the WC star `CMFGEN` models.

5.3.5 Models with additional blanketing

Line-blanketing accounts for the influence of extreme UV line 'blocking' by Fe-group elements on the populations and ionisation structure throughout the wind. For the sake of computation speed, the `CMFGEN` models for WN stars presented in previous sections contained a limited number of the atomic species responsible for blanketing. The main implication of neglecting some relatively minor blanketing elements is an overestimation of ionisation throughout the wind. A given $T_\star$ will therefore lead to a higher ionisation spectrum if less blanketing is included, resulting in temperatures being underestimated. Luminosities will also be underestimated using models with reduced blanketing.

To investigate the magnitude of these simplifications, I modelled a small number of WN stars using versions of the WNL and WNE (weak) `CMFGEN` models (Table 5.3) with additional blanketing species. Namely, the larger WNL model contained ArIII–V, CaIII–V and NiIII–V. The larger WNE (weak) model contained additional species CIII, OII–VI, NeII–IV, SiIII, SIV–VI, ArIII–VII, CaIII–VII, FeIII, NiIII–VII. I used the larger WNL model to re-derive parameters for Wd1–V (WN8) and Wd1–P (WN7), and the larger WNE model to re-derive parameters for Wd1–O (WN6). As expected, using the same diagnostics as for models with less blanketing (Section 5.3.2), I derived temperatures that were 2000–3000 kK higher and luminosities ∼10% higher than with the original models. I did not use an expanded WC star model to re-analyse any stars, as that detailed in Table 5.3 contained sufficient blanketing.

These systematic parameter shifts are small; typically the same order of magnitude or smaller than general uncertainties of the modelling technique (see following section). Therefore, in the discussion that follows, in order to present a self-consistent set of results, I refer exclusively to the parameters derived using smaller models.

5.3.6 Parameter uncertainties

Due to the large amount of time required to compute each model, it is unfeasible to calculate statistical errors on the derived parameters. This would require computation of a large numbers of models in the parameter space surrounding each best-fitting model. Instead, during the fitting process I estimated the range in each parameter that would provide acceptable fits to the data. These ranges of values act as estimates of the uncertainties. I found the following: $\pm 2500K$ for $T_\star$, ± 0.1–0.2 dex in $\log(L/L_\odot)$ for single WN and WC stars (depending on the coverage and reliability of available photometry), ± 0.2 dex in $\log(L/L_\odot)$ for dusty WC or binary WN stars, 0.05 dex for $\dot{M}$ and $\pm 150\,\mathrm{kms}^{-1}$

for v_∞.

The dominant source of uncertainty in luminosities is in the distance. As discussed in Section 5.1.2, I assumed 4.0±0.5 kpc - a 12.5% (±0.1 dex in L) uncertainty. The next largest source of uncertainty is reddening. With RIJHK$_S$ photometry available for every star, this can be well-constrained, increasing L uncertainties to ±0.15 dex at most - less if shorter wavelength photometry is available. As K$_S$ photometry is primarily used to derive luminosity, the accuracy of this is worth considering. As discussed in Section 5.2.4, most K$_S$ photometry is accurate to ±0.05 mag, however a small number (indicated in Table 5.2) are only accurate ± 0.1 mag, corresponding to ∼10 % in flux and hence 0.04 dex in L. In these cases I put more emphasis on H-band flux, which is more sensitive to reddening, and hence I estimate a total uncertainty rising to ±0.2 in $\log(L/L_\odot)$.

The addition of further flux components such as a binary companion of black-body representing thermal dust emission adds uncertainty to the luminosity. Although the wavelength dependence of line-dilution is effective at constraining the relative contributions of O-star and dust, I estimate an uncertainty of ±0.2 dex in these cases.

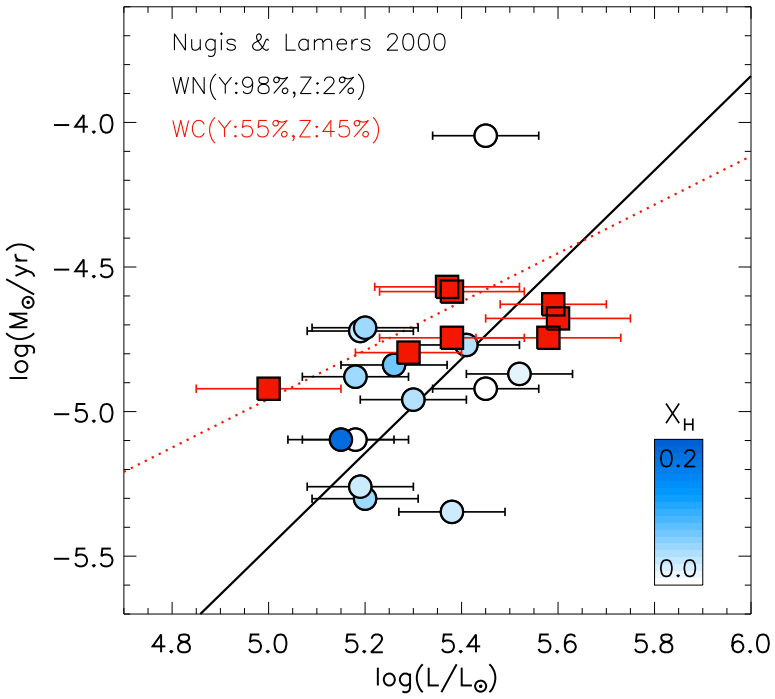

Figure 5.6: Mass-loss rates versus luminosity for the WR stars in Wd1 given by `CMFGEN` analysis (Table 5.4). Blue circles represent WN stars - colour coded according to their surface hydrogen mass fraction X_H. Red squares represent WC stars. Uncertainties in $\dot{M}$ are comparable to symbol sizes (0.05 dex). Empirical $\dot{M}(L)$ relations from Nugis & Lamers (2000) are shown by lines, for WC stars (dotted, their equation 21) and WN stars (solid, their equation 20).

Table 5.4: Stellar parameters derived for WR stars in Wd1 (identified in Fig 5.2 and Table 5.2). The spectral and SED fits used to derive parameters are shown in Appendices F & D and G & E for WN and WC stars respectively.

Star	Sp. Type	$T_\star$ (kK)	$\log(L/L_\odot)$ WR (O-star)	$\dot{M}$ ($\times 10^{-5}\, M_\odot yr^{-1}$)	v_∞ (kms^{-1})	H/He (#)	X_H
A	WN7b+?	65	5.45 (<4.8)	9.0	2700	0.00	0.00
B	WN7+?	48	5.26 (5.1)	1.45	1600	0.30	0.07
D	WN7	53	5.18	1.32	1300	0.20	0.05
G	WN7	62	5.23	1.90	1100	0.10	0.02
I	WN8	47	5.20	1.95	1100	0.20	0.05
J	WN5	38	5.38	0.45	1900	0.10	0.02
O	WN6	42	5.45	1.20	1900	0.00	0.00
P	WN7	46	5.30	1.10	1150	0.15	0.04
Q	WN6	50	5.18	0.80	1400	0.00	0.00
R	WN5	50	5.20	0.50	1500	0.20	0.05
U	WN6	38	5.52	1.35	2200	0.05	0.01
V	WN8	36	5.41	1.70	1150	0.15	0.04
W	WN7	46	5.15	0.80	1800	0.90	0.18
X	WN5	51	5.19	0.55	1500	0.10	0.02
						C/He (#)	X_C
C	WC9d	40	5.38 (4.7)	1.80	1300	0.20	0.38
E	WC9	35	5.59	2.35	1100	0.07	0.17
F	WC9d	52	5.00 (5.1)	1.20	1000	0.20	0.38
H	WC9d	35	5.58 (5.6)	1.80	1100	0.10	0.23
K	WC8	50	5.29	1.60	1700	0.30	0.47
M	WC9d	49	5.37 (4.9)	2.70	1150	0.25	0.43
N	WC9d	39	5.60 (5.5)	2.10	1300	0.20	0.38
T	WC9d	50	5.38 (4.8)	2.60	1200	0.20	0.38

5.4 Results and discussion

The stellar parameters obtained for all WR stars in Wd1, by the methods described above, are given in Table 5.4. In Figure 5.6 I plot the clumping-corrected mass-loss rates against luminosity for WR stars in Wd1. Recall from Section 1.4.1 that stellar winds are theoretically predicted to intensify with luminosity and metallicity (Eq. 1.14). I also show the empirical $\dot{M}(L, Y, Z)$ relationship of Nugis & Lamers (2000) in Figure 5.6, for typical H-free WN (X=0,Y=0.98,Z=0.02) and WC (X=0,Y=0.55,Z=0.45) stars. As for the Galactic sample shown in Fig. 1.20, the WC stars are largely consistent with the Nugis & Lamers relation, and the WN stars show considerable scatter around the relation, with the strong-line Wd1–A lying well above. I conclude that the empirical $\dot{M}-L$ relation provides a useful parameterisation of mass-loss for stellar models in this luminosity regime, but its accuracy is limited to approximately $\sim$0.5 dex in $\dot{M}$.

In Figure 5.7 I present a H-R diagram showing effective temperature ($T_\star$) and luminosity (L) for all analysed WR stars. A comparison is made between these and the results of other analyses of Galactic WC (left panel) and WN stars (right panel). The points representing WN stars are shaded to indicate their surface hydrogen abundance (X_H). Amongst the WC stars, carbon abundances and mass-loss rates do not vary enough to warrant such distinctions. I find WN and WC with similar luminosities, in the range $\log(L/L_\odot)$ 5.2–5.6, with the WC star Wd1–F extending this range down to $\log(L/L_\odot) \simeq 5.0$. I measure a wide range of temperatures for the WN stars, $T_\star = 36$–65 kK, and a smaller range for WC stars of $T_\star = 35$–52 kK. Hydrogen surface abundances in the WN stars are uniformly low, with a median H/He = 0.1 by number ($X_H = 0.02$), with the notable exception of Wd1–W which has H/He = 0.9 ($X_H = 0.18$). The WC stars display a narrow range of carbon abundances, C/He = 0.1–0.3, and have similar terminal wind velocities, $v_\infty \simeq 1200\,\mathrm{kms}^{-1}$.

5.4.1 Comparison to other Galactic WR stars

Hamann et al. (2006) present a model grid analysis, using the PoWR model atmosphere code, of $\sim$60 lightly-reddened Galactic WN stars of all spectral types, mostly outside of massive clusters. They identify two distinct groups of WN stars in the H-R diagram; one with high luminosity ($\log(L/L_\odot) = 6.0$–6.5) and a narrow range in temperature ($T_\star = 40$–50 kK), and one with lower luminosity ($\log(L/L_\odot) = 5.3$–5.8) and a broader temperature range ($T_\star = 45$–100 kK). The latter group are uniformly H-poor, whereas the former have a range in surface H abundance (see Figure 5.7**b**). The WN stars in Wd1

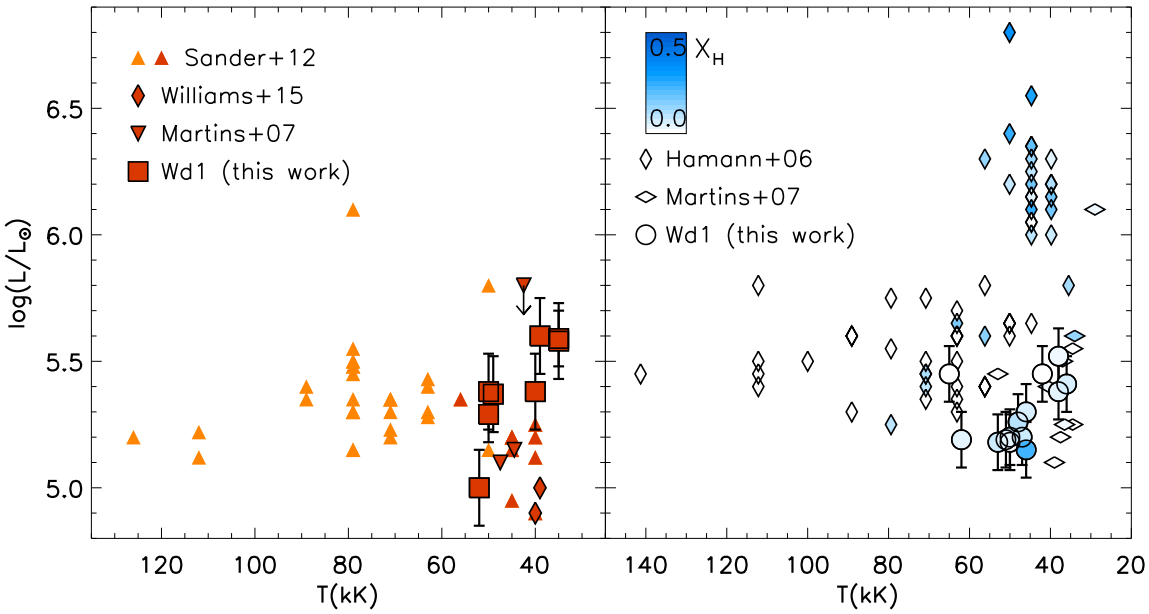

Figure 5.7: **a**(*Left*) H-R diagram showing the location of WC stars analysed in this work (squares), together with the Galactic field sample analysed by Sander et al. (2012) (orange WC4–8, red WC9), WC9 stars in the GC cluster (Martins et al., 2007) and the WC9 stars WR 93 and WR 103 (Williams et al., 2005). Error bars show a 0.11 dex (0.15 dex) uncertainty on L for single (dusty) WC stars. Temperature uncertainties ($\sim$2.5 kK) are comparable to symbol sizes. **b**(*right*) As left, showing WN stars analysed in this work (circles), together with the Galactic field sample analysed by Hamann et al. (2006), and WN7–8 stars in the GC cluster (Martins et al., 2007). Symbols are coloured to represent surface hydrogen mass fraction. Error bars show 0.11 dex uncertainty on L. Temperature uncertainties ($\sim$2.5 kK) are comparable to symbols sizes.

are consistent in luminosity with the lower H-free group, with some found at even lower luminosity ($\log(L/L_{\odot}) \simeq 5.2$). Taking only WN6-8 subtypes - to ensure a meaningful comparison to the Wd1 WN stars - Hamann et al. (2006) measure a median surface hydrogen mass fraction of $X_H = 0.1$, significantly higher than 0.02 median in the Wd1 WN stars. This is strong evidence that the WN stars in Wd1 are hydrogen poor compared to their counterparts in the field.

The GC cluster, with an age of 6 ± 2 Myr (Paumard et al., 2006), is host to a similar (but less numerous) population of WR stars to Wd1. Martins et al. (2007) present `CMFGEN` analyses of 8 WN5-8 stars, and 3 WC9 stars in the GC cluster based on K-band spectroscopy. For the WN stars they measure $\log(L/L_{\odot}) = 5.1$–5.6 and $T_{\star} = 35$–55 kK, strikingly similar to the Wd1 WN stars (see Figure 5.7**b**). The K-band spectral range contains limited information regarding hydrogen abundance, however Martins et al. (2007) argue that all WN stars they analyse show a low H abundance, H/He ≤ 0.1 ($X_H = 0.02$), with the exception of one WN7 star with H/He $\simeq 1$($X_H \simeq 0.2$).

Sander et al. (2012) analyse ~ 40 unobscured Galactic WC stars with a grid of models, generated using the `PoWR` atmosphere code. Their sample includes 4 WC8 stars and 13 WC9 stars - the only WC types present in Wd1. I show their results in Figure 5.7**a**. For the WC9 stars they find temperatures $T_{\star} = 40$–45 kK (except one with $T_{eff} = 56$ kK) and luminosities $\log(L/L_{\odot}) = 4.9$–5.3, with WC8 at higher temperatures ($T_{\star} = 50$–60 kK) and marginally higher luminosity ($\log(L/L_{\odot}) = 5.1$–5.4). I measure consistent luminosities for four of the WC9 stars in Wd1, but three (Wd1–E, H, N) are higher with $\log(L/L_{\odot}) \simeq 5.6$ and extend below the temperature range measured by Sander et al. (2012), indicating they have unusually large radii for WC stars. The four WC9 stars with $\log(L/L_{\odot}) < 5.4$ and the WC8 star Wd1–K all have temperatures consistent with those measured by Sander et al. (2012).

Of the three WC9 stars in the GC cluster analysed by Martins et al. (2007), two have luminosities $\log(L/L_{\odot}) \sim 5.2$, and an upper limit of $\log(L/L_{\odot}) < 5.8$ was placed on the third. All three have temperatures $T_{\star} \sim 45$ kK, towards the hotter end of the range I measure for Wd1 WC9 stars (Figure 5.7**a**).

5.4.2 Comparison to the predictions of single-star evolution

In Figure 5.8 I show the evolution of T_{eff} and L in single-star models with initial masses from $32\,M_{\odot}$ to $120\,M_{\odot}$ at solar metallicity ($Z = 0.014$) (Ekström et al., 2012). I show models including the effects of stellar rotation (left panel) and without rotation (right panel). In Table 5.5 I give the values of parameters in single-star (Ekström et al., 2012)

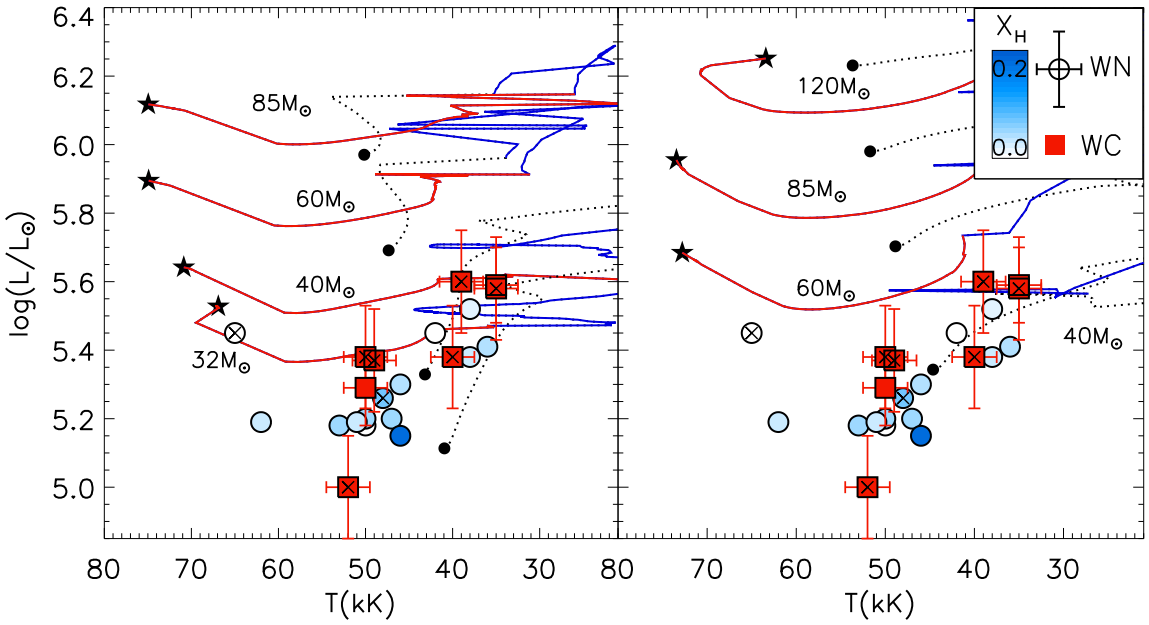

Figure 5.8: (*Left*) H-R diagram showing the locations of WR stars in Wd1, as derived from `CMFGEN` analyses presented here. WN stars are shown as varying shades of blue, according to their surface hydrogen mass fraction (see key), and symbol sizes are proportional to $\log \dot{M}$. Typical error bars are shown by the symbol in the top right corner of right panel. Lines represent single-star evolutionary tracks of various initial mass (labelled) *with* stellar rotation (Ekström et al., 2012). black points mark the starting points of these tracks, and stars the end points (end of Silicon burning). The tracks are coloured according to their surface abundances, and hence expected spectroscopic appearance. black dotted sections are non-WR, blue sections have T>10^4 K and $X_H < 0.4$ (WN) and red sections have $X_C > X_N$ (WC). (*Right*) same as left but showing single-star tracks without stellar rotation.

Table 5.5: Model parameters at the time step closest to an age of 5 Myr. *(Upper)* single-star models (Ekström et al., 2012). The non-rotating 60 $M_\odot$ model reaches the end of core C-burning when younger than 5 Myr. *(Lower)* Average (or a range where a significant spread is present) parameters for primary stars in close binary systems (Eldridge et al., 2008). All primary stars $\gtrsim 60\,M_\odot$ reach the the end of core C-burning when younger than 5 Myr (~ 4.1 Myr for 60 $M_\odot$).

M ($M_\odot$)	v_{ini} (kms^{-1})	T (kK)	$\log(L/L_\odot)$	$\dot{M}$ ($10^{-5}\,M_\odot yr^{-1}$)	X_H	X_C
25	300	34	5.08	0.002	0.71	1.8×10^{-3}
32	0	28	5.40	0.004	0.72	2.3×10^{-3}
32	300	35	5.40	0.008	0.67	1.4×10^{-3}
40	0	19	5.67	4.36	0.00	1.3×10^{-4}
40	300	38	5.65	0.28	0.51	6.7×10^{-4}
60	300	74	5.89	2.0	0.00	0.49
M_P			$\log(L/L_\odot)$		X_H	X_C
25			5.11		0.71	3.4×10^{-3}
40			5.26–5.38		0.024	0.15–0.40

and close binary models (Eldridge et al., 2008) at an age of 5 Myr - the adopted age of Wd1.

I note that simply reproducing the locations of WR stars in the H-R diagram does not constitute agreement between observation and theory. The known age and coevolution of Wd1 provide an additional constraint, such that L, T, and surface abundances must also be reproduced at a compatible age. The time evolution of surface abundances also stand as a test of mass-loss and chemical mixing. To illustrate this, I colour the lines in Fig. 5.8 representing stellar models to indicate the WR phases they putitavely correspond to. To do this I followed Georgy et al. (2012) in defining a WR star as having $T_{eff} > 10^4$ K and $X_H < 0.3$. Once below this X_H criteria, the star is a WN until carbon exceeds nitrogen by mass at the surface, at which point the star becomes a WC. I neglect to define the WO or WN/C phases, as these are very short lived and no such stars are observed in Wd1. The 32 $M_\odot$ and 40 $M_\odot$ models, with and without rotation respectively, are the lowest initial mass to evolve beyond the He-ZAMS to high ($T_{eff} > 30$ kK) temperatures.

At this point, it is important to recall the definition of $T_\star$ from the `CMFGEN` analysis. Since T_{eff} in evolutionary models refers to the temperature at the hydrostatic surface - which in WR stars is found deeper than the traditional definition of a photosphere ($\tau = 2/3$) - I defined WR stellar temperatures ($T_\star$) at a greater depth ($\tau \simeq 20$) to facilitate comparison with evolutionary predictions. However, I focus my comparison between

observations and stellar models on luminosity, as this is quite tightly related to the total mass of the star and to the internal physics. Effective temperatures depends on the physics of the stellar atmosphere, particularly the mass-loss rate and opacity, and is more a probe of the outer layers.

Before assessing the coincidence of Wd1 WR stars with solar metallicity single-star tracks, I will address the metallicity of Wd1. The Galactic metallicity gradient has been measured by Balser et al. (2011) - using electron temperatures of a large sample of Galactic HII-regions - to be -0.05 ± 0.02 dex kpc^{-1}. Wd1 resides at a Galactocentric radius of ~ 5 kpc, which is 3 kpc interior to the Sun. Consequently it should be moderately oxygen (and generally metal) rich, exceeding that of the Orion nebula by 40%, i.e, $\log(O/H) \sim 8.85$. In their analysis of the massive stars in the GC cluster, Martins et al. (2007) present single-star evolutionary tracks from the Geneva group at twice solar metallicity (their Fig. 23b). The most significant difference between these and tracks at solar metallicity is the luminosity reached during Helium burning. This difference grows with initial mass, as metallicity-dependant mass-loss plays a more powerful role on the main sequence in reducing the final masses of the stars. For example, the luminosity difference between 40 $M_\odot$ models at $Z_\odot$ and $2Z_\odot$ during He-burning is < 0.1 dex. In contrast, 85 $M_\odot$ models evolve down to $\log(L/L_\odot) = 5.1$, compared to 5.5 at solar metallicity. However, without access to bespoke models at the specific metallicity of Wd1, I used those calculated at solar metallicity. It must be considered, therefore, that models with initial mass $\gtrsim 60\,M_\odot$ may evolve to luminosities 0.1–0.2 dex lower than shown in Figure 5.8.

The broad-line WN star Wd1–A is the hottest and amongst the most luminous observed, suggesting it is the most evolved object. This star coincides well with the expected end-points of stellar evolution for single stars, not just in its combination of L and T, but its lack of surface H. However, no WN stars are predicted with such high temperatures, and if the 7.9d photometric period in Wd1–A (Bonanos, 2007) is due to a close binary companion, the assumption of single-star evolution may not apply. There is a clustering of WN stars in the H-R diagram around $\log(L/L_\odot) = 5.2$ and $T = 50$ kK, including the known binary star Wd1–B (P = 3.5 d). Such a grouping is expected in a coeval population, as according to single-star evolution, stars of a narrow range in initial mass (and hence luminosity) will go through the WR phase simultaneously. WN stars not belonging to this group are the hotter Wd1–G (WN7), and the cooler and more luminous Wd1–J (WN5), Wd1–O (WN6), Wd1–U(WN6) & Wd1–V(WN8). This latter group of WN stars are all consistent with the WN phase in the rotating 32 $M_\odot$ model,

and to a lesser extent the 40 $M_\odot$ non-rotating model. However, the majority of WN stars are sub-luminous compared to these single-star models, both with and without rotation.

There is a notable absence of any WR stars with $\log(L/L_\odot) > 5.6$ in Wd1. Stellar models predict that only stars with initial masses $> 60\,M_\odot$ enter the WR phase with such high luminosities, suggesting that stars initially more massive than this have already undergone core collapse (Figure 5.8). A similar conclusion can be reached by noting the absence of H-rich late-type WN stars, which have typical luminosities of $\log(L/L_\odot) = 6.2 \pm 0.2$ (Hamann et al., 2006) and are thought to descend from stars with initial mass $> 60\,M_\odot$ (Crowther et al., 1995b; Massey et al., 2001). Therefore, from the WR stars alone it is possible to infer an upper limit of the cluster turn-off mass at $60\,M_\odot$, assuming single-star evolution. However, it is possible that the most luminous WN stars currently observed in Wd1 are rejuvenated binary products, or 'massive blue stragglers'. It was proposed by Vanbeveren et al. (1998) that after approximately 4 Myr, a population of super-luminous O-type stars mimicking a younger age would appear in a coeval cluster. Such stars would supposedly proceed to pass though a H-rich WNL phase, and quite possibly evolve to look similar to the group of WN stars in Wd1 observed at $\log(L/L_\odot) \sim 5.5$ & $T \sim 40$ kK. More recently, Schneider et al. (2014) predict the most massive star in a massive coeval cluster to be a binary product by an age of 1–2 Myr, highlighting the prevalence of binary products amongst the most luminous cluster stars. If this is the case for the most luminous WN stars in Wd1, it would lower the turn-off mass inferred by the WR population, as stars with initial masses lower than 60 $M_\odot$ would be mimicking stars with higher mass. An upper limit of 60 $M_\odot$ for the turn-off in Wd1 is consistent with the analysis of OB supergiants by C05. As these are expected to be the *least* evolved post-MS objects in Wd1, their estimated masses of 30–35 $M_\odot$ provides an estimate of the turn-off. Of course, the WR stars in Wd1 are expected to have evolved from stars with initial masses higher than this, suggesting a lower progenitor mass limit of 30–35 $M_\odot$ for the WR stars evolving in isolation.

The majority of WN stars in Wd1 are sub-luminous compared to single star models, more so than could be accounted for by moderately higher metallicity models. This is a frequently observed problem revealed by an increasing number of WR star analyses. Hamann et al. (2006) observe a surplus of low-luminosity ($\log(L/L_\odot) < 5.5$) H-poor WN stars in the Galactic field population, relative to synthetic populations of single-stars simulated using Geneva stellar models (Meynet & Maeder, 2005) (Recall Fig. 1.15). The late-type WN stars in the GC analysed by Martins et al. (2007) have lower luminosities than single-star tracks at solar metallicity, but may be explained by higher metallicity

models.

The rotating 32 $M_{\odot}$ model is the lowest initial mass to experience a WC phase, with the next lowest mass model (25 $M_{\odot}$) undergoing core-collapse during the WN phase. The predicted lower limit on progenitor mass for WC stars is therefore somewhere between these values. Only the tracks including (fast) stellar rotation are capable of reproducing the positions of the WC stars in Wd1. The 40 $M_{\odot}$ and 32 $M_{\odot}$ tracks are consistent, within the uncertainties, with all WC stars excluding of Wd1-F, which is 0.2 dex less luminous than the 32 $M_{\odot}$ model. However, the criterion adopted to mark the beginning of the WC phase in evolutionary models, i.e., $X_C > X_N$ does not represent the carbon abundances in these WC stars. For example, at the WN→WC transition in the rotating 60 $M_{\odot}$ model, the surface carbon mass fraction is $X_C < 1\%$. The lowest carbon abundance I measure is C/He = 0.07 by number, corresponding to $X_C = 17\%$ (assuming pure He and C). It is clear therefore that WC stars analysed have higher carbon abundances than the evolutionary tracks with which some are consistent in the H-R diagram. Furthermore, only the 60 $M_{\odot}$ single-star and 40 $M_{\odot}$ close binary models have comparable X_C at an age of 5 Myr (Table 5.5) to match the WC stars, albeit at a much higher temperature ($T \sim 74$ kK) in the 60 $M_{\odot}$ case. Similarly, Sander et al. (2012) find that, as well as being sub-luminous compared to single-star models, nearly all WC stars and *particularly* WC9 subtypes are cooler than expected when carbon is revealed at the surface. A potential solution to this is provided by envelope inflation (recall Section 1.4.1). The WC9 stars in Wd1 may have extended sub-photospheric layers, hence displaying disproportionately large radii for their core size, explaining the cool derived temperatures.

5.4.3 Evolutionary history of the WR stars

The key to understanding the evolutionary history of the WR stars in Wd1 lies in explaining why the majority of the WN population are currently sub-luminous, and hence less massive than the predictions of stellar models. Georgy et al. (2012) discuss three scenarios whereby stars may lose more mass than prescribed by the single-star Geneva models (Ekström et al., 2012). In these models, mass-loss on the MS is dictated by the theoretical Vink et al. (2001) relation, and post-main sequence by empirical relations from de Jager et al. (1988) (RSG) and Nugis & Lamers (2000) or Gräfener & Hamann (2008) (WR). Briefly, these three scenarios are:

i) single-star channel where stars with initial mass below the current WR progenitor limit (15–20 $M_{\odot}$) display enhanced mass-loss during the RSG phase,

ii) single-star channel where massive stars already becoming WR stars lose more mass throughout their lives, possibly in the form of giant eruptions,

iii) binary star channel where additional mass-loss is caused by RLOF in CB systems.

Here I discuss which of these scenarios is most supported by the WR stars in Wd1.

There is evidence that RSG mass-loss rates are higher than assumed by evolutionary models. van Loon et al. (2005) measure mass-loss rates 3–50 times higher those suggested by de Jager et al. (1988) for dust-enshrouded RSGs, and there is evidence that RSGs do not follow a single mass-loss prescription throughout the whole phase (Smith, 2014). Even studies which measure RSG mass-loss rates in agreement with those assumed (e.g., Mauron & Josselin 2011) implicitly ignore the possibility of short-lived eruptions, which could increase the average mass lost throughout the phase. Such eruptions are evidenced by shells of material observed around (typically the most luminous) RSGs (e.g., VY CMa, Smith et al. 2001). Enhanced RSG mass-loss rates are of no consequence to WR stars unless they are capable of shedding their H-rich envelopes and returning to the blue side of the H-R diagram. Evidence for this blueward evolution exists in the prototypical post-RSG YHG IRC+10420, around which a maser emitting shell is observed, which has been shown to be the remnant of RSG mass-loss (Humphreys et al., 1997). Furthermore, Davies et al. (2008) analyse the RSGs in the $\sim$12 Myr old cluster RSG1, finding a narrow range in initial mass around 18 $M_{\odot}$, and maser emission indicating a dense circumstellar material around the most luminous RSGs. These observations, together with the presence of a slightly more luminous YHG in the same cluster, paints a picture of blue-ward evolution from RSG$\rightarrow$YHG via an enhanced mass-loss episode. However, Georgy et al. (2012) study the evolution of a 15 $M_{\odot}$ star with 10x the normal de Jager et al. (1988) mass-loss rate, and find that the H-rich envelope is not lost, preventing blueward evolution to a H-free WN or WC type star. The main problem with the low-mass post-RSG scenario (*i*) functioning in Wd1, is that the cluster is too young for 15–20 $M_{\odot}$ stars to have evolved beyond the RSG phase. A 25 $M_{\odot}$ single-star at an age of 6 Myr (upper limit on the age of Wd1) has $\log(L/L_{\odot}) = 5.17$ and $T_{eff} = 28$kK, i.e., is still evolving off the main sequence to become an RSG. The total lifetime of this model is 7.1 Myr, and core-collapse occurs in a post-RSG phase when $X_H \sim 0.2$.

For low luminosity ($\log(L/L_{\odot}) \sim 5.0$) WC stars in the Galactic field, similar to Wd1–F, Sander et al. (2012) favour higher RSG mass-loss rates, as they claim the models by Vanbeveren et al. (1998) (featuring enhanced RSG mass-loss rates) cover the required luminosity range. There is a problem with this scenario; as Langer (2012) points out, it would also imply a population of similarly luminous H-free WNE stars as progenitors,

which are not observed (Hamann et al., 2006).

The youth of Wd1 prohibits low-mass ($\lesssim 25\,M_{\odot}$) single-star progenitors for the H-poor WR stars, and Wd1 no longer contains stars with initial masses $\gtrsim 60\,M_{\odot}$. Therefore, if scenario (*ii*) is responsible for the low-luminosity H-poor WR stars, single-star progenitors must be from the approximate initial mass range 30–60 $M_{\odot}$. The simultaneous presence of 3 RSGs (Westerlund, 1987; Clark et al., 2005) with the WR stars places tighter constraints on the WR progenitor masses. Single-stars above 40 $M_{\odot}$ do not experience an RSG phase, meaning that the progenitors of the current WR stars cannot exceed this by much. Therefore scenario (*ii*) would require additional mass-loss in $\sim 50\,M_{\odot}$ stars. Such stars are not expected to obtain Eddington factors ($\Gamma = \kappa L/4\pi GMc$), close to one, and so are not candidates for enhanced mass-loss in the upper H-R diagram (Gräfener et al., 2011; Vink, 2011). The only remaining route from main-sequence to H-poor WN is therefore via a LBV phase, where large amounts of mass are lost in sporadic, erruptive events, due to an unknown physical mechanism (Smith & Owocki, 2006). The presence of LBV W243 with a luminosity $\log(L/L_{\odot}) \simeq 5.8$ (Clark & Negueruela, 2004), in excess of the WR stars, suggests that this channel could be operating in Wd1.

The prevalence of hard X-ray sources and circumstellar dust associated with the WR stars in Wd1 provides strong evidence for a high binary fraction, making scenario (*iii*) an appealing explanation for the low-L H-free WR stars. Regardless of these observations, the work of Sana et al. (2012) shows that only 1/4 of massive stars will evolve in effective isolation. It is therefore unreasonable to expect the single-star models presented in Fig 5.8 to explain the entire population. Mass and angular momentum transfer in close binary systems can have a profound effect on the stars (see Section 1.2.2). Mass-loss rates of $10^{-3}\,M_{\odot}\mathrm{yr}^{-1}$ can be reached during mass-transfer (Smith, 2014), removing large quantities of mass from a star almost instantaneously compared to nuclear timescales. This provides a means for primary stars in binary systems to lose their hydrogen envelopes and take on a WR spectral appearance as they expand off the MS. Due to the large parameter space in which CB evolution operates, detailed population synthesis models have not been created (c.f. Eldridge et al. 2008). In Section 1.2.2 I describe the uncertainties currently arresting our understanding of binary interaction. It is worth repeating here that the efficiency of mass transfer between donor and accretor is a considerable unknown, such that relative masses in post-RLOF binary systems are not tightly constrained by theory.

Eldridge et al. (2008) predict that close binary evolution lowers the minimum mass to become a WR star to approximately 15 $M_{\odot}$, down from $\sim 27\,M_{\odot}$ in single-star models

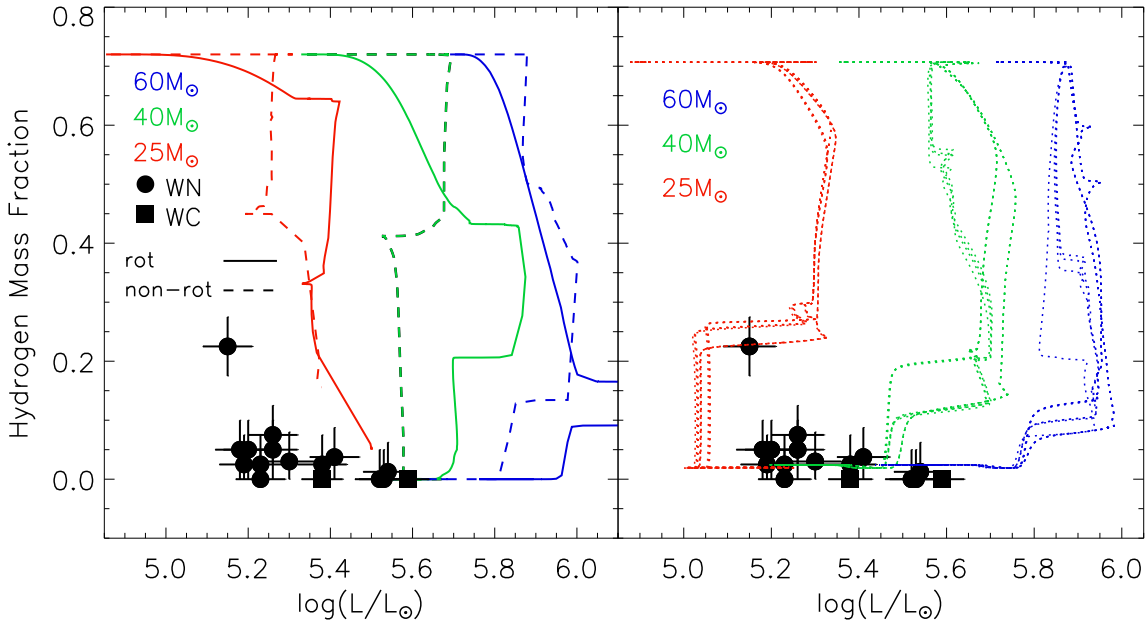

Figure 5.9: *Left* Evolution of surface hydrogen abundance with luminosity in Geneva single-star models for various initial masses, with (solid) and without (dashed) stellar rotation. *Right* same as left, for the primary stars of CB systems. For each primary mass (colour) 12 tracks are plotted, corresponding to a different combinations of initial mass ratio ($q = 0.3, 0.5, 0.7$ & 0.9) and orbital separation ($\log(r/R_\odot) = 2.0, 2.5$ & 3.0).

with rotation. This provides a natural explanation not only for the low-L of some WR stars in Wd1, but for the low surface H abundances observed in nearly all WN stars. Indeed, when RLOF ends, the stars radius will have shrunk and a small residual H layer will remain on the surface (Petrovic et al., 2005), possibly explaining the low X_H measured amongst the Wd1 WN stars. In Figure 5.9 I plot the surface H abundances and luminosities of all WR stars in Wd1, along with the evolution of these properties in single-star models with and without rotation (Ekström et al. 2012, Left panel) and the primary stars of CB systems (Eldridge et al. 2008, Right panel). It can be seen that CB evolution produces sufficiently low-L stars with low surface H abundances to match the majority of Wd1 WR stars. However, the 25 $M_{\odot}$ binary model which matches the observations has an age of $\sim$7 Myr by the time surface H has reduced to $X_H < 0.2$. The 40 $M_{\odot}$ binary model reaches H exhaustion in just over 5 Myr (Table 5.5), suggesting that primary stars of CB systems in the range 30–40 $M_{\odot}$ may be suitable progenitors for the low-L H-poor WR stars.

If significant numbers of the WN stars in Wd1 are the products of CB evolution, the accreting (secondary) stars should be detectable. Langer (2012) state that only very massive binaries with rather unequal masses can produce WR binary stars where the O-star companion is somewhat less luminous than the WR. Interestingly however, the known binary Wd1–B with a period of 3.5 d has a mass ratio $q = M_{WR}/M_O = 0.37$ (Koumpia & Bonanos, 2012) and at 1μm the WR provides $\sim$60% of the flux (Table 2.8). A similar light ratio is observed at 1μm in the Galactic WN5+O8.5V binary WR 127, which has a period of 9.55 d and $q = 0.47$. Petrovic et al. (2005) are able to reproduce WR 127 using a CB evolution model with case A mass-transfer, accounting for the effects of RLOF on rotation and hence mass-loss of the accreting star. Their model has an initial period of 6 d and $q \simeq 0.5$. However, they are unable to reproduce shorter period WR+O systems (e.g., WR 153, $P = 6.69$ d) as these evolve into contact on the MS. Additionally, to reproduce WR 127 they require a uneven mass ratio ($q = 0.5$) to limit the efficiency of mass-transfer to $\sim$10%, and hence prevent the secondary reaching a greater luminosity than the stripped primary (WR). It remains unclear how the 90% of mass lost by the primary which is not accreted is ejected from the system. Current models of CB evolution are therefore capable of producing systems with a WR star dominating optical/near-IR flux, however, in general the luminosity of the accreting star is raised above the WR component (Langer, 2012). For the WN stars I modelled as a single stars, emission line strengths were well reproduced by `CMFGEN` models with no additional continuum flux contribution. I estimate that line dilution due to a companion would be noticeable if

line strengths were reduced by half or more, corresponding to $F_O/F_{WR} < 1.0$. This places an approximate luminosity limit of the companions of $< L_{WR}$. The unseen companion stars must fulfil several requirements to be consistent with this picture; they must have stellar winds strong enough to produce X-rays from wind collisions (earlier than $\sim$B0V), have current luminosity $\log(L/L_\odot) \lesssim 5.0$, and initial mass ratios must have been less than ~ 0.5 in order to limit the efficiency of mass transfer. Early B and late O dwarfs ($\sim$B1–O7V) meet all of these requirements, as they have $\log(L/L_\odot) = 4.6$–5.0 (Martins et al., 2005), initial masses 15–25 $M_\odot$ (giving appropriate q if the Wd1 WR stars have $>40\,M_\odot$ progenitors), and have been observed in X-ray luminous WR+OBV colliding wind systems (e.g., WR 147: WN8+B0.5V, Williams et al. 1997).

5.5 Conclusions

In this chapter I have presented spectroscopic analysis of 22 WR stars in the 5 Myr old, 4 kpc distant, young massive cluster Westerlund 1. A narrow age spread in the PMS of this cluster (Kudryavtseva et al., 2012) means the high-mass stellar population may be considered coeval. It therefore serves as a stringent test of massive star evolutionary theory. Many of the WR stars in Wd1 show indirect evidence for binary companions, making it an important laboratory to study the increasingly touted role of binary interaction in producing WR stars.

I collated archival data for the WR stars in Westerlund 1, to complement a complete set of 1–2.5μm spectra and JHK$_S$ photometry (Crowther et al., 2006b). Red optical spectra were recovered for 9/22 stars, including 7/8 showing strong indirect evidence for a binary companion (dust excess, or high and hard X-ray luminosity). I re-derived R and I-band photometry for 18/22 stars by PSF fitting on archival VLT/FORS2 and MPG ESO 2.2m/WFI images respectively, using DAOPHOT. I retrieved optical photometry from the remaining 4 sources from the USNO B1.0 catalogue. Finally, I recovered mid-IR *Spitzer* IRAC photometry from the GLIMPSE survey for 5/22 stars, including 3/6 WC stars showing a dust excess.

I modelled the spectrum of each WR star using the `CMFGEN` model atmosphere code, which delivered a stellar temperature ($T_\star$, at an optical depth $\tau \sim 20$), luminosity, mass-loss rate, hydrogen (WN) or carbon (WC) abundance, and terminal wind velocity. The luminosity of each star was measured by an iterative process, simultaneously with mass-loss rate, temperature, and interstellar reddening (E(B–V)), by reproducing the SED of each object with an appropriately reddened `CMFGEN` model. Two of the WN stars

(Wd1–A & Wd1–B) were modelled as binary systems. I used a Kurucz model of an O7V star, scaled in luminosity, to approximate their companions stars. I took a similar approach when modelling the dust-producing WC stars, including both a scaled Kurucz O7V star and a scaled black-body with temperature 1400 ± 200 K, to approximate the companion star and the dust produced in the stellar wind collision.

I derived a relatively narrow range of stellar luminosities for the WN stars ($\log(L/L_{\odot}) = 5.1$–5.5), and a larger range for the WC stars ($\log(L/L_{\odot}) = 5.0$–5.6). I compared my results to Galactic field samples of WN and WC stars analysed by (Hamann et al., 2006) and (Sander et al., 2012) respectively. The WN stars are H-poor, and have consistent but low luminosities compared with other H-free WNE; the WC stars have similar temperatures to other WC9 stars (Williams et al., 2015), but generally higher luminosities. Compared to WRs in the GC cluster (Martins et al., 2007), the WC9 stars are predominantly more luminous and carbon rich, and the WN stars are very similar in T, L and X_H.

When compared with models of single-star evolution, the WC stars in Wd1 have luminosities consistent with 32–40 $M_{\odot}$ (60 $M_{\odot}$) rotating (non-rotating) models during the predicted WC phase. However, the 60 $M_{\odot}$ non-rotating model has a lifetime shorter than 5 Myr. Of the single-star models surviving to 5 Myr, only the 60 $M_{\odot}$ with rotation shows significant surface C enrichment at this age - at higher temperature and luminosity than measured for the WC stars. Therefore, the WC stars are sub-luminous and too cool when compared to single-star models with the appropriate age and surface composition.

All but ∼5 of the WN stars are sub-luminous compared with model predictions. As they are all H-poor, this low luminosity corresponds to a low current mass. I discussed several scenarios, proposed by Georgy et al. (2012), which may lead to low-L H-free WR stars. The first of these - where stars with initial mass 15–20 $M_{\odot}$ experience enhanced mass-loss as RSGs - can be ruled out in Wd1 due to its youth. The second scenario - stars in the traditional WR initial mass range >25 $M_{\odot}$ experiencing eruptive (LBV) mass-loss during pre-WR evolution - is limited to the initial mass range 40–60 $M_{\odot}$ by the presence of RSGs and absence of WNha stars in the cluster. Such stars do not approach the Eddington limit, hence an unknown mechanism must be at work. However, the presence of at least one LBV in Wd1 is promising. Thirdly, close binary evolution as a means of stripping the H envelopes from evolving stars has the most supporting evidence. Hard X-rays detected in the majority of WN suggest unseen companions, which must be relatively faint (at 1–2.5μm) compared to the WR stars, as spectral fits are adequate without extra flux contributions. Such faint companions are difficult to produce in binary interactions

leading to WR star primaries, and require highly non-conservative mass-transfer, which may occur if initial mass ratios are low (uneven). Late O and early B-type dwarf stars are compatible with the observational constraints placed on any unseen companions to the low-L WN stars. The short period of the only confirmed spectroscopic WR binary in Wd1, Wd1–B, can only be explained if the stars evolved into contact during the main sequence (Petrovic et al., 2005).

Chapter 6

Summary and future work

6.1 The Galactic WR population

In Chapter 2 I presented near-IR absolute magnitude-spectral type calibrations for WN, WC and WO type Wolf-Rayet stars, based on 126 examples with known distances (mostly by cluster or association membership). I derived distances to a further 246 WR stars, by applying these calibrations to the rapidly growing known Galactic population, and presented a 3D map of their locations. I noted that approximately half as many WC stars are available for calibration as cluster/association members than WN, consistent with the findings of Smith & Tombleson (2015) (Fig. 1.17) that WC stars are generally more dispersed. This challenges the idea that WC stars descend directly from WN, which in turn descend from the most massive O-stars. I showed the WR stars to be Cauchy distributed in their separations from the Galactic midplane, with HWHM = 39.2 pc. At least 12 stars reside at $|z| > 300$ pc. The low binary fraction and a preference for WN8 subtypes in this small sample of runaway WRs indicates a binary supernova origin for the most extreme examples.

Exploiting the Galactic metallicity gradient, I compared WR subtype number ratios measured in the inner Galaxy, solar neighbourhood, and outer Galaxy to the predictions of various metallicity-dependent evolutionary models. I measured N_{WC}/N_{WN} to be significantly higher than predicted by single-star models including fast rotation (Meynet & Maeder, 2005), suggesting that lengthened WNL and shortened WC phases resulting from stellar rotation are not widely observed at ($Z \gtrsim Z_{\odot}$). Similarly, the shortened eWNE (H-free) phase predicted by rotating models - particularly at lower metallicity - is not borne out in our measurements. Single-star models without rotation (Eldridge & Vink, 2006) and models that account for close binary interaction (Eldridge et al.,

2008) reproduce our measurements of N_{WC}/N_{WN} more closely, such that a population of non-rotating single-stars and interacting close binaries would be consistent with the measured N_{WC}/N_{WN} at all metallicities considered. However, I caution that the predictions of subytpe number ratios from evolutionary models rely on how model surface properties are interpreted as observable properties, which remains uncertain and overly simplistic (Groh et al., 2014).

In Chapter 3 I presented a toy model of the Galactic WR population, guided by the observed Galactic WR distribution. Using calibrated IR and visual absolute magnitudes, and accounting for the variation in subtypes with Galactic location, I applied a 3D dust distribution to models - spatially congruous with the gas content of the Galaxy - to derive global magnitude distributions for populations of various sizes. Comparison of these model-derived observables to a representative, complete local sample of WR systems ($m_K^{sys} < 8$) indicates a population of $\simeq$800. Using a volume-limited sample ($d < 3$kpc) I estimated that these modelled systems represent $\sim$69% of the total, hence I estimate a Galactic WR population totalling 1200^{+300}_{-100}.

An average WR phase duration of 0.25 Myr is necessary to sustain this estimated population. This exceeds the duration of the putative WR phase in rotating single-star models, and is consistent with the higher end of those predicted by non-rotating single-star and close binary evolution models at solar metallicity (Eldridge & Vink, 2006; Georgy et al., 2012; Eldridge et al., 2008). I also used the favoured model population to estimate a required depth of $K_S < 13.5$ for spectroscopic surveys, to achieve 95% completeness in Galactic WR stars, and to predict the ESA *Gaia* mission will not deliver significant numbers WR star discoveries via low-resolution spectroscopy.

The detected population of $\sim$660 represents $\sim$60% of the total, leaving $\sim$500 undiscovered. In Section 2.4 I described an ultimately unsuccessful observations of IR-selected WR candidates, towards the Perseus spiral arm of the Galaxy. However, these IR colour selection techniques has been shown to deliver WR stars with an efficiency of $\sim$15% towards the inner galaxy (Mauerhan et al., 2011), and have recently been refined (Faherty et al., 2014). Data from deeper near-IR surveys are becoming available (e.g., UKIDSS, Lawrence et al. 2007), which will be a fruitful hunting ground for the remaining Galactic WR stars. With a better understanding of the IR brightness and expected distribution of Galactic WR stars from this work, it will be possible to apply more sophisticated candidate selection techniques. Specifically, Bayesian model comparison could be applied, which could combine models of the WR population with the dominant contaminating population (other IR-excess stars) to fully utilise the information content in the surveys.

Such a technique could be developed in an analogous way to high redshift quasar searches (Mortlock, 2014).

6.2 Oxygen abundances in WC and WO stars

In Chapter 4 I presented *Herschel* PACS scans of the [OIII] 88.36μm fine-structure line in 7 carbon and oxygen-type Wolf-Rayet stars, reporting 4 robust detections. I summarised the stellar parameters of these 7 stars - newly derived in the case of WR 140 - before using line fluxes and upper limits to derive the fractional ionic abundance of O^{2+} in each. To do this I employed the method of DCH00 - an adaptation of BRA88 for clumped winds. I showed that the extent of wind clumping in the outer wind ($10^5 R_\star$) was the dominant uncertainty in calculating ionic abundance from line flux.

With the aim of establishing a total oxygen abundance in each star from the fractional abundance of O^{2+}, I used a *Spitzer* IRS spectrum of one program star WR 23 - containing fine-structure lines of Ne, S, and O - to test the ionisation structure at large radii ($> 10^3\, R_\star$) predicted by a tailored `CMFGEN` model atmosphere. I showed that, in line with predictions, the fractional abundances of other ions at various densites supports O^{2+} being the dominant oxygen ion at the formation density of [OIII] 88.36μm. This scenario was also supported by archival ISO-LWS measurements of [OIII] 51.81μm in WR 11, from which I measured O^{2+} in excellent agreement with [OIII] 88.36μm, despite its higher formation density. Therefore, I was able to interpret the derived O^{2+} abundances as true oxygen abundances in the 4 stars with robust [OIII] 88.36μm detections. Comparing to models of stellar evolution, I found surface oxygen mass fractions to be a factor of 2–5 lower than predicted, with the possible exception of WR 140. I combined carbon abundance determinations from spectral analysis with these oxygen measurements to show that C/O is uniformly higher than predicted by evolutionary models; in accordance with recent studies of cooler WC9 stars (Williams et al., 2015) and hotter WO stars (Tramper et al. 2015, in prep).

Stellar models with and without stellar rotation predict very similar C/O, suggesting that internal mixing by shear turbulence is ineffective once helium begins. This is to be expected if the star has essentially spun-down by the onset of He-burning - a distinct possibility at Galactic metallicity. I argued that the C/O discrepancy would be most easily accounted for by an decrease in the $^{12}C(\alpha,\gamma)^{16}O$ reaction rate assumed in stellar models. Now that a significant number of WC and WO stars have reliable oxygen abundance measurements, it would be timely to create stellar models with different rates

of $^{12}C(\alpha,\gamma)^{16}O$. Pure helium stellar models would be advantageous for several reasons; they have a simple structure (Langer, 1989) allowing large numbers to be produced, and because earlier (H-rich) phases of evolution only affect the C/O ratio indirectly (e.g., mass-loss affecting core sizes and therefore temperatures), bypassing them would not compromise the experiment to determine the most appropriate reaction rate.

To address the key uncertainty in clumping factor at large radii, it will be possible to use the PACS detections of the 88μm and 177μm continuum in WR 11. Schnurr & Crowther (2008) showed that different clumping laws $\big(f(r)\big)$ result in detectable differences in the mid-IR continuum level, due to the ρ^2 dependence of free-free emission. The $\sim$100μm continuum is formed at thousands of stellar radii ($R_\star$), and has rarely been observed in WR stars, making these *Hershcel* observations of critical importance.

A more ambitious goal will be to model the line profiles and strengths of the detected [OIII] 88.36μm lines. Model atmosphere solutions are rarely computed beyond $\sim 10^3 R_\star$. This will require developing `CMFGEN` model atmosphere solutions with appropriate atomic data for the tenuous wind conditions at $\geq 10^5 R_\star$.

6.3 WR stars in Westerlund 1

In Chapter 5 I presented tailored model atmosphere analysis, using `CMFGEN`, for 22 WR stars in the Galactic cluster Westerlund 1. I provided evidence for the cluster being coeval - based on a narrow age spread in PMS stars and a lack of ongoing star formation - with an age of 5 Myr. The distance to Wd1 is well known at 4 ± 0.5 kpc, making it the largest, single-age, spatially resolved massive star population known.

Data

For the analysis I utilised a complete set of 1–2.5μm spectra and JHK$_S$ photometry (Crowther et al., 2006b). I also obtained R and I-band photometry for every WR, largely re-derived from archival imaging. Photometry at these wavelengths was crucial for determining reddening when fitting model SEDs, as they sampled the rapid decline in flux shortward of 1μm. I supplemented these data with red-optical spectra for 9/22 sources, 7 of which showed convincing binary evidence. Emission line strengths in these spectra were important in determining the flux ratio between WR and companion, at wavelengths free from thermal dust emission - produced in colliding-wind WC systems. Mid-IR photometry was essential in accounting for this dust excess, as this dominated

the observed flux longwards of ∼3μm. Unfortunately, *Spitzer* IRAC phtometry was only recoverable for 3/6 dust-producing WC systems.

A complete set of mid-IR photometry for the WC9d systems would be useful for more accurate modelling of their dust components. Without this, line dilution at ∼2μm (shortward of the dust flux peak at 3–5μm) was the only means of assessing the dust contribution, which was often difficult to separate from the companion star flux, especially in cases where only a limited red optical spectrum was available. A basic black body model for the dust component provided satisfactory fits to the limited IRAC photometry available, but it has long been known that dust geometries are more complex, i.e., pinwheels and shells (Tuthill et al., 1999; Marchenko et al., 1999). Complete photometric sampling across 3–20μm, at multiple epochs, would be required to constrain radiative transfer dust models with alternative geometries. Current instruments capable of mid-IR imaging of Wd1 include FORCAST (Faint Object InfraRed Camera for the SOFIA Telescope) (Adams et al., 2010). Furthermore, the accuracy of stellar parameters would benefit greatly from a uniform set of intermediate resolution 0.5–1μm spectra, similar to those already obtained using FORS2. This wavelength range contains a greater number of CIII and CII lines than the 1–2.5μm region, which are the most effective temperature diagnostics in cool WC stars.

Analysis & Results

I modelled the spectrum and SED of each WR, incorporating all available data, including a (scaled) Kurucz O7V spectrum to represent a companion star in 2 WN systems and all 6 WC9d systems; in addition to a simple black-body ($T = 1400 \pm 200$ K) to represent dust emission in the latter. I obtained stellar temperatures, $T_\star$, by matching the relative strengths of HeII/HeI (WN & WC) and CIV/CIII/CII (WC) lines. Absolute line strengths and widths - particularly HeI 1.083μm- were used to constrain mass-loss rate and terminal velocity in each star.

The derived mass-loss rates for WN and WC stars (Fig 5.6) showed good agreement with the empirical $\dot{M}(L)$ relation of (Nugis & Lamers, 2000) - frequently employed to account for stellar mass-loss in evolutionary models. A shallower increase in $\dot{M}$ with L was observed in WC stars compared to WN, as in larger Galactic field samples. However, WN stars showed significant scatter (∼0.5 dex in $\dot{M}$) around the empirical relation.

I found the WN stars in Wd1 to be significantly H-poor compared to similar subtypes in the Galactic field population. They also have consistent, but slightly lower, luminosities on average compared with other Galactic H-free WNE. The WC stars span

a wider range in luminosity than the WN, with three exceeding any other (currently analysed) Galactic WC9 stars. These very luminous WC9 stars also have amongst the coolest temperatures known $\leq 40\,\mathrm{kK}$ - indicating unusually large radii.

The uniformity of WN star parameters (represented by a grouping in the H-R diagram, Fig 5.8), may indicate a dominant formation mechanism for WR stars at this particular age - predominantly resulting in low L and X_H. The lowest luminosity H-free WR stars predicted by single-star stellar evolution models are more luminous than measured in Wd1, and are only seen at the upper age limit of Wd1 ($\sim$6 Myr) if fast stellar rotation is included. The presence of RSGs in Wd1, which have a progenitor mass limit of $\sim 40\,M_{\odot}$ dictated by the Humphrey-Davidson limit, constrains the progenitors of the current WR population to $\sim$40–50 $M_{\odot}$ under single-star evolution. A spectroscopic analysis of the supergiant population needs to be done, as for those in RSG1 for example (Davies et al., 2008). From their luminosity, a good initial mass estimate would be possible, as stellar evolution is less dependent on uncertain mass-loss up to this point. A well-constrained initial mass range for the supergiants would provide a robust lower initial mass limit for the WR population in the case of single-star evolution.

Basic models of binary interaction can reproduce the low X_H and to a lesser extent luminosity of the current WN stars before an age of 5 Myr from (primary) progenitors in the range 30–40 $M_{\odot}$. However, without extremely inefficient mass transfer, it is unlikely that a population of H-free WR stars could be produced without *more* luminous companion stars. This is because the envelope stripped from the WR progenitor (original primary star) would rejuvenate the main-sequence H-burning companion. Uneven initial mass ratios could solve this problem, but are incompatible with massive binary statistics. Therefore, the bottom line is that the majority of H-free WR stars in Wd1 must originate from either 40–50 $M_{\odot}$ single-stars with enhanced mass-loss by some unknown process, or binary interactions featuring inefficient mass transfer.

A thorough search for binary companions to the WRs in Wd1 needs to be undertaken. The only dedicated effort has been the photometric monitoring presented by Bonanos (2007), which was limited to a small ($\sim$1 m) telescope and a short baseline of 17 d. Ritchie et al. (2010) collate archival photometric and spectroscopic observations of the WR stars, finding only 8 with published photometry at two or more epochs, and only 5 with multi-epoch visual spectra.

The wealth of indirect evidence for binary companions to the H-poor WN stars provides ample motivation for a spectroscopic monitoring campaign. Case B mass transfer - the most likely mechanism for envelope striping of the H-poor WN - is limited to systems

with periods shorter than a few hundred days, suggesting a reasonable timescale of line variability in some systems, assuming random inclinations. Detailed binary models have had some success in reproducing isolated WR+O systems (e.g., Petrovic et al. 2005), indicating a mass-transfer efficiency as low as 10% in some massive systems with initial $q{\sim}2$. If binary interactions are responsible for the majority of WN stars in Wd1 - as suggested by their low L and X_H, and X-ray properties - initial mass ratios are required to be unequal ($q \lesssim 0.5$) by CB evolution models, and the unseen companions must be fainter than the WR at optical/near-IR wavelengths. I showed that Early B/late O type stars satisfy these constraints. The detection of such stars in some of the WN systems would provide important constrains to the efficiency of mass-transfer, particularly if orbital solutions could be obtained. A failure to detect *any* companions the WN stars would be significant, and would strongly favour a single-star origin for the majority of the population.

List of Acronyms

AGB Asymptotic Giant Branch

AGN Active Galactic Nucleus

BSG Blue SuperGiant

CMZ Central Molecular Zone

CB Close Binary

CE Common Envelope

EMMI ESO Multi-Mode Instrument

FORS2 FOcal Reducer and low dispersion Spectrograph

FWHM Full Width at Half-Maximum

FWZI Full Width at Zero Intensity

GC Galactic Centre

GMC Giant Molecular Cloud

GRB Gamma Ray Burst

H-R Hertzsprung-Russell

IMF Initial Mass Function

INT Isaac Newton Telecsope

IDS Immediate Dispersion Spectrograph

IGM Inter-Galactic Medium

IR Infra-Red

IRAC Infra-red Array Camera

IRTF Infra-red Telescope Facility

IRS Infra-red Spectrograph

IMF Initial Mass Function

ISM Interstellar Medium

ISO-LWS *Infrared Space Observatory* Long Wavelength Spectrometer

LBG Lyman Break Galaxy

LBV Luminous Blue Variable

LIRG Luminous Infra-Red Galaxy

LMC Large Magellanic Cloud

MS Main Sequence

NTT New Technology Telescope

PACS Photodetector Array Camera and Spectrometer

PMS Pre-Main Sequence

PSF Point Spread Function

RSG Red SuperGiant

RLOF Roche Lobe Over-Flow

SED Spectral Energy Distribution

SFR Star Formation Rate

SuSI2 SUperb-Seeing Imager 2

SMC Small Magellanic Cloud

SN Supernova

SOFI Son OF Isaac

UV Ultra-Violet

VLT Very Large Telescope

WC Carbon-type Wolf-Rayet

Wd1 Westerlund 1

WFI Wide Field Imager

WN Nitrogen-type Wolf-Rayet

WN/C Transition Type Wolf-Rayet

WNE Early-type WN

WNL Late-type WN

WO Oxygen-type Wolf-Rayet

WR Wolf-Rayet

YHG Yellow HyperGiant

Bibliography

Abbott D. C., Lucy L. B., 1985, Astrophysical Journal, 288, 679

Abt H. A., Levy S. G., 1978, Astrophysical Journal Supplements, 36, 241

Adams J. D., Herter T. L., Gull G. E., Schoenwald J., Henderson C. P., Keller L. D., De Buizer J. M., Stacey G. J., Nikola T., 2010, in Society of Photo-Optical Instrumentation Engineers (SPIE) Conference Series Vol. 7735 of Society of Photo-Optical Instrumentation Engineers (SPIE) Conference Series, FORCAST: a first light facility instrument for SOFIA. p. 1

Aggarwal K. M., 1983, Astrophysical Journal Supplements, 52, 387

Anderson L. D., Bania T. M., Balser D. S., Cunningham V., Wenger T. V., Johnstone B. M., Armentrout W. P., 2014, Astrophysical Journal Supplements, 212, 1

Anderson L. S., 1989, Astrophysical Journal, 339, 558

Appenzeller I., Mundt R., 1989, Astronomy and Astrophysics Review, 1, 291

Appenzeller I., Fricke K., Fürtig W., Gässler W., Häfner R., Harke R., Hess H.-J., Hummel W., et al. 1998, The Messenger, 94, 1

Arnal E. M., Cappa C. E., Rizzo J. R., Cichowolski S., 1999, Astronomical Journal, 118, 1798

Arnett W. D., Bahcall J. N., Kirshner R. P., Woosley S. E., 1989, Annual Review of Astronomy and Astrophysics, 27, 629

Baade D., Meisenheimer K., Iwert O., Alonso J., Augusteijn T., Beletic J., Bellemann H., Benesch W., et al. 1999, The Messenger, 95, 15

Baldwin J. A., Phillips M. M., Terlevich R., 1981, Publications of the Astronomical Society of the Pacific, 93, 5

Balser D. S., Rood R. T., Bania T. M., Anderson L. D., 2011, Astrophysical Journal, 738, 27

Barlow M. J., Roche P. F., Aitken D. K., 1988, Monthly Notices of the Royal Astronomical Society, 232, 821

Baume G., Vázquez R. A., Carraro G., 2004, Monthly Notices of the Royal Astronomical Society, 355, 475

Beals C. S., 1929, Monthly Notices of the Royal Astronomical Society, 90, 202

Beals C. S., 1939 Vol. 6 of Trans. IAU, . p. 248

Begelman M. C., Sarazin C. L., 1986, Astrophysical Journal Letters, 302, L59

Benjamin R. A., Churchwell E., Babler B. L., Bania T. M., Clemens D. P., Cohen M., Dickey J. M., Indebetouw R., Jackson J. M. e. a., 2003, Publications of the Astronomical Society of the Pacific, 115, 953

Bestenlehner J. M., Gräfener G., Vink J. S., Najarro F., de Koter A., Sana H., Evans C. J., Crowther P. A., et al. 2014, Astronomy and Astrophysics, 570, A38

Bibby J. L., Crowther P. A., Furness J. P., Clark J. S., 2008, Monthly Notices of the Royal Astronomical Society, 386, L23

Bieging J. H., Abbott D. C., Churchwell E. B., 1982, Astrophysical Journal, 263, 207

Bilir S., Karaali S., Ak S., dağtekin N. D., Önal Ö., Yaz E., Coşkunoğlu B., Cabrera-Lavers A., 2011, Monthly Notices of the Royal Astronomical Society, 417, 2230

Bissaldi E., Calura F., Matteucci F., Longo F., Barbiellini G., 2007, Astronomy and Astrophysics, 471, 585

Blaauw A., 1961, Bulletin of the Astronomical Institutes of the Netherlands, 15, 265

Bohannan B., Crowther P. A., 1999, Astrophysical Journal, 511, 374

Bohlin R. C., Savage B. D., Drake J. F., 1978, Astrophysical Journal, 224, 132

Boily C. M., Kroupa P., 2003, Monthly Notices of the Royal Astronomical Society, 338, 665

Bonanos A. Z., 2007, Astronomical Journal, 133, 2696

Borgman J., Koornneef J., Slingerland J., 1970, Astronomy and Astrophysics, 4, 248

Bouret J.-C., Lanz T., Hillier D. J., 2005, Astronomy and Astrophysics, 438, 301

Bournaud F., Elmegreen B. G., Teyssier R., Block D. L., Puerari I., 2010, Monthly Notices of the Royal Astronomical Society, 409, 1088

Bouwens R. J., Illingworth G. D., Oesch P. A., Trenti M., Labbé I., Bradley L., Carollo M., van Dokkum P. G., Gonzalez V., Holwerda B., Franx M., Spitler L., Smit R., Magee D., 2015, Astrophysical Journal, 803, 34

Brandner W., Clark J. S., Stolte A., Waters R., Negueruela I., Goodwin S. P., 2008, Astronomy and Astrophysics, 478, 137

Braun H., Langer N., 1995, Astronomy and Astrophysics, 297, 483

Bressert E., Bastian N., Gutermuth R., Megeath S. T., Allen L., Evans II N. J., Rebull L. M., Hatchell J., Johnstone D., Bourke T. L., Cieza L. A., Harvey P. M., Merin B., Ray T. P., Tothill N. F. H., 2010, Monthly Notices of the Royal Astronomical Society, 409, L54

Breysacher J., Azzopardi M., Testor G., 1999, Astronomy and Astrophysics Supplements, 137, 117

Brinchmann J., Kunth D., Durret F., 2008, Astronomy and Astrophysics, 485, 657

Bronfman L., Casassus S., May J., Nyman L.-Å., 2000, Astronomy and Astrophysics, 358, 521

Buat V., Xu C., 1996, Astronomy and Astrophysics, 306, 61

Calzetti D., 2001, New Astronomy Reviews, 45, 601

Campbell W. W., 1894, Astronomy and Astro-Physics (formerly The Sidereal Messenger), 13, 448

Cantiello M., Yoon S.-C., Langer N., Livio M., 2007, Astronomy and Astrophysics, 465, L29

Cappa C. E., Goss W. M., Niemela V. S., Ostrov P. G., 1999, Astronomical Journal, 118, 948

Cappa C. E., Vasquez J., Pineault S., Cichowolski S., 2010, Monthly Notices of the Royal Astronomical Society, 403, 387

Cardelli J. A., Clayton G. C., Mathis J. S., 1989, Astrophysical Journal, 345, 245

Carraro G., Turner D., Majaess D., Baume G., 2012, in IAU Symposium Vol. 289, The distance to the young open cluster Westerlund 2

Castelli F., Kurucz R. L., 2004, in Piskunov, N. and Weiss, W. W. and Gray, D. F., eds, Modelling of Stellar Atmospheres Vol. 210 of IAU Symposium, New Grids of ATLAS9 Model Atmospheres. p. 20P

Castor J. I., Abbott D. C., Klein R. I., 1975, Astrophysical Journal, 195, 157

Chabrier G., 2003, Publications of the Astronomical Society of the Pacific, 115, 763

Chapman J. M., Leitherer C., Koribalski B., Bouter R., Storey M., 1999, Astrophysical Journal, 518, 890

Chené A.-N., Borissova J., Bonatto C., Majaess D. J., Baume G., Clarke J. R. A., Kurtev R., Schnurr O. e. a., 2013, Astronomy and Astrophysics, 549, A98

Chené A.-N., Moffat A. F. J., St-Louis N., Schnurr O., Crowther P. A., Artiguau E., Alecian E., Wade G. A., submitted 2014, Monthly Notices of the Royal Astronomical Society

Chiappini C., Frischknecht U., Meynet G., Hirschi R., Barbuy B., Pignatari M., Decressin T., Maeder A., 2011, Nature, 472, 454

Chieffi A., Limongi M., 2013, Astrophysical Journal, 764, 21

Chini R., Hoffmeister V. H., Nasseri A., Stahl O., Zinnecker H., 2012, Monthly Notices of the Royal Astronomical Society, 424, 1925

Chiosi C., Nasi E., Sreenivasan S. R., 1978, Astronomy and Astrophysics, 63, 103

Chiosi C., Maeder A., 1986, Annual Review of Astronomy and Astrophysics, 24, 329

Chomiuk L., Povich M. S., 2011, Astronomical Journal, 142, 197

Claeys J. S. W., de Mink S. E., Pols O. R., Eldridge J. J., Baes M., 2011, Astronomy and Astrophysics, 528, A131

Clark J. S., Negueruela I., 2002, Astronomy and Astrophysics, 396, L25

Clark J. S., Negueruela I., 2004, Astronomy and Astrophysics, 413, L15

Clark J. S., Negueruela I., Crowther P. A., Goodwin S. P., 2005, Astronomy and Astrophysics, 434, 949

Clark J. S., Muno M. P., Negueruela I., Dougherty S. M., Crowther P. A., Goodwin S. P., de Grijs R., 2008, Astronomy and Astrophysics, 477, 147

Clark J. S., Ritchie B. W., Negueruela I., 2010, Astronomy and Astrophysics, 514, A87

Clark J. S., Ritchie B. W., Najarro F., Langer N., Negueruela I., 2014, Astronomy and Astrophysics, 565, A90

Cohen M., Parker Q. A., Green A. J., 2005, Monthly Notices of the Royal Astronomical Society, 360, 1439

Cole S., Lacey C. G., Baugh C. M., Frenk C. S., 2000, Monthly Notices of the Royal Astronomical Society, 319, 168

Conti P. S., 1975, Memoires of the Societe Royale des Sciences de Liege, 9, 193

Conti P. S., 1984, in Maeder A., Renzini A., eds, Observational Tests of the Stellar Evolution Theory Vol. 105 of IAU Symposium, Basic Observational Constraints on the Evolution of Massive Stars. p. 233

Conti P. S., 1988, NASA Special Publication, 497, 81

Conti P. S., Massey P., 1989, Astrophysical Journal, 337, 251

Conti P. S., Massey P., Vreux J.-M., 1990, Astrophysical Journal, 354, 359

Conti P., Crowther P., Leitherer C., 2008, From Luminous Hot Stars to Starburst Galaxies. Cambridge Astrophysics, Cambridge University Press

Corti M., Bosch G., Niemela V., 2007, Astronomy and Astrophysics, 467, 137

Cotera A. S., Simpson J. P., Erickson E. F., Colgan S. W. J., Burton M. G., Allen D. A., 1999, Astrophysical Journal, 510, 747

Crowther P. A., Hillier D. J., Smith L. J., 1995a, Astronomy and Astrophysics, 293, 172

Crowther P. A., Smith L. J., Hillier D. J., Schmutz W., 1995b, Astronomy and Astrophysics, 293, 427

Crowther P. A., Smith L. J., Hillier D. J., 1995c, Astronomy and Astrophysics, 302, 457

Crowther P. A., Smith L. J., Willis A. J., 1995d, Astronomy and Astrophysics, 304, 269

Crowther P. A., Smith L. J., 1996, Astronomy and Astrophysics, 305, 541

Crowther P. A., 1997, Monthly Notices of the Royal Astronomical Society, 290, L59

Crowther P. A., De Marco O., Barlow M. J., 1998, Monthly Notices of the Royal Astronomical Society, 296, 367

Crowther P. A., Fullerton A. W., Hillier D. J., Brownsberger K., Dessart L., Willis A. J., De Marco O., Barlow M. J., Hutchings J. B., Massa D. L., Morton D. C., Sonneborn G., 2000, Astrophysical Journal Letters, 538, L51

Crowther P. A., Dessart L., Hillier D. J., Abbott J. B., Fullerton A. W., 2002, Astronomy and Astrophysics, 392, 653

Crowther P. A., 2003, Astrophysics and Space Science, 285, 677

Crowther P. A., Morris P. W., Smith J. D., 2006a, Astrophysical Journal, 636, 1033

Crowther P. A., Hadfield L. J., Clark J. S., Negueruela I., Vacca W. D., 2006b, Monthly Notices of the Royal Astronomical Society, 372, 1407

Crowther P. A., 2007, Annual Review of Astronomy and Astrophysics, 45, 177

Crowther P. A., Walborn N. R., 2011, Monthly Notices of the Royal Astronomical Society, 416, 1311

Cucchiara A., Levan A. J., Fox D. B., Tanvir N. R., Ukwatta T. N., Berger E., Krühler T., Küpcü Yoldaş A., et al. 2011, Astrophysical Journal, 736, 7

Currie T., Hernandez J., Irwin J., Kenyon S. J., Tokarz S., Balog Z., Bragg A., Berlind P., Calkins M., 2010, Astrophysical Journal Supplements, 186, 191

Dahlen T., Strolger L.-G., Riess A. G., Mattila S., Kankare E., Mobasher B., 2012, Astrophysical Journal, 757, 70

Dale J. E., Bonnell I. A., Clarke C. J., Bate M. R., 2005, Monthly Notices of the Royal Astronomical Society, 358, 291

Dame T. M., Hartmann D., Thaddeus P., 2001, Astrophysical Journal, 547, 792

Davies B., Figer D. F., Law C. J., Kudritzki R.-P., Najarro F., Herrero A., MacKenty J. W., 2008, Astrophysical Journal, 676, 1016

Davies B., Clark J. S., Trombley C., Figer D. F., Najarro F., Crowther P. A., Kudritzki R.-P., Thompson M., Urquhart J. S., Hindson L., 2012, Monthly Notices of the Royal Astronomical Society, 419, 1871

Davis A. B., Moffat A. F. J., Niemela V. S., 1981, Astrophysical Journal, 244, 528

De Becker M., Raucq F., 2013, Astronomy and Astrophysics, 558, A28

de Jager C., Nieuwenhuijzen H., van der Hucht K. A., 1988, Astronomy and Astrophysics Supplements, 72, 259

de La Chevrotière A., Moffat A. F. J., Chené A.-N., 2011, Monthly Notices of the Royal Astronomical Society, 411, 635

de la Fuente D., Najarro F., Trombley C., Davies B., Figer D. F., 2015, Astronomy and Astrophysics, 575, A10

De Marco O., Schmutz W., 1999, Astronomy and Astrophysics, 345, 163

De Marco O., Schmutz W., Crowther P. A., Hillier D. J., Dessart L., de Koter A., Schweickhardt J., 2000, Astronomy and Astrophysics, 358, 187

de Mink S. E., Pols O. R., Hilditch R. W., 2007, Astronomy and Astrophysics, 467, 1181

de Mink S. E., Langer N., Izzard R. G., 2011, Bulletin de la Societe Royale des Sciences de Liege, 80, 543

de Mink S. E., Langer N., Izzard R. G., Sana H., de Koter A., 2013, Astrophysical Journal, 764, 166

de Rossi M. E., Tissera P. B., Pedrosa S. E., 2010, Astronomy and Astrophysics, 519, A89

de Wit W. J., Testi L., Palla F., Zinnecker H., 2005, Astronomy and Astrophysics, 437, 247

Dearborn D. S. P., Blake J. B., 1979, Astrophysical Journal, 231, 193

Depew K., Parker Q. A., Miszalski B., De Marco O., Frew D. J., Acker A., Kovacevic A. V., Sharp R. G., 2011, Monthly Notices of the Royal Astronomical Society, 414, 2812

Dessart L., Crowther P. A., Hillier D. J., Willis A. J., Morris P. W., van der Hucht K. A., 2000, Monthly Notices of the Royal Astronomical Society, 315, 407

Divan L., Burnichon-Prévot M.-L., 1988, NASA Special Publication, 497, 1

Djurašević G., Zakirov M., Eshankulova M., Erkapić S., 2001, Astronomy and Astrophysics, 374, 638

Dobbs C. L., Burkert A., Pringle J. E., 2011, Monthly Notices of the Royal Astronomical Society, 417, 1318

Domiciano de Souza A., Kervella P., Jankov S., Vakili F., Ohishi N., Nordgren T. E., Abe L., 2005, Astronomy and Astrophysics, 442, 567

Dong H., Wang Q. D., Morris M. R., 2012, Monthly Notices of the Royal Astronomical Society, 425, 884

Doran E. I., Crowther P. A., de Koter A., Evans C. J., McEvoy C., Walborn N. R., Bastian N., Bestenlehner J. M., et al. 2013, Astronomy and Astrophysics, 558, A134

Dougherty S. M., Williams P. M., van der Hucht K. A., Bode M. F., Davis R. J., 1996, Monthly Notices of the Royal Astronomical Society, 280, 963

Dougherty S. M., Williams P. M., Pollacco D. L., 2000, Monthly Notices of the Royal Astronomical Society, 316, 143

Dougherty S. M., Clark J. S., 2007, ArXiv e-prints 0705.0971

Dray L. M., Dale J. E., Beer M. E., Napiwotzki R., King A. R., 2005, Monthly Notices of the Royal Astronomical Society, 364, 59

Dray L. M., Tout C. A., Karakas A. I., Lattanzio J. C., 2003, Monthly Notices of the Royal Astronomical Society, 338, 973

Drew J. E., Barlow M. J., Unruh Y. C., Parker Q. A., Wesson R., Pierce M. J., Masheder M. R. W., Phillipps S., 2004, Monthly Notices of the Royal Astronomical Society, 351, 206

Drissen L., Lamontagne R., Moffat A. F. J., Bastien P., Seguin M., 1986, Astrophysical Journal, 304, 188

Eddington A. S., 1924, Monthly Notices of the Royal Astronomical Society, 84, 308

Eikenberry S. S., Matthews K., LaVine J. L., Garske M. A., Hu D., Jackson M. A., Patel S. G., Barry D. J., Colonno M. R., Houck J. R., Wilson J. C., Corbel S., Smith J. D., 2004, Astrophysical Journal, 616, 506

Ekström S., Georgy C., Eggenberger P., Meynet G., Mowlavi N., Wyttenbach A., Granada A., Decressin T., Hirschi R., Frischknecht U., Charbonnel C., Maeder A., 2012, Astronomy and Astrophysics, 537, A146

Eldridge J. J., Tout C. A., 2004, Monthly Notices of the Royal Astronomical Society, 353, 87

Eldridge J. J., Vink J. S., 2006, Astronomy and Astrophysics, 452, 295

Eldridge J. J., Izzard R. G., Tout C. A., 2008, Monthly Notices of the Royal Astronomical Society, 384, 1109

Eldridge J. J., 2009, Monthly Notices of the Royal Astronomical Society, 400, L20

Eldridge J. J., Fraser M., Smartt S. J., Maund J. R., Crockett R. M., 2013, Monthly Notices of the Royal Astronomical Society, 436, 774

Elmegreen B. G., 1998, in Woodward C. E., Shull J. M., Thronson Jr. H. A., eds, Origins Vol. 148 of Astronomical Society of the Pacific Conference Series, Observations and Theory of Dynamical Triggers for Star Formation. p. 150

Espinoza P., Selman F. J., Melnick J., 2009, Astronomy and Astrophysics, 501, 563

Esteban C., Vilchez J. M., Smith L. J., Clegg R. E. S., 1992, Astronomy and Astrophysics, 259, 629

Esteban C., Rosado M., 1995, Astronomy and Astrophysics, 304, 491

Fahed R., Moffat A. F. J., Zorec J., Eversberg T., Chené A. N., Alves F., Arnold W., Bergmann T., et al. 2011, Monthly Notices of the Royal Astronomical Society, 418, 2

Fahed R., Moffat A. F. J., 2012, Monthly Notices of the Royal Astronomical Society, 424, 1601

Faherty J. K., Shara M. M., Zurek D., Kanarek G., Moffat A. F. J., 2014, Astronomical Journal, 147, 115

Fang M., van Boekel R., King R. R., Henning T., Bouwman J., Doi Y., Okamoto Y. K., Roccatagliata V., Sicilia-Aguilar A., 2012, Astronomy and Astrophysics, 539, A119

Ferrière K., 2008, Astronomische Nachrichten, 329, 992

Figer D. F., McLean I. S., Najarro F., 1997, Astrophysical Journal, 486, 420

Figer D. F., McLean I. S., Morris M., 1999, Astrophysical Journal, 514, 202

Fleming W. P. S., Pickering E. C., 1912, Annals of Harvard College Observatory, 56, 165

Foellmi C., Moffat A. F. J., Guerrero M. A., 2003, Monthly Notices of the Royal Astronomical Society, 338, 360

Fowler W. A., 1984, Science, 226, 922

Freyhammer L. M., Clausen J. V., Arentoft T., Sterken C., 2001, Astronomy and Astrophysics, 369, 561

Friend D. B., Abbott D. C., 1986, Astrophysical Journal, 311, 701

Fritz T. K., Gillessen S., Dodds-Eden K., Lutz D., Genzel R., Raab W., Ott T., Pfuhl O., Eisenhauer F., Yusef-Zadeh F., 2011, Astrophysical Journal, 737, 73

Frost C. A., Lattanzio J. C., 1996, Astrophysical Journal, 473, 383

Fujii M. S., Portegies Zwart S., 2011, Science, 334, 1380

Fullerton A. W., Massa D. L., Prinja R. K., 2006, Astrophysical Journal, 637, 1025

Fynbo H. O. U., Diget C. A., Bergmann U. C., Borge M. J. G., Cederkäll J., Dendooven P., Fraile L. M., Franchoo S. e. a., ISOLDE Collaboration 2005, Nature, 433, 136

Galama T. J., Vreeswijk P. M., van Paradijs J., Kouveliotou C., Augusteijn T., Böhnhardt H., Brewer J. P., Doublier V., et al. 1998, Nature, 395, 670

Gamen R., Gosset E., Morrell N., Niemela V., Sana H., Nazé Y., Rauw G., Barbá R., Solivella G., 2006, Astronomy and Astrophysics, 460, 777

Gamen R. C., Fernández-Lajús E., Niemela V. S., Barbá R. H., 2009, Astronomy and Astrophysics, 506, 1269

Gamen R., Collado A., Barbá R., Chené A.-N., St-Louis N., 2014, Astronomy and Astrophysics, 562, A13

Gamow G., 1943, Astrophysical Journal, 98, 500

Gaposchkin C. P., 1930, Harvard Observatory Monographs, 3, 1

Garcia-Segura G., Mac Low M.-M., Langer N., 1996a, Astronomy and Astrophysics, 305, 229

Garcia-Segura G., Langer N., Mac Low M.-M., 1996b, Astronomy and Astrophysics, 316, 133

Garmany C. D., Conti P. S., Massey P., 1980, Astrophysical Journal, 242, 1063

Garmany C. D., Stencel R. E., 1992, Astronomy and Astrophysics Supplements, 94, 211

Gaskell C. M., Cappellaro E., Dinerstein H. L., Garnett D. R., Harkness R. P., Wheeler J. C., 1986, Astrophysical Journal Letters, 306, L77

Gayley K. G., 1995, Astrophysical Journal, 454, 410

Georgelin Y. M., Georgelin Y. P., 1976, Astronomy and Astrophysics, 49, 57

Georgy C., Ekström S., Meynet G., Massey P., Levesque E. M., Hirschi R., Eggenberger P., Maeder A., 2012, Astronomy and Astrophysics, 542, A29

Gilbert A. M., Graham J. R., 2007, Astrophysical Journal, 668, 168

Gillessen S., Eisenhauer F., Fritz T. K., Pfuhl O., Ott T., Genzel R., 2013, in de Grijs R., ed., IAU Symposium Vol. 289 of IAU Symposium, The distance to the Galactic Center. pp 29–35

González-Solares E. A., Walton N. A., Greimel R., Drew J. E., Irwin M. J., Sale S. E., Andrews K., Aungwerojwit A., Barlow M. J., et al. 2008, Monthly Notices of the Royal Astronomical Society, 388, 89

Gosset E., Royer P., Rauw G., Manfroid J., Vreux J.-M., 2001, Monthly Notices of the Royal Astronomical Society, 327, 435

Grafener G., Hamann W.-R., Hillier D. J., Koesterke L., 1998, Astronomy and Astrophysics, 329, 190

Gräfener G., Koesterke L., Hamann W.-R., 2002, Astronomy and Astrophysics, 387, 244

Gräfener G., Hamann W.-R., 2005, Astronomy and Astrophysics, 432, 633

Gräfener G., Hamann W.-R., 2008, Astronomy and Astrophysics, 482, 945

Gräfener G., Vink J. S., de Koter A., Langer N., 2011, Astronomy and Astrophysics, 535, A56

Gräfener G., Owocki S. P., Vink J. S., 2012, Astronomy and Astrophysics, 538, A40

Gray D., 2005, The Observation and Analysis of Stellar Photospheres. Cambridge University Press

Groh J. H., Damineli A., Teodoro M., Barbosa C. L., 2006, Astronomy and Astrophysics, 457, 591

Groh J. H., Meynet G., Ekström S., Georgy C., 2014, Astronomy and Astrophysics, 564, A30

Gvaramadze V. V., Weidner C., Kroupa P., Pflamm-Altenburg J., 2012, Monthly Notices of the Royal Astronomical Society, 424, 3037

Hadfield L. J., van Dyk S. D., Morris P. W., Smith J. D., Marston A. P., Peterson D. E., 2007, Monthly Notices of the Royal Astronomical Society, 376, 248

Hainich R., Rühling U., Todt H., Oskinova L. M., Liermann A., Gräfener G., Foellmi C., Schnurr O., Hamann W.-R., 2014, Astronomy and Astrophysics, 565, A27

Hamann W.-R., Schmutz W., 1987, Astronomy and Astrophysics, 174, 173

Hamann W.-R., Gräfener G., Liermann A., 2006, Astronomy and Astrophysics, 457, 1015

Hanson M. M., Kurtev R., Borissova J., Georgiev L., Ivanov V. D., Hillier D. J., Minniti D., 2010, Astronomy and Astrophysics, 516, A35

Harayama Y., Eisenhauer F., Martins F., 2008, Astrophysical Journal, 675, 1319

Harries T. J., Monnier J. D., Symington N. H., Kurosawa R., 2004, Monthly Notices of the Royal Astronomical Society, 350, 565

Heckman T. M., Robert C., Leitherer C., Garnett D. R., van der Rydt F., 1998, Astrophysical Journal, 503, 646

Heckman T. M., Lehnert M. D., Strickland D. K., Armus L., 2000, Astrophysical Journal Supplements, 129, 493

Heger A., Fryer C. L., Woosley S. E., Langer N., Hartmann D. H., 2003, Astrophysical Journal, 591, 288

Heger A., Woosley S. E., Spruit H. C., 2005, Astrophysical Journal, 626, 350

Henry R. B. C., Edmunds M. G., Köppen J., 2000, Astrophysical Journal, 541, 660

Herald J. E., Hillier D. J., Schulte-Ladbeck R. E., 2001, Astrophysical Journal, 548, 932

Herrero A., Kudritzki R. P., Vilchez J. M., Kunze D., Butler K., Haser S., 1992, Astronomy and Astrophysics, 261, 209

Hill G. M., Moffat A. F. J., St-Louis N., 2002, Monthly Notices of the Royal Astronomical Society, 335, 1069

Hillenbrand L. A., Massey P., Strom S. E., Merrill K. M., 1993, Astronomical Journal, 106, 1906

Hillier D. J., 1987, Astrophysical Journal Supplements, 63, 947

Hillier D. J., 1991, Astronomy and Astrophysics, 247, 455

Hillier D. J., Miller D. L., 1998, Astrophysical Journal, 496, 407

Hillier D. J., Miller D. L., 1999, Astrophysical Journal, 519, 354

Hillier D. J., Lanz T., Heap S. R., Hubeny I., Smith L. J., Evans C. J., Lennon D. J., Bouret J. C., 2003, Astrophysical Journal, 588, 1039

Hiltner W. A., Schild R. E., 1966, Astrophysical Journal, 143, 770

Homeier N. L., Blum R. D., Pasquali A., Conti P. S., Damineli A., 2003, Astronomy and Astrophysics, 408, 153

Hopewell E. C., Barlow M. J., Drew J. E., Unruh Y. C., Parker Q. A., Pierce M. J., Crowther P. A., Knigge C., Phillipps S., Zijlstra A. A., 2005, Monthly Notices of the Royal Astronomical Society, 363, 857

Hopkins P. F., Quataert E., Murray N., 2011, Monthly Notices of the Royal Astronomical Society, 417, 950

Hopkins P. F., Kereš D., Oñorbe J., Faucher-Giguère C.-A., Quataert E., Murray N., Bullock J. S., 2014, Monthly Notices of the Royal Astronomical Society, 445, 581

Howarth I. D., 1983, Monthly Notices of the Royal Astronomical Society, 203, 301

Howarth I. D., Schmutz W., 1992, Astronomy and Astrophysics, 261, 503

Howarth I. D., Schmutz W., 1995, Astronomy and Astrophysics, 294, 529

Hubble E., Sandage A., 1953, Astrophysical Journal, 118, 353

Humphreys R. M., Davidson K., 1979, Astrophysical Journal, 232, 409

Humphreys R. M., Davidson K., 1994, Publications of the Astronomical Society of the Pacific, 106, 1025

Humphreys R. M., Larsen J. A., 1995, Astronomical Journal, 110, 2183

Humphreys R. M., Smith N., Davidson K., Jones T. J., Gehrz R. T., Mason C. G., Hayward T. L., Houck J. R., Krautter J., 1997, Astronomical Journal, 114, 2778

Hur H., Sung H., Bessell M. S., 2012, Astronomical Journal, 143, 41

Imbriani G., Limongi M., Gialanella L., Terrasi F., Straniero O., Chieffi A., 2001, Astrophysical Journal, 558, 903

Indebetouw R., Mathis J. S., Babler B. L., Meade M. R., Watson C., Whitney B. A., Wolff M. J., Wolfire M. G., Cohen M. e. a., 2005, Astrophysical Journal, 619, 931

Ishii M., Ueno M., Kato M., 1999, Publications of the Astronomical Society of Japan, 51, 417

Isserstedt J., Moffat A. F. J., Niemela V. S., 1983, Astronomy and Astrophysics, 126, 183

Johnson H. M., Hogg D. E., 1965, Astrophysical Journal, 142, 1033

Jones C. E., Tycner C., Smith A. D., 2011, Astronomical Journal, 141, 150

Jordi C., Gebran M., Carrasco J. M., de Bruijne J., Voss H., Fabricius C., Knude J., Vallenari A., Kohley R., Mora A., 2010, Astronomy and Astrophysics, 523, A48

Katz N., Weinberg D. H., Hernquist L., 1996, Astrophysical Journal Supplements, 105, 19

Kendrew S., Simpson R., Bressert E., Povich M. S., Sherman R., Lintott C. J., Robitaille T. P., Schawinski K., Wolf-Chase G., 2012, Astrophysical Journal, 755, 71

Kennicutt Jr. R. C., 1998, Annual Review of Astronomy and Astrophysics, 36, 189

Kennicutt R. C., Evans N. J., 2012, Annual Review of Astronomy and Astrophysics, 50, 531

Kettner K. U., Becker H. W., Buchmann L., Görres J., Kräwinkel H., Rolfs C., Schmalbrock P., Trautvetter H. P., Vlieks A., 1982, Zeitschrift fur Physik A Hadrons and Nuclei, 308, 73

Kimeswenger S., Weinberger R., 1989, Astronomy and Astrophysics, 209, 51

Kingsburgh R. L., Barlow M. J., Storey P. J., 1995, Astronomy and Astrophysics, 295, 75

Kippenhahn R., Weigert A., 1967, Zeitschrift für Astrophysik, 65, 251

Kirkpatrick J. D., Henry T. J., McCarthy Jr. D. W., 1991, Astrophysical Journal Supplements, 77, 417

Kistler M. D., Yüksel H., Beacom J. F., Hopkins A. M., Wyithe J. S. B., 2009, Astrophysical Journal Letters, 705, L104

Knödlseder J., Cerviño M., Le Duigou J.-M., Meynet G., Schaerer D., von Ballmoos P., 2002, Astronomy and Astrophysics, 390, 945

Koesterke L., Hamann W.-R., 1995, Astronomy and Astrophysics, 299, 503

Koornneef J., 1977, Astronomy and Astrophysics, 55, 469

Kothes R., Dougherty S. M., 2007, Astronomy and Astrophysics, 468, 993

Koumpia E., Bonanos A. Z., 2012, Astronomy and Astrophysics, 547, A30

Krabbe A., Genzel R., Eckart A., Najarro F., Lutz D., Cameron M., Kroker H., Tacconi-Garman L. E., Thatte N., Weitzel L., Drapatz S., Geballe T., Sternberg A., Kudritzki R., 1995, Astrophysical Journal Letters, 447, L95

Kratter K. M., Matzner C. D., Krumholz M. R., Klein R. I., 2010, Astrophysical Journal, 708, 1585

Kroupa P., 2001, Monthly Notices of the Royal Astronomical Society, 322, 231

Kroupa P., Weidner C., 2003, Astrophysical Journal, 598, 1076

Krumholz M. R., Klein R. I., McKee C. F., Offner S. S. R., Cunningham A. J., 2009, Science, 323, 754

Kudritzki R.-P., Puls J., 2000, Annual Review of Astronomy and Astrophysics, 38, 613

Kudryavtseva N., Brandner W., Gennaro M., Rochau B., Stolte A., Andersen M., Da Rio N., Henning T., Tognelli E., Hogg D., Clark S., Waters R., 2012, Astrophysical Journal Letters, 750, L44

Kuiper G. P., 1938, Astrophysical Journal, 88, 472

Kunz R., Fey M., Jaeger M., Mayer A., Hammer J. W., Staudt G., Harissopulos S., Paradellis T., 2002, Astrophysical Journal, 567, 643

Kurosawa R., Hillier D. J., Pittard J. M., 2002, Astronomy and Astrophysics, 388, 957

Kurtev R., Borissova J., Georgiev L., Ortolani S., Ivanov V. D., 2007, Astronomy and Astrophysics, 475, 209

Lada C. J., Lada E. A., 2003, Annual Review of Astronomy and Astrophysics, 41, 57

Lamers H. J. G. L. M., Maeder A., Schmutz W., Cassinelli J. P., 1991, Astrophysical Journal, 368, 538

Lamers H. J. G. L. M., Leitherer C., 1993, Astrophysical Journal, 412, 771

Langer N., El Eid M. F., 1986, Astronomy and Astrophysics, 167, 265

Langer N., 1987, Astronomy and Astrophysics, 171, L1

Langer N., 1989, Astronomy and Astrophysics, 210, 93

Langer N., 1991, Astronomy and Astrophysics, 248, 531

Langer N., Hamann W.-R., Lennon M., Najarro F., Pauldrach A. W. A., Puls J., 1994, Astronomy and Astrophysics, 290, 819

Langer N., Maeder A., 1995, Astronomy and Astrophysics, 295, 685

Langer N., 2012, Annual Review of Astronomy and Astrophysics, 50, 107

Lawrence A., Warren S. J., Almaini O., Edge A. C., Hambly N. C., Jameson R. F., Lucas P., Casali M., et al. 2007, Monthly Notices of the Royal Astronomical Society, 379, 1599

Lejeune T., Schaerer D., 2001, Astronomy and Astrophysics, 366, 538

Lépine S., Moffat A. F. J., 1999, Astrophysical Journal, 514, 909

Lépine S., Wallace D., Shara M. M., Moffat A. F. J., Niemela V. S., 2001, Astronomical Journal, 122, 3407

Liermann A., Hamann W.-R., Oskinova L. M., 2009, Astronomy and Astrophysics, 494, 1137

Littlefield C., Garnavich P., "Howie" Marion G. H., Vinkó J., McClelland C., Rettig T., Wheeler J. C., 2012, Astronomical Journal, 143, 136

Lockwood G. W., 1974, Astrophysical Journal, 193, 103

Longmore S. N., Bally J., Testi L., Purcell C. R., Walsh A. J., Bressert E., Pestalozzi M., Molinari S., Ott J., Cortese L., Battersby C., Murray N., Lee E., Kruijssen J. M. D., Schisano E., Elia D., 2013, Monthly Notices of the Royal Astronomical Society, 429, 987

Lonsdale C. J., Helou G., 1985, in Bulletin of the American Astronomical Society Vol. 17 of Bulletin of the American Astronomical Society, Star Formation Rates in Disk Galaxies: Comparison of Far-infrared and H-alpha Emission. p. 612

López-Sánchez Á. R., Esteban C., 2010, Astronomy and Astrophysics, 517, A85

Lortet M. C., Testor G., Niemela V., 1984, Astronomy and Astrophysics, 140, 24

Lucy L. B., Solomon P. M., 1970, Astrophysical Journal, 159, 879

Lucy L. B., Abbott D. C., 1993, Astrophysical Journal, 405, 738

Lundström I., Stenholm B., 1984, Astronomy and Astrophysics Supplements, 58, 163

Madau P., Dickinson M., 2014, Annual Review of Astronomy and Astrophysics, 52, 415

Maeder A., 1980, Astronomy and Astrophysics, 92, 101

Maeder A., Lequeux J., Azzopardi M., 1980, Astronomy and Astrophysics, 90, L17

Maeder A., 1981, Astronomy and Astrophysics, 102, 401

Maeder A., Lequeux J., 1982, Astronomy and Astrophysics, 114, 409

Maeder A., Meynet G., 1987, Astronomy and Astrophysics, 182, 243

Maeder A., Meynet G., 1989, Astronomy and Astrophysics, 210, 155

Maeder A., Meynet G., 2000, Annual Review of Astronomy and Astrophysics, 38, 143

Maíz Apellániz J., Walborn N. R., Morrell N. I., Niemela V. S., Nelan E. P., 2007, Astrophysical Journal, 660, 1480

Maíz Apellániz J., Sota A., Morrell N. I., Barbá R. H., Walborn N. R., Alfaro E. J., Gamen R. C., Arias J. I., Gallego Calvente A. T., 2013, in Massive Stars: From alpha to Omega First whole-sky results from the Galactic O-Star Spectroscopic Survey. p. 198

Makii H., Nagai Y., Shima T., Segawa M., Mishima K., Ueda H., Igashira M., Ohsaki T., 2009, Phys. Rev. C, 80, 065802

Malchenko S. L., Tarasov A. E., 2009, Astrophysics, 52, 235

Marchenko S. V., Moffat A. F. J., Koenigsberger G., 1994, Astrophysical Journal, 422, 810

Marchenko S. V., Moffat A. F. J., van der Hucht K. A., Seggewiss W., Schrijver H., Stenholm B., Lundstrom I., Setia Gunawan D. Y. A., Sutantyo W., van den Heuvel E. P. J., de Cuyper J.-P., Gomez A. E., 1998a, Astronomy and Astrophysics, 331, 1022

Marchenko S. V., Moffat A. F. J., Eenens P. R. J., 1998b, Publications of the Astronomical Society of the Pacific, 110, 1416

Marchenko S. V., Moffat A. F. J., Grosdidier Y., 1999, Astrophysical Journal, 522, 433

Marchenko S. V., Moffat A. F. J., Crowther P. A., Chené A.-N., De Serres M., Eenens P. R. J., Hill G. M., Moran J., Morel T., 2004, Monthly Notices of the Royal Astronomical Society, 353, 153

Marchenko S. V., Moffat A. F. J., Crowther P. A., 2010, Astrophysical Journal Letters, 724, L90

Marco A., Negueruela I., 2002, Astronomy and Astrophysics, 393, 195

Martin C. L., 2005, Astrophysical Journal, 621, 227

Martín M. C., Cappa C. E., Testori J. C., 2007, Revista Mexicana de Astronomia y Astrofisica, 43, 243

Martins F., Schaerer D., Hillier D. J., 2005, Astronomy and Astrophysics, 436, 1049

Martins F., Plez B., 2006, Astronomy and Astrophysics, 457, 637

Martins F., Genzel R., Hillier D. J., Eisenhauer F., Paumard T., Gillessen S., Ott T., Trippe S., 2007, Astronomy and Astrophysics, 468, 233

Martins F., Hillier D. J., Paumard T., Eisenhauer F., Ott T., Genzel R., 2008, Astronomy and Astrophysics, 478, 219

Mason B. D., Hartkopf W. I., Gies D. R., Henry T. J., Helsel J. W., 2009, Astronomical Journal, 137, 3358

Massey P., Conti P. S., 1983, Astrophysical Journal, 273, 576

Massey P., 1984, Astrophysical Journal, 281, 789

Massey P., DeGioia-Eastwood K., Waterhouse E., 2001, Astronomical Journal, 121, 1050

Massey P., Duffy A. S., 2001, Astrophysical Journal, 550, 713

Massey P., 2003, Annual Review of Astronomy and Astrophysics, 41, 15

Massey P., Olsen K. A. G., 2003, Astronomical Journal, 126, 2867

Massey P., Olsen K. A. G., Parker J. W., 2003, Publications of the Astronomical Society of the Pacific, 115, 1265

Massey P., Neugent K. F., Morrell N., Hillier D. J., 2014, Astrophysical Journal, 788, 83

Matzner C. D., 2002, Astrophysical Journal, 566, 302

Mauerhan J. C., van Dyk S. D., Morris P. W., 2009, Publications of the Astronomical Society of the Pacific, 121, 591

Mauerhan J. C., Muno M. P., Morris M. R., Stolovy S. R., Cotera A., 2010a, Astrophysical Journal, 710, 706

Mauerhan J. C., Cotera A., Dong H., Morris M. R., Wang Q. D., Stolovy S. R., Lang C., 2010b, Astrophysical Journal, 725, 188

Mauerhan J. C., Wachter S., Morris P. W., Van Dyk S. D., Hoard D. W., 2010c, Astrophysical Journal Letters, 724, L78

Mauerhan J. C., Van Dyk S. D., Morris P. W., 2011, Astronomical Journal, 142, 40

Mauron N., Josselin E., 2011, Astronomy and Astrophysics, 526, A156

McGaugh S. S., 1991, Astrophysical Journal, 380, 140

Melena N. W., Massey P., Morrell N. I., Zangari A. M., 2008, Astronomical Journal, 135, 878

Mel'Nik A. M., Dambis A. K., 2009, Monthly Notices of the Royal Astronomical Society, 400, 518

Messineo M., Davies B., Ivanov V. D., Figer D. F., Schuller F., Habing H. J., Menten K. M., Petr-Gotzens M. G., 2009, Astrophysical Journal, 697, 701

Messineo M., Davies B., Figer D. F., Kudritzki R. P., Valenti E., Trombley C., Najarro F., Rich R. M., 2011, Astrophysical Journal, 733, 41

Meynet G., Maeder A., Schaller G., Schaerer D., Charbonnel C., 1994, Astronomy and Astrophysics Supplements, 103, 97

Meynet G., 1995, Astronomy and Astrophysics, 298, 767

Meynet G., Maeder A., 1997, Astronomy and Astrophysics, 321, 465

Meynet G., Maeder A., 2000, Astronomy and Astrophysics, 361, 101

Meynet G., Maeder A., 2003, Astronomy and Astrophysics, 404, 975

Meynet G., Maeder A., 2005, Astronomy and Astrophysics, 429, 581

Mihalas D., 1978, Stellar Atmospheres. A Series of books in astronomy and astrophysics, W. H. Freeman

Mikami T., Ogura K., 2001, Astrophysics and Space Science, 275, 441

Millour F., Petrov R. G., Chesneau O., Bonneau D., Dessart L., Bechet C., Tallon-Bosc I., Tallon M., Thiébaut E., Vakili F., et al. 2007, Astronomy and Astrophysics, 464, 107

Milne E. A., 1926, Monthly Notices of the Royal Astronomical Society, 86, 459

Miszalski B., Crowther P. A., De Marco O., Köppen J., Moffat A. F. J., Acker A., Hillwig T. C., 2012, Monthly Notices of the Royal Astronomical Society, 423, 934

Moffat A. F. J., Lamontagne R., Seggewiss W., 1982, Astronomy and Astrophysics, 114, 135

Moffat A. F. J., Shara M. M., 1983, Astrophysical Journal, 273, 544

Moffat A. F. J., 1989, Astrophysical Journal, 347, 373

Moffat A. F. J., Shara M. M., Potter M., 1991, Astronomical Journal, 102, 642

Mokiem M. R., de Koter A., Vink J. S., Puls J., Evans C. J., Smartt S. J., Crowther P. A., Herrero A., Langer N., Lennon D. J., Najarro F., Villamariz M. R., 2007, Astronomy and Astrophysics, 473, 603

Momany Y., Zaggia S., Gilmore G., Piotto G., Carraro G., Bedin L. R., de Angeli F., 2006, Astronomy and Astrophysics, 451, 515

Monet D. G., Levine S. E., Canzian B., Ables H. D., Bird A. R., Dahn C. C., Guetter H. H., Harris H. C., et al. 2003, Astronomical Journal, 125, 984

Monnier J. D., Zhao M., Pedretti E., Millan-Gabet R., Berger J.-P., Traub W., Schloerb F. P., ten Brummelaar T., McAlister H., Ridgway S., Sturmann L., Sturmann J., Turner N., Baron F., Kraus S., Tannirkulam a., Williams P. M., 2011, Astrophysical Journal, 742, L1

Morgan W. W., Keenan P. C., Kellman E., 1943, An atlas of stellar spectra, with an outline of spectral classification. Chicago, Ill., The University of Chicago press [1943]

Morris P. W., Brownsberger K. R., Conti P. S., Massey P., Vacca W. D., 1993, Astrophysical Journal, 412, 324

Morris P. W., van der Hucht K. A., Crowther P. A., Hillier D. J., Dessart L., Williams P. M., Willis A. J., 2000, Astronomy and Astrophysics, 353, 624

Morris P. W., Crowther P. A., Houck J. R., 2004, Astrophysical Journal Supplements, 154, 413

Mortlock D., 2014, ArXiv e-prints 1405.4701

Morton D. C., 1967, Astrophysical Journal, 150, 535

Moustakas J., Kennicutt Jr. R. C., Tremonti C. A., 2006, Astrophysical Journal, 642, 775

Müller P. E., Vink J. S., 2014, Astronomy and Astrophysics, 564, A57

Najarro F., Hillier D. J., Kudritzki R. P., Krabbe A., Genzel R., Lutz D., Drapatz S., Geballe T. R., 1994, Astronomy and Astrophysics, 285, 573

Najarro F., Hillier D. J., Stahl O., 1997, Astronomy and Astrophysics, 326, 1117

Nakanishi H., Sofue Y., 2003, Publications of the Astronomical Society of Japan, 55, 191

Nakanishi H., Sofue Y., 2006, Publications of the Astronomical Society of Japan, 58, 847

Naylor T., 2009, Monthly Notices of the Royal Astronomical Society, 399, 432

Negueruela I., Clark J. S., 2005, Astronomy and Astrophysics, 436, 541

Negueruela I., Marco A., 2003, Astronomy and Astrophysics, 406, 119

Negueruela I., Clark J. S., Ritchie B. W., 2010, Astronomy and Astrophysics, 516, A78

Neugent K. F., Massey P., Georgy C., 2012, Astrophysical Journal, 759, 11

Neugent K. F., Massey P., 2014, Astrophysical Journal, 789, 10

Niemela V. S., Sahade J., 1980, Astrophysical Journal, 238, 244

Niemela V. S., Shara M. M., Wallace D. J., Zurek D. R., Moffat A. F. J., 1998, Astronomical Journal, 115, 2047

Nishiyama S., Tamura M., Hatano H., Kato D., Tanabé T., Sugitani K., Nagata T., 2009, Astrophysical Journal, 696, 1407

North J. R., Tuthill P. G., Tango W. J., Davis J., 2007, Monthly Notices of the Royal Astronomical Society, 377, 415

Nugis T., Lamers H. J. G. L. M., 2000, Astronomy and Astrophysics, 360, 227

Nugis T., Lamers H. J. G. L. M., 2002, Astronomy and Astrophysics, 389, 162

Nussbaumer H., Storey P. J., 1981, Astronomy and Astrophysics, 99, 177

Oskinova L. M., Ignace R., Hamann W.-R., Pollock A. M. T., Brown J. C., 2003, Astronomy and Astrophysics, 402, 755

Oskinova L. M., 2005, Monthly Notices of the Royal Astronomical Society, 361, 679

Owocki S. P., Rybicki G. B., 1984, Astrophysical Journal, 284, 337

Owocki S. P., Castor J. I., Rybicki G. B., 1988, Astrophysical Journal, 335, 914

Owocki S. P., Rybicki G. B., 1991, Astrophysical Journal, 368, 261

Packet W., 1981, Astronomy and Astrophysics, 102, 17

Paczyński B., 1967, Acta Astronomica, 17, 355

Paczynski B., 1973, in Bappu M. K. V., Sahade J., eds, Wolf-Rayet and High-Temperature Stars Vol. 49 of IAU Symposium, Evolutionary Aspects of Wolf-Rayet Stars. p. 143

Pagel B. E. J., Terlevich R. J., Melnick J., 1986, Publications of the Astronomical Society of the Pacific, 98, 1005

Paladini R., Davies R. D., De Zotti G., 2004, Monthly Notices of the Royal Astronomical Society, 347, 237

Palla F., Stahler S. W., 1999, Astrophysical Journal, 525, 772

Parker Q. A., Phillipps S., Pierce M. J., Hartley M., Hambly N. C., Read M. A., MacGillivray H. T., Tritton S. B., Cass e. a., 2005, Monthly Notices of the Royal Astronomical Society, 362, 689

Pasquali A., Comerón F., Gredel R., Torra J., Figueras F., 2002, Astronomy and Astrophysics, 396, 533

Pauldrach A., Puls J., Kudritzki R. P., 1986, Astronomy and Astrophysics, 164, 86

Paumard T., Genzel R., Martins F., Nayakshin S., Beloborodov A. M., Levin Y., Trippe S., Eisenhauer F., Ott T., Gillessen S., Abuter R., Cuadra J., Alexander T., Sternberg A., 2006, Astrophysical Journal, 643, 1011

Paunzen E., Netopil M., Zwintz K., 2007, Astronomy and Astrophysics, 462, 157

Penny L. R., Gies D. R., 2009, Astrophysical Journal, 700, 844

Petrovic J., Langer N., van der Hucht K. A., 2005, Astronomy and Astrophysics, 435, 1013

Petrovic J., Pols O., Langer N., 2006, Astronomy and Astrophysics, 450, 219

Pettini M., Shapley A. E., Steidel C. C., Cuby J.-G., Dickinson M., Moorwood A. F. M., Adelberger K. L., Giavalisco M., 2001, Astrophysical Journal, 554, 981

Pettini M., 2004, in Esteban C., García López R., Herrero A., Sánchez F., eds, Cosmochemistry. The melting pot of the elements Element abundances through the cosmic ages. pp 257–298

Pettini M., Pagel B. E. J., 2004, Monthly Notices of the Royal Astronomical Society, 348, L59

Piatti A. E., Clariá J. J., Bica E., Geisler D., Minniti D., 1998, Astronomical Journal, 116, 801

Pittard J. M., Dougherty S. M., 2006, Monthly Notices of the Royal Astronomical Society, 372, 801

Podsiadlowski P., Joss P. C., Hsu J. J. L., 1992, Astrophysical Journal, 391, 246

Poglitsch A., Waelkens C., Bauer O. H., Cepa J., Feuchtgruber H., Henning T., van Hoof C., Kerschbaum F., Krause O., Renotte E., Rodriguez L., Saraceno P., Vandenbussche B., 2008, in Society of Photo-Optical Instrumentation Engineers (SPIE) Conference Series Vol. 7010 of Society of Photo-Optical Instrumentation Engineers (SPIE) Conference Series, The Photodetector Array Camera and Spectrometer (PACS) for the Herschel Space Observatory. p. 5

Pollock A. M. T., 1987, Astrophysical Journal, 320, 283

Pollock A. M. T., Haberl F., Corcoran M. F., 1995, in van der Hucht K. A., Williams P. M., eds, Wolf-Rayet Stars: Binaries; Colliding Winds; Evolution Vol. 163 of IAU Symposium, The ROSAT PSPC survey of the Wolf-Rayet stars. p. 512

Pols O. R., 1994, Astronomy and Astrophysics, 290, 119

Porciani C., Madau P., 2001, Astrophysical Journal, 548, 522

Poveda A., Ruiz J., Allen C., 1967, Boletin de los Observatorios Tonantzintla y Tacubaya, 4, 86

Prinja R. K., Barlow M. J., Howarth I. D., 1990, Astrophysical Journal, 361, 607

Przybilla N., Butler K., Becker S. R., Kudritzki R. P., 2006, Astronomy and Astrophysics, 445, 1099

Puls J., Kudritzki R.-P., Herrero A., Pauldrach A. W. A., Haser S. M., Lennon D. J., Gabler R., Voels S. A., Vilchez J. M., Wachter S., Feldmeier A., 1996, Astronomy and Astrophysics, 305, 171

Puls J., Springmann U., Lennon M., 2000, Astronomy and Astrophysics Supplements, 141, 23

Puls J., Markova N., Scuderi S., Stanghellini C., Taranova O. G., Burnley A. W., Howarth I. D., 2006, Astronomy and Astrophysics, 454, 625

Puls J., Vink J. S., Najarro F., 2008, Astronomy and Astrophysics Review, 16, 209

Quider A. M., Pettini M., Shapley A. E., Steidel C. C., 2009, Monthly Notices of the Royal Astronomical Society, 398, 1263

Raddi R., Drew J. E., Fabregat J., Steeghs D., Wright N. J., Sale S. E., Farnhill H. J., Barlow M. J., Greimel R., Sabin L., Corradi R. M. L., Drake J. J., 2013, Monthly Notices of the Royal Astronomical Society, 430, 2169

Raddi R., Drew J. E., Steeghs D., Wright N. J., Drake J. J., Barentsen G., Fabregat J., Sale S. E., 2015, Monthly Notices of the Royal Astronomical Society, 446, 274

Rauw G., Crowther P. A., De Becker M., Gosset E., Nazé Y., Sana H., van der Hucht K. A., Vreux J.-M., Williams P. M., 2005, Astronomy and Astrophysics, 432, 985

Rauw G., Manfroid J., Gosset E., Nazé Y., Sana H., De Becker M., Foellmi C., Moffat A. F. J., 2007, Astronomy and Astrophysics, 463, 981

Rauw G., Sana H., Nazé Y., 2011, Astronomy and Astrophysics, 535, A40

Reid M. J., Menten K. M., Zheng X. W., Brunthaler A., Xu Y., 2009, Astrophysical Journal, 705, 1548

Reid M. J., McClintock J. E., Narayan R., Gou L., Remillard R. A., Orosz J. A., 2011, Astrophysical Journal, 742, 83

Renzini A., 1984, in Maeder A., Renzini A., eds, Observational Tests of the Stellar Evolution Theory Vol. 105 of IAU Symposium, Selected Topics on the Evolution of Low and Intermediate Mass Stars. p. 21

Rieke G. H., Lebofsky M. J., 1985, Astrophysical Journal, 288, 618

Ritchie B. W., Clark J. S., Negueruela I., Langer N., 2010, Astronomy and Astrophysics, 520, A48

Rix S. A., Pettini M., Leitherer C., Bresolin F., Kudritzki R.-P., Steidel C. C., 2004, Astrophysical Journal, 615, 98

Roberts M. S., 1962, Astronomical Journal, 67, 79

Robertson B. E., Ellis R. S., 2012, Astrophysical Journal, 744, 95

Rolleston W. R. J., Trundle C., Dufton P. L., 2002, Astronomy and Astrophysics, 396, 53

Rolleston W. R. J., Venn K., Tolstoy E., Dufton P. L., 2003, Astronomy and Astrophysics, 400, 21

Roman-Lopes A., 2011, Monthly Notices of the Royal Astronomical Society, 410, 161

Rosslowe C. K., Crowther P. A., 2015a, Monthly Notices of the Royal Astronomical Society, 449, 2436

Rosslowe C. K., Crowther P. A., 2015b, Monthly Notices of the Royal Astronomical Society, 447, 2322

Runacres M. C., Owocki S. P., 2002, Astronomy and Astrophysics, 381, 1015

Runacres M. C., Owocki S. P., 2005, Astronomy and Astrophysics, 429, 323

Russeil D., 2003, Astronomy and Astrophysics, 397, 133

Rygl K. L. J., Brunthaler A., Sanna A., Menten K. M., Reid M. J., van Langevelde H. J., Honma M., Torstensson K. J. E., Fujisawa K., 2012, Astronomy and Astrophysics, 539, A79

Salaris M., Cassisi S., 2014, Astronomy and Astrophysics, 566, A109

Salpeter E. E., 1955, Astrophysical Journal, 121, 161

Sana H., de Mink S. E., de Koter A., Langer N., Evans C. J., Gieles M., Gosset E., Izzard R. G., Le Bouquin J.-B., Schneider F. R. N., 2012, Science, 337, 444

Sana H., de Koter A., de Mink S. E., Dunstall P. R., Evans C. J., Hénault-Brunet V., Maíz Apellániz J., Ramírez-Agudelo O. H., et al. 2013, Astronomy and Astrophysics, 550, A107

Sana H., Gosset E., Rauw G., Sung H., Vreux J.-M., 2006, Astronomy and Astrophysics, 454, 1047

Sander A., Hamann W.-R., Todt H., 2012, Astronomy and Astrophysics, 540, A144

Sauvage M., Thuan T. X., 1992, Astrophysical Journal Letters, 396, L69

Schaerer D., Maeder A., 1992, Astronomy and Astrophysics, 263, 129

Schaerer D., Vacca W. D., 1998, Astrophysical Journal, 497, 618

Schild H., Maeder A., 1984, Astronomy and Astrophysics, 136, 237

Schiminovich D., Ilbert O., Arnouts S., Milliard B., Tresse L., Le Fèvre O., Treyer M., Wyder T. K., et al. 2005, Astrophysical Journal Letters, 619, L47

Schmutz W., Hamann W.-R., Wessolowski U., 1989, Astronomy and Astrophysics, 210, 236

Schneider F. R. N., Izzard R. G., de Mink S. E., Langer N., Stolte A., de Koter A., Gvaramadze V. V., Hußmann B., Liermann A., Sana H., 2014, Astrophysical Journal, 780, 117

Schnurr O., Casoli J., Chené A.-N., Moffat A. F. J., St-Louis N., 2008, Monthly Notices of the Royal Astronomical Society, 389, L38

Schnurr O., Crowther P. A., 2008, in Hamann W.-R., Feldmeier A., Oskinova L. M., eds, Clumping in Hot-Star Winds Mid-IR observations of WC stars, and the connection to wind clumping. p. 89

Schönberg M., Chandrasekhar S., 1942, Astrophysical Journal, 96, 161

Schürmann D., Gialanella L., Kunz R., Strieder F., 2012, Physics Letters B, 711, 35

Schweickhardt J., Schmutz W., Stahl O., Szeifert T., Wolf B., 1999, Astronomy and Astrophysics, 347, 127

Scuflaire R., Noels A., 1986, Astronomy and Astrophysics, 169, 185

Searle L., Sargent W. L. W., 1972, Astrophysical Journal, 173, 25

Shara M. M., Smith L. F., Potter M., Moffat A. F. J., 1991, Astronomical Journal, 102, 716

Shara M. M., Moffat A. F. J., Smith L. F., Niemela V. S., Potter M., Lamontagne R., 1999, Astronomical Journal, 118, 390

Shara M. M., Moffat A. F. J., Gerke J., Zurek D., Stanonik K., Doyon R., Artigau E., Drissen L., Villar-Sbaffi A., 2009, Astronomical Journal, 138, 402

Shara M. M., Faherty J. K., Zurek D., Moffat A. F. J., Gerke J., Doyon R., Artigau E., Drissen L., 2012, Astronomical Journal, 143, 149

Shenar T., Hamann W.-R., Todt H., 2014, Astronomy and Astrophysics, 562, A118

Skinner S. L., Simmons A. E., Zhekov S. A., Teodoro M., Damineli A., Palla F., 2006, Astrophysical Journal Letters, 639, L35

Skrutskie M. F., Cutri R. M., Stiening R., Weinberg M. D., Schneider S., Carpenter J. M., Beichman C., Capps R. e. a., 2006, Astronomical Journal, 131, 1163

Smartt S. J., Crowther P. A., Dufton P. L., Lennon D. J., Kudritzki R. P., Herrero A., McCarthy J. K., Bresolin F., 2001, Monthly Notices of the Royal Astronomical Society, 325, 257

Smartt S. J., Eldridge J. J., Crockett R. M., Maund J. R., 2009, Monthly Notices of the Royal Astronomical Society, 395, 1409

Smith J. D. T., Cushing M., Barletta A., McCarthy D., Kulesa C., Van Dyk S. D., 2012, Astronomical Journal, 144, 166

Smith L. F., 1968a, Monthly Notices of the Royal Astronomical Society, 138, 109

Smith L. F., 1968b, Monthly Notices of the Royal Astronomical Society, 140, 409

Smith L. F., 1968c, Monthly Notices of the Royal Astronomical Society, 141, 317

Smith L. F., 1973, in Bappu M. K. V., Sahade J., eds, Wolf-Rayet and High-Temperature Stars Vol. 49 of IAU Symposium, Classification and Distribution of WR Stars and an Interpretation of the WN Sequence. p. 15

Smith L. F., Shara M. M., Moffat A. F. J., 1990, Astrophysical Journal, 358, 229

Smith L. F., Shara M. M., Moffat A. F. J., 1996, Monthly Notices of the Royal Astronomical Society, 281, 163

Smith L. J., Crowther P. A., Prinja R. K., 1994, Astronomy and Astrophysics, 281, 833

Smith N., Humphreys R. M., Davidson K., Gehrz R. D., Schuster M. T., Krautter J., 2001, Astronomical Journal, 121, 1111

Smith N., 2006, Astrophysical Journal, 644, 1151

Smith N., Owocki S. P., 2006, Astrophysical Journal Letters, 645, L45

Smith N., Conti P. S., 2008, Astrophysical Journal, 679, 1467

Smith N., Li W., Filippenko A. V., Chornock R., 2011, Monthly Notices of the Royal Astronomical Society, 412, 1522

Smith N., 2014, Annual Review of Astronomy and Astrophysics, 52, 487

Smith N., Tombleson R., 2015, Monthly Notices of the Royal Astronomical Society, 447, 598

Sobolev V. V., 1960, Moving envelopes of stars. Cambridge: Harvard University Press, 1960

Sonneborn G., Altner B., Kirshner R. P., 1987, Astrophysical Journal Letters, 323, L35

Springel V., Hernquist L., 2003, Monthly Notices of the Royal Astronomical Society, 339, 312

Springmann U., 1994, Astronomy and Astrophysics, 289, 505

St.-Louis N., Willis A. J., Stevens I. R., 1993, Astrophysical Journal, 415, 298

Stead J. J., Hoare M. G., 2009, Monthly Notices of the Royal Astronomical Society, 400, 731

Steidel C. C., Hamilton D., 1993, Astronomical Journal, 105, 2017

Stetson P. B., 1987, Publications of the Astronomical Society of the Pacific, 99, 191

Stevens I. R., Blondin J. M., Pollock A. M. T., 1992, Astrophysical Journal, 386, 265

Stock D. J., Barlow M. J., 2010, Monthly Notices of the Royal Astronomical Society, 409, 1429

Stock D. J., Barlow M. J., Wesson R., 2011, Monthly Notices of the Royal Astronomical Society, 418, 2532

Stothers R., Chin C.-W., 1976, Astrophysical Journal, 204, 472

Stothers R., Chin C.-W., 1979, Astrophysical Journal, 233, 267

Strom S. E., Edwards S., Skrutskie M. F., 1993, in Levy E. H., Lunine J. I., eds, Protostars and Planets III Evolutionary time scales for circumstellar disks associated with intermediate- and solar-type stars. pp 837–866

Taam R. E., Sandquist E. L., 2000, Annual Review of Astronomy and Astrophysics, 38, 113

Tang X. D., Rehm K. E., Ahmad I., Brune C. R., Champagne A., Greene J. P., Hecht A. A., Henderson D., Janssens R. V. F., Jiang C. L., Jisonna L., Kahl D., Moore E. F., Notani M., Pardo R. C., Patel N., Paul M., Savard G., Schiffer J. P., Segel R. E., Sinha S., Shumard B., Wuosmaa A. H., 2007, Physical Review Letters, 99, 052502

Tapia M., Roth M., Vázquez R. A., Feinstein A., 2003, Monthly Notices of the Royal Astronomical Society, 339, 44

Tasker E. J., 2011, Astrophysical Journal, 730, 11

Todt H., Kniazev A. Y., Gvaramadze V. V., Hamann W.-R., Buckley D., Crause L., Crawford S. M., Gulbis A. A. S., et al. 2013, Monthly Notices of the Royal Astronomical Society, 430, 2302

Tognelli E., Prada Moroni P. G., Degl'Innocenti S., 2011, Astronomy and Astrophysics, 533, A109

Torres A. V., Conti P. S., Massey P., 1986, Astrophysical Journal, 300, 379

Tovmassian H. M., Navarro S. G., Cardona O., 1996, Astronomical Journal, 111, 306

Trenti M., Perna R., Jimenez R., 2015, Astrophysical Journal, 802, 103

Turner D. G., 1980, Astrophysical Journal, 235, 146

Turner D. G., Rohanizadegan M., Berdnikov L. N., Pastukhova E. N., 2006, Publications of the Astronomical Society of the Pacific, 118, 1533

Tuthill P. G., Monnier J. D., Danchi W. C., 1999, Nature, 398, 487

Tuthill P. G., Monnier J. D., Lawrance N., Danchi W. C., Owocki S. P., Gayley K. G., 2008, Astrophysical Journal, 675, 698

Underhill A. B., 1983, Astrophysical Journal, 265, 933

Underhill A. B., Hill G. M., 1994, Astrophysical Journal, 432, 770

Vallée J. P., 2008, Astronomical Journal, 135, 1301

van der Hucht K. A., Conti P. S., Lundstrom I., Stenholm B., 1981, Space Science Reviews, 28, 227

van der Hucht K. A., 2001, New Astronomy Reviews, 45, 135

van der Hucht K. A., 2006, Astronomy and Astrophysics, 458, 453

van Leeuwen F., 2007, Astronomy and Astrophysics, 474, 653

Van Loo S., Runacres M. C., Blomme R., 2004, Astronomy and Astrophysics, 418, 717

van Loon J. T., Marshall J. R., Zijlstra A. A., 2005, Astronomy and Astrophysics, 442, 597

Vanbeveren D., De Donder E., Van Bever J., Van Rensbergen W., De Loore C., 1998, New Astronomy, 3, 443

Vanbeveren D., Van Bever J., Belkus H., 2007, Astrophysical Journal Letters, 662, L107

Varricatt W. P., Ashok N. M., 2006, Monthly Notices of the Royal Astronomical Society, 365, 127

Vázquez R. A., Will J.-M., Prado P., Feinstein A., 1995, Astronomy and Astrophysics Supplements, 111, 85

Vázquez R. A., Baume G., 2001, Astronomy and Astrophysics, 371, 908

Vázquez R. A., Baume G. L., Feinstein C., Nuñez J. A., Vergne M. M., 2005, Astronomy and Astrophysics, 430, 471

Veilleux S., Cecil G., Bland-Hawthorn J., 2005, Annual Review of Astronomy and Astrophysics, 43, 769

Vink J. S., de Koter A., Lamers H. J. G. L. M., 2000, Astronomy and Astrophysics, 362, 295

Vink J. S., de Koter A., Lamers H. J. G. L. M., 2001, Astronomy and Astrophysics, 369, 574

Vink J. S., de Koter A., 2005, Astronomy and Astrophysics, 442, 587

Vink J. S., 2011, Astrophysics and Space Science, 336, 163

von Zeipel H., 1924, Monthly Notices of the Royal Astronomical Society, 84, 684

Vreux J.-M., Andrillat Y., Biemont E., 1990, Astronomy and Astrophysics, 238, 207

Wachter S., Mauerhan J. C., Van Dyk S. D., Hoard D. W., Kafka S., Morris P. W., 2010, Astronomical Journal, 139, 2330

Walborn N. R., Howarth I. D., Lennon D. J., Massey P., Oey M. S., Moffat A. F. J., Skalkowski G., Morrell N. I., Drissen L., Parker J. W., 2002, Astronomical Journal, 123, 2754

Weaver R., McCray R., Castor J., Shapiro P., Moore R., 1977, Astrophysical Journal, 218, 377

Weaver T. A., Woosley S. E., 1993, Physics Reports, 227, 65

Wegner W., 2006, Monthly Notices of the Royal Astronomical Society, 371, 185

Westerlund B., 1961, Astronomical Journal, 66, 57

Westerlund B. E., 1987, Astronomy and Astrophysics Supplements, 70, 311

White S. D. M., Frenk C. S., 1991, Astrophysical Journal, 379, 52

Williams J. P., McKee C. F., 1997, Astrophysical Journal, 476, 166

Williams P. M., van der Hucht K. A., Pollock A. M. T., Florkowski D. R., van der Woerd H., Wamsteker W. M., 1990a, Monthly Notices of the Royal Astronomical Society, 243, 662

Williams P. M., van der Hucht K. A., Sandell G., The P. S., 1990b, Monthly Notices of the Royal Astronomical Society, 244, 101

Williams P. M., van der Hucht K. A., Bouchet P., Spoelstra T. A. T., Eenens P. R. J., Geballe T. R., Kidger M. R., Churchwell E., 1992, Monthly Notices of the Royal Astronomical Society, 258, 461

Williams P. M., Dougherty S. M., Davis R. J., van der Hucht K. A., Bode M. F., Setia Gunawan D. Y. A., 1997, Monthly Notices of the Royal Astronomical Society, 289, 10

Williams P. M., Kidger M. R., van der Hucht K. A., Morris P. W., Tapia M., Perinotto M., Morbidelli L., Fitzsimmons A., Anthony D. M., Caldwell J. J., Alonso A., Wild V., 2001, Monthly Notices of the Royal Astronomical Society, 324, 156

Williams P. M., van der Hucht K. A., Rauw G., 2005, in Rauw, G., Nazé, Y., Blomme, R., Gosset, E., eds, Massive Stars and High-Energy Emission in OB Associations, Are WC9 Wolf-Rayet stars in colliding-wind binaries?. pp 65–68

Williams P. M., Marchenko S. V., Marston A. P., Moffat A. F. J., Varricatt W. P., Dougherty S. M., Kidger M. R., Morbidelli L., Tapia M., 2009a, Monthly Notices of the Royal Astronomical Society, 395, 1749

Williams P. M., Rauw G., van der Hucht K. A., 2009b, Monthly Notices of the Royal Astronomical Society, 395, 2221

Williams P. M., van der Hucht K. A., van Wyk F., Marang F., Whitelock P. A., Bouchet P., Setia Gunawan D. Y. A., 2012, Monthly Notices of the Royal Astronomical Society, 420, 2526

Williams P. M., Crowther P. A., van der Hucht K. A., 2015, Monthly Notices of the Royal Astronomical Society, 449, 1834

Willis A. J., 1982, in De Loore C. W. H., Willis A. J., eds, Wolf-Rayet Stars: Observations, Physics, Evolution Vol. 99 of IAU Symposium, The chemical composition of the Wolf-Rayet stars. pp 87–102

Witham A. R., Knigge C., Drew J. E., Greimel R., Steeghs D., Gänsicke B. T., Groot P. J., Mampaso A., 2008, Monthly Notices of the Royal Astronomical Society, 384, 1277

Wolf C. J. E., Rayet G., 1867, Comptes Rendues, 65, 292

Wolfe A. M., Gawiser E., Prochaska J. X., 2005, Annual Review of Astronomy and Astrophysics, 43, 861

Woosley S. E., Weaver T. A., 1995, Astrophysical Journal Supplements, 101, 181

Woosley S. E., Bloom J. S., 2006, Annual Review of Astronomy and Astrophysics, 44, 507

Wright E. L., Eisenhardt P. R. M., Mainzer A. K., Ressler M. E., Cutri R. M., Jarrett T., Kirkpatrick J. D., Padgett D., McMillan e. a., 2010, Astronomical Journal, 140, 1868

Wright N. J., Parker R. J., Goodwin S. P., Drake J. J., 2014, Monthly Notices of the Royal Astronomical Society, 438, 639

Yusof N., Hirschi R., Meynet G., Crowther P. A., Ekström S., Frischknecht U., Georgy C., Abu Kassim H., Schnurr O., 2013, Monthly Notices of the Royal Astronomical Society, 433, 1114

Zahn J.-P., 1992, Astronomy and Astrophysics, 265, 115

Zinnecker H., Yorke H. W., 2007, Annual Review of Astronomy and Astrophysics, 45, 481

Appendix A

Infra-red line measurements

Contents

Table A.1: J-band line equivalent width (Å) measurements for WN stars.

WR#	Sp. Type	HeII 1.012μm	HeI 1.083μm	HeII 1.163μm	SiIV(NIV) 1.1904μm	HeII 1.281μm
105	WN9h	8.50	241.0	2.74	2.19	56.36
108	WN9ha	7.87	54.97	2.88	2.51	17.58
116	WN8h	19.89	557.5	10.28	3.00	106.6
130	WN8(h)	32,87	197.3	17.03	2.93	42.54
66	WN8(h)	52.27	199.92	28.66	5.07	57.58
123	WN8o	40.28	484.0	20.38	4.92	70.63
158	WN7h	29.88	75.38	17.46	1.46	38.08
82	WN7(h)	75.9	309.1	46.68	8.85	104.9
55	WN7o	109.5	295.6	56.5	6.99	52.56
84	WN7o	134.6	266.8	80.24	10.75	56.17
68a	WN6o	85.64	65.61	46.61	4.88	18.92
155	WN6o+O9II-Ib	61.46	53.5	28.35	1.90	22.73
75	WN6b	327	661.1	174.5	15.92	120.2
134	WN6b	387.2	310.0	200.1	11.55	88.50
136	WN6b(h)	299.9	322.9	183.5	12.88	110.6
54	WN5o	236.2	106.2	-	-	61.2
61	WN5o	243.8	141.93	-	-	42.96
83	WN5o	192.4	95.3	-	-	62.89
133	WN5o	42.28	27.94	25.1	2.24	8.48
138	WN5o	107.3	73.29	57.91	6.17	35.31
157	WN5o	116.7	47.0	60.88	3.24	47.49
110	WN5–6b	423	762.7	-	-	122
62a	WN4–5o	67.2	65.13	-	-	12
1	WN4b	376.8	451.7	196.7	10.84	73.6
6	WN4b	385.8	324.5	212.9	12.18	86.40
3	WN3b	136.4	-	56.71	2.61	25.41
93a	WN2.5–3o	89.04	70.12	-	-	94.82
2	WN2b	250.3	-	133.8	6.85	35.94

Table A.2: K & L-band line equivalent (Å) width measurements for WN stars.

WR#	Sp. Type	HeI+II 2.164–2.165μm	HeII 2.189μm	HeII 3.543μm	HeII+Pfγ 3.74μm	HeII 4.650–4.654μm	HeII+Pfβ 4.762μm
105	WN9h	66.78	6.27	5.586	130.3	303.7	-
108	WN9ha	23.68	5.21	-	-	-	-
116	WN8h	106.2	8.40	9.258	170	378.8	39.2
123	WN8o	77.60	17.34	12.43	127.8	226.1	111.9
130	WN8(h)	46.17	9.45	13.11	89.69	213.4	68.68
147	WN8(h)	-	-	11.87	129.3	307.9	55.31
16	WN8h	75.47	12.25	-	-	-	-
40	WN8h	112.6	11.68	-	-	-	-
22	WN7ha	38.43	13.2	-	-	-	-
131	WN7h	32.54	15.51	-	-	-	-
158	WN7h	35.56	9.58	17.66	76.6	150.9	57.03
55	WN7o	33	30.91	-	-	-	-
120	WN7o	51.76	38.62	-	-	-	-
24	WN6ha	33.6	24.59	-	-	-	-
25	WN6ha	18.88	14.95	-	-	-	-
115	WN6o	36.3	57.68	-	-	-	-
155	WN6o+O9II-Ib	24.55	26.66	38.42	56.55	150.5	320.4
75	WN6b	74.17	109.6	-	-	-	-
134	WN6b	60.75	144.5	113	80.61	183.6	823.33
136	WN6b(h)	71.64	109.6	90.53	99.83	245.7	562.8
83	WN5o	51.72	72.65	-	-	-	-
133	WN5o	9.48	29.14	33.18	20.47	69.49	331.3
138	WN5o	32.18	58.25	53.7	55.5	-	-
157	WN5o	42.79	59.08	52.75	66.47	172.5	461.6
128	WN4(h)	44.46	77.02	-	-	-	-
1	WN4b	53.69	152.5	103.5	60.54	223.4	1133
6	WN4b	49.00	159.8	114.4	74.95	207.3	979.1
3	WN3b	30.61	49.74	-	-	-	-

Continued on next page

Table A.2 – *Continued from previous page*

WR#	Sp. Type	HeI+II 2.164–2.165μm	HeII 2.189μm	HeII 3.543μm	HeII+Pfγ 3.74μm	HeII+Pfβ 4.650–4.654μm	HeII 4.762μm
2	WN2b	-	-	100.5	-	-	-

Table A.3: Y, J & K-band line measurements for WC stars. Equivalent width (Å) or peak (continuum units).

WR#	Sp. Type	HeII 1.012μm	HeI 1.083μm	CIV (peak) 1.191μm	CIII 1.199μm	CIV 2.070–2.084μm	CIII+HeI 2.112–2.137μm	CIV 2.427μm	CIII 2.48μm
103	WC9d	-	-	-	-	49.16	64.71	-	-
106	WC9d	12.41	173.4	10.38 (1.282)	51.03	4.038	6.772	-	-
119	WC9d	18.52	275.7	21.79 (1.627)	93.85	19.85	28.7	1.208	15.33
121	WC9d	16.2	312.4	19.38 (1.505)	87.35	14.67	21.71	1.954	8.358
57	WC8	121.7	220.9	190.4 (3.438)	76.9	-	-	-	-
60	WC8	111.1	355.5	248.9 (3.00)	41.56	451.1	209.2	-	-
135	WC8	93	343.9	109.4 (2.947)	79.39	583.4	191.8	143.9	78.57
56	WC7	143.8	220.7	232 (3.581)	56.86	-	-	-	-
64	WC7	145.8	170.6	252.9 (3.768)	59.16	-	-	-	-
90	WC7	162.1	300.9	247.7 (3.339)	57.84	825.1	223.9	-	-
137	WC7pd+O9	54.57	102.7	90.92 (2.047)	27.65	464	122.3	112.2	50.06
140	WC7pd+O5	78.19	117.4	124 (1.817)	5.15	532.4	156.3	194	79.42
5	WC6	202.7	275.9	239.8 (3.594)	44.89	1339	227.9	342.3	97.57
107a	WC6	182.4	200.1	348.9 (4.176)	33.2	-	-	-	-
154	WC6	204.6	220.4	308.4 (3.546)	30.48	1388	289.3	414.3	143.4
146	WC4/5/6+O8	128.1	166.3	132.3 (1.837)	6.9	561.3	127.9	164.4	36.82
4	WC5	-	-	-	-	1501	280.3	-	-
111	WC5	217.7	188.9	334.8 (3.876)	32.16	1613	302	490.3	148.2
143	WC5	-	-	-	-	1166	263.1	-	-
52	WC4	233.7	148.5	356.4 (3.955)	32.95	1169	277.4	-	-

Table A.4: Average emission line strengths (Equivalent widths, Å) for the most prominent lines in the spectra of each WR spectral type, gathered from published spectra of apparently single WR stars. I used these values to calculate J and K_S-band continuum flux ratios in cases where WR emission lines are diluted by an unknown companion. An uncertainty of 0.1 dex is assumed on each averaged equivalent width, in accordance with the majority of studies from which individual measurements are taken.

Spectral type	Star (WR#)	Equivalent width (Å)	ref	Average (Å)
		He II 1.012μm		
WN7	55	109.5	a,b	**89**
	82	75.9	b	
	84	134.6	b	
	120	70.8	c,d	
WN6	115	126	c,d	**119**
	85	112	a	
WN4-5	83	192.4	b	**221**
	54	236.2	b	
	61	243.8	b	
	149	234	a	
	129	200	a	
WN4b	1	377	e	**412**
	18	447	a	
WN5-6b	75	327	b	**375**
	110	423	a,d	
WN7b	77sc	280	f	
WC8	135	93	e	**93**
	57	121.7	b	
	60	111.1	b	
	118-4	80	g	
	119-2	93	g	
	53	61.7	a	
WC7	56	143.8	b	**147**
	64	145.8	b	
	90	162	b	
	124-3	138	g	
WC6	154	205	e	**179**
	107a	182	b	
	23	151	a	
WC4-5	111	218	e	**225**
	17	263	a	
	52	234	b	

Continued on next page

Table A.4 – *Continued from previous page*

Spectral type	Star (WR#)	Equivalent width (Å)	ref	Average (Å)
	150	186	a	
		He I 1.083μm		
WN8	116	480	e	**308**
	130	200	e	
	16	245	d	
WN7	55	296	b	**291**
	82	309	b	
	84	267	b	
WN6	115	170	d	**170**
WN4-5	83	95	b	**114**
	54	106	b	
	61	142	b	
WN7b	77sc	930	f	**930**
WN5-6b	75	661	b	**712**
	110	763	d	
WN4b	1	452	e	
WC8	57	221	b	**412**
	60	353	b	
	118-4	537	g	
	119-2	600	g	
	135	344	e	
WC7	56	221	b	**227**
	64	171	b	
	90	301	b	
	124-3	215	g	
WC6	5	276	e	**232**
	107a	200	b	
	154	220	e	
WC4-5	52	149	b	**169**
	111	189	e	
		He I-II 2.164μm		
WN8-9	16	75	d	**73**
	105	63	d	
	116	106	e	
	130	46	e	
WN7	55	33	b	**43**
	120	52	d	
WN6	24	34	d	**35**

Continued on next page

Table A.4 – *Continued from previous page*

Spectral type	Star (WR#)	Equivalent width (Å)	ref	Average (Å)
	115	36	d	
WN4-5	129	50	h	**53**
	149	55	h	
WN7b	77sc	85	f	
WN6b	75	74	b	
WN4b	1	54	e	
		He II 2.189μm		
WN7	120	39	d	**35**
	55	31	b	
WN6	115	58	d	**42**
	24	25	d	
WN4-5	129	110	h	**105**
	149	99	h	
		C IV 2.071–2.084μm		
WC8	48-2	581	b	**466**
	77g	430	f	
	118-4	303	g	
	119-2	433	g	
	135	583	e	
WC7	67-2	783	i	**937**
	90	825	b	
	124-3	1202	g	
WC6	5	1339	e	**1530**
	48-4	1862	b	
	154	1388	e	
WC4-5	52	1169	b	**1391**
	111	1613	e	
		C III 2.104–2.115μm		
WC8	48-2	220	b	**209**
	77g	198	f	
	118-4	173	g	
	119-2	260	g	
	135	192	e	
WC7	67-2	234	i	**293**
	90	224	b	
	124-3	422	g	

Continued on next page

Table A.4 – *Continued from previous page*

Spectral type	Star (WR#)	Equivalent width (Å)	ref	Average (Å)
WC6	5	228	e	**301**
	48-4	385	b	
	154	289	e	
WC4-5	52	277	b	**290**
	111	302	e	

(a)Conti, Massey & Vreux (1990), (b)P.A. Crowther, (priv. comm.), (c)Howarth & Schmutz (1992), (d)Crowther & Smith (1996), (e)W.D. Vacca, (priv. comm.), (f)Crowther et al. (2006b), (g)Mauerhan et al. (2011), (h)Figer, McLean & Najarro (1997), (i)Roman-Lopes (2011)

Appendix B

Galactic Wolf-Rayet stars and clusters with ambiguous distances

Pismis 24 and WR 93

The open cluster Pismis 24 (Pi 24) contains the WC7+O binary system WR 93, and has conflicting distance meaurements in the literature, i.e., 2.56 ± 0.10 kpc (Massey, DeGioia-Eastwood & Waterhouse, 2001) and 1.7 ± 0.2 kpc (Fang et al., 2012). In Figure B.1 I plot Lejeune & Schaerer (2001) isochrones along with the positions of the 8 brightest O-stars in Pi 24. I took photometry and spectral types for these O-stars from Massey et al. (2001) except for Pi 24–1, which has since been resolved into two components, Pi 24–1 NE and Pi 24–1 SW (Maíz Apellániz et al., 2007), with an optical/near ultra-violet $\Delta m \sim 0.1$. I adjusted the Massey et al. photometry for Pi 24–1 to account for its binary nature, and adopted spectral types O3.5If* and O4III(f+) for Pi 24–1 NE and Pi 24–1 SW respectively (Maíz Apellániz et al., 2007). To calculate an extinction to each of the 8 O-stars, I evaluated the E_{B-V} colour excess assuming Martins & Plez (2006) intrinsic colours and an R_V=3.1 extinction law. Finally, by taking O-star temperatures and bolometric corrections from Martins, Schaerer & Hillier (2005), I found best agreement with the isochrones for a distance modulus of 11.5 ± 0.2, corresponding to $d = 2.00^{+0.19}_{-0.17}$ kpc.

Westerlund 2

The distance to the young massive open cluster Westerlund 2 - probable host of the O3If*/WN6+O3If*/WN6 binary WR 20a (Rauw, Sana & Nazé, 2011) and WR 20b (WN6ha) - remains controvertial. Literature values range from 2.5 kpc to 8 kpc, bringing the membership of the very luminous WR 20a into doubt. Rauw et al. (2007) used the

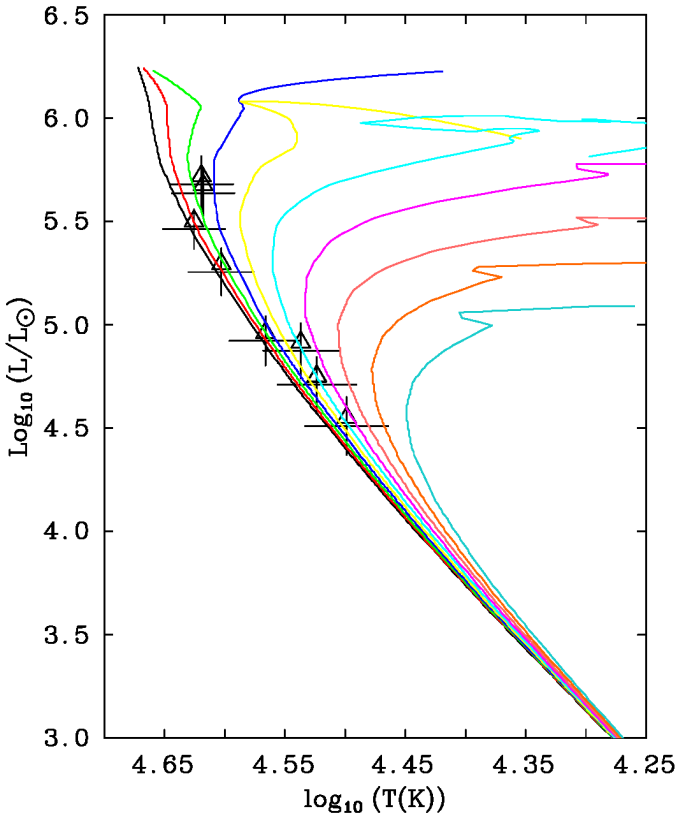

Figure B.1: Hertzsprung-Russell diagram showing positions of the 8 brightest (V-band, Massey et al. 2001) O-stars in the Pismis 24 open cluster (triangles). Stars are individually dereddened and shown at a distance modulus of 11.5, with Z=0.02 iochrones (Lejeune & Schaerer, 2001) for ages (from left to right) 6.00, 6.09, 6.19, 6.30, 6.40, 6.50, 6.59, 6.69, 6.80, and 6.90 Myr (left to right, solid lines).

light curve of WR 20a and the knowledge that both stars are of identical spectral type to derive a distance of 8.0 ± 1.0 kpc for this binary system. These authors also derive a distance to the Westerlund 2 cluster of 8.0 ± 1.4 kpc from spectro-photometry of cluster O-stars and use this agreement as evidence for membership of WR 20a. However, these distances are derived on the asumption of an $R_V = 3.1$ extinction law, yielding an average $A_V = 4.68$ for the cluster. Carraro et al. (2012) have claimed an anomalous extinction law along this line of sight with an average $R_V = 3.8 \pm 0.2$. These authors used the spectra of Rauw et al. to obtain $A_V = 7.1 \pm 1.2$, corresponding to a much smaller distance of 3.02 ± 0.52 kpc. The membership of WR 20a as two $\sim 80\,M_\odot$ stars is unfeasible at such a small distance.

WR 20b showns no evidence of binarity in the spectroscopic and photometric monitoring of Rauw et al. (2007). The asssumed intrinsic near-IR colour of WN6ha stars (Table 2.9) provides $A_{K_S} = 0.75 \pm 0.05$ ($A_V \sim 6.8$), favouring the higher extinction and lower distance estimate for Westerlund 2. The form of the extinction law to Westerlund 2 is not settled, therefore I assumed neither WR 20a or WR 20b to be members of the cluster. I included the stars of WR 20a in the calibration sample at the binary orbit-derived distance of 8.0 kpc.

The Galactic Centre

The Arches and Quintuplet clusters are found 11.6′ and 13.1′ from Sgr A* respectively, which is itself surrounded by a cluster of massive stars. The distance to the GC (R_o), and these three clusters by association, has been the subject of considerable study. The first direct parallax measurement of a GC object - the star forming region Sgr B2 - was presented by Reid et al. (2009) giving a distance of $7.9 \pm 0.8\,kpc$; from kinematic arguments Sgr B2 is estimated to be 0.13 kpc nearer than the GC. The most recent determinations of R_o are summerised by Gillessen et al. (2013), and are converging on 8 kpc. Acknowledging the spread in measurements that still remains, I assumed a distance of 8.0 ± 0.25kpc for these three clusters.

The G305 complex

There are 9 currently identified WR stars located within the boundary of the giant HII region G305.4+0.1, of which only 4 reside in the two central clusters Danks 1&2 (see Figure 16 of Mauerhan et al. 2011, and Davies et al. 2012). This is rather surprising, as one may expect to find these stars - as highly evolved descendants of massive progenitors - at the centre of these star clusters due to relaxation of their orbits. However, in the

dense environment of a cluster a massive star is more likely to encounter other massive stars or binaries, resulting in possible ejection. The apparent concentration of these 5 non-cluster WR stars in G305 around the younger Danks 1 cluster (Davies et al., 2012) supports a dynamical ejection scenario.

Located only $\sim$2.3′ from the Danks 1 cluster, WR 48–4 is the faintest WR star located within G305. Mauerhan et al. (2011) note that by assuming a WC7 spectral type and applying the K_S-band absolute magnitude-subtype calibations of Crowther et al. (2006b), this star appears to be twice as distant as the two central clusters yet is reddened by a similar amount. I considered the high IR-derived distance to WR48–4 as insignificant evidence for a chance superposition with G305. I included these 9 WRs in the calibration sample at the distance derived for the two central clusters.

Appendix C

Spatial properties of apparently single Galactic field WR stars

Table C.1: Calculated spatial locations of the 228 'field' WR stars showing no conclusive evidence for an IR-bright companion, to which our calibrated absolute magnitudes have been assigned. Shown for each object are the adopted spectral type, 2MASS photometry (unless stated), derived K_S-band extinction, heliocentric distance (d), Galactocentric radius (R_G) and vertical distance from the Galactic midplane (z).

WR#	Sp. Type	ref	J	H	K_S	$\bar{A}_{K_S}$	d(kpc)	R_G(kpc)	z(pc)
3	WN3ha	1	10.24	10.13	10.01	0.18 ± 0.02	4.53 ± 1.15	11.41 ± 1.18	-308 ± 83
4	WC5	2	8.75	8.57	7.88	0.13 ± 0.01	2.69 ± 0.49	10.15 ± 0.55	-121 ± 25
5	WC6	2	8.63	8.34	7.65	0.16 ± 0.02	2.69 ± 0.84	10.18 ± 0.88	-82 ± 32
13	WC6	2	10.14	9.64	8.86	0.29 ± 0.02	4.42 ± 1.38	9.46 ± 1.40	-40 ± 19
15	WC6	2	7.85	7.34	6.60	0.28 ± 0.02	1.57 ± 0.49	8.11 ± 0.55	-10 ± 9
16	WN8h	2	6.97	6.71	6.38	0.24 ± 0.02	2.77 ± 0.46	7.95 ± 0.52	-104 ± 20
17	WC5	2	9.93	9.74	9.17	0.07 ± 0.02	5.02 ± 0.91	8.31 ± 0.95	-303 ± 59
17-1	WN5b	3	11.73	10.38	9.53	0.85 ± 0.05	5.43 ± 0.86	8.58 ± 0.89	-41 ± 10
19	WC5+O9	4,5	9.75	9.13	8.53	0.20 ± 0.02	3.52 ± 0.64	7.93 ± 0.69	-54 ± 13
19a	WN7(h)	2	9.07	8.13	7.50	0.71 ± 0.04	2.41 ± 0.47	7.78 ± 0.53	-23 ± 8
20	WN5	2	11.00	10.43	9.93	0.45 ± 0.03	4.65 ± 0.72	8.18 ± 0.76	-130 ± 23
20b	WN6ha	2	8.65	7.80	7.18	0.75 ± 0.04	4.84 ± 0.79	8.26 ± 0.83	-10 ± 5
27	WC6	2	9.88	9.17	8.30	0.44 ± 0.03	3.18 ± 0.99	7.69 ± 1.02	26 ± 2
31c	WC6	2	11.04	10.34	9.49	0.42 ± 0.03	5.56 ± 1.74	8.09 ± 1.76	-50 ± 22
33	WC6	4	10.62	10.35	9.69	0.13 ± 0.01	6.98 ± 2.18	8.79 ± 2.19	251 ± 72
34	WN5	2	11.20	10.59	10.04	0.50 ± 0.03	4.78 ± 0.74	7.79 ± 0.78	-96 ± 18
37	WN4b	2	11.03	10.34	9.67	0.50 ± 0.03	6.36 ± 1.11	8.29 ± 1.14	-97 ± 20
38	WC4	2	11.99	11.50	10.79	0.25 ± 0.03	6.43 ± 0.98	8.32 ± 1.01	-84 ± 16
38a	WN5	2	11.53	11.21	10.70	0.40 ± 0.05	6.81 ± 1.07	8.49 ± 1.10	-90 ± 17

Continued on next page

Table C.1 – *Continued from previous page*

WR#	Sp. Type	ref	J	H	K_S	$\bar{A}_{K_S}$	d(kpc)	R_G(kpc)	z(pc)
40	WN8h	2	6.62	6.41	6.11	0.20 ± 0.02	2.48 ± 0.41	7.42 ± 0.48	-190 ± 34
42a	WN5b	2	12.08	11.31	10.81	0.38 ± 0.03	12.20 ± 1.91	11.93 ± 1.93	-84 ± 16
42b	WN4b	2	11.35	10.52	9.90	0.51 ± 0.03	7.05 ± 1.23	8.48 ± 1.25	-168 ± 33
42c	WN5	2	11.15	10.47	9.90	0.53 ± 0.03	4.41 ± 0.68	7.59 ± 0.73	-10 ± 5
42d	WN5b	2	10.20	9.52	8.91	0.45 ± 0.03	4.92 ± 0.77	7.70 ± 0.81	-21 ± 6
43-1	WN4b	6	13.16	11.57	10.47	1.13 ± 0.06	6.88 ± 1.21	8.39 ± 1.24	-59 ± 14
44	WN4	2	11.16	10.89	10.48	0.45 ± 0.03	4.83 ± 0.98	7.71 ± 1.01	125 ± 22
44a	WN5b	2	12.07	11.34	10.82	0.39 ± 0.03	12.18 ± 1.91	11.79 ± 1.93	-95 ± 18
45	WC6	2	10.60	9.99	9.19	0.35 ± 0.02	5.03 ± 1.57	7.48 ± 1.59	-33 ± 16
45a	WN5	2	11.90	11.24	10.73	0.48 ± 0.03	6.66 ± 1.03	7.93 ± 1.06	75 ± 9
45b	WN4b	2	11.45	10.61	9.92	0.57 ± 0.03	6.91 ± 1.20	7.98 ± 1.23	-28 ± 8
45-3	WN5b	3	12.57	11.57	10.94	0.57 ± 0.04	11.89 ± 1.87	11.04 ± 1.89	-152 ± 27
45-4	WN6	6	11.65	10.76	10.14	0.64 ± 0.04	6.73 ± 1.33	7.81 ± 1.35	-47 ± 13
45c	WN5	2	11.35	10.79	10.32	0.42 ± 0.03	5.66 ± 0.88	7.45 ± 0.91	-34 ± 8
46a	WN4	2	12.08	11.42	10.92	0.65 ± 0.04	5.38 ± 1.09	7.18 ± 1.12	-89 ± 22
46-1	WN6	7	11.55	10.82	10.22	0.57 ± 0.03	7.24 ± 1.43	7.89 ± 1.45	-7 ± 5
46-8	WN6	8	12.02	10.70	9.85	0.96 ± 0.05	5.08 ± 1.01	7.16 ± 1.04	-20 ± 8
46-9*	WN5	3	12.07	10.72	9.88	0.96 ± 0.06	3.60 ± 0.56	7.04 ± 0.62	4 ± 2
46-2	WN7h	7	10.56	9.64	9.03	0.68 ± 0.04	4.93 ± 0.95	7.10 ± 0.98	-31 ± 10
46-5	WN6	9	-	-	10.92	1.18 ± 0.13[7]	8.63 ± 1.97	8.49 ± 1.99	-42 ± 14
46-6	WN7	9	-	-	10.48	1.18 ± 0.13[7]	9.10 ± 2.24	8.76 ± 2.25	-45 ± 16
46-15	WN8	10	13.13	11.03	9.84	1.51 ± 0.08	7.58 ± 1.28	7.94 ± 1.30	-7 ± 4
46-12	WN4b	3	13.56	12.55	11.84	0.64 ± 0.04	16.19 ± 2.82	13.97 ± 2.83	-128 ± 26
46-14	WN5b	6	12.93	11.76	10.96	0.75 ± 0.04	11.04 ± 1.74	9.68 ± 1.76	-91 ± 17
47a	WN8h	2	10.44	9.68	9.06	0.64 ± 0.04	7.90 ± 1.30	7.67 ± 1.33	-159 ± 29
47-1	WN6	7	12.18	11.22	10.56	0.70 ± 0.04	7.96 ± 1.57	7.70 ± 1.59	7 ± 3
47b	WN9h	2	10.29	9.44	8.84	0.65 ± 0.04	7.96 ± 1.23	7.67 ± 1.26	-88 ± 17
47c	WC5	2	11.24	10.48	9.89	0.20 ± 0.02	6.60 ± 1.20	7.06 ± 1.22	-85 ± 19
48-1	WC7	7	11.06	10.09	9.31	0.41 ± 0.03	5.59 ± 0.94	6.62 ± 0.97	33 ± 2
48-5	WN6b	3	13.06	11.34	10.26	1.15 ± 0.06	7.14 ± 1.24	6.99 ± 1.27	-21 ± 7
49	WN5(h)	2	11.89	11.57	11.21	0.25 ± 0.02	9.19 ± 1.42	7.96 ± 1.44	-386 ± 63
49-1	WN8	10	13.82	11.88	10.67	1.48 ± 0.08	11.29 ± 1.91	9.28 ± 1.93	88 ± 12
52	WC4	2	8.41	8.21	7.55	0.11 ± 0.02	1.54 ± 0.23	7.19 ± 0.34	142 ± 18
52-1	WN6	6	14.77	12.69	11.55	1.42 ± 0.08	9.02 ± 1.81	7.72 ± 1.83	42 ± 5
52-2	WN6	6	12.52	11.40	10.68	0.79 ± 0.05	8.10 ± 1.60	7.15 ± 1.62	84 ± 13
54	WN5	2	10.85	10.48	10.09	0.29 ± 0.02	5.40 ± 0.84	6.39 ± 0.87	-216 ± 37
55	WN7	2	8.77	8.49	8.01	0.36 ± 0.03	3.57 ± 0.69	6.46 ± 0.74	29 ± 2
56	WC7	2	11.84	11.48	10.77	0.21 ± 0.03	12.02 ± 2.03	9.55 ± 2.04	-323 ± 58
57	WC8	2	9.09	8.75	8.01	0.37 ± 0.02	2.98 ± 0.52	6.61 ± 0.57	-242 ± 45

Continued on next page

Table C.1 – *Continued from previous page*

WR#	Sp. Type	ref	J	H	K_S	$\bar{A}_{K_S}$	d(kpc)	R_G(kpc)	z(pc)
57-1	WN7	10	15.01	12.77	11.46	1.65 ± 0.09	9.68 ± 1.92	7.77 ± 1.93	-64 ± 17
60	WC8	2	8.91	8.37	7.70	0.39 ± 0.03	2.56 ± 0.45	6.63 ± 0.51	53 ± 6
60-1	WC8	6	15.30	12.43	10.60	2.04 ± 0.11	4.56 ± 0.82	5.98 ± 0.86	34 ± 3
60-5	WC7	3	10.84	10.12	9.39	0.32 ± 0.03	6.02 ± 1.01	5.98 ± 1.04	134 ± 19
60-4	WC8	10	15.58	12.71	11.00	1.93 ± 0.11	5.75 ± 1.03	6.00 ± 1.06	35 ± 3
61	WN5	2	10.96	10.67	10.35	0.21 ± 0.02	6.32 ± 0.98	6.10 ± 1.01	-411 ± 67
61-2	WN5b	6	13.60	11.39	10.01	1.55 ± 0.09	4.92 ± 0.79	5.88 ± 0.83	11 ± 1
61-3	WC9	10	13.62	11.63	10.38	1.41 ± 0.08	4.79 ± 0.98	5.84 ± 1.02	37 ± 4
61-1	WN6	8	11.68	10.43	9.61	0.91 ± 0.05	4.68 ± 0.93	5.83 ± 0.96	72 ± 10
62	WN6b	2	9.11	8.35	7.75	0.46 ± 0.03	3.08 ± 0.53	6.24 ± 0.59	-21 ± 7
62b	WN5	2	12.01	11.44	10.97	0.42 ± 0.09	7.64 ± 1.41	5.82 ± 1.43	-153 ± 32
64	WC7	2	12.50	12.03	11.33	0.23 ± 0.02	15.35 ± 2.59	10.55 ± 2.61	775 ± 127
64-1	WN4b	6	13.84	11.83	10.64	1.32 ± 0.07	6.83 ± 1.21	5.32 ± 1.23	-38 ± 10
67-2	WC7	3	10.34	9.26	8.46	0.46 ± 0.03	3.68 ± 0.62	5.62 ± 0.67	-7 ± 5
68a	WN6	2	9.59	9.02	8.62	0.36 ± 0.02	3.80 ± 0.75	5.52 ± 0.79	-22 ± 8
68-1	WN4b	6	13.88	12.15	11.06	1.16 ± 0.07	8.88 ± 1.56	5.56 ± 1.58	-11 ± 5
70a	WN6	2	10.94	10.24	9.76	0.47 ± 0.03	6.13 ± 1.21	4.26 ± 1.24	-72 ± 18
70-1	WN7	8	13.84	12.39	11.46	1.10 ± 0.06	12.40 ± 2.42	7.51 ± 2.43	-23 ± 8
70-3	WC7	3	10.96	9.94	9.06	0.53 ± 0.03	4.68 ± 0.79	4.89 ± 0.83	9 ± 2
70-4	WN9h	11	14.58	12.22	10.87	1.72 ± 0.10	12.46 ± 1.99	7.20 ± 2.01	219 ± 32
70-5	WC9	11	11.19	9.71	8.49	1.24 ± 0.07	2.17 ± 0.44	6.31 ± 0.51	-2 ± 5
70-6	WN6b	3	15.16	12.51	10.97	1.80 ± 0.10	7.34 ± 1.30	4.29 ± 1.33	25 ± 1
70-7	WN6b	10	15.94	13.05	11.36	2.00 ± 0.11	7.99 ± 1.43	4.27 ± 1.45	52 ± 6
70-8	WN7	10	15.64	12.59	10.91	2.20 ± 0.12	5.84 ± 1.16	4.19 ± 1.19	105 ± 17
70-2	WN5b	3	10.88	9.52	8.66	0.86 ± 0.05	3.63 ± 0.57	5.20 ± 0.63	69 ± 8
70-9	WC8	10	15.56	12.87	11.31	1.75 ± 0.10	7.20 ± 1.28	4.10 ± 1.31	29 ± 2
70-11	WN7	3	12.02	10.65	9.88	0.94 ± 0.05	6.47 ± 1.25	4.05 ± 1.27	96 ± 15
71	WN6	2	9.48	9.31	9.09	0.10 ± 0.01	5.34 ± 1.05	4.93 ± 1.09	-689 ± 139
72-3	WC9	12	15.62	13.05	11.53	1.82 ± 0.10	6.74 ± 1.40	3.80 ± 1.42	92 ± 15
72-1	WC9	7	10.16	9.25	8.46	0.72 ± 0.04	2.73 ± 0.56	5.76 ± 0.61	-4 ± 5
73-1	WC7	3	15.05	12.79	11.54	1.18 ± 0.07	10.94 ± 1.88	5.42 ± 1.90	-45 ± 11
74	WN7	2	9.73	9.22	8.80	0.40 ± 0.03	5.04 ± 0.97	4.28 ± 1.00	-36 ± 11
74-1	WN9ha	10	15.50	12.28	10.59	2.37 ± 0.13	8.15 ± 1.24	3.71 ± 1.27	13 ± 1
74-2	WN7	10	15.64	12.90	11.43	1.94 ± 0.11	8.34 ± 1.66	3.64 ± 1.68	27 ± 2
75	WN6b	2	8.60	8.24	7.84	0.19 ± 0.02	3.64 ± 0.62	5.05 ± 0.67	-74 ± 16
75a	WC9	2	9.96	9.14	8.50	0.56 ± 0.03	2.98 ± 0.60	5.48 ± 0.65	-26 ± 9
75-1	WC8	6	13.28	11.76	10.73	0.97 ± 0.06	7.89 ± 1.40	3.48 ± 1.42	57 ± 7
75-14	WC9	3	14.50	12.37	11.22	1.37 ± 0.08	7.17 ± 1.50	3.34 ± 1.52	51 ± 7
75b	WC9	2	9.76	9.00	8.36	0.54 ± 0.04	2.82 ± 0.57	5.55 ± 0.63	36 ± 3

Continued on next page

Table C.1 – *Continued from previous page*

WR#	Sp. Type	ref	J	H	K_S	$\bar{A}_{K_S}$	d(kpc)	R_G(kpc)	z(pc)
75-15	WC8	12	-	13.16	11.50	1.81 ± 0.25	7.66 ± 1.61	3.32 ± 1.63	57 ± 8
75-6	WN5b	10	14.65	12.80	11.76	1.15 ± 0.07	13.28 ± 2.12	6.86 ± 2.14	37 ± 3
75-16	WC8	12	-	13.49	11.83	1.81 ± 0.25	8.90 ± 1.86	3.66 ± 1.88	43 ± 5
75-2	WC8	6	15.56	12.86	11.32	1.73 ± 0.10	7.31 ± 1.31	3.23 ± 1.33	44 ± 4
75-3	WC8	6	15.11	12.86	11.47	1.49 ± 0.09	8.75 ± 1.57	3.52 ± 1.59	43 ± 4
75-4	WN5b	6	15.00	12.70	11.34	1.55 ± 0.09	9.08 ± 1.47	3.65 ± 1.49	46 ± 4
75-17	WC8	12	16.00	14.17	12.75	1.39 ± 0.09	16.51 ± 3.05	9.73 ± 3.06	48 ± 5
75-7	WC9	10	14.97	12.96	11.63	1.49 ± 0.08	8.21 ± 1.69	3.32 ± 1.71	46 ± 5
75-8	WN4b	3	15.00	12.44	10.90	1.78 ± 0.10	6.22 ± 1.12	3.42 ± 1.14	-11 ± 6
75c	WC9	13	11.62	11.12	10.52	0.44 ± 0.03	8.00 ± 1.62	2.83 ± 1.64	406 ± 78
75d	WC9	13	10.68	9.88	9.12	0.66 ± 0.04	3.78 ± 0.77	4.72 ± 0.81	90 ± 14
75-10	WN6b	3	13.75	11.70	10.46	1.38 ± 0.08	7.03 ± 1.23	3.11 ± 1.26	63 ± 8
75-5	WC8	6	14.90	12.77	11.43	1.41 ± 0.08	8.93 ± 1.60	3.57 ± 1.62	-48 ± 12
75-12	WN6	10	15.02	12.85	11.49	1.63 ± 0.09	7.98 ± 1.63	3.15 ± 1.65	49 ± 6
75-22	WC9	12	-	13.72	12.03	2.01 ± 0.30	7.80 ± 1.99	3.14 ± 2.00	30 ± 3
75-13	WC8	10	13.60	11.67	10.39	1.30 ± 0.07	5.80 ± 1.03	3.48 ± 1.06	26 ± 1
75-23	WC9	12	10.27	9.59	8.93	0.54 ± 0.03	3.67 ± 0.75	4.80 ± 0.79	49 ± 6
76-1	WN9	10	14.84	12.00	10.42	2.05 ± 0.11	8.69 ± 1.41	3.14 ± 1.43	82 ± 10
77-1	WN7b	3	10.06	9.00	8.29	0.65 ± 0.04	4.03 ± 0.63	4.45 ± 0.67	38 ± 3
77-2	WN7	8	10.75	9.52	8.73	0.93 ± 0.05	3.83 ± 0.74	4.60 ± 0.78	5 ± 3
77-5	WN6	12	10.56	9.71	9.14	0.58 ± 0.03	4.37 ± 0.86	4.22 ± 0.90	17 ± 1
77-3	WN6	10	11.12	9.84	9.10	0.85 ± 0.05	3.79 ± 0.75	4.64 ± 0.79	-19 ± 8
77-4	WN6	3	14.14	11.85	10.59	1.58 ± 0.09	5.38 ± 1.09	3.51 ± 1.12	-54 ± 15
77-6	WN6b	3	13.56	11.93	10.95	1.04 ± 0.06	10.27 ± 1.78	3.65 ± 1.80	120 ± 17
77-7	WC9	12	-	13.46	12.06	1.60 ± 0.22	9.51 ± 2.17	3.18 ± 2.19	61 ± 10
81	WC9	2	8.29	7.76	7.12	0.48 ± 0.03	1.64 ± 0.34	6.47 ± 0.42	-55 ± 15
82	WN7(h)	2	9.48	9.04	8.69	0.32 ± 0.02	4.98 ± 0.95	3.61 ± 0.99	-182 ± 39
83	WN5	2	10.26	9.89	9.53	0.27 ± 0.02	4.20 ± 0.65	4.24 ± 0.70	-281 ± 47
84	WN7	2	9.58	8.96	8.50	0.46 ± 0.10	4.28 ± 0.93	3.95 ± 0.96	4 ± 3
84-2	WC8	12	13.98	12.20	10.98	1.21 ± 0.07	7.95 ± 1.41	1.73 ± 1.43	43 ± 4
84-1	WN9	3	12.37	10.43	9.19	1.51 ± 0.08	6.31 ± 1.00	2.28 ± 1.03	40 ± 3
84-4	WN7ha	3	10.88	10.00	9.49	0.69 ± 0.04	16.50 ± 3.02	8.86 ± 3.03	35 ± 3
84-5	WC9	12	14.34	12.78	11.59	1.24 ± 0.07	9.03 ± 1.86	1.97 ± 1.87	75 ± 11
88	WC9	2	9.03	8.56	8.05	0.36 ± 0.03	2.66 ± 0.54	5.37 ± 0.60	114 ± 19
90	WC7	2	6.25	6.09	5.52	0.05 ± 0.02	1.14 ± 0.19	6.92 ± 0.32	-76 ± 16
91	WN7b	2	9.53	8.77	8.20	0.44 ± 0.03	4.25 ± 0.66	3.92 ± 0.70	-60 ± 12
91-1	WC7	3	15.11	12.05	10.33	1.80 ± 0.10	4.69 ± 0.82	3.41 ± 0.85	80 ± 11
92	WC9	2	9.50	9.22	8.82	0.21 ± 0.02	4.07 ± 0.82	4.20 ± 0.86	-294 ± 63
93a	WN3	2	13.88	13.22	12.72	0.65 ± 0.02	10.22 ± 3.25	2.20 ± 3.27	694 ± 214

Continued on next page

Table C.1 – *Continued from previous page*

WR#	Sp. Type	ref	J	H	K_S	$\bar{A}_{K_S}$	d(kpc)	R_G(kpc)	z(pc)
93b	WO3	14	-	-	10.17	0.73 ± 0.04	2.18 ± 0.32	5.84 ± 0.40	-13 ± 5
94	WN5	2	7.09	6.19	5.91	0.32 ± 0.02	0.78 ± 0.12	7.23 ± 0.28	16 ± 1
94-1	WC9	12	15.99	12.59	10.76	2.31 ± 0.13	3.78 ± 0.81	4.24 ± 0.85	35 ± 3
98-1	WC8	12	13.52	11.70	10.56	1.17 ± 0.03	6.67 ± 1.18	1.34 ± 1.20	45 ± 5
100	WN7b	2	8.85	8.27	7.72	0.38 ± 0.03	3.50 ± 0.54	4.51 ± 0.60	-58 ± 12
100-3	WN8	12	13.90	11.52	10.17	1.71 ± 0.05	7.20 ± 1.21	0.82 ± 1.24	-17 ± 6
100-1	WN7b	3	15.12	12.61	11.08	1.75 ± 0.04	8.75 ± 1.37	0.75 ± 1.39	12 ± 1
101	WC8	2	9.62	8.78	7.89	0.66 ± 0.04	2.46 ± 0.43	5.54 ± 0.50	-42 ± 11
101-3	WN8	3	16.67	13.08	11.09	2.61 ± 0.05	7.49 ± 1.26	0.51 ± 1.28	25 ± 1
101-8	WC9	15	-	14.67	12.70	2.31 ± 0.11	9.23 ± 1.93	1.23 ± 1.94	5 ± 3
101-5	WN6b	3	-	15.21	12.22	3.68 ± 0.17	5.50 ± 1.04	2.50 ± 1.07	22 ± 1
101-9	WC9	15	-	14.62	12.02	3.17 ± 0.13	4.53 ± 0.96	3.47 ± 0.99	15 ± 1
101-1	WN9h	3	15.55	12.26	10.42	2.39 ± 0.05	7.40 ± 1.15	0.60 ± 1.18	19 ± 0
101p	WC8	3	16.32	13.05	11.20	2.16 ± 0.06	5.68 ± 1.02	2.32 ± 1.05	21 ± 1
102	WO2	2	-	-	10.62	0.50 ± 0.10	2.99 ± 0.45	5.02 ± 0.52	93 ± 11
102-12	WN9	3	-	13.61	11.14	3.20 ± 0.14	7.11 ± 1.18	0.89 ± 1.20	22 ± 1
102b	WN7b	3	15.44	12.48	10.85	1.95 ± 0.04	7.18 ± 1.11	0.82 ± 1.14	14 ± 1
102bd	WC9	3	16.26	13.47	11.49	2.26 ± 0.07	5.40 ± 1.14	2.60 ± 1.16	15 ± 1
102-17	WN6b	3	16.33	13.27	11.43	2.16 ± 0.04	7.69 ± 1.33	0.32 ± 1.35	9 ± 2
102-8	WN9	3	-	13.74	11.24	3.23 ± 0.15	7.34 ± 1.24	0.66 ± 1.26	14 ± 1
102-9	WN9	3	16.56	12.72	10.54	2.84 ± 0.05	6.37 ± 0.99	1.63 ± 1.02	12 ± 1
102-10	WN8	3	17.06	13.07	10.78	2.97 ± 0.06	5.48 ± 0.92	2.52 ± 0.95	12 ± 1
102-19	WN5	12	11.84	10.95	10.32	0.65 ± 0.04	5.08 ± 0.79	2.98 ± 0.83	73 ± 8
102-20	WC9	12	-	12.38	10.89	1.74 ± 0.26	5.22 ± 1.25	2.85 ± 1.27	-3 ± 5
102l	WN8	2	8.83	8.10	7.57	0.56 ± 0.04	4.15 ± 0.69	3.91 ± 0.73	36 ± 3
107	WN8	2	9.38	8.69	8.19	0.52 ± 0.04	5.62 ± 0.93	2.57 ± 0.96	4 ± 3
107a	WC6	2	11.17	10.31	9.38	0.53 ± 0.04	5.04 ± 1.58	3.09 ± 1.60	-17 ± 12
108	WN9ha	2	7.66	7.34	7.10	0.30 ± 0.02	4.25 ± 0.60	3.82 ± 0.65	-44 ± 9
110	WN5b	2	7.12	6.72	6.22	0.27 ± 0.02	1.55 ± 0.24	6.48 ± 0.35	30 ± 2
111-1	WN6	7	12.58	11.06	10.31	0.91 ± 0.05	6.45 ± 1.27	2.01 ± 1.30	-26 ± 9
111-5*	WN9	3	13.80	11.97	10.92	1.32 ± 0.07	15.29 ± 2.41	7.66 ± 2.43	-14 ± 5
111-6	WC9	12	14.24	13.35	10.75	2.05 ± 0.13	4.22 ± 0.92	3.99 ± 0.95	21 ± 1
111-3	WC8	6	11.21	9.70	8.57	1.05 ± 0.06	2.81 ± 0.49	5.30 ± 0.55	26 ± 1
113-1	WN7	7	9.09	8.30	7.76	0.58 ± 0.04	2.88 ± 0.56	5.27 ± 0.61	-0 ± 4
114-1	WN7b	7	12.21	11.24	10.61	0.55 ± 0.04	12.25 ± 1.91	5.52 ± 1.93	230 ± 33
114-2	WC8	12	14.45	12.90	11.69	1.13 ± 0.07	11.43 ± 2.07	4.66 ± 2.09	138 ± 22
115-1	WN6	7	10.32	9.52	8.96	0.56 ± 0.03	4.07 ± 0.80	4.32 ± 0.84	-21 ± 8
115-2	WN8	10	11.53	10.13	9.28	1.02 ± 0.06	7.36 ± 1.22	2.56 ± 1.25	-16 ± 6
115-3	WN7	10	9.59	8.82	8.30	0.56 ± 0.03	3.72 ± 0.71	4.63 ± 0.76	-8 ± 5

Continued on next page

Table C.1 – *Continued from previous page*

WR#	Sp. Type	ref	J	H	K_S	$\bar{A}_{K_S}$	d(kpc)	R_G(kpc)	z(pc)
116	WN8h	2	8.21	7.57	6.95	0.60 ± 0.03	3.07 ± 0.50	5.20 ± 0.56	3 ± 3
116-2	WN5	6	14.07	12.75	11.93	0.94 ± 0.05	9.32 ± 1.46	3.65 ± 1.48	162 ± 22
116-3	WN6ha	3	10.68	9.91	9.43	0.61 ± 0.04	14.53 ± 2.36	7.66 ± 2.37	-29 ± 8
117-1	WN7	10	9.09	8.29	7.63	0.68 ± 0.04	2.59 ± 0.50	5.67 ± 0.56	11 ± 2
118-4	WC8	10	12.18	10.52	9.36	1.12 ± 0.06	3.92 ± 0.68	4.63 ± 0.73	-7 ± 5
118-7	WC9	12	15.91	12.89	11.01	2.25 ± 0.12	4.37 ± 0.92	4.42 ± 0.95	30 ± 2
118-8	WC9	12	15.63	13.02	11.29	2.00 ± 0.11	5.55 ± 1.16	3.84 ± 1.19	23 ± 1
118-6	WN7	10	13.64	11.73	10.59	1.42 ± 0.08	7.21 ± 1.40	3.39 ± 1.43	-31 ± 10
118-9	WC9	12	14.78	13.04	11.15	1.87 ± 0.12	5.54 ± 1.20	3.89 ± 1.22	29 ± 2
119-2	WC8	10	11.83	10.49	9.56	0.83 ± 0.05	4.90 ± 0.85	4.22 ± 0.89	21 ± 1
119-3	WN7	12	13.27	11.50	10.50	1.25 ± 0.07	7.46 ± 1.46	3.47 ± 1.48	-40 ± 12
120	WN7	2	8.90	8.41	8.01	0.38 ± 0.03	3.54 ± 0.68	5.14 ± 0.73	37 ± 3
120-1	WC9	7	11.05	10.17	9.44	0.65 ± 0.04	4.41 ± 0.90	4.56 ± 0.93	24 ± 1
120-11	WC8	12	12.35	11.15	10.25	0.77 ± 0.04	6.95 ± 1.21	3.60 ± 1.23	-25 ± 8
120-7	WN7	10	10.22	9.21	8.51	0.78 ± 0.04	3.71 ± 0.71	5.00 ± 0.76	12 ± 2
120-8	WN9	3	12.86	10.82	9.66	1.47 ± 0.08	7.97 ± 1.26	3.91 ± 1.29	60 ± 6
120-3	WN9	16	11.95	10.22	9.16	1.29 ± 0.07	6.89 ± 1.08	3.82 ± 1.11	60 ± 6
120-4	WN9	16	11.85	10.26	9.27	1.20 ± 0.07	7.55 ± 1.19	3.85 ± 1.21	60 ± 6
120-5	WC8	16	12.39	10.83	9.75	1.03 ± 0.06	4.89 ± 0.85	4.37 ± 0.89	47 ± 5
120-6	WN6	11	13.51	12.83	12.32	0.48 ± 0.03	19.85 ± 3.92	13.44 ± 3.92	177 ± 31
120-9	WN7ha	3	15.15	12.55	11.14	1.95 ± 0.11	19.74 ± 3.81	13.27 ± 3.82	-16 ± 7
120-10	WN7	10	10.00	9.16	8.53	0.67 ± 0.04	3.94 ± 0.76	4.97 ± 0.80	47 ± 5
121-2	WN7	10	14.22	12.23	11.13	1.40 ± 0.08	9.29 ± 1.84	4.53 ± 1.85	8 ± 2
121-3	WN7	10	13.81	11.87	10.73	1.43 ± 0.08	7.66 ± 1.49	3.95 ± 1.51	4 ± 3
121-1	WN7h	11	10.94	10.07	9.47	0.66 ± 0.04	6.12 ± 1.18	4.27 ± 1.21	14 ± 1
121-4	WC7	12	14.13	12.13	10.66	1.31 ± 0.07	6.89 ± 1.18	4.07 ± 1.21	-62 ± 14
122-2	WN9	3	12.49	10.68	9.61	1.33 ± 0.07	8.35 ± 1.32	4.68 ± 1.34	-13 ± 5
122-3	WN6	3	12.81	11.06	9.99	1.27 ± 0.07	4.72 ± 0.94	4.90 ± 0.97	25 ± 1
122-4	WC8	10	14.70	12.67	11.25	1.45 ± 0.08	8.07 ± 1.44	5.17 ± 1.46	-45 ± 12
122-5	WC8	10	14.25	12.27	10.99	1.31 ± 0.08	7.61 ± 1.35	5.03 ± 1.37	-42 ± 11
123	WN8	2	9.52	9.28	8.92	0.26 ± 0.02	8.81 ± 1.45	4.48 ± 1.48	-711 ± 120
123-1	WN6	7	10.59	9.47	8.71	0.83 ± 0.05	3.20 ± 0.63	6.04 ± 0.68	28 ± 2
123-4	WC8	12	16.31	14.38	13.68	0.80 ± 0.09	33.24 ± 6.41	27.58 ± 6.42	-56 ± 15
123-3	WN8	10	12.22	10.81	9.94	1.05 ± 0.06	9.83 ± 1.63	6.79 ± 1.65	110 ± 15
124-8	WN6	12	8.61	7.99	7.80	0.18 ± 0.02	2.84 ± 0.56	6.36 ± 0.61	46 ± 5
124-3	WC7	12	12.95	11.82	10.77	0.71 ± 0.04	9.47 ± 1.60	7.11 ± 1.61	85 ± 11
124-9	WC6	12	13.90	12.72	11.67	0.73 ± 0.04	13.17 ± 4.12	9.88 ± 4.13	195 ± 55
124-10	WC6	12	14.35	12.59	11.33	1.06 ± 0.06	9.66 ± 3.03	7.37 ± 3.04	79 ± 19
124-6	WC6	3	12.67	10.91	9.68	1.04 ± 0.06	4.57 ± 1.43	6.08 ± 1.45	-11 ± 9

Continued on next page

Table C.1 – *Continued from previous page*

WR#	Sp. Type	ref	J	H	K_S	$\bar{A}_{K_S}$	d(kpc)	R_G(kpc)	z(pc)
124-7	WC8	12	12.83	11.02	9.58	1.40 ± 0.08	3.82 ± 0.67	6.21 ± 0.72	-5 ± 4
124-11	WN6b	3	12.65	11.19	10.25	0.95 ± 0.05	7.77 ± 1.35	6.92 ± 1.37	112 ± 16
125-1	WC8	7	10.20	9.61	9.07	0.28 ± 0.02	5.06 ± 0.87	6.56 ± 0.91	6 ± 2
125-4	WN7	10	12.71	11.07	10.12	1.18 ± 0.07	6.47 ± 1.26	6.61 ± 1.28	-1 ± 4
128	WN4(h)	2	9.97	9.84	9.62	0.25 ± 0.02	3.57 ± 0.72	6.67 ± 0.77	-216 ± 48
129	WN4	2	11.08	10.72	10.40	0.41 ± 0.03	4.75 ± 0.96	7.47 ± 0.99	222 ± 41
130	WN8h	2	8.45	7.87	7.45	0.42 ± 0.03	4.16 ± 0.69	7.52 ± 0.73	89 ± 11
132	WC6	2	10.18	9.76	9.05	0.22 ± 0.02	4.97 ± 1.55	7.80 ± 1.57	115 ± 30
142a	WC7	17	9.27	8.09	7.12	0.64 ± 0.04	1.83 ± 0.31	7.87 ± 0.40	91 ± 12
142-1	WN6	18	8.77	7.86	7.19	0.69 ± 0.04	1.70 ± 0.34	7.93 ± 0.42	106 ± 17
147	WN8(h)+OB	2	6.01	4.86	4.11	0.87 ± 0.05	0.73 ± 0.12	7.90 ± 0.28	15 ± 1
148	WN8h	2	8.76	8.53	8.32	0.15 ± 0.02	7.05 ± 1.16	10.64 ± 1.20	814 ± 131
149	WN5	2	10.62	10.06	9.61	0.40 ± 0.03	4.11 ± 0.64	8.96 ± 0.68	66 ± 7
150	WC5	2	10.72	10.31	9.60	0.22 ± 0.02	5.71 ± 1.03	10.31 ± 1.07	-228 ± 45

Spectral types: (1)Marchenko et al. (2004), (2)van der Hucht (2001), (3) this work, (4)Crowther et al. (1998), (5)Williams et al. (2009b), (6)Shara et al. (2009), (7)Hadfield et al. (2007), (8)Mauerhan et al. (2009), (9)Kurtev et al. (2007), (10)Mauerhan et al. (2011), (11)Wachter et al. (2010), (12)Shara et al. (2012), (13)Hopewell et al. (2005), (14)Drew et al. (2004), (15)Mauerhan et al. (2010c), (16)Mauerhan et al. (2010b), (17)Pasquali et al. (2002), (18)Littlefield et al. (2012).

Appendix D

Spectral energy distributions of Wolf-Rayet stars in Westerlund 1: WN stars

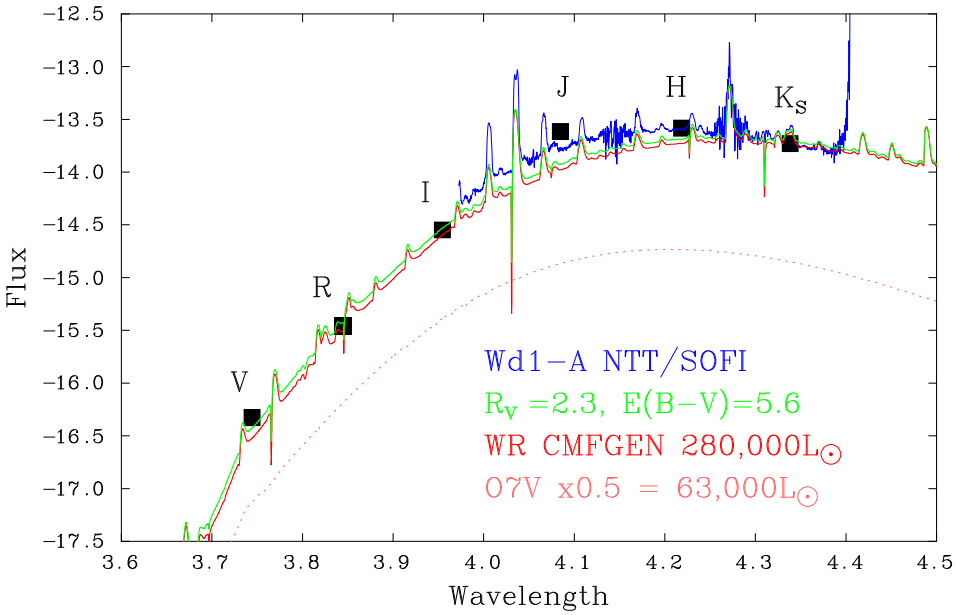

Figure D.1: SED of Wd1-A showing multi-band photometry (filled squares), flux-calibrated near-IR spectra (blue solid line), reddened CMFGEN model (red solid line), reddened and scaled Kurucz O7V model (dotted pink line), total reddened stellar model (green solid line). Applied reddening parameters and stellar luminosities are inset.

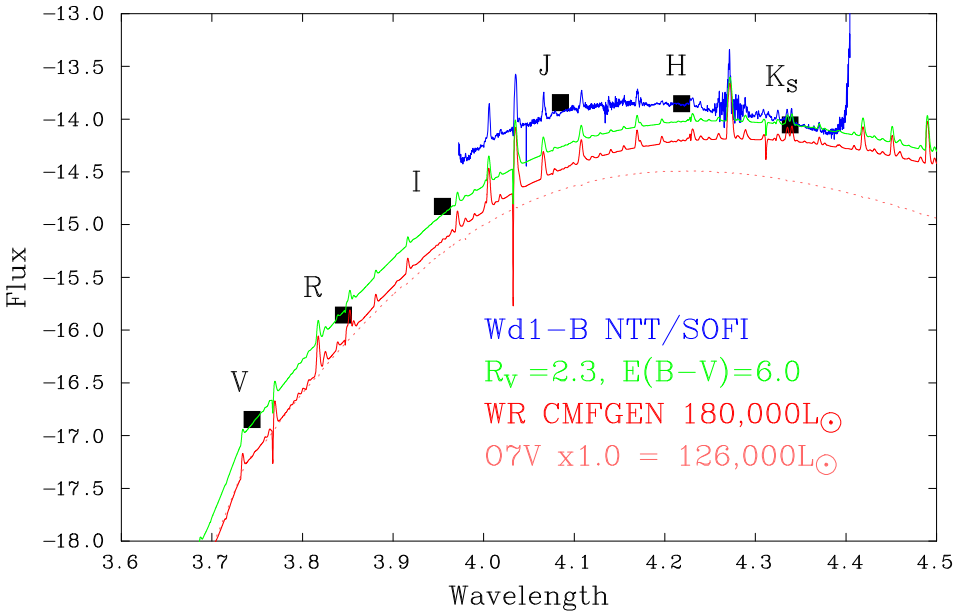

Figure D.2: As Figure D.1 for Wd1-B.

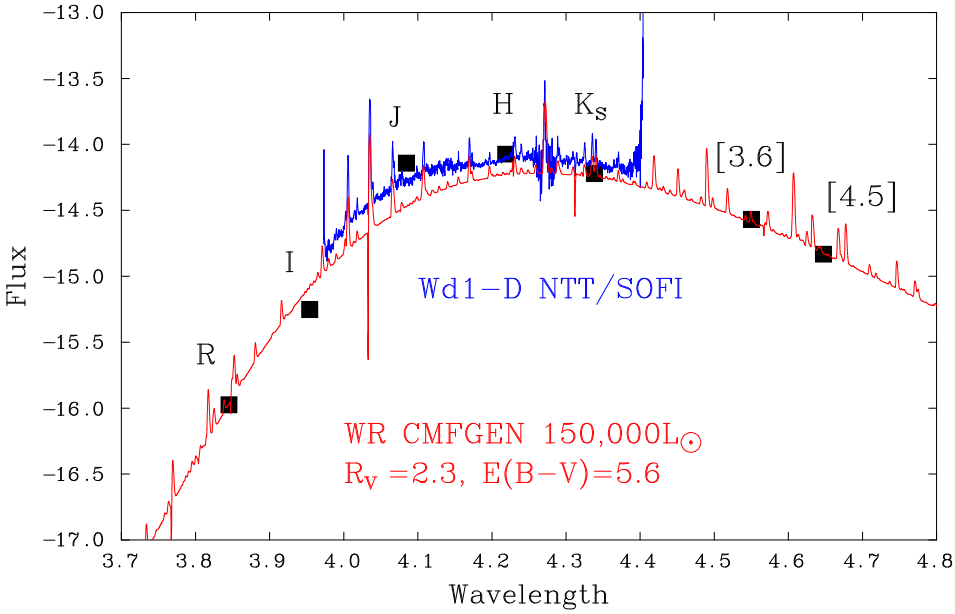

Figure D.3: SED of Wd1-D showing multi-band photometry (filled squares), flux-calibrated near-IR spectra (blue solid line) and reddened CMFGEN model (red solid line). Applied reddening parameters and stellar luminosities are inset.

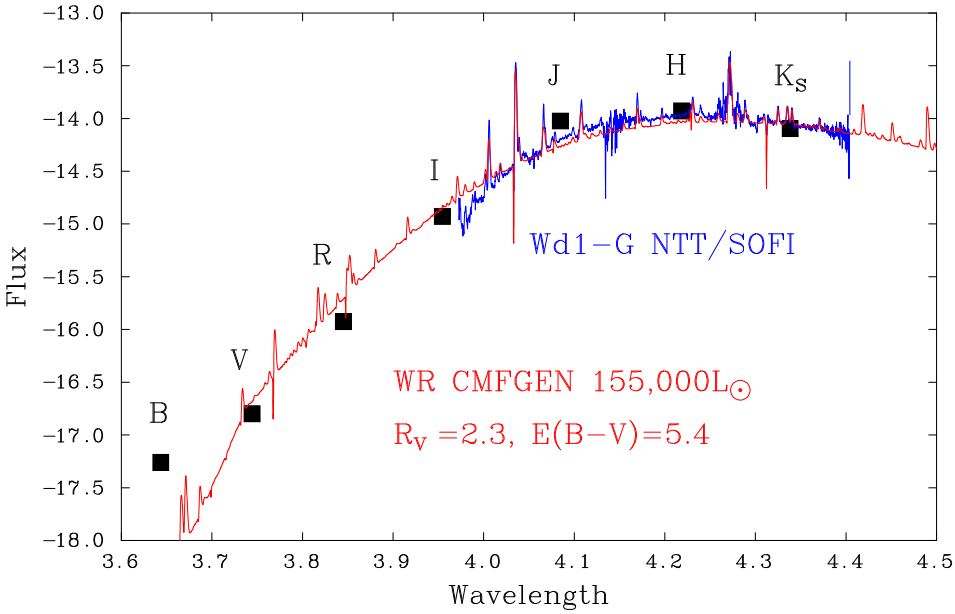

Figure D.4: As Figure D.3 of Wd1-G.

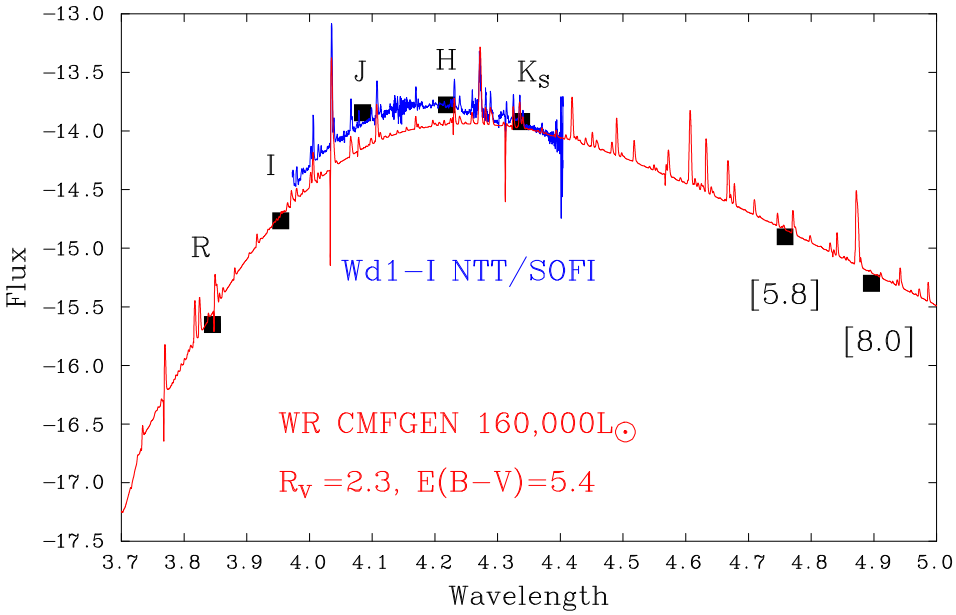

Figure D.5: As Figure D.3 of Wd1-I.

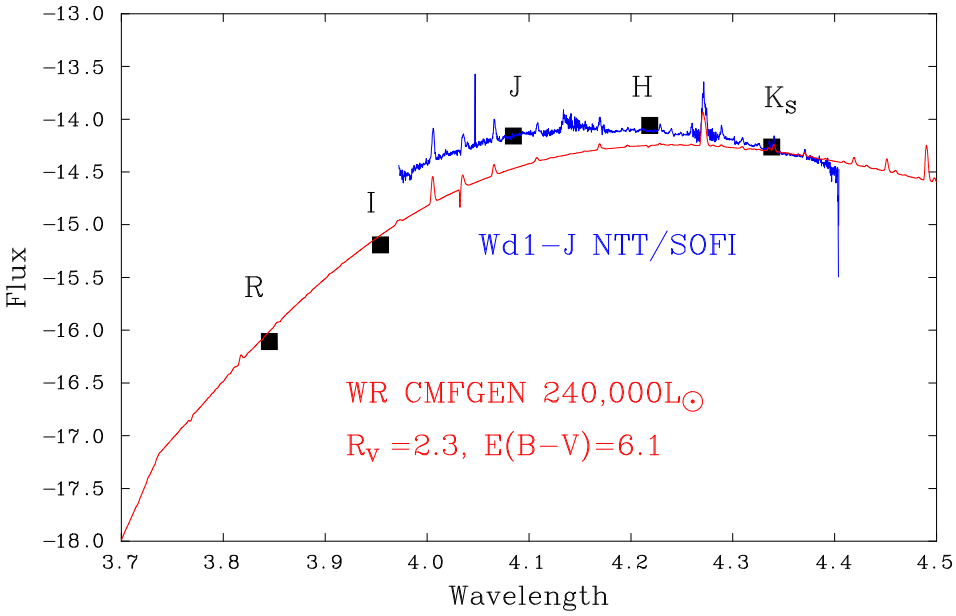

Figure D.6: As Figure D.3 of Wd1-J.

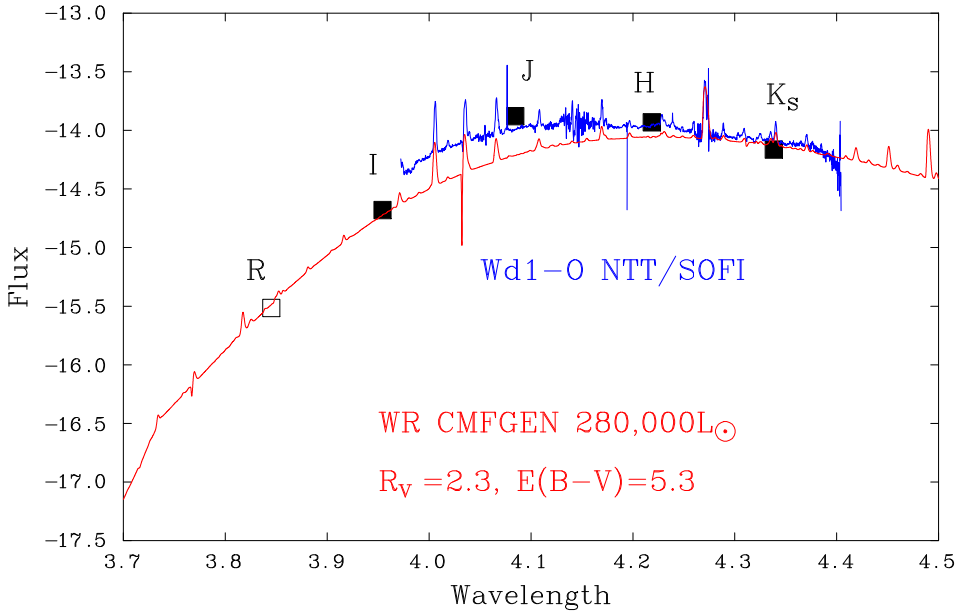

Figure D.7: As Figure D.3 of Wd1-O. Photometry from the USNO B1.0 catalogue is shown as open squares.

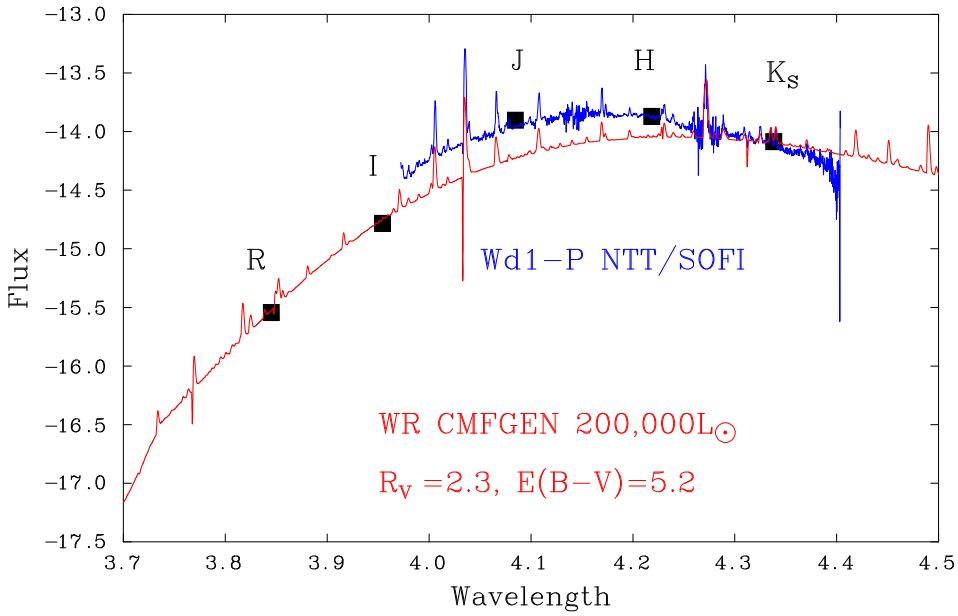

Figure D.8: As Figure D.3 of Wd1-P.

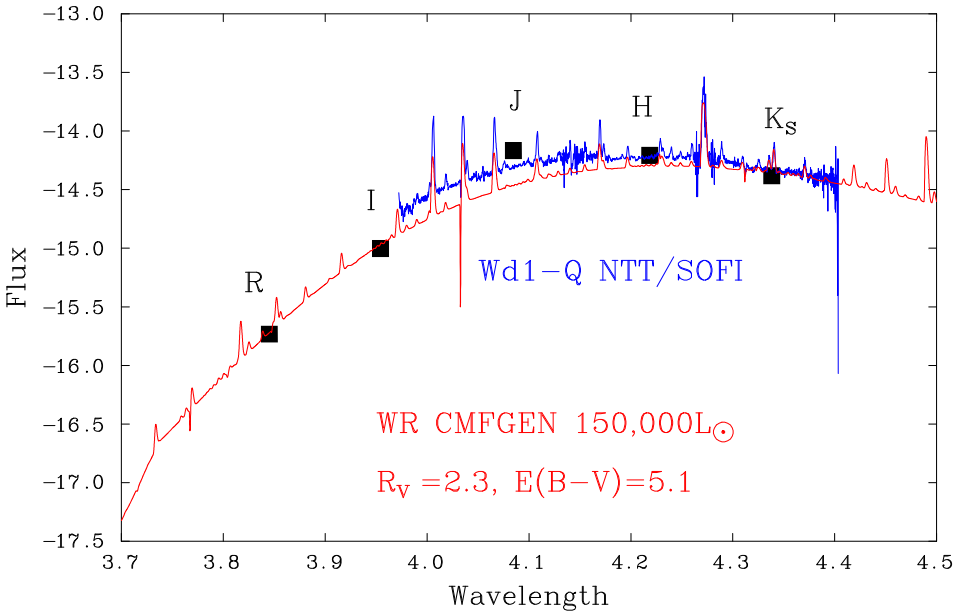

Figure D.9: As Figure D.3 of Wd1-Q.

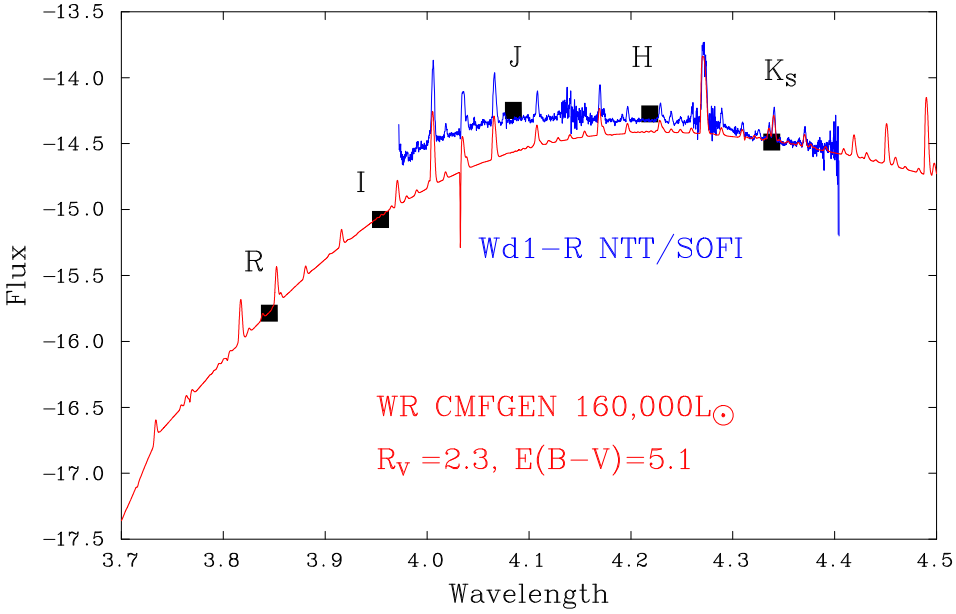

Figure D.10: As Figure D.3 of Wd1-R.

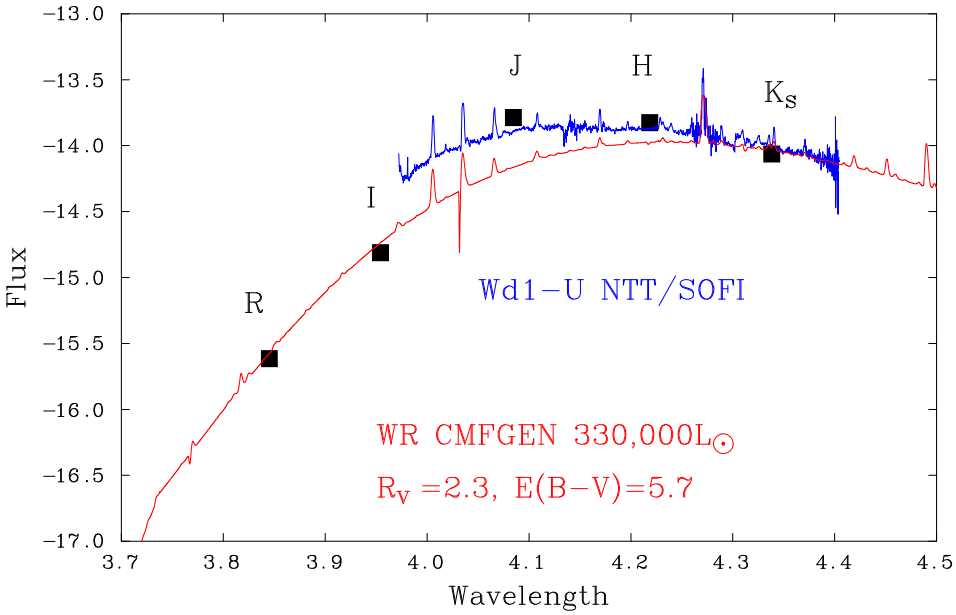

Figure D.11: As Figure D.3 of Wd1-U.

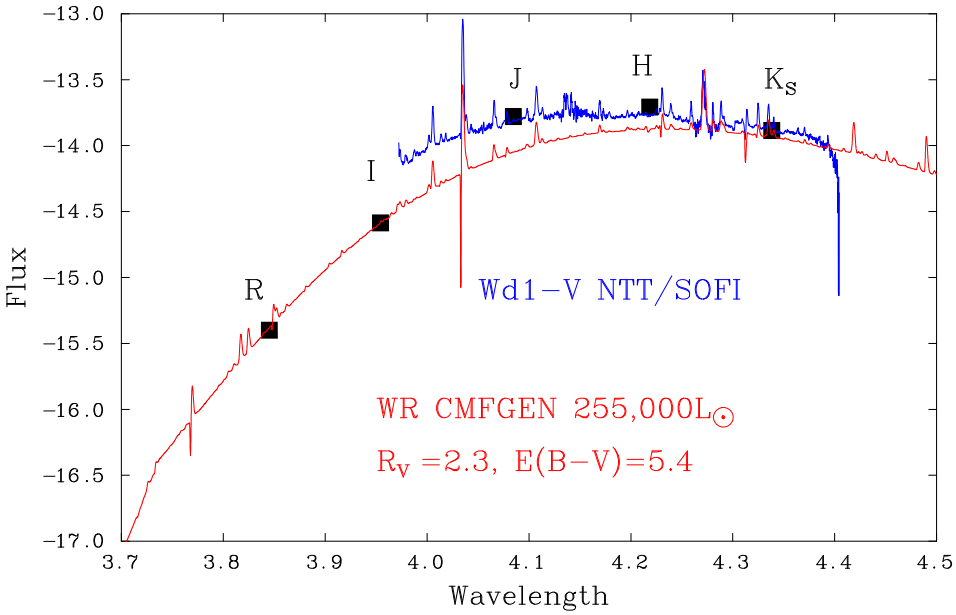

Figure D.12: As Figure D.3 of Wd1-V.

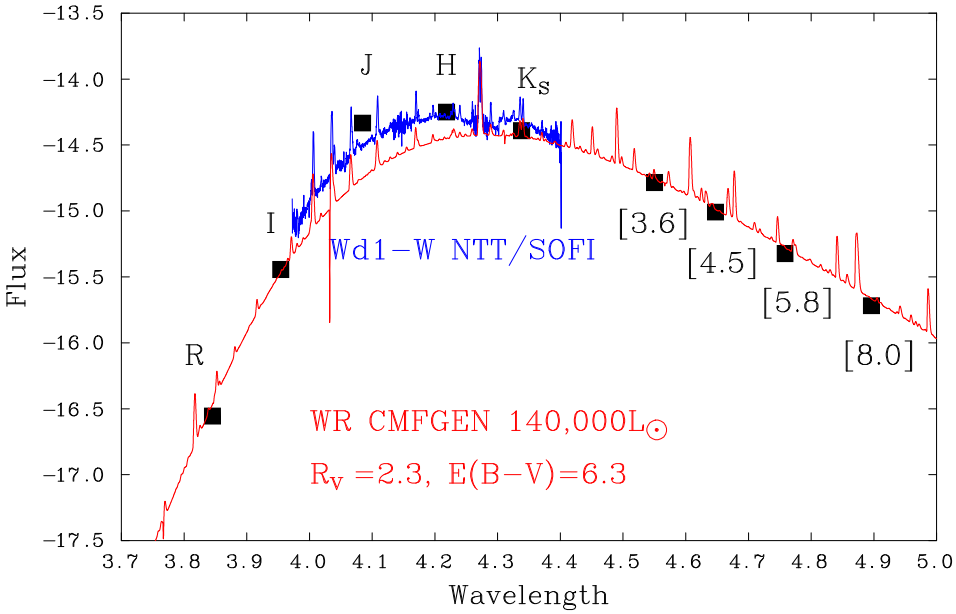

Figure D.13: As Figure D.3 of Wd1-W.

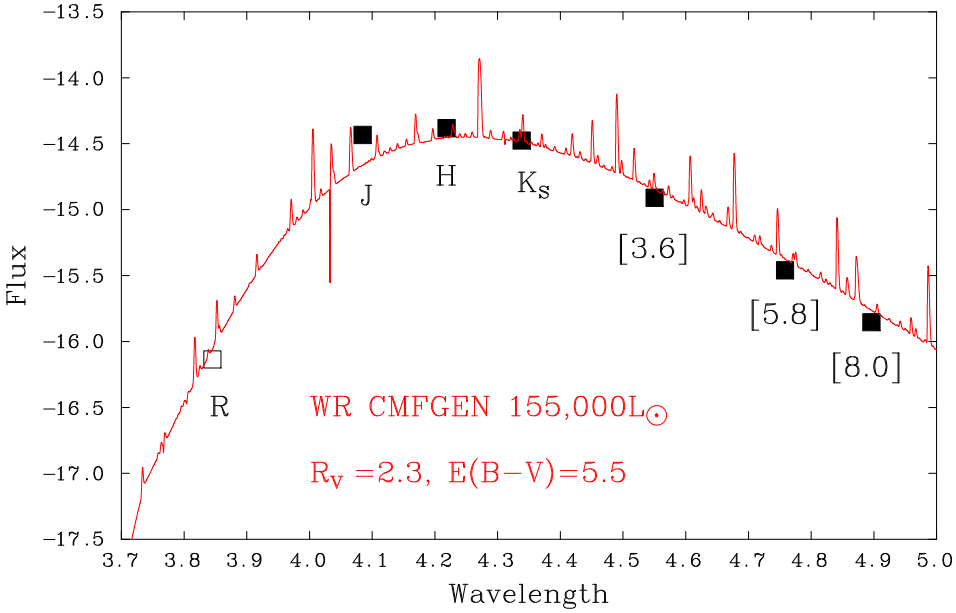

Figure D.14: As Figure D.3 of Wd1-X. Photometry from the USNO B1.0 catalogue is shown as open squares. A flux-calibrated spectrum was not available.

Appendix E

Spectral energy ditriubutions of Wolf-Rayet stars in Westerlund 1: WC stars

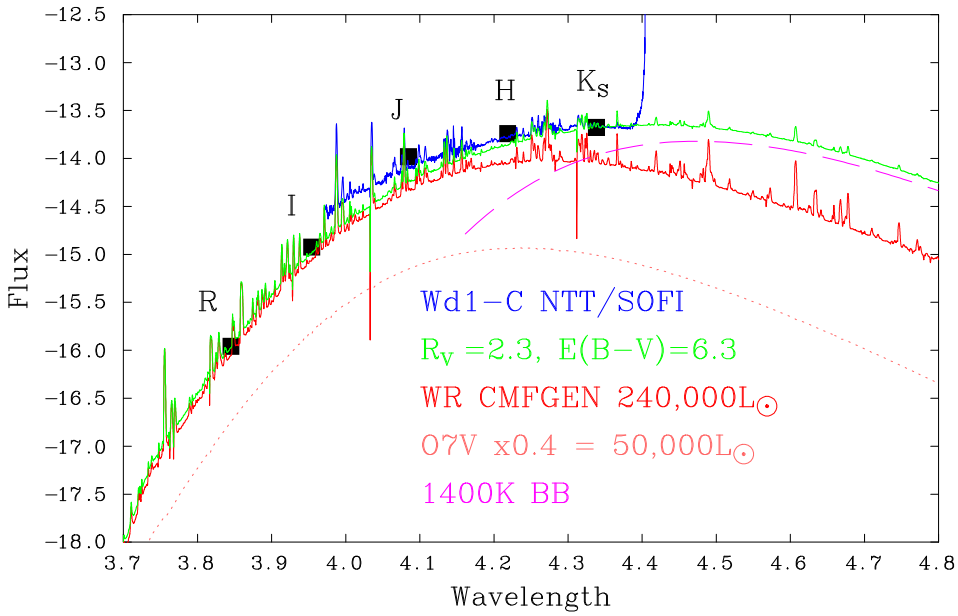

Figure E.1: SED of Wd1-C showing multi-band photometry (filled squares), flux-calibrated near-IR spectra (blue solid line), reddened CMFGEN model (red solid line), reddened and scaled Kurucz O7V model (dotted pink line), reddened and scaled isothermal black body (dashed purple line), total reddened stellar model (green solid line). The applied reddening parameters, stellar luminosities, and black body temperature are inset.

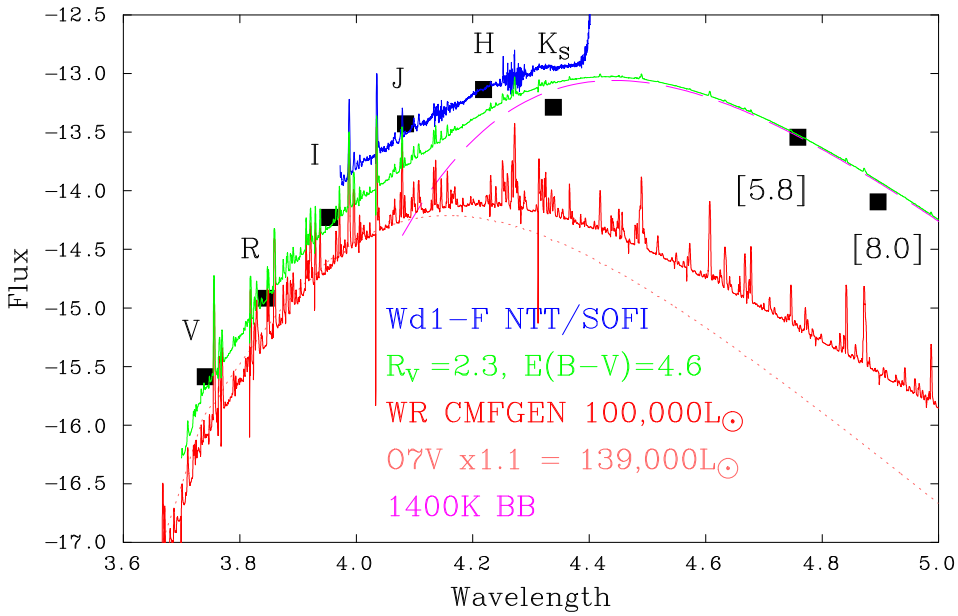

Figure E.2: As Figure E.1 for Wd1-F

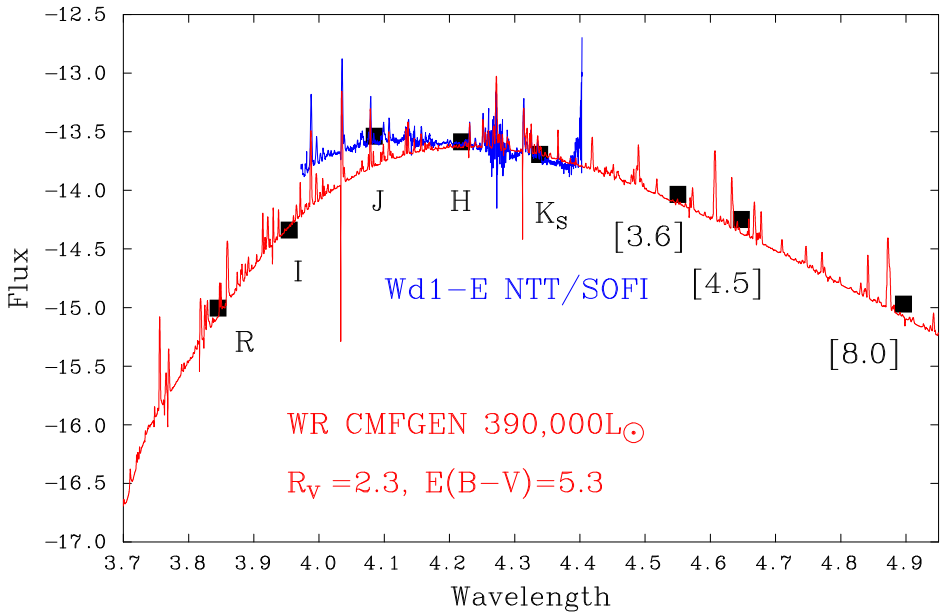

Figure E.3: SED of Wd1-E showing multi-band photometry (filled squares), flux-calibrated near-IR spectra (blue solid line), and reddened CMFGEN model (red solid line). Applied reddening parameters and stellar luminosities are inset.

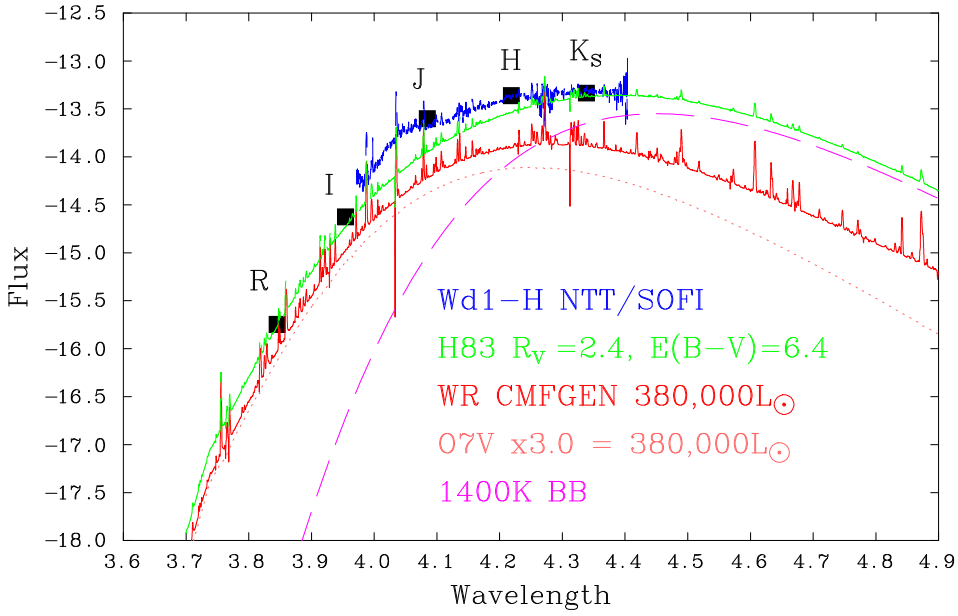

Figure E.4: As Figure E.1 for Wd1-H

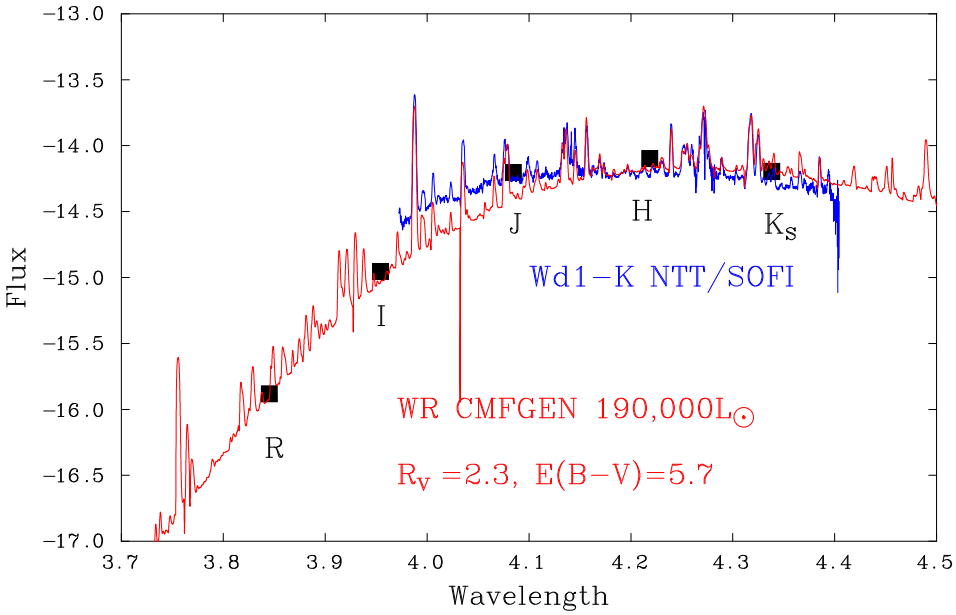

Figure E.5: As Figure E.3 for Wd1-K

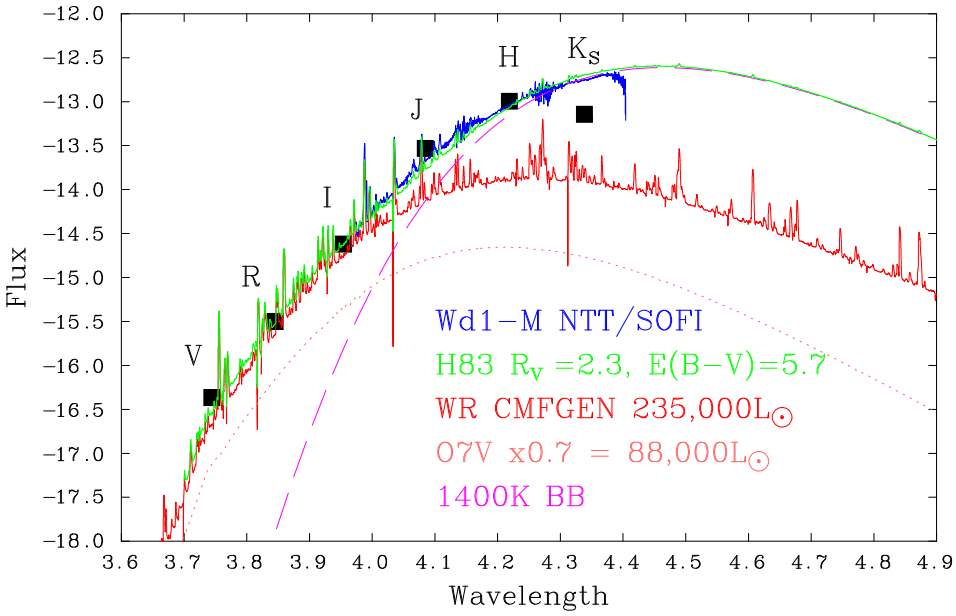

Figure E.6: As Figure E.1 for Wd1-M

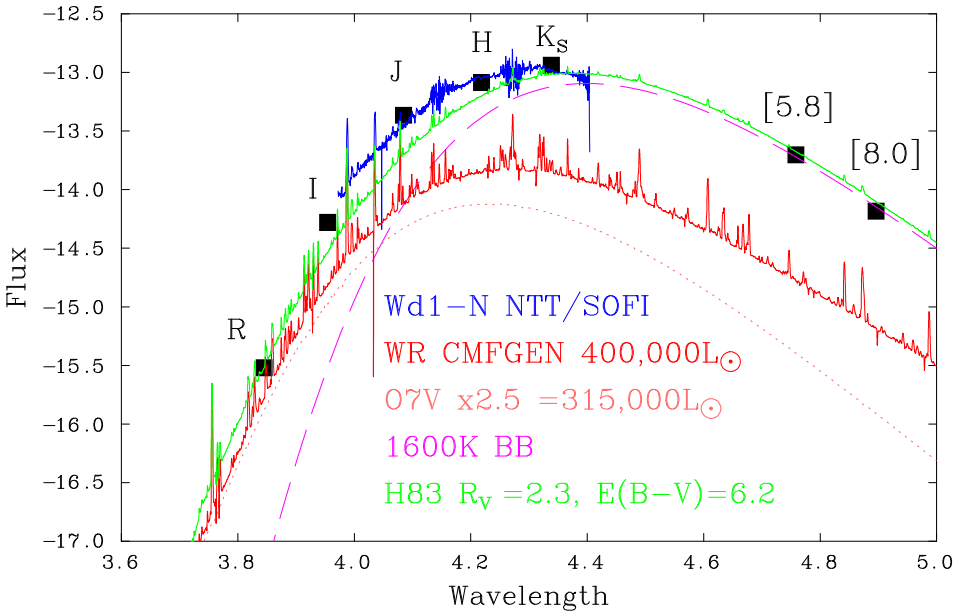

Figure E.7: As Figure E.1 for Wd1-N

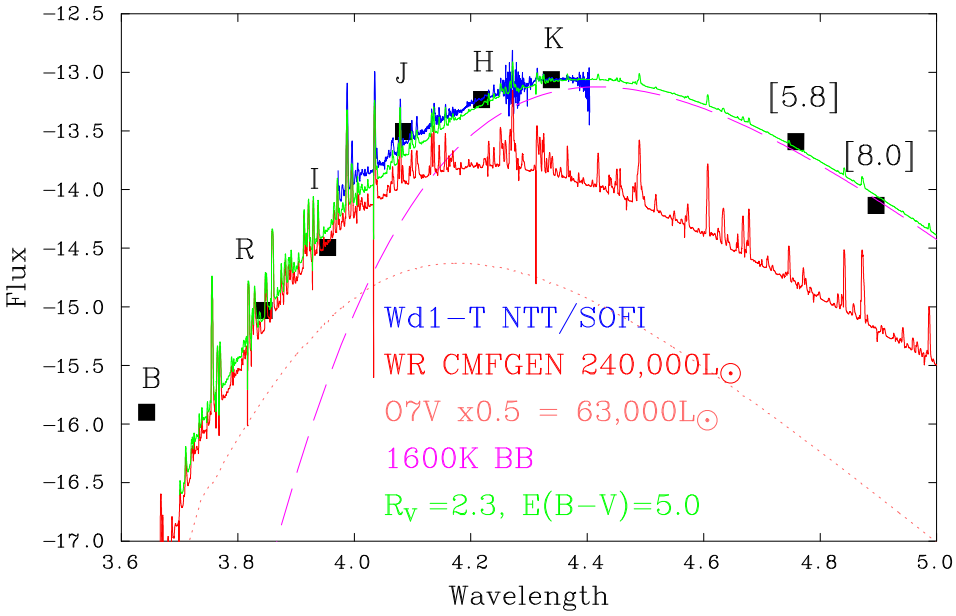

Figure E.8: As Figure E.1 for Wd1-T

Appendix F

Model fits to spectra of Wolf-Rayet stars in Westerlund 1: WN stars

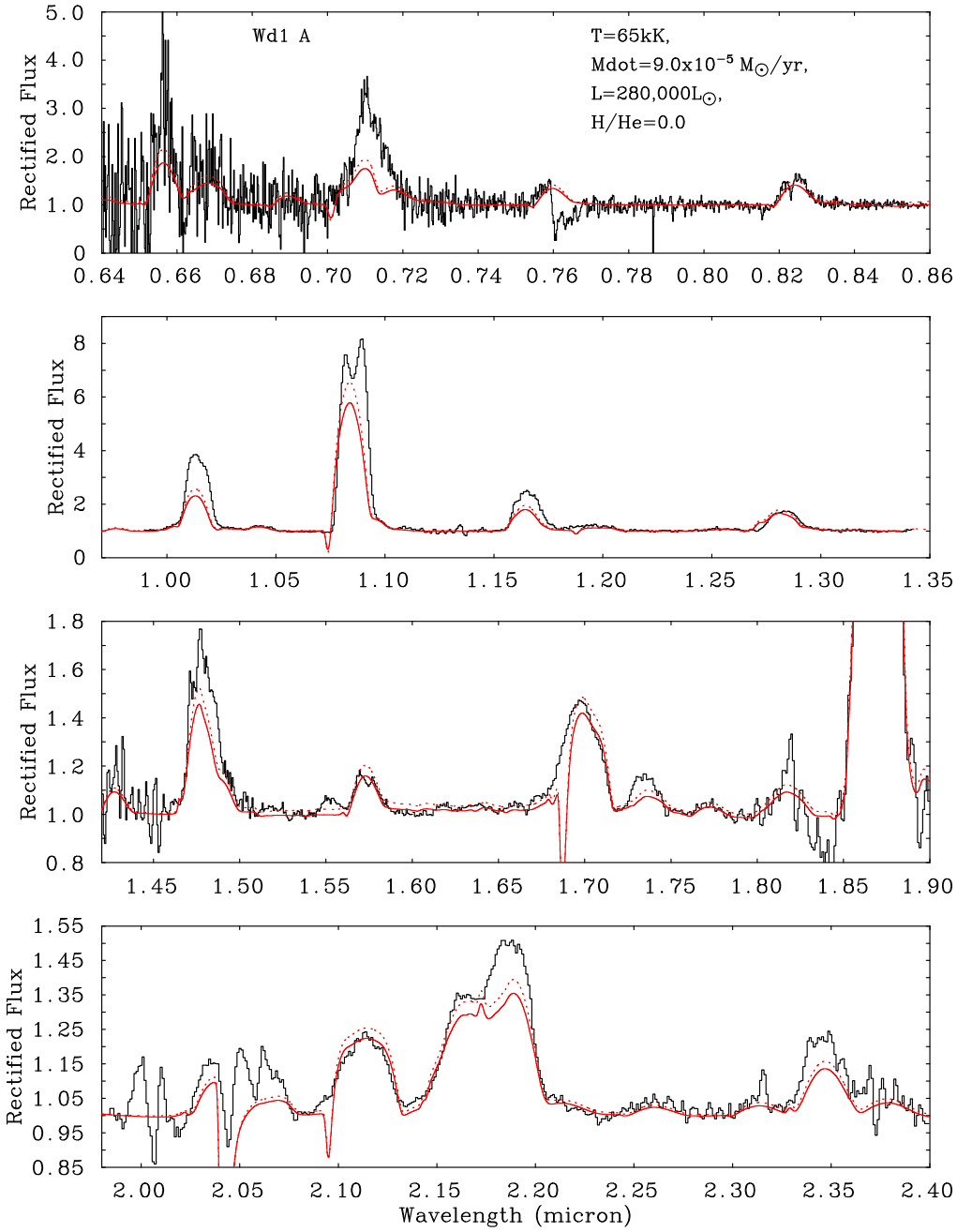

Figure F.1: Fit to the spectrum of Wd1-A, showing observed VLT/FORS2 or NTT/EMMI optical (if available) and NTT/SOFI near-IR spectra (solid black lines), CMFGEN model for the WR component (red dotted line) and combined CMFGEN + scaled Kurucz O7V model (red solid line, see Fig D.1 for SED). See Fig F.3 for identification of key diagnostic lines (Section 5.3.4 for fitting procedure). Parameters of the CMFGEN model are inset.

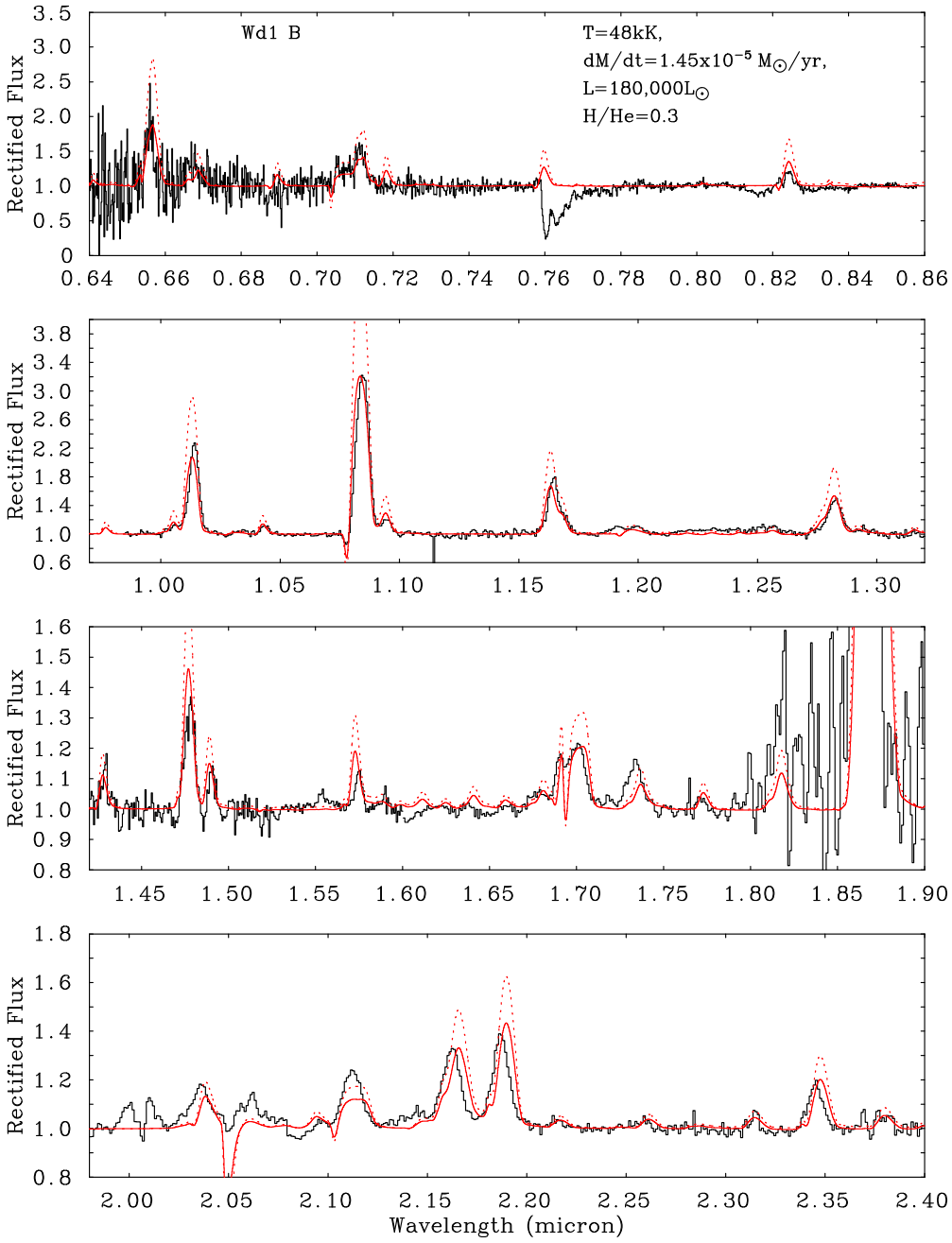

Figure F.2: As Figure F.1 for Wd1-B.

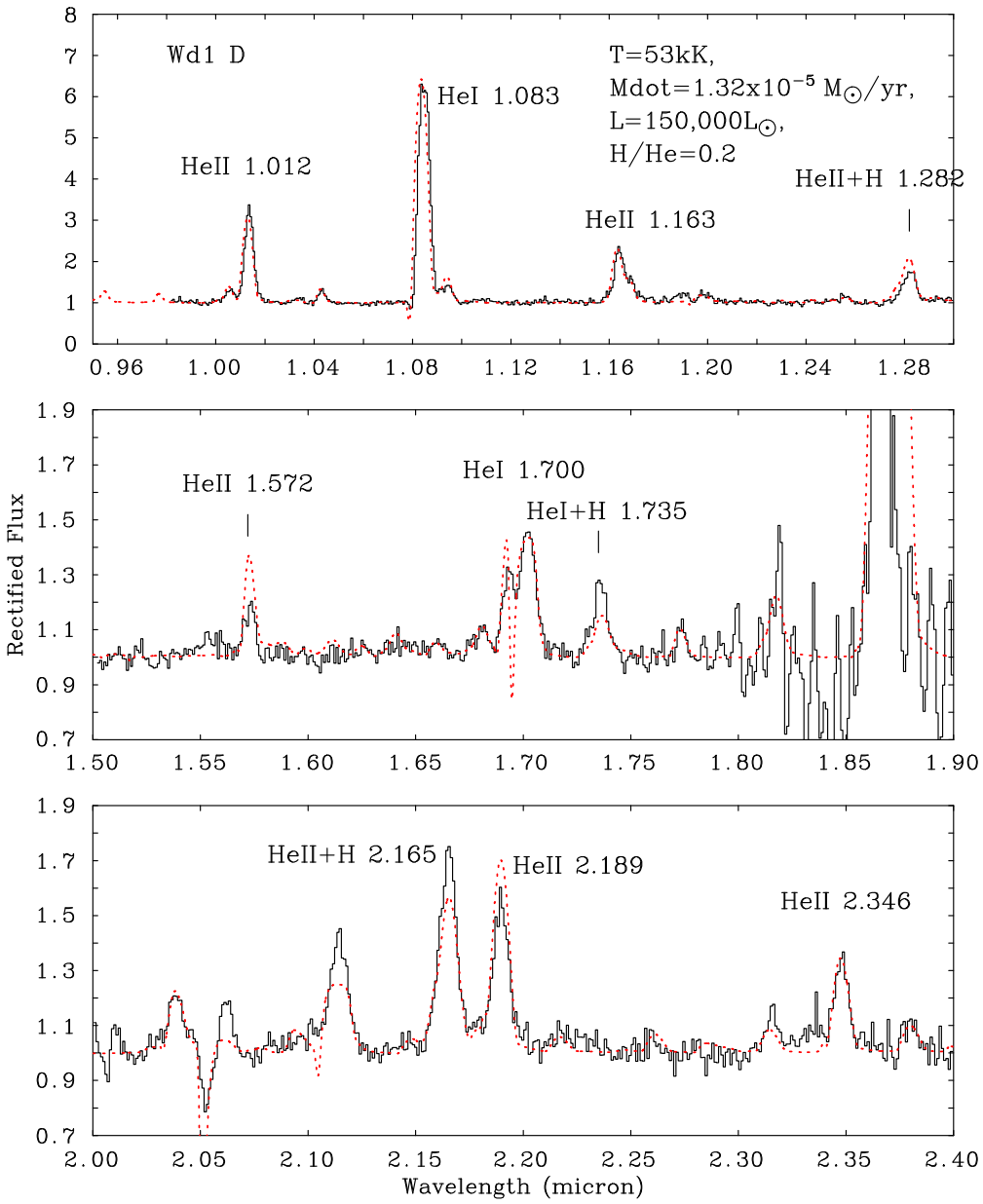

Figure F.3: Fit to the spectrum of Wd1-D, showing observed VLT/FORS2 or NTT/EMMI optical (if available) and NTT/SOFI near-IR spectra (solid black lines), and CMFGEN model for the WR star (red dotted line). Key diagnostic lines are identified (see Section 5.3.2 for fitting procedure). Parameters of the CMFGEN model are inset.

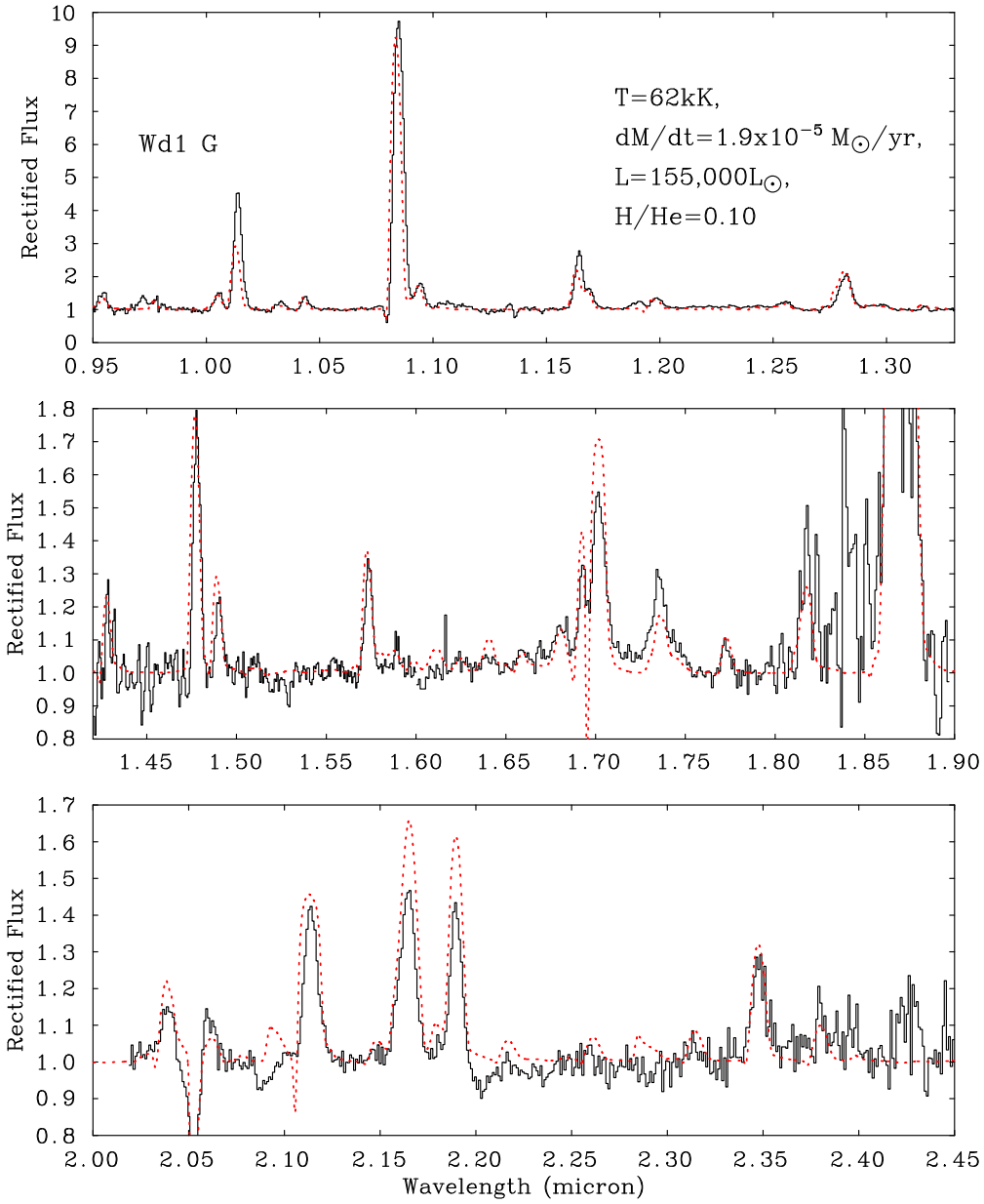

Figure F.4: As Figure F.3 for Wd1-G.

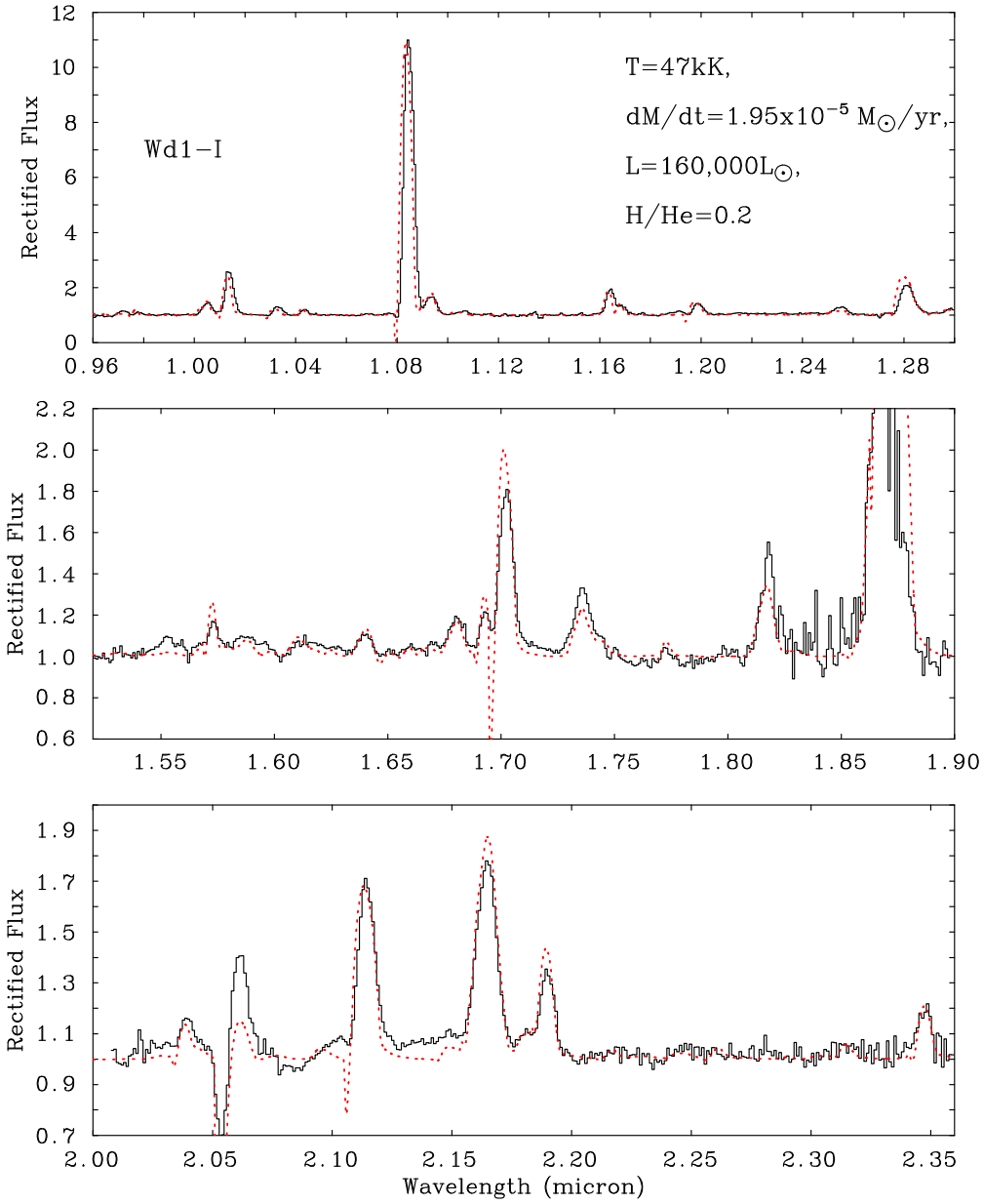

Figure F.5: As Figure F.3 for Wd1-I.

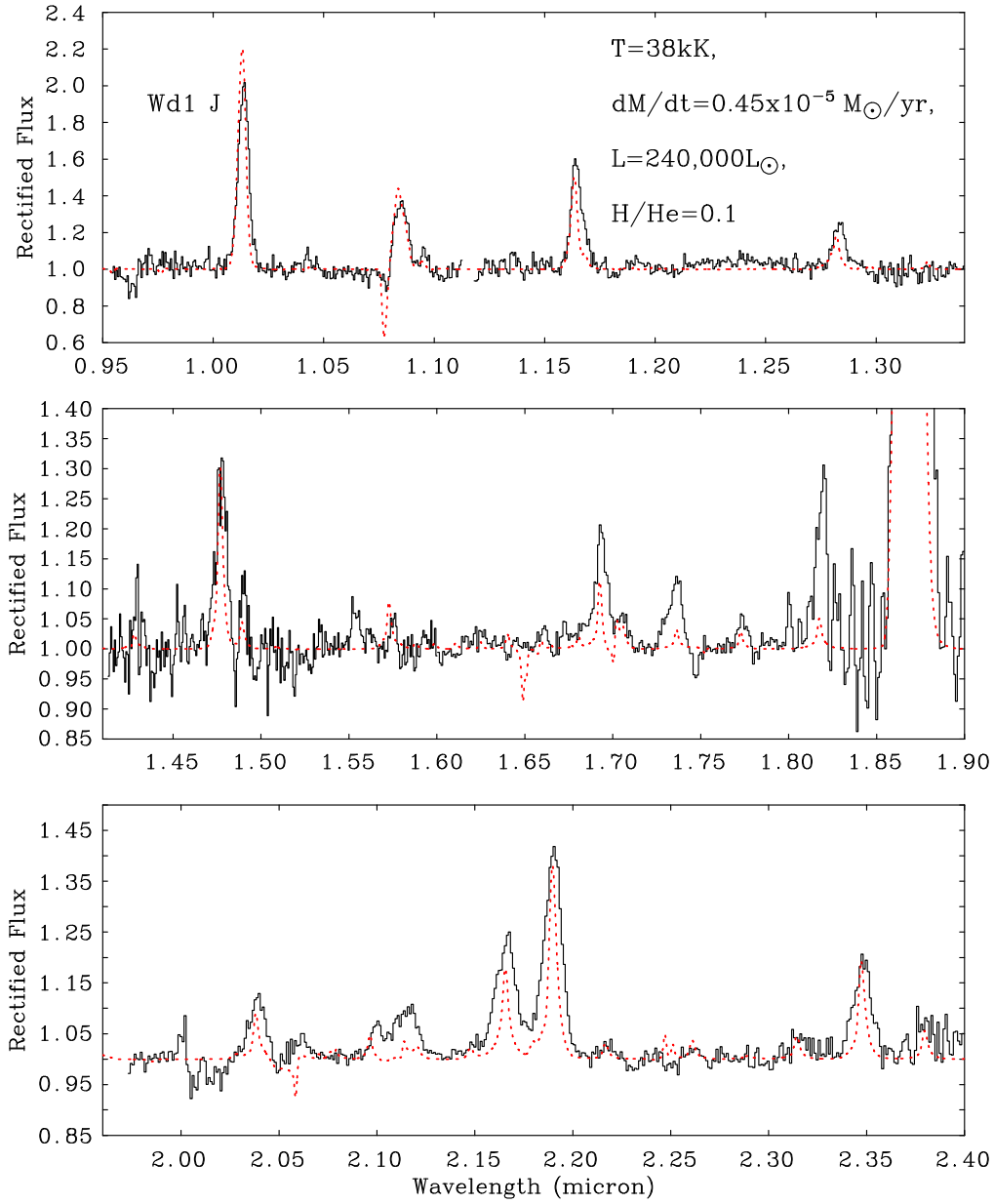

Figure F.6: As Figure F.3 for Wd1-J.

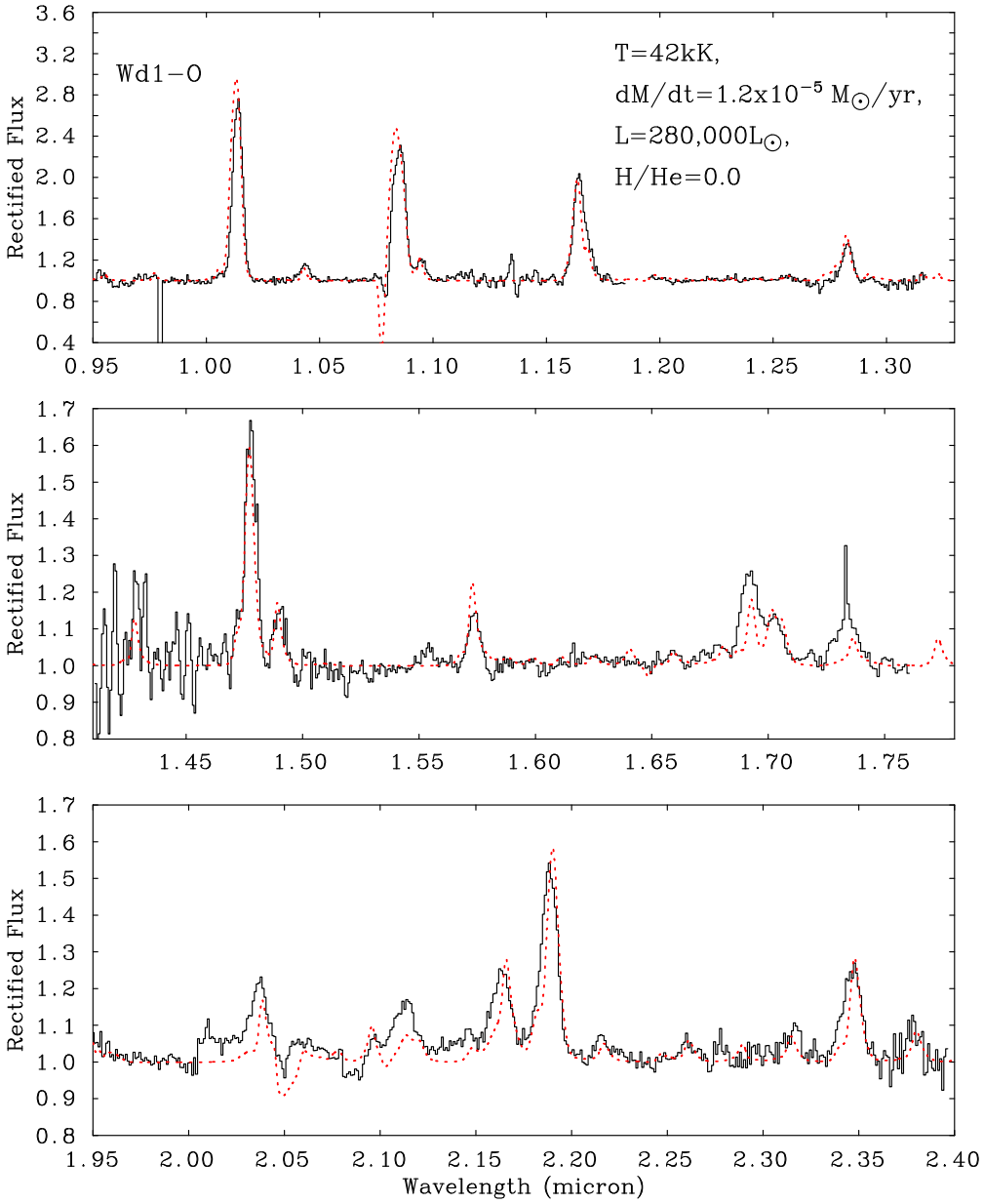

Figure F.7: As Figure F.3 for Wd1-O.

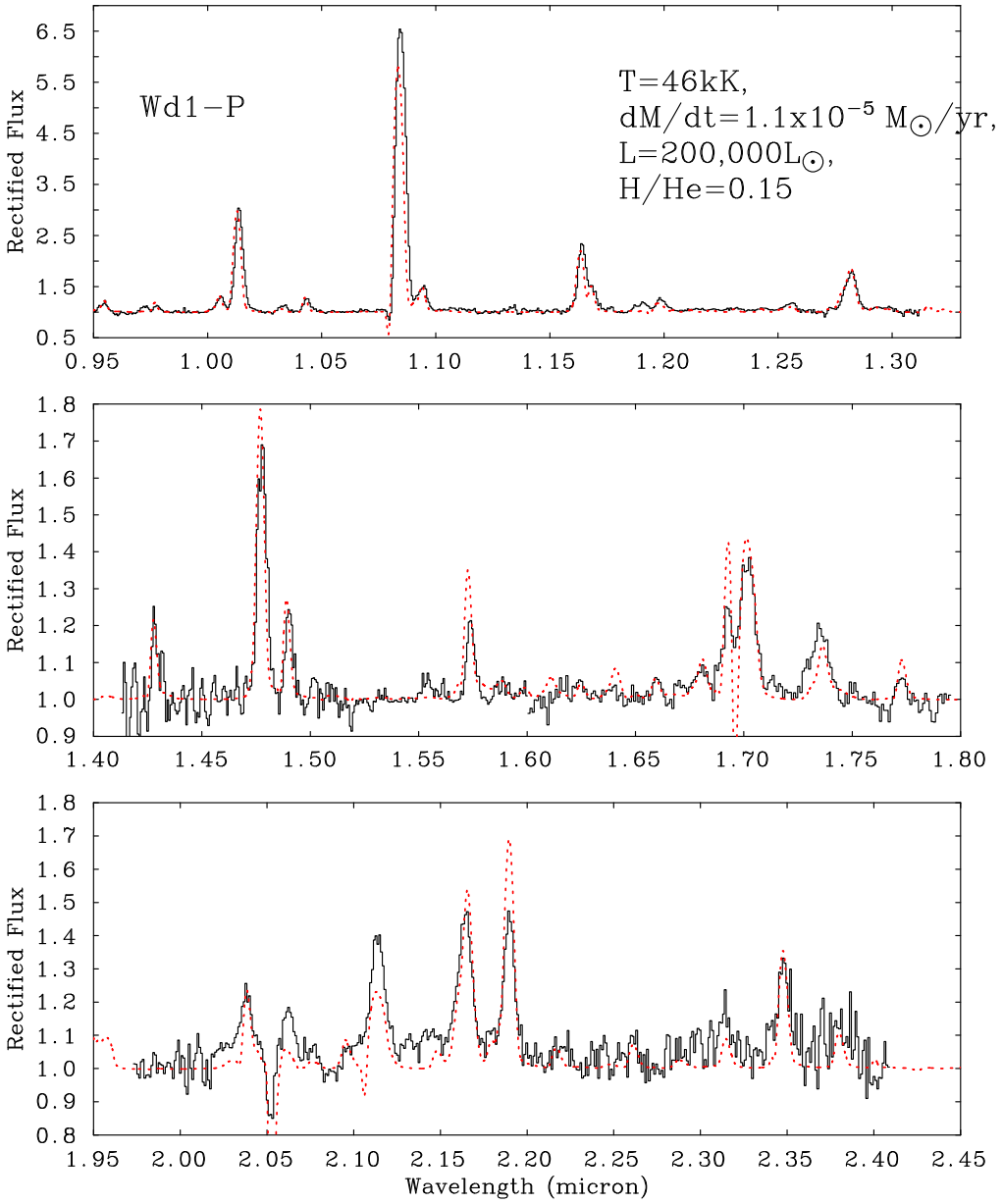

Figure F.8: As Figure F.3 for Wd1-P.

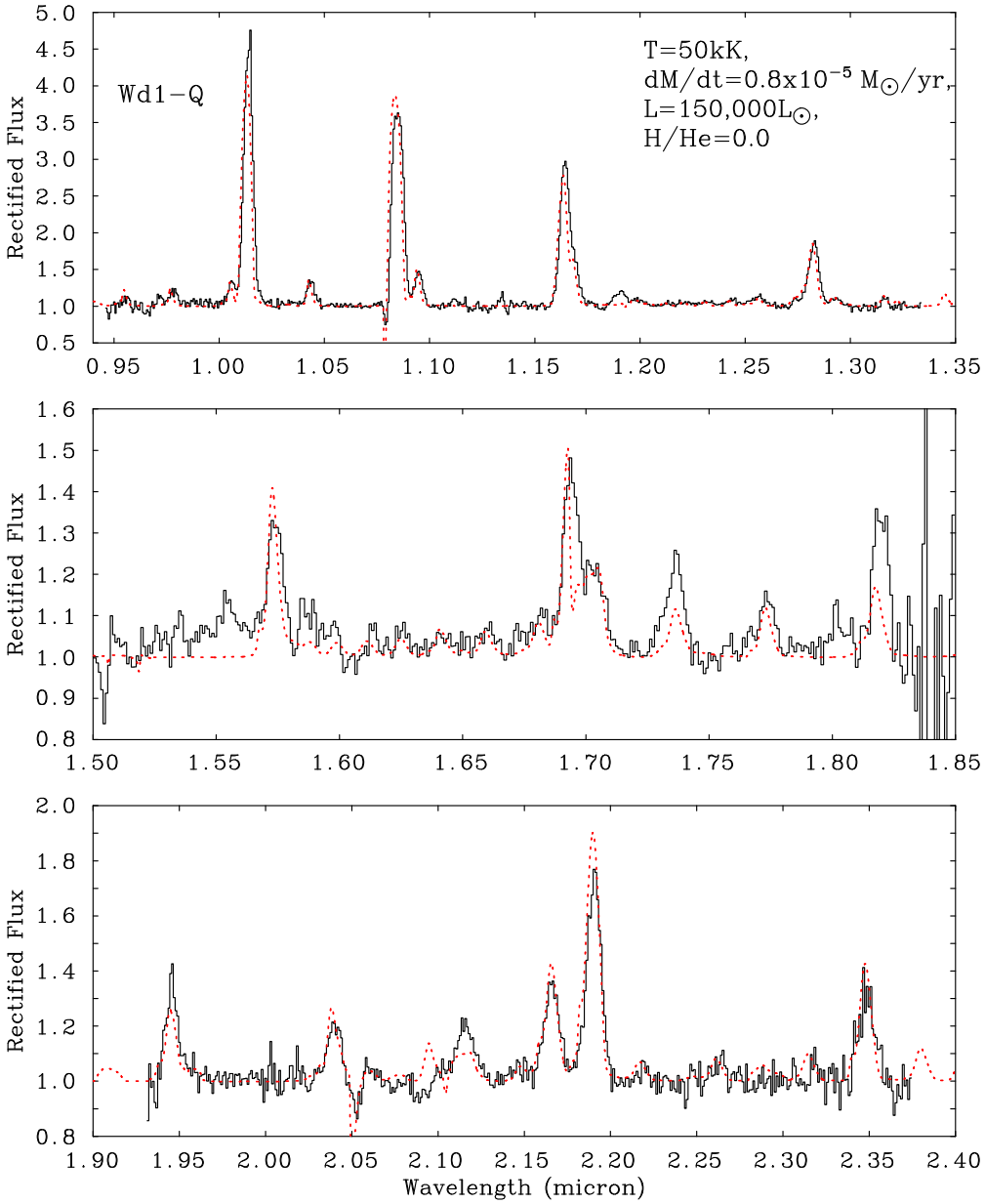

Figure F.9: As Figure F.3 for Wd1-Q.

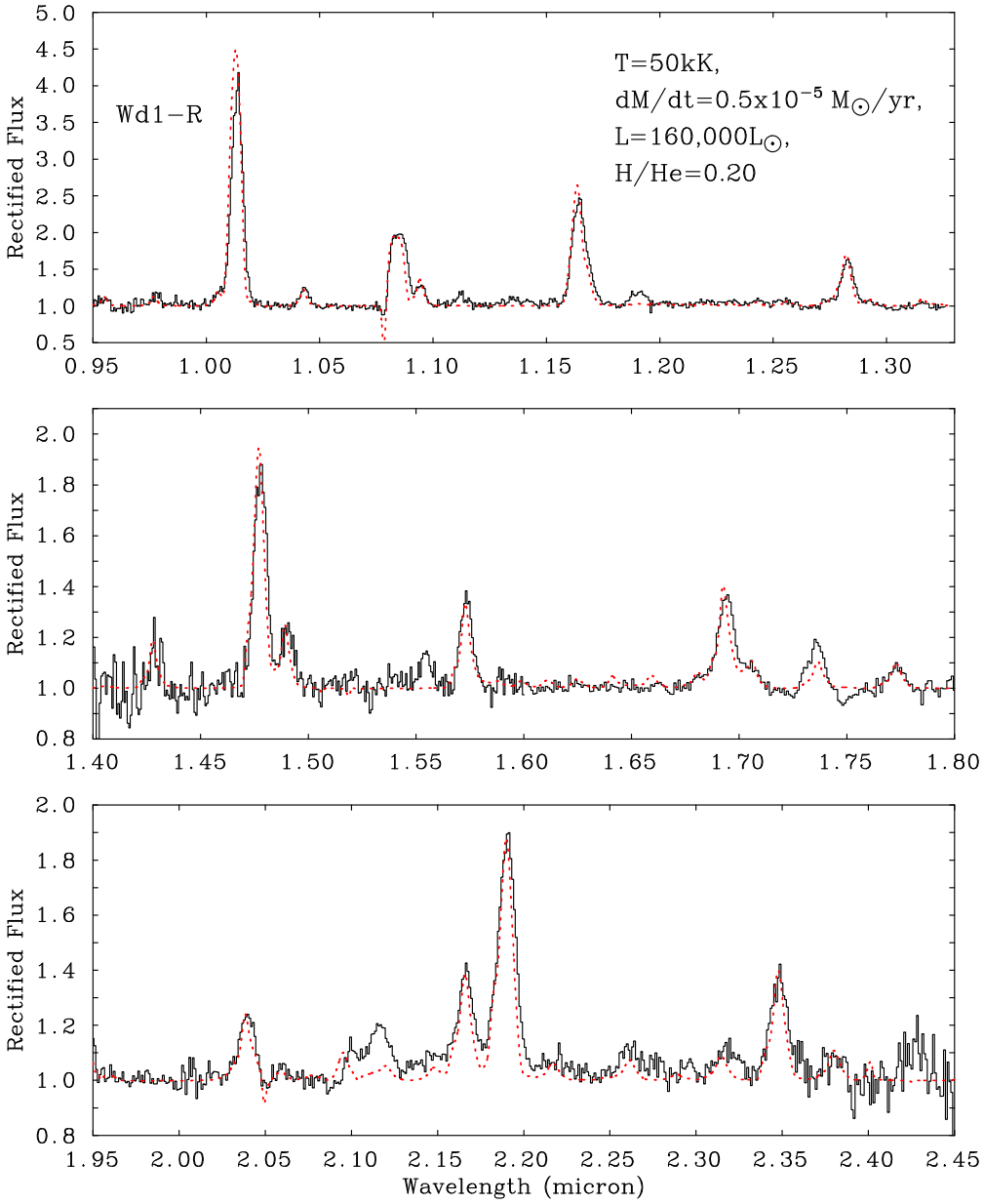

Figure F.10: As Figure F.3 for Wd1-R.

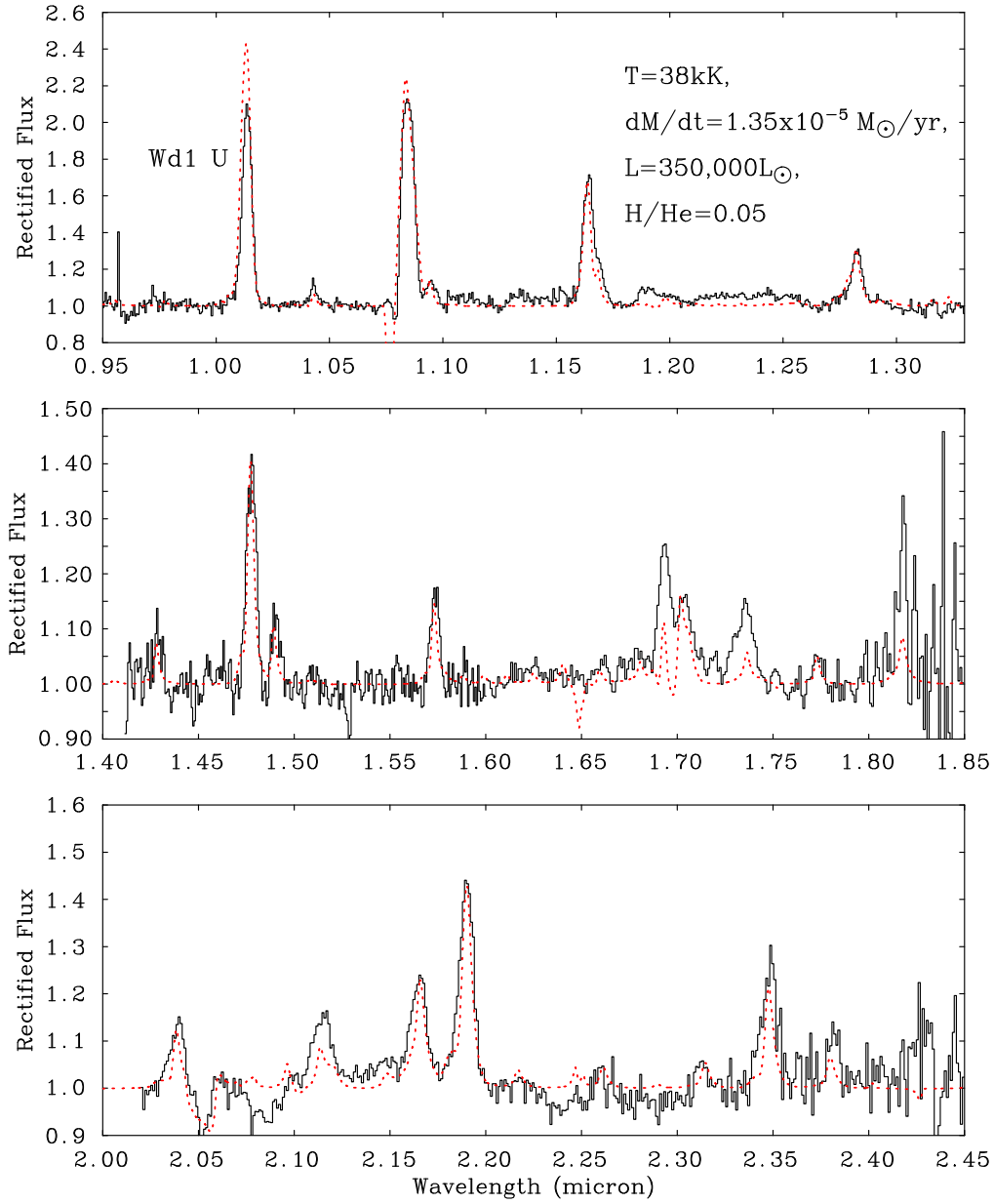

Figure F.11: As Figure F.3 for Wd1-U.

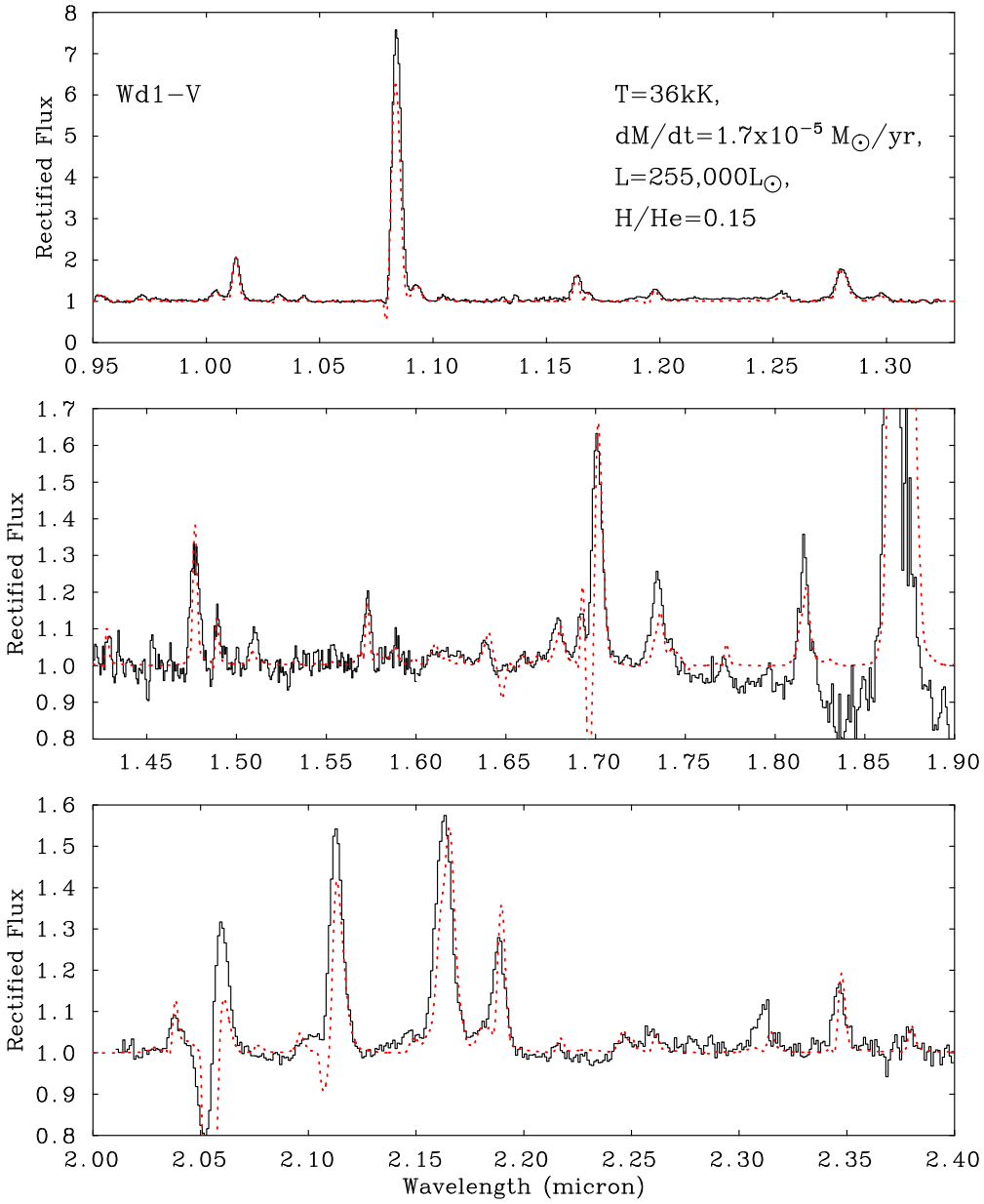

Figure F.12: As Figure F.3 for Wd1-V.

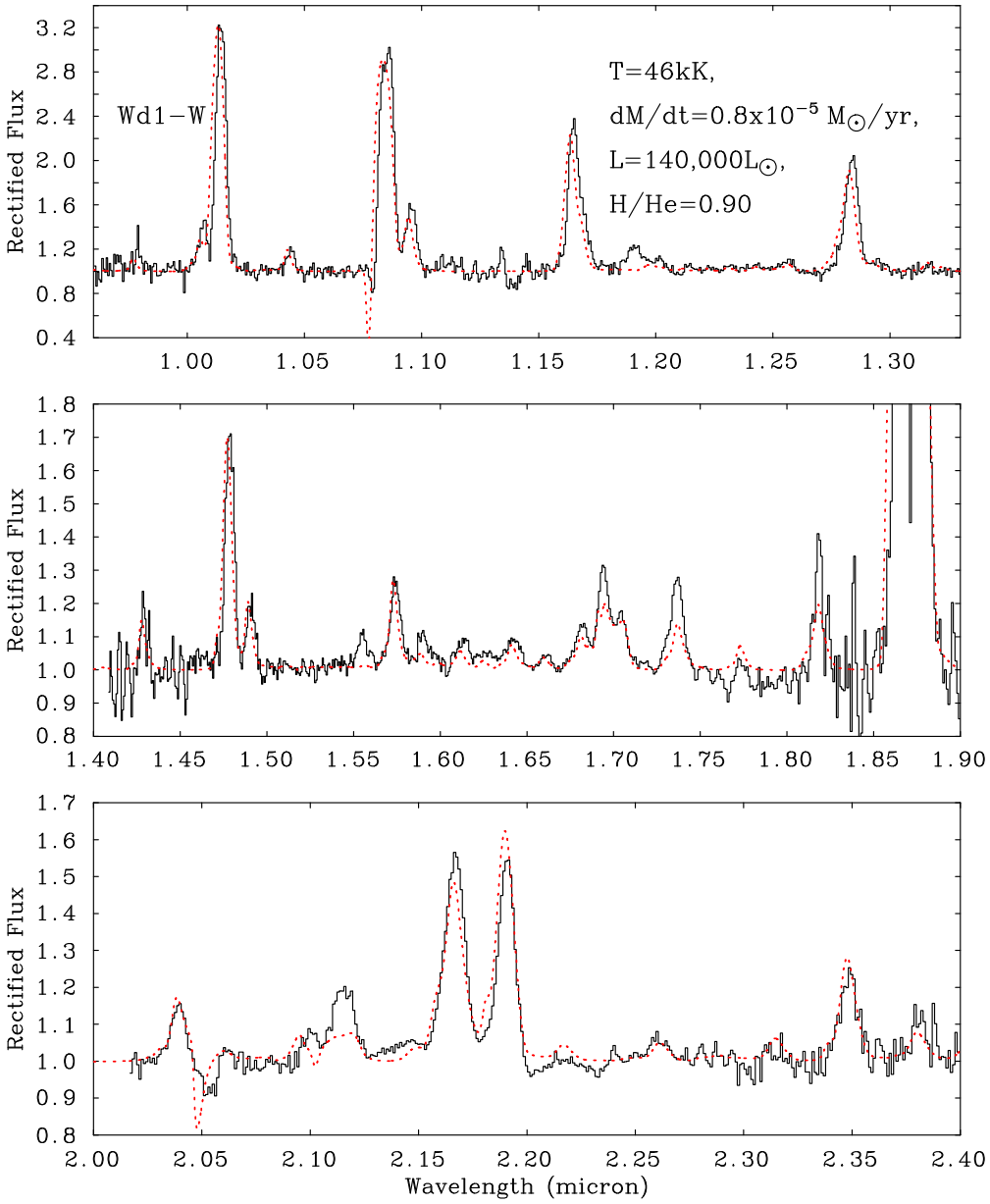

Figure F.13: As Figure F.3 for Wd1-W.

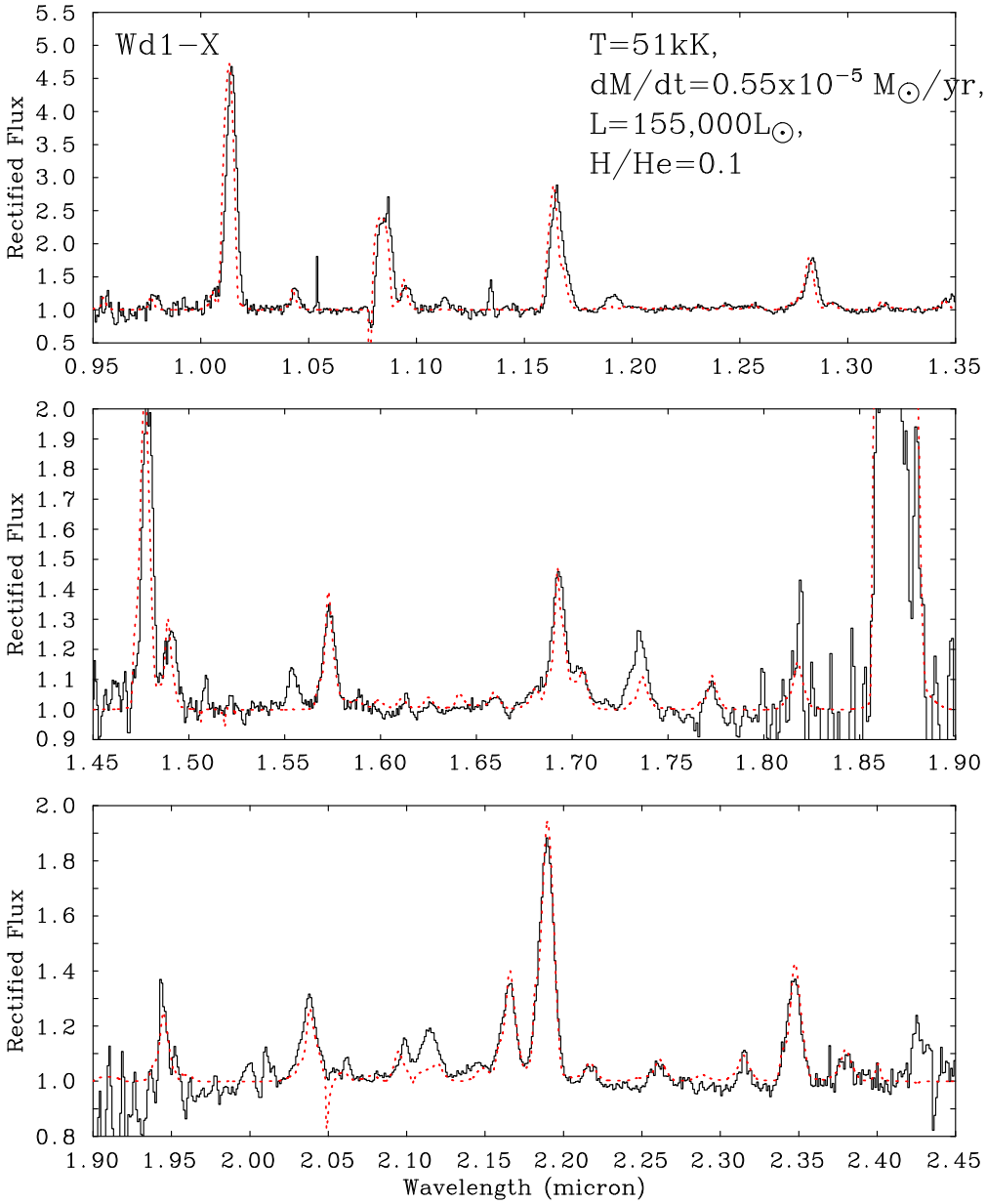

Figure F.14: As Figure F.3 for Wd1-X.

Appendix G

Model fits to spectra of Wolf-Rayet stars in Westerlund 1: WC stars

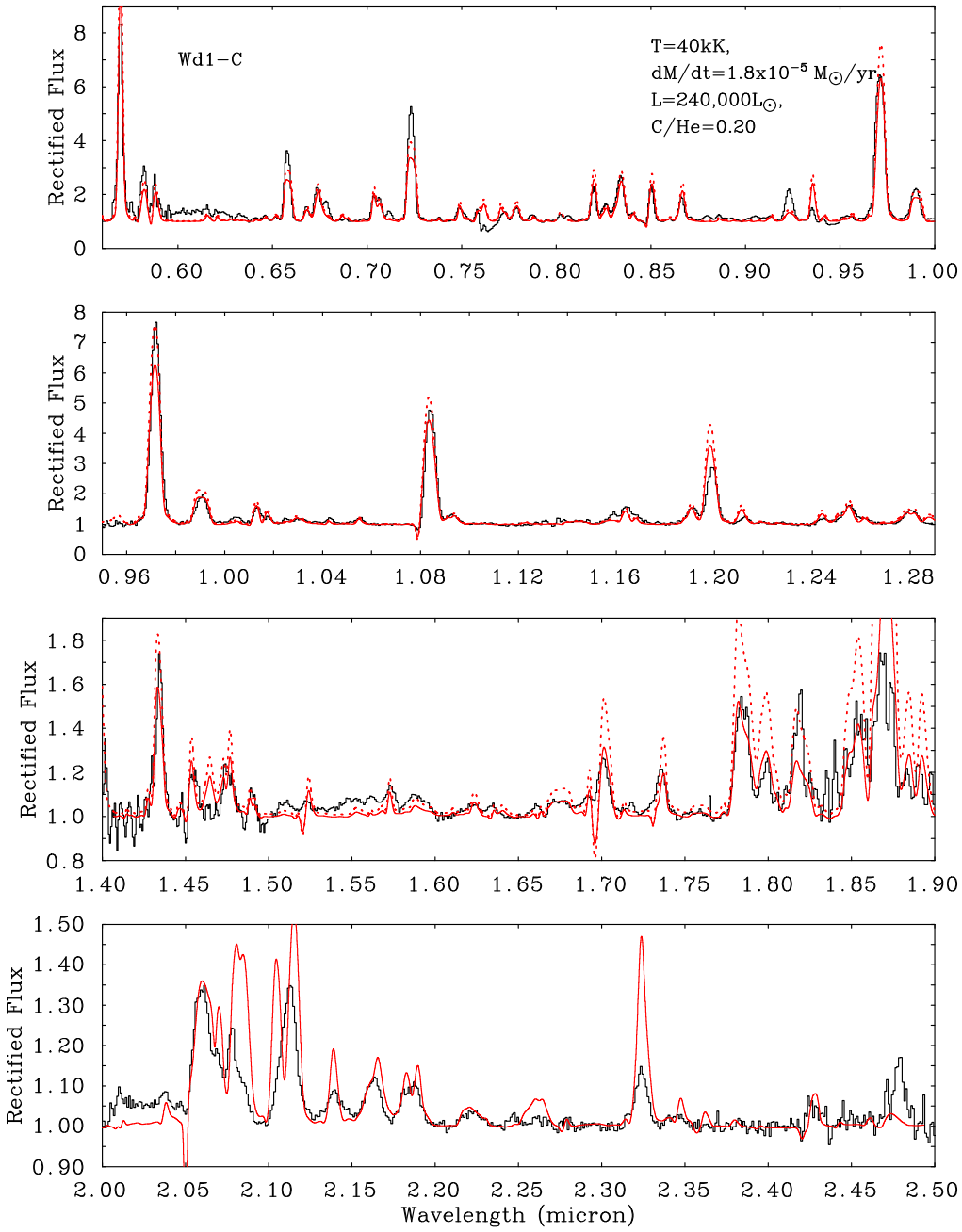

Figure G.1: Fit to the spectrum of Wd1-C, showing observed VLT/FORS2 or NTT/EMMI optical (if available) and NTT/SOFI near-IR spectra (solid black lines), CMFGEN model for the WR component (red dotted line) and combined CMFGEN + scaled Kurucz O7V model + black body (red solid line, see Fig E.1 for SED). See Fig G.8 for identification of key diagnostic lines (Section 5.3.4 for fitting procedure). Parameters of the CMFGEN model are inset. The pure un-diluted CMFGEN model is only shown for moderate amounts of dilution (low dust + O-star contribution), for clarity.

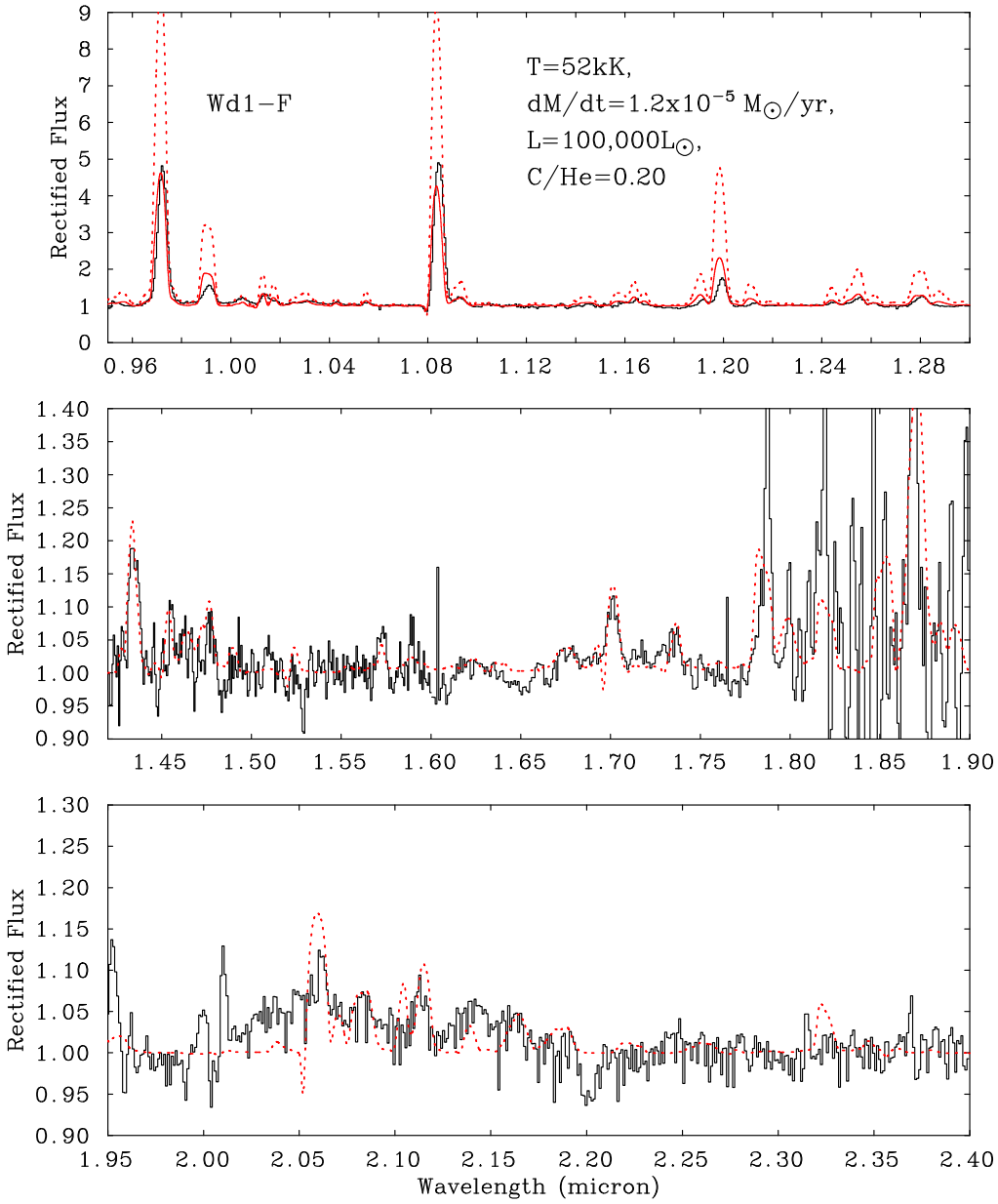

Figure G.2: As Figure G.1 for Wd1-F.

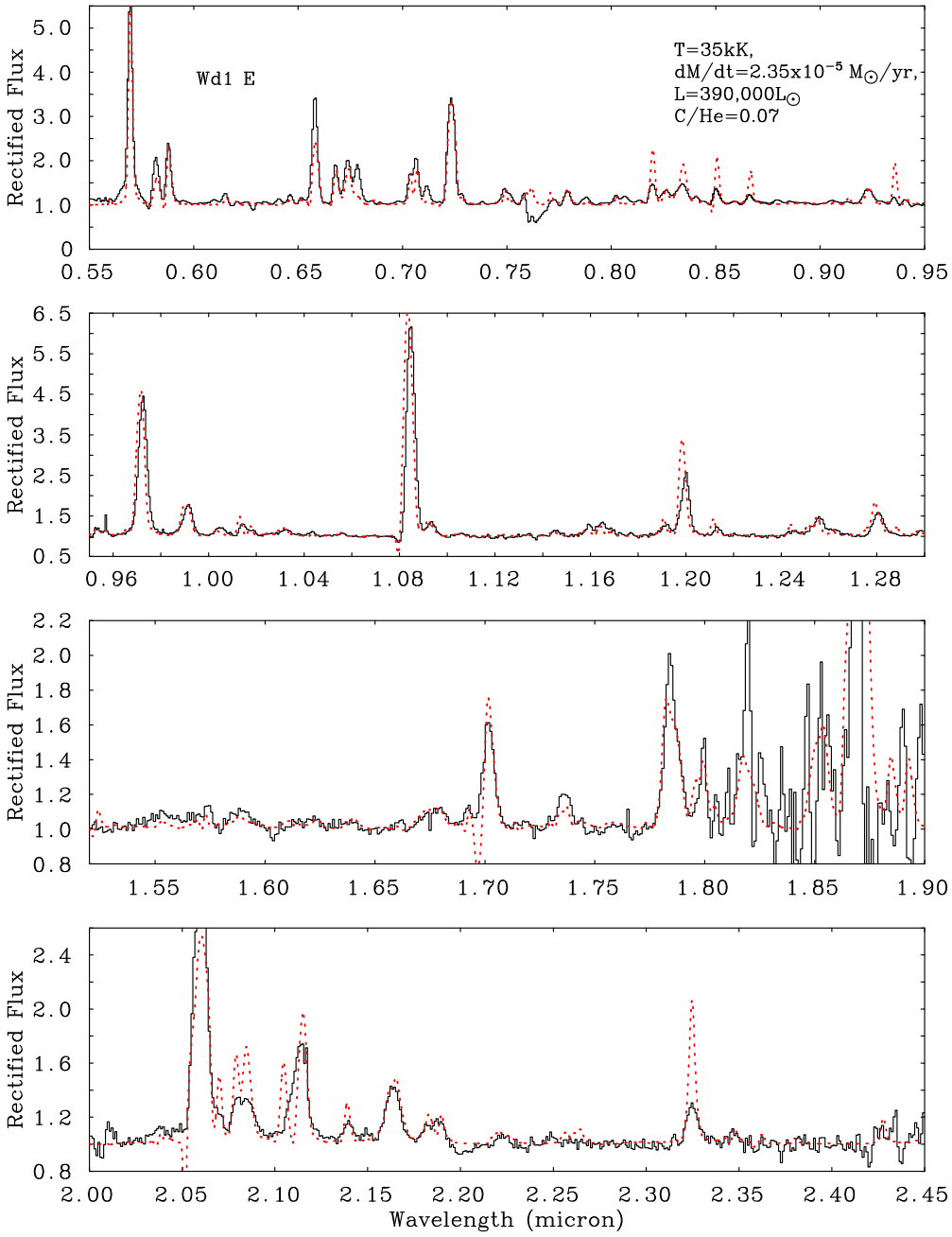

Figure G.3: Fit to the spectrum of Wd1-E, showing observed VLT/FORS2 or NTT/EMMI optical (if available) and NTT/SOFI near-IR spectra (solid black lines), and CMFGEN model for the WR component. See Fig G.8 for identification of key diagnostic lines. Parameters of the CMFGEN model are inset.

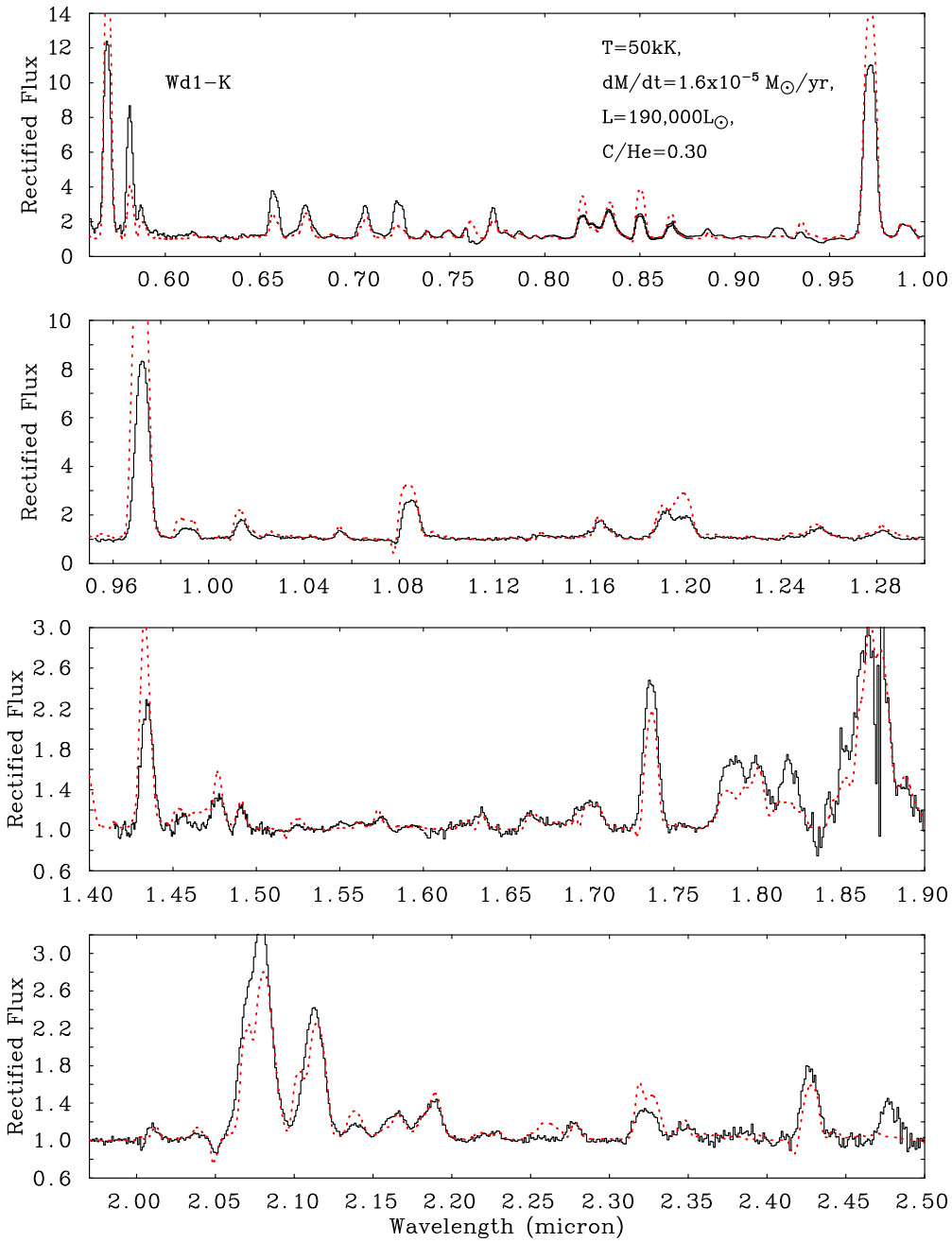

Figure G.4: As Figure G.3 for Wd1-K.

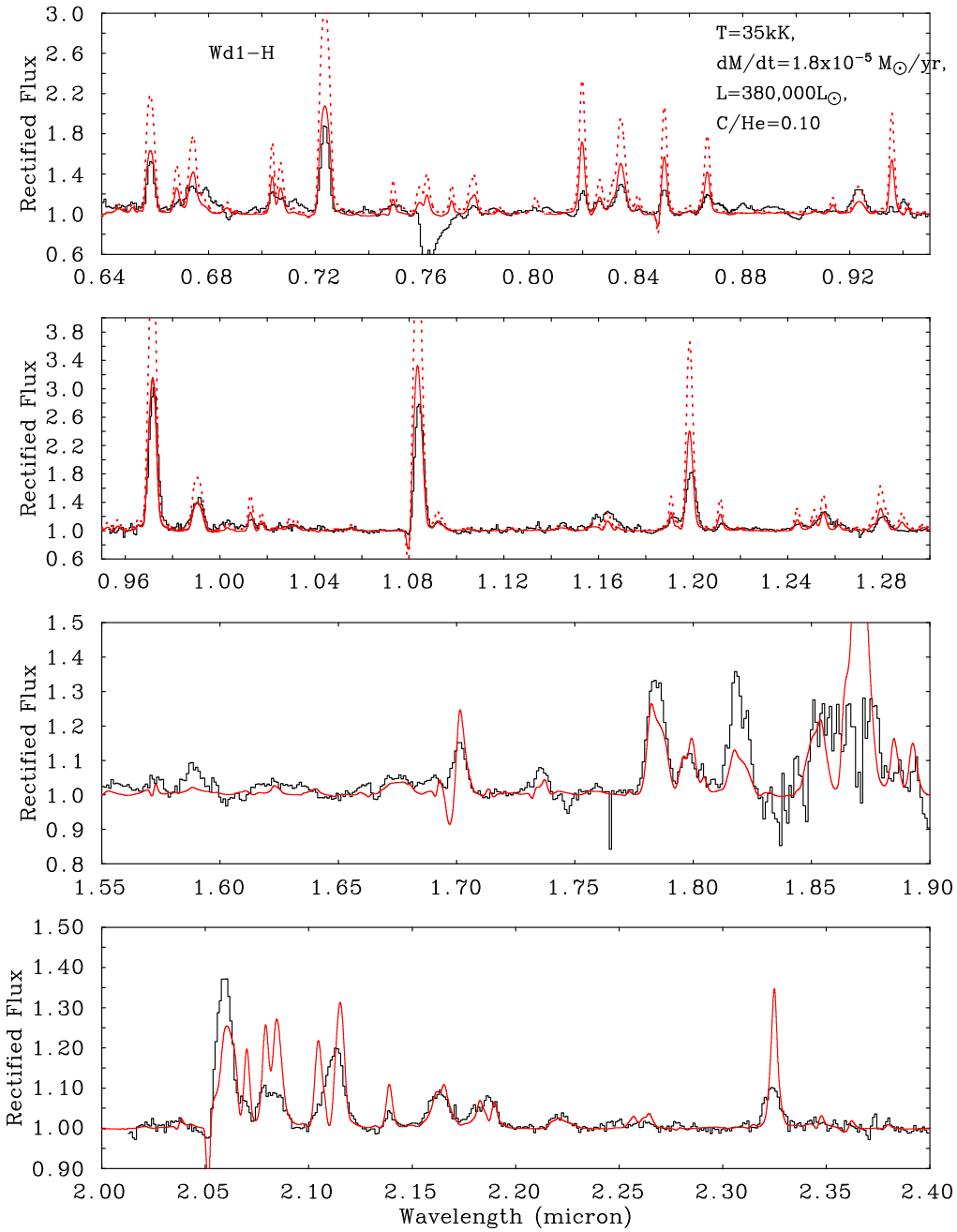

Figure G.5: As Figure G.1 for Wd1-H.

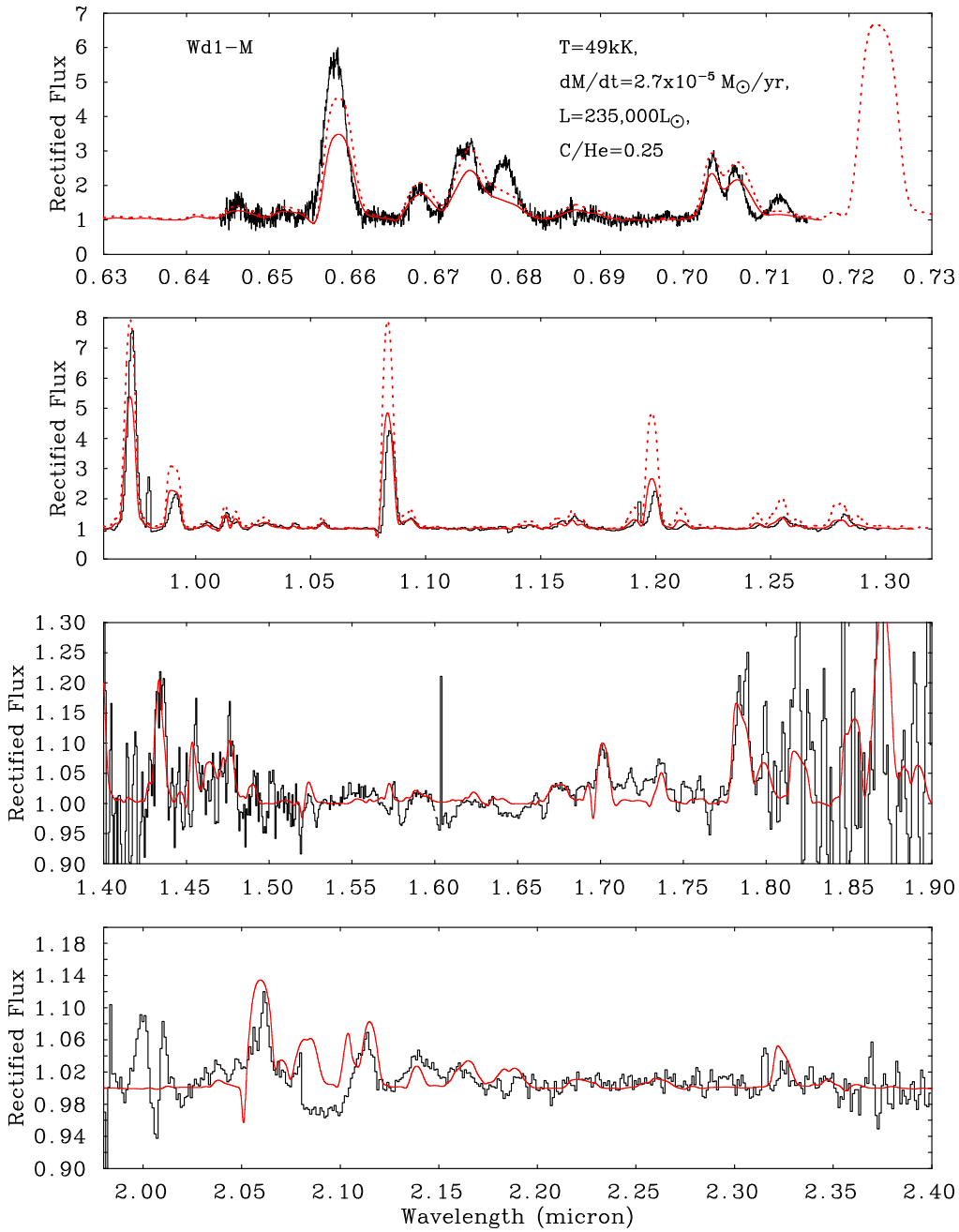

Figure G.6: As Figure G.1 for Wd1-M.

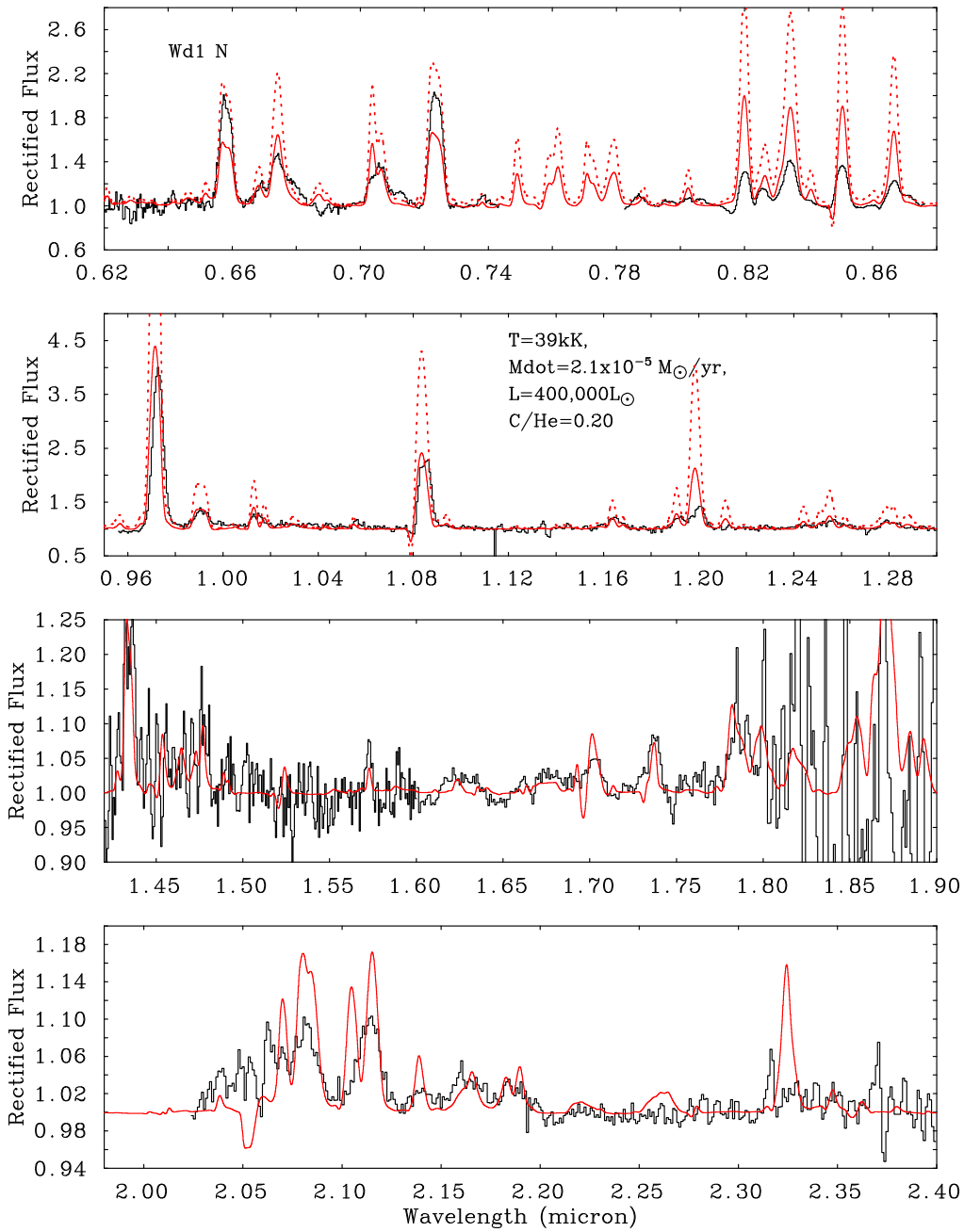

Figure G.7: As Figure G.1 for Wd1-N.

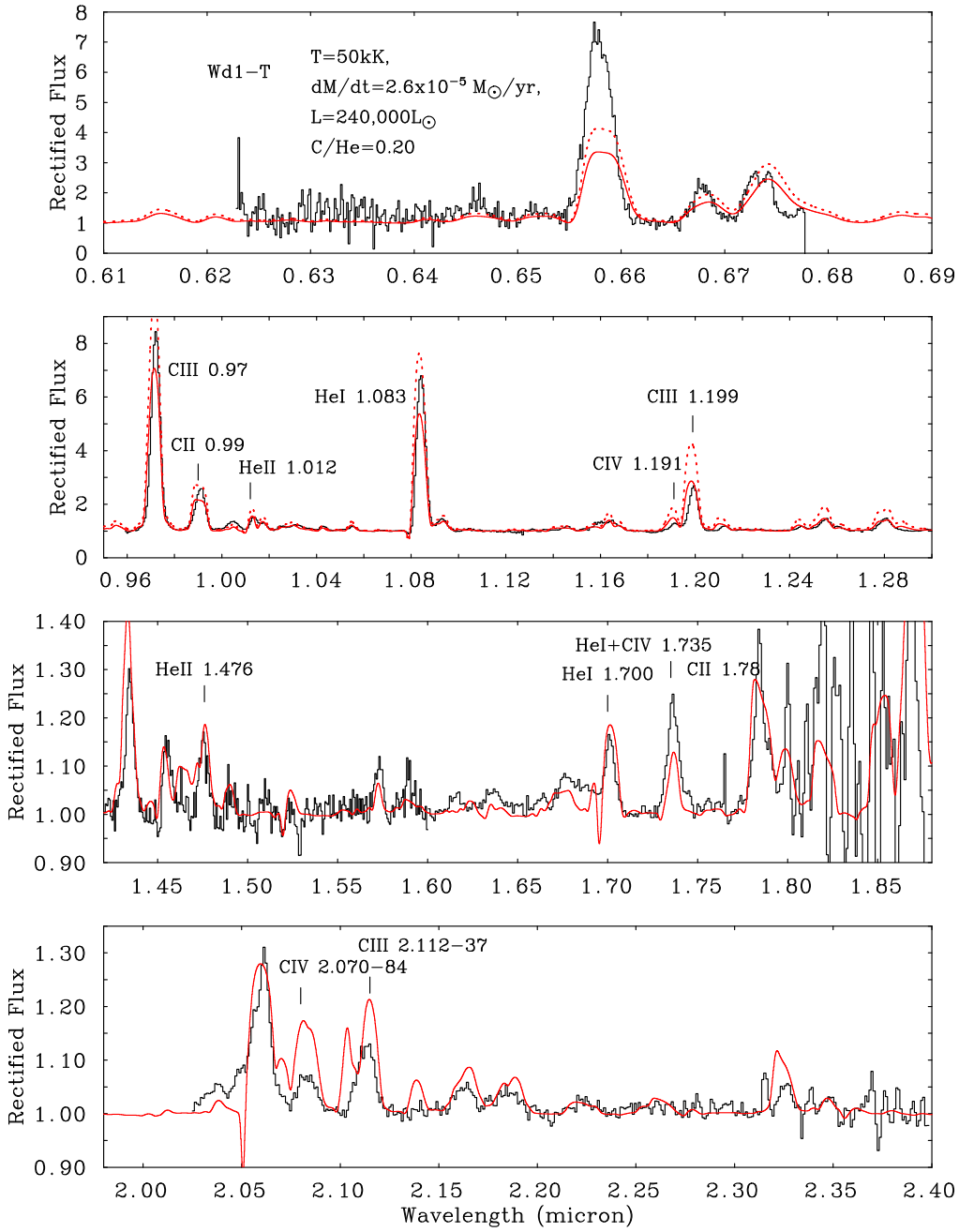

Figure G.8: As Figure G.1 for Wd1-T. Key diagnostic lines are identified (see Section 5.3.3 for fitting procedure).